Detection and characterization of exoplanets orbiting M dwarfs with two newnear-infrared instruments : ExTrA and NIRPS.

Marion Cointepas

To cite this version:

Marion Cointepas. Detection and characterization of exoplanets orbiting M dwarfs with two newnear-infrared instruments : ExTrA and NIRPS.. Astrophysics [astro-ph]. Université Grenoble Alpes [2020-..]; Université de Genève, 2023. English. NNT : 2023GRALY046 . tel-04342122

UNIVERSITÉ
DE GENÈVE

UGA
Université
Grenoble Alpes

THÈSE

Pour obtenir le grade de

DOCTEUR DE L'UNIVERSITÉ GRENOBLE ALPES
et de l'UNIVERSITÉ DE GENÈVE

École doctorale : PHYS - Physique
Spécialité : Astrophysique et Milieux Dilués
Unité de recherche : Institut de Planétologie et d'Astrophysique de Grenoble

Détection et caractérisation d'exoplanètes en orbite autour des naines M avec deux nouveaux instruments proche infrarouge : ExTrA et NIRPS.

Detection and characterization of exoplanets orbiting M dwarfs with two new near-infrared instruments: ExTrA and NIRPS.

Présentée par :

Marion COINTEPAS

Direction de thèse :

Thierry FORVEILLE Astronome, UGA	Directeur de thèse
François BOUCHY Professeur, Observatoire de Genève	Co-Directeur de thèse
Xavier BONFILS Chargé de recherche, CNRS	Co-Encadrant de thèse

Thèse soutenue publiquement le **27 juin 2023**, devant le jury composé de :

Maria Rosa ZAPATERO OSORIO Professeure, Centro de Astrobiologia, CSIC-INTA	Rapporteure
Daniel BAYLISS Professeur Assistant, Department of Physics at the University of Warwick	Rapporteur
Emeline BOLMONT Professeure Assistante, Observatoire de Genève	Examinatrice
Jean-Charles AUGEREAU Astronome, Université Grenoble-Alpes	Examinateur, Président du jury
Thierry FORVEILLE Astronome, Université Grenoble-Alpes	Directeur de thèse
François BOUCHY Professeur, Observatoire de Genève	Co-Directeur de thèse

ABSTRACT

Out of the 5322 exoplanets discovered so far, only 665 have been well characterized by measuring precisely both their radius and mass. The combination of transit photometry and high-precision velocity measurements allows to constrain the mean bulk density of the exoplanets and obtain a first-order estimate of their composition and inner structure. Cool, low mass stars are important targets to characterize exoplanets as M dwarfs represent most of the stellar population in our solar neighborhood, and are known to frequently host multiple small exoplanets. Due to the intrinsic faintness of M dwarfs at visible wavelengths, the near-infrared spectral range is preferred to study these cool stars as they emit most of their light in this region of the spectrum. ExTrA, a new near-infrared photometer and NIRPS, a new near-infrared spectrograph, both located at La Silla Observatory in Chile represent a chance to improve our understanding of planetary systems surrounding M dwarfs by measuring with precision both the planetary radius and the planetary mass.

During my PhD, I collected all potential exoplanets orbiting M dwarfs observed by the TESS mission, an all-sky survey for transiting exoplanets orbiting bright and nearby stars. From these targets, I scheduled the follow-up observations using the ExTrA facility. Started from the raw data, I generated usable light curves. I then analyzed the light curves to identify any planetary transits and modeled them to obtain the planetary parameters. While M dwarfs are good candidates for exoplanet detection, their stellar companions can cause false positives. This is why additional observations with ground-based instruments are required to confirm the companion's planetary nature, and the combination of observations with TESS in the visible and with ExTrA in the near-infrared turned out to be very useful to validate the planetary candidate and obtain a precise radius measurement. From there, more observations are needed to fully characterize exoplanets. For the different systems I published during my thesis, I gathered and modeled observations from the HARPS and ESPRESSO spectrographs.

The NIRPS spectrograph will soon also be able to provide the mass of the exoplanets detected in transits, especially around M dwarfs. I proposed two programs as part of the NIRPS Guaranteed Time Observations. The first program will use radial velocity measurements to complement our ExTrA photometry in order to populate the mass-radius diagram for mid-to-late M dwarfs. The second program attempts to discover additional planets in known systems by calculating the probability of these undetected planets' existence and the cost of detected them with current instruments like NIRPS.

The synergies between both near-infrared instruments will allow us to characterize exoplanets orbiting M dwarfs and offer a unique opportunity to study planetary formation and evolution processes around these low-mass, cool, long-lived stars.

RÉSUMÉ

Sur les 5322 exoplanètes découvertes à ce jour, seulement 665 ont été bien caractérisées en mesurant précisément à la fois leur rayon et leur masse. La combinaison de la photométrie de transit et des mesures de vitesses radiales de haute précision permet de contraindre la densité moyenne des exoplanètes et d'obtenir une première estimation de leur composition et structure interne. Les étoiles de faible masse sont des cibles importantes pour caractériser les exoplanètes car les naines M représentent la majeure partie de la population stellaire de notre voisinage et sont connues pour héberger de multiples petites exoplanètes. En raison de leur faible luminosité intrinsèque aux longueurs d'onde visibles, le proche infrarouge est privilégié pour étudier ces étoiles froides car elles émettent la plupart de leur lumière dans cette région du spectre. ExTrA et NIRPS, deux nouveaux instruments proche infrarouge, représentent une chance d'améliorer notre compréhension des systèmes planétaires entourant les naines M.

Au cours de mon doctorat, j'ai rassemblé toutes les candidats planétaires en orbite autour des naines M observées par la mission TESS, une étude globale du ciel à la recherche d'exoplanètes en transit autour d'étoiles brillantes et proches. À partir de cette liste, j'ai planifié les observations de suivi en utilisant ExTrA. À partir des données brutes, j'ai généré des courbes de lumière utilisables. J'ai ensuite analysé les courbes de lumière pour identifier les transits planétaires et je les ai modélisés pour obtenir les paramètres planétaires. Des observations supplémentaires avec des instruments au sol sont nécessaires pour confirmer la nature planétaire du compagnon car des compagnons stellaires peuvent être à l'origine de faux positifs, et la combinaison d'observations avec TESS dans le visible et avec ExTrA dans le proche infrarouge s'est avérée très utile pour valider le candidat planétaire et obtenir une mesure précise de son rayon. A partir de là, d'autres observations sont nécessaires pour caractériser complètement les exoplanètes. Pour les différents systèmes que j'ai publiés pendant ma thèse, j'ai rassemblé et modélisé des observations des spectrographes HARPS et ESPRESSO.

Le spectrographe NIRPS sera bientôt également capable de fournir la masse des exoplanètes détectées en transits, en particulier autour des naines M. J'ai proposé deux programmes dans le cadre du temps garanti d'observations (GTO) de NIRPS. Le premier utilisera des mesures de vitesses radiale pour compléter notre photométrie ExTrA afin de peupler le diagramme masse-rayon pour les naines M moyennes à tardives. Le second vise à détecter des planètes supplémentaires dans des systèmes connus en calculant la probabilité d'existence de ces planètes non détectées et le coût de leur détection avec les instruments actuels comme NIRPS.

Les synergies entre ces deux instruments dans le proche infrarouge nous permettront de caractériser les exoplanètes en orbite autour des naines M et offriront une opportunité unique d'étudier la formation et l'évolution des planètes autour de ces étoiles de faible masse, froides et à longue durée de vie.

RESUMEN

De los 5322 exoplanetas descubiertos hasta ahora, solo 665 han sido caracterizados midiendo con precisión tanto su radio como su masa. La combinación de fotometría de tránsito y mediciones de velocidad radial de alta precisión nos permite medir la densidad media de los exoplanetas y obtener una estimación a primer orden de su composición y estructura interna. Las estrellas frías de baja masa son importantes para caracterizar exoplanetas, ya que las enanas M representan la mayor parte de la población estelar en nuestro vecindario solar y se sabe que albergan con frecuencia múltiples exoplanetas pequeños. Debido a que las enanas M son intrínsecamente menos luminosas en longitudes de onda visibles, se prefiere el rango espectral del infrarrojo cercano para estudiar estas estrellas frías, porque emiten la mayor parte de su luz en esta región del espectro. Dos instrumentos nuevos que operan en el infrarrojo, ExTrA y NIRPS en el Observatorio La Silla, Chile, nos permiten mejorar el conocimiento de sistemas planetarios alrededor de enanas M, midiendo con precisión su radio y masa.

Durante mi doctorado, recopilé todos los exoplanetas orbitando enanas M observadas por la misión TESS (un telescopio espacial que observa todo el cielo en busca de exoplanetas en tránsito que orbitan estrellas brillantes y cercanas). Con estas estrellas, programé las observaciones de seguimiento utilizando la instalación ExTrA. Analicé los datos para identificar los tránsitos planetarios y los modelé para obtener los parámetros planetarios. Si bien las enanas M son buenas candidatas para la detección de exoplanetas, sus compañeros estelares pueden causar falsos positivos. Por eso se requieren observaciones adicionales con instrumentos terrestres para confirmar que las señales que vemos se deben a un planeta. La combinación de observaciones con TESS en el visible y con ExTrA en el infrarrojo cercano resultó ser muy útil para validar el candidato planetario y obtener una medición precisa del radio. A partir de ahí, se necesitan más observaciones para caracterizar completamente a los exoplanetas. Para los diferentes sistemas planetarios que publiqué durante mi tesis, tomé y modelé observaciones de los espectrógrafos HARPS y ESPRESSO.

El espectrógrafo NIRPS pronto también podrá proveer la masa de los exoplanetas detectados en tránsitos, especialmente en torno a enanas M. Propuse dos programas como parte de las Observaciones de Tiempo Garantizado de NIRPS. El primer programa utilizará mediciones de velocidad radial para complementar la fotometría de ExTrA con el fin de poblar el diagrama masa-radio para enanas M. El segundo programa intenta descubrir nuevos planetas en sistemas conocidos, y calcular el costo de detectarlos con instrumentos actuales como NIRPS.

Las sinergias entre ambos instrumentos en el infrarrojo cercano nos permitirán caracterizar exoplanetas que orbitan enanas M y ofrecerán una oportunidad única para estudiar los procesos de formación y evolución planetaria en torno a estas estrellas de baja masa, frías y de larga vida.

ACKNOWLEDGMENTS

I started my PhD just before the Covid-19 pandemic, a period that presented numerous challenges and uncertainties. Nonetheless, I made it to the finish line! I would like to express my deepest gratitude to the exceptional individuals who supported and guided me throughout this journey, enabling me to successfully obtain my doctorate.

First and foremost I am extremely grateful to my supervisors, Xavier Bonfils and François Bouchy, as well as Jose Almenara, for their invaluable advice, continuous support, and patience during my PhD. To my jury members, thank you for taking the time to read this thesis and for your constructive feedback.

In addition to my supervisors, I am thankful to the amazing people I met at IPAG and Geneva Observatory, whose support has been a constant source of motivation. Being able to discuss and collaborate with such incredible researchers and PhD students helped me so much during the most challenging times. I am fortunate to say that for some of them we became more than just colleagues, but good friends.

Marine, depuis toutes ces années, tu as toujours été là pour moi, merci d'être ma meilleure moitié.

Enfin, j'aimerais remercier ma famille qui m'a toujours soutenue. Maman, Papa, Romain, vous avez fait tellement de choses pour moi au fil du temps, aucun mot ne suffira pour décrire à quel point je vous en suis reconnaissante.

CONTENTS

LIST OF FIGURES

LIST OF TABLES

I

INTRODUCTION

"When we woke up the world was figured out
Beyond the beauty we've dreamt about
This brilliant light is brighter than we've known
Without our darkness to prove it so"
You Are Enough by Sleeping At Last

I.1 FROM SOLAR SYSTEM PLANETS TO EXOPLANETS

Humans have always been fascinated by what lies beyond Earth's horizon. We have been gazing up at the night sky and wondering about the stars and planets since ancient times. We have been able to explore space and learn more about our universe thanks to technological advancements. Despite the fact that we live on a planet with diverse ecosystems, breathtaking landscapes, and fascinating wildlife, our curiosity has always driven us to explore what lies beyond our immediate surroundings. This fascination with space has led to the development of technologies such as telescopes and satellites, all with the goal of better understanding the universe we live in.

Beyond our solar system exists a vast and yet largely unexplored universe. The study of exoplanets, planets orbiting stars outside of our solar system, has been one of the most exciting areas of research in the recent years. The first detection of an exoplanet orbiting a Sun-like stars was made by Mayor and Queloz, 1995. This exoplanet was discovered around a main-sequence star, 51 Pegasi, using the ELODIE spectrograph at the Observatoire de Haute-Provence. 51 Peg b, the exoplanet, is a 0.47 $M_{Jupiter}$ minimum-mass exoplanet with a 4.23 day orbital period and was the first of a class of exoplanets known as hot Jupiters. This is not the kind of exoplanets we expected to discover as it does not exist in our Solar system and were not predicted by the planet formation models at the time, but it kicked off the discoveries of many exoplanets, each more surprising than the last.

Since then, progress in instrumentation and data analysis have enabled the detection of thousands of exoplanets inside a wide variety of planetary systems. Some of these planets are similar in size and composition to Earth, others being completely different from what we know in our own solar system. Beyond that, exoplanet research has important implications as we can learn more about the formation and evolution of planetary systems, as well as the origins of our own solar system, by studying the properties of these exoplanets and their atmospheres.

As instrumentation improved and temporal baseline of surveys expanded, a diverse range of planetary populations began to emerge (see Figure I.1). Along with hot and warm Jupiters, a population of long-period giant exoplanets has been discovered (primarily using the radial velocity and direct imaging methods). Lower mass planets, ranging from Earth-size to Neptune-size worlds, are also being discovered (mostly by the transit and radial velocity methods). The two leading techniques to detect exoplanets (see Section I.2) are more efficient for short period exoplanets, which explains why the left side of the diagram is the most populated. The classic gas giants are on the top right (massive and long periods), and the hot Neptunes and super-Earths are on the bottom left. The relative scarcity of exoplanets in some areas of this diagram reveals important processes that formed the exoplanets and shaped the system architectures. The horizontal gap between Neptune and Jupiter, for example, is most likely caused by runaway gas accretion once a planet grows slightly larger than Neptune in the protoplanetary disk, quickly transitioning into the Saturn mass regime. The abundance of hot Jupiters on the top left is an observational bias, as these large exoplanets on short period orbits are very easy to detect. Detection efficiency rapidly decreases to the right for longer periods and at the bottom for very small exoplanets. The hot Neptune desert (Lecavelier Des Etangs, 2007; Mazeh, Holczer, and Faigler, 2016) and the Fulton gap between super-Earths and sub-Neptunes (Fulton et al., 2017) became apparent as well in this mass-period diagram.

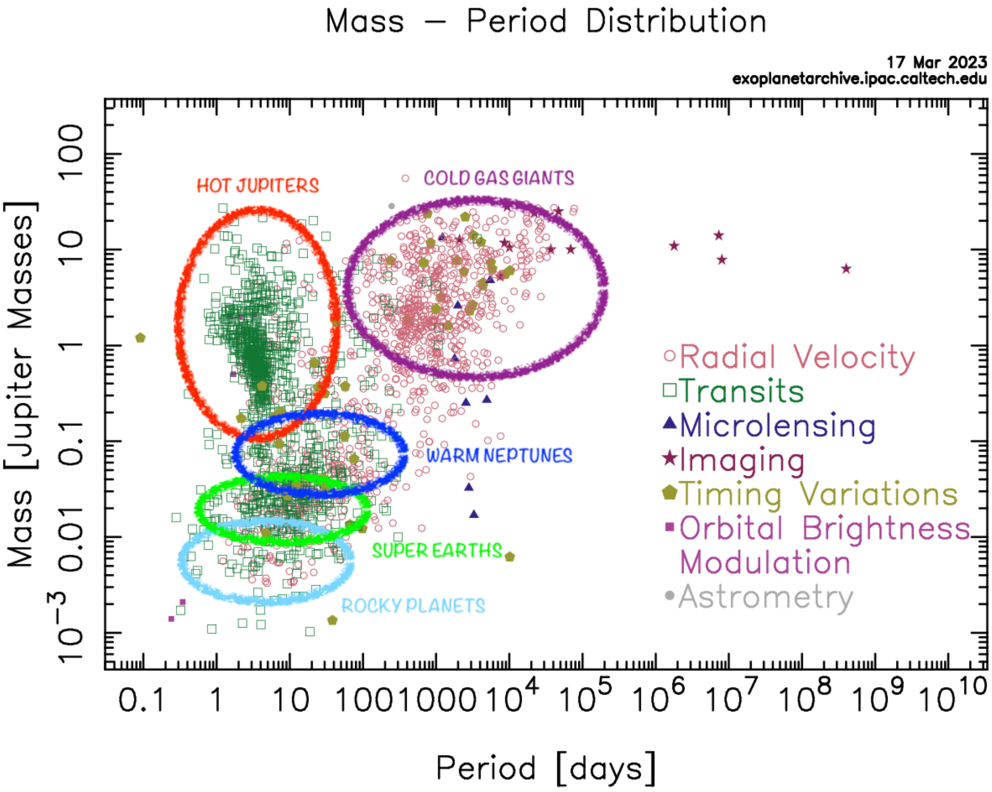

Figure I.1: Mass-Period diagram of exoplanets.
The different techniques are represented by different colored makers. I highlighted the different sub-populations of exoplanets. Credit : NASA Exoplanet Archive.

I.2 DETECTION METHODS

One of the most difficult aspects of studying exoplanets is that they are extremely distant, making direct observation difficult. Which is why the majority of these exoplanets were discovered using indirect methods, where we don't directly observe the exoplanet but rather detect its presence by measuring the star light dimming caused by the exoplanet crossing the stellar surface or by monitoring the radial velocity wobbles that the exoplanet produces on the movement of their host star.

High-contrast imaging can enable the detection of light emitted by an exoplanet. This measurement is difficult due to the low angular separations and high contrasts between the star and the exoplanet. Modern imagers, such as SPHERE at the VLT (Beuzit et al., 2008), are equipped with adaptive optics to improve spatial resolution and coronographic masks to remove stellar light (Bowler, 2016). Direct imaging is currently limited to the detection of massive exoplanets of a few Jupiter masses orbiting at a large distance from their host star. These systems also need to exhibit a favorable star-to-planet contrast ratio, and are nowadays only young systems with hot contracting exoplanets emitting more light. We can combine high-contrast imaging and high-resolution spectroscopy to directly probe the atmospheres of exoplanets. This started the development of ambitious projects such as the ELTs, which aim to characterize the atmospheres of nearby Earth-sized exoplanets (Snellen et al., 2013; Snellen et al., 2015).

Otherwise, indirect methods complement the landscape of directly imaged exoplanets as these methods are biased towards short period planets and are very successful in detected a large number of exoplanets.

I.2.1 *Radial velocity measurements*

The first ever exoplanet detecting orbiting a Sun-like star was discovered by Mayor and Queloz, 1995 using the radial velocity method. The original radial velocity curve of the star 51 Peg is displayed in Figure I.2.

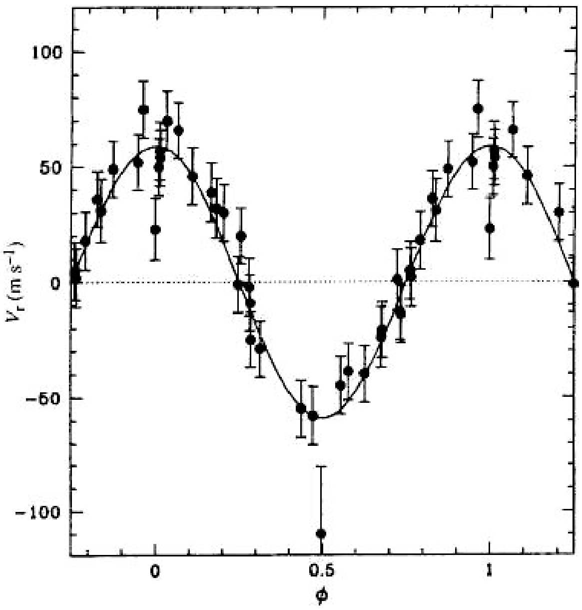

Figure I.2: Radial velocity curve of the star 51 Peg.
This original curve is phased to a period of 4.23 days, obtained with the ELODIE spectrograph (Mayor and Queloz, 1995). The signal is caused by an orbiting companion with a minimum mass of 0.47 M_J , revealing for the first time an exoplanet around another solar-type star.

The radial velocity method is a technique that measures the motion of a star caused by the gravitational pull of an exoplanet. By observing the star's motion, we can determine the exoplanet's mass and orbit. The radial velocity method or Doppler spectroscopy is an indirect method for detecting exoplanets based on the wobbles they cause in the radial velocity of their host star, the radial velocity being the line-of-sight projection of the velocity vector of the star. The star revolves around the barycenter of the star-planet system due to the reciprocal star-planet gravitational interaction. If the orbital plane is not orthogonal to the line of sight, variations in stellar radial velocity along the orbit cause periodic shifts of the stellar lines, which can be detected using a spectrograph on Earth. A schematic of the radial velocity method is presented in Figure I.3.

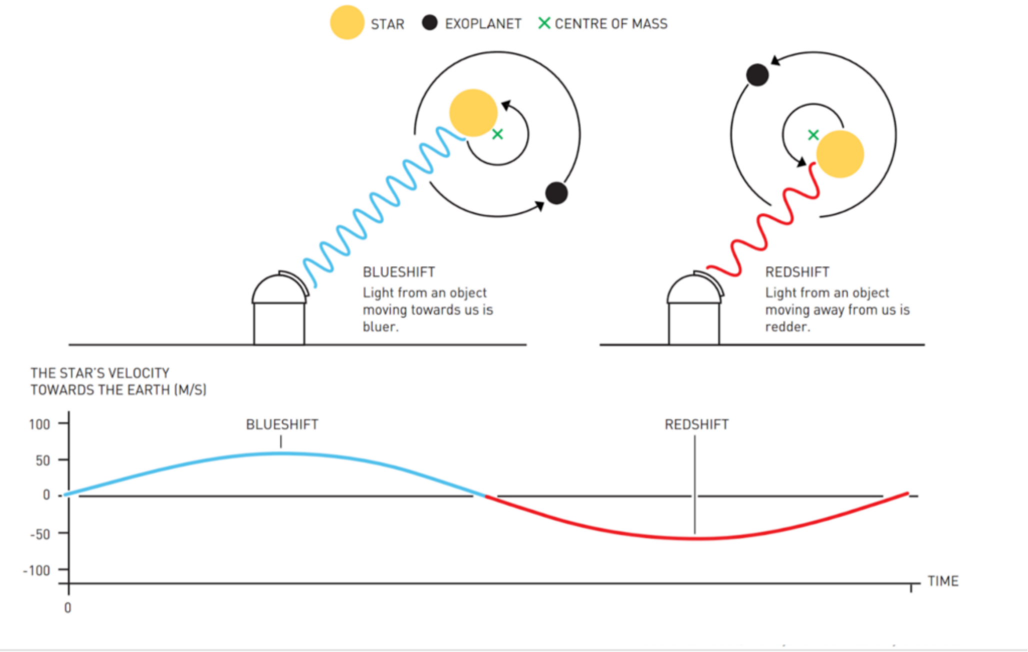

Figure I.3: Schematic of the radial velocity method.
The movement of the star around the center of mass of the system produce alternatively a blueshift and a redshift of the spectral lines that can be converted into a measure of the radial velocity of the star. Credit: Johan Jarnestad/The Royal Swedish Academy of Sciences

Using Newton's and Kepler's laws of planetary motion, the radial velocity signature v_r induced by a planet on its host star can be expressed as a function of time and system parameters.

$$v_r(t) = K[cos(\nu(t) + \omega) + e.cos(\omega)] \tag{I.1}$$

In the equation above, ω is the argument of the periapsis of the stellar orbit, e is the eccentricity, ν is the true anomaly (which also depends on the orbital period P, phase and eccentricity of the planet), and K is the semi-amplitude of the induced signal (see the Keplerian orbital parameters in Figure I.4). The semi-amplitude depends on the mass of the star, the mass of the planet, the inclination of the orbital plane of the star-planet system, the eccentricity of the orbit and the orbital period of the planet.

$$K = (\frac{2\pi G}{P})^{1/3} \frac{M_p sin(i_p)}{(M_s + M_p)^{2/3}} \frac{1}{\sqrt{1-e^2}} \tag{I.2}$$

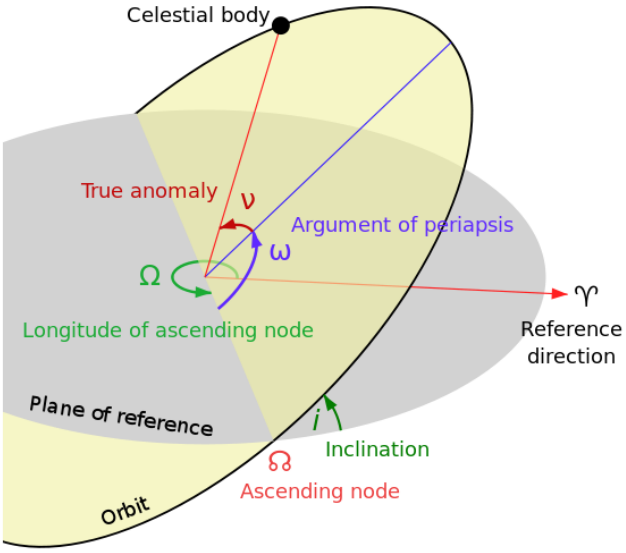

Figure I.4: Keplerian orbital elements.
The orbital plane in yellow intersects a reference plane in gray. The inclination is a vertical tilt of the ellipse with respect to the reference plane, measured at the ascending node. The argument of periapsis defines the orientation of the ellipse in the orbital plane, as an angle measured from the ascending node to the periapsis. Credit: Lasunncty at the English Wikipedia.

As a result, by monitoring the radial velocity variations of a given star, we can access the orbital properties as well as the minimum mass of the exoplanet, assuming that its orbital cycle is well-covered by the observations. In practice, the measured radial velocity is not solely due to the exoplanets in the system. Other factors, such as stellar activity, can also produce signals that make distinguishing between the two sources difficult.

To measure this radial velocity, we consider the Doppler-Fizeau effect and compute the difference in wavelengths between the stellar rest frame λ_0 and the geocentric frame λ_{obs} (c the speed of light in vacuum) using the star's absorption lines present in its spectrum.

$$v_r = c\frac{\lambda_{obs} - \lambda_0}{\lambda_0} \tag{I.3}$$

We obtain a negative/positive radial velocity measurement corresponding to a blueshift/redshift of the source, respectively.

Fischer et al., 2016 and Wright and Robertson, 2017 provided an overview of the high-precision Doppler instruments in the visible and near-infrared and their associated main surveys. HARPS (High Accuracy Radial Velocity Planet Searcher, Mayor et al., 2003) is located at Chile's La Silla Observatory. It has detected more than a hundred exoplanets and is regarded as one of the most successful planet-hunting instruments. HIRES (High Resolution Echelle Spectrometer, Vogt et al., 1994) at the Keck Observatory in Hawaii has detected dozens of exoplanets, including some of the very first confirmed exoplanets. ESPRESSO (Echelle SPectrograph for Rocky Exoplanet and Stable Spectroscopic Observations, Pepe et al., 2021) is a recent spectrograph at Chile's Paranal Observatory and is one of the most powerful planet-hunting instruments in use. CARMENES (Calar Alto high-Resolution search for M dwarfs with Exo-earths with Near-infrared and optical Echelle Spectrographs, Quirrenbach et al., 2014) is a spectrograph located at Spain's Calar Alto Observatory and is intended to detect exoplanets orbiting low-mass stars and has already discovered several super-Earths and Neptune-sized planets. These are just a few of the spectrographs that have been used to find exoplanets. Each instrument has its own set of advantages and disadvantages, and they are frequently used in tandem with other instruments and techniques to confirm the existence of exoplanets.

I.2.2 *Photometric transits*

The first transiting exoplanet orbiting a Sun-like star was discovered by Charbonneau et al., 2000; Henry et al., 2000 (it was first discovered using radial velocity technique) and the phased transit light curve of HD 209458 b is displayed in Figure I.5.

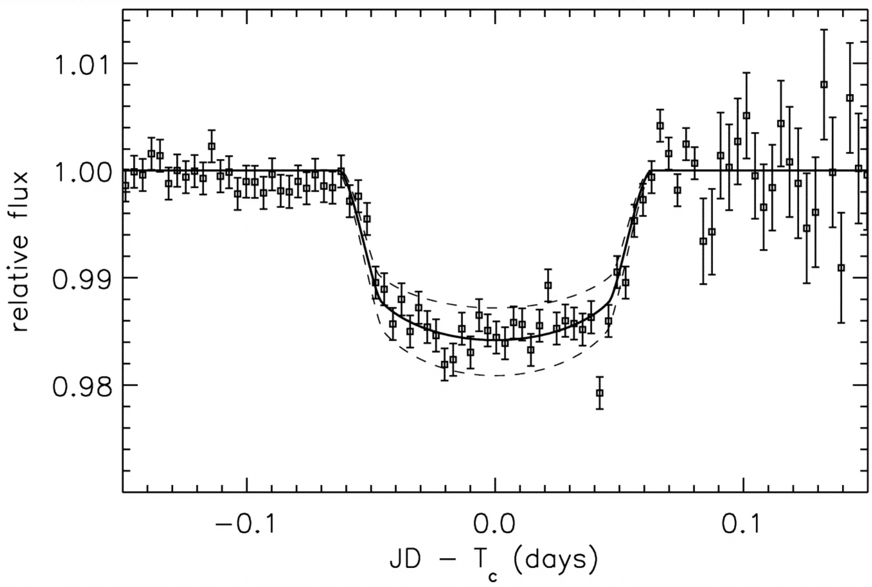

Figure I.5: Transit of HD 209458 b.

Observations obtained using the STARE Project Schmidt camera. Shown are the photometric time series, binned into 5-min averages, phased according to the best-fit orbit, plotted as a function of time from Tc. Credit : Charbonneau et al., 2000.

The transit method involves observing a decrease in the brightness of a star as an exoplanet passes in front of it. The probability of a planet to transit is strongly dependent on the planetary semi-major axis following the equation:

$$P_{transit} = \frac{R_s + R_p}{a} . \frac{1 + e\cos(\pi/2 - \omega)}{1 - e^2} \approx \frac{R_s + R_p}{a} \quad \text{(I.4)}$$

Because exoplanet size and transit depth are related, deeper transits correspond to larger exoplanets. As displayed in Figure I.6, we can directly estimate from a transit the orbital period P, equal to the time needed for a full orbit of the exoplanet, the transit depth ΔF, that gives the difference in flux with and without the transit and can be expressed as a function of the planetary radius R_p and stellar radius R_s, the total transit duration t_T, representing the time needed to reach from the first to the fourth contact of the planetary disk in front of the host star and finally the fully occulted transit duration t_F corresponding to the time between second and third contact following the equations below:

$$\Delta F = (\frac{R_p}{R_s})^2 \quad \text{(I.5)}$$

$$t_T = \frac{P}{\pi} \arcsin\left[\frac{R_s}{a} (\frac{[1 + (R_p/R_s)]^2 - [(a/R_s)\cos i]^2}{1 - \cos^2 i})^{1/2} \right] \quad \text{(I.6)}$$

$$t_F = \frac{P}{\pi} \arcsin\left[\frac{R_s}{a} (\frac{[1 - (R_p/R_s)]^2 - [(a/R_s)\cos i]^2}{1 - \cos^2 i})^{1/2} \right] \quad \text{(I.7)}$$

Transit light curves can yield the planetary radius and orbit inclination (depending on the shape of the transit curve) if the stellar properties are accurately known, and the recurrence time scale of the primary transit allows to constrain the planet orbital period. The probability of a planet transiting its host star varies as R_s/a, where a is the exoplanet's semi-major axis. Since only a fraction of the planets can be seen in transit, one must observe a large numbers of stars to find exoplanets, especially to detect planets at larger separations. This motivated the creation of transit surveys with large fields from space and from the ground.

Light curves are not completely flat during transit, but have a round 'U' shape due to stellar limb darkening, which causes a decrease in brightness near the stellar disk's edge. The line of sight is normal to the stellar surface at the midpoint of the stellar disk, but closer to the limb, the stellar surface is viewed under an angle $\pi/2 - \theta$, where *theta* is the angle between the star's surface normal and the line of sight. This translates to different stellar density and temperature structures in the line of sight, and depending on the viewing angle, a given optical depth corresponds to layers of varying temperature. The most frequently used parametrization is the quadratic limb darkening,

$$I(\mu) = 1 - a(1 - \mu) - b(1 - \mu)^2 \quad \text{(I.8)}$$

where the position on the stellar surface is given by $\mu = cos(\theta)$. I(1) is the specific intensity at the center of the disc, and a and b are the two quadratic limb-darkening coefficients, usually obtained from stellar models (Claret, 2000).

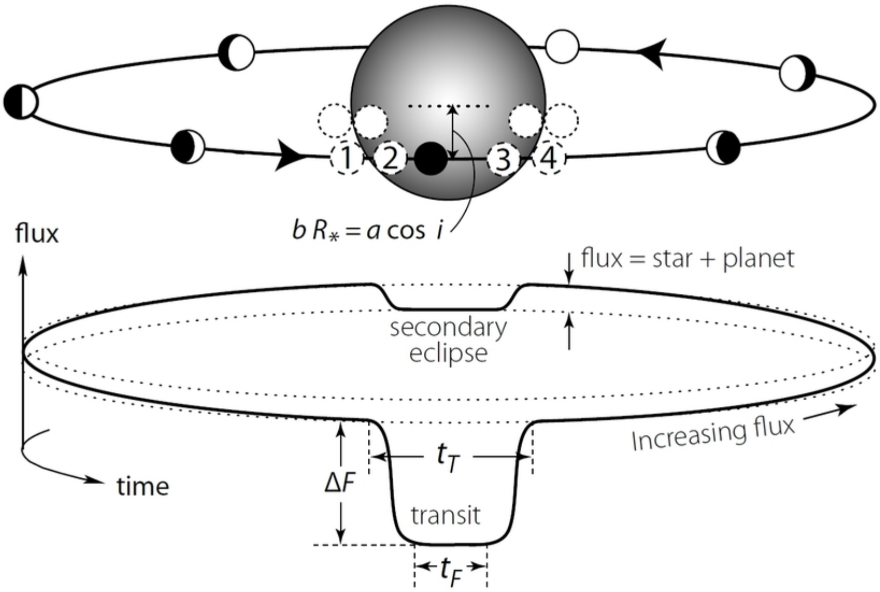

Figure I.6: Schematic of a transit.
The four basic observables from a transit light curve are shown here : the orbital period P, the transit depth ΔF, the total transit duration t_T and the fully occulted transit duration t_F. Credit : Perryman, 2011.

Space-based missions like CoRoT (Auvergne et al., 2009; Baglin et al., 2009) launched in 2006, Kepler and K2 (Borucki et al., 2010; Howell et al., 2014) launched in 2009 and now TESS (Ricker et al., 2014) launched in 2018 (see Section II.1 for a detailed description of the TESS mission) are necessary to obtain long-term continuous monitoring of a large number of stars and detect thousands of planet candidates. On the other hand, ground-based surveys looking at individual star are essential for the validation and confirmation of the existence of exoplanets detected by space missions, to find additional exoplanets in already known systems and to detect exoplanets around fainter stars. The validation of planetary candidates is important as several scenarios that can result in false positives in photometric surveys. For example, the presence of eclipsing binaries, or binary star systems, can produce light curves that resemble those of transiting planets. The use of these ground-based instruments (like MEarth, Irwin et al., 2015; TRAPPIST, Jehin et al., 2011; SPECULOOS, Jehin et al., 2018) to validate the planetary candidates and improve on the precision on the radius measurement led to the discovery of the first terrestrial exoplanets orbiting in the habitable zone of their host star like in the TRAPPIST-1 system (Gillon et al., 2016, 2017) or in the TOI-700 system (Gilbert et al., 2020, 2023).

Finally, a transit light curve cannot be used to calculate the planet's mass like the radial velocity method (see Section I.2.1). However, in multi-planetary systems, dynamical planet-planet interactions can have a effect on the exoplanet orbits, causing variations in the transit timings. By modeling these transit-timing variations (also called TTVs) with

N-body simulations, it is possible to estimate the mass of the exoplanet and probe the system's outer non-transiting exoplanets.

Combining the transit and radial velocity methods

Both the transit and radial velocity methods are useful for detecting exoplanets. However, each technique has difficulties that limit its ability to identify specific types of planets. The transit method is based on observing exoplanets that pass directly in front of their host stars, which only accounts for a small percentage of all exoplanets in our galaxy. It is also susceptible to producing false positive as a result of binary stars or background eclipsing binaries. The radial velocity method, on the other hand, is most sensitive to massive planets that orbit their host stars in close proximity. This means that smaller planets farther away from their host stars may be missed by this method.

Combining the transit method and the radial velocity method can help overcome these limitations and gain a more detailed understanding of exoplanets. We can confirm the existence of exoplanets and eliminate false positives by combining both techniques. For example, if an exoplanet is discovered using the transit method, subsequent observations using the radial velocity method can confirm its mass and density, revealing important information about its composition and internal structure. Furthermore, detecting a planet using both techniques increases the likelihood that it is a real exoplanet rather than a false positive caused by another phenomenon.

I.3 EXOPLANETS AROUND M DWARFS

The spectral type of a star is a letter given according to the shape of its spectrum and the intensity of its lines. It allows us to classify the stars in temperature and luminosity. The OBAFGKM sequence is a first-order effective temperature sequence. From the hottest to the coldest types we have 0, B, A, F, G, K, and M. We can therefore classify stars according to their brightness and temperature in the representation of the Hertzsprung-Russell (see Figure I.7). Red dwarfs or M dwarfs, are located at the bottom right of the main sequence and are the most abundant type of star in our galaxy. They are small, cool, and long-lived, making them an important target for exoplanet searches. In this section, we will explore the reasons why M dwarfs are of great interest, why they are considered a key component in the search for exoplanets but also the difficulties they represent.

I.3.1 *M dwarfs as host stars*

First and foremost, M dwarfs are abundant in our galaxy, comprising 70% of star populations in the solar neighborhood (Henry, Kirkpatrick, and Simons, 1994). They span a very wide range of masses (from 0.07 to 0.6 solar mass) and temperatures (from 2300 to

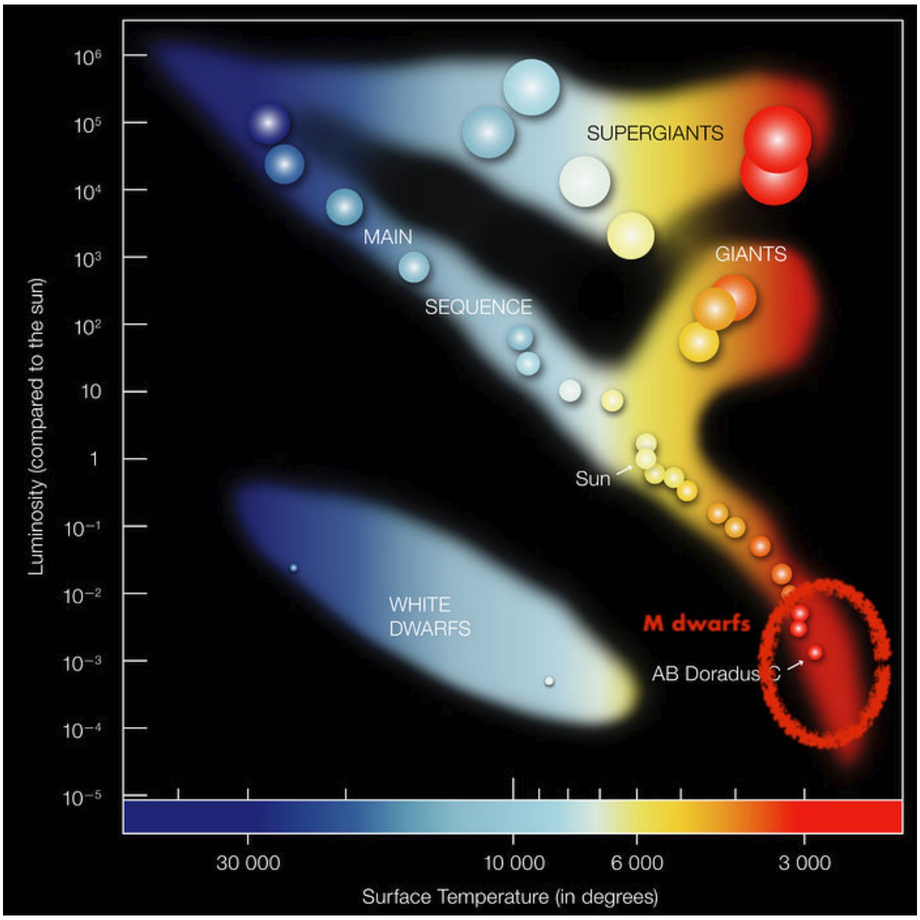

Figure I.7: Hertzprung-Russell diagram.
The temperature of stars are plotted in function of their luminosity. The position of a star in the diagram provides information about its present stage and its mass. Stars that burn hydrogen into helium lie on the diagonal branch, called the main sequence. Red dwarfs lie in the cool and faint corner. Credit: ESO.

3800K) between M9 (late) and M0 (early) stars, and unlike other stellar objects, the stellar properties of M dwarfs vary a lot from early to late M dwarfs. M dwarfs also have longer lifespans than other stars. These stars can live for tens of billions of years, meaning that if an exoplanet is discovered around an M-type star, it has the potential to be a stable and long-lived system.

These stars are also the smallest and least massive stars of the main sequence. M-dwarfs lower radius and mass compared to Sun-like stars opens the door to the detection and characterization of small exoplanets like Earth-size planets, as the contrast between the star and the exoplanet is greater both in the photometric transit and radial velocity measurement. For comparison, the size ratio of an Earth to a late M dwarf is roughly the same as Jupiter to a Sun-like star and the amplitude of the radial velocity signature induced by a

Earth-like planet, for example, increases from about 10 cm/s on a solar type star to 1 m/s on a mid M dwarf.

Another interesting aspects of M dwarfs is the potential to detect exoplanets in the habitable zone of their host stars. Indeed, their lower luminosity implies a closer-in habitable zone, corresponding to relatively short orbital periods (10–30 days). The habitable zone is defined by Kopparapu et al., 2013 as the region around a star where the exoplanet receives the right amount of irradiation to potentially have liquid water at the surface. As it is easier to detect exoplanets close to their host stars, because shorter orbital separations increase transit probability and frequency, and RV semi-amplitude, M dwarfs are interesting targets to search for habitable exoplanets. We may even discover new types of potentially habitable planets yet to be undeniably confirmed: water worlds, consisting of a rocky core covered by a thick water ocean like we expect LHS 1140 b to be (Lillo-Box et al., 2020) and Hycean worlds, a new category of planet composed of water-rich interiors with massive oceans underlying H2-rich atmospheres (Madhusudhan, Piette, and Constantinou, 2021).

M dwarfs are also intriguing targets in the context of planetary formation research because their protoplanetary disks are much less massive than those of solar-type stars, allowing researchers to investigate the impact of disk mass on planetary formation (Gaidos, 2017; Mordasini et al., 2012). Planet formation cannot be directly observed, but must be inferred by assembling pieces of information into a coherent picture. Observations can provide information on small solids (Andrews, 2020) in young protoplanetary disks or on mature planets, but measurements cannot reveal the processes that determine how solids and gas accumulate to form planets. Studies have been conducted on planet formation around M dwarfs (Pascucci et al., 2011) to propose different possible scenarios (Mercer and Stamatellos, 2020) and try to understand why these stars tend to host more exoplanets (Mulders et al., 2021). Nevertheless, the study of planet formation around M dwarfs remains an active field of research, with ongoing observations and discoveries helping us in better understanding the formation and evolution of planets around these stars.

In conclusion, M dwarfs are prime candidates for studying exoplanets for the different reasons discussed in this section. They are the most common type of star in the galaxy, and because of their small size and low luminosity, they are ideal for detecting small, rocky planets in the habitable zone of their host star. M dwarfs have variable brightness and are frequently surrounded by flares and other eruptive events. This variability can reveal important information about these stars' magnetic activity, which can then be used to investigate the properties of exoplanetary atmospheres and magnetic fields. Research into M dwarfs can provide valuable insights into the nature of star systems, as well as the formation and evolution of planetary systems.

I.3.2 *Near-infrared observations*

M dwarfs are the most common type of star and many exoplanets are likely to be discovered orbiting these stars. However, detecting small exoplanets around M dwarfs is difficult due to their intrinsic faintness. Because M-type stars emit the majority of their energy in the infrared spectrum, it is expected that near-infrared observations will be more effective in detecting small exoplanets orbiting these stars using the transit and radial velocity methods.

Indeed, the brightness of the star influences the precision measured on the transit depth. Because M-type stars are much brighter in the near-infrared than in the visible (see Figure I.8), near-infrared observations are more suited for detecting small exoplanets via the transit method. By observing the absorption of near-infrared light by atmospheric features such as water vapor and methane, near-infrared observations can also be used to characterize the atmospheres of exoplanets. In the same way, near-infrared observations are useful for measuring radial velocity because they allow to measure the star's motion with greater precision than visible light observations. M-type stars have few spectral features in the visible range, limiting the precision of radial velocity measurements. The near-infrared range, on the other hand, is rich in molecular absorption features which can be used to measure radial velocities with a greater precision.

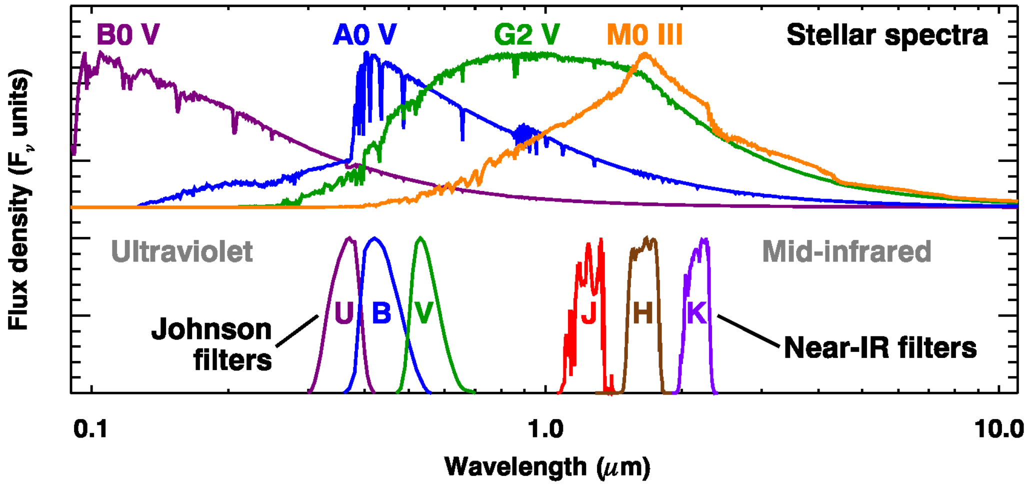

Figure I.8: Stellar spectra for different spectral type stars.
The figure above shows what the spectra from stars actually look like (using model spectra by Castelli and Kurucz, 2003). The coolest stars (red super giants and red dwarfs have similar spectrum) emit mostly in the near-infrared. Credit: Gregory C. Sloan.

The near-infrared is also useful to mitigate the effect of stellar activity. All stellar surface features (spot and plage contrasts, magnetic inhibition of surface convection) create a heterogeneous apparent surface disk, and can therefore shift the lines or affect their shape under the effect of the stellar rotation, shifting their centroids, and consequently adding a quasi-periodic signal at the stellar rotational period or at one of its harmonics (Queloz et al., 2001; Robertson and Mahadevan, 2014a; Robertson et al., 2014). Observing in the near-infrared will make it easier to distinguish between planetary and stellar activity radial velocity contributions as demonstrated by Carmona et al., 2023 (see Figure I.9). The amplitude of activity signals is lowered in the near-infrared because the contrast of dark and bright features at the stellar photosphere decreases from visible to near-infrared wavelengths.

Having both optical and near-infrared radial velocities available at the same time (by combining HARPS and NIRPS for example) is even more powerful because it allows to distinguish between signals with the same characteristics (a keplerian signal) in both spectral ranges and signals with different characteristics (activity signal) in the two spectral ranges.

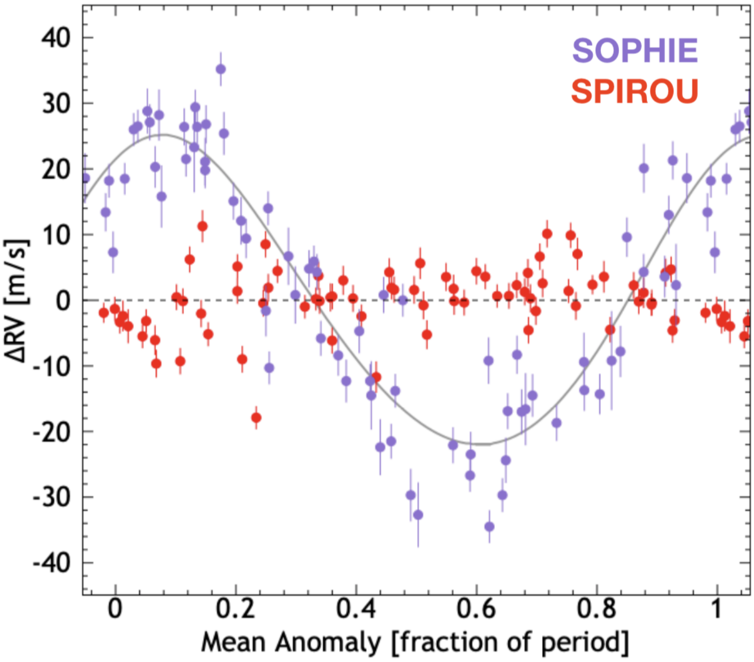

Figure I.9: Phase-folded RV measurements of Gl 388.
Observations are done with SPIRou in the near-IR (red dots) and with SOPHIE (blue dots) in the optical. The gray line represents the Keplerian model of period 2.23 days and K = 23.6 m/s derived from the SOPHIE data. Credit: Carmona et al., 2023.

Observing in the near-infrared presents however some difficulties. In the near-infrared, the Earth's atmosphere may generate noise in the data. The light emitted by a celestial object is partially or completely absorbed by the Earth's atmosphere in ground-based observations and this phenomenon is strongly wavelength dependent. Even if an observatory's location is carefully chosen to minimize the impact of the atmosphere, telluric absorption must still be corrected. In spectroscopic studies, atmospheric species imprint absorption or emission lines on top of the target's spectra and that creates the transmission spectrum of the Earth's atmosphere. Fortunately, tools have been developed (like Molecfit (Smette et al., 2015)) and are currently used to correct for this effect.

To detect exoplanets around these low-mass stars, many technological developments had to be made. CARMENES (Quirrenbach et al., 2018), HPF (Mahadevan et al., 2012),SPIRou (Artigau et al., 2014), and NIRPS (Bouchy et al., 2017) have taken a long technological development trying to reach a 1 m/s precision in the near-infrared but this precision has yet to be achieved. Reaching late M dwarfs is possible for photometric transit surveys like SPECULOOS (Delrez et al., 2018) thanks to two important developments: deep-depleted CCDs reaching quantum efficiencies around 90% at 900 nm (also used by TESS (Ricker et al., 2014)), and 4 1-m robotic telescopes. Alternatively, we can use near-infrared detectors, a choice made for ExTrA (Bonfils et al., 2015), or larger telescope mirrors.

I.4 CURRENT QUESTIONS IN EXOPLANETS

Exoplanetary science is a rapidly expanding field that seeks to study and understand planets beyond our Solar System. We went from not knowing of any planets outside the solar system to the overwhelming realization that nearly every star may have a exoplanet orbiting around in the last 30 years. The discovery of thousands of exoplanets in recent years has transformed our understanding of the abundance and diversity of planetary systems in the universe. The combined analysis of the exoplanets detected by all methods can provide interesting information, however many questions remain unanswered, and exoplanetary science remains one of the most active areas of astronomical research. Fundamental questions remain at the heart of exoplanetary science today. What is the diversity of exoplanets? How do exoplanets form and evolve?

One of the most striking aspects of the field is the diversity of exoplanetary systems. Exoplanets range in size, mass, and orbit, from hot Jupiters to super-Earths. We are trying to figure out what is causing this diversity and how it relates to the formation and evolution of exoplanetary systems, and how gas and dust in protoplanetary disks around young stars form planets. We are also interested in how planets interact with one another and with their host stars over time. This knowledge is critical for understanding the diverse planetary architectures observed in exoplanetary systems, as well as the conditions that lead to the formation of exoplanets.

When focusing on the planetary systems orbiting M dwarfs, it is worth noticing that only around a dozen systems had been well characterized when I started my thesis, and that this number has doubled since then. Despite the limited data available, these systems have already demonstrated intriguing and noteworthy characteristics, which will be discussed further in the following paragraphs.

Recent research indicates that small exoplanets tend to be more common around close-in M dwarf systems than around Solar-type stars (Bonfils et al., 2013; Dressing and Charbonneau, 2015), with an occurrence rate of 2.5 ± 0.2 planets per M dwarf with radii from 1 to 4 R_E and periods shorter than 200 days. When the high frequency of low-mass stars is combined with the occurrence rate of small planets orbiting them, there may be 10 more Earth-size exoplanets at the bottom of the main sequence than around Solar analogs. However, it remains unclear how differences in M dwarf environments influence the composition of exoplanets of a given size. We can ask ourselves if exoplanets orbiting M dwarfs are preferentially formed rocky or non-rocky with their atmosphere being stripped away. Cloutier and Menou, 2020 found an increase in the frequency of close-in rocky planets around lower-mass stars and in the relative occurrence rate of rocky to non-rocky exoplanets around mid-M dwarfs compared to mid-K dwarfs, although with a small number of confirmed transiting planets in that mass regime. However, they were not able to firmly identify the physical cause of this trend. Kubyshkina and Vidotto, 2021 found that atmospheric escape of exoplanets with the same equilibrium temperature occurs more efficiently around lower mass stars.

Despite the evidence suggesting that M dwarfs tend to form more rocky planets than volatile-rich planets, it seems that sub-Neptunes around M dwarfs actually appear to be less dense compared to those around other stars (see Figure I.10). Determining if these exoplanets continue to follow a low density pattern or not will provide critical information for M dwarf exoplanet formation scenarios. Furthermore, the sub-Neptune class, which includes super-Earths and mini-Neptunes, allows for a wide range of internal structures between Earth and Neptune that are not seen in the solar system, such as water worlds, magma ocean worlds, terrestrial planets with H2-rich atmospheres, and others. So far most of the M-dwarf host stars of transiting exoplanets are of early type. It is therefore important to also populate the mass-radius diagram with exoplanets transiting mid-to-late M dwarfs to better understand the impact of the stellar mass on the occurrence rate and bulk composition of exoplanets.

The exoplanets that we can not find in our Solar system, such as the sub-Neptunes that lie between Earth and Neptune in size, and the sub-Saturns that lie between the ice giants and gas giants, raise particularly intriguing questions about their true nature. Even within the sub-Neptune regime, the recent discovery of a bimodal distribution in radii separated by a radius valley around 1.8 R_E has opened a new window into planetary formation in the solar system's low-mass regime, which had previously been unknown (Bean, Raymond, and Owen, 2021; Fulton et al., 2017). The radius valley around M dwarfs is located at slightly smaller radii than around Sun-like stars (Cloutier and Menou, 2020) and marks the transition between rocky super-Earths and mini-Neptunes that host H/He envelopes (Owen and Wu, 2017). Several physical mechanisms have been proposed to explain the radius valley including photo-evaporation, core-powered mass loss (Gupta and Schlichting, 2020; Jin and Mordasini, 2018; Wyatt, Kral, and Sinclair, 2020), or directly as an outcome of

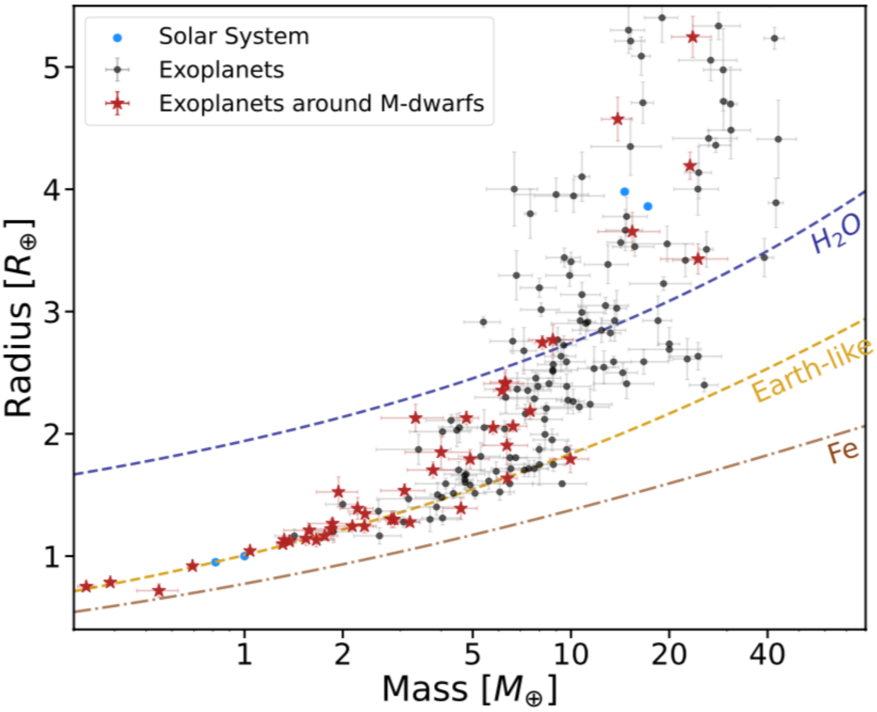

Figure I.10: Mass-Radius of known transiting exoplanets.
Exoplanets transiting M dwarfs are represented as red stars. Data from the PlanetS catalog available on DACE.

the planet formation process wherein Super-Earths form at later times in either a gas-poor or completely gas-depleted environment (Lee and Connors, 2021; Lopez and Rice, 2018). Each of these mechanisms predicts a unique dependence of the radius valley on orbital period such that measuring the radius valley's slope provides direct insight into the origin of the radius valley. Cloutier and Menou, 2020 discovered that the radius valley separating rocky and gaseous planets exhibits a negative slope with insolation around low-mass stars, as opposed to the positive slope found around Solar-type stars (see Figure I.11). This supports models of direct terrestrial planet formation in a gas-poor environment. The different slopes of gas-depleted formation and thermally-driven mass loss models naturally create a subset of the period-radius parameter space in which the two models make opposing predictions about the bulk composition of planets. Characterizing the bulk composition of additional transiting exoplanets will help to determine whether the M dwarf radius valley originated directly from planet formation or as a result of post-formation atmospheric escape.

It was also noticed that Jupiter-mass exoplanets are extremely rare in the vicinity of M dwarfs. The lack of hot Jupiters is particularly intriguing because, due to their large sizes and short periods, these planets are the easiest to detect. As a result, their absence is most likely real and not due to detection bias. Recent planetary population synthesis models

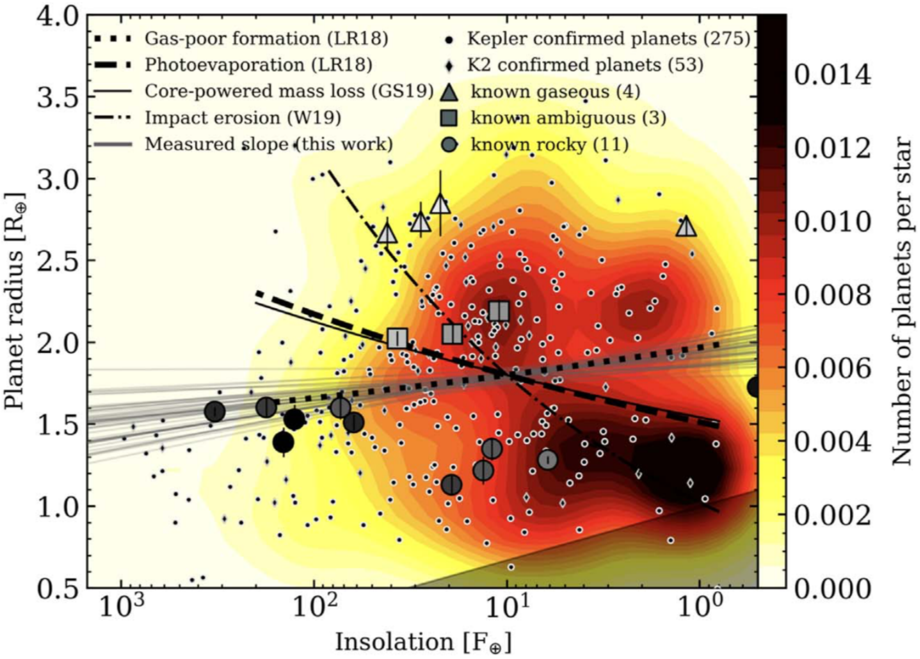

Figure I.11: Planet occurrence rates vs. insolation.
Occurrence rate map calculated from the population of confirmed planets from Kepler and K2 around low-mass dwarf stars (small circles and diamonds). Over-plotted in black are model predictions of the transition from rocky to non-rocky planets in the following scenarios: core-powered mass loss (Gupta and Schlichting, 2020), photo-evaporation (Lopez and Rice, 2018), and gas-poor formation (Lopez and Rice, 2018). Also over-plotted are planets with bulk density measurements from the literature that are classified as having either rocky (circles), gaseous (triangles), or intermediate (squares) bulk composition. Symbol colors are indicative of the MAP planet bulk densities. Credit: Cloutier and Menou, 2020.

based on the core-accretion theory predict a very low occurrence rate of giant exoplanets and even suggest it should decrease to zero for the M dwarf stellar mass range (Burn et al., 2021) due to the lack of sufficient mass surface density and the increased orbital timescales around low-mass stars (Laughlin, Bodenheimer, and Adams, 2004). However, a few of these giant exoplanets have been detected orbiting M dwarfs. To provide more information about their formation process, the validation and measurement of the masses of more giant planets transiting M dwarfs are required.

M dwarfs are different from other spectral type stars as they tend to host multi-planetary systems, which can provide much stronger tests for planetary formation theories than single planet systems (Ballard and Johnson, 2016; Fang and Margot, 2012; Steffen and Hwang, 2015). Weiss et al., 2018 have demonstrated a correlation between the size of planets in a multi-planetary system and a regular spacing between them, described as the "peas in the pod" theory. This concept has been employed to restrict planet formation models. According to Otegi, Helled, and Bouchy, 2022 that examined multi-planetary systems observed by K2 and TESS, for which both the radii and the mass were measured precisely, M-dwarf multi-planetary systems exhibit more similarity in density than in mass, indicating a possible connection in their formation mechanism. Aside from the information encoded in multi-planetary system architecture, the internal structure of exoplanets orbiting the same host star is extremely valuable for constraining models. As they share the same host star and accretion disc, the only difference in composition is the location of formation and evolution. Characterizing the bulk density of exoplanets in multi-planetary systems, as well as estimating the presence of volatiles and liquid/solid water, allows us to directly test planet formation hypotheses. It may determine whether the exoplanets' refractory ratios are similar to each other and to the host star, implying a link between stellar composition and planet composition.

The discoveries and characterizations of new exoplanets led to the challenges of understanding exoplanet atmospheres, interiors, and evolution. Understanding the internal structure and atmospheres of exoplanets is essential to our understanding of how planets form and evolve. Observations of a planet's interior are not directly possible, but an exoplanet's internal structure can be determined by its size, mass, and composition (Otegi et al., 2020). Earth, like other small, rocky planets, has a dense, iron-rich core surrounded by a silicate mantle and crust. In contrast, gas giants like Jupiter have a massive, hydrogen-rich atmosphere surrounding a relatively small rocky core. Some exoplanets, known as super-Earths are in the middle, with a rocky core and a thick atmosphere of hydrogen, helium, and other gases. The quantity of heavy elements in a planet and whether or not all planets have a core composed of rock and iron are questions that are still on-going. Indeed, determining the composition of low-mass exoplanets is difficult due to the presence of trade-offs between different components such as iron cores, silicate mantles, water content, and layers of hydrogen and helium gas, resulting in compositions degeneracies (Dorn et al., 2017). Understanding the internal structure of exoplanets could help understand the origin of the observed populations in the radius-period diagram discussed above. Another important goal, especially for sub-Neptunes is to determine the composition of the envelope, which contains information about their formation.

To gain insights into planet formation and evolution theories, we need to understand the physical and chemical mechanisms at work in exoplanet atmospheres (Seager and Deming, 2010). The atmosphere's composition and temperature can influence the planet's climate, chemistry, and ability to retain water and other volatile compounds. The planet's atmosphere can also reveal important information about its formation and history (JWST Transiting Exoplanet Community Early Release Science Team et al., 2023), such as whether it formed in a gas-rich or gas-poor environment, or whether it has been affected by volcanic or tectonic activity. The analysis of exoplanetary spectra is a critical component of this research, which is based on spectroscopic studies. The accuracy of our interpretations of exoplanetary spectra is heavily reliant on atmospheric models (Fortney, 2018), particularly when no in situ measurements are available. As a result, having reliable and precise atmospheric models to support our research efforts is critical.

Exoplanet mass and radius measurements must be very precise in order to understand their internal structure and atmospheres. These measurements can be difficult because they require sensitive observations and careful data analysis, which motivated the conception of new instruments like ExTrA and NIRPS that could push the precision already acquired in the visible into the near-infrared domain to obtain precise planetary radius and mass measurements of exoplanets orbiting M dwarfs.

MY PHD WORK - MOTIVATION OF MY THESIS

The main goal of this thesis is the study of exoplanets around M dwarfs with two new near-infrared instruments. More specifically, the idea is to get to the same precision in the near-infrared than in the visible both in photometry and in spectroscopy to better detect and characterize these exoplanets. I worked on the target selection, data analysis, and the creation of a night report for all the observations scheduled to follow-up planetary candidates. After collecting all the candidates from the TESS mission, I focused on two main instruments to achieve this goal.

In Chapter 2, I describe the TESS mission, the incredible work it has done to find planetary candidates around M dwarfs and how I selected the target sample I used during my thesis. I explained the importance of follow-up observations to validate and characterize the planet candidates found by the TESS mission.

In Chapter 3, I detail the work I've done with the ExTrA facility, a near-infrared multi-object spectrograph fed by three 60-cm telescopes located at La Silla Observatory. I screened through raw data to produce usable light curves for detecting transiting exoplanets. After creating the light curves, I analyzed them to detect any planetary transits and modeled to determine the planetary parameters. Additionally, I was responsible for selecting targets based on ExTrA various sub-programs.

In Chapter 4, I describe the new NIRPS spectrograph also installed at La Silla Observatory and complementing the HARPS spectrograph. I contributed to the NIRPS Guaranteed Time Observations by proposing two different programs. The first one to populate the mass-radius diagram of exoplanets orbiting mid-to-late M dwarfs using ExTrA and NIRPS, and the second to search for additional planets in already known TESS transiting systems using the deep search strategy.

The conclusions and future prospects related to this work are presented in the Conclusion.

II

THE TRANSITING EXOPLANET SURVEY SATELLITE

> *"May these words be the first to find your ears*
> *The world is brighter than the sun now that you're here*
> *Though your eyes will need some time to adjust*
> *To the overwhelming light surrounding us"*
> Light by Sleeping At Last

INTRODUCTION

Following the success of the CoRoT (Auvergne et al., 2009; Baglin et al., 2009) and Kepler (Borucki et al., 2010) missions, as well as other ground-based surveys, the next step for the exoplanet community was to design a photometric space mission covering the full sky and allowing the discovery of transiting planets around bright stars amenable for radial velocity follow-up. The Transiting Exoplanet Survey Satellite (TESS) represents a significant leap forward in the search for exoplanets. TESS is detecting exoplanets using the transit method but differs from other missions in that it can observe a larger portion of the sky at once (24 x 90 degree field of view), and switching to a different portion every month. TESS surveys nearly the entire sky over the course of its mission, focusing on different areas each year. TESS represents an opportunity for the exoplanet community to broaden our understanding of the universe. Even if the mission is still ongoing, TESS is already making significant contributions to the field of exoplanet research because of its cutting-edge capabilities and broad survey area.

II.1 THE TESS SPACE MISSION

TESS (see Figure II.1) is searching for exoplanets that are passing in front of bright and nearby stars (Ricker et al., 2014). It was launched on 18 April 2018 into a highly elliptical 13.7-day orbit around the Earth-Moon system. The orbit places the spacecraft in a 2:1 resonance with the Moon and is inclined with respect to the ecliptic plane. TESS is using four wide-field optical CCD cameras to monitor at least 200,000 main-sequence stars for temporary brightness drops caused by planetary transits over the course of its two-year primary mission and extended missions. TESS stars are typically 10 to 100 times brighter than the stars observed during with the Kepler and CoRoT missions. This makes the spectroscopy and radial velocity follow-up much more efficient to validate the planetary candidates and measure the mass of the exoplanets detected by TESS. TESS is expected to discover thousands of exoplanets smaller than Neptune, including dozens the size of Earth. As of March, 2023, TESS has already discovered 282 exoplanets and released more than 6000 candidates. The nominal mission goal was to search the entire sky in two years for 50 exoplanets smaller than $4R_{Earth}$ that are amenable to radial velocity follow-up observations to provide exoplanet masses and atmospheric compositions.

Figure II.1: Artist's impression of TESS.
An artist's impression of the Transiting Exoplanet Survey Satellite (TESS) with illustrated exoplanets transiting their host star in the background. Credit: MIT.

The TESS Input Catalog (TIC; Stassun et al., 2018) is a catalog of luminous sources in the sky used by the TESS mission to select target stars to observe and provide stellar parameters. The TIC allows the identification of optimal targets for exoplanet transit searches as well as the calculation of flux contamination in the TESS aperture for each target. Combined with Gaia Data Release 2 (Gaia Collaboration et al., 2018), it also provides accurate stellar radii to estimate planetary radii, which will be used to determine which targets will receive photometric and spectroscopic follow-up. A small part of the stars in the TIC were selected as part of the Candidates Target List (CTL) to be observe with the 2-minute cadence. CTL targets are chosen based on their potential for follow-up observations, with an emphasis on small, nearby stars. A year after the start of the TESS mission, Stassun et al., 2019 published a revised version of the TIC and CTL catalogs based on the incorporation of the Gaia DR2. The number of stars in this new TICv8 catalog has increased by a factor of 3.5 when compared to the original version, the stars with T_{eff} value has more than doubled, and the number of stars with estimated radii has grown by a factor of ~ 20.

To collect the light from these stars, the satellite uses four cameras with 10.5 cm apertures, each of them with a field of view of 24°x24°. Four pixels of 21 arcsec each capture 90% of the total energy of the point-spread function. Depending on the star's ecliptic latitude, each star will be observed for a period ranging from one month (one TESS sector is around 27 days) to one year if the star is located at the ecliptic pole (see Figure II.2). TESS can cover 42.7% of the sky in 13 sectors. TESS's wide red bandpass (600 to 1000 nm) allows the detection of Earth-sized and super-Earth-sized exoplanets transiting M-dwarf stars, which are significantly smaller and cooler than our Sun.

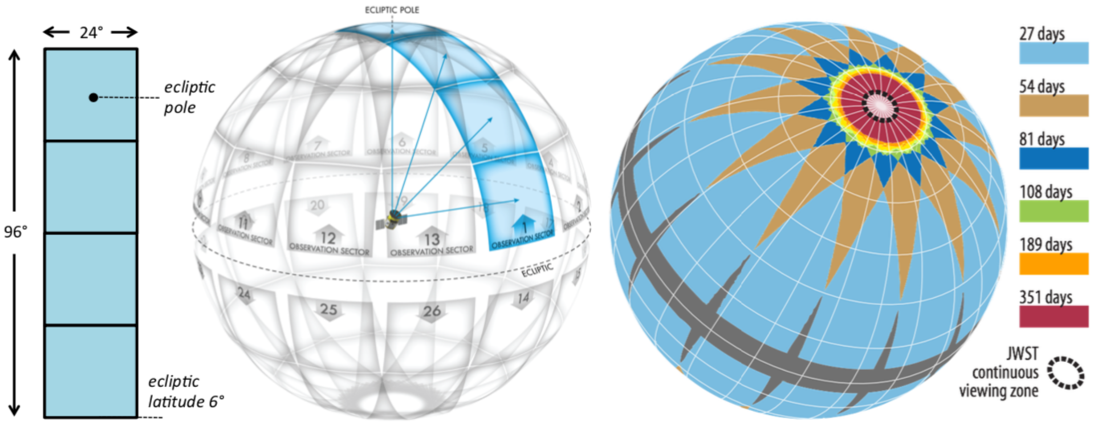

Figure II.2: TESS sky coverage for the primary mission.
Left: The combined field of view of the four TESS cameras. *Middle*: Division of the celestial sphere into 26 observation sectors (13 per hemisphere). *Right*: Duration of observations on the celestial sphere, taking into account the overlap between sectors. The dashed black circle enclosing the ecliptic pole shows the region which JWST will be able to observe at any time.

During the primary mission, luminosity measurements of selected target stars were taken every 2 minutes, and full-frame images (FFIs) of all stars every 30 minutes. After demonstrating improvements in the data compression capabilities, the FFIs in the extended mission are recorded on-board every 10 min. The Science Processing Operations Center (SPOC; Jenkins et al., 2016) pipeline is then used to process the 2-min data, and the Quick Look Pipeline (QLP; Huang et al., 2020a,b) is used for the FFIs. These pipelines search for periodic flux decreases, known as Threshold Crossing Events (TCEs), in both short and long cadence data to identify potential transiting exoplanets. The light curves are first run through a software that filters out obvious non-planetary signals before being manually vetted to identify a set of TESS Objects of Interest (TOIs). The TOI catalog contains planetary candidates for future observations, as well as a small number of previously known exoplanets. Targets are assigned consecutive TOI IDs and multi-planetary systems are assigned suffixes (.01, .02, etc.) to distinguish the different planetary candidates. Following that, follow-up observations from the ground are used to confirm the planetary nature of the candidate and measure precisely planetary parameters. A summary of the TESS primary mission is described in Guerrero et al., 2021, where they announced that the data collected during the first two years of observation yielded 2241 TOIs, and of the 1676 TOIs not later ruled out as False Positives, 1575 TOIs had periods less than 50 days, and 654 TOIs had radii smaller than $4R_{Earth}$.

TOIs are found orbiting a diverse stellar population, however for the purpose of my PhD, my interest goes towards TOIs orbiting M dwarfs. Figure II.3 shows that for M and K-type stars, small TOIs predominate, demonstrating TESS's capabilities to detect small exoplanets around small stars. During its primary mission, TESS observed TOI-700, and made its first discovery of an Earth-sized exoplanet, TOI-700 d, orbiting in the habitable zone of its M2 host star (Gilbert et al., 2020; Rodriguez et al., 2020; Suissa et al., 2020), reinforcing the idea that TESS is the perfect mission to provide small size candidates orbiting M-dwarfs.

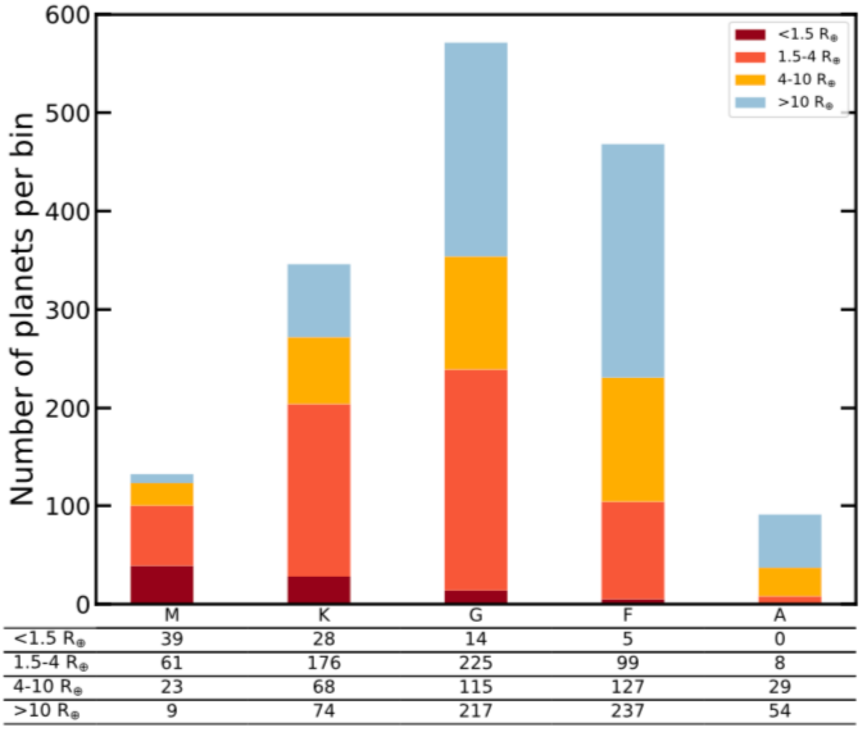

	M	K	G	F	A
<1.5 R⊕	39	28	14	5	0
1.5-4 R⊕	61	176	225	99	8
4-10 R⊕	23	68	115	127	29
>10 R⊕	9	74	217	237	54

Figure II.3: Radius distribution for TOIs.
The radius distribution of TOIs observed during the TESS primary mission is subdivided by host star spectral type (M, K, G, F, and A). False-positive TOIs and TOIs with no planetary radius are not included. Credit: Guerrero et al., 2021.

II.2 TESS FOLLOW-UP OBSERVATIONS

TESS aims to find small exoplanets orbiting bright stars that can be studied in details with follow-up observations, usually performed from the ground. These follow-up observations from the ground are required to constrain precise ephemeris and orbital parameters of the transiting object. Because TESS has a large field of view of 1440x1440 arcminutes, stars within 2.5 arcminutes of each other are extremely difficult to distinguish. TESS could attribute a drop in flux to a transiting exoplanet, when it is actually an eclipsing binary or an event that occurred on a nearby star. Following observations will allow for the validation of the planetary candidate, the estimation of the planetary mass through radial velocity measurements (Cloutier et al., 2018) and the characterization of exoplanet atmosphere using transmission spectroscopy (Kempton et al., 2018).

The TESS Follow-up Observing Program (TFOP) coordinates the majority of the follow-up observations of TOIs and other TESS planet candidates. Most of the follow-up work falls into five areas, each of which will have its own Sub Group (SG) (see Figure II.4). The SG1 uses seeing-limited photometry to detect false positives caused by nearby eclipsing binaries contaminating a candidate in the TESS image and to provide better light curves, ephemerides, and/or transit timing variations (TTVs). The SG2 is dedicated to reconnaissance spectroscopy, and provides spectroscopic parameters that more precisely constrain the masses and radii of host stars, detects false positives caused by spectroscopic binaries, and identifies stars that are not suitable for precise RV measurements. The SG3 provides high-resolution imaging with adaptive optics or speckle imaging to identify nearby objects not resolved in the TIC or by seeing-limited photometry. The SG4 works toward determining the planetary mass relative to the host star using precise radial velocity measurements. The SG5 uses space-based photometry with facilities such as HST, Spitzer, CHEOPS, and JWST, primarily to confirm and/or improve TESS photometric ephemerides, but also to provide improved light curves for transit events or, in some cases, TTVs.

In the course of my PhD, I have been involved especially in the SG1 doing ground-based photometry with ExTrA to validate the planetary nature of the companion and improve on the radius ratio measurement (see Section III.5.1). The large pixels of TESS means that in many cases follow-up photometry is needed to make sure the transit is happening on target. For shallow transits of less than 1 mmag, ground-based facilities can be used to rule out nearby eclipsing binaries (NEBs) on faint targets which are blended in the TESS pixel. With ExTrA we also have the opportunity to observe the transit in a different wavelength range from TESS (see Section III.1.1). I also followed the activity of the SG4 that focuses on precise RV measurement to confirm and characterize the exoplanet (see Section II.5 as an example).

The majority of the information gathered by the different sub groups is available via the Exoplanet Follow-up Observing Program for TESS (ExoFOP-TESS[1]) as reduced data,

---

[1] https://exofop.ipac.caltech.edu/tess/

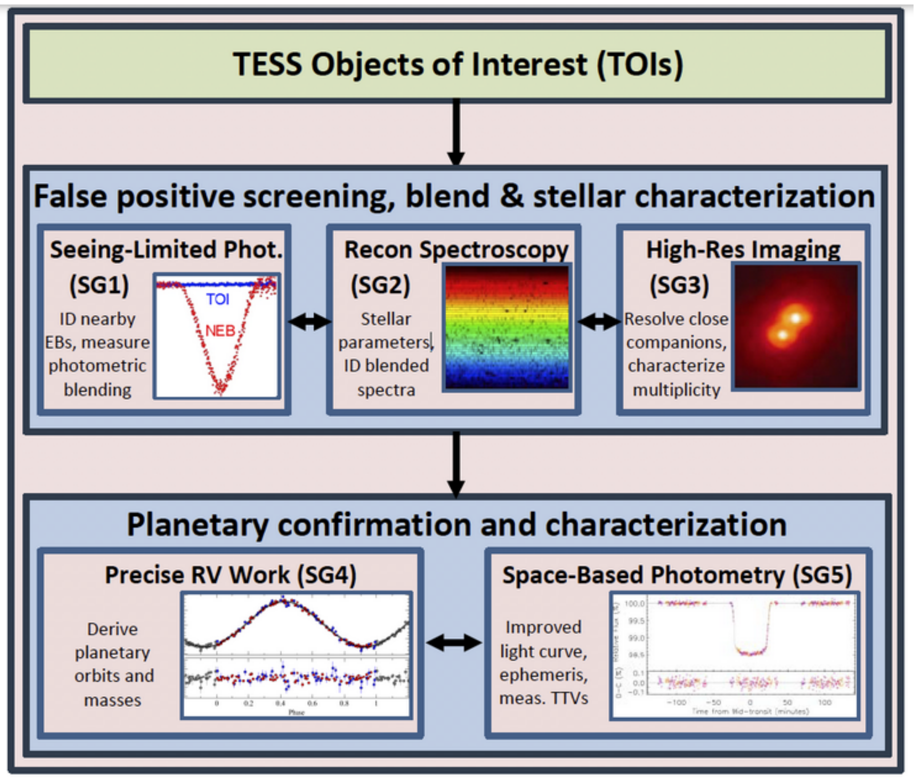

Figure II.4: TFOP sub groups.
The 5 sub groups of the TESS Follow-up Observing Program. Image credits clockwise from top left: KELT Survey, NOAO/AURA/NSF, Buchhave et al., 2011, Berta et al., 2012, Malavolta et al., 2016.

observing notes, and/or updated planetary and stellar parameters. I will use some of this information as priors for the modeling of TESS and ExTrA photometry (see Sections II.4 and III.3.2), and to collect complementary observations when writing a discovery paper (see Sections II.5 and III.4). I am also using ExoFOP-TESS to upload the analyses made with the ExTrA transits for the community to reach out to me if they are interested in adding these transits to their analysis (see Section III.7).

II.3 TESS OBJECTS OF INTEREST AROUND M DWARFS

To successfully detect new exoplanets orbiting M dwarfs with ExTrA and NIRPS, I first needed a sample of candidates to observe and confirm the presence of an exoplanet orbiting the target star. To organize myself, I created a table regrouping all the TESS candidates around M dwarfs that I update monthly with new TESS sectors, publications and results from the SG1 follow-up program to optimize the follow-up observations done with ExTrA. Indeed, a TOI's disposition is constantly updated as new observations are obtained. For example, if SG1 discovers an eclipsing binary that was blended in the TESS pixel and is responsible for the transit, the TOI's status is changed to NEB (for Near Eclipsing Binary). Similarly, TOIs are routinely re-assessed as TESS collects more data on them; this can include resolving false positives or discovering new candidates in the system. To sort out those candidates, I selected from the TOIs catalog systems with a stellar temperature below 4100K (it may seem high as it corresponds to the stellar temperature of a K7 star but as the uncertainties on this value can be important, I wanted to make sure I collected all potential candidates), and with a radius strictly smaller than 1 R_{Sun} to avoid red giant stars and stars with unknown radius (which are put automatically equal to 1 R_{Sun} within TFOP). I gathered all the TOIs matching these criteria in a table and added some valuable information that would be useful for follow-up observations. Out of the 441 TOIs currently in this table (as of March 2023), 28 were already known exoplanets before TESS observed them, 43 have been confirmed and published with a planetary radius and mass, 36 have been validated but without a mass estimation yet and 321 are still planet candidates. These TOIs are displayed in Period-Radius and Insolation-Radius diagrams in Figure II.5. The other TOIs are either ambiguous planet candidates, with lost ephemeris, or the planet candidate is found to be orbiting another star, ...

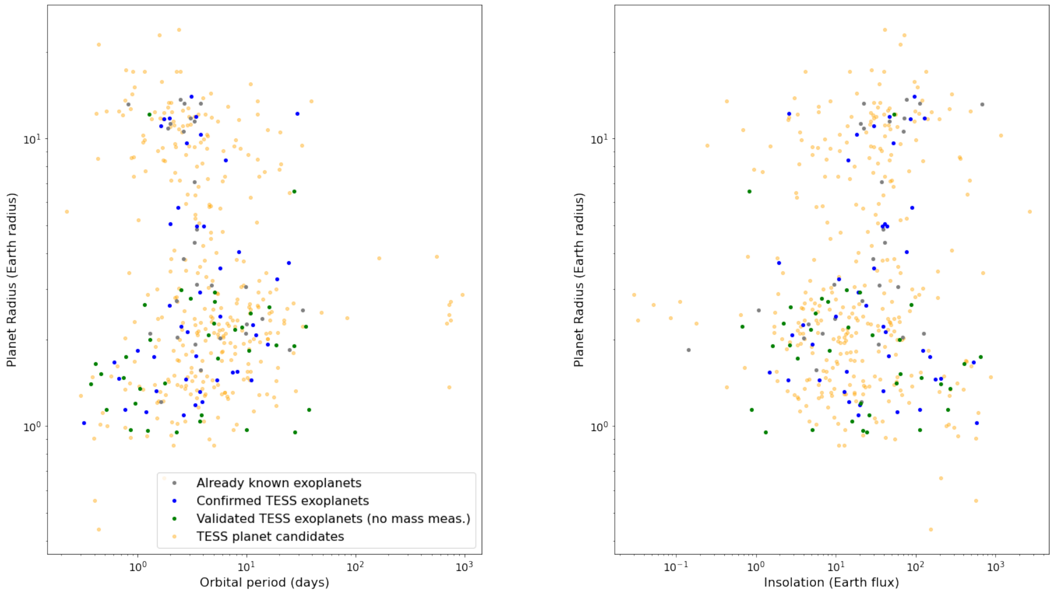

Figure II.5: Period-radius and Insolation-radius diagrams of TOIs around M dwarfs. The list is extracted directly from the table gathering the TESS candidates around M dwarfs last updated in March 2023.

II.3.1 *Parameters from TESS Follow-up Observing Program*

From the different working groups composing the TESS follow-up program, I gathered standard information on the star named as a TIC and on the planetary candidate named as a TOI, as well as the TESS sectors when the target was observed. To easily identify the star, I added to my table the position of the target on the sky using its right ascension and declination and its apparent magnitudes in different bands (TESS bandpass, V, J, K).

Regarding the planetary candidate, I chose to highlight the transit parameters such as the transit depth, the orbital period of the exoplanet, the time-of-transit center (or epoch) and the estimated planetary radius coming from the TESS automatic pipeline. These are the most useful information for follow-up observations as it will help us decide for which target and when we could possibly observe and validate the transit with our ground-based instrument ExTrA (see more detail in Chapter III). The distance of the exoplanet to the star in stellar radius unit, the exoplanet insolation and transmission spectroscopic metric from Kempton et al., 2018 that provides indication for the atmospheric characterization of the exoplanet, are also displayed. Finally, I collected the estimated planetary mass and semi-amplitude K in $\mathrm{m/s}$ calculated using Chen and Kipping, 2017 and an optimistic spectrograph time computed from the expected semi-amplitude and magnitude of the star to estimate the mass of the exoplanet using the radial velocity method.

II.3.2 *Additional computed parameters*

Stellar parameters

To make the sample homogeneous, I recomputed the stellar parameters for all the selected TOIs. Precise and accurate parameters for late-type (late K and M) dwarf stars are critical for characterizing any orbiting exoplanets, but such determinations have been impacted by these stars complex spectra and differences from the Sun. I first collected the stars magnitude in the K_s bandpass centered at 2.15μm from the Two Micron All Sky Survey (2MASS) (Skrutskie et al., 2006). Observations were made using two dedicated 1.3m telescopes located at Mount Hopkins, Arizona, and Cerro Tololo, Chile and cover 99.998% of the celestial sphere in the near-infrared. Distances were provided in the latest TESS Input Catalog (Paegert et al., 2021) using the parallax measured with the GAIA satellite (Gaia Collaboration et al., 2018). The apparent shift in the position of stars in the sky also known as parallax is caused by Earth's yearly orbit around the Sun. Parallax measurements can be used to calculate the distance to the stars: stars closer to us have a apparent shift in the sky larger than stars further away. Combining the apparent magnitude in the K_s band and the distance, we can compute the absolute magnitude in the K band and use this value to derive the star mass, radius and effective temperature.

Mann et al., 2015 used an empirically calibrated method to estimate spectroscopic effective stellar temperature and the Stefan-Boltzmann law to calculate the radii of 183 nearby

K7-M7 single stars. After that, they developed model-independent relationships between T_{eff} or absolute magnitude and radius, as well as between color and T_{eff}. The relationship between absolute K_s magnitude and stellar radius can predict radii with a $\sim$ 3% accuracy. In a later paper, Mann et al., 2019 presented an empirical relationship between the absolute K_s magnitude and M_{star} spanning a stellar mass range from 0.075 to 0.70 M_{Sun} and derived from 62 nearby binaries. They calculated the total mass of each system using their orbital parameters, with precision better than 1% in the best cases and calibrated the $M_{Ks} - M_*$ relation using these total masses, K_s magnitudes and system parallaxes. This work can be used directly via the code available on this M$_-M_K-$[2] GitHub page and is meant to provide realistic masses and uncertainties of low-mass stars given K_s magnitude and distance. With both stellar mass and radius, we infer the stellar density for each star in our sample and we use that value as a prior during the modeling of the TESS and/or ExTrA photometry.

We estimated the stellar effective temperature using the color-T_{eff} relation presented in Mann et al., 2015. We computed T_{eff} for each star in our sample using the V-J color, as well as the J-H color that was found to mitigate the lack of information on the stellar metallicity. This method is different from the one used to estimate the stellar temperature in the TICv8 catalog (Stassun et al., 2019), where they calculated it from Gaia G_{BP} and G_{RP} magnitudes using custom relations developed in Mann, Gaidos, and Ansdell, 2013 from photometrically calibrated spectra, but the values are consistent within 1σ.

Expected planetary mass

Otegi, Bouchy, and Helled, 2020 presented in their paper an updated exoplanet catalog based on precise mass and radius measurements of transiting exoplanets. The resulting mass-radius diagram shows two distinct populations, corresponding to rocky and volatile-rich exoplanets which overlap in both mass and radius. They showed that the population of rocky exoplanets has a relatively low density variability and ends at a mass of $\sim$ 25 M_{Earth}, possibly indicating the maximum core mass that can be formed. They separated the two populations using the composition line of pure water and infer two new empirical mass-radius relations based on this data. The two equations are presented below. While their results for the two regimes are consistent with previous research, the mass-radius relationships better match the population in the transition region from rocky to volatile-rich exoplanets. Depending on the estimated radius of each TOI, we computed the estimated mass for the two populations using the two equations below.

$$M = \begin{cases} (0.90 \pm 0.06)\, R^{(3.45\pm0.12)} & , if\ \rho > 3.3\, g\, cm^{-3} \\ (1.74 \pm 0.38)\, R^{(1.58\pm0.10)} & , if\ \rho < 3.3\, g\, cm^{-3} \end{cases} \tag{II.1}$$

SNR and expected precision

---

[2] https://github.com/awmann/M$_-M_K-$

A signal-to-noise ratio (SNR) is provided from the data validation report of the TESS pipeline to estimate the quality of the TESS data. However some of the values did not seem coherent with the precision on the radius ratio. We decided to recompute the SNR of TESS using the ratio between the the transit depth and the uncertainty value of the transit depth proposed by TFOP. This information on the quality of the TESS photometry is used later on to estimate for which candidates we hope to obtain a better precision than TESS with a few ExTrA transits.

II.3.3 *Summary of follow-up observations*

Another very important use of this table is to gather the follow-up observations of the different TOIs. As a TFOP member I have access to information on the follow-up observations from photometric and velocimetric instruments which I displayed on this table, as well as planetary radius and mass obtained from published articles.

I am also using this table to select the different target that we observe with ExTrA. Starting with our first published results of ExTrA capabilities (see Section III.4), where we obtained a precision of 0.1mmag/30min bin for a star with $J = 10.91$, we were able to estimate the SNR that we expect for any star of the table depending on its magnitude and the transit depth and duration, and how many transits we would need to observe with ExTrA to obtain the same precision as for TOI-269 b, or a SNR of 200 depending which case scenario happens with the smallest number of transits. After the observations are done with ExTrA, I update the table to follow the progress on each target.

The first lines of the table with all parameters (version of April 2023) is presented below and the full list of TOIs with some of the columns in Appendix A. From left to right, is displayed the TIC ID, TOI name, current disposition from TESS SG1 (Planet Candidate, Validated Planet, Planet, ...), star magnitude in multiple bands, right ascension and declination of the star, transit parameters with the epoch and depth, the period and radius of the candidate, the stellar temperature estimated by TFOP and the one I estimated using Mann et al., 2015, the estimated planet insolation and habitable zone around the star, the stellar radius and mass from the TESS community and the ones I recomputed using Mann et al., 2015 and Mann et al., 2019, the scaled semi-major axis of the orbit, the predicted semi-amplitude of the signal in radial velocity, the estimated planetary mass using Chen and Kipping, 2017 and Otegi, Bouchy, and Helled, 2020, the transmission spectroscopic metric by Kempton et al., 2018, the TESS sectors where/when the target was observed, and some relevant notes from the TESS SG2 and SG4. We also present the different estimated SNR from TESS and ExTrA (using two different analysis on TOI-269 b), the number of ExTrA transits required to get the expected precision or a SNR of 200, and the estimated time for a 3-sigma mass measurement. In the last part, we have an overview of already existing observations, with the published planetary radius and/or mass, the complementary observations, other existing names for the planet, observations with ExTrA and for which science objective (if the TOI name is in green, the transit is visible in the

ExTrA photometry, in orange the target was observed but no clear transit is visible in the data), some additional comment, the published paper relative to the planet, if I already fitted the TESS photometry and a link to the ExoFOP TESS web page for more information.

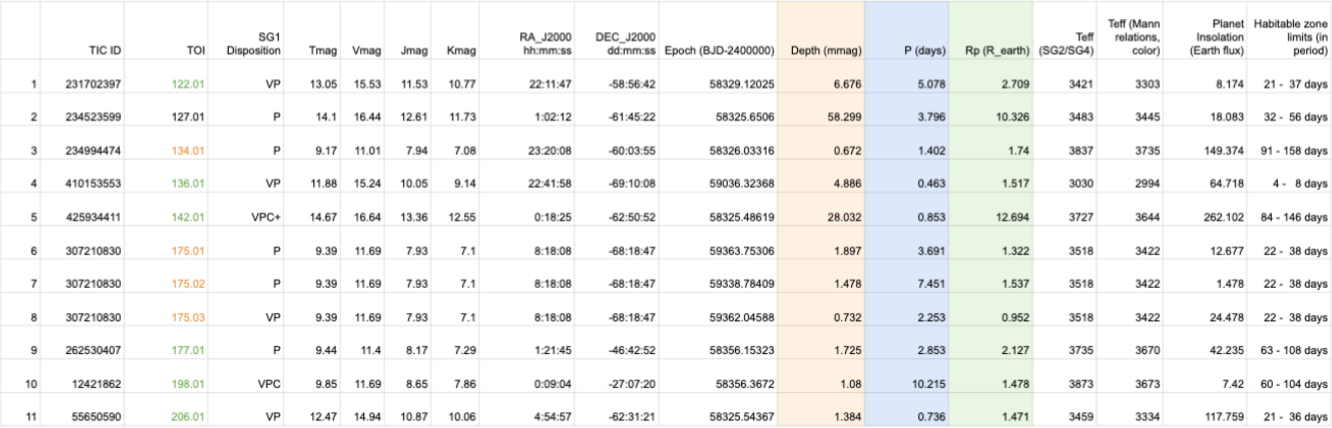

	TIC ID	TOI	SG1 Disposition	Tmag	Vmag	Jmag	Kmag	RA_J2000 hh:mm:ss	DEC_J2000 dd:mm:ss	Epoch (BJD-2400000)	Depth (mmag)	P (days)	Rp (R_earth)	Teff (SG2/SG4)	Teff (Mann relations, color)	Planet Insolation (Earth flux)	Habitable zone limits (in period)
1	231702397	122.01	VP	13.05	15.53	11.53	10.77	22:11:47	-58:56:42	58329.12025	6.676	5.078	2.709	3421	3303	8.174	21 - 37 days
2	234523599	127.01	P	14.1	16.44	12.61	11.73	1:02:12	-61:45:22	58325.6506	58.299	3.796	10.326	3483	3445	18.083	32 - 56 days
3	234994474	134.01	P	9.17	11.01	7.94	7.08	23:20:08	-60:03:55	58326.03316	0.672	1.402	1.74	3837	3735	149.374	91 - 158 days
4	410153553	136.01	VP	11.88	15.24	10.05	9.14	22:41:58	-69:10:08	59036.32368	4.886	0.463	1.517	3030	2994	64.718	4 - 8 days
5	425934411	142.01	VPC+	14.67	16.64	13.36	12.55	0:18:25	-62:50:52	58325.48619	28.032	0.853	12.694	3727	3644	262.102	84 - 146 days
6	307210830	175.01	P	9.39	11.69	7.93	7.1	8:18:08	-68:18:47	59363.75306	1.897	3.691	1.322	3518	3422	12.677	22 - 38 days
7	307210830	175.02	P	9.39	11.69	7.93	7.1	8:18:08	-68:18:47	59338.78409	1.478	7.451	1.537	3518	3422	1.478	22 - 38 days
8	307210830	175.03	VP	9.39	11.69	7.93	7.1	8:18:08	-68:18:47	59362.04588	0.732	2.253	0.952	3518	3422	24.478	22 - 38 days
9	262530407	177.01	P	9.44	11.4	8.17	7.29	1:21:45	-46:42:52	58356.15323	1.725	2.853	2.127	3735	3670	42.235	63 - 108 days
10	12421862	198.01	VPC	9.85	11.69	8.65	7.86	0:09:04	-27:07:20	58356.3672	1.08	10.215	1.478	3873	3673	7.42	60 - 104 days
11	55650590	206.01	VP	12.47	14.94	10.87	10.06	4:54:57	-62:31:21	58325.54367	1.384	0.736	1.471	3459	3334	117.759	21 - 36 days

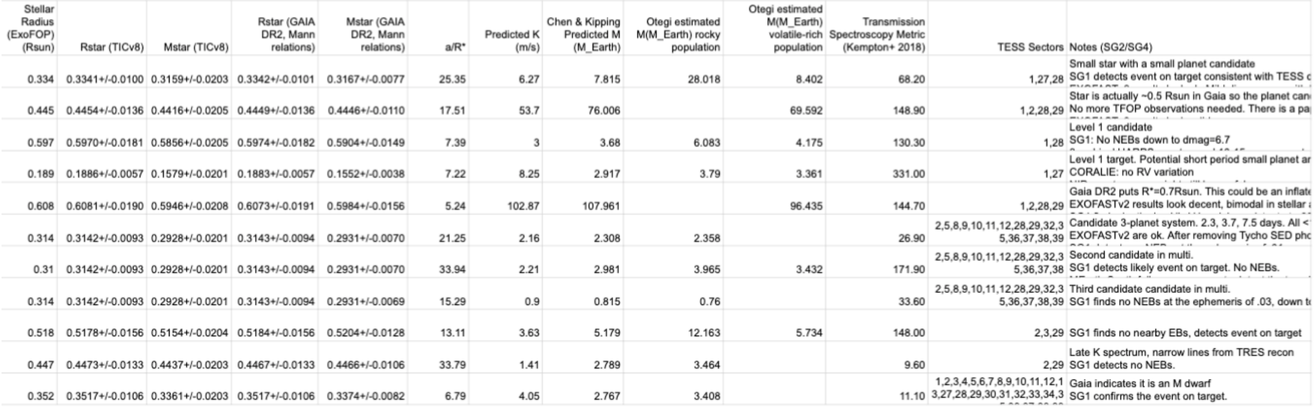

Stellar Radius (ExoFOP) (Rsun)	Rstar (TICv8)	Mstar (TICv8)	Rstar (GAIA DR2, Mann relations)	Mstar (GAIA DR2, Mann relations)	a/R*	Predicted K (m/s)	Chen & Kipping Predicted M (M_Earth)	Otegi estimated M(M_Earth) rocky population	Otegi estimated M(M_Earth) volatile-rich population	Transmission Spectroscopy Metric (Kempton+ 2018)	TESS Sectors	Notes (SG2/SG4)
0.334	0.3341+/-0.0100	0.3159+/-0.0203	0.3342+/-0.0101	0.3167+/-0.0077	25.35	6.27	7.815	28.018	8.402	68.20	1,27,28	Small star with a small planet candidate SG1 detects event on target consistent with TESS c
0.445	0.4454+/-0.0136	0.4416+/-0.0205	0.4449+/-0.0136	0.4446+/-0.0110	17.51	53.7	76.006		69.592	148.90	1,2,28,29	Star is actually ~0.5 Rsun in Gaia so the planet can No more TFOP observations needed. There is a pa
0.597	0.5970+/-0.0181	0.5856+/-0.0205	0.5974+/-0.0182	0.5904+/-0.0149	7.39	3	3.68	6.083	4.175	130.30	1,28	Level 1 candidate SG1: No NEBs down to dmag=6.7
0.189	0.1886+/-0.0057	0.1579+/-0.0201	0.1883+/-0.0057	0.1552+/-0.0038	7.22	8.25	2.917	3.79	3.361	331.00	1,27	Level 1 target. Potential short period small planet ar CORALIE: no RV variation
0.608	0.6081+/-0.0190	0.5946+/-0.0208	0.6073+/-0.0191	0.5984+/-0.0156	5.24	102.87	107.961		96.435	144.70	1,2,28,29	Gaia DR2 puts R*=0.7Rsun. This could be an inflate EXOFASTv2 results look decent, bimodal in stellar
0.314	0.3142+/-0.0093	0.2928+/-0.0201	0.3143+/-0.0094	0.2931+/-0.0070	21.25	2.16	2.308	2.358		26.90	2,5,8,9,10,11,12,28,29,32,35,36,37,38,39	Candidate 3-planet system. 2.3, 3.7, 7.5 days. All < EXOFASTv2 are ok. After removing Tycho SED pho
0.31	0.3142+/-0.0093	0.2928+/-0.0201	0.3143+/-0.0094	0.2931+/-0.0070	33.94	2.21	2.981	3.965	3.432	171.90	2,5,8,9,10,11,12,28,29,32,35,36,37,38	Second candidate in multi. SG1 detects likely event on target. No NEBs.
0.314	0.3142+/-0.0093	0.2928+/-0.0201	0.3143+/-0.0094	0.2931+/-0.0069	15.29	0.9	0.815	0.76		33.60	2,5,8,9,10,11,12,28,29,32,35,36,37,38,39	Third candidate candidate in multi. SG1 finds no NEBs at the ephemeris of .03, down t
0.518	0.5178+/-0.0156	0.5154+/-0.0204	0.5184+/-0.0156	0.5204+/-0.0128	13.11	3.63	5.179	12.163	5.734	148.00	2,3,29	SG1 finds no nearby EBs, detects event on target
0.447	0.4473+/-0.0133	0.4437+/-0.0203	0.4467+/-0.0133	0.4466+/-0.0106	33.79	1.41	2.789	3.464		9.60	2,29	Late K spectrum, narrow lines from TRES recon SG1 detects no NEBs.
0.352	0.3517+/-0.0106	0.3361+/-0.0203	0.3517+/-0.0106	0.3374+/-0.0082	6.79	4.05	2.767	3.408		11.10	1,2,3,4,5,6,7,8,9,10,11,12,13,27,28,29,30,31,32,33,34,3	Gaia indicates it is an M dwarf SG1 confirms the event on target.

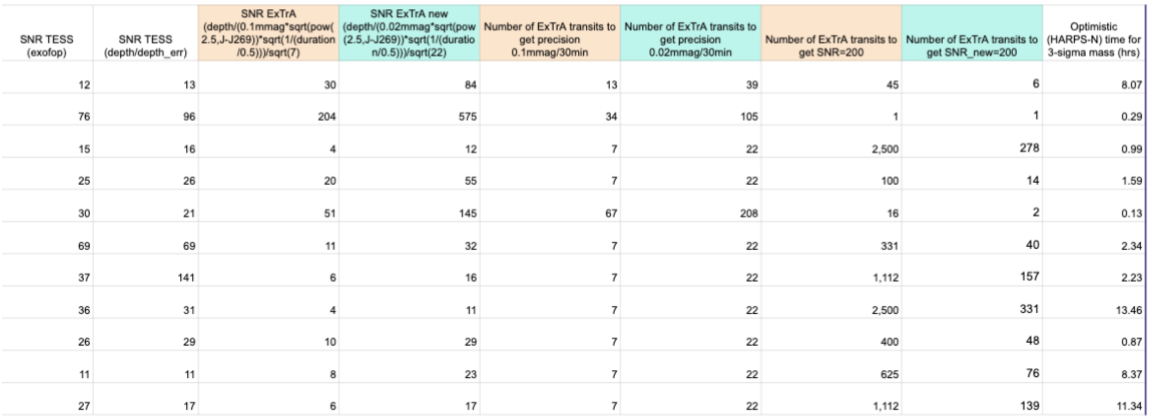

SNR TESS (exofop)	SNR TESS (depth/depth_err)	SNR ExTrA (depth/(0.1mmag*sqrt(pow(2.5,J-J269))*sqrt(1/(duration/0.5)))/sqrt(7)	SNR ExTrA new (depth/(0.02mmag*sqrt(pow(2.5,J-J269))*sqrt(1/(duration/0.5)))/sqrt(22)	Number of ExTrA transits to get precision 0.1mmag/30min	Number of ExTrA transits to get precision 0.02mmag/30min	Number of ExTrA transits to get SNR=200	Number of ExTrA transits to get SNR_new=200	Optimistic (HARPS-N) time for 3-sigma mass (hrs)
12	13	30	84	13	39	45	6	8.07
76	96	204	575	34	105	1	1	0.29
15	16	4	12	7	22	2,500	278	0.99
25	26	20	55	7	22	100	14	1.59
30	21	51	145	67	208	16	2	0.13
69	69	11	32	7	22	331	40	2.34
37	141	6	16	7	22	1,112	157	2.23
36	31	4	11	7	22	2,500	331	13.46
26	29	10	29	7	22	400	48	0.87
11	11	8	23	7	22	625	76	8.37
27	17	6	17	7	22	1,112	139	11.34

HARPS/CORALIE/CARMENES/OTHERS Mass (M_earth)	Observations	Names	Observations ExTrA	ExTrA WP	Commentaires	Articles	Radius estimation from article (R_earth)	fit TESS	ExoFOP-TESS Object page
	LCO-CTIO, TRAPPIST,		Oui	WP1		https://arxiv.org/pdf/2010.15905.pdf	2.72±0.18	OK	ExoFOP
	HATSouth	HATS-71 b	No need	WP1(stop)		https://arxiv.org/pdf/1812.09406.pdf	1.080±0.016RJ	OK	ExoFOP
4.60±0.56	HARPS, LCO-SAAO, SMARTS,		Oui (too small depth)		ESPRESSO-GTO (P105)	https://arxiv.org/pdf/1812.08145.pdf https://arxiv.org/pdf/2001.09175.pdf	1.39±0.09	OK	ExoFOP
	LCO-CTIO, MKO CDK700	LHS 3844	Oui	WP1(stop)	paper in prep(Nicola)	https://arxiv.org/pdf/1809.07242.pdf	1.32±0.02	OK	ExoFOP
			Oui	WP1				OK	ExoFOP
2.46 ± 0.31	SSO, LCO, MEarth, SMARTS, Magellan,	L 98-59 b	Oui, now	WP2	ESPRESSO-GTO (P105) 4th non-transiting planet	https://arxiv.org/pdf/1903.08017.pdf https://arxiv.org/pdf/1905.10669.pdf	1.35 ± 0.07	OK	ExoFOP
2.26 ± 0.50	SSO, LCO, MEarth, SMARTS, Magellan,	L 98-59 c	Oui	WP2	ESPRESSO-GTO (P105) 4th non-transiting planet	https://arxiv.org/pdf/1903.08017.pdf https://arxiv.org/pdf/1905.10669.pdf	1.57 ± 0.14	OK	ExoFOP
upper 0.98	SSO, LCO, MEarth, SMARTS, Magellan,	L 98-59 d	Oui (too small depth)	WP2	ESPRESSO-GTO (P105) 4th non-transiting planet	https://arxiv.org/pdf/1903.08017.pdf https://arxiv.org/pdf/1905.10669.pdf	0.80 ± 0.05	OK	ExoFOP
3.34 ± 0.72	HARPS, Minerva, PFS	GJ 3090	Oui		2nd planet in RV (17Me @ 13d)	https://arxiv.org/abs/2207.14121	2.13 ± 0.11	OK	ExoFOP
	HARPS, CORALIEvett, LCO,		Oui	WP1	ESPRESSO-GTO (P105)	paper in prep by Oddo et al. (CHEOPS)		OK	ExoFOP
			Oui	stop (old WP1)	NE-CAM (22/11/19)	https://arxiv.org/abs/2201.12661	1.30 ± 0.05	OK	ExoFOP

II.4 ANALYSIS OF TESS LIGHT CURVES

The TESS photometric data are processed by the NASA Ames Science Processing Operations Center (SPOC; Jenkins et al., 2016) and the Massachusetts Institute of Technology (MIT) Quick-Look Pipeline (QLP; Huang et al., 2020a,b). SPOC and QLP are both light curve extraction pipelines, with the exception that QLP only extracts light curves from FFIs. These systems were identified as potential candidates by either the SPOC or the QLP, and then designated as TESS Objects of Interest (TOIs; Guerrero et al., 2021). The MAST archive[3] provides calibrated FFIs, target pixel files, and data validation reports. Photometric time series from SPOC with 2min cadence data and QLP light curves are also easily accessible.

SPOC produces calibrated pixels, Simple Aperture Photometry (SAP) flux (Morris et al., 2017) and Pre-search Data Conditioning (PDCSAP) corrected flux time series (Stumpe et al., 2012). For the latter, systematic noise of non-stellar origin, such as instrumental effects and scattered moonlight, is removed. The detrending algorithm can in some cases also remove periodic stellar variability, especially if the period is longer than the observation baseline. The light curves are also corrected for dilution, based on the positions and TESS magnitudes listed in the TIC. SPOC conducts their exoplanet search on the PDCSAP light curves (Jenkins, 2002; Jenkins et al., 2010) and produces validation reports for all targets (Li et al., 2019; Twicken et al., 2018).

The MIT developed the Quick Looks Pipeline (QLP), which extracts photometry for all stars in the TIC and observed by TESS from the FFIs. According to Huang et al., 2020a, the SAP flux is extracted and detrended using a high-pass filter while excluding anomalous exposures (Huang et al., 2020b). The detrending algorithm, which is an implementation of a Kepler-style basis spline, removes contributions from both stellar signals and instrumental noise (Vanderburg and Johnson, 2014). The detrended flux time series from QLP is called KSPSAP and differs from PDCSAP primarily in the post-processing of the light curves.

I analyzed consistently all the TESS light curves provided by MAST for the TOIs orbiting M dwarfs to have an idea of the quality of the data, the variations in the photometry and have a first look on the transits. To model the TESS photometry, I used the software package juliet developed by Espinoza, Kossakowski, and Brahm, 2019 and publicly available on GitHub. The procedure to use juliet to model photometric data is described in Section III.3.2. The batman package (Kreidberg, 2015) is used to model the transit, and the fit is done using nested sampling algorithm that we parametrized using non-informative priors except for the period P, the time-of-transit center t_0, and the stellar density ρ_*. I decided to use Gaussian process (GP) to correct for the remaining systematics in the TESS photometry (see Section III.3.2.2 on the use of GPs to model systematics in the photometric data). Two specific routines were created to model the TESS light curves, one for the 2min cadence SPOC data and the other for the 30min cadence QLP data, and provides as an output the

---

[3] https://mast.stsci.edu/portal/Mashup/Clients/Mast/Portal.html

posterior parameters of the transit fit and the fitted light curves. Some example plots are presented in Figure II.6.

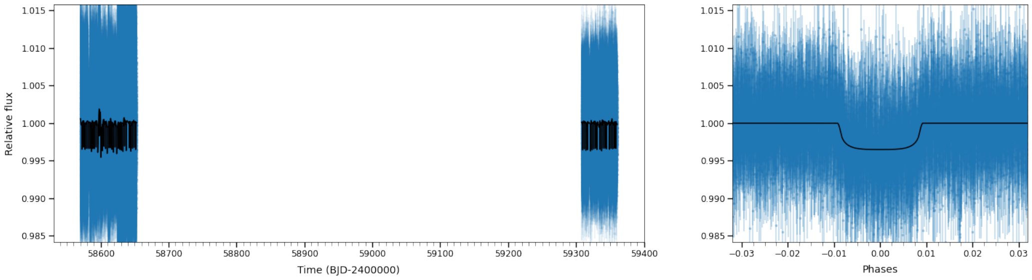

(a) Modeling of the TESS photometry of TOI-771 using the extracted PDCSAP 2min cadence data from SPOC.

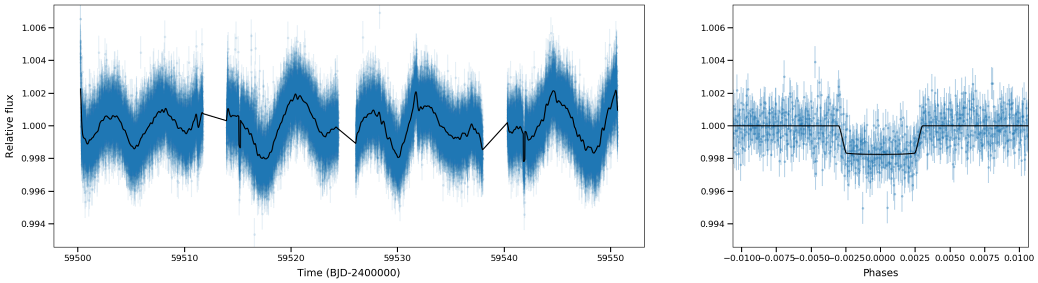

(b) Modeling of the TESS photometry of TOI-5554 using the extracted PDCSAP 2min cadence data from SPOC. We can see some variations in the photometry that are well corrected by the GP.

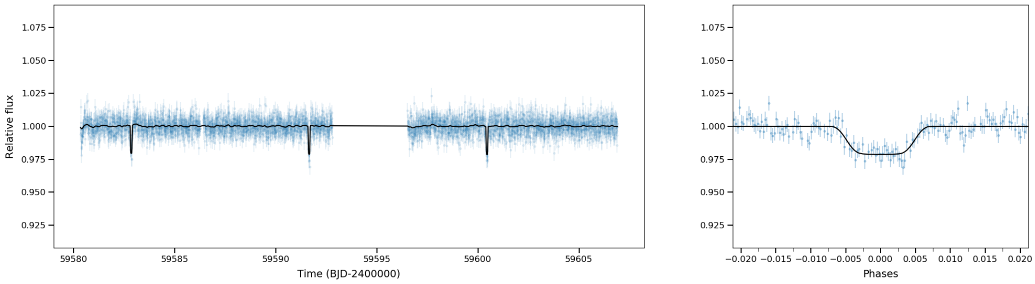

(c) Modeling of the TESS photometry of TOI-5573 using the extracted 30min cadence data from QLP.

Figure II.6: Examples of TESS photometry.
Plots from the modeling of the TESS photometry. *Left*: TESS photometry time series from one or multiple sectors along with the maximum a posteriori (solid black line). *Right*: Phase-folded light curve to the period of the exoplanet (black line corresponds to the maximum a posteriori).

II.5 TOI-663 : A NEWLY DISCOVERED MULTI-PLANETARY SYSTEM.

In this section, I will present a draft of a new discovery paper that I have been working on to validate and characterize a multi-planetary systems with three transiting mini-Neptunes first detected by the TESS mission and orbiting around a M dwarf. For this paper, I gathered multiple photometry and radial velocity datasets and modeled them jointly to characterize the three exoplanets.

Astronomy & Astrophysics manuscript no. output
September 25, 2023

TOI-663 : a newly discovered multi-planetary system with three transiting mini-Neptunes orbiting an early M star.

M. Cointepas[1,2] ★, F. Bouchy[2], J.M. Almenara[1], X. Bonfils[1], N. Astudillo-Defru[3], H. Knierim[7], M. Stalport[25], L. Mignon[2], N. Grieves[2], J. Bean[35], M. Brady[35], J. Burt[17], B.L. Canto Martins[9], K.A. Collins[4], K.I. Collins[5], X. Delfosse[1], J. R. de Medeiros[9], B.-O. Demory[39], C. Dorn[8], T. Forveille[1], A. Fukui[27,10], T. Gan[6], Y. Gómez Maqueo Chew[40], S. Halverson[17], R. Helled[7], I. Helm[5], T. Hirano[31,32], K. Horne[24], S. B. Howell[16], K. Isogai[28,29], D. Kasper[35], K. Kawauchi[30,29], J.H. Livingston[31,32,33], B. Massey[22], R. A. Matson[20], F. Murgas[10,11], N. Narita[27,31,10], E. Palle[10,11], H.M. Relles[4], L. Sabin[41], N. Schanche[44], R.P. Schwarz[4], A. Seifahrt[35], A. Shporer[12], G. Stefansson[37,43], J. Sturmer[36], M. Tamura[34,31,32], T.-G. Tan[26], J.D. Twicken[42,16], N. Watanabe[29], R.D. Wells[39], F.P. Wilkin[23], G.R. Ricker[12], S. Seager[12,13,14], J.N. Winn[37], and J.M. Jenkins[16]

(Affiliations can be found after the references)

Received ; Accepted

ABSTRACT

We present here the detection of three exoplanets orbiting the early M dwarf TOI-663 (TIC 54962195, $V = 13.7$ mag, $J = 10.4$ mag, $R_\star = 0.512 \pm 0.015\ R_\odot$, $M_\star = 0.514 \pm 0.012\ M_\odot$, d = 64 pc). TOI-663 b, c and d, with respective radii of $2.27 \pm 0.10\ R_\oplus$, $2.26 \pm 0.10\ R_\oplus$, $1.92 \pm 0.13\ R_\oplus$, and masses of $4.45 \pm 0.65\ M_\oplus$, $3.65 \pm 0.97\ M_\oplus$, $<5.2\ M_\oplus$ at 99%, are located just above the radius valley which separates rocky and volatile-rich exoplanets. The planet candidates are identified in two TESS sectors and are validated with ground-based photometric follow-up, precise radial-velocity measurements and high-resolution imaging. We used the software package `juliet` to model jointly the photometric and radial-velocity datasets, with Gaussian processes applied to correct for systematics. The three planets discovered in the TOI-663 system are low-mass mini-Neptunes with radii significantly larger than those of rocky analogues, implying that volatiles, such as water, must predominate. In addition to this internal structure analysis, we also performed a dynamical analysis that confirmed the stability of the system. The three exoplanets in the TOI-663 system, similarly to other sub-Neptunes orbiting M dwarfs, have been found to have lower densities than planets of similar size orbiting stars of different spectral types.

Key words. Planetary systems – Techniques: photometric – Techniques: radial velocities – Stars : low-mass – Planets and satellites: detection

1. Introduction

Small exoplanets discovered around other stars could be similar or very different to those of our solar system in terms of composition, formation history, and atmospheric properties. They are also difficult to study due to the small transit and radial-velocity (RV) signals they produce. But recent surveys have helped improve the sensitivity towards the detection of smaller exoplanets like the Transiting Exoplanet Survey Satellite (TESS) that was launched in 2018 to conduct an all-sky survey and discover transiting planets around the nearest and brightest stars (Ricker et al. 2015).

When looking for small and cool exoplanets, low-mass stars have distinct advantages and are particularly interesting. The transit depth and radial-velocity semi-amplitude caused by small exoplanets orbiting M dwarfs are much greater than those caused by similar planets orbiting larger stars of earlier spectral types, making such planets easier to detect. More importantly, such systems are excellent candidates for atmospheric characterization using transmission or thermal emission spectroscopy (e.g., Kempton et al. 2018, Batalha et al. 2018). To determine which planets are predominantly rocky or volatile-rich and whether they could have a significant atmosphere, precise radius measurements from transit surveys must be combined with mass measurements from dynamical observations, such as precise RV measurements. Exoplanets with precise mass, radius and bulk density measurements orbiting M dwarfs are thus important objects for better understanding the so-called radius valley separating the population of super-Earths and mini-Neptunes (e.g. Fulton et al. 2017; Mayo et al. 2018; Cloutier & Menou 2020; Hardegree-Ullman et al. 2020).

The radius valley around M dwarfs is located at slightly smaller radii than around Sun-like stars (Fulton et al. 2017; Cloutier & Menou 2020) and marks the transition between rocky super-Earths and mini-Neptunes that host H/He envelopes (Owen & Wu 2017). A variety of physical mechanisms have been proposed to explain the emergence of the radius valley including photo-evaporation, core-powered mass loss (Jin & Mordasini 2018; Gupta & Schlichting 2020; Wyatt et al. 2020), or directly as an outcome of the planet formation process wherein Super-Earths form at later times in either a gas-poor or completely gas-depleted environment (Lee & Connors 2021; Lopez & Rice 2018). Each of these mechanisms predicts a unique dependence of radius valley on orbital period such that measuring the radius valley's slope provides direct insight into the origin of the radius valley. Cloutier & Menou (2020) discov-

---

★ Corresponding author: `marion.cointepas@univ-grenoble-alpes.fr` ered that the radius valley separating rocky and gaseous planets exhibits a negative slope with insolation around low-mass stars, as opposed to the positive slope found around Solar-type stars. This supports models of direct terrestrial planet formation in a gas-poor environment. The different slopes of models of gas-depleted formation and thermally-driven mass loss naturally carve out a subset of the period-radius parameter space within which the two models make opposing predictions about the bulk composition of planets. Characterizing the bulk composition of transiting planets allows us to determine whether the M dwarf radius valley originated directly from planet formation or as a result of post-formation atmospheric escape.

Multiple transiting planet systems are particularly interesting as they provide a unique opportunity for direct comparative planetology (Millholland et al. 2017) because the exoplanets formed within the same protoplanetary disk and evolved around the same host star. These systems also allow studies of planet-planet interactions (Barros et al. 2015) and planetary formation and migration (Delisle 2017). The discovery and accurate characterization of a system with multiple transiting planets thus represent a significant addition to the current knowledge about planetary systems formation. Furthermore transiting multi-planetary systems may contain additional long-period planets not yet detected. Indeed, deep searches to find additional exoplanets have already been conducted for a few stars and both photometry and RV follow-up of transiting systems have successfully detected additional transiting exoplanets (e.g. Trappist-1 system (Gillon et al. 2017; Luger et al. 2017) or LHS 1140 system (Lillo-Box et al. 2020)).

Here we present the discovery of three new exoplanets orbiting around the same M1 type star. This discovery was made using the TESS satellite, multiple ground-based photometry facilities like ExTrA and the LCO network, and precise radial velocity measurements from HARPS, MAROON-X, IRD and ESPRESSO. Section 2 presents an analysis of the stellar properties of TOI-663. Section 3 describes the observations and data used in this study, including photometry from space and from the ground, radial velocity measurements and high resolution imaging. Section 4 presents the global analysis of the available data in order to constrain the planetary properties. Section 5 presents the discussion and conclusion.

2. Stellar parameters

TOI-663 is an M-type star located at a distance of 64.23±0.18 pc (Gaia Collaboration et al. 2018, Lindegren et al. 2018, and Bailer-Jones et al. 2018). The astrometry, photometry, and stellar parameters are reported in Table 1.

TOI-663 mass and radius are derived from the stellar parallax and K_s-band magnitude, used to compute the absolute K_s-band magnitude M_{K_s}, and the empirically-derived M dwarf mass-luminosity and radius-luminosity relations from Mann et al. (2019) and Mann et al. (2015) respectively. The analysis by Mann includes stars with close-to-solar metallicities. We used `SpecMatch-Emp`[1] (Yee et al. 2017) and HARPS high-resolution spectra of TOI-663 to estimate the stellar metallicity, for which we found a value around 0.07 ± 0.12 dex (but the five best matches are spread over ~ 0.5 dex so the metallicity remains poorly constrained), confirmed the stellar radius and obtained a more precise effective temperature than the one computed from the Mann et al. (2015, 2019) empirical relations.

Table 1. Stellar parameters for TOI-663 (TIC 54962195, UCAC4 408-053407, 2MASS J10401596-0830385, WISE J104015.85-083039.4, APASS 3855837).

Parameter	Value	Refs
Astrometry		
Right ascension (J2015.5), α	$10^{h}40^{m}15.8^{s}$	1,2
Declination (J2015.5), δ	$-08^{\circ}30'39.9''$	1,2
Parallax, [mas]	15.639 ± 0.023	1,2
Distance, d [pc]	64.23 ± 0.18	1,2
Proper motion RA [mas/year]	-141.994 ± 0.030	1,2
Proper motion D [mas/year]	-83.131 ± 0.029	1,2
Photometry		
V [mag]	13.667 ± 0.023	3
TESS magnitude [mag]	11.7602 ± 0.0074	3
J [mag]	10.448 ± 0.026	4
H [mag]	9.828 ± 0.022	4
K_s [mag]	9.607 ± 0.021	4
Stellar parameters		
Spectral type	M1V	5
M_{K_s} [mag]	5.571 ± 0.022	8
Effective temperature, $T_{\rm eff}$ [K]	3681 ± 70	7,8
Surface gravity, $\log g$ [cgs]	4.7266 ± 0.0085	3
Metallicity, [Fe/H] [dex]	0.07 ± 0.12	7,8
Stellar radius, $R_\star$ [$R_\odot$]	0.512 ± 0.015	1,6,8
Stellar mass, $M_\star$ [$M_\odot$]	0.514 ± 0.012	1,6,8
$\log R'_{HK}$	-4.81 ± 0.15	8

References : 1) Gaia Collaboration et al. (2018), 2) Lindegren et al. (2018), 3) Stassun et al. (2019), 4) Cutri et al. (2003), 5) Pecaut & Mamajek (2013), 6) Mann et al. (2015, 2019), 7) Yee et al. (2017), 8) This work

We determine the stellar radius of TOI-663 independently by modeling the spectral energy distribution (SED) with stellar atmosphere and evolution models. To construct the SED, we used the magnitudes from Gaia DR2 (Evans et al. 2018; Maíz Apellániz & Weiler 2018), the 2-Micron All-Sky Survey (2MASS, Skrutskie et al. 2006a; Cutri et al. 2003), and Wide-field Infrared Survey Explorer (WISE, Wright et al. 2010; Cutri & et al. 2013). We modeled these magnitudes using the procedure described in Díaz et al. (2014). We used informative priors for the effective temperature ($T_{\rm eff}$), and metallicity ([Fe/H]) from the analysis of the HARPS co-added spectra with `SpecMatch-Emp` (Yee et al. 2017), and for the distance from Gaia DR2 (Gaia Collaboration et al. 2018; Bailer-Jones et al. 2018). Non-informative priors were used for the rest of parameters. We used the PHOENIX/BT-Settl stellar atmosphere models (Allard et al. 2012). The data with the maximum a posteriori (MAP) stellar atmosphere model is shown in Figure 1. We obtained a stellar radius of 0.504 ± 0.010 $R_\odot$, consistent with the estimation from Mann et al. (2015) presented in Table 1.

We tried to determine the stellar rotation period of TOI-663. We studied activity indices from the HARPS spectra to see if there was some periodicity in the S_{index} of the Sodium lines or in the S_{index} of the $H\alpha$ line. After removing any long-term variation, we did not find a significant peak in the periodograms. The flux around the calcium lines is very low in the HARPS

---

[1] https://github.com/samuelyeewl/specmatch-emp

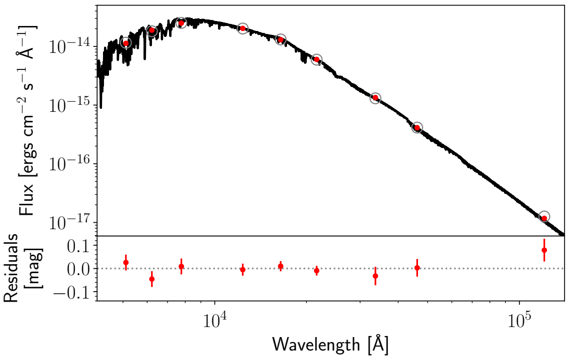

Fig. 1. Spectral energy distribution of TOI-663. The solid line is the MAP PHOENIX/BT-Settl interpolated synthetic spectrum, red circles are the absolute photometric observations, and gray open circles are the result of integrating the synthetic spectrum in the observed band-passes.

spectra but using the ESPRESSO spectra, we were able to measure the value of $\log R'_{HK} = -4.783 \pm 0.063$, derived from the calcium doublet of the ESPRESSO combined spectra. This indicates that the star has likely a rotation period estimated to $P_{\rm rot} = 30 \pm 3.1$ days (Astudillo-Defru et al. 2017a). According to this rotation period and the stellar radius, we expect the v.sin(i) to be less than a km/s, which is consistent with the values of FWHM of the CCF from the ESPRESSO spectra. No sign of periodicity were found in the All Sky Automated Survey (ASAS, Pojmanski 2002) and the Zwicky Transient Facility (ZTF Bellm et al. 2019) photometry as well as in the HARPS dataset (see Figure 2). Unfortunately, this difficulty to find the rotation period of the star prevented us from determining the age of the system using gyrochronology.

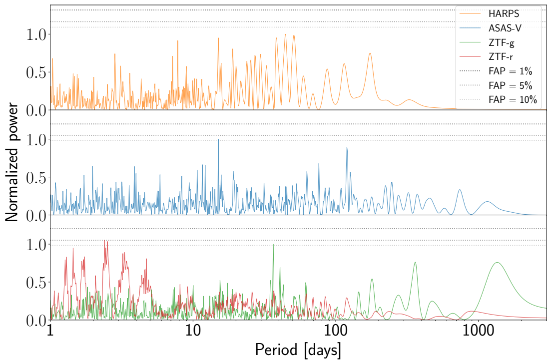

Fig. 2. Periodogram of the ASAS and ZTF photometry and HARPS radial velocity measurements.

3. Observations

3.1. TESS photometry

TOI-663 (TIC 54962195) was observed in two TESS sectors (9 and 35), one during the primary mission (February/March 2019) and one during the first extended mission (February/March 2021) with a two-minute cadence. The TESS Science Processing Operations Center (SPOC; Jenkins et al. 2016) at NASA Ames processed the TESS photometric data and the resulting Presearch Data Conditioning Simple Aperture Photometry (PDCSAP; Smith et al. 2012, Stumpe et al. 2012, 2014) light curve of TOI-663 was corrected for dilution in the TESS aperture by known contaminating sources. It is critical to ensure that no visually close-by targets that could affect the depth of the transit are present in the 21" TESS pixel and to check for contaminating eclipsing binaries. Figure 3 shows a plot of the target pixel file (TPF) and the aperture mask that is used for the simple aperture photometry (SAP). We can see that one star overlaps the TESS aperture but its faintness results in minimal dilution of the TESS light curve. The SPOC conducted a transit search of the sector 9 light curve on 25 April 2019 and the combined light curve for sectors 9 and 35 on 27 May 2021 with an adaptive, noise-compensating matched filter (Jenkins 2002; Jenkins et al. 2010, 2020). The sector 9 search produced Threshold Crossing Events (TCEs) with orbital periods of 2.60d and 4.70d; the combined search produced a third TCE with period of 7.10d. An initial limb-darkened transit model was fitted (Li et al. 2019) and a suite of diagnostic tests were conducted to help make or break the planetary nature of each signal (Twicken et al. 2018). The transit signatures passed all diagnostic tests presented in the SPOC Data Validation reports, and all TIC objects other than the target star were excluded as the transit source in each case. The TESS Science Office reviewed the vetting information and issued alerts for TOI-663.01 and TOI-663.02 on 7 May 2019, and TOI-663.03 on 8 July 2021 (Guerrero et al. 2021).

Canto Martins et al. (2020) conducted a search for rotation period in TESS TOIs using fast Fourier transform, Lomb-Scargle, and wavelet techniques, accompanied by a rigorous visual inspection, and found that TOI-663 does not show any sign of chromospheric activity throughout the observed time ranges.

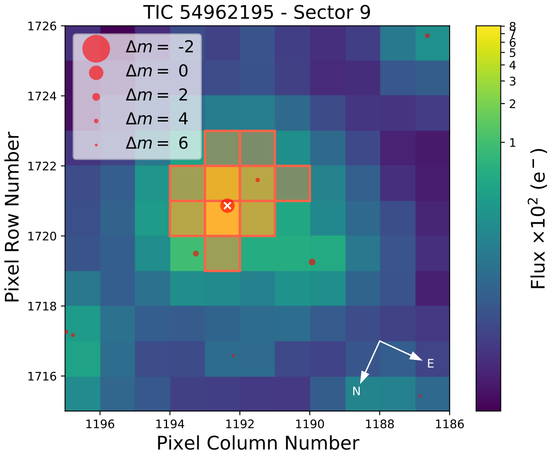

Fig. 3. TESS target pixel file image of TOI-663 in Sector 9 (created with `tpfplotter`, Aller et al. 2020). The electron counts are color-coded. The red bordered pixels are used in the SPOC simple aperture photometry. The size of the red circles indicates the Gaia DR2 magnitudes of all nearby stars.

3.2. Ground-based photometry

The *TESS* pixel scale is ∼ 21″ pixel^{-1} and photometric apertures typically extend out to roughly 1 arcminute, generally causing multiple stars to blend in the *TESS* aperture. To definitely exclude the presence of another star causing the signal in the *TESS* data, and to monitor for potential transit timing variations relative to a linear ephemeris, we conducted ground-based photometric follow-up observations of the field around TOI-663 as part of the `TESS` Follow-up Observing Program[2] Sub Group 1 (TFOP; Collins 2019). All the follow-up photometry is summarized in Table 2.

3.2.1. ExTrA photometry

ExTrA (Bonfils et al. 2015) is a near-infrared (0.85 to 1.55 μm) multi-object spectrograph fed by three 60-cm telescopes located at La Silla Observatory in Chile. Seven full transits (and three partial transits) of TOI-663.01, six full transits of TOI-663.02, and two full transits of TOI-663.03 were observed using the ExTrA telescopes (see Table 2). We used 8″ aperture fibers and the low-resolution mode (R∼20) of the spectrograph with an exposure time of 60 seconds. Five fiber positioners are used at the focal plane of each telescope to select light from the target and four comparison stars chosen with 2MASS J-magnitudes (Skrutskie et al. 2006b) and *Gaia* effective temperatures (Gaia Collaboration et al. 2018) similar to the target. The resulting ExTrA data were analyzed using a custom data reduction software to produce a synthetic photometry in a 0.85-1.55 micron bandpass, described in more detail in Cointepas et al. (2021).

3.2.2. LCOGT

We observed nine and four full predicted transit windows of TOI-663.01 and TOI-663.02, respectively, using the Las Cumbres Observatory Global Telescope (LCOGT; Brown et al. 2013) 1.0 m network nodes. We used the `TESS Transit Finder`, which is a customized version of the `Tapir` software package (Jensen 2013), to schedule our transit observations. The 1 m telescopes are equipped with 4096 × 4096 SINISTRO cameras having an image scale of 0.″389 per pixel, resulting in a 26′×26′ field of view. The images were calibrated by the standard LCOGT `BANZAI` pipeline (McCully et al. 2018). Differential photometric data were extracted using `AstroImageJ` (Collins et al. 2017a). We detected transit-like signals in all 13 light curves using photometric apertures that exclude flux from all known neighbors of TOI-663, confirming the event on-target relative to all known Gaia DR3 and TICv8 stars.

3.2.3. MuSCAT

We observed one transit of TOI-663.02 on 2020 March 24 UT with the multi-band imager MuSCAT (Narita et al. 2015) on the NAOJ 188 cm telescope at the Okayama Astro-Complex in Okayama, Japan. MuSCAT has three optical channels each equipped with a 1k × 1k CCD camera with a pixel scale of 0.″361 pixel^{-1}, enabling g-, r-, and z_s-band simultaneous imaging. The observation was performed with exposure times of 30, 15, and 30 s for the g, r, and z_s bands, respectively. We used optical diffusers to obtain slightly defocused images. We performed image calibration and aperture photometry to extract relative light curves using a custom pipeline described in Fukui et al. (2011).

3.2.4. MuSCAT2

We observed one transit of TOI-663.01 on 2020 January 17 UT with the multi-band imager MuSCAT2 (Narita et al. 2019) on the 1.52m TCS telescope at the Teide Observatory in the Canary Islands, Spain. MuSCAT2 has four optical channels each equipped with a 1k × 1k CCD camera with a pixel scale of 0.″44 pixel^{-1}, enabling g-, r-, i-, and z_s-band simultaneous imaging. The observation was performed with exposure times of 60, 30, 30, and 15 s for the g, r, i, and z_s bands, respectively. We performed image calibration and aperture photometry to extract relative light curves using a dedicated MuSCAT2 pipeline described in (Parviainen et al. 2020).

3.2.5. GMU

TOI-663.01 was observed on the night 2021 February 07 in R band with 90 second exposures with the George Mason University 0.8m Ritchey-Chretien telescope using the automated software control from Reefe et al. (2022). Intermittent clouds were present throughout the night, and a detection of the transit was not obtained. Data were reduced with a custom Python code. Data was plate-solved with astrometry.net, and aperture photometry, light curve extraction and detrending performed with AstroImageJ (Collins et al. 2017b). The results are available at ExoFOP at the NASA Exoplanet Archive.

3.2.6. OAAlbanya

TOI-663.02 was observed on the night of 2020 March 19 UT in Ic band using an exposure of 120 seconds and with a good focus. The observation was performed from the 0.4m Schmidt-Cassegrain telescope from Observatori Astronòmic Albanyà, at an altitude of 230m in the North-East of Spain. The night was mostly transparent during the window of observation, with some minor clouds at the out of transit phase of the observation. Data reduction was performed with aperture differential photometry using the AstroimageJ suite. Results showed a tentative signal coherent with an on-time transit, with high RMS related to the predicted depth, but consistent with an event nevertheless. The data set was detrended using the airmass values and the movement of the Y-axis of the image sequence to reduce systematics.

3.2.7. PEST

We observed TOI-663.01 and TOI-663.02 on 2020 April 28 UT and 2020 April 26 UT respectively with the Perth Exoplanet Survey Telescope (PEST) in Rc band. PEST is located near Perth, Australia. At the time, the 0.3 m telescope was equipped with a 1530 × 1020 SBIG ST-8XME camera with an image scale of 1.″2 pixel^{-1} resulting in a 31′ × 21′ field of view. A custom pipeline based on `C-Munipack`[3] was used to calibrate the images and extract the differential photometry.

3.2.8. SAINT-EX

Time series observations of the transit of TOI-663.01 were acquired with the SAINT-EX Observatory (Search And characterIsatioN of Transiting EXoplanets) on the night of 2020 February 05 UT. SAINT-EX is a 1-m F/8 Ritchey-Chrétien telescope that resides within the Observatorio Astronómico Nacional located at the Sierra de San Pedro Mártir in Baja California, Méx-

---

[2] https://tess.mit.edu/followup

[3] http://c-munipack.sourceforge.net

Table 2. Summary of ground-based follow-up observations

Telescope/Observatory	UTC Date	Filter	Coverage	TOI	Use
ExTrA (2 telescopes)/La Silla	2020-01-09	0.85-1.55 μm	No egress	.01	TTV
ExTrA (3 telescopes)/La Silla	2020-03-22	0.85-1.55 μm	Full	.01	TTV
ExTrA (2 telescopes)/La Silla	2021-02-15	0.85-1.55 μm	Full	.01	Global + TTV
ExTrA (2 telescopes)/La Silla	2021-02-28	0.85-1.55 μm	Full	.01	TTV
ExTrA (2 telescopes)/La Silla	2021-03-13	0.85-1.55 μm	Full	.01	Global + TTV
ExTrA (2 telescopes)/La Silla	2021-05-04	0.85-1.55 μm	Full	.01	TTV
ExTrA (3 telescopes)/La Silla	2022-03-04	0.85-1.55 μm	Full	.01	TTV
ExTrA (2 telescopes)/La Silla	2022-03-30	0.85-1.55 μm	Full	.01	TTV
ExTrA (2 telescopes)/La Silla	2022-04-20	0.85-1.55 μm	No ingress	.01	Global + TTV
ExTrA (2 telescopes)/La Silla	2022-05-03	0.85-1.55 μm	No ingress	.01	TTV
GMU	2021-02-07	R	Partial	.01	None
LCO-McD	2021-02-08	zs	Full	.01	TTV
LCO-CTIO	2020-02-05	ip	Full	.01	TTV
LCO-CTIO	2020-02-18	ip	Full	.01	TTV
LCO-SAAO	2021-01-28	zs	Full	.01	Global + TTV
LCO-SAAO	2021-02-23	ip	Full	.01	TTV
LCO-SSO	2020-04-15	zs	Full	.01	Global + TTV
LCO-SSO	2020-04-28	zs	Full	.01	TTV
LCO-SSO	2020-05-11	zs	Full	.01	Global + TTV
LCO-SSO	2021-01-18	zs	Full	.01	Global + TTV
MuSCAT2/Teide Observatory	2020-01-17	g,r,i,zs	Full	.01	TTV
PEST	2020-04-28	Rc	Full	.01	None
SAINT-EX/San Pedro Mártir Observatory	2020-02-05	zs	Full	.01	TTV
ExTrA (2 telescopes)/La Silla	2021-02-15	0.85-1.55 μm	Full	.02	Global + TTV
ExTrA (2 telescopes)/La Silla	2021-03-06	0.85-1.55 μm	Full	.02	TTV
ExTrA (2 telescopes)/La Silla	2021-03-20	0.85-1.55 μm	Full	.02	Global + TTV
ExTrA (2 telescopes)/La Silla	2021-04-22	0.85-1.55 μm	Full	.02	TTV
ExTrA (1 telescopes)/La Silla	2021-06-08	0.85-1.55 μm	Full	.02	TTV
ExTrA (2 telescopes)/La Silla	2022-04-09	0.85-1.55 μm	Full	.02	TTV
LCO-CTIO	2020-03-01	ip	Full	.02	Global + TTV
LCO-CTIO	2020-03-15	gp	Full	.02	TTV
LCO-SAAO	2020-06-07	zs	Full	.02	Global + TTV
LCO-SAAO	2021-02-06	zs	Full	.02	TTV
MuSCAT/Okayama Observatory	2020-03-24	g, r, zs	Full	.02	Global + TTV
OAAlbanya	2020-03-19	Ic	Full	.02	TTV
PEST	2020-04-26	Rc	Full	.02	TTV
ExTrA (1 telescopes)/La Silla	2022-04-13	0.85-1.55 μ m	Full	.03	Global + TTV
ExTrA (2 telescopes)/La Silla	2022-04-20	0.85-1.55 μ m	Full	.03	Global + TTV

ico (31.04342 N,115.45476 W) at an altitude of 2780 m (Demory et al. 2020). The observations were acquired with a deep-depleted Andor Ikon CCD in the z' filter and consisted of 396 datapoints which cover a full transit of TOI-663.01. Each observation had an exposure time of 2.0 s spanning 5 h of continuous observations. The data were reduced and the aperture photometry was done, using the custom pipeline PRINCE done on site, as detailed in Demory et al. (2020). For the final light curve, the aperture of 14 pixels was chosen. We then analyzed the light curve with AIJ (Collins et al. 2017b) to correct for airmass and total counts in the aperture thus reducing systematics.

3.3. Radial velocities

3.3.1. HARPS

We obtained 40 spectra of TOI-663 with the High Accuracy Radial velocity Planet Searcher (HARPS; Mayor et al. 2003) echelle spectrograph at the ESO 3.6m telescope at La Silla Observatory in Chile. The HARPS optical spectrograph has a resolution of R=115,000 and is stabilized in pressure and temperature, in order to achieve a sub-m/s precision. The observations span 463 days and were taken between UT 2020 March 02 and UT 2021 June 7 (Prog-ID 105.20AK.002,106.215E.004,1102.C-0339). The second fiber was on sky during the observations.
These data were reduced with the Data Reduction Software[4]. Radial velocities were computed through maximum likelihood

---

[4] http://www.eso.org/sci/facilities/lasilla/instruments/harps/doc/DRS.pdf

between individual spectra and the median stellar spectrum, where spectral zones containing tellurics were flagged. Details of the procedure are given in Astudillo-Defru et al. (2017b). The HARPS radial velocities of TOI-663 have a median uncertainty per data point of 4.5 m/s.

3.3.2. ESPRESSO

We obtained ten spectra of TOI-663 with the Echelle SPectrograph for Rocky Exoplanets and Stable Spectroscopic Observations (ESPRESSO; Pepe et al. 2021) at the 8.2 m ESO Very Large Telescope (VLT) array, at the Paranal Observatory in Chile. The observations were obtained from 2022 April 05 to 2022 April 18 for an ESPRESSO program designed to test if the density of sub-Neptunes orbiting M-dwarfs is different than sub-Neptunes orbiting more massive stars (Program ID: 109.2391.001; PI: Grieves). We observed TOI-663 in HR2x1 mode (1 UT, R~140,000) over a spectral range from ~380 to ~780 nm. ESPRESSO is contained in a temperature and pressure controlled vacuum vessel to minimize the night spectral drift.

ESPRESSO observations can be carried out with simultaneous calibration using a Fabry-Pérot etalon on a second calibration fiber. However, given the relatively faint magnitude of TOI-663 (V = 13.67) we did not use the Fabry-Pérot etalon for simultaneous calibration, and the calibration fiber was pointed at the sky for background calibration that is used as a sky subtraction calibration in the data processing. The ESPRESSO RVs were processed using the Data Analysis Center for Exoplanets (DACE), a facility dedicated to extrasolar planets data visualisation, exchange, and analysis hosted by the University of Geneva[5]. The RV and stellar activity indicators provided in DACE are computed by cross-correlating the calibrated spectra with stellar templates for the specific spectral type, using the latest version (3.0.0) of the publicly-available ESPRESSO Data Reduction Software[6]. The ten ESPRESSO RVs of TOI-663 have a median uncertainty of 1.58 m/s.

3.3.3. MAROON-X

We obtained 14 spectra of TOI-663 with MAROON-X (Seifahrt et al. 2018) at Gemini North in two campaigns from UT 2021 February 22 to 2021 March 04 and UT 2021 April 19 to 2021 April 30 under Prog-ID GN-2021A-Q-230. MAROON-X is a fairly new EPRV spectrograph operating in the red-optical wavelength regime, delivering R ≃ 85,000 from 500–920 nm in two arms, dubbed blue (500–670 nm) and red (650–920 nm). Spectra were taken with a fixed exposure time of 20 min and showed an average peak SNR of 100 in the red arm. The data were reduced by the instrument team using a custom python3 data reduction pipeline to produce optimum extracted and wavelength calibrated 1D spectra. The radial velocity analysis was performed using `serval` (Zechmeister et al. 2018), a template matching RV retrieval code in a custom python3 implementation. On average, the RV uncertainty per datapoint was 2.3 m/s for the blue and 1.7 m/s for the red arm. MAROON-X is using a stabilized Fabry-Perot etalon for wavelength and drift calibration (Seifahrt et al. 2022) and can deliver 30 cm/s on-sky RV precision over short timescales (Trifonov et al. 2021) but suffers from inter-run RV offsets which in the case of our observations had a prior of 1.5 ± 0.5 m/s for the blue and 1.6 ± 0.5 m/s for the red channel.

3.3.4. IRD

We observed TOI-663 with the InfraRed Doppler (IRD) instrument (Tamura et al. 2012; Kotani et al. 2018) on the Subaru 8.2m telescope. IRD simultaneously covers Y, J, and H−bands with the spectral resolving power of $\lambda/\Delta\lambda \approx 70,000$. A total of six near-infrared spectra were secured between UT 2021 February 2 and June 8, each with an integration time of 1200 − 1500 sec. One frame was interrupted by bad weather, which we discarded in the subsequent analysis. We reduced the raw frames with the standard reduction procedure, and measured the relative radial velocities using the custom RV-analysis pipeline for IRD (Hirano et al. 2020). Except for the frame affected by bad weather, the extracted one-dimensional spectra had the typical S/N ratios of 51 − 73 per pixel at 1000 nm, and derived radial velocities had the statistical errors of 3.5 − 4.8 m s^{-1}.

3.4. *High Resolution Imaging*

As part of our standard process for validating transiting exoplanets to assess the possible contamination of bound or unbound companions on the derived planetary radii (Ciardi et al. 2015), we observed the TOI 663 with near-infrared adaptive optics (AO) imaging at Keck and with optical speckle imaging at Gemini. Gaia DR3 is also used to provide additional constraints on the presence of undetected stellar companions as well as wide companions.

3.4.1. Near-Infrared Adaptive Optics Imaging

The Keck Observatory observations were made with the NIRC2 instrument on Keck-II behind the natural guide star AO system (Wizinowich et al. 2000) on 2019-Jun-10 UT in the standard 3-point dither pattern that is used with NIRC2 to avoid the left lower quadrant of the detector which is typically noisier than the other three quadrants. The dither pattern step size was 3″ and was repeated twice, with each dither offset from the previous dither by 0.5″. NIRC2 was used in the narrow-angle mode with a full field of view of ~ 10″ and a pixel scale of approximately 0.0099442″ per pixel. The Keck observations were made in the narrowband Br-γ filter (λ_o = 2.1686; $\Delta\lambda$ = 0.0326 μm) and in the Jcont filter (λ_o = 1.2132; $\Delta\lambda$ = 0.0198 μm), both with an integration time of 10 seconds for a total of 90 seconds on target per filter.

The science frames were flat-fielded and sky-subtracted. The flat fields were generated from a median average of dark subtracted flats taken on-sky. The flats were normalized such that the median value of the flats is unity. The sky frames were generated from the median average of the dithered science frames; each science image was then sky-subtracted and flat-fielded. The reduced science frames were combined into a single combined image using an intra-pixel interpolation that conserves flux, shifts the individual dithered frames by the appropriate fractional pixels, and median-coadds the frames. The final resolutions of the combined dithers were determined from the full-width half-maximum of the point spread functions: 0.052″ at 2 μm and 0.064″ at 1.2 μm.

The sensitivities of the final combined AO image were determined by injecting simulated sources azimuthally around the primary target every 20° at separations of integer multiples of the central source's FWHM (Furlan et al. 2017). The brightness of each injected source was scaled until standard aperture photometry detected it with 5σ significance. The resulting brightness of the injected sources relative to TOI-663 set the contrast limits at

---

[5] https://dace.unige.ch/dashboard/index.html

[6] https://www.eso.org/sci/software/pipelines/espresso/espresso-pipe-recipes.html

that injection location. The final 5σ limit at each separation was determined from the average of all of the determined limits at that separation and the uncertainty on the limit was set by the rms dispersion of the azimuthal slices at a given radial distance. The Keck data have a sensitivity close-in of Δmag = 2.2 mag at $0.06''$(Br-γ) and δmag = 2.4 mag at $0.07''$($Jcont$), and deeper sensitivity at wider separations (δmag = 7.7 mag at $\gtrsim 0.5''$); the final sensitivity curves for the Keck Br-γ imaging is shown in (Figure 4). No close-in ($\lesssim 1''$) stellar companions were detected by Keck in agreement with the optical speckle imaging.

3.4.2. Optical Speckle Imaging

TOI-663 was observed on 2019 June 10 and 2020 January 12 UT using the 'Alopeke and Zorro speckle instruments on Gemini South/North respectively. Zorro and 'Alopeke (Scott et al. 2021) both provide simultaneous speckle imaging in two bands (562 nm and 832 nm) with output data products including a reconstructed image and robust contrast limits on companion detections (Howell et al. 2011). Both data sets gave consistent results and Figure 5 shows the Gemini South Zorro resultant 5-sigma contrast curves and the reconstructed 832-nm speckle image. We find that TOI-663 is a single star with no companion brighter than about 5 to 9 magnitudes, respectively, from 0.1 arcsec to 1.2 arcsec. At the distance of TOI-663 (64 pc), these angular limits correspond to spatial limits of 6.4 to 77 AU.

3.4.3. Gaia Assessment

In addition to the high resolution imaging, we used Gaia to identify any wide stellar companions that may be bound members of the system. Typically, these stars are already in the TESS Input Catalog and their flux dilution to the transit has already been accounted for in the transit fits and associated derived parameters. There are no additional widely separated companions identified by Gaia that have the same distance and proper motion as TOI-663 (see also Mugrauer & Michel 2020, 2021).

Additionally, the Gaia DR3 astrometry provides additional information on the possibility of inner companions that may have gone undetected by either Gaia or the high resolution imaging. The Gaia Renormalized Unit Weight Error (RUWE) is a metric, similar to a reduced chi-square, where values that are $\lesssim$ 1.4 indicate that the Gaia astrometric solution is consistent with the star being single whereas RUWE values $\gtrsim$ 1.4 may indicate an astrometric excess noise, possibly caused by the presence of an unseen companion (e.g., Ziegler et al. 2020). TOI-663 has a Gaia DR3 RUWE value of 1.6 - while this value is slightly higher than the nominal value of 1.4, the 1.4 RUWE boundary is more of a guideline as opposed to a hard cut-off. Additionally, TOI-663 does not appear in the Gaia DR3 binary table; as such, the Gaia astrometric fit is still consistent with a single star model. However, this RUWE value could be linked to the long term radial velocity trend seen in the HARPS dataset which could be associated with a bound companion.

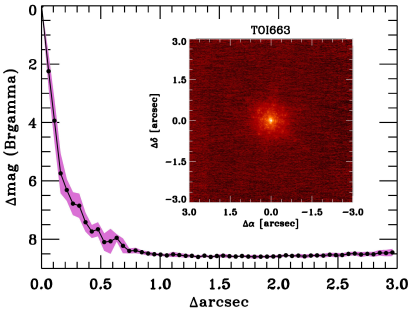

Fig. 4. Keck NIR AO imaging and sensitivity curve for TOI-663 taken in the Br-γ filter. The image reaches a contrast of ~ 7.7 magnitudes fainter than the host star within $0.''5$. *Inset:* Image of the central portion of the data.

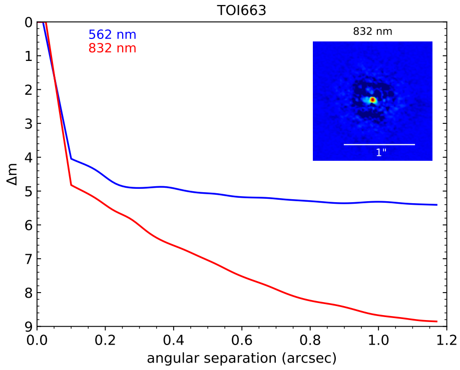

Fig. 5. This figure shows the 5σ speckle imaging contrast curves of Gemini South Zorro in both filters as a function of the angular separation out to 1.2 arcsec, the end of speckle coherence. The inset shows the reconstructed 832 nm image with a 1 arcsec scale bar. The star, TOI-663, was found to have no close companions to within the angular and contrast levels achieved.

4. Analysis and modeling

We used the software package `juliet` (Espinoza et al. 2019) to model the photometric and radial-velocity data. The algorithm is built on many publicly available tools for the modeling of transits (`batman`, Kreidberg 2015), RVs (`radvel`, Fulton et al. 2018), and Gaussian processes (GPs) (`george`, Ambikasaran et al. 2015; `celerite`, Foreman-Mackey et al. 2017). In order to compare different models, `juliet` efficiently computes the Bayesian evidence ($\ln Z$) using `dynesty` (Speagle 2020), a python package to estimate Bayesian posteriors and evidence using nested sampling methods. Instead of starting with an initial parameter vector centered on a likelihood maximum discovered through optimization techniques, nested sampling algorithms sample directly from the given priors. Throughout our various analyses, we ensured that we had enough live points given the number of free parameters to avoid missing peaks in the parameter space. Here we decided to conduct two independent analyses of our data. We started the analysis using only TESS photometry, and the resulting planet parameters were used as priors in a subsequent RV analysis. As the result of these two analyses, we were able to constrain the priors of some parameters and use them for a joint analysis of all our data.

4.1. TESS photometry

First, using `juliet`, we modeled the TESS PDCSAP light curve where our planet candidates was initially detected. The transit model fits the stellar density $\rho_\star$ along with the planetary and jitter parameters. Except for the stellar density, which we calculated in Section 2, we used ExoFOP priors for the orbital parameters. We adopted a few parametrization modifications when dealing with the transit photometry. We assigned a quadratic limb-darkening law for TESS, as shown to be appropriate for space-based missions (Espinoza & Jordán 2015), which was then parameterized with the uniform sampling scheme (q_1, q_2) introduced by Kipping (2013). Additionally, rather than fitting directly for the planet-to-star radius ratio ($p = R_p/R_\star$) and the impact parameter of the orbit ($b = a/R_\star \cos i$), `juliet` used the parameterization introduced in Espinoza (2018) and fit for the parameters r_1 and r_2 to guarantee full exploration of physically plausible values in the (p,b) plane. We assume circular orbits. Based on our analysis of nearby companions, we set the TESS dilution factor to one. In addition, we added in quadrature a jitter term σ_{TESS} to the TESS photometric uncertainties, which may be underestimated due to additional systematics in the space-based photometry. Figure 6 depicts the best-fit transit model for the two TESS sectors. In the same figure, we also showed the phase-folded light curve for each planet.

4.2. Radial velocity analysis

For the radial velocity modeling using `juliet`, we tested a 3-planet and 4-planet model including or not a linear long-term trend and Gaussian processes and we compared the evidences to select the one with the highest probability. We used as prior for each candidate the period and time-of-transit center estimated from the TESS photometry analysis and assume circular orbits. After fitting all of our datasets with a 3-planet model including a trend seen in the HARPS dataset, we saw that the model did not fit properly our set of radial velocity measurements for the different instruments. As a model with only 3 planets and a trend does not seem to match our data, we tested two different models: adding a Gaussian process or considering the possibility of having a 4th non-transiting exoplanet in the system. We looked for another periodic signal in the radial velocity datasets. We found a potential peak at longer period around 25.8 days in the HARPS dataset compatible at the ~1.4-sigma level with the estimated rotational period derived from the $\log R'_{HK}$ value (see Section 2). We fitted a 4-planet model to our radial velocity datasets (considering this new planet is not transiting and with a period range between 8 and 30 days) and found that the evidence of this model ($\ln Z = 293.33 \pm 0.66$) was slightly lower than the evidence for the model with 3 exoplanets, a long-term trend and a GP ($\ln Z = 294.60 \pm 0.67$), although the model comparison does not favor one model over the other (Kass & Raftery 1995). For the joint fit of photometry and RVs we adopted the model with 3 exoplanets, a long-term trend and a GP, as the signal of a possible 4th exoplanet was not convincing and the GP allows a better description of the residuals of the 3-planet model. The long-term trend was estimated at $0.0229^{+0.0091}_{-0.0085}$ m/day in the joint fit presented in the next section.

4.3. Joint fit of all data

We performed a joint analysis using `juliet` of the TESS photometry complemented by some ground-based photometry from ExTrA, LCOGT and MuSCAT and velocity data from HARPS, ESPRESSO, MAROON-X and IRD to obtain the most precise parameters of the TOI-663 system. Each individual ground-based light curve presented in Section 3 was analyzed for the TTVs analysis (see Section 4.5). From this, we decided to only select a few of these transits for the global analysis to improve on the radius measurement. To choose which transits to use, we kept a first selection of transits for which the posterior of the time-of-transit center was more constrained after the fit (a non-uniform posterior on t_0), and then we only selected the nights with the smallest systematics visible in the data. We selected all transits available for TOI-663.03 as it was the least constrained by the TESS photometry.

After a verification that the depth of the transits were consistent in the different wavelength ranges, we decided to fit only one set of r_1 and r_2 parameters for each planet. To detrend the photometry data, we used time-dependent Gaussian processes. We chose the approximate Matern kernel proposed by Foreman-Mackey et al. (2017) because there are no obvious quasi-periodic oscillations in the light curves. We don't have a sufficient precision on the RV data to constrain the eccentricity of the different planets in this system so we decided to fix them at 0 to decrease the number of free parameters. Multi-planet systems tend to have low eccentricities but this decision is explained in more detail in the analysis in Section 4.4. We seek the posterior distribution of 127 free parameters in total, and due to the large number of parameters, we perform this fit using `dynesty`. We constrained our priors using previous `juliet` results before the final run for the joint modeling to optimize the computation time due to the large parameter space. Because we used rather broad priors for the planetary parameters in the separate fits of TESS and HARPS data, nested sampling is an efficient method for exploring the parameter space, and because most of the planetary parameters are specific to a given data type, they would not change significantly in a joint fit.

Table 3 shows the posteriors the planetary parameters derived using the stellar parameters presented in Section 2. Figures 7, 8, and 9 show the results of the photometry of our joint fit to the data for the three exoplanets. In Figures 10 and 11, we present the radial-velocity component of the joint fit and the phase-folded data. The corner plots of the radial velocity semi-amplitude for the three planets are presented in Figure B.1.

4.4. Stability of the system

From our global fit, we find that the three planets currently have period ratios P_c/P_b=1.807 and P_d/P_c=1.513. We investigated the short-term dynamics in this three-planet system. Our objective is both to get a first hint on the range of orbital eccentricities compatible with the system stability, and to look for potential mean-motion resonances (MMR). As such, we built a two-dimensional chaos map. It consists in a 121×121 grid of simulations in the parameter space exploring the orbital eccentricity of the middle planet e_c on one axis and the orbital period of that same planet P_c on the other axis (Fig. 12). All the other dynamical parameters were initially fixed to their estimation resulting from the global fit, hence with the hypothesis that e_b=0=e_d and ω_i=0 for i=b,c,d. Each subsequent box in the grid defines a unique set of system orbital parameters that we used as initial conditions for numerical integrations of the equations of motion. We used the IAS15 adaptive timestep integrator to perform the numerical integrations (Rein & Spiegel 2015). IAS15 is part of

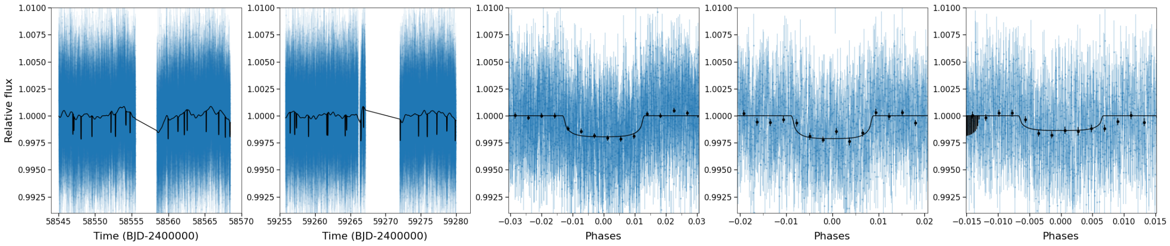

Fig. 6. Modeling of the TESS data. Two left panels: TESS photometry time series from Sectors 9 and 35 along with the maximum a posteriori (solid black line). Three right panels: Phase-folded light curve to the period of the planet (black points correspond to 1/6 of the transit duration for each planet). The three panels are associated with the b/c/d planets respectively. The dark area to the left on the far right plot is due to the transit of the other exoplanets that happened close to the transit of TOI-663 d.

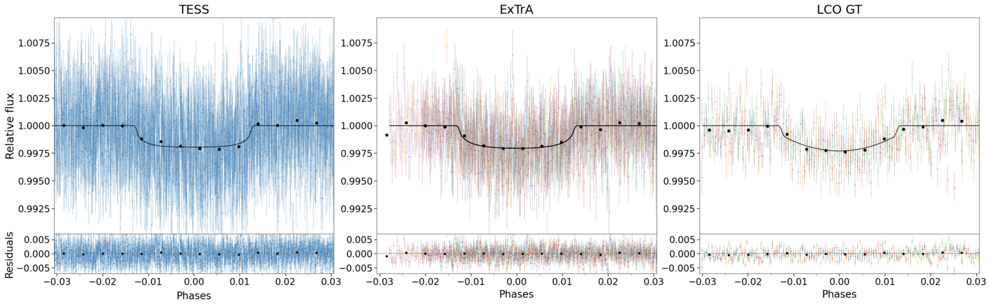

Fig. 7. Phase-folded light curves for TOI-663 b for the TESS (17 transits), ExTrA (three transits with two telescopes each) and LCO-GT (four transits) photometry. The black line is the maximum a posteriori model, the black points are data binned to 1/6 of the transit duration.

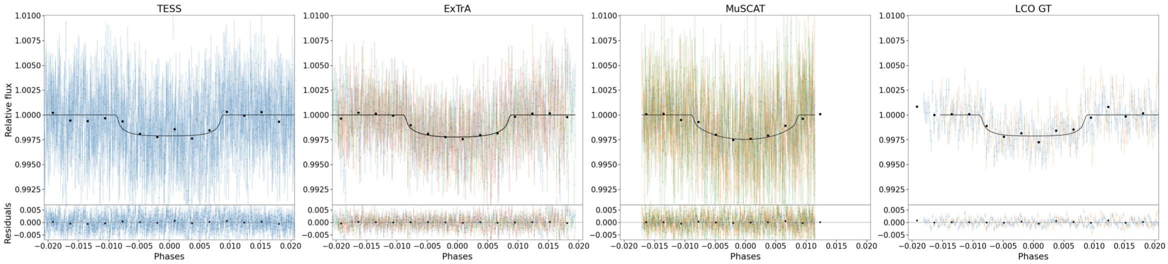

Fig. 8. Phase-folded light curves for TOI-663 c for the TESS (eight transits), ExTrA (two transits with two telescopes each), MuSCAT (one transit with three filters) and LCO-GT (two transits) photometry. The black line is the maximum a posteriori model, the black points are data binned to 1/6 of the transit duration.

the python package REBOUND[7] (Rein & Liu 2012). We also included a correction for general relativity effects following Anderson et al. (1975) and implemented in REBOUNDx (Tamayo et al. 2020). Each set of initial conditions was integrated over 10kyr, during which the mean longitudes of the planets were regularly recorded in output. After the numerical integrations, we used the mean longitude time series to derive the numerical analysis of fundamental frequencies (NAFF) fast chaos indicator (Laskar 1990, 1993). This quantity informs about the strength of chaos in a planetary system via the variations of the orbital mean-motions, according to the following formula

$$\mathrm{NAFF} = \max_j \left[log_{10} \frac{\mid n_{j,2} - n_{j,1} \mid}{n_{j,0}} \right]. \quad (1)$$

In this equation, n_1 and n_2 depict the orbital mean-motion computed over the first and second half of the integration, respectively. n_0 is the initial mean motion. The mean-motion difference between the two integration halves is computed on each planet j, and the maximum value defines the NAFF of the planetary system. We refer to Stalport et al. (2022) for a more detailed synthesis of this process, and for a discussion of the link between NAFF and the orbital stability.

In Fig. 12, we report the results as a color code, where the bluer regions indicate smaller NAFF, and hence, weaker chaos. Orbital eccentricities e_c larger than 0.1 are strongly disfavored, given the resulting strong chaos. While this exact threshold should be taken with caution since it results from a partial exploration of the parameter space, it provides us with insights on the range of eccentricity allowed by orbital stability. Only small values are not destructive for the system. This justifies the assumption of null eccentricities to favor the convergence of our

---

[7] `https://rebound.readthedocs.io/en/latest/`

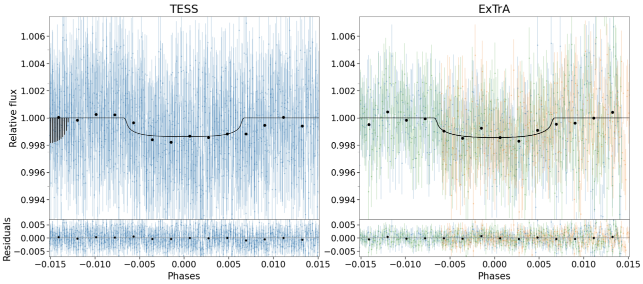

Fig. 9. Phase-folded light curves for TOI-663 d for the TESS (seven transits) and ExTrA (two transits, one with one telescope and the other with two telescopes) photometry. The black line is the maximum a posteriori model, the black points are data binned to 1/6 of the transit duration. The dark area to the left on the far right plot is due to the transit of the other exoplanets that happened close to the transit of TOI-663 d.

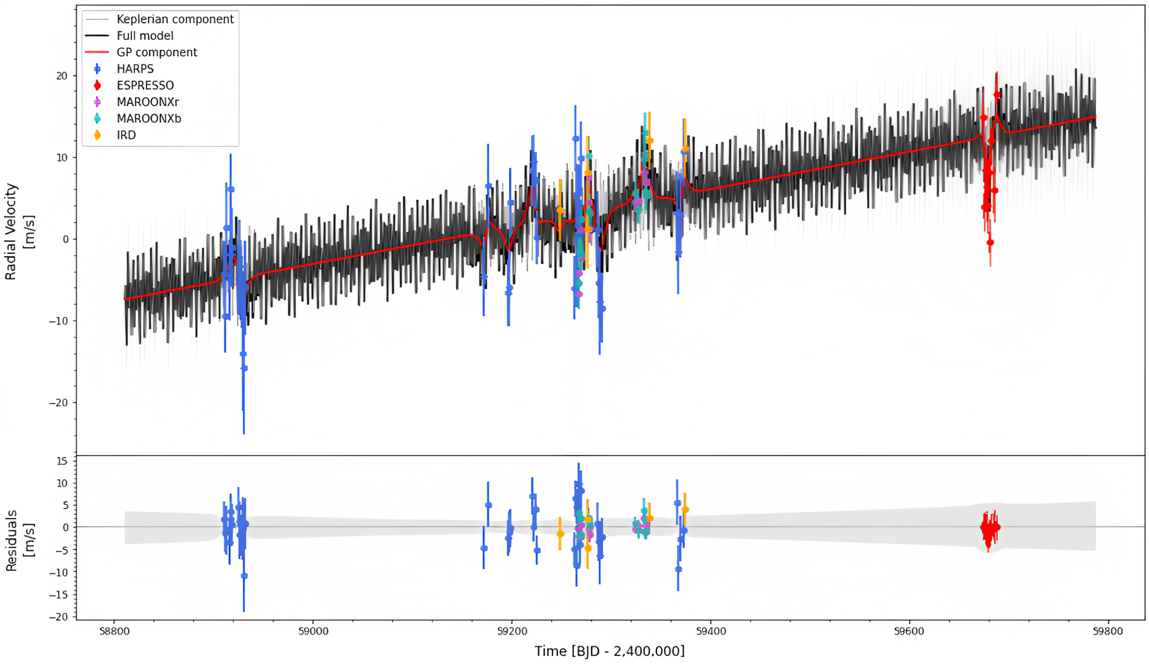

Fig. 10. Radial-velocity measurements from HARPS, ESPRESSO, MAROON-X and IRD for TOI-663. The data points with errors are shown in colors; the black line and gray band correspond respectively to the median and 1σ of 1000 randomly chosen posterior samples from the joint fit.

global fit. Additionally, two vertical features are detected. They overlap with the 9:5 MMR between planets b and c, and 3:2 MMR between planets c and d. A vertical line is drawn at the orbital period of planet c as derived from our global fit, which shows that the system does not fall in any of those features. We do not find the planets in any low-order MMR.

In the previous section, the possibility of a 4th planet in the TOI-663 system is mentioned. This additional candidate would have a significantly longer orbital period (more than three times the period of planet d), hence likely not affecting the orbital stability of the inner system.

4.5. TTVs analysis

Using `juliet`, we calculated transit timing variations (TTVs) for all photometric datasets. Rather than fitting a period P and a time of transit center t_0, `juliet` searches for individual transit times. We combined multiple transits happening at the same time in order to reduce the uncertainties on the estimation of the time of transit center. The results of the analysis showing the difference between the observed transit times and the calculated linear ephemeris from TESS transits and for the different planets are presented in Fig. 13. The data show no significant variation at the level of 4, 5 and 8 minutes RMS for TOI-663 b, TOI-663 c and TOI-663 d respectively, consistent with the uncertainties on the measured values.

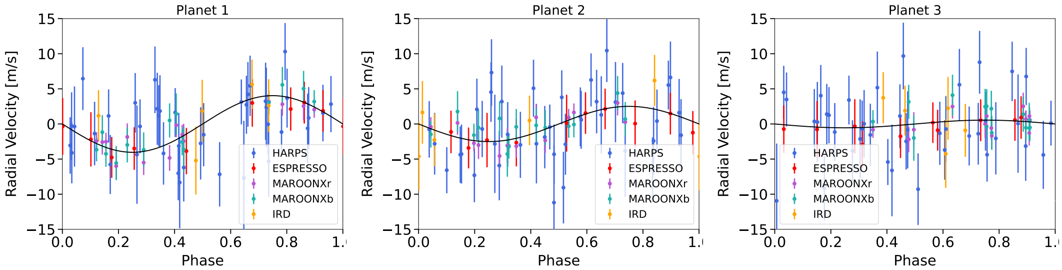

Fig. 11. RVs phase-folded to the periods of the planets. The black line is the best-fit model from the joint fit.

Table 3. Posterior stellar and planetary parameters obtained from our joint photometric and radial-velocity `juliet` analysis for TOI-663. The posterior estimate corresponds to the median value. Error bars denote the 68% posterior credible intervals.

Parameter name	Posterior estimate for TOI-663 b	Posterior estimate for TOI-663 c	Posterior estimate for TOI-663 d
Posterior parameters			
Period (days)	$2.5989020^{+0.0000032}_{-0.0000030}$	$4.6955507^{+0.0000095}_{-0.0000094}$	$7.1027268^{+0.0000297}_{-0.0000279}$
t_0 (BJD$_{\mathrm{TDB}}$)	$2458544.38918^{+0.00068}_{-0.00071}$	$2458543.40593^{+0.00105}_{-0.00107}$	$2458547.11249^{+0.00230}_{-0.00215}$
r_1	$0.458^{+0.083}_{-0.081}$	$0.483^{+0.070}_{-0.086}$	$0.445^{+0.101}_{-0.077}$
r_2	$0.0407^{+0.0012}_{-0.0012}$	$0.0404^{+0.0013}_{-0.0013}$	$0.0345^{+0.0021}_{-0.0021}$
K (m/s)	$3.25^{+0.45}_{-0.47}$	$2.18^{+0.58}_{-0.57}$	<2.7 at 99%
Derived transit and RVs parameters			
$p = R_p/R_\star$	$0.0407^{+0.0012}_{-0.0012}$	$0.0404^{+0.0013}_{-0.0013}$	$0.0345^{+0.0021}_{-0.0021}$
$b = (a/R_\star)\cos(i_p)$	$0.19^{+0.12}_{-0.12}$	$0.23^{+0.11}_{-0.13}$	$0.17^{+0.15}_{-0.12}$
i_p (deg)	$89.14^{+0.57}_{-0.60}$	$89.30^{+0.41}_{-0.35}$	$89.60^{+0.27}_{-0.36}$
Derived physical parameters*			
$M_p(M_\oplus)$	$4.45^{+0.63}_{-0.66}$	$3.65^{+0.97}_{-0.97}$	<5.2 at 99%
$R_p(R_\oplus)$	$2.27^{+0.10}_{-0.09}$	$2.26^{+0.10}_{-0.10}$	$1.92^{+0.13}_{-0.13}$
$\rho_p(g/cm^3)$	$2.07^{+0.42}_{-0.38}$	$1.73^{+0.54}_{-0.49}$	<4.0 at 99%
$a_p(au)$	0.0295 ± 0.0011	0.0437 ± 0.0016	$0.0576^{+0.0021}_{-0.0022}$
$T_{eq}(K)$ †	674 ± 30	553 ± 24	482 ± 21
$S\,(S_\oplus)$	$49.1^{+9.3}_{-8.1}$	$22.3^{+4.2}_{-3.7}$	$12.9^{+2.4}_{-2.1}$

[*] We sample from a normal distribution for the stellar mass, stellar radius, and stellar temperature that is based on the results from Section 2.
[†] Equilibrium temperature was calculated assuming 0.3 Bond albedo and the semi-major axis distance considering an uniform temperature across the entire planet's surface.

5. Discussion & Conclusion

In this paper, we present the validation and characterization of three mini-Neptunes transiting the M dwarf TOI-663. The exoplanets were detected by the TESS mission, then confirmed and characterized from ground-based transit follow-up observations and from precise RV measurements.

5.1. Mass-radius diagram and internal structure

TOI-663 b, c and d, with respective radii of 2.27 ± 0.10 $R_\oplus$, 2.26 ± 0.10 $R_\oplus$, 1.92 ± 0.13 $R_\oplus$, and masses of 4.45 ± 0.65 $M_\oplus$, 3.65 ± 0.97 $M_\oplus$, 1.9 ± 1.3 $M_\oplus$, lie at the edge of the population of mini-Neptunes. However, the determination of the mass of planet d is at the ∼1.7 sigma level, which is not significant to precisely characterize this exoplanet. We can only conclude to an upper limit for planet d of <5.2 $M_\oplus$ at 99%. We plan to observe TOI-663 the coming semesters using the combination of HARPS and NIRPS (Bouchy et al. 2017) to characterize the long-term trend found in the HARPS dataset, improve the mass measurements and better characterize possible additional signals in this system.

The three detected planets of the TOI-663 system are low-mass mini-Neptunes. Their radii are considerably larger than rocky analogues (Fig. 14) and hence their radii must be dominated by volatiles, e.g., water.

To estimate the range of compositions for TOI-663 b, TOI-663 c, and TOI-663 d, we employ a layered interior model consisting of up to four layers: a H-He atmosphere, a water layer, a

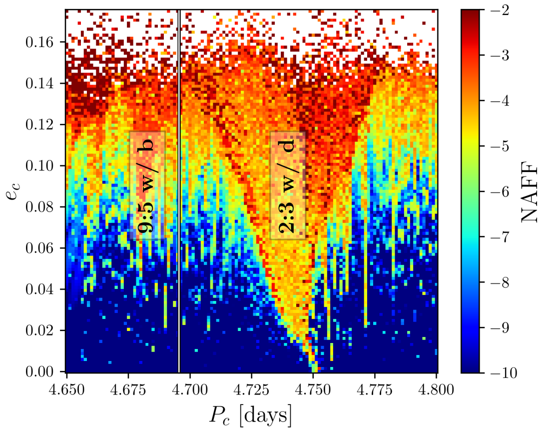

Fig. 12. Chaos map around our best-fit solution. The map has a resolution of 121×121 pixels, which represent as many system configurations that were numerically integrated to derive a NAFF chaos estimation as defined in Eq. (1). We report the results in the form of a color code, where the bluer regions of the map refer to systems with smaller NAFF, and hence weaker chaos. The nearby principal MMR are indicated, and the vertical line marks the orbital period of planet c as estimated from our global fit.

silicate mantle, and an iron core (see Dorn et al. 2017). We solve the standard structure equations for each layer and use a nested sampling algorithm to construct structure models that reproduce the measured masses and radii of the planets, to quantify the degeneracy between various interior parameters and produce posterior probability distributions (Buchner et al. 2014) assuming a solar Mg/Si ratio (Lodders 2020) and an age of 5 Gyr. For the water layer, we employ the AQUA equation of state (Haldemann et al. 2020).

In a first scenario, we allow the water mass fraction to be up to 50% underneath a H/He layer. The results are summarized in the upper half of Table 4. Within these constraints, we find that the three TOI-663 planets have a similar composition of roughly 30% core, 40% mantle, and 30% water layer mass fraction, with a small H-He atmosphere of $\log(M_{\rm atm}/M_{\rm p}) = -4$ to -5.

In order to estimate the maximum water mass fraction in the planets, we also consider internal structures with no H/He atmospheres ($M_{\rm atm} = 0$) and without limiting the total water mass fraction. Additionally, we follow Dorn & Lichtenberg (2021) by assuming an isothermal temperature profile until 0.1 bar followed by an adiabatic profile. The results for this case are summarized in the lower half of Table 4. We find that the water mass fraction is about 20% larger than in the constrained case, i.e., approximately 50%. Accordingly, the core and mantle mass fractions are reduced by ~10%, i.e., $M_{\rm core}/M_p \sim 20\%$ and $M_{\rm mantle}/M_p \sim 30\%$, respectively.

Overall, the TOI-663 planets are expected to be water-rich and may have small H-He atmospheres. It should be noted, however, that while disfavored by the nested sampling algorithm, an Earth-like composition with a small H-He atmosphere (< 1%) can also fit the observed mass and radius of the TOI-663 planetary system. Moreover, pollution of the H-He envelope could lead to contraction of the atmosphere, and hence, a higher atmospheric mass fraction (Lozovsky et al. 2018). In addition, we have estimated here the amount of *surface* water and neglected any water dissolved deep in the interior, which could result in higher water mass fractions (Dorn & Lichtenberg 2021). Also, the host star elemental mass fractions can differ from solar abundances, which can, e.g., change the composition of the planet's mantle. Furthermore, the system's age is unknown, which could affect the characterization of the TOI-663 planetary system. Nonetheless, while these uncertainties could change the exact values of the nested sampling algorithm, it is clear that the composition of the TOI-663 planets is water-rich.

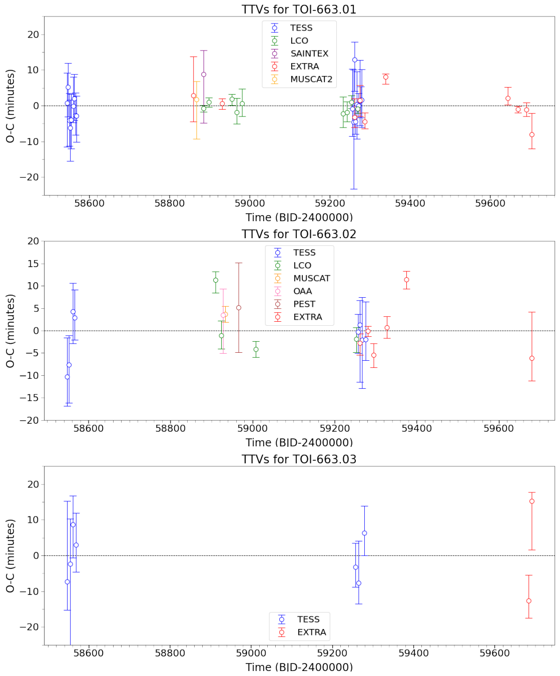

Fig. 13. Transit time variations. The observation minus the calculated linear ephemeris (O-C) diagram derived using all photometric datasets (with a transit) available through TFOP. *Top*: TOI-663.01 *Middle*: TOI-663.02 *Bottom*: TOI-663.03

Interestingly, Luque & Pallé (2022) proposed a population of planets around M dwarfs that are water-rich worlds. On one hand, the planets of TOI-663 may indeed be part of water-rich worlds as we analyzed above. On the other hand, the planets do not follow the density trend of the proposed water-rich population as obtained from Zeng et al. (2019), which however does neglect density variations due to differing equilibrium temperatures or ages. Furthermore, Rogers et al. (2023) show that the water-rich worlds can be equally well described by compositions that include H/He envelopes. In general, additional constraints are needed to further reduce the existing degeneracy between hydrogen and water dominated envelopes, i.e., spectral data from JWST.

From a formation point of view, significant water budgets on the TOI-663 planets are feasible. High water budgets on the TOI-663 planets may be inherited from formation outside of the snow-line (Mordasini et al. 2009) as well as the production of endogenic water (Kimura & Ikoma 2020). How much endogenic water can be produced by redox reactions between a primordial H/He envelope in contact with an oxidized mantle for such small sub-Neptunes as the TOI-663 planets is still poorly known, but recent studies indicate that this is an important aspect to consider (Misener & Schlichting 2023).

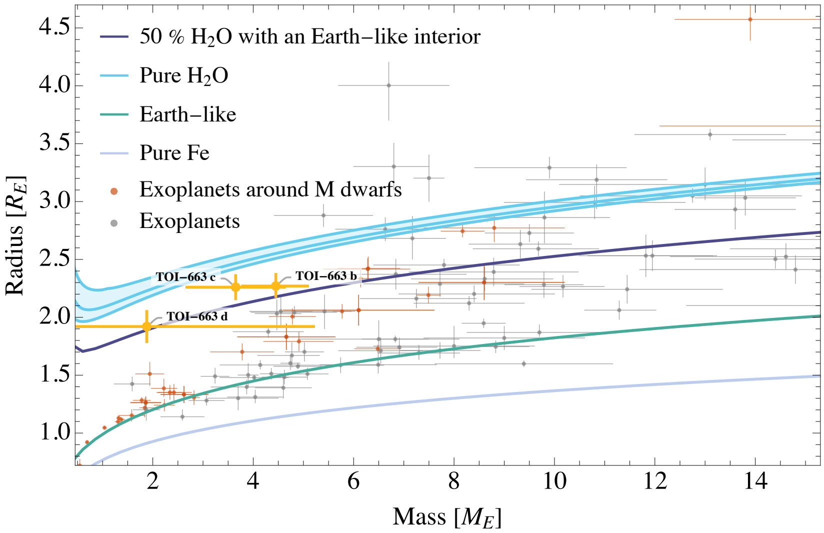

Fig. 14. Mass-radius diagram of the detected exoplanets (Otegi et al. 2020) and the TOI-663 planetary system. The green, gray, and dark blue lines show the mass-radius relation for an Earth-like, a pure-iron composition, and a 50% water content with and Earth-like interior respectively. The blue region shows the M-R relation of pure water for the equilibrium temperature range of the planets in the TOI-663 system.

Table 4. Nested sampling results for a maximum water mass fraction of 50 % (top) and assuming no H-He atmosphere and no limit on the water mass fraction (bottom).

planet	M_{core}/M_p	M_{mantle}/M_p	M_{water}/M_p	$\log(M_{\mathrm{atm}}/M_p)$
TOI-663 b	0.30 ± 0.19	0.42 ± 0.23	0.28 ± 0.13	−4.84 ± 1.81
TOI-663 c	0.30 ± 0.19	0.42 ± 0.23	0.28 ± 0.13	−4.09 ± 1.34
TOI-663 d	0.39 ± 0.23	0.39 ± 0.24	0.22 ± 0.12	−5.00 ± 1.43
TOI-663 b	0.16 ± 0.10	0.28 ± 0.15	0.56 ± 0.09	N/A
TOI-663 c	0.12 ± 0.08	0.26 ± 0.17	0.62 ± 0.13	N/A
TOI-663 d	0.18 ± 0.13	0.35 ± 0.22	0.47 ± 0.13	N/A

Despite evidence that M dwarfs tend to form more rocky planets, the mass-radius diagram of known exoplanets with precise mass (<25%) and radius (<8%), shown in Figure 14, shows that sub-Neptunes around M dwarfs appear to be less dense than those around other stars. The 3 exoplanets of the TOI-663 system tend to agree with this observation.

5.2. Position around the radius valley

Using data from the Kepler and K2 missions, Cloutier & Menou (2020) discovered that the radius valley separating rocky and gaseous planets has a negative slope with insolation around low-mass stars, as opposed to the positive slope found around Solar-type stars (Martinez et al. 2019). This supports models of the direct formation of gas-poor terrestrial planets whose atmospheres were not removed through photo-evaporation (Owen & Wu 2017; Jin & Mordasini 2018; Lopez & Rice 2018), core-powered mass loss (Ginzburg et al. 2018; Gupta & Schlichting 2019, 2020), or impact erosion(Schlichting et al. 2015; Wyatt et al. 2020). In contrast to Cloutier & Menou (2020), Van Eylen et al. (2021) show the opposite trend of the slope of the radius valley with orbital period, which is similar to the positive slope found around Solar-type stars. To resolve the discrepancy, they state that a larger sample of well-studied planets orbiting M dwarf stars is required. Unfortunately, the three TOI-663 exoplanets are located above the radius valley and do not help to constrain either of the two models.

5.3. Similarity of multi-planetary systems

M dwarfs tend to host multi-planetary systems, which can provide much stronger tests for planetary formation theories than single planet systems (Fang & Margot 2012; Steffen & Hwang 2015; Ballard & Johnson 2016). Weiss et al. (2018) have demonstrated a correlation between the size of planets in a multi-planetary system and a regular spacing between them, described as the "peas in the pod" theory. This concept has been employed to restrict planet formation models. According to Otegi et al. (2022) that examined multi-planetary systems observed by K2 and TESS, for which both the radii and the mass were measured precisely, M-dwarf multi-planetary systems exhibit more similarity in density than in mass, indicating a possible connection in their formation mechanism. The densities of the three exoplanets of the TOI-663 system are consistent with each other within 1 sigma, and therefore compatible with the observation of Otegi et al. (2022).

5.4. Potential for atmospheric characterization

Regarding atmospheric characterization, we calculated the transmission spectroscopic metric (TSM) in the J magnitude using the equation from Kempton et al. (2018) and obtained the following values for TOI-663 b, TSM = 76^{+16}_{-12}, for TOI-663 c, TSM = 75^{+29}_{-17}, and for TOI-663 d, TSM = 78^{+120}_{-35}. This value takes into account the equilibrium temperature of the exoplanet computed at its semi-major axis distance. Unfortunately, they all fall below the criteria of Kempton et al. (2018) to be part of the best candidates for transmission spectroscopy.

Acknowledgements. We are grateful to the ESO/La Silla staff for their continuous support. We acknowledge funding from the European Research Council under the ERC Grant Agreement n. 337591-ExTrA. This paper includes data collected by the TESS mission. Funding for the TESS mission is provided by the NASA Explorer Program. We acknowledge the use of public TESS Alert data from the pipelines at the TESS Science Office and at the TESS Science Processing Operations Center. Resources supporting this work were provided by the NASA High-End Computing (HEC) program through the NASA Advanced Supercomputing (NAS) Division at Ames Research Center for the production of the SPOC data products. We thank the Swiss National Science Foundation (SNSF) and the Geneva University for their continuous support to our planet search programs. This work has been in particular carried out in the frame of the National Centre for Competence in Research 'PlanetS' supported by the Swiss National Science Foundation (SNSF). This work made use of `tpfplotter` by J. Lillo-Box (publicly available in www.github.com/jlillo/tpfplotter), which also made use of the python packages `astropy`, `lightkurve`, `matplotlib` and `numpy`. This research was carried out in part at the Jet Propulsion Laboratory, California Institute of Technology, under a contract with the National Aeronautics and Space Administration (NASA). Some of the observations in this paper made use of the High-Resolution Imaging instrument Zorro and were obtained under Gemini LLP Proposal Number: GN/S-2021A-LP-105. Zorro was funded by the NASA Exoplanet Exploration Program and built at the NASA Ames Research Center by Steve B. Howell, Nic Scott, Elliott P. Horch, and Emmett Quigley. Zorro was mounted on the Gemini South telescope of the international Gemini Observatory, a program of NSF's OIR Lab, which is managed by the Association of Universities for Research in Astronomy (AURA) under a cooperative agreement with the National Science Foundation on behalf of the Gemini partnership: the National Science Foundation (United States), National Research Council (Canada), Agencia Nacional de Investigación y Desarrollo (Chile), Ministerio de Ciencia, Tecnología e Innovación (Argentina), Ministério da Ciência, Tecnologia, Inovações e Comunicações (Brazil), and Korea Astronomy and Space Science Institute (Republic of Korea). Some observations in this paper were obtained with MAROON-X, a visitor instrument on the Gemini North telescope, located within the Maunakea Science Reserve and adjacent to the summit of Maunakea. We are grateful for the privilege of observing the Universe from a place that is unique in both its astronomical quality and its cultural significance. This work is based upon observations carried out at the Observatorio Astronómico Nacional on the Sierra de San Pedro Mártir (OAN-SPM), Baja California, México. SAINT-EX observations and team were supported by the Swiss National Science Foundation (PP00P2-163967 and PP00P2-190080), the Centre for Space and Habitability (CSH) of the University of Bern, the National Centre for Competence in Research PlanetS, supported by the Swiss National Science Foundation (SNSF), and UNAM PAPIIT-IG101321. This work makes use of observations from the LCOGT network. Part of the LCOGT telescope time was granted by NOIRLab through the Mid-Scale Innovations Program (MSIP). MSIP is funded by NSF. This research has made use of the Exoplanet Follow-up Observation Program (ExoFOP; DOI: 10.26134/ExoFOP5) website, which is operated by the California Institute of Technology, under contract with the National Aeronautics and Space Administration under the Exoplanet Exploration Program. Funding for the TESS mission is provided by NASA's Science Mission Directorate. This work is partly supported by JSPS KAKENHI Grant Numbers JP17H04574, JP18H05439, JP 18H05442, JP19K14783, JP20K14521, JP21H00035, JP21K13955, JP21K20376, Grant-in-Aid for JSPS Fellows, Grant Number JP20J21872, JST CREST Grant Number JPMJCR1761, and Astrobiology Center SATELLITE Research project AB022006. This article is based on observations made with the MuSCAT2 instrument, developed by ABC, at Telescopio Carlos Sánchez operated on the island of Tenerife by the IAC in the Spanish Observatorio del Teide. M.T. is supported by JSPS KAKENHI grant Nos.18H05442. C.D. acknowledges support from the Swiss National Science Foundation under grant TMSGI2_211313. This material is based upon work supported by the National Science Foundation Graduate Research Fellowship under Grant No. DGE 1746045. GS acknowledges support provided by NASA through the NASA Hubble Fellowship grant HST-HF2-51519.001-A awarded by the Space Telescope Science Institute, which is operated by the Association of Universities for Research in Astronomy, Inc., for NASA, under contract NAS5-26555. JRM and BLCM acknowledge continuous grants from the brazilian funding agencies CAPES (Finance Code 001) and CNPq. The material is based upon work supported by NASA under award number 80GSFC21M0002.

References

Allard, F., Homeier, D., & Freytag, B. 2012, Philosophical Transactions of the Royal Society of London Series A, 370, 2765
Aller, A., Lillo-Box, J., Jones, D., Miranda, L. F., & Barceló Forteza, S. 2020, A&A, 635, A128
Ambikasaran, S., Foreman-Mackey, D., Greengard, L., Hogg, D. W., & O'Neil, M. 2015, IEEE Transactions on Pattern Analysis and Machine Intelligence, 38, 252
Anderson, J. D., Esposito, P. B., Martin, W., Thornton, C. L., & Muhleman, D. O. 1975, ApJ, 200, 221
Astudillo-Defru, N., Delfosse, X., Bonfils, X., et al. 2017a, A&A, 600, A13
Astudillo-Defru, N., Forveille, T., Bonfils, X., et al. 2017b, A&A, 602, A88
Bailer-Jones, C. A. L., Rybizki, J., Fouesneau, M., Mantelet, G., & Andrae, R. 2018, AJ, 156, 58
Ballard, S. & Johnson, J. A. 2016, ApJ, 816, 66
Barros, S. C. C., Almenara, J. M., Demangeon, O., et al. 2015, MNRAS, 454, 4267
Batalha, N. E., Lewis, N. K., Line, M. R., Valenti, J., & Stevenson, K. 2018, ApJ, 856, L34
Bellm, E. C., Kulkarni, S. R., Graham, M. J., et al. 2019, PASP, 131, 018002
Bonfils, X., Almenara, J. M., Jocou, L., et al. 2015, in Society of Photo-Optical Instrumentation Engineers (SPIE) Conference Series, Vol. 9605, Techniques and Instrumentation for Detection of Exoplanets VII, ed. S. Shaklan, 96051L
Bouchy, F., Doyon, R., Artigau, É., et al. 2017, The Messenger, 169, 21
Brown, T. M., Baliber, N., Bianco, F. B., et al. 2013, PASP, 125, 1031
Buchner, J., Georgakakis, A., Nandra, K., et al. 2014, A&A, 564, A125
Canto Martins, B. L., Gomes, R. L., Messias, Y. S., et al. 2020, ApJS, 250, 20
Chen, Y., Girardi, L., Bressan, A., et al. 2014, MNRAS, 444, 2525
Ciardi, D. R., Beichman, C. A., Horch, E. P., & Howell, S. B. 2015, ApJ, 805, 16
Cloutier, R. & Menou, K. 2020, AJ, 159, 211
Cointepas, M., Almenara, J. M., Bonfils, X., et al. 2021, A&A, 650, A145
Collins, K. 2019, in American Astronomical Society Meeting Abstracts, Vol. 233, American Astronomical Society Meeting Abstracts #233, 140.05
Collins, K. A., Kielkopf, J. F., Stassun, K. G., & Hessman, F. V. 2017a, AJ, 153, 77
Collins, K. A., Kielkopf, J. F., Stassun, K. G., & Hessman, F. V. 2017b, AJ, 153, 77
Cutri, R. M. & et al. 2013, VizieR Online Data Catalog, II/328
Cutri, R. M., Skrutskie, M. F., van Dyk, S., et al. 2003, VizieR Online Data Catalog, II/246
Delisle, J. B. 2017, A&A, 605, A96
Demory, B. O., Pozuelos, F. J., Gómez Maqueo Chew, Y., et al. 2020, A&A, 642, A49
Díaz, R. F., Almenara, J. M., Santerne, A., et al. 2014, MNRAS, 441, 983
Dorn, C. & Lichtenberg, T. 2021, The Astrophysical Journal Letters, 922, L4
Dorn, C., Venturini, J., Khan, A., et al. 2017, A&A, 597, A37
Dotter, A., Chaboyer, B., Jevremović, D., et al. 2008, ApJS, 178, 89
Espinoza, N. 2018, Research Notes of the American Astronomical Society, 2, 209
Espinoza, N. & Jordán, A. 2015, MNRAS, 450, 1879
Espinoza, N., Kossakowski, D., & Brahm, R. 2019, MNRAS, 490, 2262
Evans, D. W., Riello, M., De Angeli, F., et al. 2018, A&A, 616, A4
Fang, J. & Margot, J.-L. 2012, ApJ, 761, 92
Foreman-Mackey, D., Agol, E., Ambikasaran, S., & Angus, R. 2017, AJ, 154, 220
Fukui, A., Narita, N., Tristram, P. J., et al. 2011, PASJ, 63, 287
Fulton, B. J., Petigura, E. A., Blunt, S., & Sinukoff, E. 2018, PASP, 130, 044504
Fulton, B. J., Petigura, E. A., Howard, A. W., et al. 2017, AJ, 154, 109
Furlan, E., Ciardi, D. R., Everett, M. E., et al. 2017, AJ, 153, 71
Gaia Collaboration, Brown, A. G. A., Vallenari, A., et al. 2018, A&A, 616, A1
Gillon, M., Triaud, A. H. M. J., Demory, B.-O., et al. 2017, Nature, 542, 456
Ginzburg, S., Schlichting, H. E., & Sari, R. 2018, MNRAS, 476, 759
Gomes da Silva, J., Santos, N. C., & Bonfils, X. 2011, in Astronomical Society of the Pacific Conference Series, Vol. 448, 16th Cambridge Workshop on Cool Stars, Stellar Systems, and the Sun, ed. C. Johns-Krull, M. K. Browning, & A. A. West, 1117
Guerrero, N. M., Seager, S., Huang, C. X., et al. 2021, ApJS, 254, 39
Gupta, A. & Schlichting, H. E. 2019, MNRAS, 487, 24
Gupta, A. & Schlichting, H. E. 2020, MNRAS, 493, 792
Haldemann, J., Alibert, Y., Mordasini, C., & Benz, W. 2020, A&A, 643, A105
Hardegree-Ullman, K. K., Zink, J. K., Christiansen, J. L., et al. 2020, ApJS, 247, 28

Hirano, T., Kuzuhara, M., Kotani, T., et al. 2020, PASJ, 72, 93

Howell, S. B., Everett, M. E., Sherry, W., Horch, E., & Ciardi, D. R. 2011, AJ, 142, 19

Jenkins, J. M. 2002, ApJ, 575, 493

Jenkins, J. M., Chandrasekaran, H., McCauliff, S. D., et al. 2010, in Society of Photo-Optical Instrumentation Engineers (SPIE) Conference Series, Vol. 7740, Software and Cyberinfrastructure for Astronomy, ed. N. M. Radziwill & A. Bridger, 77400D

Jenkins, J. M., Tenenbaum, P., Seader, S., et al. 2020, Kepler Data Processing Handbook: Transiting Planet Search, Kepler Data Processing Handbook (KSCI-19081-003)

Jenkins, J. M., Twicken, J. D., McCauliff, S., et al. 2016, in Society of Photo-Optical Instrumentation Engineers (SPIE) Conference Series, Vol. 9913, Software and Cyberinfrastructure for Astronomy IV, 99133E

Jensen, E. 2013, Tapir: A web interface for transit/eclipse observability, Astrophysics Source Code Library

Jin, S. & Mordasini, C. 2018, ApJ, 853, 163

Kass, R. E. & Raftery, A. E. 1995, Journal of the American Statistical Association, 90, 773

Kempton, E. M. R., Bean, J. L., Louie, D. R., et al. 2018, PASP, 130, 114401

Kimura, T. & Ikoma, M. 2020, Monthly Notices of the Royal Astronomical Society, 496, 3755

Kipping, D. M. 2013, MNRAS, 435, 2152

Kotani, T., Tamura, M., Nishikawa, J., et al. 2018, in Society of Photo-Optical Instrumentation Engineers (SPIE) Conference Series, Vol. 10702, Ground-based and Airborne Instrumentation for Astronomy VII, ed. C. J. Evans, L. Simard, & H. Takami, 1070211

Kreidberg, L. 2015, PASP, 127, 1161

Kürster, M., Endl, M., Rouesnel, F., et al. 2003, in ESA Special Publication, Vol. 539, Earths: DARWIN/TPF and the Search for Extrasolar Terrestrial Planets, ed. M. Fridlund, T. Henning, & H. Lacoste, 485–489

Laskar, J. 1990, Icarus, 88, 266

Laskar, J. 1993, Physica D, 67, 257

Lee, E. J. & Connors, N. J. 2021, ApJ, 908, 32

Li, J., Tenenbaum, P., Twicken, J. D., et al. 2019, PASP, 131, 024506

Lillo-Box, J., Figueira, P., Leleu, A., et al. 2020, A&A, 642, A121

Lindegren, L., Hernández, J., Bombrun, A., et al. 2018, A&A, 616, A2

Lodders, K. 2020, Solar Elemental Abundances

Lopez, E. D. & Rice, K. 2018, MNRAS, 479, 5303

Lozovsky, M., Helled, R., Dorn, C., & Venturini, J. 2018, ApJ, 866, 49

Luger, R., Sestovic, M., Kruse, E., et al. 2017, Nature Astronomy, 1, 0129

Luque, R. & Pallé, E. 2022, Science, 377, 1211

Maíz Apellániz, J. & Weiler, M. 2018, A&A, 619, A180

Mann, A. W., Dupuy, T., Kraus, A. L., et al. 2019, ApJ, 871, 63

Mann, A. W., Feiden, G. A., Gaidos, E., Boyajian, T., & von Braun, K. 2015, ApJ, 804, 64

Martinez, C. F., Cunha, K., Ghezzi, L., & Smith, V. V. 2019, ApJ, 875, 29

Mayo, A. W., Vanderburg, A., Latham, D. W., et al. 2018, AJ, 155, 136

Mayor, M., Pepe, F., Queloz, D., et al. 2003, The Messenger, 114, 20

McCully, C., Volgenau, N. H., Harbeck, D.-R., et al. 2018, in Society of Photo-Optical Instrumentation Engineers (SPIE) Conference Series, Vol. 10707, Proc. SPIE, 107070K

Millholland, S., Wang, S., & Laughlin, G. 2017, ApJ, 849, L33

Misener, W. & Schlichting, H. E. 2023, arXiv preprint arXiv:2303.09653

Mordasini, C., Alibert, Y., & Benz, W. 2009, Astronomy & Astrophysics, 501, 1139

Mugrauer, M. & Michel, K.-U. 2020, Astronomische Nachrichten, 341, 996

Mugrauer, M. & Michel, K.-U. 2021, Astronomische Nachrichten, 342, 840

Narita, N., Fukui, A., Kusakabe, N., et al. 2015, Journal of Astronomical Telescopes, Instruments, and Systems, 1, 045001

Narita, N., Fukui, A., Kusakabe, N., et al. 2019, Journal of Astronomical Telescopes, Instruments, and Systems, 5, 015001

Otegi, J. F., Bouchy, F., & Helled, R. 2020, A&A, 634, A43

Otegi, J. F., Helled, R., & Bouchy, F. 2022, A&A, 658, A107

Owen, J. E. & Wu, Y. 2017, ApJ, 847, 29

Parviainen, H., Palle, E., Zapatero-Osorio, M. R., et al. 2020, A&A, 633, A28

Pecaut, M. J. & Mamajek, E. E. 2013, ApJS, 208, 9

Pepe, F., Cristiani, S., Rebolo, R., et al. 2021, A&A, 645, A96

Pojmanski, G. 2002, Acta Astron., 52, 397

Reefe, M., Alfaro, O., Foster, S., et al. 2022, Journal of Astronomical Telescopes, Instruments, and Systems, 8, 027002

Rein, H. & Liu, S. F. 2012, A&A, 537, A128

Rein, H. & Spiegel, D. S. 2015, MNRAS, 446, 1424

Ricker, G. R., Winn, J. N., Vanderspek, R., et al. 2015, Journal of Astronomical Telescopes, Instruments, and Systems, 1, 014003

Rogers, J. G., Schlichting, H. E., & Owen, J. E. 2023, arXiv preprint arXiv:2301.04321

Schlichting, H. E., Sari, R., & Yalinewich, A. 2015, Icarus, 247, 81

Scott, N. J., Howell, S. B., Gnilka, C. L., et al. 2021, Frontiers in Astronomy and Space Sciences, 8, 138

Seifahrt, A., Bean, J. L., Kasper, D., et al. 2022, in Society of Photo-Optical Instrumentation Engineers (SPIE) Conference Series, Vol. 12184, Ground-based and Airborne Instrumentation for Astronomy IX, ed. C. J. Evans, J. J. Bryant, & K. Motohara, 121841G

Seifahrt, A., Stürmer, J., Bean, J. L., & Schwab, C. 2018, in Society of Photo-Optical Instrumentation Engineers (SPIE) Conference Series, Vol. 10702, Ground-based and Airborne Instrumentation for Astronomy VII, ed. C. J. Evans, L. Simard, & H. Takami, 107026D

Skrutskie, M. F., Cutri, R. M., Stiening, R., et al. 2006a, AJ, 131, 1163

Skrutskie, M. F., Cutri, R. M., Stiening, R., et al. 2006b, AJ, 131, 1163

Smith, J. C., Stumpe, M. C., Van Cleve, J. E., et al. 2012, PASP, 124, 1000

Speagle, J. S. 2020, MNRAS, 493, 3132

Stalport, M., Delisle, J. B., Udry, S., et al. 2022, A&A, 664, A53

Stassun, K. G., Oelkers, R. J., Paegert, M., et al. 2019, AJ, 158, 138

Steffen, J. H. & Hwang, J. A. 2015, MNRAS, 448, 1956

Stumpe, M. C., Smith, J. C., Catanzarite, J. H., et al. 2014, PASP, 126, 100

Stumpe, M. C., Smith, J. C., Van Cleve, J. E., et al. 2012, PASP, 124, 985

Tamayo, D., Rein, H., Shi, P., & Hernandez, D. M. 2020, MNRAS, 491, 2885

Tamura, M., Suto, H., Nishikawa, J., et al. 2012, in Society of Photo-Optical Instrumentation Engineers (SPIE) Conference Series, Vol. 8446, Ground-based and Airborne Instrumentation for Astronomy IV, ed. I. S. McLean, S. K. Ramsay, & H. Takami, 84461T

Trifonov, T., Caballero, J. A., Morales, J. C., et al. 2021, Science, 371, 1038

Twicken, J. D., Catanzarite, J. H., Clarke, B. D., et al. 2018, PASP, 130, 064502

Van Eylen, V., Astudillo-Defru, N., Bonfils, X., et al. 2021, MNRAS, 507, 2154

Weiss, L. M., Marcy, G. W., Petigura, E. A., et al. 2018, AJ, 155, 48

Wizinowich, P., Acton, D. S., Shelton, C., et al. 2000, PASP, 112, 315

Wright, E. L., Eisenhardt, P. R. M., Mainzer, A. K., et al. 2010, AJ, 140, 1868

Wyatt, M. C., Kral, Q., & Sinclair, C. A. 2020, MNRAS, 491, 782

Yee, S. W., Petigura, E. A., & von Braun, K. 2017, ApJ, 836, 77

Zechmeister, M., Reiners, A., Amado, P. J., et al. 2018, A&A, 609, A12

Zeng, L., Jacobsen, S. B., Sasselov, D. D., et al. 2019, Proceedings of the National Academy of Sciences, 116, 9723

Ziegler, C., Tokovinin, A., Briceño, C., et al. 2020, AJ, 159, 19

---

[1] Univ. Grenoble Alpes, CNRS, IPAG, F-38000 Grenoble, France

[2] Observatoire de Genève, Département d'Astronomie, Université de Genève, Chemin Pegasi 51b, 1290 Versoix, Switzerland

[3] Departamento de Matemática y Física Aplicadas, Universidad Católica de la Santísima Concepción, Alonso de Rivera 2850, Concepción, Chile

[4] Center for Astrophysics | Harvard & Smithsonian, 60 Garden Street, Cambridge, MA 02138, USA

[5] George Mason University, 4400 University Drive, Fairfax, VA, 22030 USA

[6] Department of Astronomy and Tsinghua Centre for Astrophysics, Tsinghua University, Beijing 100084, China

[7] Institute for Computational Science, University of Zurich, Winterthurerstr. 190, CH-8057 Zurich, Switzerland

[8] Institute for Particle Physics and Astrophysics, ETH Zürich, Wolfgang-Pauli-Strasse 27, CH-8093 Zurich, Switzerland

[9] Departamento de Física, Universidade Federal do Rio Grande do Norte, 59072-970 Natal, RN, Brazil

[10] Instituto de Astrofísica de Canarias (IAC), E-38200 La Laguna, Tenerife, Spain

[11] Dept. Astrofísica, Universidad de La Laguna (ULL), E-38206 La Laguna, Tenerife, Spain

[12] Department of Physics and Kavli Institute for Astrophysics and Space Research, Massachusetts Institute of Technology, Cambridge, MA 02139, USA

[13] Department of Earth, Atmospheric and Planetary Sciences, Massachusetts Institute of Technology, Cambridge, MA 02139, USA

[14] Department of Aeronautics and Astronautics, MIT, 77 Massachusetts Avenue, Cambridge, MA 02139, USA

[15] Department of Astrophysical Sciences, Princeton University, NJ 08544, USA

[16] NASA Ames Research Center, Moffett Field, CA 94035, USA

[17] Jet Propulsion Laboratory, California Institute of Technology, 4800 Oak Grove drive, Pasadena, CA, 91109, USA

[18] NASA Exoplanet Science Institute-Caltech/IPAC, Pasadena, CA 91125, USA

[19] Astronomy Department, University of California, Berkeley, CA 94720, USA

[20] U.S. Naval Observatory, 3450 Massachusetts Avenue NW, Washington, D.C. 20392, USA
[21] Department of Physics & Astronomy, Swarthmore College, Swarthmore PA 19081, USA
[22] Villa '39 Observatory, Landers, CA 92285, USA
[23] Department of Physics and Astronomy, Union College, 807 Union St., Schenectady, NY 12308, USA
[24] SUPA Physics and Astronomy, University of St. Andrews, Fife, KY16 9SS Scotland, UK
[25] Space sciences, Technologies and Astrophysics Research (STAR) Institute, University of Liège, Allée du 6 Août 19C, 4000 Liège, Belgium
[26] Perth Exoplanet Survey Telescope, Perth, Western Australia, Australia
[27] Komaba Institute for Science, The University of Tokyo, 3-8-1 Komaba, Meguro, Tokyo 153-8902, Japan
[28] Okayama Observatory, Kyoto University, 3037-5 Honjo, Kamogatacho, Asakuchi, Okayama 719-0232, Japan
[29] Department of Multi-Disciplinary Sciences, Graduate School of Arts and Sciences, The University of Tokyo, 3-8-1 Komaba, Meguro, Tokyo
[30] Department of Physical Sciences, Ritsumeikan University, Kusatsu, Shiga 525-8577, Japan
[31] Astrobiology Center, 2-21-1 Osawa, Mitaka, Tokyo 181-8588, Japan

[32] National Astronomical Observatory of Japan, 2-21-1 Osawa, Mitaka, Tokyo 181-8588, Japan
[33] Department of Astronomical Science, The Graduated University for Advanced Studies, SOKENDAI, 2-21-1, Osawa, Mitaka, Tokyo, 181-8588, Japan
[34] Department of Astronomy, Graduate School of Science, The University of Tokyo, 7-3-1 Hongo, Bunkyo-ku, Tokyo 113-0033, Japan

[35] Department of Astronomy and Astrophysics, The University of Chicago, 5640 South Ellis Avenue, Chicago, IL 60637, USA
[36] Landessternwarte, Zentrum für Astronomie der Universität Heidelberg, Königstuhl 12, 69117 Heidelberg, Germany
[37] Department of Astrophysical Sciences, Princeton University, 4 Ivy Lane, Princeton, NJ 08540, USA
[38] Institut für Astrophysik und Geophysik, Georg-August-Universität Göttingen, Friedrich-Hund-Platz 1, 37077 Göttingen, Germany
[39] Center for Space and Habitability, University of Bern, Gesellschaftsstrasse 6, 3012, Bern, Switzerland
[40] Universidad Nacional Autónoma de México, Instituto de Astronomía, AP 70-264, CDMX 04510, México
[41] Universidad Nacional Autónoma de México, Instituto de Astronomía, AP 106, Ensenada 22800, BC, México
[42] SETI Institute, Mountain View, CA 94043, USA
[43] NASA Sagan Fellow
[44] Department of Astronomy, University of Maryland, College Park, MD 20742

Appendix A: Radial velocity measurements

Appendix B: Corner plot of some parameters from the join fit of all data.

Table A.1. Radial velocity measurements for the different spectrographs used in this analysis.

Time (BJD - 2400000)	RV (km/s)	RV err (km/s)	Instrument
58910.723746	34.324020	0.004000	HARPS
58911.771067	34.318880	0.004440	HARPS
58912.716950	34.329700	0.005490	HARPS
58915.705378	34.323300	0.004940	HARPS
58916.751278	34.326390	0.003840	HARPS
58917.771100	34.334450	0.004290	HARPS
58918.715956	34.327300	0.004800	HARPS
58924.721557	34.323460	0.004360	HARPS
58925.718218	34.324960	0.005640	HARPS
58926.725780	34.323560	0.004520	HARPS
58927.736396	34.322920	0.004490	HARPS
58928.709603	34.321810	0.004390	HARPS
58929.717392	34.314330	0.007000	HARPS
58930.707725	34.312610	0.008150	HARPS
58931.737397	34.322390	0.005710	HARPS
59171.848568	34.323730	0.004830	HARPS
59176.826197	34.334770	0.005100	HARPS
59196.785378	34.321760	0.004010	HARPS
59197.791841	34.322360	0.004700	HARPS
59198.795178	34.332740	0.004190	HARPS
59220.777917	34.336650	0.004230	HARPS
59221.761564	34.337840	0.003190	HARPS
59223.747478	34.335450	0.003470	HARPS
59224.732789	34.328460	0.003270	HARPS
59262.759243	34.322320	0.003830	HARPS
59263.749363	34.340640	0.004060	HARPS
59264.712802	34.333680	0.003770	HARPS
59265.741670	34.324630	0.004580	HARPS
59266.698914	34.329960	0.004020	HARPS
59267.741355	34.332680	0.004740	HARPS
59268.788980	34.328840	0.004230	HARPS
59269.672306	34.338130	0.004470	HARPS
59286.794959	34.329480	0.004600	HARPS
59287.761950	34.322910	0.004330	HARPS
59288.761531	34.320690	0.006520	HARPS
59290.717159	34.319910	0.004200	HARPS
59366.521206	34.331450	0.005130	HARPS
59367.552764	34.326720	0.005090	HARPS
59369.521491	34.331190	0.005140	HARPS
59372.544956	34.338960	0.004120	HARPS
59674.553825	34.274761	0.001426	ESPRESSO
59675.576856	34.263909	0.001523	ESPRESSO
59676.670671	34.268350	0.002146	ESPRESSO
59677.512074	34.266289	0.003088	ESPRESSO
59678.659022	34.263947	0.002010	ESPRESSO
59679.625607	34.268052	0.001628	ESPRESSO
59680.566038	34.259502	0.001265	ESPRESSO
59682.524050	34.272004	0.001389	ESPRESSO
59685.570917	34.265878	0.002843	ESPRESSO
59687.548051	34.277600	0.001226	ESPRESSO
59267.876851	33.052791	0.002311	MAROON-X blue
59268.007143	33.048796	0.003156	MAROON-X blue
59269.852498	33.056575	0.002331	MAROON-X blue
59269.981134	33.052285	0.002319	MAROON-X blue
59276.915064	33.064205	0.002425	MAROON-X blue
59277.880398	33.057519	0.002386	MAROON-X blue
59278.032393	33.057208	0.002369	MAROON-X blue
59323.793794	33.059731	0.001462	MAROON-X blue
59327.768365	33.057727	0.001732	MAROON-X blue
59332.910732	33.063903	0.002816	MAROON-X blue
59333.769718	33.064511	0.001553	MAROON-X blue
59333.894284	33.067126	0.002444	MAROON-X blue
59334.771413	33.059801	0.001489	MAROON-X blue
59334.858713	33.059432	0.001687	MAROON-X blue
59267.876851	33.048031	0.001835	MAROON-X red
59268.007143	33.050574	0.002479	MAROON-X red
59269.852498	33.055762	0.001778	MAROON-X red
59269.981134	33.052448	0.001904	MAROON-X red
59276.915064	33.062313	0.001993	MAROON-X red
59277.880398	33.059240	0.001935	MAROON-X red
59278.032393	33.055978	0.001772	MAROON-X red
59323.793794	33.059169	0.001161	MAROON-X red
59327.768365	33.059375	0.001376	MAROON-X red
59332.910732	33.062870	0.001697	MAROON-X red
59333.769718	33.065211	0.001285	MAROON-X red
59333.894284	33.064958	0.001632	MAROON-X red
59334.771413	33.061625	0.001232	MAROON-X red
59334.858713	33.061741	0.001275	MAROON-X red
59248.003442	-0.00625	0.00376	IRD
59275.916993	-0.00858	0.00484	IRD
59275.975987	-0.00166	0.00446	IRD
59338.810860	0.00222	0.00353	IRD
59373.773176	0.00134	0.00364	IRD

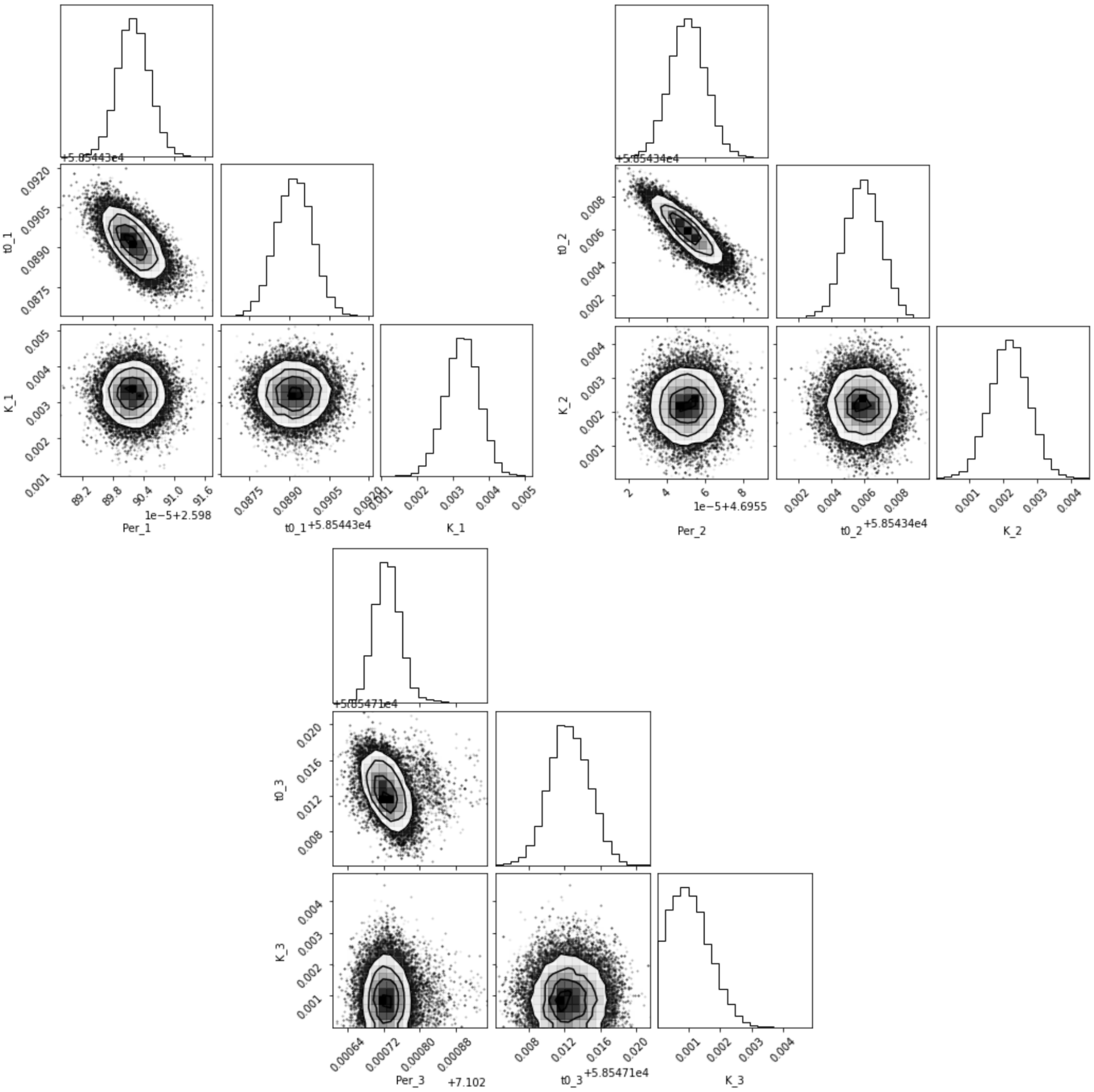

Fig. B.1. Corner plots showing the posterior distributions of the period (days), time of transit center (BJD_{TDB}) and radial velocity semi-amplitude (km/s) for the three planets from the joint modeling of photometry and radial velocity datasets.

III

THE PHOTOMETRIC EXPERIMENT EXTRA

"I couldn’t help but ask for you to say it all again
I tried to write it down, but I could never find a pen
I’d give anything to hear you say it one more time
That the universe was made just to be seen by my eyes"
Saturn by Sleeping At Last

INTRODUCTION

I spent most of my PhD journey working with ExTrA, the facility located at La Silla Observatory in Chile. This facility includes an near-infrared multi-object spectrograph fed by three 60-cm telescopes. The project aimed at extending the precision of visible photometry to near-infrared photometry using the spectroscopic information to select the best wavelength bands and remove what could cause color-dependent systematics and disrupt ground-based observations. With this unique approach, ExTrA is hoping to uncover transiting rocky planets orbiting in the habitable zone of nearby M dwarfs. These discoveries could be further studied using advanced telescopes such as the VLT, JWST, and ELT, paving the way for an exo-life laboratory. My work involved detecting transiting exoplanets by screening through raw data to create usable light curves. Once the light curves created, I analyzed them to identify any planetary transits and modeled them to obtain the planetary parameters. As part of my work, I was also in charge of the target selection based on different sub-programs. While M dwarfs are favorable targets for exoplanet detection, their stellar companions can cause false positives and interfere with planet characterization. That’s why follow-up observations using ground-based instruments are necessary to validate the planetary nature of the companion.

III.1 THE INSTRUMENT

ExTrA is composed of three 60-cm telescopes feeding a near-infrared spectrograph. The project is described in details in Bonfils et al., 2015. The telescopes are placed in three domes and an auxiliary building houses the spectrograph, main server, weather station, all-sky camera, and a webcam. A picture of ExTrA is presented in Figure III.1.

Figure III.1: The ExTrA facility.
Picture of the three domes and auxiliary building of ExTrA, at La Silla Observatory in Chile. Credit: A. Ghizzi Panizza/ESO.

III.1.1 *Overall description of the instrument*

On each telescope, 5 Field Units (FUs) are used in place of a CCD camera to pick up light from the target and 4 selected comparison stars. The spectro-photometry of the target will be compared to the spectro-photometry of the four comparison stars. The FUs are made up of fibers, precisely positioned to ensure photometric stability. The three telescopes are independent, and all fibers from all three feed a single near-infrared spectrograph with a low spectral resolution, where two different prisms are available with resolutions of R$\sim$20 or R$\sim$200, and wavelength coverage from 0.85 to 1.55 microns. ExTrA has a large field of view of 1 degree to have enough convenient comparison stars to select from, and a guiding camera is used to reduce the guiding error to less than 0.05 arcsec over an integration.

The FUs collect and inject the telescope beams of the target and the 4 comparison stars into the optical fibers. Each FU is made up of two "buttons": one for science and one for centering. The centering button is made up of a bundle of 19 fibers. They provide a 'pixelated' view of the field near the star. The flux distribution between fibers is used to compute the actual position of the star. We can correct between this position and the predicted position before moving the star and then apply a relative movement precise to 1 micron to center the star in the science button. Each science button is made up of two channels: one for bright stars with an aperture of 8 arcsec and another optimized for fainter stars with an aperture of 4 arcsec in order to reduce the background contribution coming from the sky. Each channel has two fibers: one to collect the star's light and the other to collect the sky background near the star. The schematic of the instrument is showed in Figure III.2. Each telescope has 5 FUs, each with 4 science fibers and one fiber bundle, for a total of 60 fibers and 15 bundles of 20 meters length connecting the focal planes of the telescopes to the spectrograph. Only 30 fibers are used simultaneously (either the 8 arcsec or 4 arcsec aperture).

The spectrograph can image the fiber bundles in centering mode and disperse the science fibers with a prism using a different light path (see Figure III.3). A flipping mirror in the science light path is used to select the centering mode. To ensure precision and repeatability of measurements, the spectrograph science optical path contains no moving parts. The spectrograph is housed in a thermally controlled isolated room in the auxiliary building.

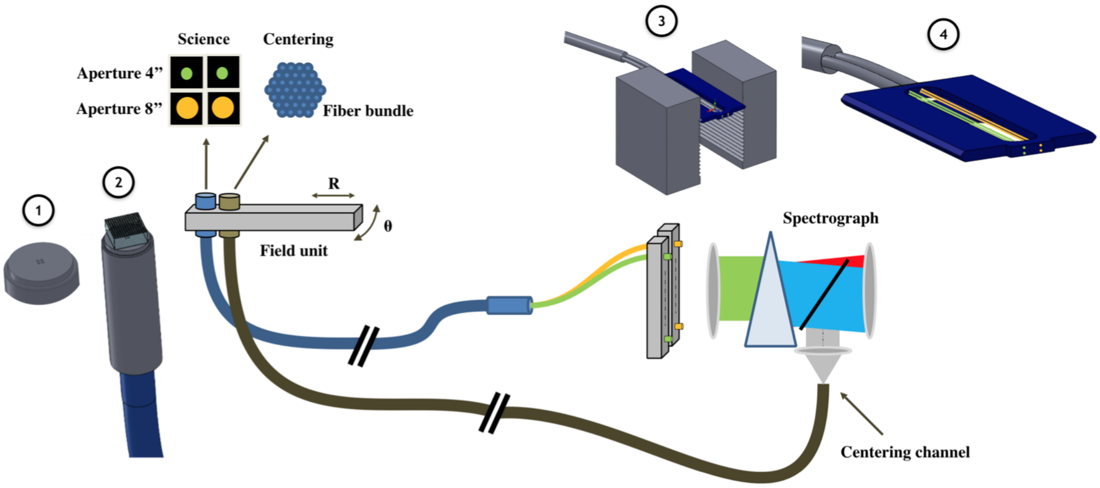

Figure III.2: ExTrA fiber system schematic.
Design of the fiber system from FUs to spectrograph, with 3D implementation of some parts: science button detail (1), science button with microlens (2), drawer arrangement at the spectrograph image plane (3), and drawer detail (4).

III.1.2 *Specificities*

When compared to current ground-based photometric instruments, ExTrA experimental setup has several advantages and we hope that this new concept will overcome the limitations of previous photometric surveys. Let me describe how in the next paragraphs.

The spectra of comparison stars never perfectly match the spectrum of the target in traditional differential photometry. When the atmospheric absorption is chromatic, the amount of light filtered out by the Earth’s atmosphere varies slightly between the target and the comparison stars. As a result, ground-based transit searches must choose a narrow band-pass with as few telluric lines as possible. However, ExTrA possesses a multi-object spectrograph with 200 spectral channels of less than 6nm resolution (R$\sim$200). The resolution enables differential photometry with much narrower spectral channels, which leads to

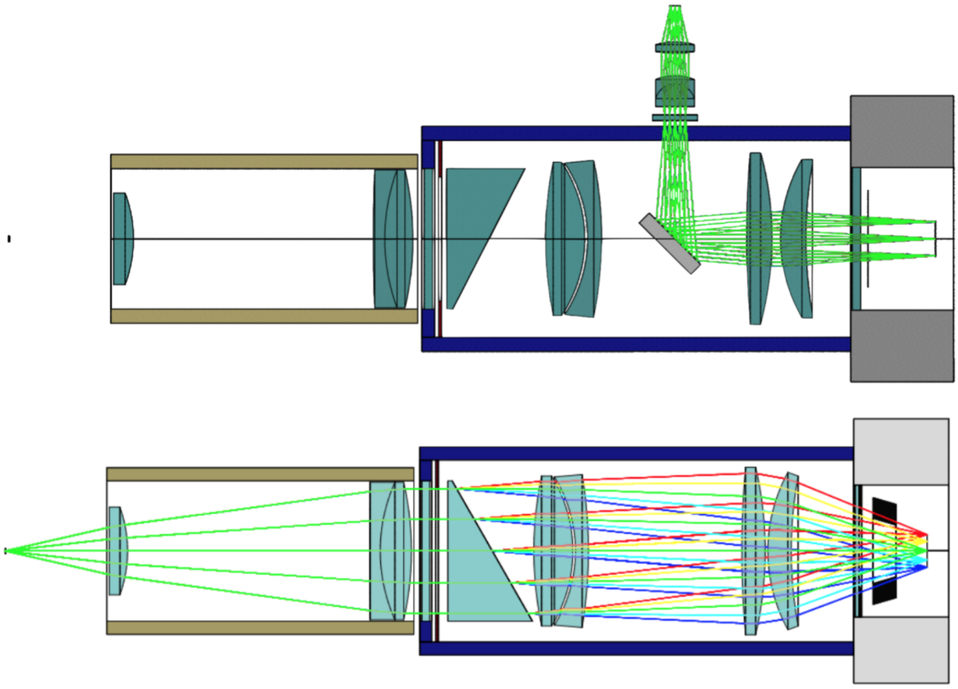

Figure III.3: ExTrA spectrograph.
The two configurations of the spectrograph: centering mode (upper panel), and science mode (lower panel).

much finer atmospheric variation correction. And the wide spectral domain allows for the simultaneous collection of more photons, resulting in an increased efficiency. The spectral resolution is then degraded by performing differential photometry on individual spectral channels, resulting in broad band light curves with high signal-to-noise ratios.

Detectors with large areas are typically required for ground-based transit searches but large infrared detectors are expensive. ExTrA has the advantage of multiplexing, meaning that we can record light from multiple telescopes using a single spectrograph, so a single camera. The spectrograph will also use the detector area much more efficiently than imagers, allowing for smaller detectors and a less expensive camera. This provides an opportunity to observe at infrared wavelengths at a low cost, which is a huge advantage when observing M dwarfs that emits most of their photons in this wavelengths range, as we can see in Figure III.4.

Pixels on the detector have flaws. A good differential photometry practice is to always guide on the same pixel. Although it can help reducing some systematics, seeing variations and guiding errors remain and make maintaining an identical illumination for a given pixel impossible. Defocusing the telescope is another common practice by sampling the comparison stars and target point spread functions using more pixels (up to a few hundred), and then the systematics average down with the square root of their number. ExTrA distributes each spectra across 3000 pixels, ensuring excellent detector systematics averaging.

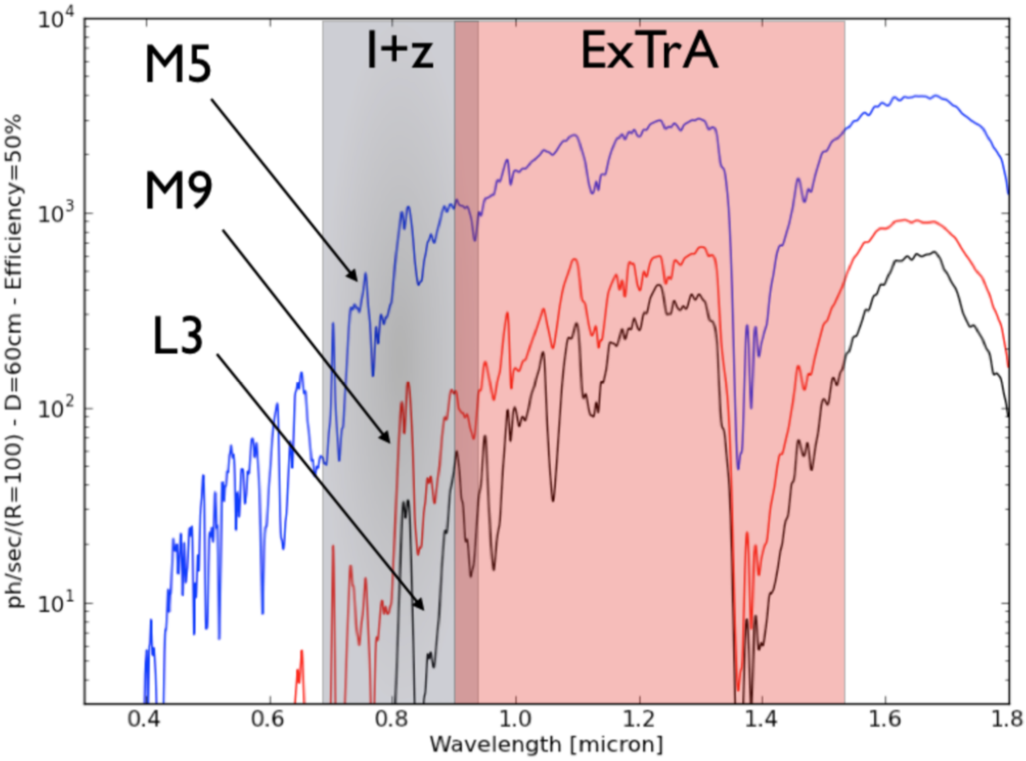

Figure III.4: Photon distribution of different spectral type stars.
The photon distribution is computed per R=100 resolution element for a M5@15pc, a M9@10pc, and a L3@10pc dwarfs, as would be recorded with a telescope of 60-cm diameter, with a 50% efficiency, and through the Earth atmosphere. The gray zone labeled 'I+z' is the typical band pass of ground-based transit surveys. The red zone labeled ExTrA is our spectral window. Stellar spectra are derived from NextGen models and the Earth atmospheric transmission from ATRAN.

III.2 OPERATIONS, SCHEDULING AND OBSERVATIONS

ExTrA observations are made entirely remotely. We select targets and observe them when a transit is expected to happen (see Section III.5 for the different ExTrA science cases). To do so we use a transit predictor tool, developed by a member of the ExTrA science team, that takes as input the ephemeris computed using the TESS photometry or more precise ephemeris and displays for the selected night which transits are visible from La

Silla Observatory as well as the time and duration of the transits. A few targets, usually 2 to 3 per night, are then selected to be observed. During the first couple of years of ExTrA observations, we decided that the three telescopes would observe the same target in order to properly estimate the capabilities of the instrument. The three telescopes can of course observe different targets at the same time in order to increase the efficiency of our survey.

For each target, the field of observation is prepared in advance using a custom software and the same one is used for each observation of a specific star (the field of view for the TRAPPIST-1 star is displayed as an example in Figure III.5). In addition of selecting the desired field of view for the observation, the size of the fiber (4" or 8"), the resolution of the prism ($R{\sim}20$ or $R{\sim}200$) and the exposure time are also decided. An exposure time of 60 seconds is used for all ExTrA transit observations, and the observations usually last the duration of the expected transit + 30min to an hour baseline before and after the transit. A limit at a J magnitude of 9 was first chosen to select between a high or low resolution mode. We adjusted this limit to a J magnitude of 8.5 according to dispersion plots as a function of the J magnitude. For the fiber size, the interest is to reduce the sky contribution for the faintest stars. From the scatter plots as a function the J magnitude, we decided to that for $J >\sim 13$, the 4 arcsec fiber should be used. The 4 arcsec fiber is also preferred if the target has close contaminants, but it is more sensitive to star motion in the field. We also give instructions on how to focus, in order to collect the entire PSF of the star inside the fiber, and how to center the star in the fiber. For the centering, we hope to achieve a precision of less than 3 arcsec. The last centering offset obtained before the start of the observation is indicated in the report of each sequence (see Figure III.11). The guiding and centering are very sensitive to the seeing conditions.

The experiment is controlled by a main server from the auxiliary building. In order for all the computers to communicate between each other and pilot the telescope, we use TANGO controls as well as custom Python functions. TANGO controls is a free open source device-oriented controls toolkit for controlling any kind of hardware or software. It provides a complete set of features for controlling equipment and lot of services for managing systems.

The contribution of the solar continuum coming from the brightness of the Moon diminishes as one moves into the red, and at wavelengths longer than 900 nm, the emission bands produced by atmospheric OH are the dominant source of night sky radiation. Even in the presence of a full moon, they completely dominate the night sky emission at even longer wavelengths, in the near-IR (Patat, 2004). However, we noticed that even though ExTrA is observing in the near-infrared, our photometry was directly impacted by the Moon. We noticed that the fluxes on the different sky fibers separated as seen in the bottom panel of Figure III.6) and that impacted our final light curves (top panel of Figure III.6). One explanation could be the reflection of the Moon light inside the telescope before culmination. We adjusted our observations in consequence to avoid this effect.

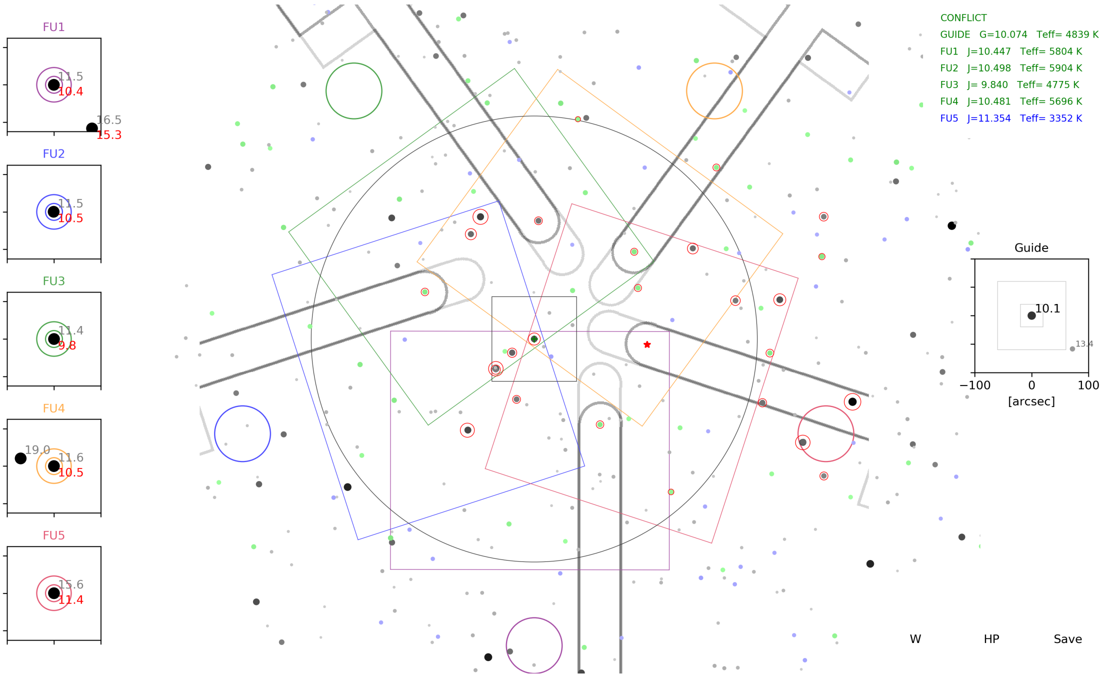

```
CONFLICT
GUIDE   G=10.074   Teff= 4839 K
FU1   J=10.447   Teff= 5804 K
FU2   J=10.498   Teff= 5904 K
FU3   J= 9.840   Teff= 4775 K
FU4   J=10.481   Teff= 5696 K
FU5   J=11.354   Teff= 3352 K
```

Figure III.5: TRAPPIST-1 field-of-view.

Snapshot of the software to prepare ExTrA observations for TRAPPIST-1. The field-of-view of one telescope has a diameter of 1° (gray circle). Each one of the 5 Field Units (FUs) can be positioned in part of the focal plane shown with rectangles of 5 different colors. Each FU is placed over a particular comparison star (green stars) or the target (red star). On the left, the location of each FU is magnified and, to scale, the fiber apertures drawn with color circles (first circle is 4", second circle is 8"). This enables to check if other stars appear near the fibers. In red is the J magnitude of the star, in gray the Gaia magnitude. The guiding star is located in the center and a magnified image is shown on the right. The five arms correspond to the selected stars with their 2MASS J magnitude and Gaia DR2 temperature indicated on the top right of the figure.

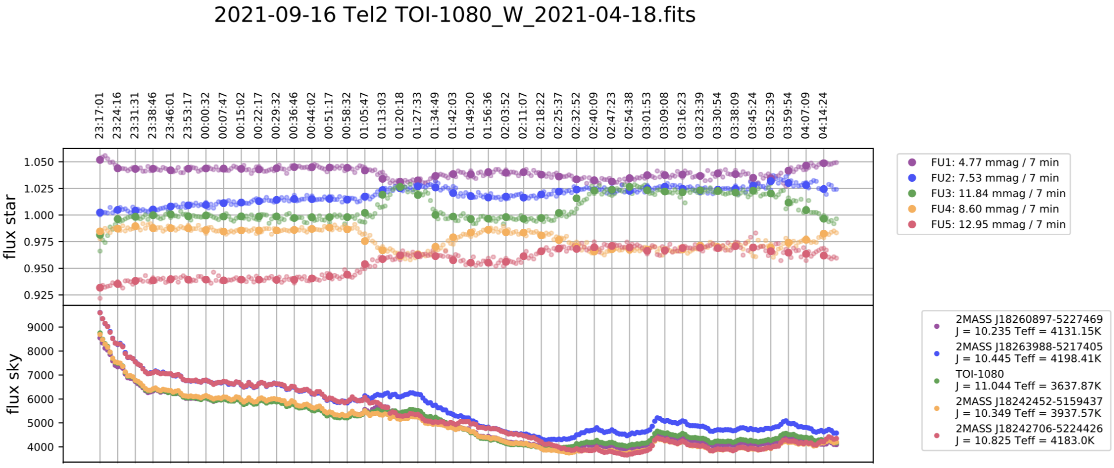

Figure III.6: Portion of the ExTrA nightly report to show the Moon's impact. Report created after the observation sequence of TOI-1080 using telescope 1 on September 16th, 2021. The description of how the reports are created is presented in SectionIII.3.1.

III.3 DATA ANALYSIS

Following the observational phase, the next step consists in conducting a comprehensive analysis of the acquired data. Generating and modeling a light curve to find a transit involves multiple steps. We first collect the data obtained from a photometer or a space-based telescope that continuously monitors the brightness of a star over time. I mostly worked with observations from the three ExTrA telescopes and the TESS satellite. The observational data is then processed to remove any systematic effects and noise. This includes removing any outliers, correcting for any systematic trends, and normalizing the data. This step corresponds to the production of the light curves and will be described in the first subsection. Once our light curves are ready, we define a model which takes into account the transit of the planet : its orbital period, the size of the planet, and the shape of the transit, and if necessary noise models. The model is then fit to the light curve using statistical methods. The modeling of our light curves is described in the second subsection. As we have a rather high number of free parameters and use most of the time Gaussian processes in our fit (see Section III.3.2.2), we decided to use nested sampling algorithms that allow us to properly explore the parameter space. The quality of the fit is evaluated by comparing the model to the data or different models with each other, and examining the residuals of the fit. Once we decided which model is the most reliable, the transit parameters such as the transit depth, duration, and orbital period can be extracted from the model. These parameters can then be used to estimate the size and other properties of the transiting planet.

III.3.1 *Light curves extraction*

After the observations are done, the raw images are first transformed into extracted spectra. The format of the data is presented in Figure III.7.

To describe the creation of the ExTrA light curves, I will use as an example the night of March 1, 2020 when we observed a transit of TOI-269 b. The article regarding the confirmation of this new exoplanet with ExTrA can be found in Section III.4.

We observed TOI-269 with a 8" fiber aperture using the low resolution mode ($R \sim 20$) with an exposure time of 60 seconds. To accurately point our target and comparison stars, we use Gaia DR2 4770833527616320512 as a guiding star. The five stars we selected for this field of view are 2MASS J05021375-5416532 positioned on FU1, 2MASS J05032583-5353188 on FU3, 2MASS J05020219-5351064 on FU4, 2MASS J05001046-5407021 on FU5, and our target star TOI-269 on FU2. The field of view of TOI-269 used for each night of observations with ExTrA is presented in the appendix of the article in Section III.4.

We start our procedure by looking at the master flat used to calibrate our data. In Figure III.8, we can see that for the low resolution mode (R$\sim$20), the spectrum of the star only covers 43 pixels of the 640 available in the detector in the spectral dimension, and we will

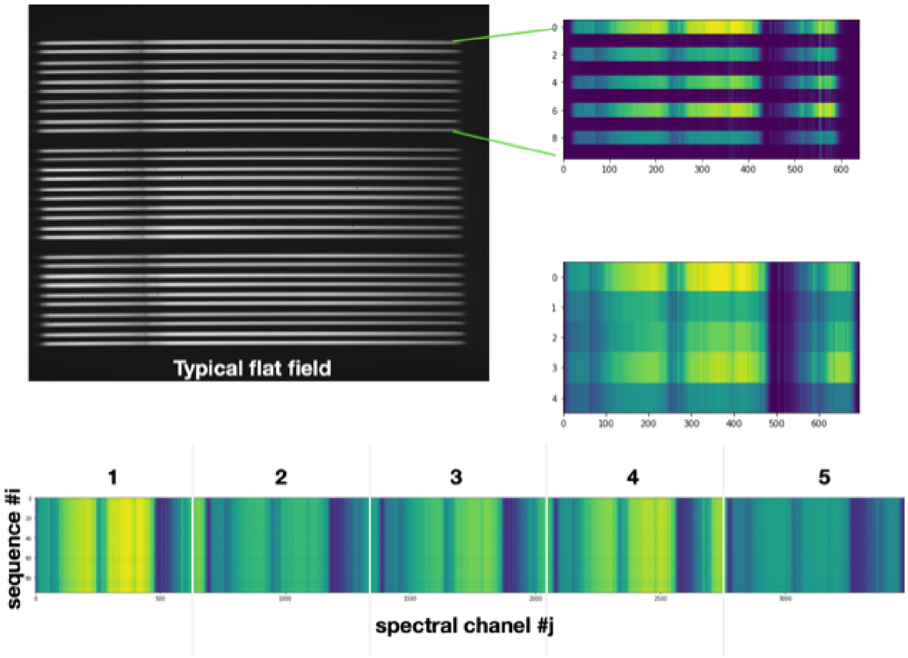

Figure III.7: ExTrA raw data.
Top figures: Each horizontal line corresponds to a fiber. On the left, is displayed a typical flat field where we can see the 10 fibers (5 for target fibers and 5 sky fibers) for each telescope. To the right we present the 10 fibers from one telescope observing a target (the dark lines correspond to the sky fibers) and below the 5 star-sky fluxes. *Bottom figure*: The fibers are now displayed as columns, with the x axis being the flux spread on the different pixels of the detector, and the y axis the sequence composed of multiple exposures.

focus our analysis on this subsection of the detector.

Our data product for the observation sequence of a specific star is composed of three dimensions : the time of each exposure, the different fibers, and the pixels that can be swapped with wavelength values. We first subtract the flux from each sky fiber to each corresponding star fiber and normalize by the flat. We obtain a 2D flux of each object as showed in Figure III.9. We check the absolute flux of all the stars to ensure that the night was clear and that there was no significant flux loss that could cause problems with the photometry.

We normalize by dividing all fluxes by the median flux and create a template of all the exposures to remove outliers (see Figure III.10). Each points with more than a 5σ deviation from the template is masked, and using these new cleaned spectra we create a new template.

We distribute a weight (proportional to the variance of the flux versus time) for each pixel/wavelength in order to mitigate the effect of Earth's atmosphere especially in the

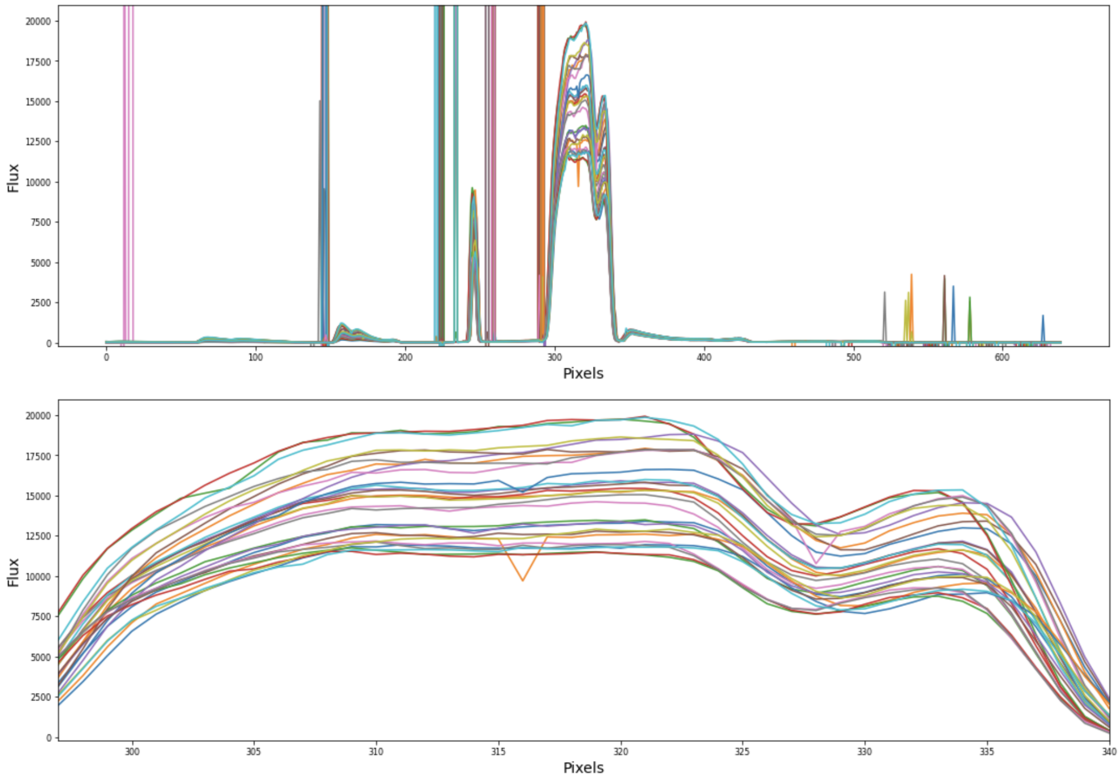

Figure III.8: ExTrA Master flat.
Master Flat used to calibrate for the low resolution data. *Top*: Flux as a function of pixel, with each curves corresponding to a fiber ((5 fibers on stars + 5 fibers on sky)* 3 telescopes = 30 fibers). *Bottom*: Zoom in on the 43 pixels representing the first order spectrum.

water bands. We then obtain the differential photometry for each star (our target and the 4 comparison stars) by normalizing with a template that includes the photometry of the different stars.

For each observation sequence and each telescope, a PDF file is created (see Figure III.11) to gather in one document the 5 light curves, as well as the flux from the sky fibers, the raw star flux subtracted from the sky, the airmass and dome azimuth, the sky-ambient temperature and humidity indicative of the weather, the guiding error, and two overscan regions.

The final photometry is affected by some systematic effects which are still under investigation. One of them may come from the fact that there are some differential motions of the stars during the observing sequence which introduce differential centering on the fibers aperture. A decorrelation with the position of the star inside the fiber is not possible because we can’t monitor the XY position of the star inside the fiber aperture during an acquisition. This problem is being investigated by observing the same field with the centering bundle

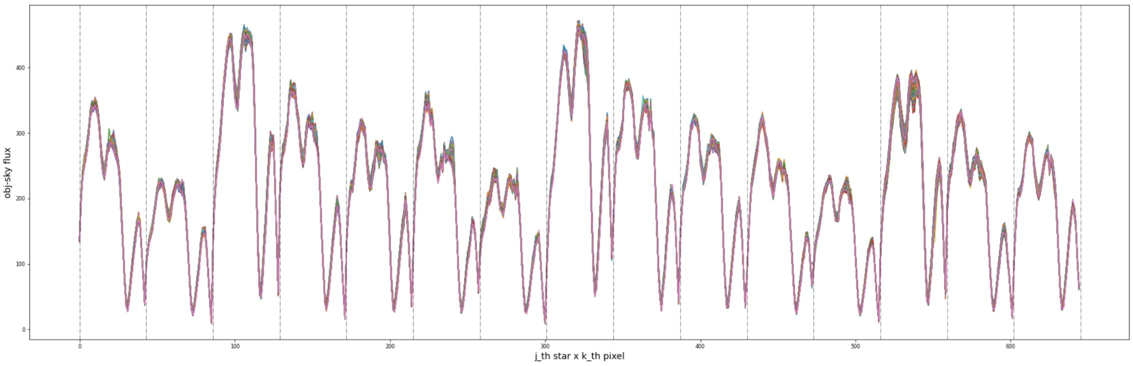

Figure III.9: ExTrA normalized flux.
Sky subtracted and flat normalized flux for each object fiber. The dotted vertical lines separate the spectrum of the different objects. We can see the spectrum of the target star and 4 comparison stars for each of the three telescopes. Each curves corresponds to one 60s exposure (237 exposures total for this observation sequence).

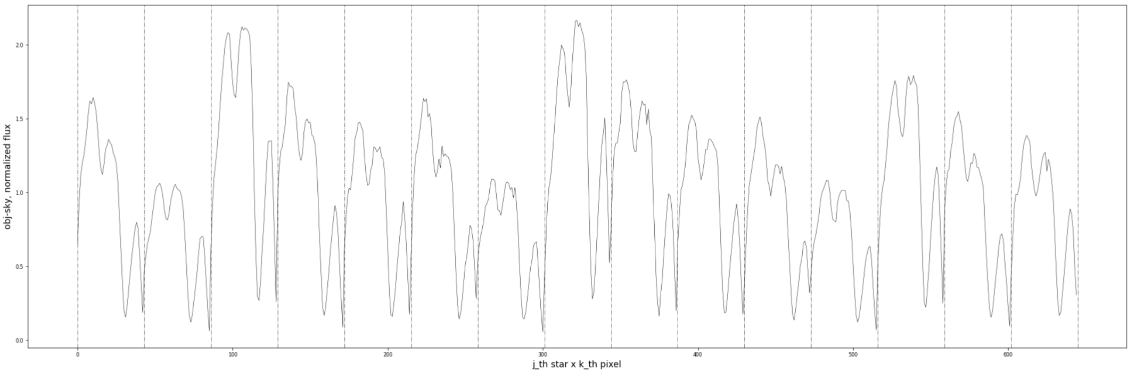

Figure III.10: Template corresponding to the median over the temporal sequence.

only during a whole night, and then applying the measured offsets on all subsequent nights.

III.3.2 *Modeling the light curves*

Once the procedure to create the ExTrA light curves was added to the routine that is controlling the observations every night, I was able to start working on analyzing those light curves to search for transit signals.

III.3.2.1 *juliet modeling tool*

To model our photometry data, and have the possibility to also model the photometry and radial velocity jointly, I decided to use the juliet tool developed by Espinoza, Kossakowski,

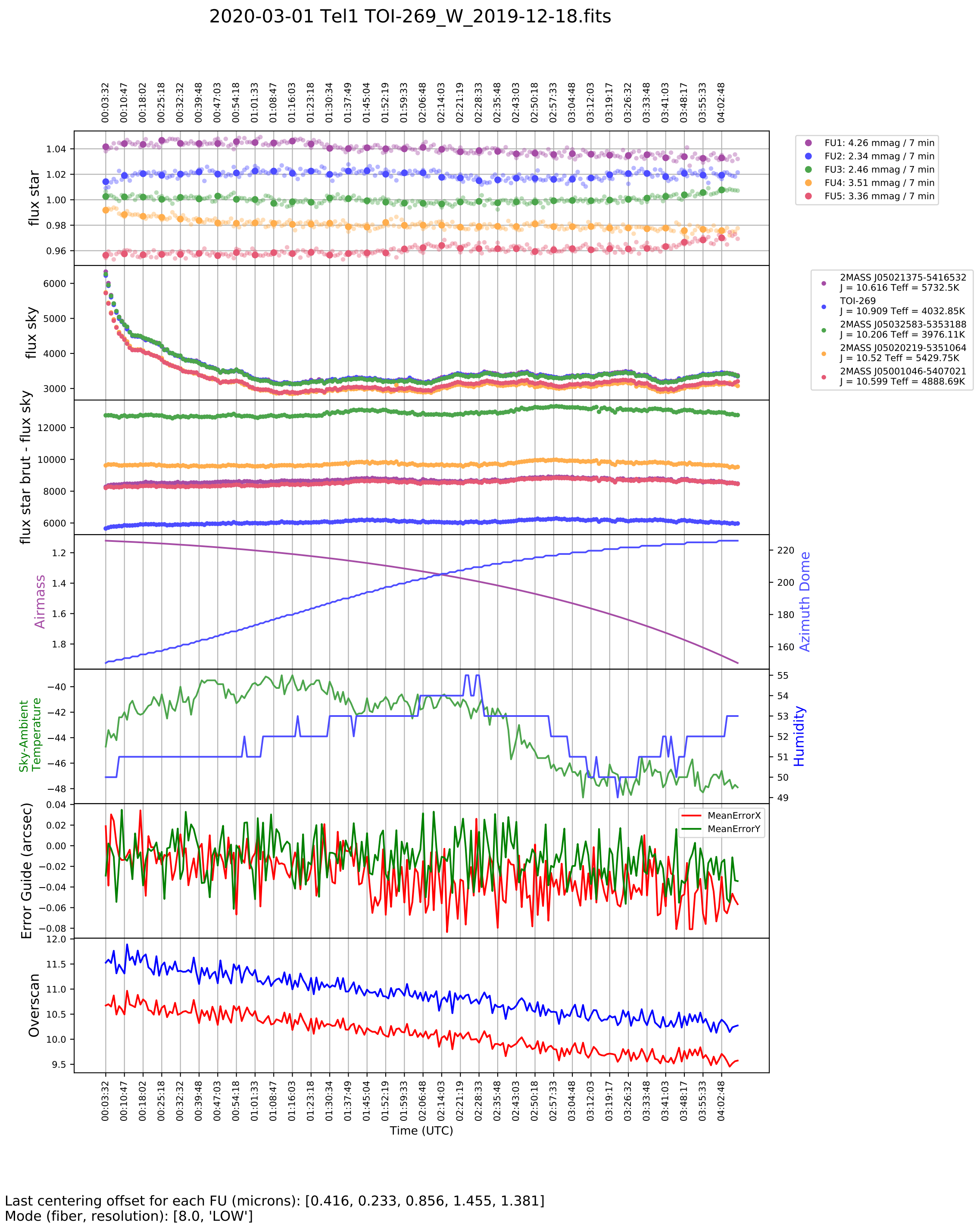

2020-03-01 Tel1 TOI-269_W_2019-12-18.fits

Last centering offset for each FU (microns): [0.416, 0.233, 0.856, 1.455, 1.381]
Mode (fiber, resolution): [8.0, 'LOW']

Figure III.11: ExTrA nightly report.
Report created after the observation sequence of TOI-269 using telescope 1 on March 1st, 2020.

and Brahm, 2019 and publicly available on GitHub.

juliet is a flexible tool to analyze transits and/or radial velocities measurements. It is built using many existing python packages for modeling transits, radial velocities, and stochastic processes like Gaussian Processes (GPs) and can be used for the analysis of transit photometry and radial-velocity measurements from multiple instruments at the same time, using nested sampling algorithms that allows not only to perform a thorough sampling of the parameter space, but also model comparison.

The transit model is generated within juliet by using batman (Kreidberg, 2015), which has many flexible options useful for transit modeling. The transit parameters that are allowed to vary for each transiting planet are the planet-to-star radius ratio $p = R_p/R_{star}$, the semi-major axis in stellar unit a/R_{star}, the impact parameter of the orbit $b = (a/R_{star}) * cos(i)$, where i is the inclination of the planetary orbit with respect to the plane of the sky, the period of the orbit P, the time-of-transit center t_0, the argument of periastron passage ω and the eccentricity of the orbit e.

juliet offers the option to parameterize either p and b or use the sampling scheme detailed in Espinoza, 2018, which samples another set of two parameters r_1 and r_2 defined between 0 and 1 and that explores all physically meaningful ranges for p and b, ensuring the condition $b < 1 + p$ is always satisfied and samples for which $b \geq 1 + p$ are rejected. juliet allow us to fit for the stellar density common for all transiting exoplanets in the same system, rather than individual values of a/R_{star} for each transiting exoplanet in the system. I always parametrized the model using the stellar density as I estimated homogeneously the stellar radius and mass of all TESS targets around M dwarfs (see Section II.3.2).

The eccentricity and argument of periastron passage can be parametrized directly, which is convenient when a circular orbit is chosen so the eccentricity can be fixed to 0. These two parameters can also be parametrized using the transformations $S_1 = \sqrt{e}sin(\omega)$ and $S_2 = \sqrt{e}cos(\omega)$, in which case $e = S_1^2 + S_2^2$ and $\omega = atan2(S1, S2)$. I decided to use this last set of parameters when I wanted to fit for an eccentric orbit as the priors required are simply uniform distributions between -1 and 1, and within juliet it is always ensured that the eccentricity is smaller than 1.

For the limb-darkening coefficients, juliet offers the parametrization proposed by Kipping, 2013, where q_1 and q_2 defined between 0 and 1 are sampled to produce only physically possible limb-darkening coefficients. A pair of limb-darkening coefficients is necessary for each instrument used in the analysis. During my analysis, I found that the limb-darkening parameters were not constrained by the light curves and the posterior distributions were still uniform.

juliet also enables us to model radial velocity measurements using radvel (Fulton et al., 2018), which is complementary to the photometry when we want to characterize exoplanets. The corresponding model consists of a Keplerian signal for each planet in the system, the systemic velocity dependent on the instrument used, and an optional long-term trend that could indicate the presence of a long-period companion or stellar activity. To define the keplerian, we use the semi-amplitude of the variation K, the period of the orbit P, the time-of-transit center t_0, the argument of periastron passage ω and the eccentricity of the orbit e. All the keplerian parameters are common with the transit model except for the semi-amplitude, specific to radial velocity data.

In addition to the planetary and stellar parameters, we can model for the noise using for example a jitter term added in quadrature to each of the error bars of the data points that can be assimilated to a white noise model. However, a white noise model is often not enough to describe the systematics present in the data. This sentence is especially true for the ExTrA data as we noticed since the beginning that we had large variations in our data that we could not correlate with usual parameters like the airmass or the position of the telescope. The systematics were different for observations on the same star for two different nights of observations, or even between the telescopes that were observing the same star at the same time. For this reason we decided to model our noise using Gaussian Process in order to have a non-parametric approach to correct for the systematics. The correction of the ExTrA light curves using GPs is described in the next subsection.

Finally, once the parameters are selected, juliet uses nested sampling algorithms to perform posterior sampling to obtain the posterior distribution of the parameters given the data and to estimate Bayesian evidences used to compare different models. To do so, nested sampling algorithms sample a defined number of live points from the priors given by the user and sequentially replace the live point with the lowest likelihood by a new live point with a larger likelihood at each iteration. For each iteration, the Bayesian evidence is updated and the algorithm stops when a convergence criterion is reached. Different python packages are available for nested sampling and we decided to use dynesty (Speagle, 2020) as it is more suited to tackle large-dimensional problems. Because computing model evidences requires a extensive exploration of the priors, nested sampling algorithms are very efficient at deeply exploring the parameter space. This approach differs from Markov-Chain Monte Carlo (MCMC) algorithms such as the classical Metropolis-Hastings algorithms or widely used fast algorithms such as emcee (Foreman-Mackey et al., 2013), which require initial guesses of the parameters to achieve convergence in a reasonable amount of time. This difference is important for posterior exploration of models using GPs, where a search for optimal parameters before the posterior exploration is time-consuming. The larger the prior volume, the longer it takes for the nested sampling algorithm to converge, but juliet offers the possibility of multi-threading to help with this time issue for typical exoplanetary science problems.

All the parameters used within juliet are described in Table III.1.

III.3.2.2 *Gaussian process to correct systematic effect*

In the field of exoplanet discovery and characterization, Gaussian processes (GPs) have become a popular model for correcting datasets from non-white noise, also known as

Table III.1: List of parameters that define the model for the photometry and radial velocity for each instrument i. The planetary parameters have to be given to every planet we consider in the system.

Parameter name	Units	Description
Photometry		
Planetary parameters		
P	days	Orbital period
t_0	days (BJD TBD)	Time-of-transit center
p	-	Planet-to-star radius ratio *
b	-	Impact parameter *
e	-	Eccentricity of the orbit †
ω	deg	Argument of periastron †
$\rho_\star$	kg/m3	Stellar density
Instrumental parameters		
D_i	-	Dilution factor
M_i	Relative flux	Relative flux offset
$q_{1,i}$	-	Limb-darkening parameter
$q_{2,i}$	-	Limb-darkening parameter
Radial velocity		
Additional planetary parameters		
K	m/s or km/s	RV semi-amplitude
Instrumental parameters		
μ_i	m/s or km/s	Systemic RV
Noise model		
White noise parameter		
$\sigma_{w,i}$	ppm - m/s or km/s	Jitter term
Gaussian Process (approximate Matern Kernel)		
σ_{GP}	ppm - m/s or km/s	Amplitude of the GP
ρ_{GP}	days	Time scale of the GP

* In addition of fitting directly for (p, b), we also fit using the (r1, r2) parametrization.

† In addition of fitting for (e, ω) directly, we also fit using the parameters $S_1 = \sqrt{e} sin(\omega)$ and $S_2 = \sqrt{e} cos(\omega)$.

red noise. GPs are essentially an infinite-dimensional Gaussian distribution with a mean function and a covariance, auto-correlation, or "kernel" function. They allow us to learn unknown functions and their error bars directly from the data, which is especially useful when there is no good parametric model available. Furthermore, GPs can be extremely versatile and powerful for modeling systematics.

Despite their usefulness, GPs have some limitations that we have to take into account. Although techniques such as george and celerite (Foreman-Mackey et al., 2017) have been developed to reduce computation time, GPs are still computationally expensive. The celerite method for example uses a specific model for the covariance that can improve the computational efficiency of many astronomical data analysis problems. This method's main limitation is that it can only be applied to one-dimensional datasets. In our case, we will only use the time component to detrend our dataset, so this is not an issue. We could think of applying the Gaussian process to the wavelength component instead of time component to correct for chromatic effects, but unfortunately I did not have the time to explore this idea during my PhD.

GPs are also sensitive to kernel selection. I decided to use the approximate 3/2 Matern kernel from the python package celerite (Foreman-Mackey et al., 2017) as it described best stochastic effect without any sign of periodicity, which matches with the systematics present in the ExTrA photometry. Finally you have to ensure that you fit what you mean to fit, and make sure the GP is not fitting some part of your planetary signal, or even the entire planet signal if you are looking for additional planets. To do so, we made sure that the timescale of the GP was different from the duration of the transit that we wanted to observe but that solution only works if we already have prior knowledge on the planet candidate.

There are different applications for GPs in astrophysics, the most common being separating stellar activity and planetary signals, where we can model activity in RVs and activity indicators simultaneously using a GP. I used GPs mostly to model instrumental systematics seen in the ExTrA and TESS photometry, and other instruments datasets. The approximate Matern kernel used in all my models is composed of two hyper-parameters : one for the amplitude of the GP and one for the time-scale of the GP. This parametrization seems to fit well the systematics present within the ExTrA light curves.

III.3.2.3 *Creation of automatic routines to model photometric and velocimetric datasets*

As discussed in the previous subsections, juliet is therefore a very useful tool to model different datasets, which is why I had to master it during my PhD as I was using it for all the modeling that I needed to do. I created multiple routines that implemented juliet, in order to model only the TESS photometry (see Section II.4), the TESS and ExTrA photometry using a common transit depth for both instruments (see the automatic code used for all TOIs observed in Appendix A) and also different depths to check the chromaticity of the transit signal and finally some joint modeling of photometry and radial velocity combined.

The first routine that I developed was to fit the TESS photometry for each TOIs orbiting M dwarfs in the table presented in the previous chapter. The routine takes as input the name of the TOI and a table downloaded from ExoFOP with the estimated values for the period P, the time-of-transit center t_0, and the stellar density ρ_*.

The second and third routines I put together was to fit jointly the TESS and ExTrA photometry, with the purpose of validating the TESS planetary candidates and improve on the planetary parameters as part of the WP1 objective (see Section III.5.1). These two routine are identical except for the planet-to-star radius ratio where I fit only one set of (p,b) parameters for both instrument in one routine, and two different p parameters for the other one (pTESS, pExTrA, b) to check for chromaticity in the transit depth as TESS and ExTrA observations are made at different wavelength ranges.

As for the first routine, the only input is the TOI number and a table gathering all the TOIs downloaded from ExoFOP with prior information on the period and time of transit-center and the stellar parameters. The estimations for the duration and depth of the transit are also retrieved in order to automatically scale the plot representing the phase-folded light curves to the size of the transit. The TESS photometry is downloaded from the MAST website Mast Portal[1], and only in-transit data (a window of 3 times the duration of the transit) is selecting for the fit in order to save computation time.

The planetary parameters and TESS instrumental parameters are defined and non-informative priors are used except for the period and time-of-transit center, where the estimations from ExoFOP confirmed by the TESS photometry fit from the first routine are used as normal priors, and the stellar density, for which the stellar radius and stellar mass from ExoFOP calculated in the same way I mentioned in Section II.3.2 are used to compute the stellar density which is put as a normal prior too.

The routine looks for the ExTrA observations related to this TOI, searching for the '.fits' file with the target name located on the same server. For both TESS and ExTrA photometry, the code recovers the time of observation, the flux and the uncertainty on the flux. I added a criteria to remove the noisiest light curves of ExTrA from the fit to not degrade the estimations of the planetary parameters. The parameters related to the ExTrA instrument are added. The decision to consider each night of observation as a different instrument was made to better correct for the systematics. We also decided that one GP per telescope was the best compromise between computation time and correction of the systematics.

After the fit is complete and the convergence criteria is reached, the outputs are a text file with the estimation of the parameters, as well as an overview of the positions of the samples and where the posterior distributions were taken from those samples provided by dynesty. The routine I created also plots the time series of the TESS and ExTrA transits (see

---

[1] https://mast.stsci.edu/portal/Mashup/Clients/Mast/Portal.html

Figure III.12), as well as the phase-folded light curves of both instruments (see top panels of Figures III.15 and III.14), each individual ExTrA transits (see Figure III.13), and histograms of the posterior distributions of the radius ratio and planetary radius (see bottom panels of Figure III.14). When the same transit depth is fitted, the histogram shows the comparison between the posteriors of the planetary radius estimated from TESS and ExTrA combined and the planetary radius estimated from TESS only computed in a previous fit using the first routine (see Section II.4). When different depths are fitted, the histogram shows the comparison between the posteriors of the planetary radius estimated from ExTrA and the planetary radius estimated from TESS within the same fit (see bottom left panel of Figure III.15). I also display the difference between the posterior distribution of the radius ratio for ExTrA and the posterior distribution of the radius ratio for TESS (see bottom right panel of Figure III.15). If the depths are similar, this new distribution is centered in 0 (gray line). I added two vertical green lines corresponding to 95% of the distribution (or 2σ) to see if the transit depths are still compatible with each other within this range.

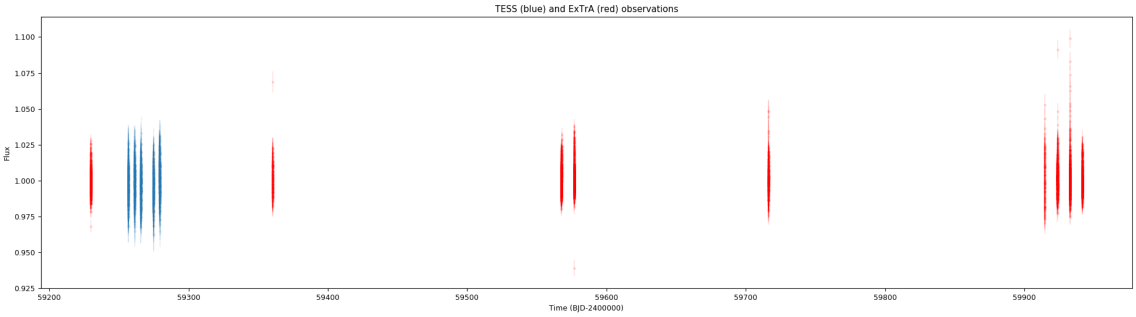

Figure III.12: Modeling of TOI-1883.01 transits with a common depth.
Plot from the routine that models the TESS and ExTrA photometry for TOI-1883.01 with the same transit depths for both instruments that represent the time series used for the fit.

The last routine is neither unique nor automatic, but specific to the TOIs I published as first author, in which I led the global analysis by gathering all photometric and velocimetric datasets to obtained the most precise parameters for the exoplanet. It is very similar to the ones described above, with the addition of the radial velocity modeling to complement our photometric datasets. This type of routine is easily adjustable as you would only need to change the input files relevant to the target you want to model and adjust the priors of your fit depending on previous knowledge on the target. Examples of what can produce such analysis are described in my first paper in Section III.4 and another discovery paper in Section II.5.

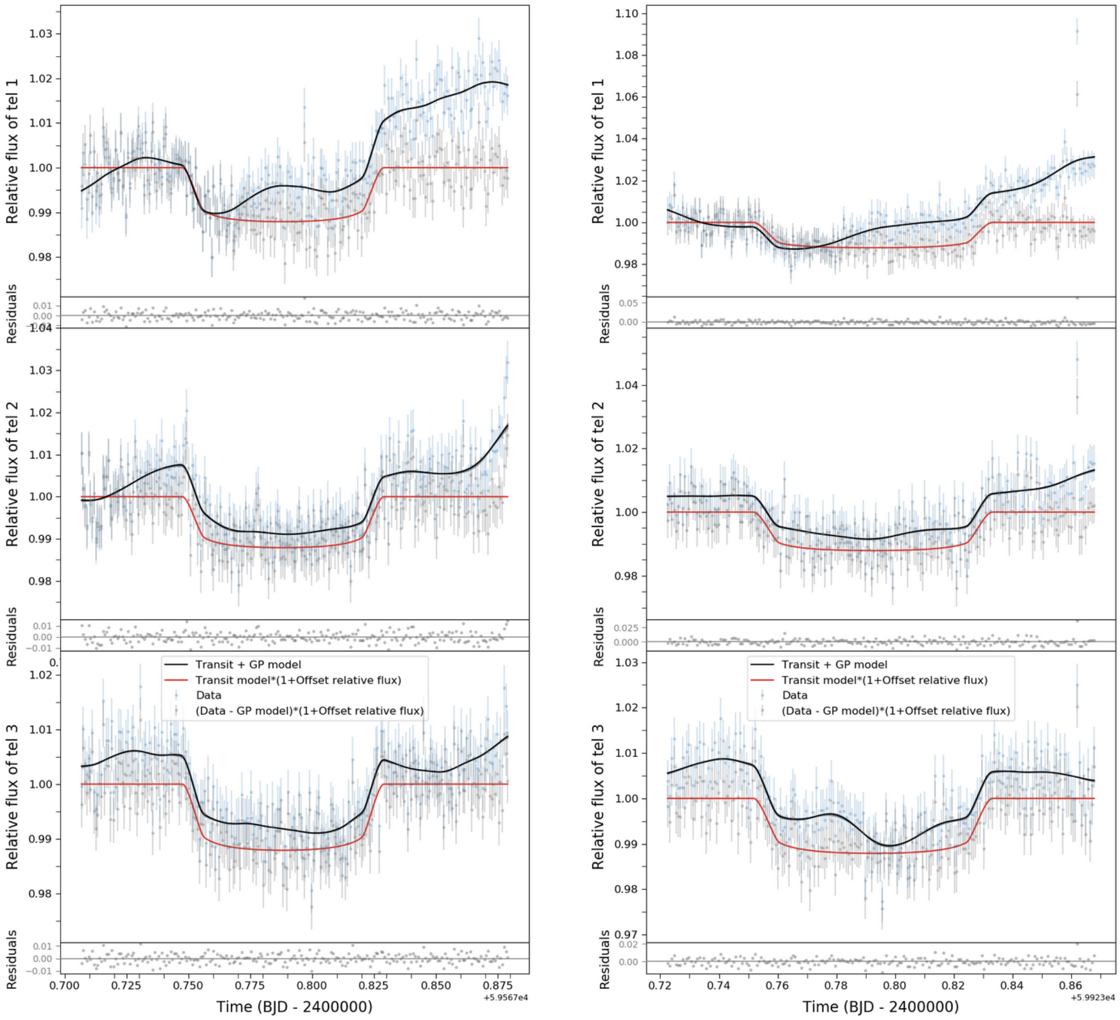

Figure III.13: ExTrA transits of TOI-1883.01.

Plot from the routine that models the TESS and ExTrA photometry for TOI-1883.01 with the same transit depths for both instruments. 6 transits of TOI-1883.01 are presented here, corresponding to two different nights of observations (columns) using each time the three ExTrA telescopes (lines). In blue dots is our raw data, modeled in black by the transit + GP. In gray dots is the detrended light curves, with the maximum a posteriori model transit in red. The residuals below correspond to the modeled transit subtracted from detrended data points.

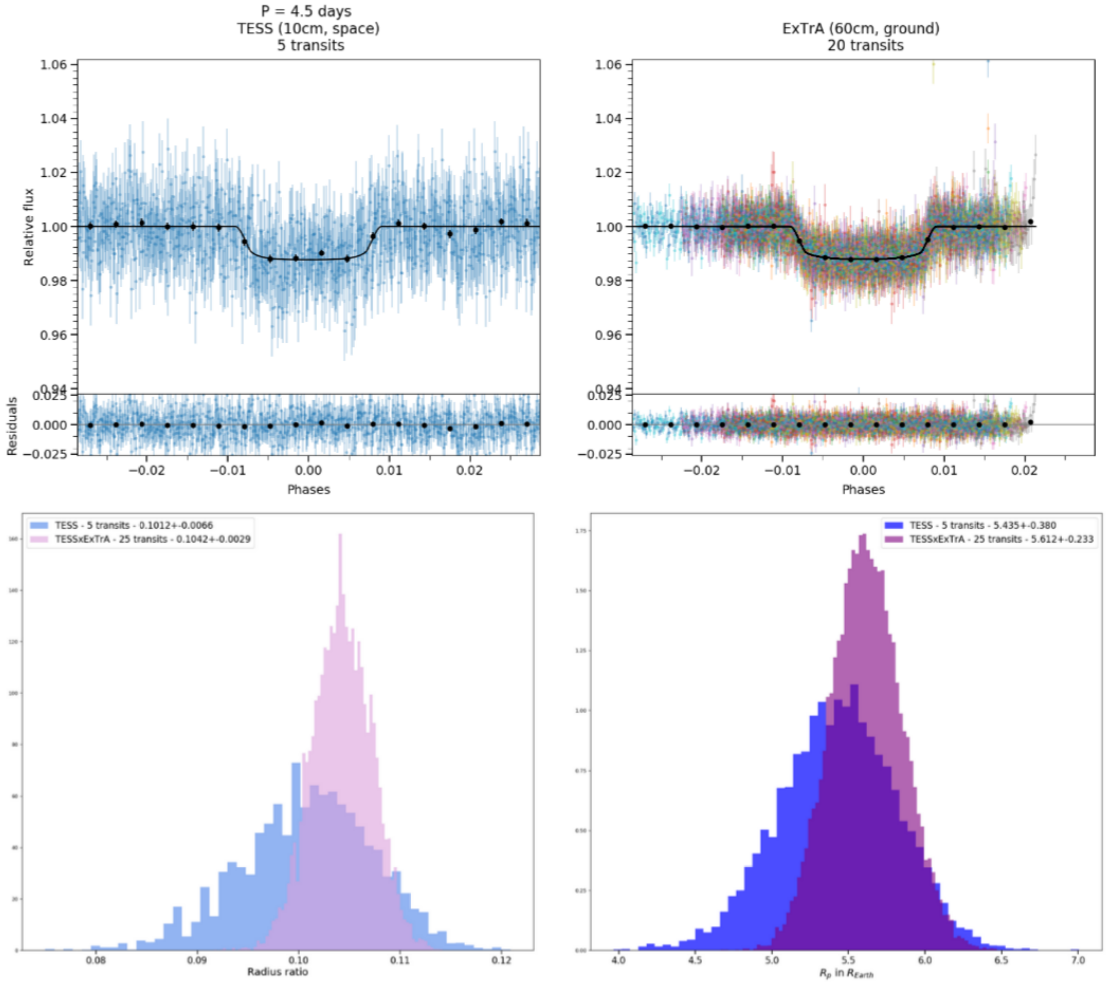

Figure III.14: Modeling of TOI-1883.01 transits with the same transit depth.
Plots from the routine that models the TESS and ExTrA photometry for TOI-1883.01 with the same transit depths for both instruments. *Top*: Phase-folded light curves of TESS and ExTrA with the corresponding number of transits fitted (the black line is the maximum a posteriori model, the black points are binned data to 1/6 of the transit duration). *Bottom left*: Histogram of the posterior distribution of the radius ratio of the joint fit (in light purple), and of a fit with only the TESS photometry (in light blue). *Bottom right*: Histogram of the posterior distribution of the planetary radius of the joint fit (in dark purple), and of a fit with only the TESS photometry (in dark blue).

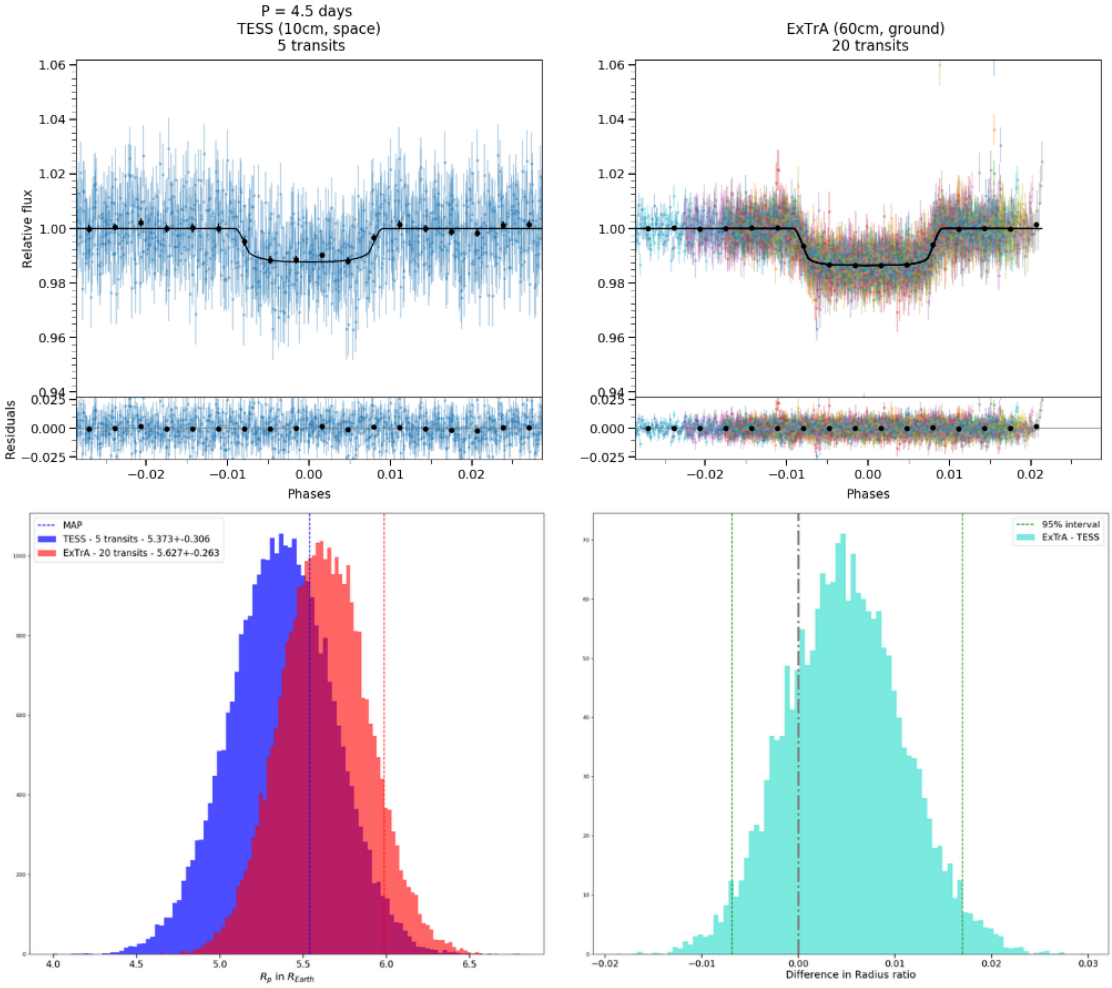

Figure III.15: Modeling of TOI-1883.01 transits with different transit depths.
Plots from the routine that models the TESS and ExTrA photometry for TOI-1883.01 with a different transit depth for each instrument. *Top*: Phase-folded light curves of TESS and ExTrA with the corresponding number of transits fitted (the black line is the maximum a posteriori model, the black points are binned data to 1/6 of the transit duration). *Bottom left*: Histogram of the posterior distribution of the radius ratio for TESS (in blue) and for ExTrA (in red). *Bottom right*: Histogram of the difference of posterior distributions of the radius ratio between ExTrA and TESS. The green vertical lines correspond to 95% or 2σ of the distribution. The gray vertical line is centered on 0.

III.4 TOI-269 B: AN ECCENTRIC SUB-NEPTUNE TRANSITING A M2 DWARF

One of the first targets ExTrA observed is TOI-269, where we were able to confirm the presence of a mini-Neptune orbiting this M2 type star. We observed it 3 nights with ExTrA when transits were expected to happen given the ephemeris calculated with TESS. Other facilities had obtained observations for this specific target so I gathered them all. We obtained two transits from the LCOGT network and 81 spectra with HARPS as part of dedicated program on M-dwarfs. I used the software package juliet to model separately and jointly the photometric and radial velocity datasets as described in the previous section. This analysis revealed an eccentric orbit for TOI-269 b with almost the highest value for planets with periods shorter than 10 days and radius smaller than 10 Earth radii. We did multiple tests to confirm this result and then turned to possible explanations such as planet-planet migration, excitation from a distant planet or atmospheric escape. This first analysis of the ExTrA photometry showed us that we could improve the precision of the radius measurement for some TESS candidates. This motivated the creation of the first work package of ExTrA, explained in the next section.

A&A 650, A145 (2021)
https://doi.org/10.1051/0004-6361/202140328

Astronomy & Astrophysics

TOI-269 b: an eccentric sub-Neptune transiting a M2 dwarf revisited with ExTrA*

M. Cointepas[1,2], J. M. Almenara[1], X. Bonfils[1], F. Bouchy[2], N. Astudillo-Defru[3], F. Murgas[1,21,22], J. F. Otegi[13,2], A. Wyttenbach[1], D. R. Anderson[4,7,8], É. Artigau[14], B. L. Canto Martins[20], D. Charbonneau[9], K. A. Collins[9], K. I. Collins[10], J.-J. Correia[1], S. Curaba[1], A. Delboulbé[1], X. Delfosse[1], R. F. Díaz[16], C. Dorn[13], R. Doyon[15], P. Feautrier[1], P. Figueira[17,18], T. Forveille[1], G. Gaisne[1], T. Gan[11], L. Gluck[1], R. Helled[13], C. Hellier[4], L. Jocou[1], P. Kern[1], S. Lafrasse[1], N. Law[5], I. C. Leão[20], C. Lovis[2], Y. Magnard[1], A. W. Mann[5], D. Maurel[1], J. R. de Medeiros[20], C. Melo[17], T. Moulin[1], F. Pepe[2], P. Rabou[1], S. Rochat[1], D. R. Rodriguez[29], A. Roux[1], N. C. Santos[18,19], D. Ségransan[2], E. Stadler[1], E. B. Ting[27], J. D. Twicken[28,27], S. Udry[2], W. C. Waalkes[12], R. G. West[7,8], A. Wünsche[1], C. Ziegler[6], G. Ricker[23], R. Vanderspek[23], D. W. Latham[9], S. Seager[23,24,25], J. Winn[26], and J. M. Jenkins[27]

(Affiliations can be found after the references)

Received 12 January 2021 / Accepted 30 March 2021

ABSTRACT

We present the confirmation of a new sub-Neptune close to the transition between super-Earths and sub-Neptunes transiting the M2 dwarf TOI-269 (TIC 220 479 565, $V = 14.4$ mag, $J = 10.9$ mag, $R_\star = 0.40\,R_\odot$, $M_\star = 0.39\,M_\odot$, $d = 57$ pc). The exoplanet candidate has been identified in multiple TESS sectors, and validated with high-precision spectroscopy from HARPS and ground-based photometric follow-up from ExTrA and LCO-CTIO. We determined mass, radius, and bulk density of the exoplanet by jointly modeling both photometry and radial velocities with `juliet`. The transiting exoplanet has an orbital period of $P = 3.6977104 \pm 0.0000037$ days, a radius of $2.77 \pm 0.12\,R_\oplus$, and a mass of $8.8 \pm 1.4\,M_\oplus$. Since TOI-269 b lies among the best targets of its category for atmospheric characterization, it would be interesting to probe the atmosphere of this exoplanet with transmission spectroscopy in order to compare it to other sub-Neptunes. With an eccentricity $e = 0.425^{+0.082}_{-0.086}$, TOI-269 b has one of the highest eccentricities of the exoplanets with periods less than 10 days. The star being likely a few Gyr old, this system does not appear to be dynamically young. We surmise TOI-269 b may have acquired its high eccentricity as it migrated inward through planet-planet interactions.

Key words. planets and satellites: detection – stars: low-mass – techniques: photometric – techniques: radial velocities

1. Introduction

Low-mass stars offer particular advantages, and are particularly interesting, when looking for small and cool exoplanets. The transit depth and the radial-velocity semi-amplitude provoked by rocky exoplanets around M dwarfs is much higher than those caused by similar planets orbiting around larger stars of earlier spectral type, which makes such planets easier to detect. Even more importantly, such systems are also ideal targets for atmospheric characterization by transmission or thermal emission spectroscopy (e.g., Kempton et al. 2018, Batalha et al. 2018). Planets orbiting around M dwarfs are therefore important objects to obtain precise mass, radius, and bulk density measurements of transiting exoplanets smaller than Neptune, which are crucial to better understanding the so-called radius valley between the super-Earth and sub-Neptune populations (e.g., Fulton et al. 2017, Mayo et al. 2018, Cloutier & Menou 2020, and Hardegree-Ullman et al. 2020).

The Transiting Exoplanet Survey Satellite (TESS, Ricker et al. 2015) is a NASA all-sky survey designed to detect transiting exoplanets orbiting nearby stars, with a specific focus on exoplanets smaller than Neptune. With its array of four cameras, the satellite has been delivering, since July 2018, both 2 min cadence photometry on pre-selected targets and full-frame images (FFIs) with a cadence of 30 min (no longer the case, however, for the extended mission that began on July 5, 2020, when TESS started collecting FFIs at 10 min cadence). Each pointing corresponds to a sector of the sky that is observed for a period of about 27 days. TESS is focusing on relatively bright stars, which is crucial for the confirmation of transiting candidates and to enable follow-up observations and characterization of confirmed exoplanets. TESS has identified more than 200 exoplanet candidates orbiting M dwarfs to date, including a few super-Earths with masses measured thanks to high-precision radial velocities (e.g., GJ357 b – Luque et al. 2019; LTT3780 b – Cloutier et al. 2020).

The Exoplanets in Transits and their Atmospheres (ExTrA) facility (Bonfils et al. 2015) was developed to specifically perform from the ground high-precision spectro-photometry in the near-infrared on mid- to late M dwarf stars. ExTrA consists of a set of three 60 cm telescopes equipped with multi-object fiber positioners and a low-resolution near-IR spectrograph. ExTrA is being used to confirm TESS planet detections, refine transit parameters, and search for additional exoplanets in the same systems.

In this paper, we report the discovery of a new transiting exoplanet around the M2 dwarf TOI-269, which was first detected as a candidate by TESS. The target was then

---

* ExTrA photometric data are only available at the CDS via anonymous ftp to `cdsarc.u-strasbg.fr` (`130.79.128.5`) or via `http://cdsarc.u-strasbg.fr/viz-bin/cat/J/A+A/650/A145`

Table 1. Stellar parameters for TOI-269 (TIC 220 479 565, UCAC4 180-005252, 2MASS J05032306-5 410 378, WISE J050323.09-541 039.1, APASS 26 149 036).

Parameter	Value	Refs
Astrometry		
Right ascension (J2015.5), α	$05^{\mathrm{h}}03^{\mathrm{m}}23.11^{\mathrm{s}}$	1,2
Declination (J2015.5), δ	$-54°10'39.8''$	1, 2
Parallax (mas)	17.508 ± 0.023	1, 2
Distance, d (pc)	57.023 ± 0.076	1, 2
Proper motion RA (mas yr^{-1})	26.472 ± 0.43	1, 2
Proper motion D (mas yr^{-1})	120.750 ± 0.43	1, 2
Photometry		
V (mag)	14.37 ± 0.11	3
TESS magnitude (mag)	12.2958 ± 0.0074	3
J (mag)	10.909 ± 0.026	4
H (mag)	10.304 ± 0.022	4
K_{s} (mag)	10.100 ± 0.023	4
Stellar parameters		
Spectral type	M2V	5
$M_{K_{\mathrm{s}}}$ (mag)	6.320 ± 0.023	6
Effective temperature, T_{eff} (K)	3514 ± 70	6, 7
Surface gravity, $\log g$ (cgs)	4.831 ± 0.029	6
Metallicity, [Fe/H] (dex)	-0.29 ± 0.12	6, 7
Stellar radius, $R_\star$ ($R_\odot$)	0.398 ± 0.012	6
Stellar mass, $M_\star$ ($M_\odot$)	0.3917 ± 0.0095	6
$\log R'_{\mathrm{HK}}$	-5.320 ± 0.142	6

References. (1) Gaia Collaboration (2018), (2) Lindegren et al. (2018), (3) Stassun et al. (2019), (4) Cutri et al. (2003), (5) Pecaut & Mamajek (2013), (6) this work, (7) Yee et al. (2017).

confirmed with ground-based photometry and its mass measured thanks to HARPS radial velocities (RVs). Section 2 presents a detailed analysis of the stellar properties of TOI-269. Section 3 describes the observations and data used in this study, including a description of ExTrA. Section 4 presents the global analysis of the available data in order to constrain the planetary properties. Section 5 presents a discussion of our results, and Sect. 6 presents our conclusions.

2. Stellar parameters

TOI-269 is an M dwarf at a distance of 57.023 ± 0.076 pc (Gaia Collaboration 2018, Lindegren et al. 2018, and Bailer-Jones et al. 2018). The astrometry, photometry, and stellar parameters are reported in Table 1.

We derived the mass of the star with the empirical relationship between $M_{K_{\mathrm{s}}}$ and $M_\star$ of Mann et al. (2019) and using their `M_-M_K-` code[1]. An apparent magnitude of $K_{\mathrm{s}} = 10.100 \pm 0.023$ leads to an absolute magnitude of $M_{K_{\mathrm{s}}} = 6.320 \pm 0.023$ and a mass of $M_\star = 0.3917 \pm 0.0095\ M_\odot$. We used another empirical relation from Mann et al. (2015) to estimate the radius of the star also from the value of the apparent magnitude and found $R_\star = 0.398 \pm 0.012\ R_\odot$, which is the same value as provided in the TESS Input Catalog (TIC-v8; Stassun et al. 2019). With both mass and radius we infer a stellar density of $\rho_\star = 8.76 \pm 0.87\ \mathrm{g\,cm^{-3}}$. The analysis by Mann includes stars with close-to-solar metallicities. However, using `SpecMatch-Emp`[2] (Yee et al. 2017) and HARPS high-resolution spectra of TOI-269, we estimated that the star has a metallicity of [Fe/H] = -0.29 ± 0.12 (Yee et al. 2017). To verify the impact of such sub-solar metallicity on the stellar parameters, we performed an analysis of the spectral energy distribution combined with stellar evolution model (Appendix C). It leads to similar results for the stellar mass and radius. To be more conservative, in the rest of this paper we use the relations in Mann et al. (2015, 2019) without taking into account the stellar metallicity. With `SpecMatch-Emp`, we also obtain an effective temperature $T_{\mathrm{eff}} = 3514 \pm 70$ K and radius $R_\star = 0.41 \pm 0.04\ R_\odot$. We report the T_{eff} value in Table 1, but discard the $R_\star$ value, which we found to be less precise than that of the Mann et al. (2015) relationship. An analysis of the WISE (Wright et al. 2010) data for TOI-269 shows no IR excess, pointing to the absence of circumstellar material around the star, at least in the WISE bands.

We estimated the age of the star using gyrochronology with the different rotation periods that we calculated (see Sects. 3.2.3 and 3.3). We used the relation from Engle & Guinan (2011), which determines the stellar age through measures of the rotation period of the star. If we used the estimation of the rotation period from the HARPS spectra ($P_{\mathrm{rot}} = 69 \pm 15$ days), we obtained a stellar age of 4.19 ± 0.97 Gyr. We also calculated the age with the rotation period measured from WASP-South ($P_{\mathrm{rot}} = 35.7 \pm 2.0$ days) and found 2.16 ± 0.27 Gyr. At this point, we cannot conclude which rotation period is the correct one, but it appears that the system is not newly formed. We confirmed these estimations using the relations from Barnes (2010), Barnes & Kim (2010), and Meibom et al. (2015), which describe the rotational evolution of main sequence stars taking into account the stellar mass dependence, as we obtained an age of $5.8^{+2.4}_{-1.9}$ Gyr from the HARPS rotation period and $2.36^{+0.45}_{-0.35}$ Gyr from the WASP-South data. In terms of activity, we found the star to be rather quiet and slowly rotating (see next section).

3. Observations

3.1. TESS photometry

TOI-269 was observed in six TESS sectors (3, 4, 5, 6, 10, and 13) from September 2018 to July 2019 with the two-minute cadence. The TESS photometric data were processed by the NASA Ames Science Processing Operations Center (SPOC; Jenkins et al. 2016). The resulting Presearch Data Conditioning Simple Aperture Photometry (PDCSAP; Smith et al. 2012, Stumpe et al. 2012, 2014) light curve of TOI-269 was corrected for dilution by known contaminating sources in the TESS aperture. Given the large TESS pixel size of 21", it was essential to verify that no visually close-by targets were present that could affect the depth of the transit and to check for a contaminating eclipsing binary. A plot of the target pixel file (TPF) and the aperture mask that is used for the simple aperture photometry (SAP), generated with `tpfplotter` (Aller et al. 2020), is shown in Fig. 1. We can see that one star overlaps the TESS aperture, but its faintness results in minimal dilution of the TESS light curve. The CROWDSAP value in the TESS data (which is the ratio of target flux to total flux in the aperture) ranges from 0.9829 to 0.9932 in all TESS sectors used for this analysis. This value corresponds to the ~1% dilution expected from the star visible in the TESS aperture with a magnitude difference of 5 with TOI-269.

A potential transit signal with 3.698-day period was identified in the SPOC transit search (Jenkins 2002, Jenkins et al. 2010, 2020) of the TOI-269 light curve. This was promoted to

---

[1] https://github.com/awmann/M_-M_K-

[2] https://github.com/samuelyeewl/specmatch-emp

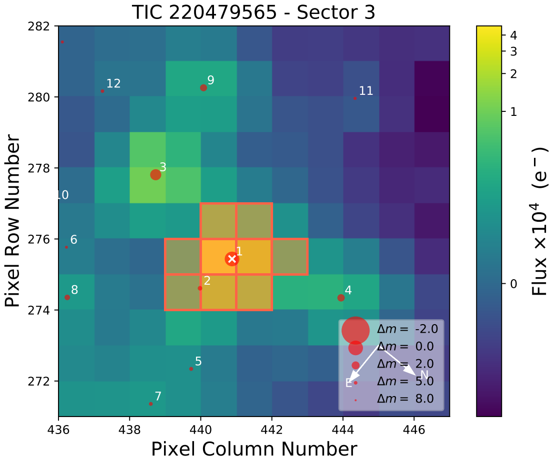

Fig. 1. TESS target pixel file image of TOI-269 in Sector 3 (created with `tpfplotter`, Aller et al. 2020). The electron counts are color-coded. The red bordered pixels are used in the simple aperture photometry. The size of the red circles indicates the *Gaia* DR2 magnitudes of all nearby stars.

TOI planet candidate status and designated as TOI-269.01 by the TESS Science Office based on the SPOC data validation results; the results indicate that the 4900 ppm signature based on 35 individual transits was consistent with that of a transiting planet (Twicken et al. 2018, Li et al. 2019). The difference image centroids analysis performed in the data validation (DV) report shows that the source of the transits is within 1 arcsec of the target, and furthermore that the DV reports are very clean; the transiting planet's signature passes all of DV tests, including the odd/even transit depth test, the ghost diagnostic, and the statistical bootstrap test. These tests are described in Twicken et al. (2018) and can exclude a false positive created by the second star in TESS aperture.

A recent work by Canto Martins et al. (2020), which reports a search for rotation period among 1000 TESS TOIs using fast Fourier transform, Lomb-Scargle, and wavelet techniques, accompanied by a rigorous visual inspection shows that TOI-269 does not indicate any sign of chromospherical activity all along the observed time ranges, and that it is among the quietest stars in the sample.

3.2. Ground-based photometry

3.2.1. ExTrA photometry

ExTrA is a new facility composed of three 60 cm telescopes that are located at La Silla Observatory (Bonfils et al. 2015). It is dedicated to searching for exoplanets transiting nearby M dwarfs with near-infrared photometry. The instrument relies on a new approach that involves combining photometry with spectroscopic information in order to mitigate the disruptive effect of Earth's atmosphere, as well as effects introduced by instruments and detectors. On each telescope five field units (FUs) are used to collect the light from the main target and four selected comparison stars. The FUs are composed of fibers accurately positioned that all feed a single near-infrared spectrograph with low spectral resolution ($R \sim 200$ or $R \sim 20$) and that covers the 0.9–1.6 μm range. The wide spectral domain enables the simultaneous collection of more photons which increases the sensitivity. ExTrA has the advantage of multiplexing, meaning that we can use a single spectrograph (so a single detector) to record the light from several telescopes. Although all three telescopes can observe the same field, most of the time they will observe different fields in order to maximize the transit search efficiency. For now all the telescopes are observing the same target in order to better understand the performance and limitations of the instrument.

On each telescope each FU is composed of two "buttons": the science button and the centering button. The centering button is composed of a bundle of 19 fibers in a hexagonal arrangement, used to calculate the position of the stars accurately, and then apply a relative offset to center the star in the science button. Each science button is composed of two channels, one with an aperture of 8" (optimized for bright stars), and a second one with an aperture of 4" in order to reduce the background contribution (optimized for faint stars). Finally, each channel has two fibers: one to collect the light of the star and another to collect the sky background close to the star. Thus, the spectrograph images the fiber bundles in centering mode, and with a different light path disperses the science fibers using a prism.

We observed TOI-269 with an 8" fiber aperture using the low-resolution mode ($R \sim 20$). We used *Gaia* DR2 4770833527616320512 as a guiding star to correctly point our target and comparison stars. The five stars we observed for that specific field of view were 2MASS J05021375-5 416 532 on the field unit 1 (FU1), 2MASS J05032583-5 353 188 on the FU3, 2MASS J05020219-5 351 064 on the FU4, 2MASS J05001046-5 407 021 on the FU5, and finally our target star, which was positioned on the FU2. The four comparison stars come from the 2MASS catalog (Skrutskie et al. 2006). The field of view of TOI-269 used for each night of observations with ExTrA is presented in Fig. A.1. At low resolution the spectrum of the star only covers 43 pixels of the 640 available in the detector in the spectral dimension. We first subtracted the sky flux and normalized by the flat. We made sure by looking at the absolute flux of all the stars that the night was clear and that we did not have any strong flux loss that could cause issues in the photometry. We created a template of all the exposures to remove any outliers. We distributed a weight (proportional to the variance of flux versus time) for each pixel/wavelength in order to mitigate the effect of the Earth's atmosphere, especially in the water bands. We then obtained the differential photometry for each star (our target and the four comparison stars) by normalizing with a template that includes the photometry of the different stars. The photometry is still affected by some systematic effects that are still under investigation. One of them may come from the fact that there are some differential motions of the stars during the observing sequence which introduce differential centering on the fibers aperture. A decorrelation with the position of the star inside the fiber is not possible because we cannot monitor the XY position of the star inside the fiber aperture during an acquisition. This problem is being investigated by observing the same field with the centering bundle only during a whole night, and then applying the measured offsets on all subsequent nights. For this work, we only present the light curve of our main target TOI-269 and we removed systematic trends applying Gaussian processes that allow us to model non-white noise effects for which we do not have a good model at hand. TOI-269 b transits were observed with ExTrA on December 18, 2019, December 29, 2019, and March 1, 2020, with an exposure time of 60 s. Telescope 1 was not in operation during the first two nights. In total, seven light curves of TOI-269 were obtained with ExTrA.

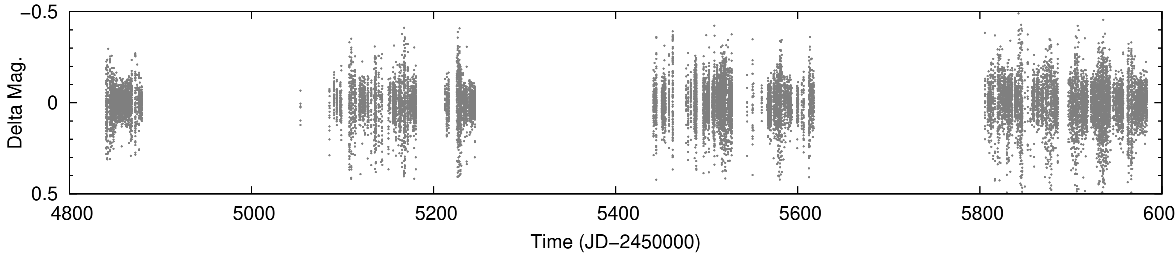

Fig. 2. WASP-South light curve of TOI-269 showing the time sampling.

3.2.2. LCOGT photometry

We observed full transits of TOI-269 b in Sloan i'-band on UTC 2019 March 02 (and respectively UTC 2020 October 13, only used in Sect. 4.4 as the global analysis had already been done at this time) from the LCOGT (Brown et al. 2013) 1.0 m network nodes at Cerro Tololo Inter-American Observatory (CTIO) (and Siding Spring Observatory). We also observed an ingress with nearly full transit coverage in I_c-band on UTC 2019 April 07 from the LCOGT 1.0 m network node at CTIO. We used the `TESS Transit Finder`, which is a customized version of the `tapir` software package (Jensen 2013) to schedule our transit observations. The 4096 × 4096 LCOGT SINISTRO cameras have an image scale of 0.389″ per pixel, resulting in a 26′ × 26′ field of view. The images were calibrated by the standard LCOGT `BANZAI` pipeline (McCully et al. 2018), and photometric data were extracted with `AstroImageJ` (Collins et al. 2017). The images were mildly defocused and have typical stellar point spread functions with a full width half maximum (FWHM) of ∼2″.3; circular apertures with radius ∼4″.3 were used to extract the differential photometry.

3.2.3. WASP-South photometry

The field of TOI-269 was observed by WASP-South (an array of eight cameras using 200 mm, $f/1.8$ lenses backed by 2048 × 2048 CCDs; Pollacco et al. 2006) over the three consecutive years, 2009, 2010, and 2011. Observations spanned 180 days in each year, accumulating a total of 18 100 photometric data points (Fig. 2). At a magnitude of V = 14.4, TOI-269 is at the faint end of the WASP range, but the field is relatively sparse, and the next-brightest star in the 48 arcsec extraction aperture is 4 magnitudes fainter.

Combining all the data, and searching for a rotational modulation using the methods presented in Maxted et al. (2011), we find a possible periodicity of 35.7 ± 2.0 days, where the error allows for possible phase changes over the observation span (Fig. 3). The modulation has an amplitude of 10 mmag, and an estimated false alarm probability of less than 1%.

3.3. Radial velocities: HARPS

We obtained 81 spectra of TOI-269 with the High Accuracy Radial velocity Planet Searcher (HARPS; Mayor et al. 2003) echelle spectrograph at the ESO 3.6 m telescope at La Silla Observatory in Chile. The HARPS optical spectrograph has a resolution of R = 115,000 and is stabilized in pressure and temperature, in order to achieve a sub-m s^{-1} precision. The observations span 275 days and were taken between UT January 18, 2019, and October 20, 2019 (Prog-ID 1102.C-0339(A)).

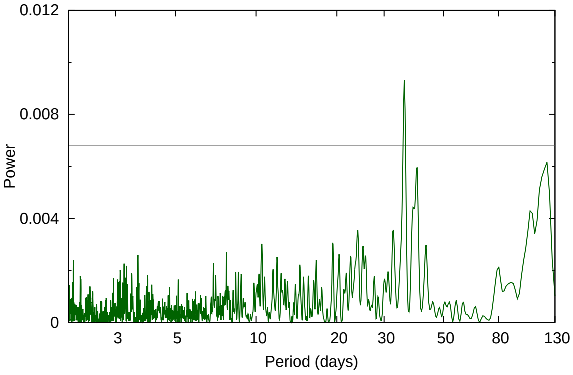

Fig. 3. Periodogram of the WASP-South light curves of TOI-269 from 2009–2011, showing a possible rotational modulation with a period of 36 days. The horizontal line corresponds to the estimated 1% false alarm level.

The HARPS observations were acquired without simultaneous wavelength calibration and with an exposure time of 1800 s, although seven of them have exposures of 1200 or 2400 s, resulting in a total open shutter time of 41.2 h. These data were reduced with the Data Reduction Software[3]. Radial velocities were computed through maximum likelihood between individual spectra and a master stellar spectrum following the recipes described in Astudillo-Defru et al. (2017b). Reduced spectra have a median signal-to-noise ratio of ∼13 at 650 nm, resulting in a median radial velocity precision of 7.5 m s^{-1} and presenting a dispersion of 8.5 m s^{-1}.

We also performed an analysis with HARPS data using the DACE platform[4] (Buchschacher & Alesina 2019) that can be used to compute periodograms for parameters available in RVs data and to represent correlations between different indicators. We did not find any sign of a strong stellar activity in the different indicators (CCF-FWHM, S-index, Na-index) derived from the spectra except in Hα with a peak around 54 days. The low value of log $R'_{\rm HK} = -5.32 \pm 0.14$, derived from the HARPS combined spectra, indicates a chromospherically inactive star with likely a long rotation period estimated to $P_{\rm rot}$ = 69 ± 15 days, according to Astudillo-Defru et al. (2017a).

This value is compatible with 2σ to the WASP-South value, but we could also imagine that the signal found in the WASP data comes from two stellar spots at the surface of the star and could correspond to $P_{\rm rot}/2$.

---

[3] `http://www.eso.org/sci/facilities/lasilla/instruments/harps/doc/DRS.pdf`

[4] `https://dace.unige.ch`

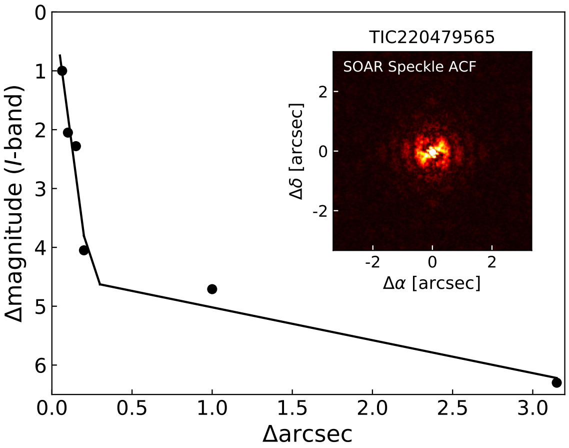

Fig. 4. I-band 5σ contrast curve from SOAR speckle imaging of TOI-269 (TIC 220 479 565). The inset depicts the corresponding speckle auto-correlation function.

3.4. SOAR speckle imaging

High angular resolution imaging is needed to search for nearby sources that could contaminate the TESS photometry, resulting in an underestimated planetary radius, or could be the source of astrophysical false positives, such as background eclipsing binaries. We searched for stellar companions to TOI-269 with speckle imaging on the 4.1 m Southern Astrophysical Research (SOAR) telescope (Tokovinin 2018) on 18 February 2019 UT, observing in Cousins I band, a visible band-pass similar to TESS. More details of the observations are available in Ziegler et al. (2020). The 5σ detection sensitivity and speckle auto-correlation functions from the observations are shown in Fig. 4. No nearby stars were detected within 3″ of TOI-269 in the SOAR observations.

4. Analysis and modeling

We used the software package `juliet` (Espinoza et al. 2019) to model separately and jointly the photometric and radial-velocity data. The algorithm is built on many publicly available tools for the modeling of transits (`batman`, Kreidberg 2015), RVs (`radvel`, Fulton et al. 2018), and Gaussian processes (GPs) (`george`, Ambikasaran et al. 2015; `celerite`, Foreman-Mackey et al. 2017). In order to compare different models, `juliet` efficiently computes the Bayesian evidence (lnZ) using `dynesty` (Speagle 2020), a python package to estimate Bayesian posteriors and evidence using nested sampling methods. Nested sampling algorithms sample directly from the given priors instead of starting off with an initial parameter vector around a likelihood maximum found via optimization techniques, as is done in common sampling methods. During our different analysis, we made sure that we had enough live points given the number of free parameters so that we would not miss peaks in the parameter space. We started the analysis using only TESS photometry, and then HARPS RVs measurements in order to constrain the priors and use them for a joint analysis of all our data.

4.1. TESS photometry

First, using `juliet`, we modeled the TESS PDCSAP light curve where our planet candidate was initially detected. The transit model fits the stellar density $\rho_\star$ along with the planetary and jitter parameters. We chose the priors of the orbital parameters from ExoFOP, except for the stellar density that we calculated in Sect. 2. We adopted a few parametrization modifications when dealing with the transit photometry. We assigned a quadratic limb-darkening law for TESS, as shown to be appropriate for space-based missions (Espinoza & Jordán 2015), which was then parameterized with the uniform sampling scheme (q_1, q_2) introduced by Kipping (2013). Additionally, rather than fitting directly for the planet-to-star radius ratio ($p = R_\mathrm{p}/R_\star$) and the impact parameter of the orbit ($b = a/R_\star \cos i$), `juliet` used the parameterization introduced in Espinoza (2018) and fit for the parameters r_1 and r_2 to guarantee full exploration of physically plausible values in the (p,b) plane. We fixed the TESS dilution factor to one based on our analysis of nearby companions. Furthermore, we added in quadrature a jitter term σ_TESS to the TESS photometric uncertainties, which might be underestimated due to additional systematics in the space-based photometry. The details of the priors and posteriors, and the description of each parameter are presented in Table B.1. The best-fit transit model for the six sectors of TESS photometry is shown in Fig. 5. We also represented the phase-folded light curve in the same figure.

4.2. HARPS radial velocities

As the star does not seem to be very active and has a long rotation period, we decided that Gaussian processes were not required to model the HARPS data. However, a small long-period trend seems visible in our dataset so we decided to add a linear drift to the fit. We first computed the periodogram of the RV time series where we subtracted the possible linear trend, and then the Keplerian corresponding to the TOI-269 b period (see Fig. 6). We then analyzed the radial-velocity data from HARPS using `juliet`. The intercept of the linear model, which represents here the systemic velocity of the star, is computed at time $t_\gamma = 2\,458\,639$ BJD$_\mathrm{UTC}$, close to the middle of our observations. This configuration of one planet with a possible additional long-term trend (that is compatible with zero within 2σ) in the data appears to be the simplest and model that best explains the current dataset. The priors are taken from the TESS analysis and an overview of the HARPS data. The details of the priors and posteriors, and the description of each parameter are presented in Table B.2.

4.3. Joint fit of all data

To obtain the most precise parameters of the TOI-269 system, we performed a joint analysis of the TESS, LCO, and ExTrA photometry and velocity data from HARPS using `juliet`. This time we fitted for the eccentricity and applied the classical parameterization of (e, ω) into $(\sqrt{e}\sin\omega, \sqrt{e}\cos\omega)$, always ensuring that $e \leq 1$. We decided to use time-dependent Gaussian processes on the ExTrA and LCO-CTIO photometry as the data had not been detrended yet. We decided on the approximate Matern kernel introduced in Foreman-Mackey et al. (2017) because when looking at the light curves there are no evident quasi-periodic oscillations. We only use the three-transit duration around transit data for TESS for reasons of computation time.

In total, we looked for the posterior distribution of 51 free parameters, and as it is a large number of parameters, we used `dynesty` to perform this fit. Before the final run for the joint modeling, we constrained our priors using the previous results from `juliet` in order to optimize the search for the posteriors and the computation time due to the large parameter space. Since

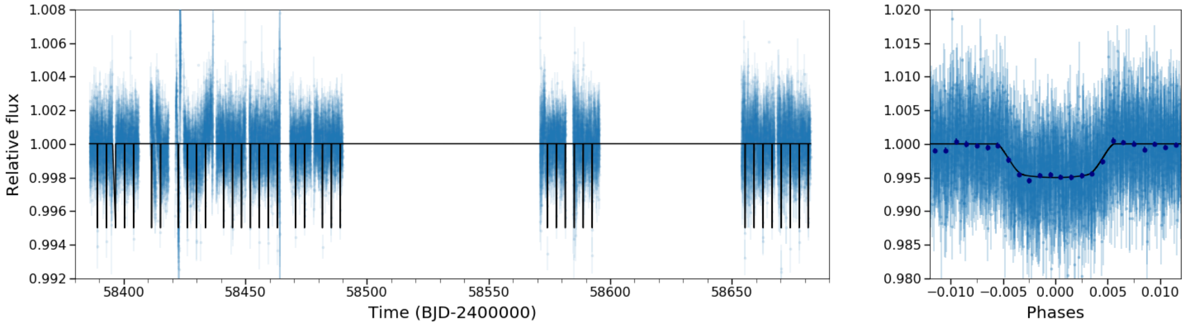

Fig. 5. Modeling of the TESS data. *Left panel*: TESS photometry time series (20 min binned data) from Sectors 3, 4, 5, 6, 10, and 13 along with the median of 1000 randomly chosen posterior samples (solid black line). *Right panel*: phase-folded light curve to the period of the planet (dark blue points correspond to ~5 min binned data).

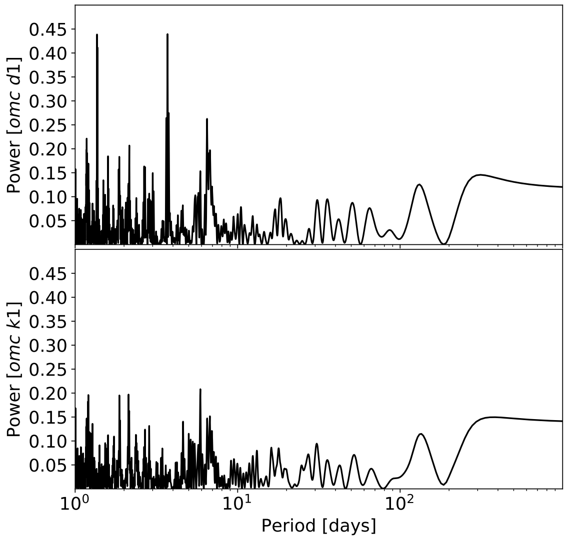

Fig. 6. Analysis of the HARPS radial velocities. Periodogram for RV time series where a linear drift was subtracted is shown in the *top panel*. We can see a peak at 3.7 days corresponding to the period of the planet, and another at 1.36 days corresponding to its alias. Both peaks have a false alarm probability ≪1%. The *lower panel* is the periodogram for RVs where a linear drift and Keplerian (for the first planet) were subtracted; the highest peak at 5.9 days has a false alarm probability of 20.8%.

we used rather large priors for the planetary parameters for the fit of TESS data and HARPS data separately, nested sampling is an efficient method for the exploration of the parameter space, and as most of the planetary parameters are specific to a given data type, they would not change significantly in a joint fit. Using prior knowledge from the previous fit for the joint modeling was therefore justified. Table B.3 and Tables 2 and B.4 show respectively the priors and posteriors of all the parameters, along with the transit, RVs and physical parameters derived using the stellar parameters presented in Sect. 2. Figure 7 shows the results of our joint fit to the data for ExTrA[5]. The GPs we used to account for the systematics clearly capture the observed trends in the ExTrA photometry. We show the phased transits of the photometry instruments after subtracting the GP component from the ExTrA and LCO-CTIO data in Fig. 8. In Figs. 9 and 10, we present the radial-velocity component of the joint fit modeled by the median and one-sigma error of 1000 randomly chosen posterior samples, and the phase-folded data with the maximum a posteriori model.

This analysis revealed an eccentric orbit for TOI-269 b, which is discussed in the next section.

In order to estimate the precision of the new instrument ExTrA, we computed the standard deviation of the residuals of TESS and ExTrA data phased at the period of the planet (see Fig. 8 for the residuals of the phase-folded light curves) for different bin sizes (from 2 to 64 min bins) and present the results in Fig. 11. We can see that combining 7 ExTrA transits is similar to combining 35 TESS transits to obtain the same precision on the dispersion of the residuals, potentially correlated to the precision on the radius ratio. We established that we need to fit the TESS and ExTrA light curves simultaneously to constrain the parameters of the Gaussian processes, so that they filter ExTrA photometry on a different timescale than the transit itself, but we do obtain a better precision (1–5 transits) to measure the depth of the transit with fewer ExTrA observations.

4.4. TTVs analysis

We calculated the transit timing variations (TTVs) with all the photometric datasets (TESS, LCOGT, ExTrA) using `juliet`. Instead of fitting a period P and a time-of-transit center t_0, `juliet` looks for the individual transit times. We fitted each ExTrA transit individually and one transit time for each night of observations, which is more coherent for the analysis. Combining the three telescopes reduces the error bars on each ExTrA estimation. The results of the analysis showing the difference between the observed transit times and the calculated linear ephemeris from all the transits is presented in Fig. 12. No significant variation appears in the data.

5. Discussion

5.1. Mass-radius diagram and internal structure

TOI-269 b, with a radius of 2.77 ± 0.12 $R_\oplus$ and a mass of 8.8 ± 1.4 $M_\oplus$, lies within the population of sub-Neptunes. With a stellar irradiation of 19 times the Earth, TOI-269 b lies in the gas-dominated sub-Neptune population described by

---

[5] The raw and detrended fluxes are available in electronic form at the CDS.

Table 2. Posterior stellar and planetary parameters obtained from our joint photometric and radial-velocity `juliet` analysis for TOI-269.

Parameter name	Posterior estimate	Description
Posterior parameters for TOI-269		
$\rho_\star$ (g cm^{-3})	$8.98^{+0.83}_{-0.81}$	Stellar density
$q_{1,\mathrm{TESS}}$	$0.39^{+0.33}_{-0.24}$	Quadratic limb-darkening parameterization
$q_{2,\mathrm{TESS}}$	$0.22^{+0.30}_{-0.16}$	Quadratic limb-darkening parameterization
$q_{1,\mathrm{LCO}}$	$0.35^{+0.28}_{-0.19}$	Quadratic limb-darkening parameterization
$q_{2,\mathrm{LCO}}$	$0.36^{+0.35}_{-0.25}$	Quadratic limb-darkening parameterization
$q_{1,\mathrm{ExTrA}}$	$0.133^{+0.16}_{-0.089}$	Quadratic limb-darkening parameterization
$q_{2,\mathrm{ExTrA}}$	$0.43^{+0.36}_{-0.30}$	Quadratic limb-darkening parameterization
Posterior parameters for TOI-269 b		
P_b (days)	$3.6977104^{+0.0000037}_{-0.0000037}$	Period of the planet
t_0 (BJD TBD)	$2458381.84668^{+0.00033}_{-0.00033}$	Time of transit-center for the planet
$r_{1,\mathrm{b}}$	$0.700^{+0.078}_{-0.15}$	Parameterization for p and b
$r_{2,\mathrm{b}}$	$0.0638^{+0.0020}_{-0.0021}$	Parameterization for p and b
$S_{1,\mathrm{b}} = \sqrt{e_\mathrm{b}}\sin(\omega_\mathrm{b})$	$0.614^{+0.077}_{-0.10}$	Parameterization for e and ω
$S_{2,\mathrm{b}} = \sqrt{e_\mathrm{b}}\cos(\omega_\mathrm{b})$	$0.18^{+0.15}_{-0.16}$	Parameterization for e and ω
K_b (m s^{-1})	$7.6^{+1.2}_{-1.2}$	Radial-velocity semi-amplitude of the planet
Long-term trend in RVs		
RV slope (m s^{-1} day^{-1})	$0.0161^{+0.0081}_{-0.0081}$	Linear trend : first parameter
RV intercept (km s^{-1}) at t_γ	$37.22864^{+0.00082}_{-0.00082}$	Linear trend: second parameter
Derived transit and RVs parameters		
$p = R_\mathrm{p}/R_\star$	$0.0638^{+0.0020}_{-0.0021}$	Planet-to-star radius ratio
$b = (a/R_\star)\cos(i_\mathrm{p})$	$0.55^{+0.12}_{-0.22}$	Impact parameter of the orbit
i_p (deg)	$88.14^{+0.78}_{-0.90}$	Inclination of the orbit
e_b	$0.425^{+0.082}_{-0.086}$	Eccentricity of the orbit
ω_b (deg)	74^{+15}_{-15}	Argument of periastron
Derived physical parameters $^{(*)}$		
$M_\mathrm{p}(M_\oplus)$	$8.8^{+1.4}_{-1.4}$	Planetary mass (in Earth mass)
$R_\mathrm{p}(R_\oplus)$	$2.77^{+0.12}_{-0.12}$	Planetary radius (in Earth radius)
ρ_p(g cm^{-3})	$2.28^{+0.48}_{-0.42}$	Planetary density
a_p (au)	$0.0345^{+0.0015}_{-0.0015}$	Semi-major axis
$T_\mathrm{eq}(K)$	531^{+25}_{-25}	Equilibrium temperature of the planet $^{(\dagger)}$
$S\,(S_\oplus)$	$19.0^{+4.0}_{-3.3}$	Planetary insolation (in Earth flux)

Notes. The posterior estimate corresponds to the median value. Error bars denote the 68% posterior credibility intervals. $^{(*)}$We sample from a normal distribution for the stellar mass, stellar radius, and stellar temperature that is based on the results from Sect. 2. $^{(\dagger)}$Equilibrium temperature was calculated assuming 0.3 Bond albedo and the semi-major axis distance.

Fulton et al. (2018). Figure 13 shows M–R curves tracing the compositions of pure-iron, Earth-like, and pure-water planets and a planet with 95% water and 5% H–He atmosphere subjected to a stellar radiation of $F/F_\oplus = 20$ (similar to that of TOI-269 b). For reference, also shown are exoplanets with accurate and reliable mass and radius determinations (Otegi et al. 2020a, accessible on the Data & Analysis Center for Exoplanet, DACE[6]). TOI-269 b sits above the pure-water curve and below the 5% H–He curve, implying that the H–He mass fraction is unlikely to exceed a few percent.

Determining the planetary internal structure is extremely challenging since various compositions can lead to identical mass and radius (e.g., Rogers & Seager 2010, Lopez & Fortney 2014, Dorn et al. 2015, 2017, Lozovsky et al. 2018, and Otegi et al. 2020b). With the aim of at least partially breaking the degeneracy, and in order to determine how well a given interior model compares with the other possible models that also fit the data, we use a generalized Bayesian inference method with a Nested sampling scheme. This approach allows us to quantify the degeneracy and correlation of the planetary structural parameters and to estimate the most likely region in the parameter space. We modeled the interior of TOI-269 b considering a pure-iron

---

[6] `https://dace.unige.ch/exoplanets/`

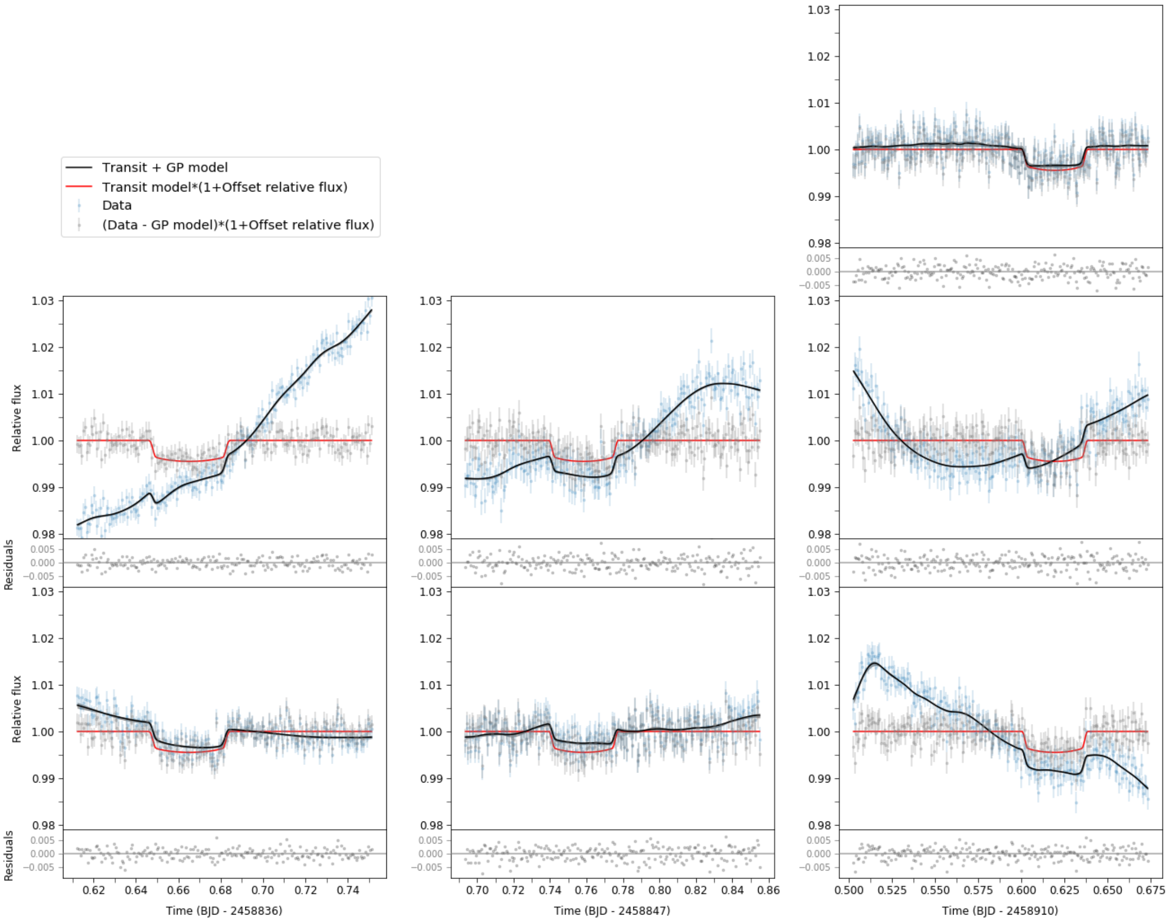

Fig. 7. ExTrA light curves for the three nights of observations (columns) and for each telescope (*first line* corresponding to telescope 1, *second line* to telescope 2, and *third line* to telescope 3). Our raw data are shown in blue, and modeled using Gaussian processes in black. The detrended light curves are shown (gray dots), with the maximum a posteriori model transit (in red). The residuals below correspond to the modeled transit subtracted from detrended data points.

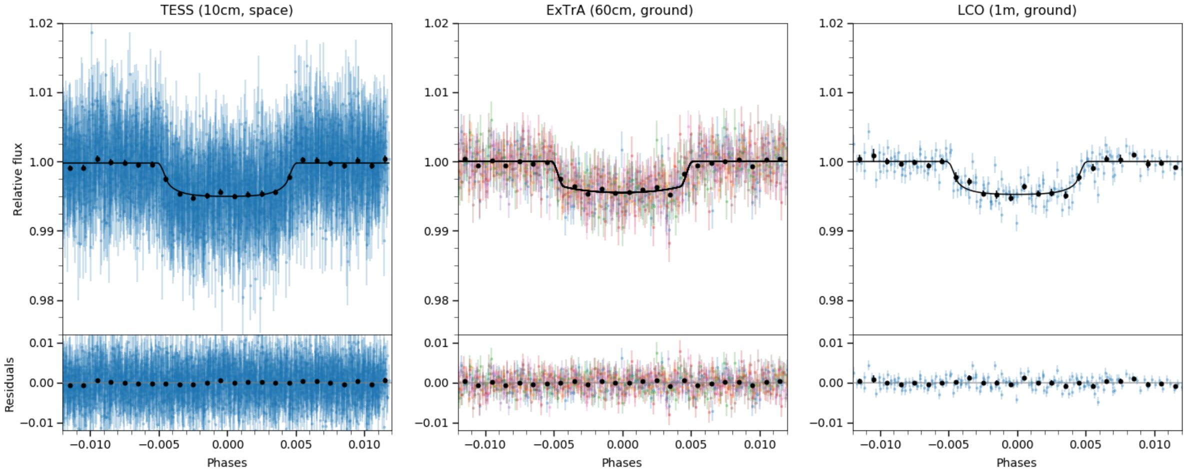

Fig. 8. Photometry data for TESS (35 transits), ExTrA (7 transits; corrected for the GP component), and LCO-CTIO (2 transits; corrected for the GP component) phase-folded to the period of the planet. The black line is the maximum a posteriori model; the black points are ~5 min binned data.

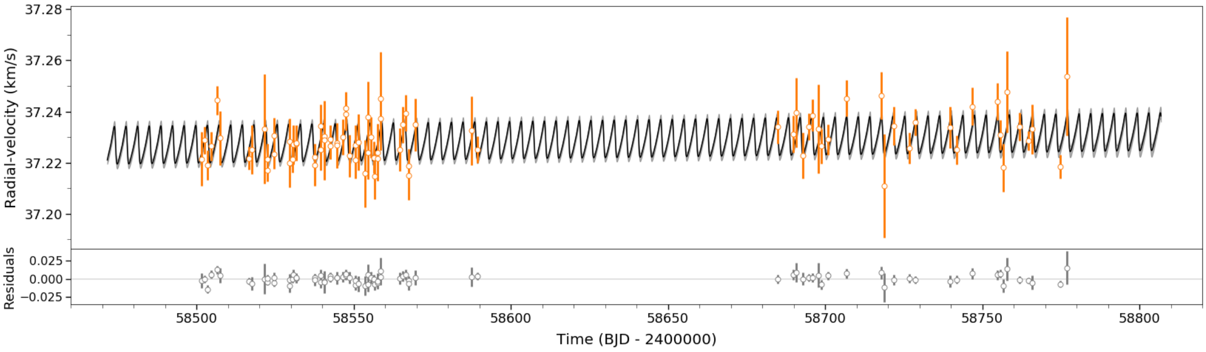

Fig. 9. HARPS radial-velocity measurements for TOI-269. The data points with errors are shown in orange; the black line and gray band correspond respectively to the median and 1σ of 1000 randomly chosen posterior samples from the joint fit.

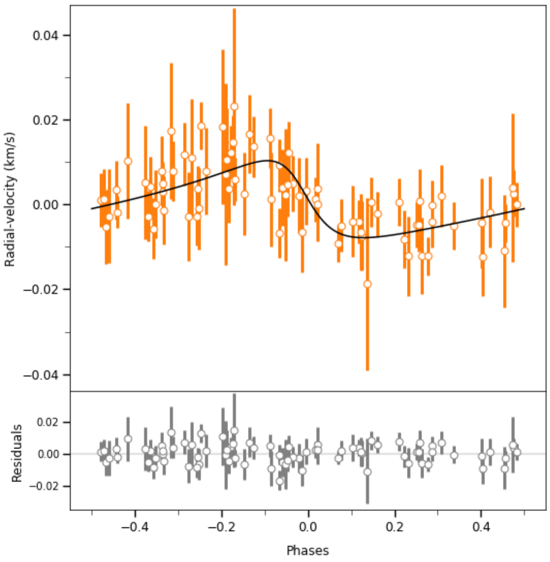

Fig. 10. HARPS RVs phase-folded to the period of the transiting planet. The black line is the best-fit model from the joint fit.

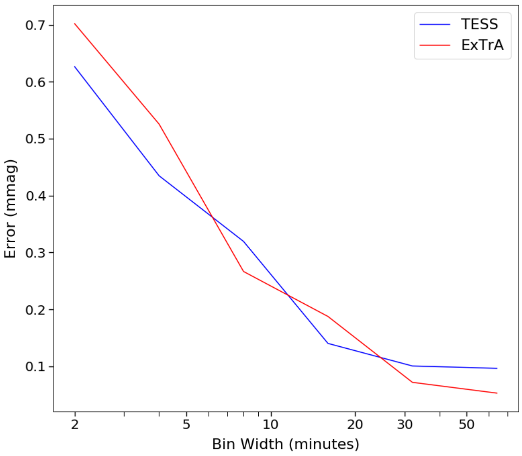

Fig. 11. Dispersion of the residuals for TESS (35 combined transits) and ExTrA (7 combined transits) data for different bin sizes.

core, a silicate mantle, a pure-water layer, and a H–He atmosphere. The equations of state (EOSs) used for the iron core are taken from Hakim et al. (2018), the EOS of the silicate-mantle is calculated with `PERPLE_X` from Connolly (2009) using the thermodynamic data of Stixrude & Lithgow-Bertelloni (2011), and the EOS for the H–He envelope are from Chabrier et al. (2019) assuming a proto-solar composition. For the pure-water layer the AQUA EOS from Haldemann et al. (2020) is used. The thickness of the planetary layers were set by defining their masses and solving the structure equations. To obtain the transit radius, we follow Guillot (2010) and evaluate the location where the chord optical depth $\tau_{\rm ch}$ is 2/3. It has been suggested that stellar abundances can be used as a proxy for the planetary bulk abundances to reduce the degeneracy (Dorn et al. 2017, Brugger et al. 2017, and Otegi et al. 2020b), but the result is debated (Plotnykov & Valencia 2020), and we therefore opted not to use them.

Figure 14 shows a ternary diagram and an illustration of the inferred internal composition of TOI-269 b. The ternary diagram shows the strong degeneracy of internal composition leading to the same mass and radius, which cover almost the whole diagram. We find a median H–He mass fraction of 0.8%, which corresponds to a lower bound since enriched H–He atmospheres are more compressed and, therefore increase the planetary H–He mass fraction. Formation models suggest that sub-Neptunes are very likely to be formed via envelope enrichment (Venturini & Helled 2017). We also find that TOI-269 b can have a significant water layer, accounting for nearly half of the planetary mass with a thickness of about one Earth radius ($1.02^{+0.39}_{-0.37}$). The iron core and silicate mantle have estimated relative mass fractions of 19% and 26%, with large uncertainties. The degeneracy between the core and mantle in this M–R regime does not allow us to accurately estimate the masses of these two constituents. Since interior models cannot distinguish between water and H–He as the source of low-density material, we also ran a three-layer model which leaves out the H_2O envelope. Under this assumption we find that the planet would be nearly 4^{+1}_{-1}% H-He, 43^{+24}_{-23}% iron, and 52^{+22}_{-23}% rock by mass. These estimations with the three-layer model set maximum limits since any water added would decrease these mass fractions.

5.2. A significantly eccentric orbit

In our joint fit of photometric and velocimetric data, we derived a non-zero eccentricity of $0.425^{+0.082}_{-0.086}$, with 99% of the posterior values between 0.210 and 0.577. As shown on an eccentricity-period diagram with exoplanets smaller than 10

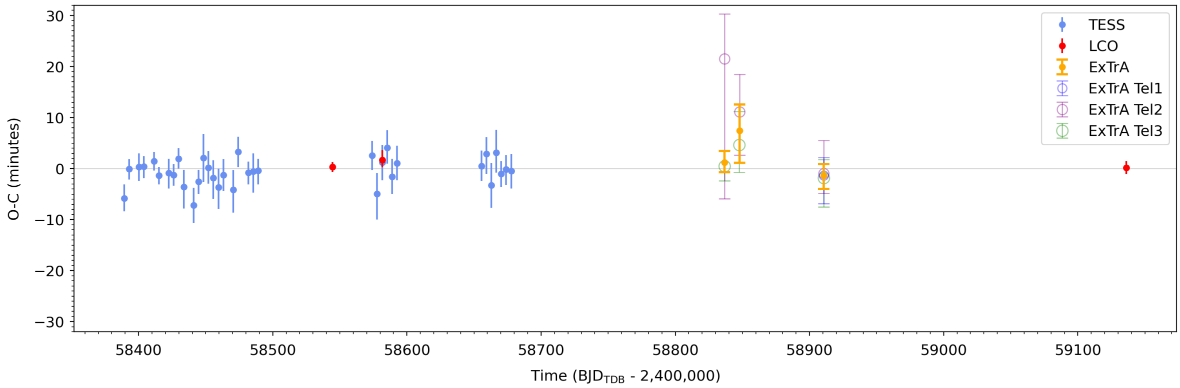

Fig. 12. Transit time variations. The observation minus the calculated linear ephemeris (O–C) diagram derived using TESS (light blue), LCO-CTIO (red), and ExTrA data (dark blue corresponding to telescope 1, purple to telescope 2, green to telescope 3, and yellow to a transit time fit of all the telescopes available for each night).

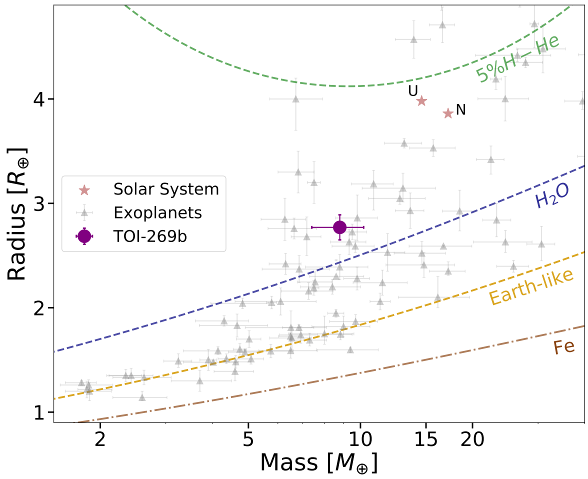

Fig. 13. Mass-radius diagram of exoplanets with accurate mass and radius determination (Otegi et al. 2020a). Also shown are the composition lines of iron, an Earth-like planet, pure water, and 95% water + 5% H–He subjected to an insolation flux of $20S_\oplus$ (similar to that of TOI-269b). The EOSs used for the iron core are taken from Hakim et al. (2018), the EOS of the silicate-mantle is calculated with `PERPLE_X` from Connolly (2009), and for pure-water the AQUA EOS from Haldemann et al. (2020) is used.

Earth radii (Fig. 15), TOI-269 b has a remarkable eccentricity with almost the highest value for planets with periods shorter than 10 days.

To understand which part of our data constrains the eccentricity most, we applied different fits and compared their posterior distributions (Fig. 16). First, we fitted only the photometry using data from TESS, ExTrA, and LCO, and without a prior on the stellar density. This yielded a broad distribution of eccentricities showing that, although compatible with zero, the photometry alone poorly constrains the eccentricity value. Second, we fitted only the HARPS radial velocities, and we obtained an eccentricity of $0.25^{+0.13}_{-0.10}$, close to the 2σ threshold chosen by Lucy & Sweeney (1971) to consider an eccentricity value to be significantly different than zero. As expected, the posterior distribution is also narrower, showing that radial velocity alone constrains the eccentricity more than the photometry alone does. Actually, when fitting both photometry and radial-velocity data together (but still without a prior on the stellar density), we obtained a similar posterior distribution on eccentricities than that of our fit with only radial velocity.

In Fig. 16, we also show the posterior distributions for the stellar density when relevant (i.e., not when fitting RV alone). With posterior values ranging from 10 to $100\,\mathrm{g\,cm^{-3}}$, we see that the stellar density is poorly constrained by either photometry alone or both photometry and radial velocity. Most of these values are actually too high for such an early M dwarf. We also see that there is a strong correlation between the stellar density and the eccentricity of the planet. This introduces the importance of the prior on the stellar density. In Fig. 16, we add the result of our joint fit of both photometric and velocimetric data including the prior knowledge on the stellar density (see Sect. 2). The narrow prior on stellar density selects a fraction of an otherwise broad $e-\rho_{\rm star}$ posterior density distribution. At this point we can thus conclude that if some of the eccentricity is already encoded in the radial-velocity data, most of the constraints eventually come from the prior on the stellar density.

To lend more credit to this remarkable result, we also modeled the data by imposing a circular orbit to TOI-269 b. It leads to a stellar density $>25.8\,\mathrm{g\,cm^{-3}}$ with a 99% confidence level, which is not compatible with the radius and mass estimation we provided in Sect. 2, and therefore also excludes that the orbit could be circular. As a side note, we also tried to account for the finite integration time of the observations, in case the too long integration times would bias the light curve toward lower stellar densities (Kipping 2010), but it did not change our posterior distribution for the stellar density.

Granted with a robust non-zero eccentricity, we turn to possible explanations. Because the star is likely a few billion years old (Sect. 2), TOI-269 b probably did not acquire its eccentricity recently. It may have reached its present orbit with planet-planet migration and acquired a high eccentricity in the process. We looked at the circularization timescale following Patra et al. (2017). Determining which tidal quality factor to use for a specific exoplanet is not simple, so we looked at the problem the other way around. Given the two ages that we estimated for TOI-269, we would need a tidal quality factor Qp larger than 1.5×10^5 and 2.8×10^5 in order to explain why the exoplanet is not on a circular orbit yet. This range of values is high

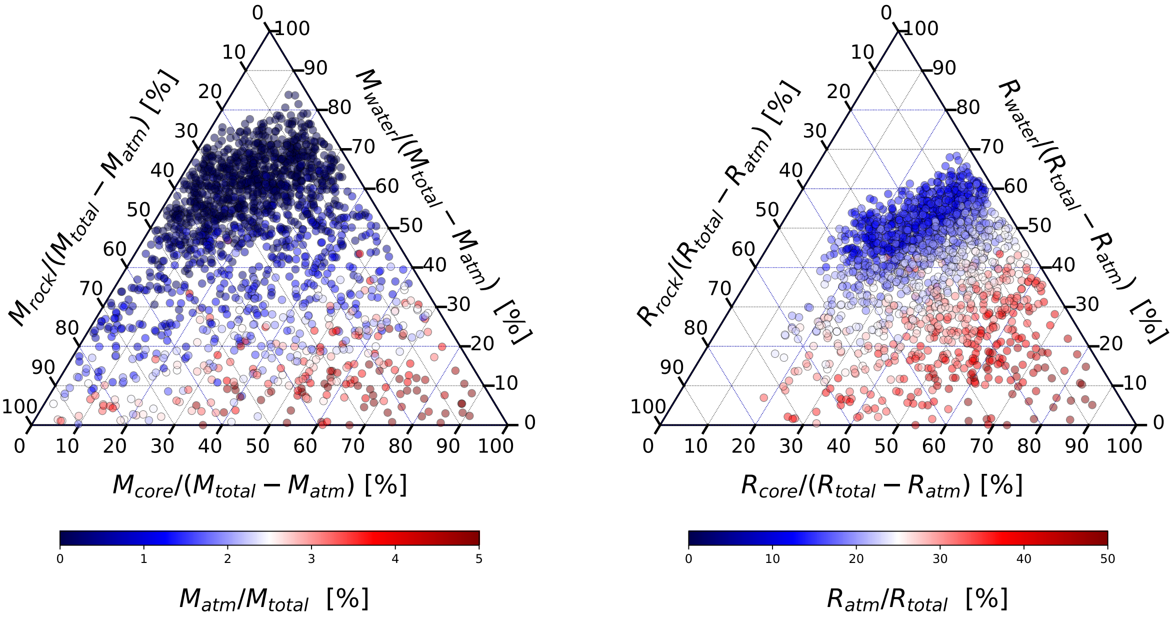

Fig. 14. Ternary diagram of the inferred internal composition of TOI-269 b in mass (*left*) and radius (*right*).

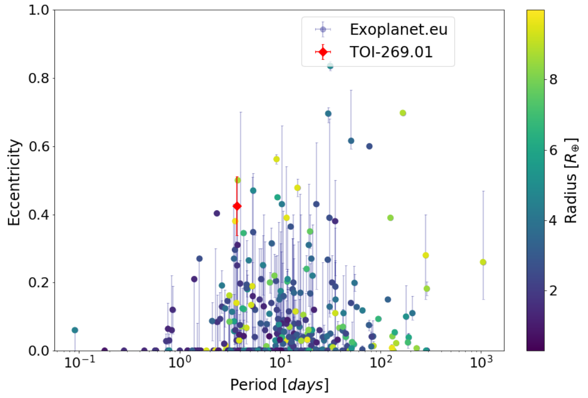

Fig. 15. Orbital eccentricity as a function of the orbital period with the planetary radius (see color scale at right) from the Exoplanet.eu catalog.

compared to the tidal quality factors calculated for the Solar System planets, where Qp is around 10–100 for the rocky planets (Goldreich & Soter 1966) and up to ~30 000 for Jupiter using the excitation frequency of Io (Lainey et al. 2009). However, in studies that target exoplanets (e.g., Hansen 2012) it was shown that Qp can go as high as 10^7–10^8 for exoplanets that orbit close to the host star. The discrepancy between the values of Qp for Jupiter and for the close-in exoplanets can be explained by the fact that these planets are likely to be in synchronous rotation, contrary to Jupiter, which has a fast rotation. A slower synchronous rotation would make the dissipation via inertial waves less efficient (e.g., Ogilvie & Lin 2004), and therefore the planets would take more time to circularize. The observations can give us an upper value for Qp, in order to explain why the planet is not circularized yet, but we would need models of the internal structure and tidal dissipation specifically of TOI-269 b to constrain this

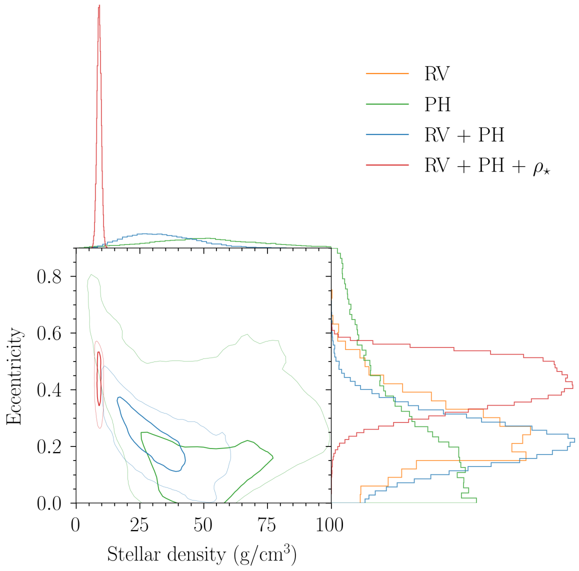

Fig. 16. Two-parameter joint posterior distributions for the stellar density and planet eccentricity for three different analyses (photometry only; joint radial velocity and photometry; and joint radial velocity and photometry with a stellar density prior computed from the stellar radius and mass derived in Sect. 2). The 39.3% and 86.5% two-variable joint confidence regions are denoted by a thick and a thin line, respectively. Histograms of the marginal posterior samples are presented at the top and at the right (for the eccentricity, the radial velocity-only analysis is also shown).

factor more closely, and helps us give a lower limit on Qp for example. It is also interesting to note that Correia et al. (2020) proposed other mechanisms to explain non-null eccentricity of other warm Neptunes, including excitation from distant planet

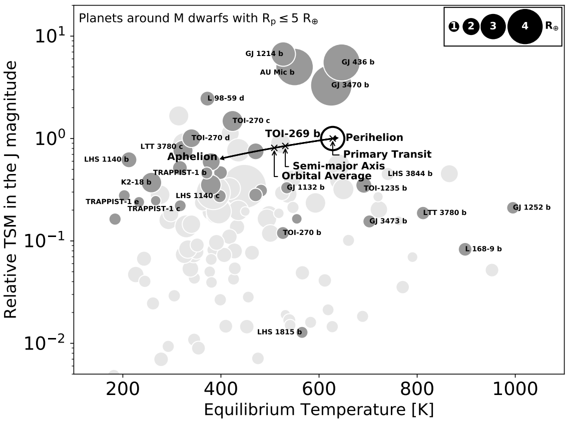

Fig. 17. Transmission spectroscopic metric in the J magnitude as a function of the planetary equilibrium temperature. The TSM values are shown relatively to the TOI-269 b (eccentricity-corrected) reference value of 89^{+19}_{-14}. Only planets orbiting M dwarf ($T_{\text{eff}} \leq 3875$ [K]) and with $R_p \leq 5\,R_\oplus$ were selected. TOI-269 b is shown as a black circle. The black arrow shows the range of equilibrium temperature depending on planet position during the orbit. The crosses show the locations of the orbital average, the semi-major axis, and the primary transit. Other planets with and without measured masses are shown in dark gray and light gray, respectively.

or atmospheric escape. We note that the RVs include a possible trend (0.0161 ± 0.0081 m s^{-1} day^{-1}), and therefore a possible hint of an outer companion. Given the ~275-day time span of observations with HARPS, if the possible companion were to have an orbital period of twice this time span, its mass would be $30 \pm 15\,M_\oplus$.

5.3. Potential for atmospheric characterization

We calculated the transmission spectroscopic metric (TSM) in the J magnitude using the equation from Kempton et al. (2018) and obtained a value of $\text{TSM} = 75^{+16}_{-12}$. This value takes into account the equilibrium temperature when the planet is at a distance corresponding to its semi-major axis. For an eccentric orbit and for transmission spectroscopy it would be more exact to take into account the planet equilibrium temperature at the exact transit moment (see details below). By doing so a corrected TSM of 89^{+19}_{-14} is computed. To put this value into context, we also computed the TSM for exoplanets with $R_p \leq 5\,R_\oplus$ orbiting M dwarf host stars ($T_{\text{eff}} \leq 3875$ (K)) using the NASA exoplanet archive on February 16, 2021. The TSM values are shown relatively to the TOI-269 b value in Fig. 17. TOI-269 b lies among the best targets of its category (sub-Neptunes around M dwarfs). So far, the atmospheric characterization of sub-Neptune planets mostly delivered non-detections (e.g., on the warm GJ 1214 b by Kreidberg et al. 2014), and the few detections obtained did not bring conclusive results on their actual atmospheric contents. For example, the more temperate K2-18 b (Cloutier et al. 2017) exhibits a near-infrared absorption in its transmission spectrum first interpreted as due to water (Benneke et al. 2019, Tsiaras et al. 2019), but Bézard et al. (2020) argued that methane could be responsible for this feature. Thus, it would be very interesting to probe with transmission spectroscopy the atmospheres of newly discovered temperate and warm sub-Neptunes such as TOI-269 b, TOI-270 c or d (Günther et al. 2019, Van Eylen et al. 2021), or LTT 3780 c (Cloutier et al. 2020, Nowak et al. 2020) in order to see if they exhibit atmospheric features and if so, what their natures are. Finally, detecting any atmospheric features could help in constraining the extent and the mean molecular weight of the atmosphere, and give some constraints on possible interior structures (see Sect. 5.1).

Interestingly, the orbit of TOI-269 b is found to be significantly eccentric. The change in stellar irradiation due to the eccentricity throughout the orbital revolution brings a change in equilibrium temperature by a factor of $\sqrt{\frac{1+e}{1-e}} \sim 1.6 \pm 0.1$. Thus, the planet temperature passes from ~400 K near aphelion to ~630 K near perihelion. Depending of the actual atmospheric conditions, some species such as sulfuric acid may condense and vaporize throughout an orbital revolution, but details of such phenomena are beyond the scope of this paper. We also note that the primary transit happens ~1.5h after perihelion (at ~1.02 times the perihelion radius), when the planet is the hottest. This means that TOI-269 b is a slightly better target for transmission spectroscopy than by only considering the semi-major axis or the orbital average equilibrium temperature (see Fig. 17).

Moreover, the currently found high eccentricity could hint that the planet may have recently arrived in its position. As the host star is an M dwarf with a convective envelope, strong tidal interactions are supposed to circularize the planetary orbit rapidly (Correia et al. 2020). If the planet migrated recently (e.g., due to a Lidov-Kozai mechanism), it is possible that strong to moderate atmospheric escape also started recently and would be still in process (Bourrier et al. 2018a). Such a scenario is supported by the observation of atmospheric evaporation in the Neptune-sized planets GJ 436 b (Ehrenreich et al. 2015), GJ 3470 b (Bourrier et al. 2018b, Palle et al. 2020), and HAT-P-11 b (Allart et al. 2018), which all possess eccentric orbits. Observing evaporation in an eccentric sub-Neptune would be very informative on the architecture and history of the system. For example, this is possible by detecting the meta-stable helium infrared triplet at 1083 nm (Oklopčić & Hirata 2018, Spake et al. 2018) at high resolution (Allart et al. 2018, Nortmann et al. 2018). Even though no helium detection has been reported to date for sub-Neptune planets (Kasper et al. 2020, Gaidos et al. 2020a,b), TOI-269 b could have a helium signal of 0.5–1.5% (≳50–150 scale-height, depending on the atmospheric escape rate, thermospheric temperature, and stellar high-energy irradiation; Nortmann et al. 2018; Kasper et al. 2020) that could be detected with several transit observations with a high-resolution infrared spectrograph such as NIRPS (Bouchy et al. 2017).

6. Conclusions

We presented the discovery and characterization of a sub-Neptune transiting the M dwarf TOI-269. The planet was detected by the TESS mission, then confirmed via ground-based transit follow-up observations with multiple instruments and from precise RV measurements with HARPS by measuring its mass. TOI-269 b contributes to the TESS Level One Science Requirement of delivering 50 transiting small planets (with radii smaller than $4R_e$) with measured masses to the community. It will be re-observed in five sectors during the TESS year-3 extended mission from Sept 2020 to April 2021, which will provide new timing to perform a better TTV analysis.

The estimated average density of TOI-269 b is $2.28^{+0.48}_{-0.42}$ g/cm^3, which is significantly lower than the typical density of rock planets and indicates the presence of a volatile envelope. Internal structure models with four layers (an iron core, silicate mantle, water ocean, and H-He atmosphere), although strongly degenerated, suggest that TOI-269 b has between 0.4% and 4% H–He by mass. Our analysis suggests that TOI-269 b would be an interesting target for atmospheric characterization in order to compare it with other sub-Neptunes.

The ExTrA observations of this target allowed us to test the precision of our instrument. Early M dwarfs with many TESS transits are not the primary targets for ExTrA. It will be more competitive around late stars with one or a few TESS transits in order to obtain a better precision for the planetary radius and for the transit timings. As for measuring radii, we were able to show here that the precision of one transit with ExTrA is comparable to that of five transits with TESS (see Fig. 11). ExTrA could also detect other planets in already-known planetary systems.

With such a high eccentricity, TOI-269 b is reminiscent of GJ 436 b (Bourrier et al. 2018b) and follow-up observations similar to those conducted for this planet would thus provide an instructive comparison. TOI-269 b is probably too far away to detect an atmospheric escape in Ly-α (Ehrenreich et al. 2015), but could be attempted with transmission spectroscopy of the helium triplet (Sect. 5.3). In addition, further RV monitoring will be valuable and, actually, already anticipated with the forthcoming near-infrared spectrograph NIRPS (Bouchy et al. 2017). They may detect the companion responsible for the possible RV trend that we have identified in this paper, and will also measure the Rossiter-McLaughlin anomaly to see if, like GJ 436 b, TOI-269 b also has a misaligned orbit (Bourrier et al. 2018b).

Acknowledgements. We are grateful to the ESO/La Silla staff for their continuous support. We thank the referee for his careful reading of the manuscript and his thoughtful comments. We acknowledge funding from the European Research Council under the ERC Grant Agreement no. 337591-ExTrA. This paper includes data collected by the TESS mission. Funding for the TESS mission is provided by the NASA Explorer Program. We acknowledge the use of public TESS Alert data from the pipelines at the TESS Science Office and at the TESS Science Processing Operations Center. Resources supporting this work were provided by the NASA High-End Computing (HEC) program through the NASA Advanced Supercomputing (NAS) Division at Ames Research Center for the production of the SPOC data products. This work makes use of observations from the LCOGT network. This work made use of `tpfplotter` by J. Lillo-Box (publicly available in `www.github.com/jlillo/tpfplotter`), which also made use of the python packages `astropy`, `lightkurve`, `matplotlib` and `numpy`. We thank the Swiss National Science Foundation (SNSF) and the Geneva University for their continuous support to our planet search programs. This work has been in particular carried out in the frame of the National Centre for Competence in Research 'PlanetS' supported by the Swiss National Science Foundation (SNSF). We thank La Silla observatory staff for their support. N.A.-D. acknowledges the support of FONDECYT project 3180063. A.W. acknowledges the financial support of the SNSF by grant number P400P2_186765. This material is based upon work supported by the National Science Foundation Graduate Research Fellowship Program under Grant No. DGE-1650115. This work was supported by FCT – Fundação para a Ciência e a Tecnologia through national funds and by FEDER through COMPETE2020 - Programa Operacional Competitividade e Internacionalização by these grants: UID/FIS/04434/2019; UIDB/04434/2020; UIDP/04434/2020; PTDC/FIS-AST/32113/2017 and POCI-01-0145-FEDER-032113; PTDC/FIS-AST/28953/2017 and POCI-01-0145-FEDER-028953. Based in part on observations obtained at the Southern Astrophysical Research (SOAR) telescope, which is a joint project of the Ministério da Ciência, Tecnologia e Inovações (MCTI/LNA) do Brasil, the US National Science Foundation's NOIRLab, the University of North Carolina at Chapel Hill (UNC), and Michigan State University (MSU). FPE would like to acknowledge the Swiss National Science Foundation (SNSF) for supporting research with HARPS through the SNSF grants nr. 140649, 152721, 166227 and 184618. J.R.M. acknowledges continuous grants from CNPq, CAPES and FAPERN brazilian agencies. C.D. acknowledges support from the Swiss National Science Foundation under grant PZ00P2_174028. This work is supported by the French National Research Agency in the framework of the Investissements d'Avenir program (ANR-15-IDEX-02), through the funding of the "Origin of Life" project of the Univ. Grenoble-Alpes. B.L.C.M. and I.C.L. acknowledge continuous grants from CNPq, CAPES and FAPERN brazilian agencies. We thank Emeline Bolmont for interesting discussion about tidal dissipation.

References

Alibert, Y., Mordasini, C., Benz, W., & Naef, D. 2010, in EAS Publications Series, 42, eds. K. Goździewski, A. Niedzielski, & J. Schneider, 209
Allard, F., Homeier, D., & Freytag, B. 2012, Phil. Trans. R. Soc. London Ser. A, 370, 2765
Allart, R., Bourrier, V., Lovis, C., et al. 2018, Science, 362, 1384
Aller, A., Lillo-Box, J., Jones, D., Miranda, L. F., & Barceló Forteza, S. 2020, A&A, 635, A128
Ambikasaran, S., Foreman-Mackey, D., Greengard, L., Hogg, D. W., & O'Neil, M. 2015, IEEE Trans. Pattern Anal. Mach. Intell., 38, 252
Astudillo-Defru, N., Delfosse, X., Bonfils, X., et al. 2017a, A&A, 600, A13
Astudillo-Defru, N., Forveille, T., Bonfils, X., et al. 2017b, A&A, 602, A88
Bailer-Jones, C. A. L., Rybizki, J., Fouesneau, M., Mantelet, G., & Andrae, R. 2018, AJ, 156, 58
Barnes, S. A. 2010, ApJ, 722, 222
Barnes, S. A., & Kim, Y.-C. 2010, ApJ, 721, 675
Batalha, N. E., Lewis, N. K., Line, M. R., Valenti, J., & Stevenson, K. 2018, ApJ, 856, L34
Benneke, B., Wong, I., Piaulet, C., et al. 2019, ApJ, 887, L14
Bézard, B., Charnay, B., & Blain, D. 2020, Nat. Astron., submitted [arXiv:`2011.10424`]
Bonfils, X., Almenara, J. M., Jocou, L., et al. 2015, in Society of Photo-Optical Instrumentation Engineers (SPIE) Conference Series, 9605, Techniques and Instrumentation for Detection of Exoplanets VII, 96051L
Bouchy, F., Doyon, R., Artigau, É., et al. 2017, The Messenger, 169, 21
Bourrier, V., Lecavelier des Etangs, A., Ehrenreich, D., et al. 2018a, A&A, 620, A147
Bourrier, V., Lovis, C., Beust, H., et al. 2018b, Nature, 553, 477
Brown, T. M., Baliber, N., Bianco, F. B., et al. 2013, PASP, 125, 1031
Brugger, B., Mousis, O., Deleuil, M., & Deschamps, F. 2017, ApJ, 850, 93
Buchner, J., Georgakakis, A., Nandra, K., et al. 2014, A&A, 564, A125
Buchschacher, N., & Alesina, F. 2019, in Astronomical Society of the Pacific Conference Series, 521, Astronomical Data Analysis Software and Systems XXVI, eds. M. Molinaro, K. Shortridge, & F. Pasian, 757
Canto Martins, B. L., Gomes, R. L., Messias, Y. S., et al. 2020, ApJS, 250, 20
Chabrier, G., Mazevet, S., & Soubiran, F. 2019, ApJ, 872, 51
Charbonneau, D., Berta, Z. K., Irwin, J., et al. 2009, Nature, 462, 891
Chen, Y., Girardi, L., Bressan, A., et al. 2014, MNRAS, 444, 2525
Cloutier, R., & Menou, K. 2020, AJ, 159, 211
Cloutier, R., Astudillo-Defru, N., Doyon, R., et al. 2017, A&A, 608, A35
Cloutier, R., Eastman, J. D., Rodriguez, J. E., et al. 2020, AJ, 160, 3
Collins, K. A., Kielkopf, J. F., Stassun, K. G., & Hessman, F. V. 2017, AJ, 153, 77
Connolly, J. A. D. 2009, Geochem. Geophys. Geosyst., 10, Q10014
Correia, A. C. M., Bourrier, V., & Delisle, J. B. 2020, A&A, 635, A37
Cutri, R. M., et al. 2013, VizieR Online Data Catalog, II/328
Cutri, R. M., Skrutskie, M. F., van Dyk, S., et al. 2003, VizieR Online Data Catalog, II/246
Díaz, R. F., Almenara, J. M., Santerne, A., et al. 2014, MNRAS, 441, 983
Dorn, C., Khan, A., Heng, K., et al. 2015, A&A, 577, A83
Dorn, C., Venturini, J., Khan, A., et al. 2017, A&A, 597, A37
Dotter, A., Chaboyer, B., Jevremović, D., et al. 2008, ApJS, 178, 89
Ehrenreich, D., Bourrier, V., Wheatley, P. J., et al. 2015, Nature, 522, 459
Engle, S. G., & Guinan, E. F. 2011, in ASP Conf. Ser., 451, 9th Pacific Rim Conference on Stellar Astrophysics, eds. S. Qain, K. Leung, L. Zhu, & S. Kwok, 285
Espinoza, N. 2018, Res. Notes Am. Astron. Soc., 2, 209
Espinoza, N., & Jordán, A. 2015, MNRAS, 450, 1879
Espinoza, N., Kossakowski, D., & Brahm, R. 2019, MNRAS, 490, 2262
Evans, D. W., Riello, M., De Angeli, F., et al. 2018, A&A, 616, A4
Feroz, F., Hobson, M. P., & Bridges, M. 2009, MNRAS, 398, 1601
Foreman-Mackey, D. 2016, J. Open Source Softw., 1, 24
Foreman-Mackey, D., Agol, E., Ambikasaran, S., & Angus, R. 2017, AJ, 154, 220
Fulton, B. J., Petigura, E. A., Howard, A. W., et al. 2017, AJ, 154, 109
Fulton, B. J., Petigura, E. A., Blunt, S., & Sinukoff, E. 2018, PASP, 130, 044504
Gaia Collaboration, (Brown, A. G. A., et al.) 2018, A&A, 616, A1
Gaidos, E., Hirano, T., Mann, A. W., et al. 2020a, MNRAS, 495, 650
Gaidos, E., Hirano, T., Wilson, D. J., et al. 2020b, MNRAS, 498, L119
Goldreich, P., & Soter, S. 1966, Icarus, 5, 375
Guillot, T. 2010, A&A, 520, A27
Günther, M. N., Pozuelos, F. J., Dittmann, J. A., et al. 2019, Nat. Astron., 3, 1099
Hakim, K., Rivoldini, A., Van Hoolst, T., et al. 2018, Icarus, 313, 61
Haldemann, J., Alibert, Y., Mordasini, C., & Benz, W. 2020, A&A, 643, A105
Hansen, B. M. S. 2012, ApJ, 757, 6

Hardegree-Ullman, K. K., Zink, J. K., Christiansen, J. L., et al. 2020, ApJS, 247, 28
Harpsøe, K. B. W., Hardis, S., Hinse, T. C., et al. 2013, A&A, 549, A10
Jenkins, J. M. 2002, ApJ, 575, 493
Jenkins, J. M., Chandrasekaran, H., McCauliff, S. D., et al. 2010, in Society of Photo-Optical Instrumentation Engineers (SPIE) Conference Series, 7740, Software and Cyberinfrastructure for Astronomy, ed. N. M. Radziwill & A. Bridger, 77400D
Jenkins, J. M., Twicken, J. D., McCauliff, S., et al. 2016, in Society of Photo-Optical Instrumentation Engineers (SPIE) Conference Series, 9913, Software and Cyberinfrastructure for Astronomy IV, 99133E
Jenkins, J. M., Tenenbaum, P., Seader, S., et al. 2020, Kepler Data Processing Handbook: Transiting Planet Search, Kepler Data Processing Handbook (KSCI-19 081-003)
Jensen, E. 2013, Tapir: A web interface for transit/eclipse observability, Astrophysics Source Code Library
Kasper, D., Bean, J. L., Oklopčić, A., et al. 2020, AJ, 160, 258
Kempton, E. M. R., Bean, J. L., Louie, D. R., et al. 2018, PASP, 130, 114401
Kipping, D. M. 2010, MNRAS, 408, 1758
Kipping, D. M. 2013, MNRAS, 435, 2152
Kreidberg, L. 2015, PASP, 127, 1161
Kreidberg, L., Bean, J. L., Désert, J.-M., et al. 2014, Nature, 505, 69
Lainey, V., Arlot, J.-E., Karatekin, Ö., & van Hoolst, T. 2009, Nature, 459, 957
Li, J., Tenenbaum, P., Twicken, J. D., et al. 2019, PASP, 131, 024506
Lindegren, L., Hernández, J., Bombrun, A., et al. 2018, A&A, 616, A2
Lopez, E. D., & Fortney, J. J. 2014, ApJ, 792, 1
Lozovsky, M., Helled, R., Dorn, C., & Venturini, J. 2018, ApJ, 866, 49
Lucy, L. B., & Sweeney, M. A. 1971, AJ, 76, 544
Luque, R., Pallé, E., Kossakowski, D., et al. 2019, A&A, 628, A39
Maíz Apellániz, J., & Weiler, M. 2018, A&A, 619, A180
Mann, A. W., Feiden, G. A., Gaidos, E., Boyajian, T., & von Braun, K. 2015, ApJ, 804, 64
Mann, A. W., Dupuy, T., Kraus, A. L., et al. 2019, ApJ, 871, 63
Maxted, P. F. L., Anderson, D. R., Collier Cameron, A., et al. 2011, PASP, 123, 547
Mayor, M., Pepe, F., Queloz, D., et al. 2003, The Messenger, 114, 20
Mayo, A. W., Vanderburg, A., Latham, D. W., et al. 2018, AJ, 155, 136
McCully, C., Volgenau, N. H., Harbeck, D.-R., et al. 2018, in Society of Photo-Optical Instrumentation Engineers (SPIE) Conference Series, 10 707, Proc. SPIE, 107070K
Meibom, S., Barnes, S. A., Platais, I., et al. 2015, Nature, 517, 589
More, R. M., Warren, K. H., Young, D. A., & Zimmerman, G. B. 1988, Phys. Fluids, 31, 3059
Nortmann, L., Pallé, E., Salz, M., et al. 2018, Science, 362, 1388
Nowak, G., Luque, R., Parviainen, H., et al. 2020, A&A, 642, A173
Ogilvie, G. I., & Lin, D. N. C. 2004, ApJ, 610, 477
Oklopčić, A., & Hirata, C. M. 2018, ApJ, 855, L11
Otegi, J. F., Bouchy, F., & Helled, R. 2020a, A&A, 634, A43
Otegi, J. F., Dorn, C., Helled, R., et al. 2020b, A&A, 640, A135
Palle, E., Nortmann, L., Casasayas-Barris, N., et al. 2020, A&A, 638, A61
Patra, K. C., Winn, J. N., Holman, M. J., et al. 2017, AJ, 154, 4
Pecaut, M. J., & Mamajek, E. E. 2013, ApJS, 208, 9
Plotnykov, M., & Valencia, D. 2020, MNRAS, 499, 932
Pollacco, D. L., Skillen, I., Collier Cameron, A., et al. 2006, PASP, 118, 1407
Ricker, G. R., Winn, J. N., Vanderspek, R., et al. 2015, J. Astron. Telesc. Instrum. Syst., 1, 014003
Rogers, L. A., & Seager, S. 2010, ApJ, 716, 1208
Skrutskie, M. F., Cutri, R. M., Stiening, R., et al. 2006, AJ, 131, 1163
Smith, J. C., Stumpe, M. C., Van Cleve, J. E., et al. 2012, PASP, 124, 1000
Spake, J. J., Sing, D. K., Evans, T. M., et al. 2018, Nature, 557, 68
Speagle, J. S. 2020, MNRAS, 493, 3132
Stassun, K. G., Oelkers, R. J., Paegert, M., et al. 2019, AJ, 158, 138
Stixrude, L., & Lithgow-Bertelloni, C. 2011, Geophys. J. Int., 184, 1180
Stumpe, M. C., Smith, J. C., Van Cleve, J. E., et al. 2012, PASP, 124, 985
Stumpe, M. C., Smith, J. C., Catanzarite, J. H., et al. 2014, PASP, 126, 100
Tokovinin, A. 2018, PASP, 130, 035002
Tsiaras, A., Waldmann, I. P., Tinetti, G., Tennyson, J., & Yurchenko, S. N. 2019, Nat. Astron., 3, 1086
Twicken, J. D., Catanzarite, J. H., Clarke, B. D., et al. 2018, PASP, 130, 064502
Van Eylen, V., Astudillo-Defru, N., Bonfils, X., et al. 2021, MNRAS, submitted [arXiv:2101.01593]
Venturini, J., & Helled, R. 2017, ApJ, 848, 95
Winters, J. G., Medina, A. A., Irwin, J. M., et al. 2019, AJ, 158, 152
Wright, E. L., Eisenhardt, P. R. M., Mainzer, A. K., et al. 2010, AJ, 140, 1868
Yee, S. W., Petigura, E. A., & von Braun, K. 2017, ApJ, 836, 77
Ziegler, C., Tokovinin, A., Briceno, C., et al. 2020, VizieR Online Data Catalog, J/AJ/159/19

---

[1] Univ. Grenoble Alpes, CNRS, IPAG, 38000 Grenoble, France
e-mail: `marion.cointepas@univ-grenoble-alpes.fr`
[2] Observatoire de Genève, Département d'Astronomie, Université de Genève, Chemin Pegasi 51b, 1290 Versoix, Switzerland
[3] Departamento de Matemática y Física Aplicadas, Universidad Católica de la Santísima Concepción, Alonso de Rivera 2850, Concepción, Chile
[4] Astrophysics Group, Keele University, Staffordshire ST5 5BG, UK
[5] Department of Physics and Astronomy, The University of North Carolina at Chapel Hill, Chapel Hill, NC 27599-3255, USA
[6] Dunlap Institute for Astronomy and Astrophysics, University of Toronto, 50 St. George Street, Toronto, Ontario M5S 3H4, Canada
[7] Department of Physics, University of Warwick, Coventry, UK
[8] Centre for Exoplanets and Habitability, University of Warwick, Gibbet Hill Road, Coventry, UK
[9] Center for Astrophysics | Harvard & Smithsonian, 60 Garden Street, Cambridge, MA 02138, USA
[10] George Mason University, 4400 University Drive, Fairfax, VA 22030, USA
[11] Department of Astronomy and Tsinghua Centre for Astrophysics, Tsinghua University, Beijing 100084, PR China
[12] Department of Astrophysical and Planetary Sciences, University of Colorado, Boulder, CO 80309, USA
[13] Institute for Computational Science, University of Zurich, Winterthurerstr. 190, 8057 Zurich, Switzerland
[14] Département de physique, Université de Montréal, 2900 boul. Édouard-Montpetit, Montréal, QC H3C 3J7, Canada
[15] Université de Montréal, Département de Physique & Institut de Recherche sur les Exoplanètes, Montréal, QC H3C 3J7, Canada
[16] International Center for Advanced Studies (ICAS) and ICIFI(CONICET), ECyT-UNSAM, Campus Miguelete, 25 de Mayo y Francia(1650), Buenos Aires, Argentina
[17] European Southern Observatory, Alonso de Córdova 3107, Vitacura, Región Metropolitana, Chile
[18] Instituto de Astrofísica e Ciências do Espaço, Universidade do Porto, CAUP, Rua das Estrelas, 4150-762 Porto, Portugal
[19] Departamento de Física e Astronomia, Faculdade de Ciências, Universidade do Porto, Rua do Campo Alegre, 4169-007 Porto, Portugal
[20] Departamento de Física, Universidade Federal do Rio Grande do Norte, 59072-970 Natal, RN, Brazil
[21] Instituto de Astrofísica de Canarias (IAC), E-38200 La Laguna, Tenerife, Spain
[22] Dept. Astrofísica, Universidad de La Laguna (ULL), 38206 La Laguna, Tenerife, Spain
[23] Department of Physics and Kavli Institute for Astrophysics and Space Research, Massachusetts Institute of Technology, Cambridge, MA 02139, USA
[24] Department of Earth, Atmospheric and Planetary Sciences, Massachusetts Institute of Technology, Cambridge, MA 02139, USA
[25] Department of Aeronautics and Astronautics, MIT, 77 Massachusetts Avenue, Cambridge, MA 02139, USA
[26] Department of Astrophysical Sciences, Princeton University, NJ 08544, USA
[27] NASA Ames Research Center, Moffett Field, CA 94035, USA
[28] SETI Institute, Mountain View, CA 94043, USA
[29] Space Telescope Science Institute, 3700 San Martin Drive, Baltimore, MD 21218, USA

Appendix A: ExTrA field of view of TOI-269

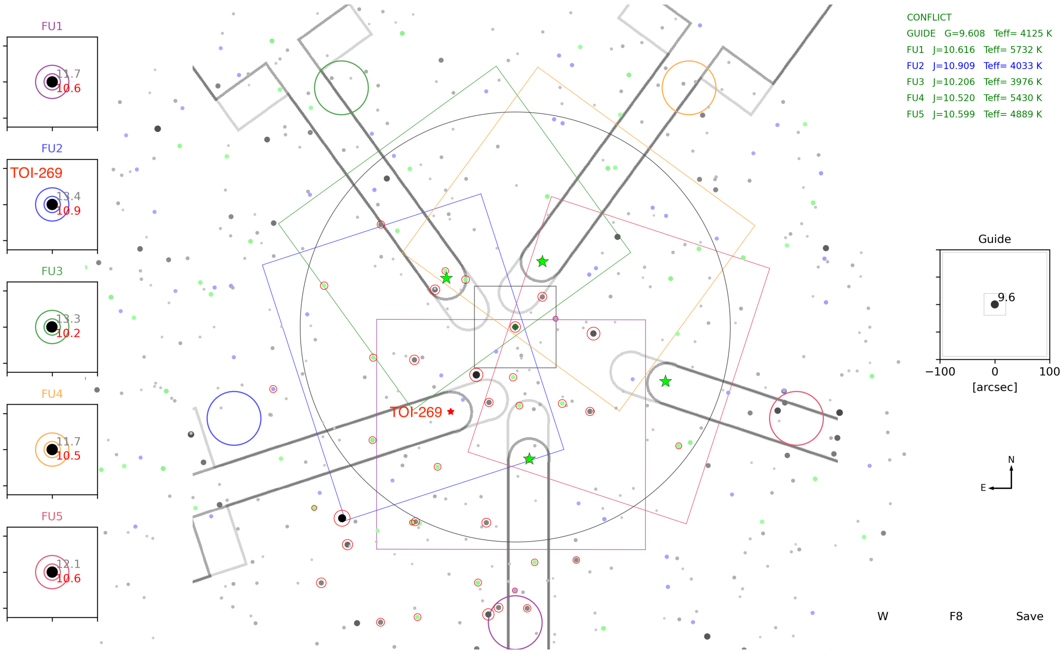

Fig. A.1. Snapshot of the software for preparing observations for ExTrA. The field of view of one telescope has a diameter of 1° (gray circle). Each of the five field units (FUs) can be positioned in the part of the focal plane shown with a rectangle of corresponding color. In this figure the field of TOI-269 is shown. Each FU is placed over a particular comparison star (green stars) or the target (red star). On the left the location of each FU is magnified and the fiber apertures are drawn to scale (colored circles; the first circle is 4”, the second circle is 8”). This is used to check if other stars appear near the fibers. In red is the *J* magnitude of the star, in gray the *Gaia* magnitude. The guiding star is located at the center and a magnified image is shown on the right. The five arms correspond to the selected stars with their 2MASS *J* magnitude and *Gaia* DR2 temperature indicated at the top right of the figure.

Appendix B: Prior and posterior values for the different fits

Table B.1. Prior and posterior values for the photometry fit of TESS data.

Parameter name	Prior	Posterior	Description
Parameters for TOI-269 b			
P_b (days)	$\mathcal{N}(3.7, 0.1^2)$	$3.697722^{+0.000017}_{-0.000016}$	Period of the planet
t_0 (BJD TDB)	$\mathcal{N}(2458381.84, 0.1^2)$	$245831.84601^{+0.00058}_{-0.00058}$	Time of transit-center for the planet
$\rho_\star$ (g cm^{-3})	$\mathcal{N}(8.760, 0.870)$	$9.10^{+0.82}_{-0.74}$	Stellar density
$r_{1,\mathrm{b}}$	$\mathcal{U}(0, 1)$+	$0.8983^{+0.0091}_{-0.0099}$	Parametrization for p and b
$r_{2,\mathrm{b}}$	$\mathcal{U}(0, 1)$	$0.0725^{+0.0024}_{-0.0021}$	Parametrization for p and b
e_b	0.	0.	Eccentricity
ω_b (degrees)	90.	90.	Argument of periastron
Parameters for TESS			
D_TESS	1.	1.	Dilution factor for TESS
M_TESS	$\mathcal{N}(0, 0.1^2)$	$-0.000015^{+0.000016}_{-0.000016}$	Relative flux offset for TESS
$\sigma_{\mathrm{w,TESS}}$ (ppm)	$\log\mathcal{U}(0.01, 100)$	$0.58^{+8.1}_{-0.55}$	Extra jitter term for TESS lightcurve
$q_{1,\mathrm{TESS}}$	$\mathcal{U}(0, 1)$	$0.128^{+0.22}_{-0.099}$	Quadratic limb-darkening parametrization
$q_{2,\mathrm{TESS}}$	$\mathcal{U}(0, 1)$	$0.42^{+0.34}_{-0.28}$	Quadratic limb-darkening parametrization

Notes. The posterior estimate corresponds to the median value. Error bars denote the 68% posterior credibility intervals.

Table B.2. Prior and posterior values for the RVs fit of the HARPS measurements.

Parameter name	Prior	Posterior	Description
Parameters for TOI-269 b			
P_b (days)	$\mathcal{N}(3.697722, 0.000017^2)$	$3.697723^{+0.000018}_{-0.000017}$	Period of the planet
t_0 (BJD TDB)	$\mathcal{U}(2458381.84601, 0.00058)$	$3.697722^{+0.000017}_{-0.000016}$	Time of transit-center for the planet
K_b (m s^{-1})	$\mathcal{U}(0, 20)$	$7.2^{+1.3}_{-1.2}$	Radial-velocity semi-amplitude of the planet
$S_{1,b} = \sqrt{e_b}\sin(\omega_b)$	$\mathcal{U}(-1, 1)$	$0.34^{+0.21}_{-0.30}$	Parametrization for e and ω
$S_{2,b} = \sqrt{e_b}\cos(\omega_b)$	$\mathcal{U}(-1, 1)$	$0.30^{+0.13}_{-0.20}$	Parametrization for e and ω
RV parameters for HARPS			
$\sigma_{w,HARPS}$ (km s^{-1})	$\log\mathcal{U}(10^{-4}, 10^{-2})$	$0.00039^{+0.00078}_{-0.00024}$	Extra jitter term for HARPS
RV slope (km s^{-1} days^{-1})	$\mathcal{U}(-1., 1.)$	$\left(1.81^{+0.86}_{-0.89}\right) \times 10^{-5}$	Linear trend : first parameter
RV intercept (systemic velocity in km s^{-1})	$\mathcal{U}(37.18, 37.28)$	$37.22861^{+0.00092}_{-0.00077}$	Linear trend : second parameter

Notes. The posterior estimate corresponds to the median value. Error bars denote the 68% posterior credibility intervals.

Table B.3. Prior values for the joint fit of TESS, ExTrA, LCO, and HARPS.

Parameter name	Prior	Description
Parameters for TOI-269 b		
P_b (days)	$\mathcal{U}(3.69769, 3.69773)$	Period of the planet
t_0 (BJD TDB)	$\mathcal{U}(2458381.845, 2458381.849)$	Time of transit-center for the planet
$\rho_\star$ g/cm^3	$\mathcal{N}(8.760, 0.870)$	Stellar density
$r_{1,b}$	$\mathcal{U}(0.3, 1)$	Parametrization for p and b
$r_{2,b}$	$\mathcal{U}(0, 0.1)$	Parametrization for p and b
$S_{1,b} = \sqrt{e_b}\sin(\omega_b)$	$\mathcal{U}(-1, 1)$	Parametrization for e and ω
$S_{2,b} = \sqrt{e_b}\cos(\omega_b)$	$\mathcal{U}(-1, 1)$	Parametrization for e and ω
K_b (km s^{-1})	$\mathcal{U}(0, 0.016)$	Radial-velocity semi-amplitude of the planet
Parameters for TESS photometry		
D_{TESS}	1.0	Dilution factor for TESS
M_{TESS}	$\mathcal{N}(0, 0.1^2)$	Relative flux offset for TESS
$\sigma_{w,TESS}$ (ppm)	$\log\mathcal{U}(1, 100)$	Extra jitter term for TESS lightcurve
$q_{1,TESS}$	$\mathcal{U}(0, 1)$	Quadratic limb-darkening parametrization
$q_{2,TESS}$	$\mathcal{U}(0, 1)$	Quadratic limb-darkening parametrization
Parameters for LCO-CTIO photometry		
D_{LCO}	1.0	Dilution factor for LCO-CTIO
M_{LCO}	$\mathcal{N}(0, 0.1^2)$	Relative flux offset for LCO-CTIO
$\sigma_{w,LCO}$ (ppm)	$\log\mathcal{U}(1, 2000)$	Extra jitter term for LCO-CTIO lightcurve
$q_{1,LCO}$	$\mathcal{U}(0, 1)$	Quadratic limb-darkening parametrization
$q_{2,LCO}$	$\mathcal{U}(0, 1)$	Quadratic limb-darkening parametrization
Parameters of the GP		
$\sigma_{GP,LCO}$ (relative flux)	$\log\mathcal{U}(10^{-6}, 1)$	Amplitude of the GP
$\rho_{GP,LCO}$ (days)	$\log\mathcal{U}(10^{-3}, 10)$	Time-scale of the Matern kernel
Parameters for ExTrA photometry		
D_{ExTrA}	1.0	Dilution factor for ExTrA
M_{ExTrA}	$\mathcal{N}(0, 0.1^2)$	Relative flux offset for each ExTrA light curve
$\sigma_{w,ExTrA}$ (ppm)	$\log\mathcal{U}(1, 1000)$	Extra jitter term for each ExTrA light curve
$q_{1,ExTrA}$	$\mathcal{U}(0, 1)$	Quadratic limb-darkening parametrization
$q_{2,ExTrA}$	$\mathcal{U}(0, 1)$	Quadratic limb-darkening parametrization
Parameters of the GP for each ExTrA light curve (one for each night and each telescope)		
$\sigma_{GP,ExTrA}$ (relative flux)	$\log\mathcal{U}(10^{-6}, 1)$	Amplitude of the GP
$\rho_{GP,ExTrA}$ (days)	$\log\mathcal{U}(10^{-3}, 10)$	Time-scale of the Matern kernel

Table B.3. continued.

Parameter name	Prior	Description
RV parameters for HARPS		
$\sigma_{\rm w,HARPS}$ (km s^{-1})	$\log\mathcal{U}(10^{-4}, 10^{-2})$	Extra jitter term for HARPS
RV slope (km s^{-1} days^{-1})	$\mathcal{U}(-10^{-4}, 10^{-4})$	Linear trend: first parameter
RV intercept (systemic velocity) (km s^{-1})	$\mathcal{U}(37.22, 37.24)$	Linear trend: second parameter

Table B.4. Posterior parameters for the different instruments used in the `juliet` analysis for TOI-269 b.

Parameter name	Posterior estimate	Description
Posterior parameters for TESS photometry		
$M_{\rm TESS}$ (ppm)	$0.00033^{+0.00012}_{-0.00012}$	Relative flux offset
$\sigma_{\rm w,TESS}$ (ppm)	$9.6^{+34}_{-7.4}$	Extra jitter term
Posterior parameters for LCO-CTIO photometry		
$M_{\rm LCO}$ (ppm)	$0.0009^{+0.0022}_{-0.0020}$	Relative flux offset
$\sigma_{\rm w,LCO}$ (ppm)	890^{+120}_{-120}	Extra jitter term
Parameters of the GP		
$\sigma_{\rm GP,LCO}$ (relative flux)	$0.0030^{+0.0044}_{-0.0014}$	Amplitude of the GP
$\rho_{\rm GP,LCO}$ (days)	$0.094^{+0.14}_{-0.051}$	Time-scale of the Matern kernel
RV parameters for HARPS		
$\sigma_{\rm w,HARPS}$ (m s^{-1})	$0.39^{+0.68}_{-0.24}$	Extra jitter term
Posterior parameters for ExTrA photometry		
Posterior parameters for night 1 of observations		
Telescope 2		
$M_{\rm ExTrA}$ (ppm)	$0.00005^{+0.050}_{-0.038}$	Relative flux offset
$\sigma_{\rm w,ExTrA}$ (ppm)	22^{+160}_{-19}	Extra jitter term
$\sigma_{\rm GP,ExTrA}$ (relative flux)	$0.059^{+0.095}_{-0.031}$	Amplitude of the GP
$\rho_{\rm GP,ExTrA}$ (days)	$0.23^{+0.23}_{-0.10}$	Time-scale of the Matern kernel
Telescope 3		
$M_{\rm ExTrA}$ (ppm)	$-0.005^{+0.013}_{-0.025}$	Relative flux offset
$\sigma_{\rm w,ExTrA}$ (ppm)	27^{+210}_{-24}	Extra jitter term
$\sigma_{\rm GP,ExTrA}$ (relative flux)	$0.019^{+0.052}_{-0.013}$	Amplitude of the GP
$\rho_{\rm GP,ExTrA}$ (days)	$0.37^{+0.76}_{-0.25}$	Time-scale of the Matern kernel
Posterior parameters for night 2 of observations		
Telescope 2		
$M_{\rm ExTrA}$ (ppm)	$0.0010^{+0.018}_{-0.012}$	Relative flux offset
$\sigma_{\rm w,ExTrA}$ (ppm)	34^{+290}_{-31}	Extra jitter term
$\sigma_{\rm GP,ExTrA}$ (relative flux)	$0.0163^{+0.028}_{-0.0079}$	Amplitude of the GP
$\rho_{\rm GP,ExTrA}$ (days)	$0.124^{+0.13}_{-0.052}$	Time-scale of the Matern kernel
Telescope 3		
$M_{\rm ExTrA}$ (ppm)	$-0.0008^{+0.0023}_{-0.0017}$	Relative flux offset
$\sigma_{\rm w,ExTrA}$ (ppm)	29^{+240}_{-26}	Extra jitter term
$\sigma_{\rm GP,ExTrA}$ (relative flux)	$0.00232^{+0.0075}_{-0.00096}$	Amplitude of the GP
$\rho_{\rm GP,ExTrA}$ (days)	$0.035^{+0.13}_{-0.021}$	Time-scale of the Matern kernel
Posterior parameters for night 3 of observations		
Telescope 1		
$M_{\rm ExTrA}$ (ppm)	$-0.00077^{+0.00036}_{-0.00032}$	Relative flux offset
$\sigma_{\rm w,ExTrA}$ (ppm)	26^{+210}_{-23}	Extra jitter term
$\sigma_{\rm GP,ExTrA}$ (relative flux)	$0.00067^{+0.00061}_{-0.00061}$	Amplitude of the GP
$\rho_{\rm GP,ExTrA}$ (days)	$0.016^{+0.42}_{-0.012}$	Time-scale of the Matern kernel

Notes. The posterior estimate corresponds to the median value. Error bars denote the 68% posterior credibility intervals.

Table B.4. continued.

Parameter name	Posterior estimate	Description
Telescope 2		
$M_{\rm ExTrA}$ (ppm)	$-0.016^{+0.041}_{-0.039}$	Relative flux offset
$\sigma_{\rm w,ExTrA}$ (ppm)	30^{+260}_{-27}	Extra jitter term
$\sigma_{\rm GP,ExTrA}$ (relative flux)	$0.055^{+0.11}_{-0.034}$	Amplitude of the GP
$\rho_{\rm GP,ExTrA}$ (days)	$0.33^{+0.41}_{-0.17}$	Time-scale of the Matern kernel
Telescope 3		
$M_{\rm ExTrA}$ (ppm)	$0.0053^{+0.018}_{-0.0098}$	Relative flux offset
$\sigma_{\rm w,ExTrA}$ (ppm)	27^{+220}_{-24}	Extra jitter term
$\sigma_{\rm GP,ExTrA}$ (relative flux)	$0.0160^{+0.026}_{-0.0073}$	Amplitude of the GP
$\rho_{\rm GP,ExTrA}$ (days)	$0.071^{+0.076}_{-0.029}$	Time-scale of the Matern kernel

Appendix C: Spectral energy distribution

Table C.1. Modeling of the spectral energy distribution: parameter, prior, posterior median, and 68.3% CI for each of the analyses.

Parameter		Prior	Posterior BT-Settl	Posterior BT-Settl + Dartmouth	Posterior BT-Settl + `PARSEC`
Effective temperature, $T_{\rm eff}$	(K)	$N(3514, 70)$	3578^{+44}_{-38}	3586^{+24}_{-20}	3562 ± 37
Surface gravity, $\log g$	(cgs)	$U(-0.5, 6.0)$	$5.46^{+0.37}_{-0.52}$	4.8648 ± 0.0055	$4.833^{+0.021}_{-0.036}$
Metallicity, (Fe/H)	(dex)	$N(-0.29, 0.12)$	-0.32 ± 0.11	-0.325 ± 0.082	$-0.403^{+0.073}_{-0.085}$
Distance	(pc)	$N(57.023, 0.076)$	57.023 ± 0.076	57.022 ± 0.077	57.022 ± 0.079
$E_{\rm (B-V)}$	(mag)	$U(0,3)$	$0.028^{+0.036}_{-0.020}$	$0.025^{+0.030}_{-0.018}$	$0.022^{+0.030}_{-0.016}$
Jitter *Gaia*	(mag)	$U(0, 1)$	$0.069^{+0.10}_{-0.034}$	$0.075^{+0.098}_{-0.034}$	$0.082^{+0.12}_{-0.040}$
Jitter 2MASS	(mag)	$U(0, 1)$	$0.025^{+0.043}_{-0.018}$	$0.030^{+0.045}_{-0.021}$	$0.026^{+0.044}_{-0.018}$
Jitter WISE	(mag)	$U(0, 1)$	$0.025^{+0.044}_{-0.018}$	$0.023^{+0.040}_{-0.017}$	$0.029^{+0.053}_{-0.021}$
Radius, $R_\star$	($R_\odot$)	$U(0, 100)$†	0.3926 ± 0.062	0.3910 ± 0.0032	$0.3948^{+0.0064}_{-0.0052}$
Mass, $M_\star$	($M_\odot$)			0.4103 ± 0.0045	$0.390^{+0.014}_{-0.023}$
Density, $\rho_\star$	(g cm^{-3})			9.670 ± 0.180	$8.920^{+0.540}_{-0.800}$
Age	(Gyr)			$5.3^{+3.5}_{-2.4}$	$0.143^{+0.15}_{-0.049}$
Luminosity	($L_\odot$)			$0.02276^{+0.00063}_{-0.00050}$	$0.02261^{+0.00066}_{-0.00054}$

Notes. $N(\mu,\sigma)$: normal distribution prior with mean μ, and standard deviation σ. U(l,u): uniform distribution prior in the range $[l, u]$. † For the BT-Settl analysis only.

We performed an independent determination of the stellar parameters of TOI-269 modeling the spectral energy distribution (SED) with stellar atmosphere and evolution models. We constructed the SED using the magnitudes from *Gaia* DR2 (Evans et al. 2018; Maíz Apellániz & Weiler 2018), the 2-Micron All-Sky Survey (2MASS, Skrutskie et al. 2006; Cutri et al. 2003), and the Wide-field Infrared Survey Explorer (WISE, Wright et al. 2010; Cutri & et al. 2013). We modeled these magnitudes using the procedure described in Díaz et al. (2014). We used informative priors for the effective temperature ($T_{\rm eff}$), and metallicity ([Fe/H]) from the analysis of the HARPS co-added spectra with `SpecMatch-Emp` (Yee et al. 2017), and for the distance from *Gaia* DR2 (Gaia Collaboration 2018; Bailer-Jones et al. 2018). We used non-informative priors for the rest of the parameters. We used the PHOENIX/BT-Settl stellar atmosphere models (Allard et al. 2012), and two stellar evolution models: Dartmouth (Dotter et al. 2008) and `PARSEC` (Chen et al. 2014). We did three analyses, one using stellar atmosphere models only (BT-Settl) and another two with the stellar atmosphere models and each of the stellar evolution models (BT-Settl + Dartmouth, BT-Settl + `PARSEC`). The priors, posterior median, and 68.3% credible intervals (CI) for jump and derived parameters are listed in Table C.1. The data with the maximum a posteriori (MAP) stellar atmosphere model is shown in Fig. C.1.

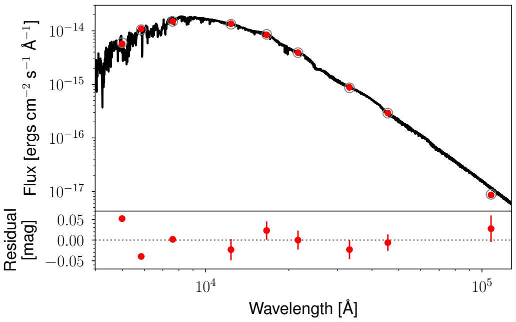

Fig. C.1. Spectral energy distribution of TOI-269. The solid line is the MAP PHOENIX/BT-Settl interpolated synthetic spectrum, red circles are the absolute photometric observations, and gray open circles are the result of integrating the synthetic spectrum in the observed band-passes.

III.5 SCIENCE CASES DEFINITION AND TARGET SELECTION

Using transit photometry, the ExTrA project aims at detecting small exoplanets orbiting M dwarf stars. ExTrA observation time has been divided into different work packages, each with its own set of objectives that correspond to a specific science case. In each work package, we have carefully selected a subset of targets from the TOI catalog that are best suited to address the specific scientific questions of that package. As of March 2023, ExTrA has already observed $\sim$ 160 different TOIs.

III.5.1 *WP1 - Transit validation and radius ratio improvement*

After publishing the first validation paper of an exoplanet orbiting a M dwarf using ExTrA photometry, we realized that we could obtain the same precision on the residuals of the fitted light curves as TESS but with less ExTrA transits. This motivated the creation of the first work package of ExTrA dedicated to validating the TESS planetary candidates using ExTrA near-infrared observations and improving on the current planetary radius estimation. We chose TOIs with stellar effective temperatures T_{eff} less than 3800K that are visible by the ExTrA telescopes at La Silla Observatory. We selecting targets for which 5 ExTrA transits were expected to get a similar or better signal-to-noise ratio than TESS at that time (without taking into account future TESS observations or additional photometry). We included planetary candidates that had not yet been validated by reconnaissance spectroscopic or photometric follow-up because we believe ExTrA's near-infrared wavelength coverage will help rule out eclipsing binaries as the source of the transit signal. The results of this study are currently being summarized in a paper and I present a preliminary draft hereafter.

Astronomy & Astrophysics manuscript no. output
May 1, 2023

Validation of new transiting systems with the ExTrA telescopes in the context of TESS planetary candidates follow-up.

M. Cointepas[1, 2] ⋆, J.M. Almenara[1], X. Bonfils[1], F. Bouchy[2], and T. Forveille[1]

(Affiliations can be found after the references)

Received ; accepted

ABSTRACT

The NASA TESS (Transiting Exoplanet Survey Satellite) mission promises to improve our understanding of the population of small exoplanets orbiting M-type stars by collecting an all-sky sample for population studies. To assemble such a sample, hundreds of planet candidates must be confirmed with additional follow-up observations. Here, we present 15 exoplanet candidates orbiting M dwarfs that were detected using TESS data and re-observed with the ExTrA facility. These exoplanets have orbital periods between 1 and 11 days and orbit relatively bright M stars with. We vet and validate the transits as planetary signals using follow-up observations for 15 new TESS exoplanets.

Key words. Planetary systems – Techniques: photometric – Stars : low-mass – Planets and satellites: detection

1. Introduction

We have now confirmed and validated more than 5300 exoplanets (NASA Exoplanet Archive). Because of this large sample size, our understanding of exoplanetary systems, their properties, and formation and evolutionary processes has grown significantly over the last three decades. But the sample of exoplanets orbiting low mass stars remains small and requires an intense follow-up of TESS planetary candidates using facilities dedicated to the observation of these exoplanets orbiting M dwarfs.

The ExTrA (Exoplanets in Transits and their Atmospheres) facility (Bonfils et al. 2015) was designed to perform high-precision spectro-photometry in the near-infrared on mid-to-late M-dwarf stars from the ground, at la Silla Observatory in Chile. ExTrA is made up of three 60-cm telescopes with multi-object fiber positioners and a low-resolution nIR spectrograph. Part of ExTrA's observing time is being used to confirm TESS planet detections, refine transit parameters, and look for additional exoplanets in already known planetary systems.

According to recent research, small exoplanets are more common in close-in M dwarf systems than in Solar-type stars (Bonfils et al. 2013; Dressing & Charbonneau 2015), with an occurrence rate of $2.5pm0.2$ planets per M dwarf with radii ranging from 1 to 4 R_E and periods less than 200 days. It is unclear, however, how differences in M dwarf environments affect the composition of exoplanets of a given size.

Bryant et al. (2023) recently studied the occurrence rate of giant planets orbiting low-mass stars using TESS photometry and demonstrated this occurrence rate to be non-zero. They showed that, when compared to occurrence rate studies for higher mass host stars (Beleznay & Kunimoto 2022), giant planets are less common around low-mass stars than solar-type stars, as predicted by the core-accretion planet formation theory (Laughlin et al. 2004; Burn et al. 2021). Their new results provide evidence that giant planets are less common around late M-dwarfs than early M-dwarfs but that giant planets can still exist around stars with masses as low as 0.2 - 0.3 M_{Sun}. This result contradicts currently accepted planet formation models and they discuss some possibilities for how these planets could have formed.

We present here the validation of 15 systems initially detected by the TESS pipeline and observed with ExTrA and imaging facilities. We first describe the target selection in Section 2 and photometric observations with TESS and ExTrA, and high-resolution imaging in Section 3. We present our stellar sample of validated systems in Section 4, including host star properties and how these values were derived. We present our modeling of TESS and ExTrA photometry in Section 5. We then discuss results and validation of new planetary systems in Section 6, present our discussion in Section 7, and concluding and summarizing our work in Section 8.

2. Target selection

In this section, we describe how we selected the target sample of TOIs for which we decided to take ExTrA observations when transits were expected to happen. The main science goal of this program is to improve on the planetary parameters, especially the radius ratio compared to TESS photometry only estimations. After our first published results using ExTrA on TOI-269 b (Cointepas et al. 2021), we noticed that for some targets, we were able to get a similar of better precision than TESS with a few ExTrA transits. We decided then to dedicate observation time to refining TESS transit parameters.

We selected TOIs with a stellar effective temperature T_{eff} below 3800K observable from La Silla Observatory where the ExTrA telescopes are located. From those, we selected candidates for which 5 ExTrA transits were expected to improve on the signal to noise ratio (S/N) compared to the TESS one (com-

---

⋆ Corresponding author:
`marion.cointepas@univ-grenoble-alpes.fr`

puted as $depth/depth_{err}$) available at that time. We included planetary candidate that were not yet validated by reconnaissance spectroscopic or photometric follow-up as we expect that the wavelength coverage of ExTrA in the near-infrared could help rule out eclipsing binaries as the source of the transit signal. The initial sample for which we obtained ExTrA observations consisted of 56 TOIs. Out of these TOIs, we published some systems individually, we removed the systems where other stars were contaminating the ExTrA aperture, and we took out the published planets when we could not get a better precision on the planetary radius. We attempted to validate 26 new planets in this work, but were only able to do so for 15 of them for now. We discuss possible explanations on the non validated systems in Section 7.

3. Observations

In this section, we outline the observations of our targets using TESS and ExTrA. For those targets which have not yet been validated, we present the imaging observations gathered using ExoFOP.

3.1. TESS photometry

The 15 exoplanets described in this paper were first identified as transiting planet candidates in the TESS photometry. TESS is conducting an all-sky survey of nearby bright stars in search of transiting exoplanets (Ricker et al. 2015). It was launched in April 2018 and surveys sections of the sky for approximately 27 days at a time. The TESS photometric data is processed by the NASA Ames Science Processing Operations Center (SPOC; Jenkins et al. 2016) and the Massachusetts Institute of Technology (MIT) Quick-Look Pipeline (QLP; Huang et al. (2020a,b)). SPOC and QLP are both light curve extraction pipelines, with the exception that QLP only extracts light curves from FFIs. These systems were identified as potential candidates by either the SPOC or the QLP, and then designated as TESS Objects of Interest (TOIs; Guerrero et al. (2021)). The planet candidates for which we propose a validation or improvement on the radius ratio measurement are presented in Table 1.

It is critical to check for contaminating eclipsing binaries and ensure that no visually close-by targets that could affect the depth of the transit are present in the 21" TESS pixel. The plots of the target pixel file (TPF) and the aperture mask used for simple aperture photometry (SAP) are shown in Figures 1, 2 and 3. No TPF was found for TOI-4201, TOI-4666 and TOI-5344.

3.2. ExTrA photometry

ExTrA is a new facility consisting of three 60-cm telescopes at La Silla Observatory (Bonfils et al. 2015). Its mission is to use near-infrared photometry to find exoplanets transiting nearby M dwarfs. The instrument employs a novel approach that combines photometry with spectroscopic data to mitigate the disruptive effects of the Earth's atmosphere as well as effects introduced by instruments and detectors. 5 Field Units (FUs) are used on each telescope to collect the light from the main target and four selected comparison stars. The FUs are made up of precisely placed fibers that feed a single near-infrared spectrograph with low spectral resolution ($R \sim 200$ or $R \sim 20$) that covers the 0.9-1.6 micron range. The broad spectral domain allows for the simultaneous collection of more photons, increasing sensitivity. ExTrA has the advantage of multiplexing, which means that we can record light from multiple telescopes using a single spectrograph (and thus a single detector). The resulting ExTrA data were analyzed using custom data reduction software.

3.3. High-contrast imaging

We obtained high-contrast imaging with multiple large ground-based telescopes to assess the impact of possible contamination from nearby stars and rule out the possibility of stellar companions for the planet candidates that were not yet validated. Bound stellar companions can produce false-positive transit signals if they are eclipsing binaries, in addition to diluting transit signals and underestimating planet radii (Ciardi et al. 2015). The different observations are displayed in Figures4,5 and 6. No imaging observations were found for TOI-2496, TOI-4201, TOI-4666 and TOI-5344.

4. Stellar parameters

We estimated consistently the stellar parameters for all the TESS candidates. The stellar radii are derived from the stellar parallax and K_s-band magnitude, used to compute the absolute K_s-band magnitude M_{K_s}, and the empirically-derived M dwarf radius-luminosity relations Mann et al. (2015). The stellar masses are computed using similar work from Mann et al. (2019). The results are presented in Table 2.

4.1. GAIA RUWE

The Gaia DR3 astrometry sheds light on the possibility of inner companions that were missed by Gaia or high resolution imaging. The Gaia Renormalized Unit Weight Error (RUWE) is a metric in which values below 1.4 indicate that the Gaia astrometric solution is consistent with the star being single, whereas values greater than 1.4 may indicate astrometric excess noise caused by the presence of an unseen companion (Ziegler et al. 2020). The only TOI in our list with a Gaia DR3 RUWE value above 1.4 is TOI-2496 (RUWE = 1.7). While this value is slightly higher than the nominal value of 1.4, the 1.4 RUWE boundary is more of a guideline as opposed to a hard cut-off.

5. Analysis

In order to model jointly the photometric data of the TESS and ExTrA instruments, we used the software package `juliet` (Espinoza et al. 2019). The algorithm is built on many publicly available tools for the modeling of transits (`batman`, Kreidberg 2015) and Gaussian Processes (GPs) (`george`, Ambikasaran et al. 2015; `celerite`, Foreman-Mackey et al. 2017). `juliet` computes the Bayesian evidence (lnZ) using `dynesty` (Speagle 2020), a python package to estimate Bayesian posteriors and evidences using nested sampling methods. Nested sampling algorithms sample directly from the given priors instead of starting off with an initial parameter vector around a likelihood maximum found via optimization techniques, as done in common sampling methods. The transit model fits the stellar density $\rho_\star$ along with the planetary and jitter parameters. We chose to put informative priors on the two orbital parameters (P and t_0)

Table 1. TESS observations of the systems observed with ExTrA.

TOI ID	TIC ID	Sectors	TESS transits	Pipeline	RA	Dec
TOI 210	TIC 141608198	[1-5,7-13,27-39]	61	SPOC	05:55:50.84	-73:59:07.04
TOI 218	TIC 32090583	[1-4,6-13,27-34,36-39]	1213	SPOC	03:53:41.28	-68:44:19.06
TOI 519	TIC 218795833	[7,34]	37	SPOC	08:18:25.62	-19:39:46.0
TOI 521	TIC 27649847	[7,34,44-46]	71	SPOC	08:13:22.62	+12:13:19.59
TOI 530	TIC 387690507	[6,33,44,45]	16	SPOC	06:53:39.08	+12:52:53.685
TOI 654	TIC 35009898	[9,36,45,46]	57	SPOC	10:58:53.89	-05:32:51.16
TOI 667	TIC 101955023	[9,10,36]	40	SPOC	10:14:50.18	-47:09:17.77
TOI 672	TIC 151825527	[9,10,36]	17	SPOC	11:11:57.81	-39:19:41.21
TOI 700	TIC 150428135	[1,3-11,13,27,28,30,31,33-38]	??	SPOC	06:28:22.97	-65:34:43.01
TOI 732	TIC 36724087	[9,35]	??	SPOC	10:18:34.78	-11:43:04.08
TOI 756	TIC 73649615	[10,11,37]	50	SPOC	12:48:24.9	-45:28:13.7
TOI 771	TIC 277634430	[10-12,37,38]	48	SPOC	10:56:27.33	-72:59:06.63
TOI 1080	TIC 161032923	[13]	7	SPOC	18:25:28.4	-52:12:52.46
TOI 1883	TIC 348755728	[35]	5	SPOC	08:56:21.42	-12:55:50.32
TOI 2407	TIC 153078576	[3,4,30,31]	17	SPOC	03:18:59.17	-46:27:28.89
TOI 2496	TIC 160328683	[32,33]	31	SPOC	06:04:47.08	-32:34:48.71
TOI 2952	TIC 302527524	[9-11,36-38]	8	QLP	08:56:46.24	-68:30:37.63
TOI 4201	TIC 95057860	[6]	3	QLP	06:01:53.93	-13:27:40.94
TOI 4552	TIC 248250955	[12,39]	152	SPOC	17:38:51.42	-47:38:13.36
TOI 4666	TIC 165202476	[31]	8	QLP	03:45:09.57	-39:03:47.455
TOI 4860	TIC 335590096	[36]	11	QLP	12:14:15.35	-13:10:29.4
TOI 5344	TIC 16005254	[43,44]	9	QLP	04:13:03.89	+20:54:54.56

Table 2. Stellar parameters of the TOIs.

TOI ID	Tmag - Vmag - Jmag	Stellar temperature	Spectral type	Stellar radius	Stellar mass
TOI 210	12.51 - 15.37 - 10.87	3264 ± 157	M3.5	0.3308 ± 0.0100	0.3126 ± 0.0077
TOI 218	13.55 - 16.45 - 11.68	3249 ± 157	M5	0.2841 ± 0.0085	0.2579 ± 0.0063
TOI 519	14.53 - 17.35 - 12.85	3324 ± 157	M3.5	0.3554 ± 0.0110	0.3418 ± 0.0088
TOI 521	12.43 - 14.69 - 10.92	3465 ± 157	M2.5	0.4199 ± 0.0125	0.4168 ± 0.0099
TOI 530	13.45 - 15.40 - 12.11	3566 ± 157	M2	0.5444 ± 0.0164	0.5447 ± 0.0134
TOI 654	12.17 - 14.54 - 10.74	3424 ± 157	M3	0.4276 ± 0.0128	0.4255 ± 0.0102
TOI 667	10.94 - 13.68 - 9.24	3261 ± 157	M3.5	0.2266 ± 0.0070	0.1940 ± 0.0050
TOI 672	11.56 - 13.58 - 10.36	3659 ± 157	M1	0.5436 ± 0.0163	0.5439 ± 0.0133
TOI 700	10.88 - 13.15 - 9.47	3494 ± 157	M2.5	0.4200 ± 0.0126	0.4169 ± 0.0101
TOI 732	10.53 - 13.14 - 9.01	3331 ± 157	M3.5	0.3747 ± 0.0112	0.3645 ± 0.0088
TOI 756	12.40 - 14.61 - 11.14	3533 ± 157	M2	0.5083 ± 0.0152	0.5105 ± 0.0123
TOI 771	12.07 - 14.89 - 10.51	3306 ± 157	M3.5	0.2422 ± 0.0073	0.2108 ± 0.0051
TOI 1080	12.68 - 15.35 - 11.04	3227 ± 157	M4	0.2000 ± 0.0060	0.1667 ± 0.0040
TOI 1883	13.35 - 15.79 - 11.87	3477 ± 157	M2.5	0.4942 ± 0.0150	0.4965 ± 0.0122
TOI 2407	12.53 - 14.68 - 11.13	3596 ± 157	M1.5	0.5252 ± 0.0157	0.5269 ± 0.0128
TOI 2496	14.20 - nan - 12.50	3273 ± 157	M3.5	0.5805 ± 0.0181	0.5764 ± 0.0149
TOI 2952	12.64 - 14.75 - 11.20	3558 ± 157	M2	0.5087 ± 0.0152	0.5109 ± 0.0123
TOI 4201	13.50 - 15.16 - 12.26	3790 ± 157	M0.5	0.6138 ± 0.0185	0.6037 ± 0.0151
TOI 4552	11.86 - 14.44 - 10.26	3264 ± 157	M3.5	0.2856 ± 0.0086	0.2596 ± 0.0063
TOI 4666	13.33 - 15.33 - 11.98	3666 ± 157	M1	0.5857 ± 0.0176	0.5808 ± 0.0145
TOI 4860	13.77 - 16.47 - 12.06	3237 ± 157	M4	0.3522 ± 0.0110	0.3381 ± 0.0089
TOI 5344	13.22 - 15.40 - 11.80	3575 ± 157	M2	0.5834 ± 0.0176	0.5788 ± 0.0145

and the stellar density (computed from the stellar radius and mass) using the values from ExoFOP TESS. We adopted a few parametrization modifications when dealing with the transit photometry. We assigned a quadratic limb-darkening law for TESS, as shown to be appropriate for space-based missions (Espinoza & Jordán 2015), which was parametrized with the uniform sampling scheme (q_1, q_2) introduced by Kipping (2013).

Two different parametrizations were used for the planet-to-star radius ratio ($p = R_p/R_\star$) and the impact parameter of the orbit ($b = a/R_\star \cos i$). I first fitted two different planet-to-star radius ratio parameters (one for TESS and one for ExTrA) to check for chromaticity in the transit depth as TESS and ExTrA observations are made at different wavelength ranges. Then I used the parametrization introduced in Espinoza (2018) and fit for the parameters r_1 and r_2 to guarantee full exploration of physically plausible values in the (p,b) plane to compare the precision on the radius ratio from a combined fit of TESS and ExTrA to a previous fit of TESS photometry only.

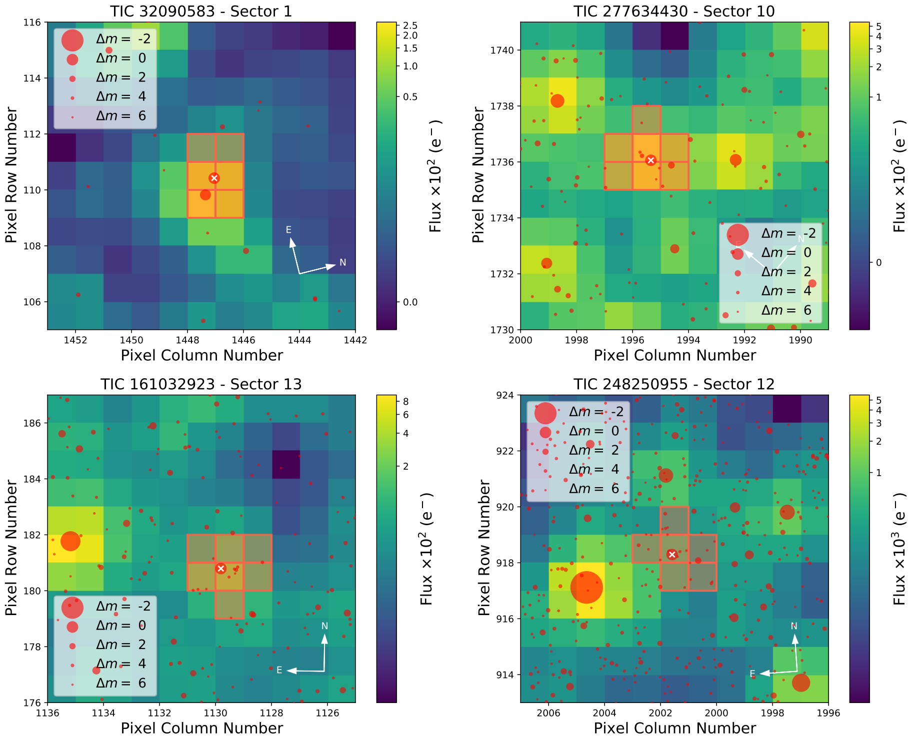

Fig. 1. TESS Pixel Files for the 4 super-Earth candidates

We fixed the TESS dilution factor to one based on our analysis of nearby companions. Furthermore, we added in quadrature a jitter term σ_{TESS} to the TESS photometric uncertainties, which might be underestimated due to additional systematics in the space-based photometry. We decided to use time-dependent Gaussian processes on the TESS and ExTrA photometry as the data was not detrended yet. We chose the approximate Matern kernel introduced in Foreman-Mackey et al. (2017) because when looking at the ExTrA light curves there are no evident quasi-periodic oscillations. We used `dynesty` to perform this fit as there is a large number of free parameters. The posterior values for the planetary radius, computed using the stellar radius from Section 4, are presented in Table 3.

6. Results

6.1. Validation of planetary candidates

The ExTrA observations were able for now to validate the planetary nature of the companion for 15 targets and improve on the known radius measurement for several targets. An overview of all the original targets observed as part of WP1 is presented in Figure 7. We also compared the uncertainties on the radius ratio measurements for both TESS and TESS+ExTrA to estimate the improvement made by adding the ExTrA photometry (see Figure 8. We displayed the planetary radius measurements in Figure 9, to compare the estimations from TESS photometry, TESS+ExTrA combined and published results. For the non yet published candidates, we also used a model with different transit depths for TESS and ExTrA to make sure no sign of chromaticity was present between the datasets. The results of those fit can be found in Appendix.

6.1.1. Super-Earths

The phase-folded light curves of TESS and ExTrA for all the super-Earths candidates are presented in Figure 10.

TOI-218.01

We find that TOI-218 b is a Terran world (as defined in Chen & Kipping (2017)) orbiting a M4 dwarf star on a 0.463d orbit. We find it has a radius of $1.216 \pm 0.061 R_E$ and a predicted mass of $1.77^{+0.33}_{-0.29} M_E$ for a rocky composition.

TOI-771.01

We find that TOI-771 b is a Terran world orbiting a M4 dwarf star on a 2.326d orbit. We find it has a radius of $1.391^{+0.055}_{-0.054} R_E$ and a predicted mass of $2.81^{+0.40}_{-0.36} M_E$ for a rocky composition.

TOI-1080.01

We find that TOI-1080 b is a Terran world orbiting a M4 dwarf star on a 3.965d orbit. We find it has a radius of $1.281^{+0.080}_{-0.081} R_E$ and a predicted mass of $2.12^{+0.49}_{-0.43} M_E$ for a rocky composition.

TOI-4552.01

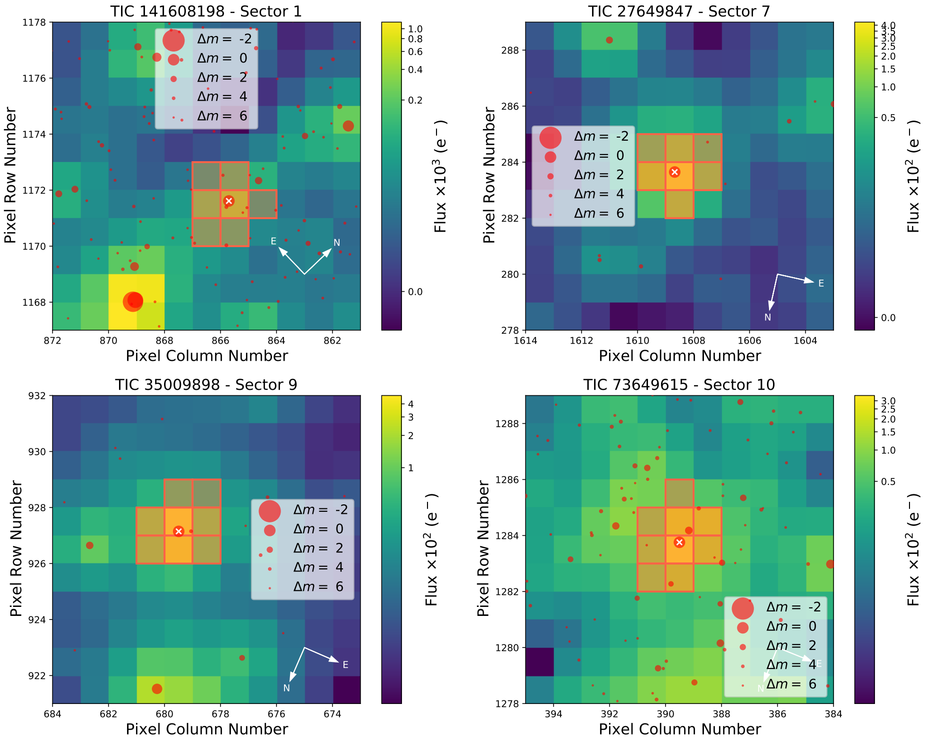

Fig. 2. TESS Pixel Files for the 4 sub-Neptune candidates

We find that TOI-4552 b is a Terran world orbiting a M3 dwarf star on a 0.301d orbit. We find it has a radius of $1.081^{+0.067}_{-0.066} R_E$ and a predicted mass of $1.18^{+0.27}_{-0.23} M_E$ for a rocky composition.

6.1.2. Sub-Neptunes

The phase-folded light curves of TESS and ExTrA for all the sub-Neptunes candidates are presented in Figure 11.

TOI-210.01

We find that TOI-210 b is a Neptunian world (as defined in Chen & Kipping (2017)) orbiting a M4 dwarf star on a 9.011d orbit. We find it has a radius of $2.219^{+0.078}_{-0.077} R_E$ and a predicted mass of $14.1^{+1.8}_{-1.6} M_E$ for a rocky composition and a predicted mass of $6.13^{+0.34}_{-0.33} M_E$ for a more volatile rich composition.

TOI-521.01

We find that TOI-521 b is a Neptunian world orbiting a M3 dwarf star on a 1.543d orbit. We find it has a radius of $2.023 \pm 0.087 R_E$ and a predicted mass of $10.2^{+1.6}_{-1.4} M_E$ for a rocky composition and a predicted mass of $5.30^{+0.36}_{-0.35} M_E$ for a more volatile rich composition.

TOI-654.01

We find that TOI-654 b is a Neptunian world orbiting a M3 dwarf star on a 1.528d orbit. We find it has a radius of $2.334^{+0.088}_{-0.087} R_E$ and a predicted mass of $16.7^{+2.3}_{-2.1} M_E$ for a rocky composition and a predicted mass of $6.64^{+0.40}_{-0.39} M_E$ for a more volatile rich composition.

TOI-756.01

We find that TOI-756 b is a Neptunian world orbiting a M2 dwarf star on a 1.239d orbit. We find it has a radius of $2.76^{+0.15}_{-0.16} R_E$ and a predicted mass of $30.0^{+6.1}_{-5.5} M_E$ for a rocky composition and a predicted mass of $8.67 \pm 0.076 M_E$ for a more volatile rich composition.

6.1.3. Gas Giants

The phase-folded light curves of TESS and ExTrA for all the gas giants candidates are presented in Figures 12 and 13.

TOI-672.01

We find that TOI-672 b is a gas giant orbiting a M1 dwarf star on a 3.634d orbit. We find it has a radius of $5.31 \pm 0.17 R_E$ and a predicted mass of $24.4 \pm 1.2 M_E$ for a volatile rich composition.

TOI-1883.01

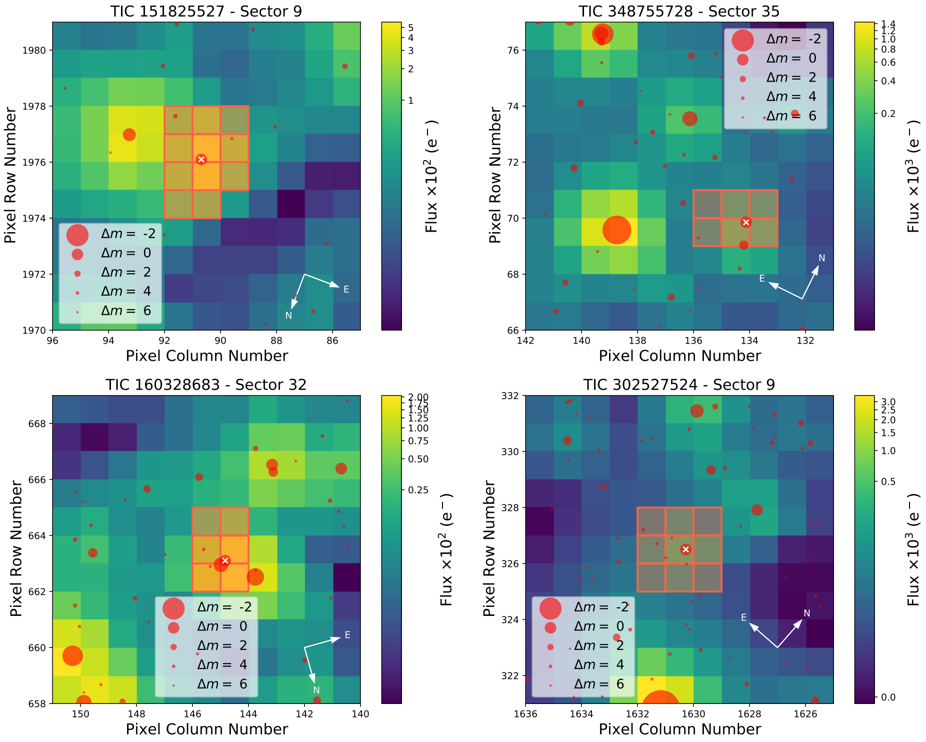

Fig. 3. TESS Pixel Files for the 4 gas giants candidates

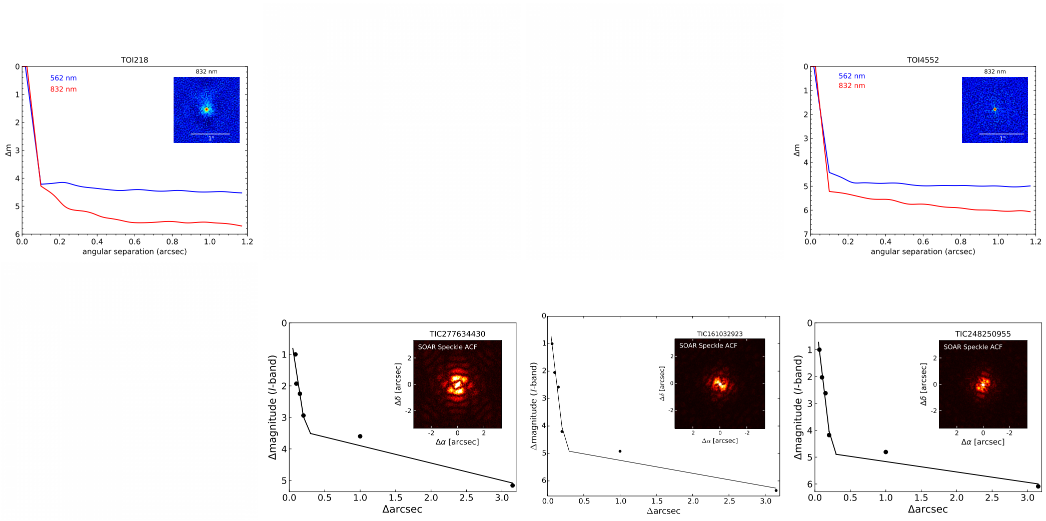

Fig. 4. Imaging for the 4 super-Earth candidates

We find that TOI-1883 b is a gas giant orbiting a M3 dwarf star on a 4.506d orbit. We find it has a radius of 5.61 ± 0.23R_E and a predicted mass of $26.5^{+1.8}_{-1.7}M_E$ for a volatile rich composition.

TOI-2496.01

No imaging. We find that TOI-2496.01 could be a gas giant orbiting a M4 dwarf star on a 1.575d orbit. We find it has a potential radius of $17.0^{+1.2}_{-1.4}R_E$ and a predicted mass of $154^{+17}_{-19}M_E$ for a volatile rich composition.

TOI-2952.01

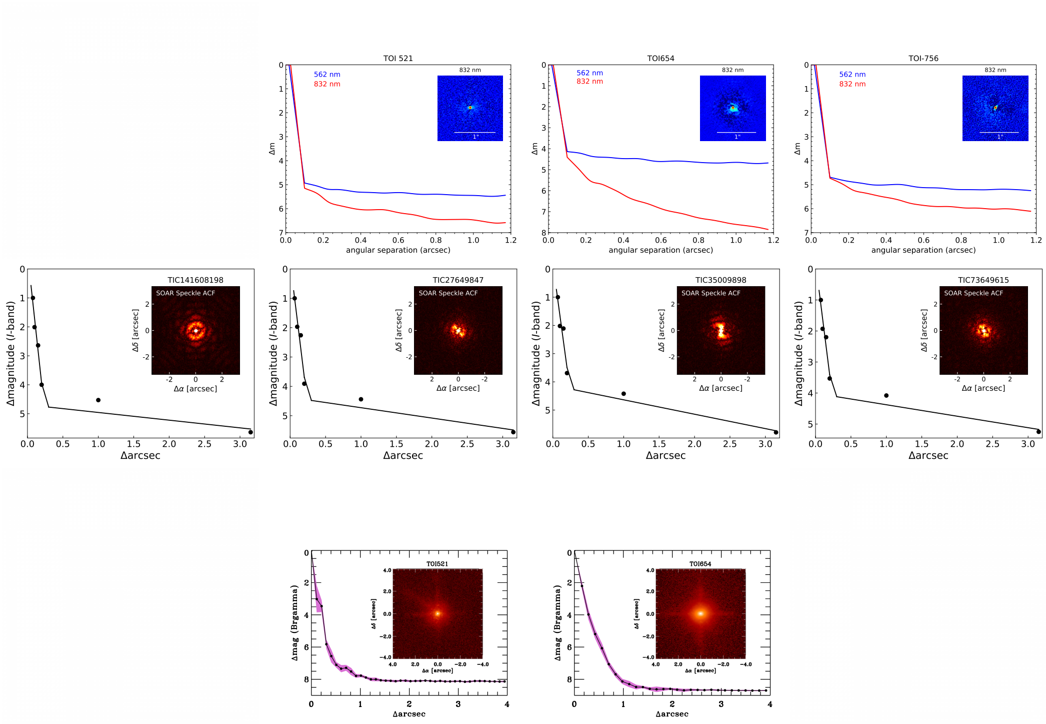

Fig. 5. Imaging for the 4 sub-Neptune candidates

We find that TOI-2952 b is a gas giant orbiting a M2 dwarf star on a 10.784d orbit. We find it has a radius of $6.56 \pm 0.23 R_E$ and a predicted mass of $33.9 \pm 1.9 M_E$ for a volatile rich composition.

TOI-4201.01

No imaging, no TPF. We find that TOI-4201.01 could be a gas giant orbiting a M0 dwarf star on a 3.581d orbit. We find it has a potential radius of $11.75^{+0.43}_{-0.41} R_E$ and a predicted mass of $85.3^{+5.0}_{-4.6} M_E$ for a volatile rich composition.

TOI-4666.01

No imaging, no TPF. We find that TOI-4666.01 could be a gas giant orbiting a M1 dwarf star on a 2.909d orbit. We find it has a potential radius of $12.19^{+0.40}_{-0.38} R_E$ and a predicted mass of $90.5^{+4.7}_{-4.5} M_E$ for a volatile rich composition.

TOI-5344.01

No imaging, no TPF. We find that TOI-5344.01 could be a gas giant orbiting a M2 dwarf star on a 3.793d orbit. We find it has a potential radius of $10.17 \pm 0.34 R_E$ and a predicted mass of $68.0 \pm 3.6 M_E$ for a volatile rich composition.

6.2. Improvement on the planetary radius measurement

Out of the TOIs observed, some of them have been published since we started this program. We compared the precision on the planetary radius published to the results of our modeling. For 8 of them we obtained a better precision on the planetary radius : TOI-519.01, TOI-530.01, TOI-667.01, TOI-700.01, TOI-732.01 and .02, TOI-2407.01, and TOI-4860.01. However, we noticed that for 2 of them (TOI-519.01 and TOI-530.01), this improvement was caused by a more precise stellar radius, and the published value of radius ratio was better than the one we obtained in this analysis.

7. Discussion

8. Conclusion

Acknowledgements. We are grateful to the ESO/La Silla staff for their continuous support. We acknowledge funding from the European Research Council under the ERC Grant Agreement n. 337591-ExTrA. This paper includes data collected by the TESS mission. Funding for the TESS mission is provided by the NASA Explorer Program. We acknowledge the use of public TESS Alert data from the pipelines at the TESS Science Office and at the TESS Science Processing Operations Center. Resources supporting this work were provided by the NASA High-End Computing (HEC) program through the NASA Advanced Supercomputing (NAS) Division at Ames Research Center for the production of the SPOC data products. We thank the Swiss National Science Foundation (SNSF) and the Geneva University for their continuous support to our planet search programs. This work has been in particular carried out in the frame of the National Centre for Competence in Research 'PlanetS' supported by the Swiss National Science Foundation (SNSF).

References

Ambikasaran, S., Foreman-Mackey, D., Greengard, L., Hogg, D. W., & O'Neil, M. 2015, IEEE Transactions on Pattern Analysis and Machine Intelligence, 38, 252
Beleznay, M. & Kunimoto, M. 2022, MNRAS, 516, 75

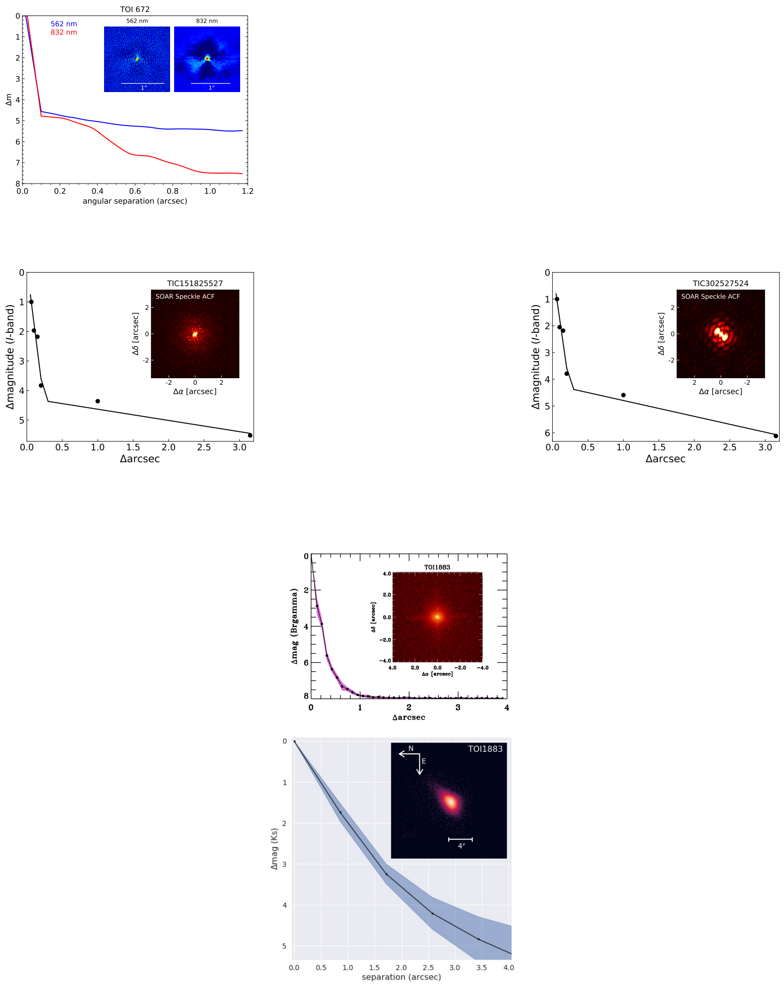

Fig. 6. Imaging for the 3 gas giants candidates

Bonfils, X., Almenara, J. M., Jocou, L., et al. 2015, in Society of Photo-Optical Instrumentation Engineers (SPIE) Conference Series, Vol. 9605, Techniques and Instrumentation for Detection of Exoplanets VII, 96051L

Bonfils, X., Delfosse, X., Udry, S., et al. 2013, A&A, 549, A109

Bryant, E. M., Bayliss, D., & Van Eylen, V. 2023, MNRAS[`arXiv:2303.00659`]

Burn, R., Schlecker, M., Mordasini, C., et al. 2021, A&A, 656, A72

Chen, J. & Kipping, D. 2017, ApJ, 834, 17

Ciardi, D. R., Beichman, C. A., Horch, E. P., & Howell, S. B. 2015, ApJ, 805, 16

Cointepas, M., Almenara, J. M., Bonfils, X., et al. 2021, A&A, 650, A145

Dressing, C. D. & Charbonneau, D. 2015, ApJ, 807, 45

Espinoza, N. 2018, Research Notes of the American Astronomical Society, 2, 209

Espinoza, N. & Jordán, A. 2015, MNRAS, 450, 1879

Espinoza, N., Kossakowski, D., & Brahm, R. 2019, MNRAS, 490, 2262

Foreman-Mackey, D., Agol, E., Ambikasaran, S., & Angus, R. 2017, AJ, 154, 220

Guerrero, N. M., Seager, S., Huang, C. X., et al. 2021, ApJS, 254, 39

Huang, C. X., Vanderburg, A., Pál, A., et al. 2020a, Research Notes of the American Astronomical Society, 4, 204

Huang, C. X., Vanderburg, A., Pál, A., et al. 2020b, Research Notes of the American Astronomical Society, 4, 206

Jenkins, J. M., Twicken, J. D., McCauliff, S., et al. 2016, in Society of Photo-Optical Instrumentation Engineers (SPIE) Conference Series, Vol. 9913, Software and Cyberinfrastructure for Astronomy IV, 99133E

Kipping, D. M. 2013, MNRAS, 435, 2152

Kreidberg, L. 2015, PASP, 127, 1161

Laughlin, G., Bodenheimer, P., & Adams, F. C. 2004, ApJ, 612, L73

Mann, A. W., Dupuy, T., Kraus, A. L., et al. 2019, ApJ, 871, 63

Mann, A. W., Feiden, G. A., Gaidos, E., Boyajian, T., & von Braun, K. 2015, ApJ, 804, 64

Ricker, G. R., Winn, J. N., Vanderspek, R., et al. 2015, Journal of Astronomical Telescopes, Instruments, and Systems, 1, 014003

Smith, J. C., Stumpe, M. C., Van Cleve, J. E., et al. 2012, PASP, 124, 1000

Speagle, J. S. 2020, MNRAS, 493, 3132

Stumpe, M. C., Smith, J. C., Catanzarite, J. H., et al. 2014, PASP, 126, 100

Stumpe, M. C., Smith, J. C., Van Cleve, J. E., et al. 2012, PASP, 124, 985

Ziegler, C., Tokovinin, A., Briceño, C., et al. 2020, AJ, 159, 19

---

[1] Univ. Grenoble Alpes, CNRS, IPAG, F-38000 Grenoble, France

[2] Observatoire de Genève, Département d'Astronomie, Université de Genève, Chemin Pegasi 51b, 1290 Versoix, Switzerland

Table 3. Comparison of the planetary radius from this analysis (TESS only and TESS+ExTrA) and from the literature

TOI	R_p (TESS only) in R_E	R_p (TESS+ExTrA) in R_E	R_p (literature) in R_E
210.01	2.265 ± 0.087	2.220 ± 0.078	none
218.01	1.210 ± 0.080	1.216 ± 0.061	none
519.01	37.195 ± 1.933	11.975 ± 0.412	$0.75 \pm 0.21 R_J = 8.41 \pm 2.35 R_E$
521.01	1.967 ± 0.086	2.023 ± 0.087	none
530.01	8.495 ± 0.323	8.513 ± 0.290	$0.83 \pm 0.05 R_J = 9.30 \pm 0.56 R_E$
654.01	2.342 ± 0.100	2.334 ± 0.088	none
667.01	1.194 ± 0.042	1.189 ± 0.041	1.16 ± 0.11
672.01	5.271 ± 0.169	5.310 ± 0.163	none
700.01	3.948 ± 0.669	2.656 ± 0.122	$2.63 + 0.24 - 0.23$
732.01	1.163 ± 0.073	1.170 ± 0.064	1.33 ± 0.07
732.02	2.264 ± 0.165	2.335 ± 0.141	2.30 ± 0.16
756.01	2.693 ± 0.169	2.764 ± 0.154	none
771.01	1.436 ± 0.061	1.392 ± 0.053	none
1080.01	1.314 ± 0.152	1.282 ± 0.081	none
1883.01	5.435 ± 0.380	5.612 ± 0.233	none
2407.01	3.896 ± 0.163	3.825 ± 0.150	4.14 ± 0.16
2496.01	54.814 ± 6.607	17.038 ± 1.272	none
2952.01	6.489 ± 0.377	6.555 ± 0.232	none
4201.01	11.379 ± 0.690	11.808 ± 0.420	none
4552.01	1.145 ± 0.085	1.080 ± 0.066	none
4666.01	12.488 ± 0.554	12.192 ± 0.396	none
4860.01	8.559 ± 0.445	8.202 ± 0.297	$0.76 + 0.14 - 0.04 R_J = 8.29 + 1.57 - 0.45 R_E$
5344.01	9.937 ± 0.454	10.167 ± 0.350	none

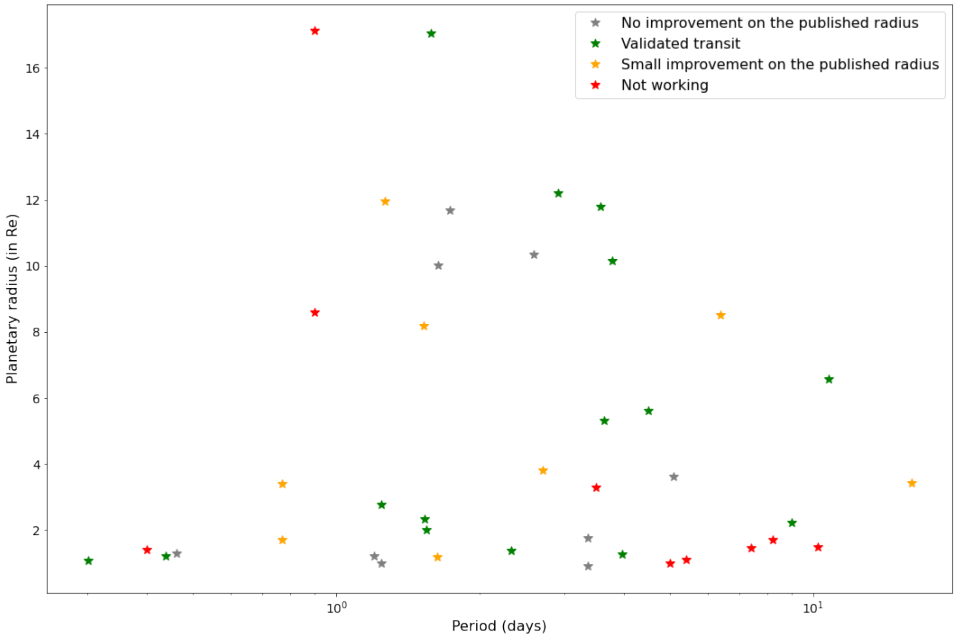

Fig. 7. Target summary for the WP1. All the targets observed by ExTrA as part of the WP1 are presented here. The different outcomes are displayed by different colors.

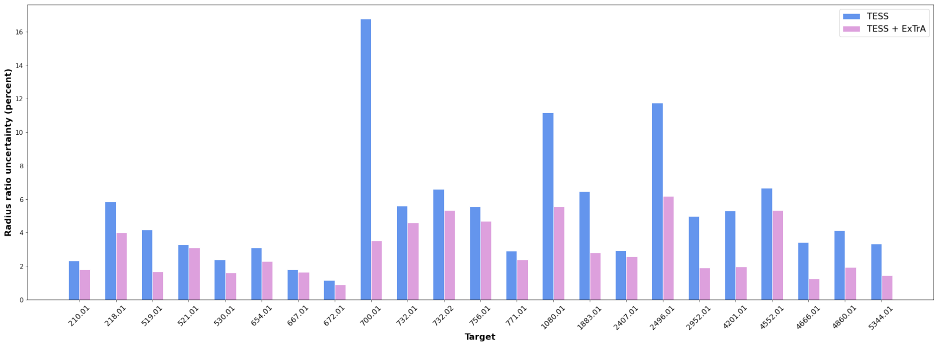

Fig. 8. Comparison of the uncertainties on the radius ratio measurements between TESS and ExTrA.

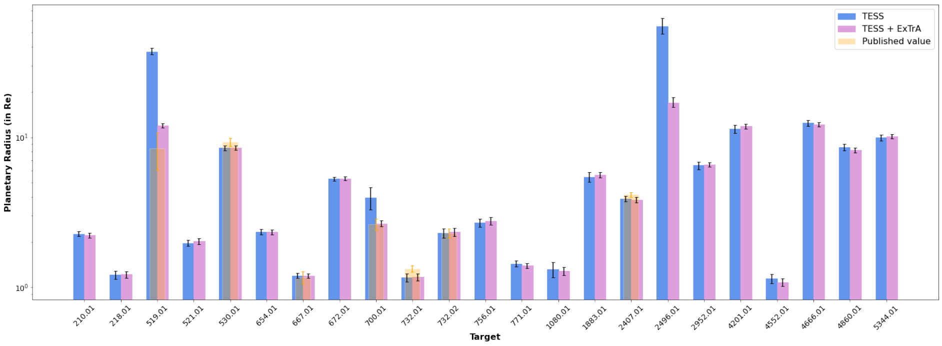

Fig. 9. Planetary radius measurements from TESS only, TESS and ExTrA combined and published values.

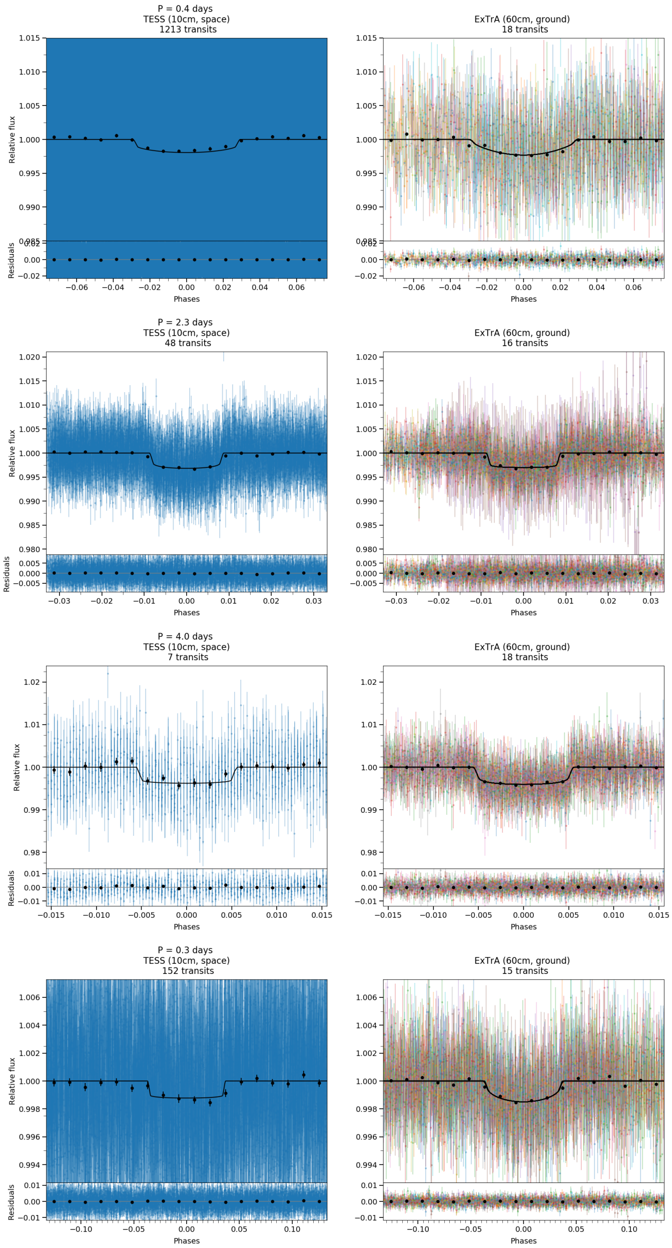

Fig. 10. TESS and ExTrA phase-folded light curves for TOI-218.01, TOI-771.01, TOI-1080.01 and TOI-4552.01. Above each curve is written the telescope, the size of its primary mirror, where it is located, and below the total number of transits phase-folded. The black line is the maximum a posteriori model, the black points are data binned to 1/6 of the transit duration.

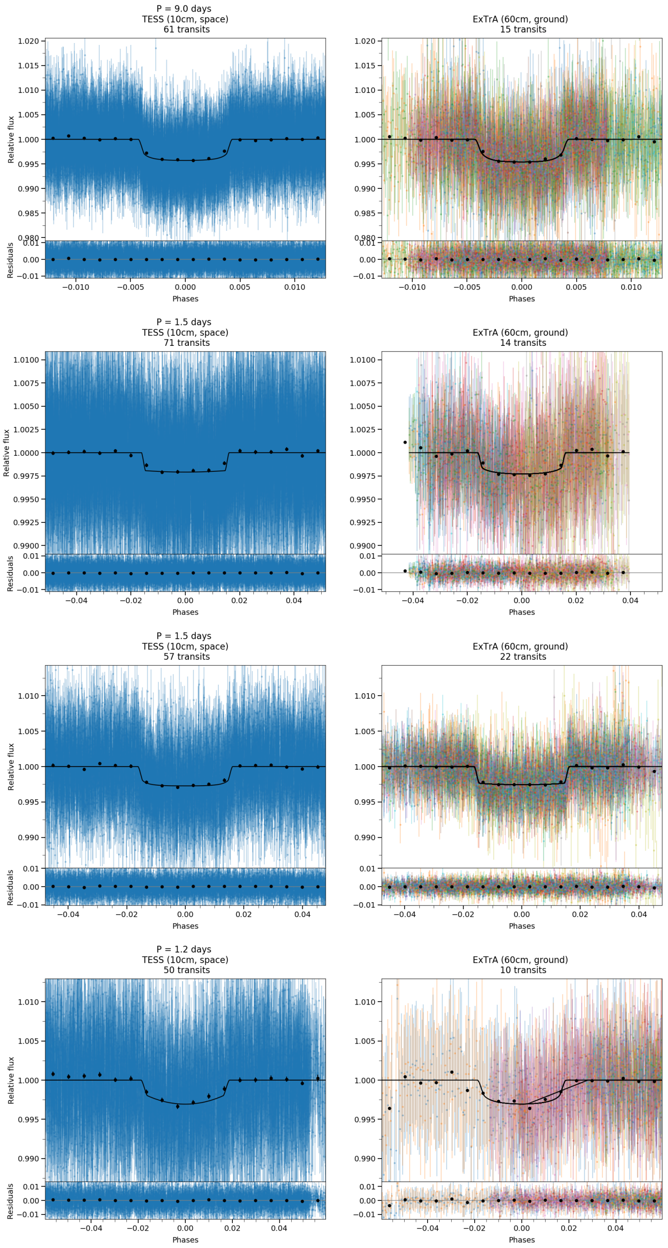

Fig. 11. TESS and ExTrA phase-folded light curves for TOI-210.01, TOI-521.01, TOI-654.01 and TOI-756.01. Above each curve is written the telescope, the size of its primary mirror, where it is located, and below the total number of transits phase-folded. The black line is the maximum a posteriori model, the black points are data binned to 1/6 of the transit duration.

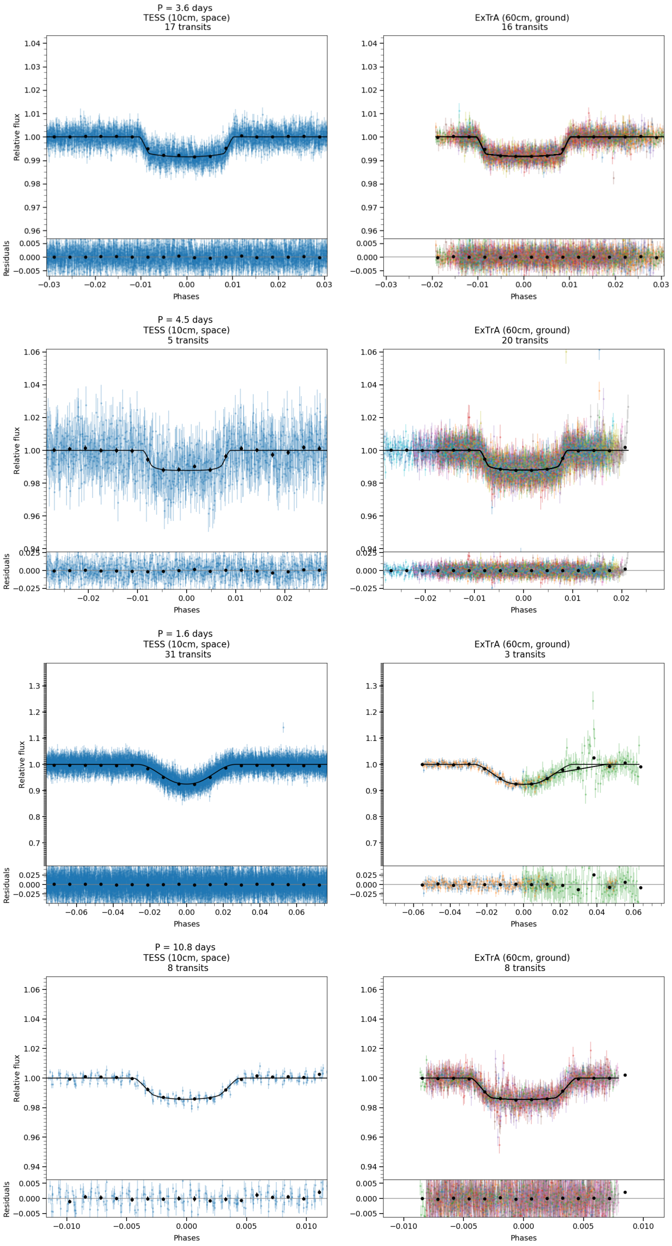

Fig. 12. TESS and ExTrA phase-folded light curves for TOI-672.01, TOI-1883.01, TOI-2496.01 and TOI-2952.01. Above each curve is written the telescope, the size of its primary mirror, where it is located, and below the total number of transits phase-folded. The black line is the maximum a posteriori model, the black points are data binned to 1/6 of the transit duration.

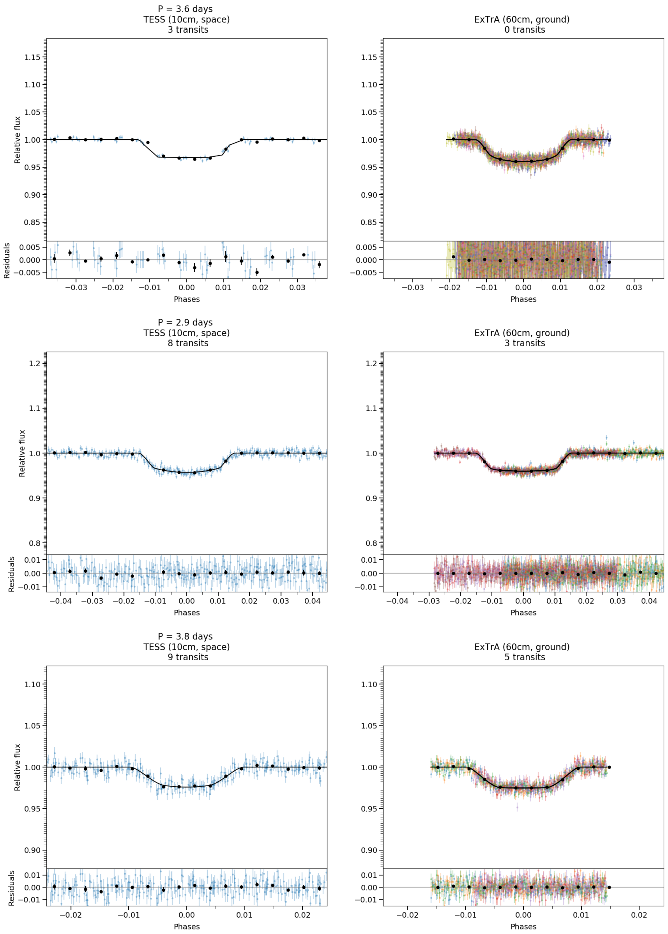

Fig. 13. TESS and ExTrA phase-folded light curves for TOI-4201.01, TOI-4666.01 and TOI-5344.01. Above each curve is written the telescope, the size of its primary mirror, where it is located, and below the total number of transits phase-folded. The black line is the maximum a posteriori model, the black points are data binned to 1/6 of the transit duration.

Appendix A: Modeling of TESS and ExTrA photometry with different transit depths.

We fitted TESS and ExTrA light curves with different transit depths to verify if there was some sign of chromaticity. Presented below are the histograms of the posteriors of the planetary radii from the TESS photometry (in blue) and the ExTrA photometry (in red). We also displayed the difference between the ExTrA and TESS planetary radius posterior distributions to ensure that the two transit depths were consistent within 2 σ.

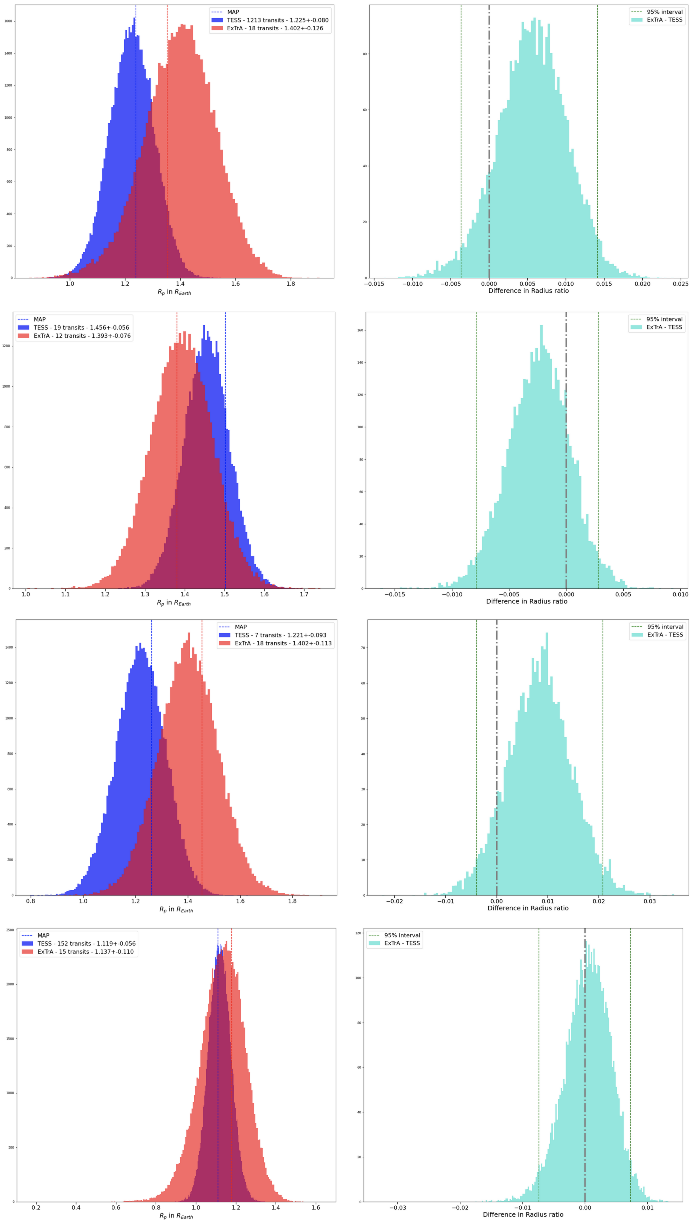

Fig. A.1. Modeling of the TESS and ExTrA photometry for TOI-218.01, TOI-771.01, TOI-1080.01 and TOI-4552.01.*Left*: Histogram of the posterior distribution of the radius ratio for TESS (in blue) and for ExTrA (in red). The colored dotted vertical lines correspond to the Maximum A Posteriori for each distribution.*Right*: Histogram of the difference of posterior distributions of the radius ratio between ExTrA and TESS. The green vertical lines correspond to 95% or 2σ of the distribution. The gray vertical line is centered on 0.

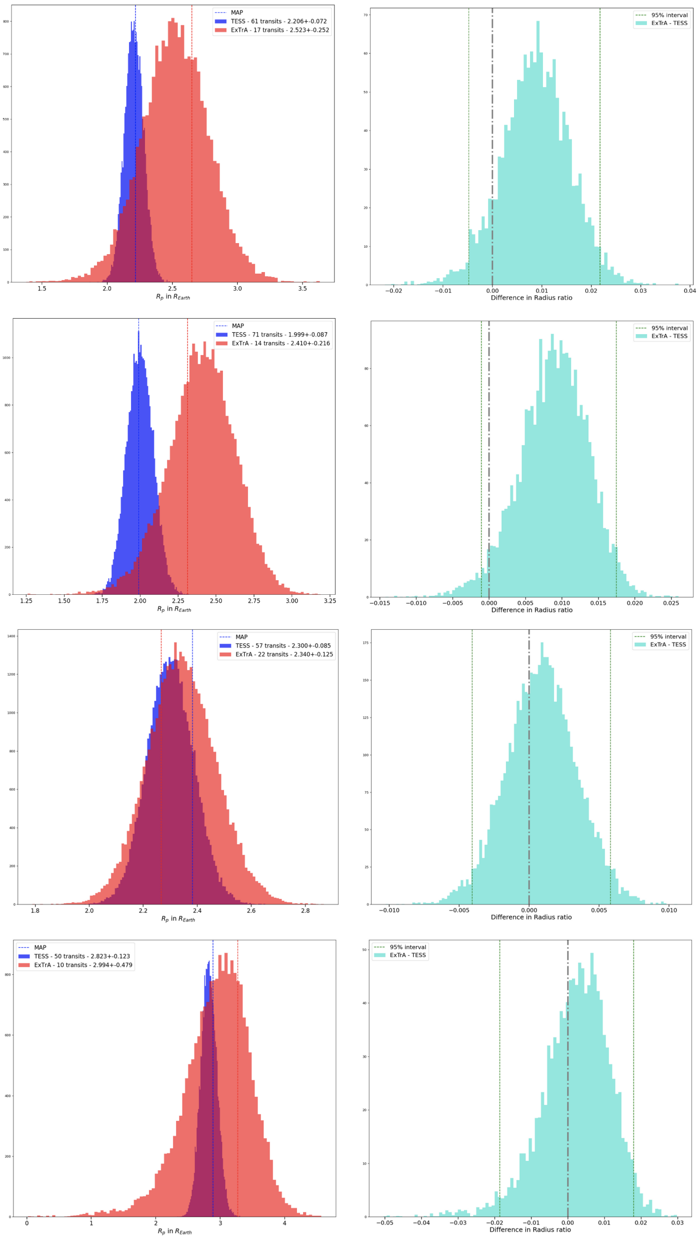

Fig. A.2. Modeling of the TESS and ExTrA photometry for TOI-210.01, TOI-521.01, TOI-654.01 and TOI-756.01. *Left*: Histogram of the posterior distribution of the radius ratio for TESS (in blue) and for ExTrA (in red). The colored dotted vertical lines correspond to the Maximum A Posteriori for each distribution.*Right*: Histogram of the difference of posterior distributions of the radius ratio between ExTrA and TESS. The green vertical lines correspond to 95% or 2σ of the distribution. The gray vertical line is centered on 0.

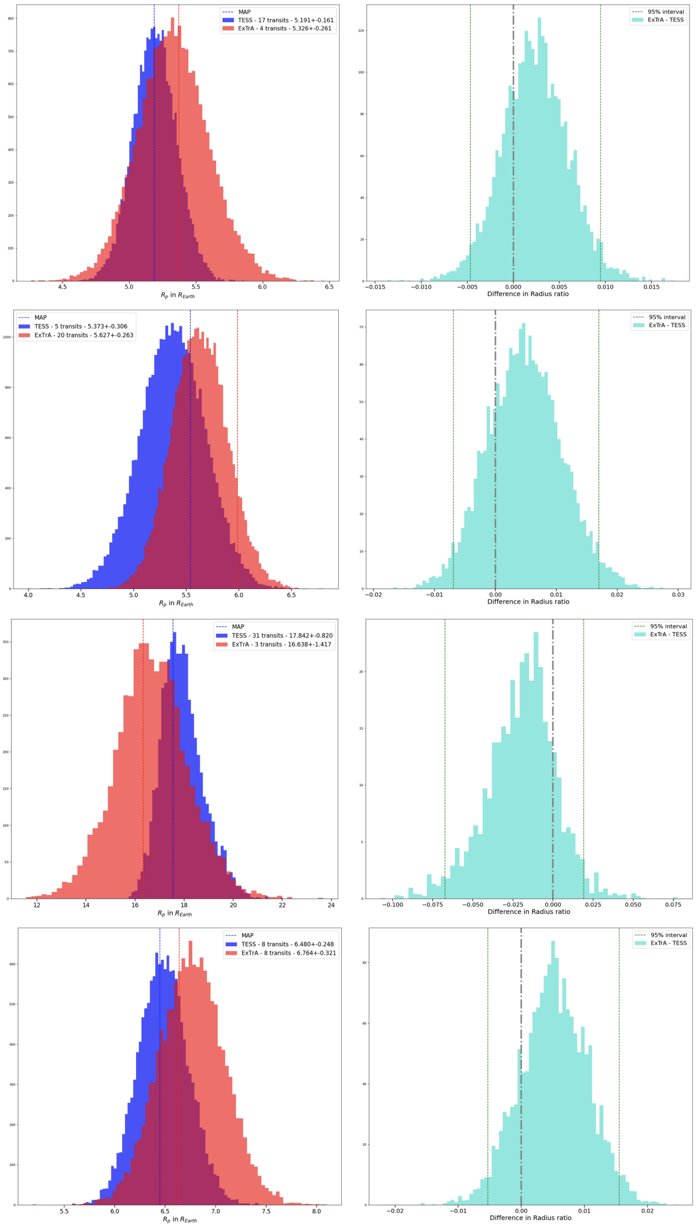

Fig. A.3. Modeling of the TESS and ExTrA photometry for TOI-672.01, TOI-1883.01, TOI-2496.01 and TOI-2952.01. *Left*: Histogram of the posterior distribution of the radius ratio for TESS (in blue) and for ExTrA (in red). The colored dotted vertical lines correspond to the Maximum A Posteriori for each distribution.*Right*: Histogram of the difference of posterior distributions of the radius ratio between ExTrA and TESS. The green vertical lines correspond to 95% or 2σ of the distribution. The gray vertical line is centered on 0.

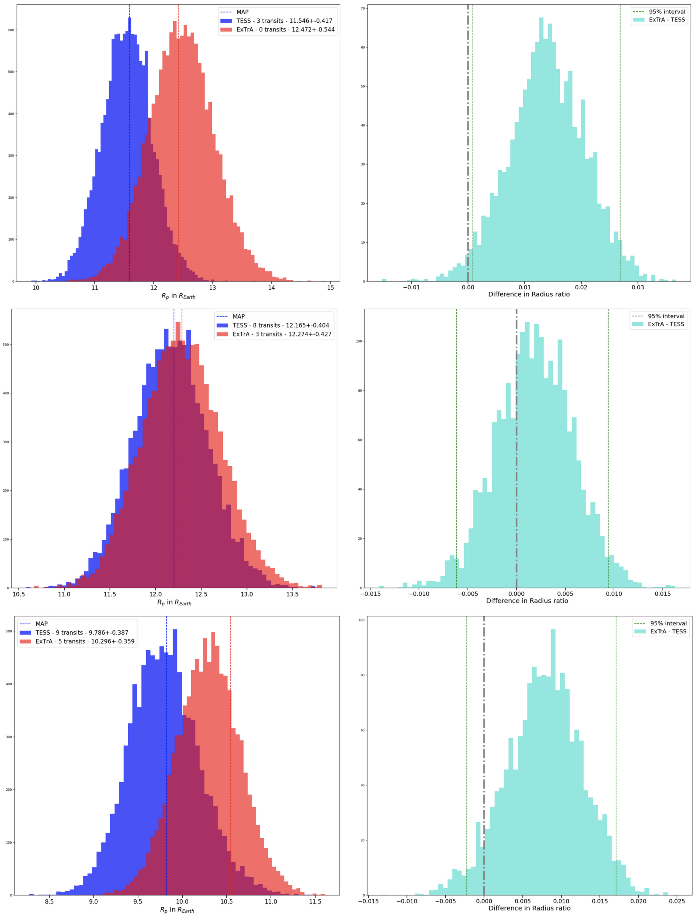

Fig. A.4. Modeling of the TESS and ExTrA photometry for TOI-4201.01, TOI-4666.01 and TOI-5344.01. *Left*: Histogram of the posterior distribution of the radius ratio for TESS (in blue) and for ExTrA (in red). The colored dotted vertical lines correspond to the Maximum A Posteriori for each distribution.*Right*: Histogram of the difference of posterior distributions of the radius ratio between ExTrA and TESS. The green vertical lines correspond to 95% or 2σ of the distribution. The gray vertical line is centered on 0.

III.5.2 *WP2 - Transit timing variations and additional companions*

The second work package of ExTrA is dedicated to multi-planetary systems. Systems with two or more exoplanets are important for several reasons. The discovery of multiple exoplanets in a single system sheds light on how planets form and evolve. Theories about the formation of planetary systems can be developed and tested by studying the properties of these planets, such as their radius, masses, orbits, and compositions. The discovery of multiple exoplanets in a single system also emphasizes the incredible diversity of planetary systems in the universe. These systems can have a wide variety of architectures and properties, providing a wealth of data to test theories about the formation and evolution of planets. Multiple exoplanet systems can also assist us in better understanding the process of planetary migration. Planets can move from their original positions as a result of gravitational interactions with other planets or the protoplanetary disk. Multiple planets in a system can help us constrain possible migration paths and better understand the factors that influence planetary migration.

By observing multiple transits of an exoplanet, especially in already known multi-planetary systems, we can detect transit timing variations (TTVs). TTVs, see Figure III.16, are deviations in an exoplanet's transit timing across its host star that can be caused by gravitational interactions with other exoplanets in the system (Agol and Fabrycky, 2018; Agol et al., 2005; Holman and Murray, 2005). Depending on the orbits and masses of the interacting planets, these variations can be periodic or irregular. TTVs can be used to detect additional planets in a system that would otherwise be missed by other methods, as well as to constrain the properties of known planets. TTVs are used to measure the mass of an exoplanet by observing the planet's transit timings across the face of its host star over time, modeling the gravitational interactions between the exoplanet and its companion planets, and inferring the mass of the companion planet from the observed variations in transit timings.

The Kepler-36 system contains the best-characterized pair of small planets discovered to date using TTVs (Carter et al., 2012). This system has the smallest fractional separation between any pair of adjacent orbits of any multi-planet system for which densities of the planets have been measured, and this pair also has one of the largest density contrasts. The TRAPPIST-1 system is also well known for having the masses and densities of all 7 exoplanets measured using the TTV method as demonstrated in Grimm et al., 2018. Using a novel method applied to a set of 284 individual transit timing, they found out that TRAPPIST-1 c and e likely have largely rocky interiors, while planets b, d, f, g, and h require envelopes of volatiles in the form of thick atmospheres, oceans, or ice, in most cases with water mass fractions less than 5%.

An observing program dedicated to these multi-planet systems was therefor essential for ExTrA as transit timing variations afford a means of measuring the density of exoplanets. The transit depth provides the radius-ratio of the planet to the star, whereas if two planets transit and show TTVs, their TTVs provide an estimate of the perturbing planet's mass

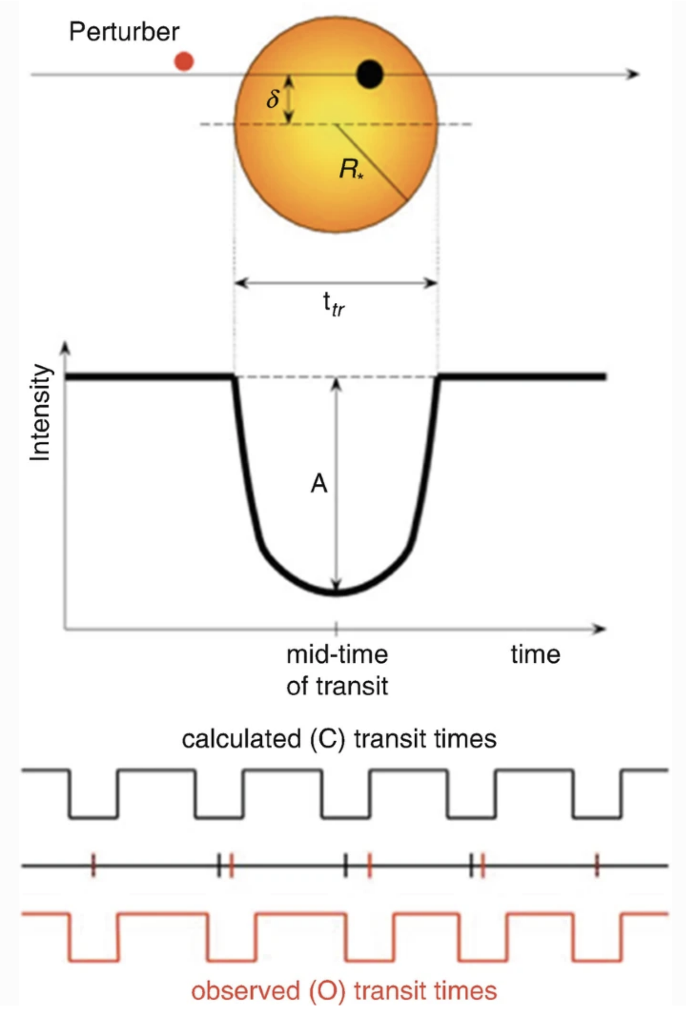

Figure III.16: TTVs.
Schematic view of transit timing variation from Haghighipour, 2015.

ratio to the star. As a result of two transiting, interacting planets, we can estimate the density ratio of the planets to the star, and thus the density of the planets. One issue could be the eccentricity dependence with the stellar density, but multi-transiting planet systems typically require low eccentricities to be stable.

For this work package, we selected multi-planetary systems from TESS's M dwarfs sample, to which we added TESS candidates with possible additional exoplanets detected in RV measurements.

Preliminary results on TOI-3494

TOI-3494.01 was a planetary candidate that we observed in the context of ExTrA WP1. The $2.4 R_{Earth}$ planetary candidate with a 7.75-days period found by TESS showed about an hour amplitude TTVs. The TESS and ground-based follow-up transits were analyzed with a photo-dynamical model, and an outer planet in 2:1 mean motion resonance was detected. An upper limit for the mass of the transiting planet of $36 M_{Earth}$ and a mass for the outer planet of $4.9^{+3.3}_{-2.4} M_{Earth}$ were measured. As a result, the transiting candidate's nature is confirmed, and a new exoplanet is discovered in this system that will be published soon (Almenara et al. in prep). The TESS and ground-based transits are presented in Figure III.17. Adding the ExTrA transits to the photo-dynamical analysis (see Figure III.18), especially as a better timing precision is obtained on the ExTrA transits compared to the TESS transits, allowed to constrain the ephemeris of TOI-3494.01, avoiding for example to miss the most recent transit observed (last red dot on Figure III.18) by a couple of hours, and revealing the presence of an additional exoplanet in the system.

The strength of TTVs is determined by a number of factors, including the masses and orbital parameters of the planets in the system. TTVs are generally stronger for longer period planets than for shorter period planets. This is because the gravitational influence of a distant planet on transit timing is greater than that of a nearby planet, that would only undergo the gravitational pull of the star. When planets are in resonance, their gravitational interaction can lead to larger TTVs compared to planets that are not in resonance. Indeed, resonant planets have a stronger gravitational interaction with each other as they are more likely to be close to each other in their orbits at certain times. This means that their gravitational influence on each other is stronger, and this can result in larger TTVs.

During these first analyses on the ExTrA transits, we noticed that having two telescopes observing the same transit at the same time increased the precision up to a few minutes. Knowing that, we used photo-dynamical models to predict the expected amplitude of TTVs from the multi-planetary systems of the WP2. Unfortunately, we don't expect to be able to detect a lot of TTV signals with our current precision.

III.5.3 *Other science cases*

As ExTrA has proven its capability to obtain a good precision when observing very cold targets, we decided to dedicate some observation time to study these objects. To study in details temperate Earth-sized exoplanets, one of the most promising options is the detection of such planets in transit in front of stars that are small and close enough to allow for detailed atmospheric characterization. We started observing a small sample of 5 stars selected from the ultra-cool dwarf target list of the SPECULOOS survey (Sebastian et al., 2021). The photometry has yet to be analyzed as part of this current project.

As part of an internship, we developed an optimal strategy for detecting additional transiting exoplanets called the deep search project (see the Deep search project applied to NIRPS in Section IV.2.2). The main idea was that now that we have access to a large amount of TESS data, we can estimate the number of missed exoplanets orbiting TESS M dwarfs and calculate the cost of detecting them using various velocimetric and photo-

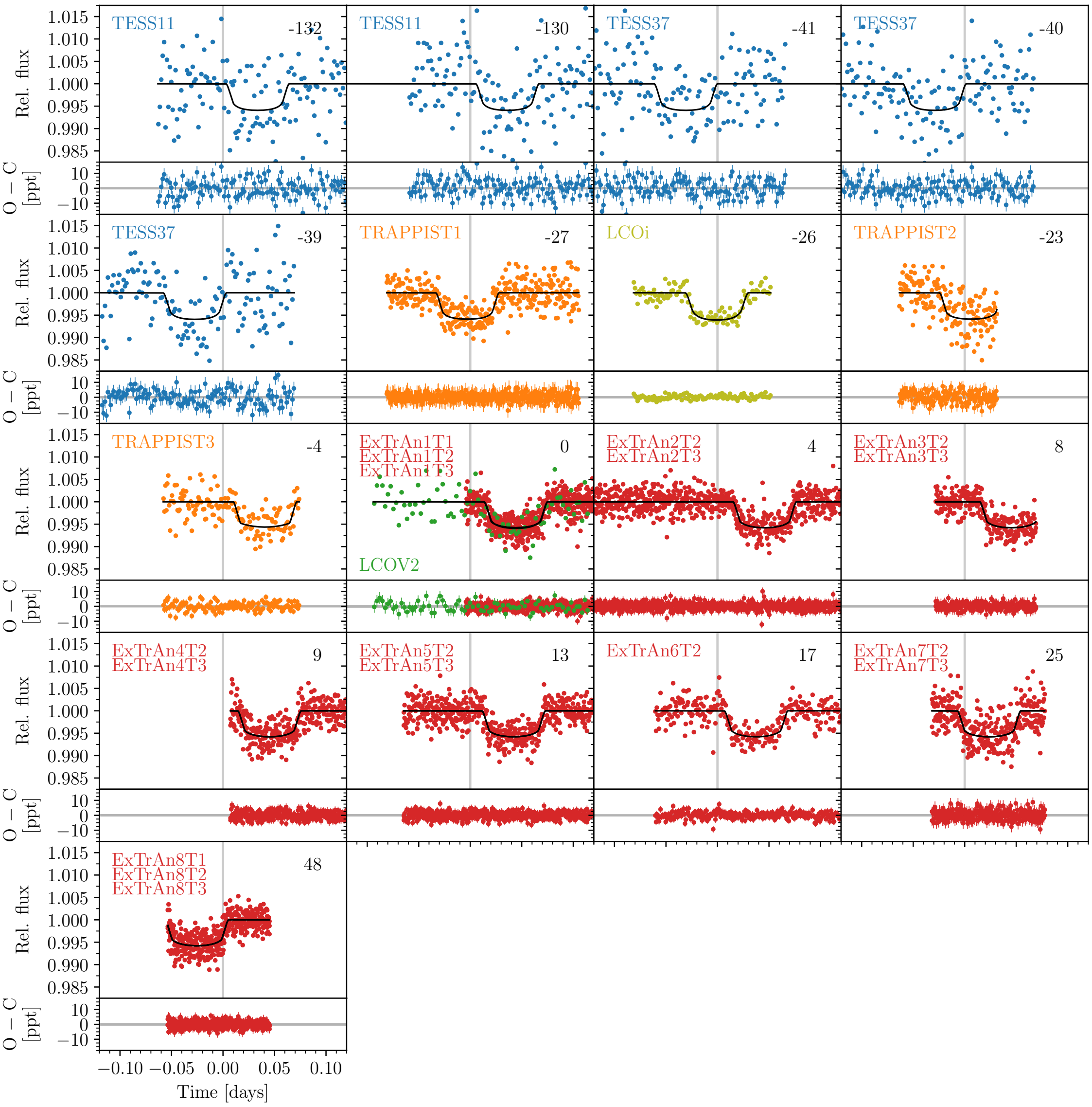

Figure III.17: Transits of TOI-3494.01.
TESS and ground-based photometry used for the dynamical analysis of TOI-3494.01.

metric instruments. The ultimate purpose was to determine how to best utilize a given telescope time in order to maximize the rate of new detections. We are currently applying this technique by observing 7 TESS systems for which we expect additional exoplanets missed by TESS. This is an on-going project and the photometry has yet to be analyzed.

ExTrA also participate in non-exoplanet related projects such as the optical and near-infrared spectro-photometric monitoring campaign to study the stable accretion and episodic outflows in the young transition disk system GM Aurigae (Bouvier et al., 2023).

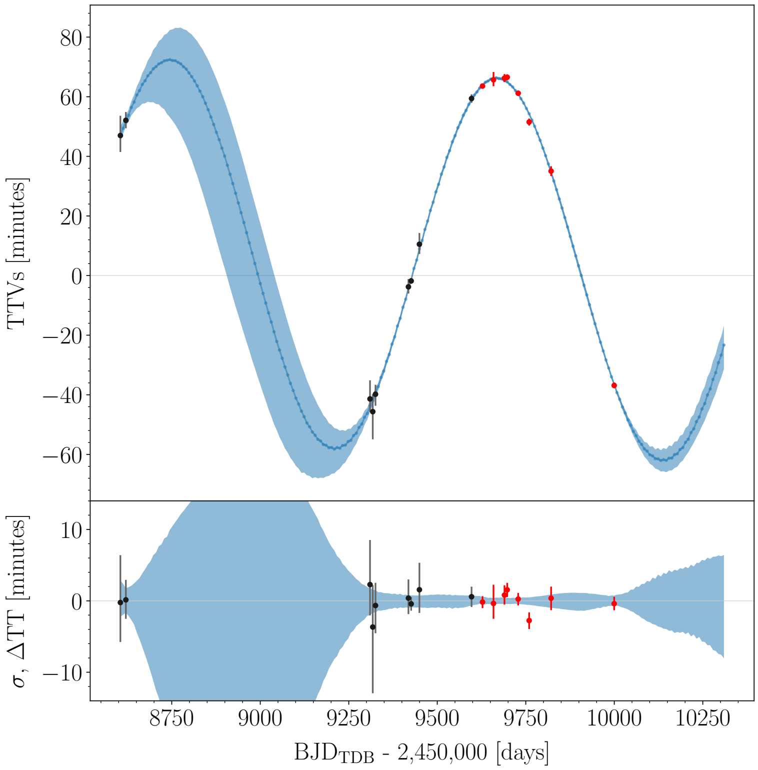

Figure III.18: Photo-dynamical model of TOI-3494.01.
The black dots showed the TESS and ground-based transits, the ExTrA transits are highlighted in red.

The emission lines observed in the ExTrA spectra are presented in Figure III.19.

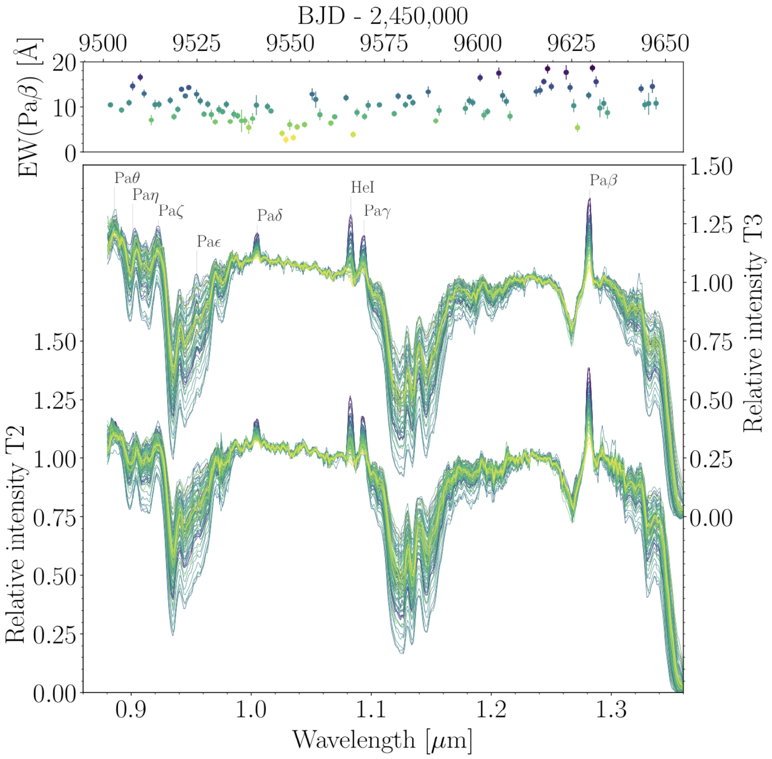

Figure III.19: ExTrA spectra of the young transition disk system GM Aurigae
Median spectrum for each night from the ExTrA-T2 telescope (lower part, 88 spectra) and ExTrA-T3 telescope (upper part, 69 spectra). The main emission lines are indicated. The color is proportional to the equivalent widths of the Paβ line shown in the top panel as a function of Julian date. Credit: Bouvier et al., 2023.

III.6 PRECISION OF EXTRA AND OTHER INSTRUMENTS

Using the observations done with ExTrA for the past few years, we compared the precision of the light curves as a function of the J magnitude of the star and present the results in Figure III.20.

Photometric surveys from the ground are a powerful tool for detecting exoplanets around M dwarfs. Others photometric surveys are also targeting M dwarfs to detect exoplanets but ExTrA is the only one with a near-infrared camera.

MEarth (Irwin et al., 2015) is made up of two robotically controlled observatories. Both MEarth-North and MEarth-South observatories are composed of eight identical telescopes. A 40cm primary mirror on each telescope focuses starlight onto a high-quality CCD camera, which records the infrared brightness of each star. The project has already discovered several interesting planetary systems (Berta-Thompson et al., 2015; Charbonneau et al., 2009; Dittmann et al., 2017), with transits of a few mmag around bright M dwarfs (with J

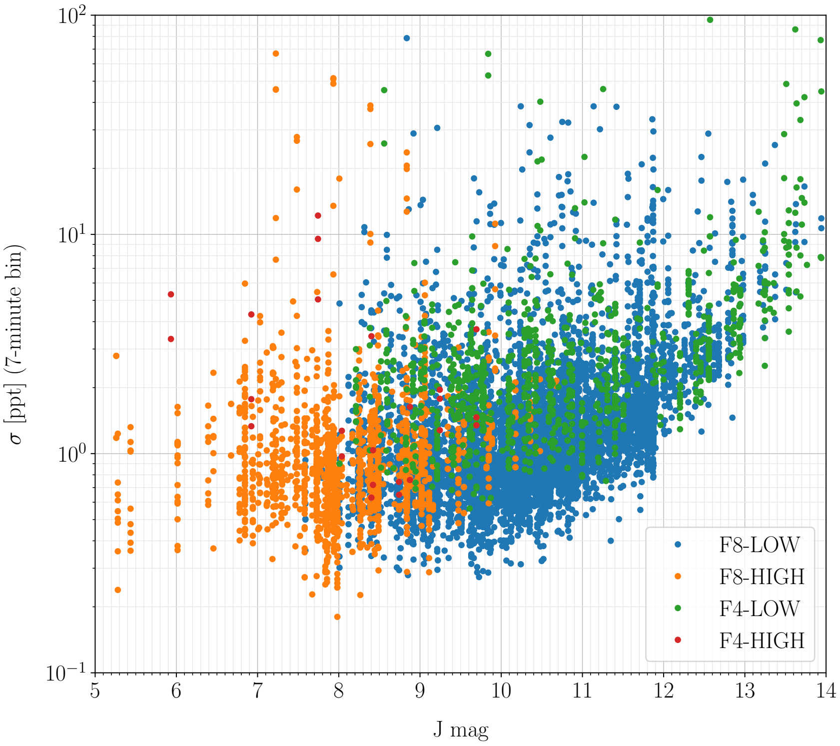

Figure III.20: Precision on the ExTrA light curves as a function of the J magnitude. We used a 30-min sliding window averaging method to correct for the transits and systematics signals.

magnitudes between 9.24 and 9.75).

TRAPPIST (Gillon et al., 2011) is a 60-cm robotic telescope that was installed at the ESO La Silla Observatory in April 2010 (with a similar project in the northern hemisphere). It is equipped with a high-quality CCD camera mounted on a 60cm light weight optical tube. The exoplanet photometry can be done using the broad band filters Johnson B, V , R, Cousins Ic, Sloan z′, and a special ′I + z′ filter. TRAPPIST's most famous discovery is the TRAPPIST-1 system (J=11.35), whose first light curves showed 11 transit-like signatures with amplitudes close to 1% for the three internal planets (Gillon et al., 2016).

The SPECULOOS (Search for habitable Planets EClipsing ULtra-cOOl Stars) project (Jehin et al., 2018) is based at the ESO's Paranal Observatory in Chile's Atacama desert (with a similar project in the northern hemisphere). It consists of four robotic telescopes of Ritchey-Chrétien design, each with a 1 m primary mirror and equipped with near-infrared optimized CCD cameras. The photometric precision of the instrument ranges from a few percents for the faintest detected objects, to a few mmag for intermediate-brightness stars, to ~0.5 mmag for the brightest unsaturated objects (Delrez et al., 2018). Delrez et al., 2022 published the discovery of two temperate super-Earths transiting a nearby late-type M dwarf with a J magnitude of 12.26. After TESS revealed a first candidate with a ∼0.7%-deep transit-like signature, an intense monitoring with SPECULOOS revealed a second transit signal, with a transit depth of about 0.6%.

III.7 OTHER CONTRIBUTIONS TO TESS EXOPLANET DISCOVERY PAPERS

Other members of the ExTrA team led the discovery papers for TOI-177 b also known as GJ 3090 b (Almenara et al., 2022a), a mini-Neptune above the radius valley with a potential second exoplanet detected in the radial velocity data, and TOI-3884 b (Almenara et al., 2022b), where follow-up observations collected by the ExTrA facility and the Las Cumbres Observatory Global Telescope revealed that the transit of the sub-Saturn exoplanet is chromatic and well modeled if the exoplanet orbits a star with a large polar spot (see Figure III.21).

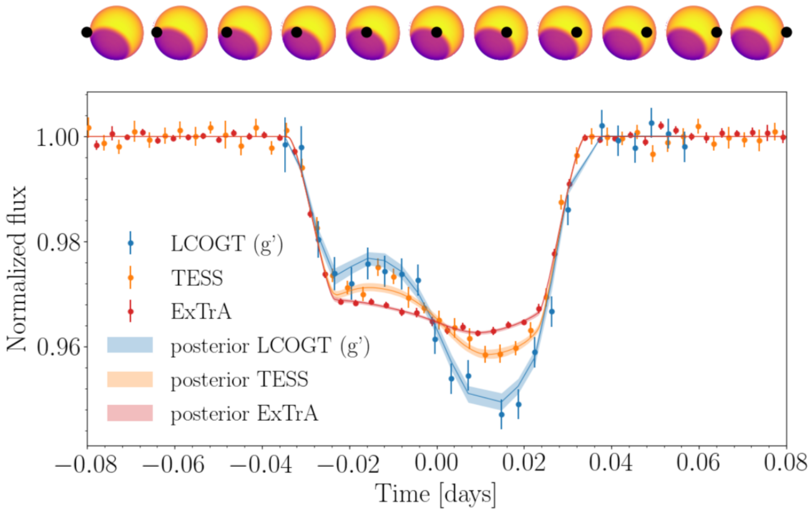

Figure III.21: Chromatic transit of TOI-3884 b.
Phased transits observed by LCOGT, TESS, and ExTrA, and the posterior model of a planet transiting a star with a polar spot. *Above the panel*: Model of the stellar surface and the planet for the median posterior values, as seen by TESS at different times during the transit. Credit: Almenara et al., 2022b.

I also contributed to the following papers by monitoring the TESS planetary candidates and planning the observations with ExTrA when transits were expected to happen, analyzing the photometry and modeling the transit, following the TESS follow-up observation group activities and providing ExTrA light curves to validate the planetary candidate in a near-infrared spectral range, alongside a section describing our observations. These paper led to the discovery of TOI-1231 b (Burt et al., 2021), a temperate Neptune-sized exoplanet and one of the coolest small exoplanets accessible for atmospheric studies so far, TOI-620 b (Reefe et al., 2022), a low-density Neptune-size exoplanet, LP 791-18 d (Peterson et al., Nature paper accepted), where the gravitational interaction with the sub-Neptune LP 791-18 c prevents the orbit of LP 791-18 d from being completely circularized, resulting in continued tidal heating of LP 791-18 d interior and likely strong volcanic activity at the surface as illustrated in Figure III.22, TOI-4306.01 and TOI-4306.02 also known as SPECULOOS-2 b and SPECULOOS-2 c (Delrez et al., 2022), two temperate super-Earths with the second one located within the conservative habitable zone, very close to its inner limit (see Figure III.23), TOI-3235 b (Hobson et al., 2023), a short-period Jupiter-size exoplanet orbiting an M dwarf with a stellar mass close to the critical mass at which stars transition from partially to fully convective, TOI-715 b (Dransfield et al., 2023), an exoplanet located within the most conservative definitions of the habitable zone for rocky planets, TOI-4184 b (Barkaoui et al., 2023), located at the edge of the sub-Jovian desert in the radius-period plane, TOI-4201 b and TOI-5344 b (Hartman et al., 2023), two giant planets transiting M dwarf stars, .

Figure III.22: Artist's view of LP 791-18 d
LP 791-18 d, illustrated here, is an Earth-size world about 90 light-years away. The gravitational tug from a more massive planet in the system, shown as a blue disk in the background, may result in internal heating and volcanic eruptions – as much as Jupiter's moon Io, the most geologically active body in the solar system. Credit: NASA's Goddard Space Flight Center/Chris Smith (KRBwyle).

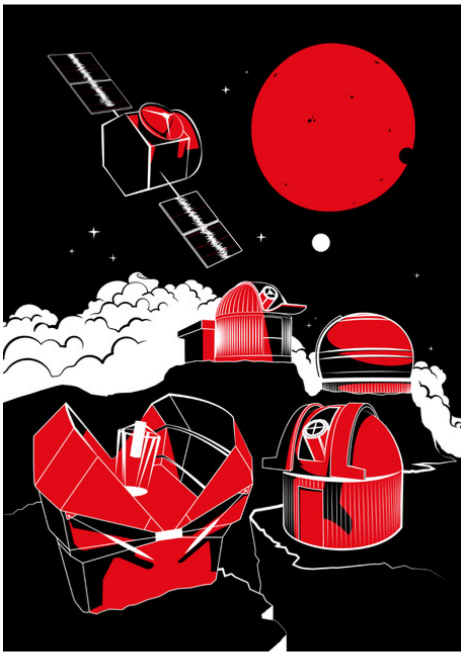

Figure III.23: Artist's view of the detection of SPECULOOS-2 b and SPECULOOS-2 c. Is shown here the red star and its two planets, and some of the telescopes used for the discovery. Credit: University of Birmingham/Amanda J. Smith.

Figure III.24: Artist's view of ExTrA.
Collaboration between Joana De Almeida Pereira, student at the École supérieure de bande dessinée et d'illustration (ESBDI) de Genève and myself.

IV

THE NEAR-INFRARED SPECTROGRAPH NIRPS

"We know it all by heart
The whole is greater
Than the sum of its parts
We heard it all before
And beauty there echoes
The speck of our souls"
Bad Blood by Sleeping At Last

INTRODUCTION

In the study and characterization of exoplanets, radial velocity measurements are complementary to the photometry to obtain the mass of the planetary companion and therefor estimate its bulk density. The Near Infrared Planet Searcher, abbreviated "NIRPS," is a spectrograph designed to observe in the near-infrared spectral domain from the southern hemisphere. The main goal of NIRPS is to perform precise radial-velocity follow-up on transiting planet candidates identified by space missions, sometimes already validated using ground-based photometry, and especially to monitor M dwarfs in order to find and characterize small exoplanets, including rocky exoplanets, in the habitable zone of their host star. In May 2015, ESO invited the NIRPS team to adapt the original NIRPS design for simultaneous observation with the HARPS spectrograph at the Cassegrain focus of the ESO 3.6-meter telescope at La Silla Observatory.

IV.1 OVERALL DESCRIPTION OF THE INSTRUMENT

NIRPS is a fiber-fed cross-dispersed echelle spectrograph equipped with adaptive optics and located in a cryogenic vacuum tank in the Coudé floor of the 3.6-m telescope at La Silla Observatory in Chile (see Figure IV.1). NIRPS is observing in the Y, J, and H-bands with a wavelength range of 0.971-1.854 μm, which corresponds to 70 orders in one single exposure. We expect it to deliver radial velocities with a precision of around 1 m/s. The spectrograph has a compact design for better thermal stability. A more detailed description of the instrument can be found in Bouchy et al., 2017; Wildi et al., 2022.

Figure IV.1: NIRPS tank.
Cylindrical cryogenic chamber within which the NIRPS optical parts are installed. The cryogenic chamber keeps the components in a vacuum environment and cooled down to a freezing -190 degrees Celsius.

NIRPS is composed of four different subsystems: the front-end connected to the 3.6m telescope, the calibration unit, the fiber link, the spectrograph. A schematic of the subsystems is presented in Figure IV.2.

The front-end is made up of various sub-modules that are located in a base plate that is connected directly to the 3.6-m telescope's Cassegrain rotator (Blind et al., 2022). It extracts the 700 nm to 2400 nm wavelength range from the telescope beam using a dichroic and corrects for atmospheric dispersion. A dichroic filter is a type of color filter that selectively allows certain wavelength band to pass while reflecting others. The visible light is routed directly into the HARPS Cassegrain Fiber Adapter or "bonnette" as it was before NIRPS, and the near infrared light goes into the NIRPS fibers. Even if telescope pointing and guiding are perfect at a given reference wavelength, atmospheric dispersion shifts the image centroid at different wavelengths, affecting fibre injection. As a result, an Atmospheric Dispersion Corrector (ADC) is required to meet the instrument requirements (Cabral et al., 2022).

NIRPS is the first spectrograph with an Adaptive Optics (AO) system (Conod et al., 2016). The instrument is equipped with a multi-mode fiber (also called few mode fiber), which is much less affected by AO correction residuals than a single-mode fiber, allowing for a better coupling efficiency in degraded seeing and on fainter targets with relaxed AO specifications (Blind, Conod, and Wildi, 2017). NIRPS couples starlight into a fiber corresponding to 0.4" on the sky as efficiently or better than HARPS or ESPRESSO couples

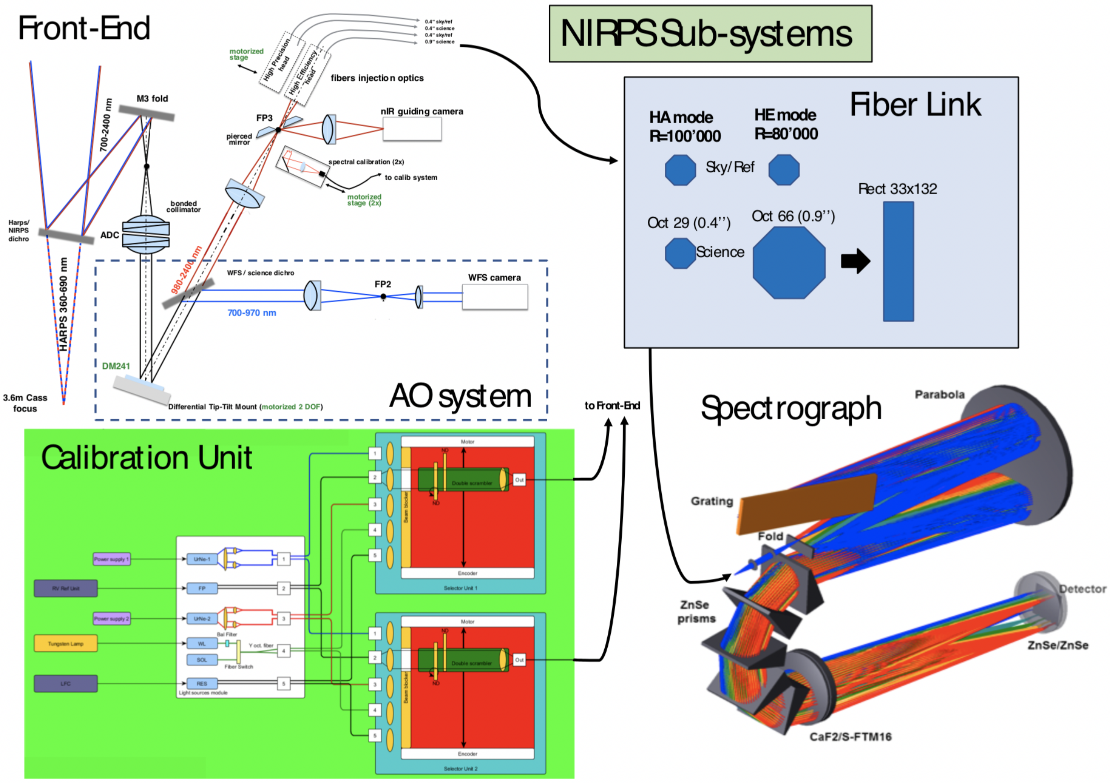

Figure IV.2: NIRPS subsystems.
The different subsystems are presented here : the Front-End, the Calibration Unit, the Fiber Link and the Spectrograph

light into a 1.0" fiber thanks to the high-order AO system. This allows the spectrograph to be much smaller, more thermally stable, and less expensive (Wildi et al., 2017). The AO system is built using a wavefront sensor operating between 700 and 950 nm coupled to a deformable mirror with a loop frequency ranging from 250 to 1000 Hz for scrambling. However, the tip-tilt scan of the fiber tip appeared to be the most efficient scrambling strategy with the AO of NIRPS: it preserves coupling into fiber and can couple to any given mode of the fiber, in contrast to other classical optical aberrations (Blind, Conod, and Wildi, 2017). The AO system works up to magnitude of I = 14.5. The spectrograph is very compact thanks to the AO system, which allows for a reduction of a factor of two in fiber size.

The fiber link converts the front-end's beam and injects it into an optical fiber that transports light to the spectrograph, with the possibility to scramble the light. Scrambling the light is useful to stabilize the position of the light's photo-center to a fraction of the fiber diameter. It has two observation modes. The High Accuracy (HA) mode, which uses a 0.4 arcsec octagonal fiber to achieve a spectral resolution of ∼82'000. The High Efficiency (HE) mode, which uses a 0.9 arcsec octagonal fiber that is sliced in two halves at the pupil level and feeds a rectangular fiber to achieve a spectral resolution of ∼75'000. Both observing modes, HA and HE, have a 0.4 arcsec simultaneous reference fiber for sky or drift (using the Fabry-Perot) measurement. The reference fiber collects sky light through a second hole 37 arcseconds away from the main scientific target and invisible to the nIR guiding camera. The other option is to track instrumental drifts using the Fabry-Perot. This mode was designed for high SNR scientific exposures where the limiting factor is not the photon noise on the target but potential instrumental drifts within the spectrograph.

The fiber stretcher is a device that reduces the impact of modal noise in few mode fibers by rapidly modulating phase between modes and homogenizing output illumination. This allows for a significant reduction in the impact of external factors and the stabilization of the cross-correlation function between the measured spectrum and the mask from one observation to the next, avoiding drifts and noise of more than 1 m/s. Optical fibers (and even more non-circular ones) are known for their excellent near-field scrambling properties, which led to the very successful concept of a double scrambler, which exchanges near and far-field properties and scrambles both efficiently. One advantage of the double scrambler is improving grating illumination stability. From the standpoint of RV stability, it appears that the stretcher and AO scrambling each provide an increase in stability, down to about 1 m/s. When they are combined, they accumulate to first order and stability drops to a few tens of centimeters per second. The HA mode was the first equipped with fiber stretcher and AO scrambling, and demonstrated a higher stability of modal noise pattern over a day and for varying telescope pointings which is why it was decided to add a fiber stretcher for all fibers (Blind et al., 2022).

The spectrograph is located at the back-end within a cryostat. The cryogenic enclosure is kept at 80 K and at a pressure of 10^{-6} mbar. A parabola collimates the fibre beam and relays it to the echelle grating. The grating distorts the collimated beam, which is then redirected to the parabola. The diffracted collimated beam is focused by the parabola and folded back to the parabola by the flat mirror. The parabola brings the diffracted beam together with the cross disperser, which is made up of 5 refractive prisms that rotate the beam by 180 degrees. The diffracted and cross-dispersed beam is focused on the detector by the refractive camera (see Figure IV.2) . The spectrograph is fed by two fibers : a object fiber and a reference fiber, and forms the spectra of the light from both fibers side by side on the detector. The NIRPS detector is a 4096×4096 pixels high-performance infrared focal plane array Hawaii-4RG (Thibault et al., 2022). The exposure meter algorithm uses individual reads of 5.5733 sec to measure the stellar flux and the mid-time of the exposure. The conversion factor of the NIRPS's detector is $\sim$1.27 e-/ADU and the saturation level is fixed to 45'000 ADU/pixel on the data reduction pipeline.

The calibration unit is very similar to the ESPRESSO one (see ESPRESSO User Manual and Pepe et al., 2021). There are different calibration sources available for the spectrograph : a uranium-neon hollow-cathode lamp, a stabilized Fabry-Perot etalon and a laser frequency comb is expected for 2023. The light from the calibration source can be fed into either of the two fibers ('object' or 'reference').

HARPS and NIRPS will observe simultaneously most of the time, even though NIRPS can be used alone. This will allow to construct a single powerful high-resolution, high-fidelity spectrograph covering the range of 0.37 to 1.85 micron. As radial velocities in the near infrared are less affected by stellar spot variations than in the visible, this combination will allow for better calibration of stellar activity.

The Top level requirements of NIRPS were initially for the spectrograph to ensure high radial velocity precision and high spectral fidelity at the level of 1 m/s in less than 30 min for an M3 star with a magnitude of H=9. These requirements would enable to achieve the science goals outlined in Section IV.2.1.

Comparison with other near-infrared spectrographs

While optical precise radial velocity has reached 1 m/s accuracy for a number of instruments (e.g., HARPS (Pepe et al., 2002), ESPRESSO (Pepe et al., 2021)), near-infrared precise radial velocity (primarily Y, J, H, and, for some instruments, K band) is still in its early stages. Several near-infrared instruments (e.g., SPIRou (Donati et al., 2020), CARMENES-IR (**quirrenbach2018**), HPF (Kanodia et al., 2018), IRD (Hirano et al., 2020; Kotani et al., 2018), GIANO-B (Origlia et al., 2014)) have seen first light in recent years. These spectrographs are presented in Table IV.1. NIRPS is however the only one in the Southern Hemisphere.

Table IV.1: Near-infrared spectrographs.

Instrument	Telescope	Wavelength coverage	Resolution	Fiber diameter	Precision	Specificities
NIRPS	ESO 3.6 m	0.95-1.8 microns	$\sim$75 000-$\sim$90 000	0.4" or 0.9"	$\sim$1 m/s	Adaptive Optics, combined with HARPS
SPIRou	CFHT 3.6 m	0.95-2.35 microns	$\sim$75 000	1.3"	$\sim$2 m/s	Spectro-polarimetry
CARMENES-IR	Calar Alto Observatory 3.5 m	0.96-1.71 microns	$\sim$80 000	1.5"	5-10 m/s	combined with CARMENES-VIS
HPF	Hobby-Eberly Telescope 10 m	0.81-1.28 microns	$\sim$53 000	1.7"	$\sim$1.53 m/s	
IRD	Subaru 8.2 m	0.97-1.75 microns	$\sim$75 000	0.48"	$\sim$2 m/s	
GIANO-B	TNG 3.5 m	0.9-2.45 microns	$\sim$50 000	1"	$\sim$10 m/s	combined with HARPS-N

IV.2 PROPOSALS FOR THE NIRPS GUARANTEED TIME OBSERVATIONS

Guaranteed Time Observations is granted for providing hardware or software that improves ESO's scientific capabilities. The total number of GTO nights granted to the NIRPS team is 725 nights that will be scheduled over the first 5 years of operation of the instrument (2023 - 2028).

IV.2.1 *Overview of the scientific work packages*

NIRPS was designed to investigate different aspects offered by M dwarfs as exoplanet hosts, with a focus on three main science cases : the Work Package 1 to do a blind radial velocity survey for exoplanets orbiting M dwarfs to find golden targets for direct imaging studies with future extreme adaptive optics imagers on the ELT, the Work Package 2 to measure the mass and deduce the density of transiting exoplanets around M dwarfs, and the Work Package 3 to characterize exoplanets atmospheres via high-resolution transmission spectroscopy.

WP1

The proposed blind radial-velocity search for exoplanets around low-mass stars is an ambitious project to understand planet formation, particularly its sensitivity to initial conditions in the proto-planetary disk, and identify Earth-like exoplanets for future in-depth atmospheric characterization and direct imaging. The time allocated was divided in three major scientific themes in order to complete this ambitious radial velocity blind search.

One goal of this project is to find the most promising Earth-like exoplanets for future atmospheric characterization and high-contrast imaging using the next generation of world-class observatories. The objective is to compile a comprehensive list of such systems, with a particular emphasis on planetary systems orbiting nearby M dwarfs, which provide the best targets due to their contrast and separation. This census is important for the 2027-2030 horizon because the upcoming Extremely Large Telescopes (ELTs) will provide a opportunity to study the atmospheres of non-transiting exoplanets (Birkby et al., 2013; Snellen et al., 2015). Through transmission spectroscopy and reflected light, ANDES at the ELT will be able to characterize much lower mass planets, including rocky planets orbiting nearby M dwarfs, and detect bio-markers in their atmospheres (Marconi et al., 2020). While exoplanets have been discovered around our nearest stellar neighbors (Anglada-Escudé et al., 2016; Astudillo-Defru et al., 2017; Bonfils et al., 2013), the list around the nearest M dwarfs is far from complete. The NIRPS sample aims to fill this gap by including nearby M dwarf stars that have received insufficient precise radial velocity observations to constrain planetary candidates, as well as known planetary systems for which the NIRPS and HARPS wavelength coverage will provide improved sensitivity due to its unprecedented stellar activity filtering.

A second goal of the WP1 is understanding the formation and evolution of planetary systems, which requires the identification of their global architecture. Despite knowing over 5000 exoplanets, our understanding of planetary systems' inner and outer regions is still incomplete. To better understand the coupling of these regions during the formation and evolution of planetary systems, NIRPS will combine three approaches. First, we will employ a deep search strategy (see as an example Ballard et al., 2011) to conduct RV follow-up on known transiting planetary systems in the vicinity of M dwarfs (see a detailed description of this approach in Section IV.2.2). Second, we'll begin characterizing 18 M dwarfs with at least one cold massive planet beyond the ice-line in order to probe their inner region. This will allow us to confirm the two families of scenarios proposed to explain the presence of super-Earths and Neptunes in our solar system : the inward-migration theory (Alibert et al., 2006) and the in-situ formation theory (Chiang and Laughlin, 2013). The systems' architectures with cold Jupiters will be used to validate such scenarios. Finally, we will begin radial velocity monitoring of controversial multi-planetary systems in order to better understand the impact of stellar activity and the importance of the rotation period (see Robertson and Mahadevan, 2014b as an example).

The study of planets orbiting low-mass stars is essential for understanding planetary formation and the physical processes involved, such as orbital migration and accretion (Alibert and Benz, 2017). The temperature and mass of the star are extremely important in determining the initial conditions in the proto-planetary disk, which affects planet formation. Super-Earths with orbital periods of less than 100 days have been found to be more common around early-to-mid M dwarfs than around Sun-like stars (Bonfils et al., 2013; Sabotta et al., 2021). We propose to use NIRPS's near-infrared capabilities to detect and precisely work on previously unseen targets such as ultra-cool dwarfs, young and active M dwarfs, close binaries, and dust-emitting young dwarfs. We will observe ultra-cool dwarfs, stars that are too faint to observe with HARPS or ESPRESSO in the optical domain, which will significantly expand the parameter space explored by precise radial velocity and allow for the most precise study of the impact of stellar mass on planetary formation. We will also conduct a blind search for new planetary systems around single and binary young stars, allowing us to distinguish the effects of planetary formation from those of secular evolution (long-term dynamical evolution, mean motion resonance configuration, change of eccentricities distribution). We expect to obtain a larger sample of age-calibrated exoplanet systems due to the efficiency of infrared velocimetry in filtering out the impact of activity, which is critical for detecting planets around young and active stars (Cale et al., 2021; Donati et al., 2016). This focused search for planets will help answering fundamental questions about exoplanets, such as the effects of planetary migration on final orbital architectures, interactions with proto-planetary and debris disks (Baruteau et al., 2014), and the stability of habitable atmospheric conditions over time.

The proposed targets for P111 starting in April 2023 are presented in Figure IV.3.

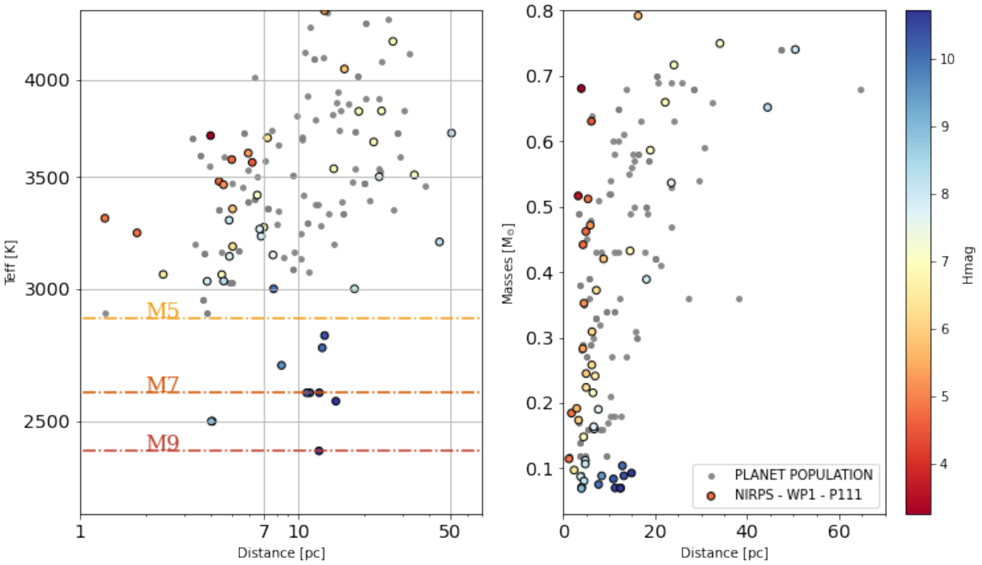

Figure IV.3: NIRPS WP1 project.
Masses and effective temperature as a function of the distance: known exoplanets around cool stars. The stellar sample selected in WP1 for P111 is presented here. Data retrieved from exoplanets.eu, March 27, 2023.

WP2

Measuring the precise mass of transiting exoplanets is critical to constrain their internal structure. Exoplanets smaller than 4 R_E, also called super-Earths and sub-Neptunes, have been found to be the most common type of exoplanets in the solar neighborhood, according to the Kepler and TESS surveys. But these small exoplanets have a bimodal distribution (Fulton et al., 2017), which is likely related to various atmospheric escape mechanisms. NIRPS will conduct a mass characterization program for the small transiting exoplanets orbiting mid-to-late type M dwarfs, primarily detected in transit using the TESS photometry and ground-based follow-up programs. This program will pave the mass-radius diagram of multi-planetary systems (see Figure IV.4), provide mass measurements of a sample of temperate small exoplanets amenable to atmospheric characterization with JWST and even obtain ultra-precise mass measurements of a sample of rocky exoplanets with the goal of constraining their core mass fraction.

The Kepler and TESS space missions have greatly expanded our understanding of exoplanets, revealing that super-Earth and mini-Neptune systems are common in the universe. To gain a better understanding of exoplanets, we must first understand the diverse nature of planetary systems, their formation, and individual planet properties. Exoplanets transiting M dwarfs are especially interesting in this regard because their small size and low irradiation levels allow us to detect smaller and cooler planets more easily than those orbiting larger, hotter stars. The environment for planet formation around M dwarfs, on the other hand, differs from that of Solar-type stars due to their longer hot proto-stellar phase, lower proto-planetary disk mass, and intense activity at young ages, which may affect the formation and composition of the planets they host. This second program aims to determine the mass, bulk density, and bulk composition of exoplanets transiting M dwarfs across a wide range of parameters in order to gain insight into the formation and evolution of M dwarf exoplanets. Seven complementary sub-programs are planned to achieve this goal.

It is unusual to find massive exoplanets orbiting M-type dwarf stars. According to recent planetary population synthesis models based on core accretion theory, the likelihood of finding such planets is extremely low, and may even be zero (Burn et al., 2021), due to insufficient mass density and longer orbital times around low-mass stars (Laughlin, Bodenheimer, and Adams, 2004). Despite the fact that the occurrence rate is much lower than that of FGK stars, there are five well-known examples of these planets orbiting M dwarfs and Bryant, Bayliss, and Van Eylen, 2023 identified fifteen potential giant planets from the TESS survey. Gaining a better understanding of these giant planets' formation processes necessitates validating and measuring their masses as they form.

Recent research indicates that close-in M dwarf systems have more low-mass planets than Solar-type stars (Bonfils et al., 2013; Dressing and Charbonneau, 2015), but it is unclear how the differences in M dwarf environments affect the composition of planets with a given radius. Although M dwarfs are thought to produce more rocky planets than volatile-rich planets (Cloutier and Menou, 2020), the density of sub-Neptunes around M dwarfs appears to be lower than that of other stars. Understanding whether these planets continue to have low densities or have higher densities will provide important information on the formation of M dwarf planets. Furthermore, planets' atmospheric escape is more efficient around lower mass stars (Kubyshkina and Vidotto, 2021). It is critical to study exoplanets transiting mid-to-late M dwarfs and populate the mass-radius diagram with their data to gain a better understanding of the impact of stellar mass on the occurrence and bulk composition of exoplanets (see the detailed project in Section IV.2.3).

The radius valley is an important indicator of planet formation and evolution. It is found at slightly smaller radii around M dwarfs than around Sun-like stars and marks the transition from rocky Super-Earths to gas-enveloped terrestrials (Cloutier and Menou, 2020; Fulton et al., 2017). Several physical mechanisms have been proposed to explain the emergence of the radius valley, including thermally-driven atmospheric mass loss (Gupta and Schlichting, 2020; Jin and Mordasini, 2018; Wyatt, Kral, and Sinclair, 2020) and the planet formation process (Lee and Connors, 2021; Lopez and Rice, 2018). The radius valley's slope with respect to the orbital period gives direct insight into its origin. Cloutier and Menou, 2020 observed that the radius valley separating rocky and gaseous planets has a negative slope with insolation around low-mass stars, supporting models of direct formation of terrestrial planets in a gas-poor environment. The slopes of the gas-depleted formation and thermally-driven mass loss models produce a subset of the Period-Radius parameter space with opposing predictions about the bulk composition of planets in that subspace. The bulk composition of transiting exoplanets must be characterized to determine whether the M dwarf radius valley results directly from planet formation or from post-formation atmospheric escape.

Planetary mass and radius measurements, particularly the iron core mass fraction, can provide valuable information about the internal structure of terrestrial exoplanets. Precise mass measurements for transiting planets smaller than 1.7 R_{Earth} (Cloutier and Menou, 2020) using the precise radial velocity measurements have revealed that many rocky planets have compositions similar to Earth, with a 33% iron core and a 67% silicate mantle. However, there is some variability in the internal compositions of small planets, as they appear to have a wider range of Fe/Si ratios than their host stars (Adibekyan et al., 2021; Plotnykov and Valencia, 2020), which have a high degree of homogeneity in Mg/Si and Fe/Si abundances (Bedell et al., 2018). This difference asks the question of whether the differences in stellar abundances and rocky planet compositions are real and important for understanding terrestrial planet formation, or if they are simply the result of imprecise inferences about planet compositions. To address this issue, ultra-precise planetary mass measurements and core mass fractions with an absolute uncertainty of 10% are required.

The transit of exoplanets in the habitable zone can be studied more effectively around M-dwarfs, which have a lower mass than Sun-like stars. This is because the smaller size of M-dwarfs generates radial velocity signals in meters per second rather than centimeters per second, allowing the mass of Earth-size planets to be determined. Furthermore, due to their lower luminosity, M-dwarfs have a closer-in habitable zone, resulting in relatively short orbital periods of 10-30 days. The discovery of exoplanetary systems containing an M-dwarf host and a transiting exoplanet within or near the HZ represents a fantastic opportunity for additional atmospheric characterization using the James Webb Space Telescope (JWST). These systems may even reveal new types of potentially habitable planets, with a rocky core covered by a thick water ocean (Lillo-Box et al., 2020), and Hycean worlds, which have an H2 atmosphere on top of a condensed H2O-rich interior (Madhusudhan, Piette, and Constantinou, 2021). However, in order to probe the atmospheres of temperate super-Earths and mini-Neptunes with JWST, prior knowledge of their mass is required, as this parameter is critical for correctly interpreting their transmission spectra (Batalha et al., 2019).

When compared to single-planet systems, studying multi-planetary systems can provide more robust tests for planetary formation theories (Ballard and Johnson, 2016; Fang and Margot, 2012; Steffen and Hwang, 2015). The sizes of exoplanets in multi-planetary systems have been discovered to be correlated, and there is frequently regular spacing between the planets, a theory known as "peas in a pod." This phenomenon has been used to constrain models of planet formation. Recent research (Otegi, Helled, and Bouchy, 2022) found that for M-dwarfs, the multi-planetary systems are more similar in density than in mass, indicating that they formed in a similar manner. In addition to multi-planetary system architecture, the internal structure of planets within the same system can provide valuable information for constraining models. Because they share the same host star and accretion disc, differences in composition are determined solely by their birth and evolution locations. Determining the bulk composition of planets in multi-planetary systems, as well as estimating the presence of volatiles and liquid/solid water, can help test planetary formation hypotheses and determine if there is a link between stellar and planet composition.

In recent decades, the detection and characterization of exoplanets has favored older planets, with the majority of observed planets being more than 1 Gyr old (Berger et al., 2020). Observing and characterizing younger planets transiting M dwarf stars is of great interest because it allows us to study the early stages of planetary evolution and gain a better understanding of how mature planets form. Many planetary properties will change over time as a result of various processes such as migration, gravitational contraction, atmospheric heating, mass loss, and core-envelope interactions. Young planets provide snapshots of the first few hundred million years of planet formation, when physical properties and system architectures evolve the fastest (Owen and Wu, 2013). As a result, probing a population of younger planets is important for constraining planetary system formation and evolution models. Young exoplanets, despite their scientific importance, are difficult to detect, due to the active nature of their host stars. Recent studies have focused on relatively young planet-hosting systems, and while obtaining precise masses of young planets remains a significant challenge (Plavchan et al., 2020), it is useful to continue these efforts. Near-infrared radial velocities are less affected by spot-driven stellar activity than traditional visible radial velocities (Carleo et al., 2020). However, some young M dwarfs emit stellar flares, which may affect the exoplanet atmosphere (Airapetian et al., 2020). It is therefore important to detect and characterize planets transiting flaring M-dwarfs in order to understand the impact of stellar activity on planetary formation and atmospheric erosion.

WP3

The in-depth look into exoplanets through high-resolution time-series spectroscopy will help understand the chemistry and dynamics of exoplanet atmospheres and their orbital architectures. NIRPS will observe the atmospheres of a population of exoplanets across a large range in mass, radius, irradiation, age, and the host star spectral type (see Figure IV.5). The precise chemical inventories, Temperature-Pressure profiles, mass-loss rates, as well as dynamical and orbital constraints will reshape the field towards population-based studies built on a uniform data acquisition, reduction, and analysis strategy.

While exoplanet detection and characterization are the main scientific objectives of NIRPS, a number of other significant science projects are planned including dynamical studies of ultra-cool dwarfs in young moving groups and stellar variability studies that attempt to measure minute variations in line profiles, such as Doppler imaging of ultra-cool stars and brown dwarfs. NIRPS will also be able to identify nearby stellar component and blended binaries using the AO guiding camera, and monitor the Sun observed as a star

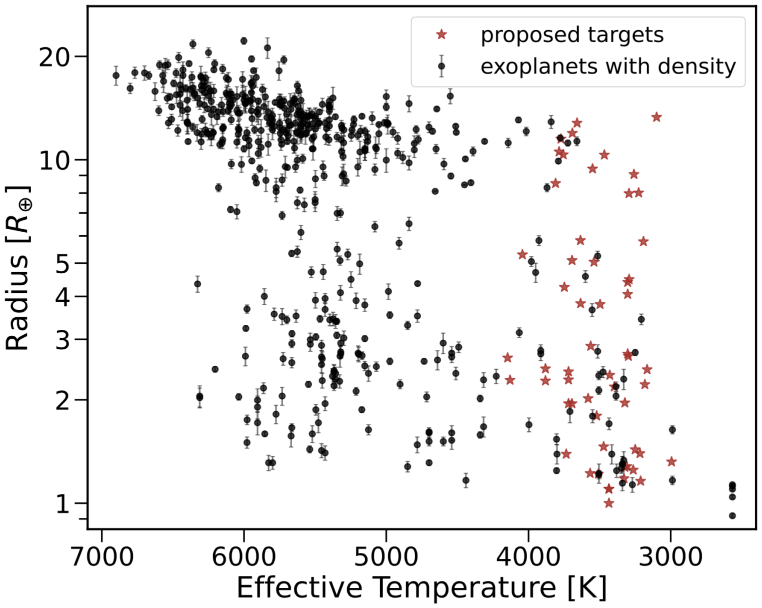

Figure IV.4: NIRPS WP2 project.
Radius versus host star effective temperature of exoplanets with mass precision $<$ 25% and radius precision $<$ 8% from PlanetS catalog extended from Otegi, Bouchy, and Helled, 2020. The WP2 targets for P111 (first period of the GTO) are shown with red stars.

using the HELIOS solar telescope (see Figure IV.6).

Other science cases already proposed for the NIRPS GTO involve the improvement of metallicity determination of M dwarfs with FGK binaries by creating a library of high signal-to-noise near-infrared spectra from a sample of FGK and M type binaries and obtaining coherent metallicities and abundances for the M dwarfs; and the study of radial-velocity variations in cool giants to disentangle exoplanets signals from stellar activity. Acquiring precise RV on these cool stars will allow us to learn whether more massive stars tend to form more massive exoplanets and the role of metallicity in this process, and to investigate the planetary architecture properties at different stellar evolutionary stages.

My contribution to the NIRPS GTO

I contributed to the NIRPS GTO by proposing two different programs related to the WP1 and WP2, described in detail in the next sections. In addition to proposing these two different programs, I also participated in the preparation of the upcoming first semester of observations with NIRPS. As I am involved in WP1 and WP2 through my proposals, I also played an active role in the planning and coordination of the observation schedule for these two work packages. I collaborated closely with other team members of NIRPS to ensure that the observation time was optimized and allocated appropriately based on the target's priority level. To achieve this, I provided and regularly updated important parameters for

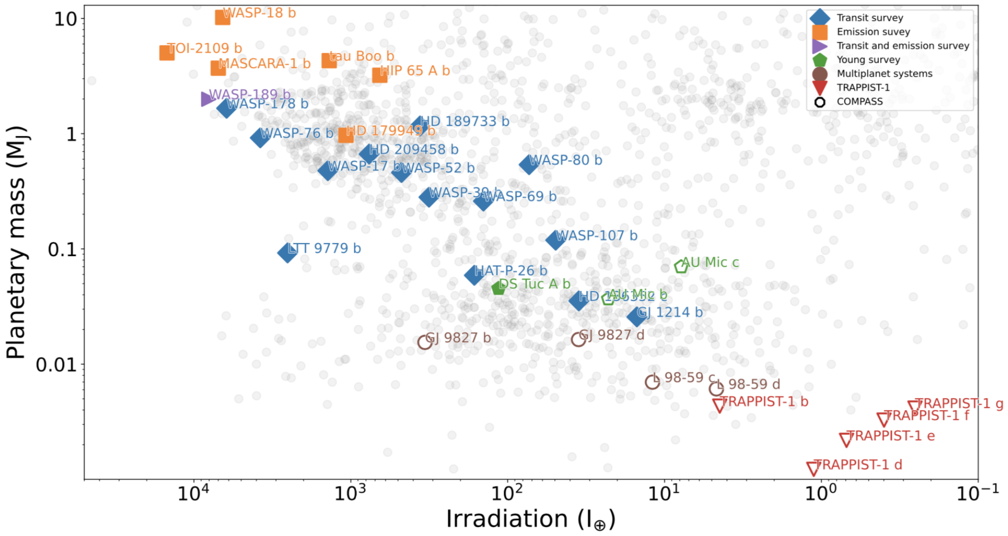

Figure IV.5: NIRPS WP3 project.

Exoplanet population in a mass-irradiation diagram. The exoplanets to be observed in P111 are highlighted for the different sub-packages within WP3. COMPASS (Characterizing Obliquities for a Multi-Planetary Architectures System Survey) investigates the frequency of mutually-misaligned small exoplanets orbiting the same star.

Figure IV.6: Picture of HELIOS.

HELIOS feeds sunlight via fibre optics to the HARPS and NIRPS spectrographs, improving its exoplanet detection techniques while improving our understanding of stellar activity.

the selection of priority targets to be observed by sharing information obtained as part as the TFOP group and searching for additional information on the targets using the Gaia data.

IV.2.2 *Deep Search for additional exoplanets with NIRPS*

IV.2.2.1 *General overview of the project*

This project was mainly completed during the internship of Augustin Patey entitled "Toward an optimal strategy to detect exo-Earths in transit". The TESS telescope presented in Chapter II is currently using the transit method to detect exoplanets. Ballard, 2019 proposed an estimate of the number of exoplanets that would be detected by TESS around M dwarfs, as well as the number of exoplanets that TESS would have missed. The main idea of this project was, using the TESS data that we currently have, to estimate again the number of missed exoplanets around TESS M dwarfs and compute the cost of detecting them using a variety of velocimetric and photometric instruments. The final step was to figure out how to best use given telescope time to maximize the rate of new detections.

Assuming a planet's orbit has a uniformly distributed orientation, the probability of it being oriented to transit is such that only a fraction of existing exoplanets can be detected using this method. Despite this unfavorable statistic, exoplanets' orbits within the same planetary system tend to be relatively coplanar ($\sim 2°$). As a result, for a given star, one transiting exoplanet detection biases the statistic for potential other exoplanets orbiting the star in favor of a well-oriented orbit. We developed a survey strategy that targets systems known to have a favorable orientation (meaning a transiting exoplanet), optimizing the rate of new detections. Unlike traditional blind searches, we refer to this strategy as the deep search for transiting exoplanets.

Deep searches to find additional exoplanets have already been conducted for a few stars and both photometry and RV follow-ups of transiting systems have successfully detected additional transiting exoplanets (e.g. Trappist-1 system (Gillon et al., 2017; Luger et al., 2017) or LHS 1140 system (Lillo-Box et al., 2020)).

For this project, we used the list of all transiting systems from TESS candidates orbiting M-dwarfs presented in Section II.3 and determined their likelihood of hosting more exoplanets than those already discovered. To do this, we created fictive planetary systems based on known statistical distributions (Dressing and Charbonneau, 2015 for the occurrence rate and Ballard and Johnson, 2016 for the planet multiplicity). Our simulations are anchored to real TESS systems by using the prior knowledge we have on the single or multiple planetary candidates already detected by TESS, as well as the prior knowledge we have on stellar properties detailed in Section II.3. We used the Hill criterion to ensure that the fictive systems were stable. The Hill criterion is an analytic criterion for the critical separation in a two-planet system, beyond which the system is Hill stable and the exoplanets will never have a close encounter (Gladman, 1993). We used the modeling of TESS light curves (described in Section II.4) in order to derive impact parameters and therefore better constrain the orientation of the systems. We removed fictive exoplanets that would have appeared in TESS light curves and we kept only those below TESS sensitivity.

An occurrence map of additional exoplanets

Our first goal is to estimate how likely additional exoplanets are to exist within a given known TESS planetary system and how likely it is for these exoplanets to transit. Monte-Carlo simulations are used to generate fictive systems in which trials always start with a given star and its already known exoplanets, and additional exoplanets are randomly generated based on multi-planetary system statistics.

Ballard and Johnson, 2016 distinguish two types of planetary systems called the Kepler Dichotomy: those with a few exoplanets (1 to 2 per system) and a high mutual inclination ($> 8°$), and those with more exoplanets (above 5 per system) and a lower mutual inclination ($\sim 2°$). For the deep search strategy, we will only focus on the second type of planetary systems as we are interested mainly in discovering new (transiting) planet candidates. Johansen et al., 2012 gives us the ability to identify and discard some of this first population's exoplanets. They discussed that exoplanets larger than $\sim 4R_{Earth}$ belong exclusively to single transiting systems, and thus to systems with either one exoplanets or more exoplanets but high mutual inclinations. The majority of planet candidates in our input catalog have radii less than $6R_{Earth}$, with a smaller fraction ranging from 6 to 30 R_{Earth}. For our analysis, we decided to use $6R_{Earth}$ as the threshold to distinguish between the two types of planetary systems and exclude the large exoplanets from our sample. On the other hand, if a system already has two or more known transiting exoplanets, it can be easily attributed to the second population of exoplanets and assumed to have low mutual inclinations. The remaining systems with a single transiting exoplanet smaller than $6R_{Earth}$ can be belong to either population. For those systems, we assume the occurrence rate is 47%, as reported by Ballard and Johnson, 2016 for multiple transiting systems.

The Kepler Dichotomy feature has been challenged by He et al., 2020, who proposed a continuous distribution of mutual inclinations. However, their study focused on FGK stars, so we will still use the M-dwarf statistics and Kepler dichotomy developed in Ballard and Johnson, 2016.

To create a fictive system, we first enter as input some previously known parameters like the stellar radius, the orbital period and the radius of each already known planet candidates. We then derive the total number of exoplanets and the mutual inclination of the system from Ballard and Johnson, 2016, with the constraint that the number of planet is at least equal to the number of known candidates. For each fictive planet, we draw an eccentricity from Limbach and Turner, 2015, a planetary radius between 0.5 and 4 R_{Earth} from Dressing and Charbonneau, 2015, we compute an estimated mass from Otegi, Bouchy, and Helled, 2020, and finally we draw an orbital period between 0.5 and 200 days from Dressing and Charbonneau, 2015, making sure that the period meets the Hill criterion with the periods already drawn to ensure the theoretical stability of the system. A set of 10’000 fictive systems is computed for each TOI, taking the TESS candidate into account. Each fictive planet is sorted in a Period-Radius grid, using the bins from Dressing and Charbonneau, 2015. Counting the fictive planets in each bin and averaging them across the 10’000 systems produces our new expected occurrence rate. We can now create an Occurrence Map (O-Map) of additional exoplanets (see Figure IV.7 as an example), where the known candidates are highlighted in the blue cells).

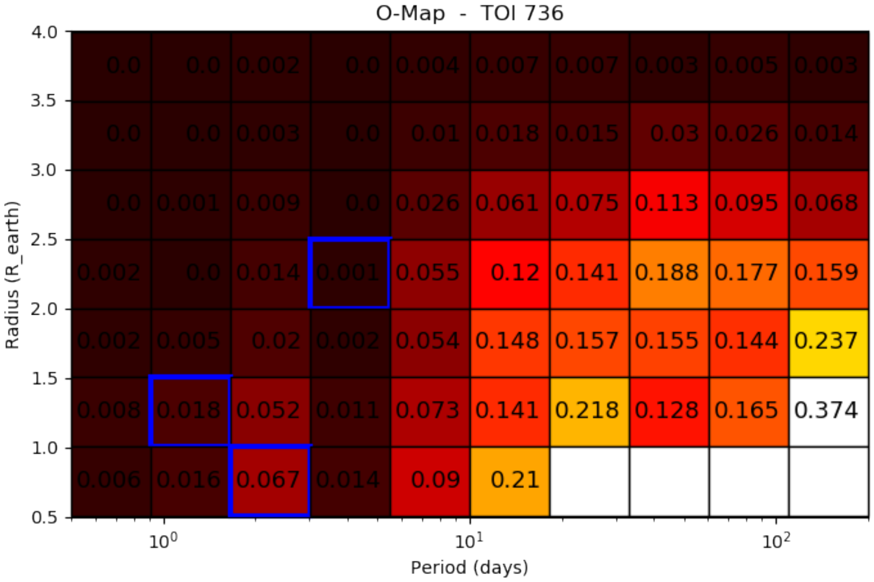

0.0	0.0	0.002	0.0	0.004	0.007	0.007	0.003	0.005	0.003
0.0	0.0	0.003	0.0	0.01	0.018	0.015	0.03	0.026	0.014
0.0	0.001	0.009	0.0	0.026	0.061	0.075	0.113	0.095	0.068
0.002	0.0	0.014	0.001	0.055	0.12	0.141	0.188	0.177	0.159
0.002	0.005	0.02	0.002	0.054	0.148	0.157	0.155	0.144	0.237
0.008	0.018	0.052	0.011	0.073	0.141	0.218	0.128	0.165	0.374
0.006	0.016	0.067	0.014	0.09	0.21				

Figure IV.7: Occurrence Map of TOI-736.
The cells highlighted in blue are the bins in which the previous candidates are located. The lack of fictive exoplanets inside the period bins of the actual candidates is explained by the Hill criterion ensuring the theoretical stability of the fictive systems.

The presence of TESS candidates transiting their host star indicates that the systems have a much more favorable orbital inclination than a general case, considering average mutual inclinations of $\sim 2^\circ$. As a result, we assumed that the system’s global inclination is given by the orbital inclination of the actual known candidate. But this inclination is not very well constrained. To take into account this uncertainty due to the global quality of the data and the methods used to fit the TESS light curves, we decided to use as input the full posterior distribution of impact parameters for each TOI fitted in Section II.4, and from there infer a distribution in orientation that would reflect the lack of knowledge on the real impact parameter of the candidate. We also had to take into account that the fitting algorithm did not converge for several TOIs with only a few transits recorded, resulting in a quasi-uniform posterior distribution or even inconsistent values such as an average above 1. In these scenarios we either assumes a Gaussian distribution if an impact parameter existed in the literature, or a uniform distribution to describe our lack of knowledge for this system.

We used the approach developed by Beatty and Seager, 2010 to compute the probability of each planet transiting given the global orientation distribution described above and the system's mutual inclination. The criterion for a well oriented planet corresponds to impact parameter between $-1 - \frac{R_{planet}}{R_{star}}$ and $1 + \frac{R_{planet}}{R_{star}}$. The TESS survey is so complete in some areas of the Period-Radius parameter space that a non-detection implies that there is no transiting planet in that area. We therefor exclude transits that would have been detected by TESS by setting the criterion of detection of a candidate at a TESS S/N above 6. From this, we create a transit probability map (TP-Map) as a function of the system's orbital period, radius, and mutual inclination (see Figure IV.8 as an example). Proceeding in the same way as for O-Maps, we can now build transiting occurrence maps (TO-Maps) like the one shown in Figure IV.9.

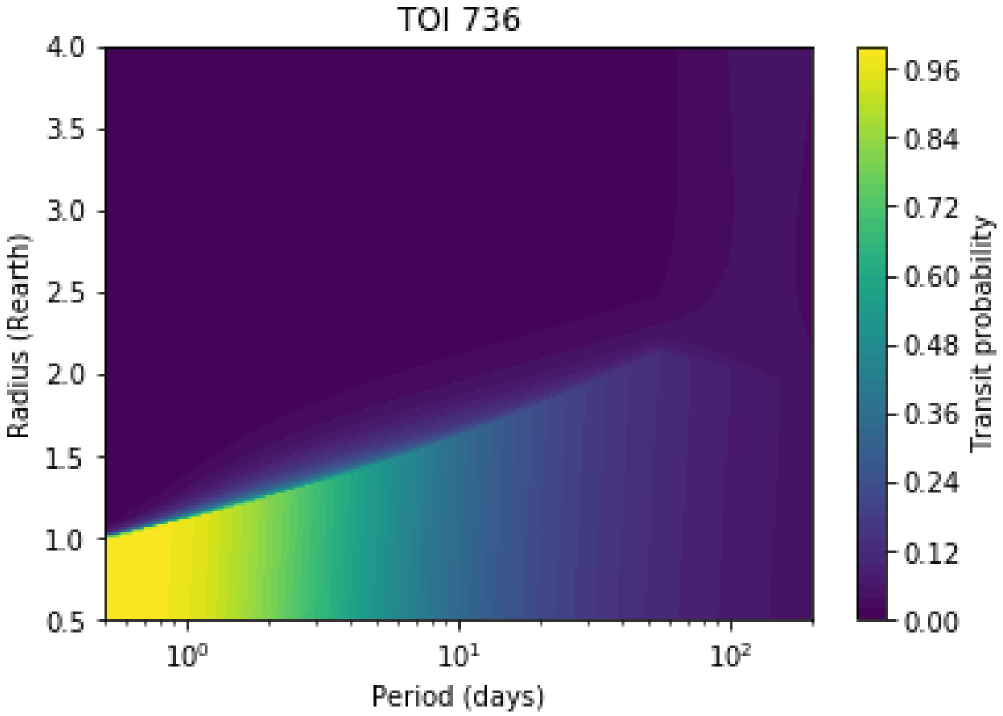

Figure IV.8: Transiting Probability Map of TOI-736.
This map shows the transit probabilities taking TESS completeness into account.

Radial velocity survey

The first application for our simulated planetary systems is to suggest optimized scheduling for ground-based surveys using the radial velocity method. For this purpose, we want to calculate the cost of detecting a planet given its main characteristics and the main char-

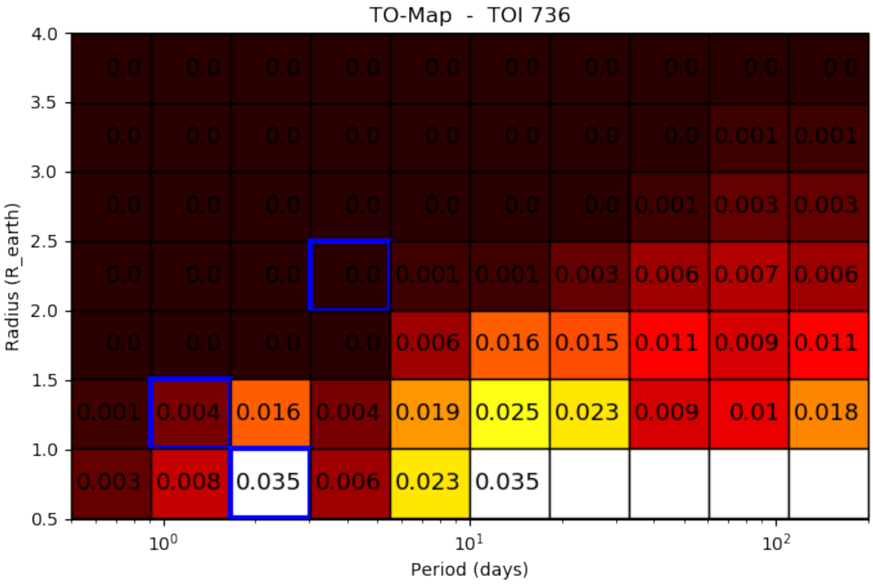

Figure IV.9: Transiting Occurrence Map of TOI-736.
The cells highlighted in blue are the bins in which the previous candidates are located.

acteristics of its host star. We will then be able to determine what portion of the planetary parameter space will be covered by a survey targeting any of the TESS M-dwarfs for a certain amount of time. Using the set of 10'000 simulated systems for a target star, we can predict the probability of an additional detection, along with expected values for the detection's characteristics, by simply integrating the transit probabilities over the region of the parameter space covered by the survey and averaging over the 10'000 systems. Cloutier et al., 2018 presents a method and a tool to compute the cost of measuring planetary masses with a given precision for TESS candidates. We adapted this tool and converted the cost of mass measurements into a cost of planet detection. We assumed the latter cost to be twice as high as the former, as in the worst case where we would be obtain these measurements at zero phases, we can solve the issue by doubling the number of measurements and homogeneously distribute these measurements to treat every possible phase equally. We ignored the impact of other planets orbiting the star.

Cloutier et al., 2018 gives the dependency of N_{RV}, the number of measurements needed, on the semi-amplitude K measurement variance σ_K and from there we derive N_{RV} as a function of the orbital period the mass of the planet. Given these dependencies, we computed N_{RV} for each spectrograph and star, using a standard planet with a period of one day and a mass of one Earth mass. Following that, we generalized to each simulated planet in our sample. As an example, we present in Figure IV.10 the time of observation needed to detect hypothetical new exoplanets around TOI-736, with NIRPS, as function of the position of the planet in the period-mass space. As expected, large candidates with a short orbital period would be the fastest to detect.

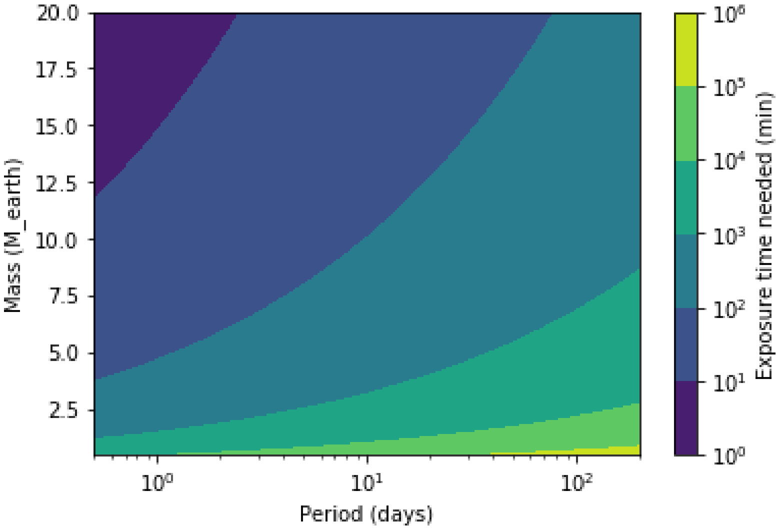

Figure IV.10: Detection cost of an additional planet around TOI-736.
Map of observation time or total exposure time needed for the detection of hypothetical planets orbiting TOI-736 with NIRPS.

The total exposure time must be divided into several measurements under two constraints: first, at least 20 different measurements must be performed so that each degree of freedom can be fairly estimated. Second, we want the exposure time of one observation to be less than 40 minutes. After some tests done with NIRPS, we realized that an exposure of 40 minutes would saturate the detector and we divided this value by two for the planning of the GTO observations. We take the fewest number of measurements while respecting these two criteria, in order to reduce the total overhead time of the telescope.

After applying the different filters mentioned above, we are now able to predict, for a certain amount of telescope time, the expected number of additional detections around our M dwarfs target sample. After deciding on a 100 night survey (each night lasting 9 hours), the goal is now to determine which stars to target and for how long in order to maximize the total expected number of new detections. Because our problem here is similar to the Knapsack Problem, we decided to use the greedy approximation algorithm with a few modifications. We first created a sorted list of the expected number of additional planets for each star, in 10-minute increments. The problem is deciding which item to take from each list while staying within the time limit. The results presented for hypothetical survey scheduling are approximations to the optimal solution. We set a time limit for each star to limit sub-optimal cases. This limit is chosen to maximize the algorithm's output.

This method can be applied to many spectrographs located at various observatories around the world: NIRPS and HARPS (La Silla Observatory, Chile), ESPRESSO (VLT, Chile), SPIRou (CFHT, Hawaii), SOPHIE (OHP, France), ... Several merit functions are tried, among which maximizing transiting detections, total detections, transiting planets inside the habitable zone, transiting planets with insolation under 1 Earth flux. As a output of the code, a table is generating presenting a chronological scheduling with the expected number of new detections. The corresponding fictive planets in the generated data for the targeted TOI are gathered in a Period-Radius and Insolation-Radius diagrams (see Figure IV.11), where actual TESS candidates are also displayed to compare the positions of the candidates in the parameter space. The table displays the expected number of transit detections and the total expected number of detections for each TOI proposed. Because the RV method is not limited to transiting exoplanets, we expect to detect a lot more non-transiting exoplanets.

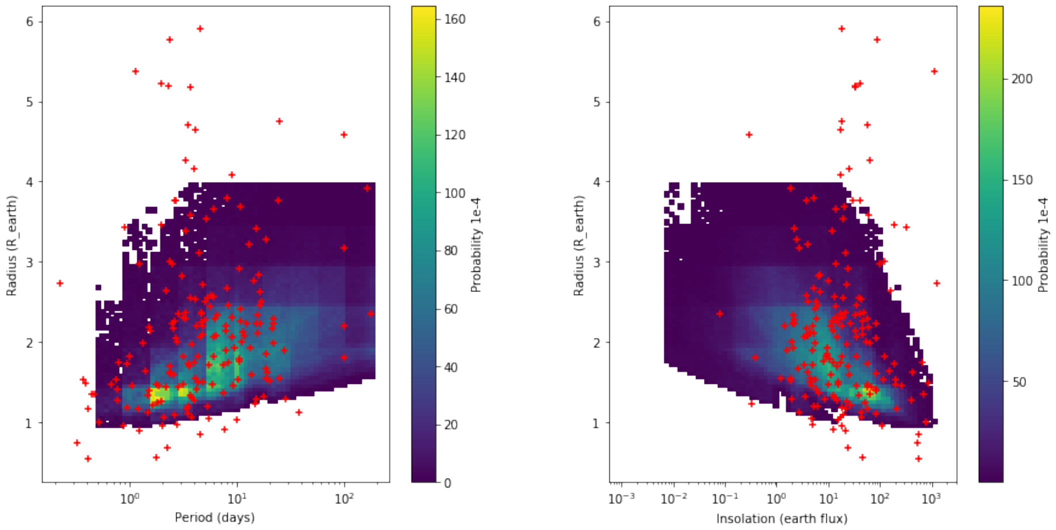

Figure IV.11: Period-radius and Insolation-radius diagrams
Expected additional transiting detections with NIRPS for 100 night survey. Red points are the TESS catalog candidates.

Photometry survey

Another way to exploit the computed sets of planetary systems is to predict the result of a ground-based survey using the transit method. We introduce a detection limit in signal depth, as well as a completeness function in orbital period, for ground instruments such as the ExTrA telescopes. Together, they constrain the parameter space within which we can calculate the probability of a new detection.

A ground survey's completeness is highly dependent on the orbital period P. If the transit occurs during the day, it is impossible to observe it for specific periods (like a 1 or 2 day period). Because the orbital phase is not fixed for the sets of planetary systems, we must average the completeness over all possible phases. The completeness of the observation is determined by the length of the observation: the longer it is, the longer the observable orbital periods are. The completeness is also determined by the length of the night, or more precisely by the length of the star observation window. We uniformly take several thousands of phases between t_0 and $t_0 + P$ for a given observation time, a given star, and a given orbital period. From each phase, defined as a transit instant, we compute the next transits, inside the time of observation. If the total number of transits on the night exceeds a fixed limit (e.g., 1 or 2 transits), the completeness for this phase is set to 1, otherwise 0. After doing this for each phase, the average of all phases yields a number between 0 and 1. The observation window is defined as the star having an airmass lower than 1.5. It is determined by the telescope's altitude, the star's declination, and the time of year. Assuming that the observation is made at an appropriate time of year, we only consider the star's declination and the telescope's altitude. We deduce the length of the observation window from these curves by stating which longitudes have air masses lower than 1.5. Given that a star sweeps 360° of longitude in a day, we convert the longitude interval into a duration.

Adding a detection limit to signal depth requires calculating a theoretical depth for the fictive exoplanets. Knowing that depth varies with planetary radius as R_p^2, we take the depth of the TESS candidate as a reference and infer a hypothetical depth for the potential new exoplanets for a given position in the Period-Radius space. As for the RV method, the aim is to find a theoretically optimal scheduling for a photometric survey. We use the same algorithm to maximize the expected number of detections, in a fixed total survey time. The parameter to adjust here is how many nights to spend on each target. The number of consecutive nights influences the completeness function in orbital period: the longer the survey, the more complete it is in period. We could now apply this algorithm to any photometric survey instrument, but for the remaining of the section, we would go back to radial velocity follow-up using NIRPS.

A paper is currently in preparation to present the Deep Search project described above.

IV.2.2.2 *Selected targets for NIRPS*

In a first analysis in June 2021, using the candidates list from TESS at that time, we found that among 202 M-dwarf hosts, TESS missed 49 ± 7 exoplanets. The discovery of these additional planets would complete the systems' architecture and provide new information in the understanding of the formation and evolution of multi-planetary systems. Multi-planetary systems are unique chance to perform comparative exoplanetology and, in particular, to understand how stellar irradiation shapes the small exoplanets (Owen and Wu, 2017; Van Eylen et al., 2018). As a result, we propose to dedicate some of the NIRPS GTO to do a radial velocity search for these missing planets, stating with the ones with the highest merit. We ranked all systems based on their potential for discovering additional planets and chose 32 to follow up with NIRPS (see Table IV.2). The total exposure time is based on the SNR estimation from Cloutier et al., 2018. We decided to divide this total time in 20-minute exposures as a first approach, but the exposure time can be adjusted depending on the brightness of the target. By observing these targets for 100 nights, we expect to find around 40 new candidates, 8 of these transiting their host star. We will also be able to measure the mass of 32 known TESS candidates with at least a 15% precision using the same data set (and improve already known mass measurements). The precision on the mass measurement of the known TESS candidate is computed using the NIRPS Science Team ETC. During the commissionings, we noticed that the photon noise was higher than expected, forcing to increase the exposure times by a factor of 3. However, we did not take into account HARPS in our estimation, for which we expect to reduce the exposure time by two to obtain the same precision. Taken all this into account, we expect the need to increase our exposure time by a factor 1.5 to reach the desired precision.

IV.2.3 *Toward the most precise Mass-Radius diagram for mid-to-late M-dwarf small exoplanets*

In the last three decades, more than 5000 exoplanets have been discovered, with significant statistical properties emerging. Previous research, based on empirical evidence from Kepler photometry (Dressing and Charbonneau, 2015; Gaidos et al., 2016) and radial velocity surveys (Bonfils et al., 2013), suggested that the mass and radius distribution of exoplanets differs between M and FGK stars. Various physical processes may take place, and we can ask ourselves if planet formation is more efficient around M dwarfs (Ballard, 2019; Ballard and Johnson, 2016; Dressing and Charbonneau, 2015), and if exoplanets orbiting this type of star have more rocky compositions (Mulders, Pascucci, and Apai, 2015).

However, when looking at the mass-radius diagram of known planets (see Figure IV.12), we observe that sub-Neptunes around M dwarfs appear to be less dense than sub-Neptunes around other type of stars. Determining whether these planets continue to have lower densities or, on the other hand, have more rocky compositions will provide critical information for understanding the formation scenario of exoplanets orbiting M dwarfs.

Another finding is a bimodal distribution of planets with radius below 4 R_{Earth} (see Figure IV.13). The two modes appear to separate rocky from volatile-rich planets at a planetary radius around 1.8 R_{Earth} (Fulton et al., 2017; Zeng et al., 2019), possibly depending on orbital period (Van Eylen et al., 2018) and stellar mass (Cloutier and Menou, 2020). The interpretation of these demographics has resulted in an important theoretical work, and photo-evaporation and orbital evolution models have been shown to reproduce the desert (Owen and Wu, 2017).

To determine which planets are rocky and whether they have atmospheres, precise radius measurements from transit surveys must be combined with mass measurements from dynamical observations, such as precise radial velocity measurements with NIRPS. ExTrA, described in the previous chapter, is currently used to improve the precision of

Table IV.2: Optimal survey scheduling for 100 nights of observation with NIRPS.

TOI	Number of TESS candidates	H mag	Number of 20min exposures	Expected total detections	Expected transiting detections	TESS candidate	TESS cand. expected K (m/s)	TESS cand. mass meas. precision (n_σ)
4342	2	9.18	90	2.684	0.510	2.3Re@5.5d - 2.5Re@10.7d	2.99 - 3.28	9.6 - 10.5
4337	1	8.59	90	1.659	0.491	2.8Re@2.3d	5.58	17.9
2221	1	4.83	90	1.831	0.401	4.0Re@8.5d	6.33	162.3
3884	1	10.55	90	1.470	0.360	5.7Re@4.5d	23.52	44.8
4506	1	10.83	90	1.832	0.347	2.9Re@5.4d	11.04	27.0
277	1	9.77	90	1.412	0.318	4.3Re@4.0d	10.68	22.4
2457	1	9.13	90	1.558	0.311	2.8Re@14.2d	3.11	9.5
5146	1	8.81	90	1.727	0.297	2.3Re@10.1d	2.54	8.1
5095	1	10.73	90	1.456	0.293	3.1Re@3.5d	10.11	19.3
5155	1	10.02	90	1.130	0.292	3.1Re@9.8d	3.81	7.0
1083	1	10.07	90	1.330	0.291	3.2Re@13.0d	3.67	8.7
4675	1	9.19	90	1.540	0.291	2.2Re@3.6d	3.00	9.2
5139	1	10.86	90	0.865	0.281	7.1Re@5.9d	19.37	23.4
1883	1	11.23	90	0.846	0.277	5.9Re@4.5d	17.83	29.5
2552	1	10.01	90	1.190	0.260	3.0Re@2.4d	6.5	17.1
2501	1	9.91	90	1.214	0.231	2.9Re@5.3d	16.79	31.0
4526	1	11.03	90	1.095	0.229	2.7Re@2.3d	8.16	15.5
249	1	9.50	88	1.473	0.228	2.3Re@6.6d	2.97	5.4
761	1	9.15	90	1.525	0.227	2.6Re@10.6d	3.99	12.2
663	3	9.83	84	1.824	0.221	2.3Re@2.6d - 2.4Re@4.7d - 1.9Re@7.1d	4.68 - 4.19 - 4.69	9.5 - 8.5 - 9.5
4508	1	9.71	90	1.703	0.221	2.1Re@3.5d	4.69	12.3
435	1	11.10	86	0.726	0.217	5.3Re@3.4d	14.03	15.7
5511	1	10.85	43	0.590	0.103	5.8Re@4.7d	17.09	15.5
2453	1	10.40	80	1.192	0.214	3.0Re@4.4d	6.27	14.0
532	1	10.75	56	0.686	0.150	5.6Re@2.3d	17.86	17.0
2406	1	12.13	90	1.059	0.183	2.8Re@3.1d	12.20	14.7
5486	1	10.34	79	1.058	0.190	3.8Re@2.0d	10.57	20.8
2407	1	10.56	70	1.079	0.200	3.8Re@2.7d	10.13	13.3
5532	1	9.70	65	1.123	0.156	2.2Re@5.7d	2.57	4.0
672	1	9.70	46	1.167	0.137	5.1Re@3.6d	14.28	21.4
2781	1	11.05	65	0.619	0.179	5.9Re@2.8d	17.42	17.9
4668	1	11.55	21	0.232	0.049	5.2Re@1.0d	27.30	15.9
TOTAL				**40.894**	**8.158**			

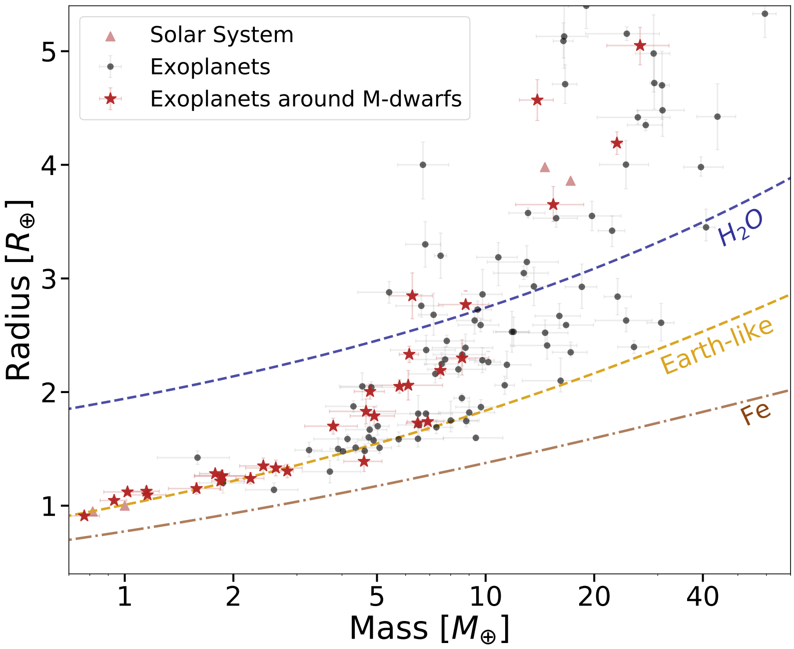

Figure IV.12: Mass-radius diagram of known exoplanets.
Are presented here the exoplanets with mass precision $< 25\%$ and radius precision $< 8\%$. The red stars represent the population of exoplanets orbiting M dwarfs.

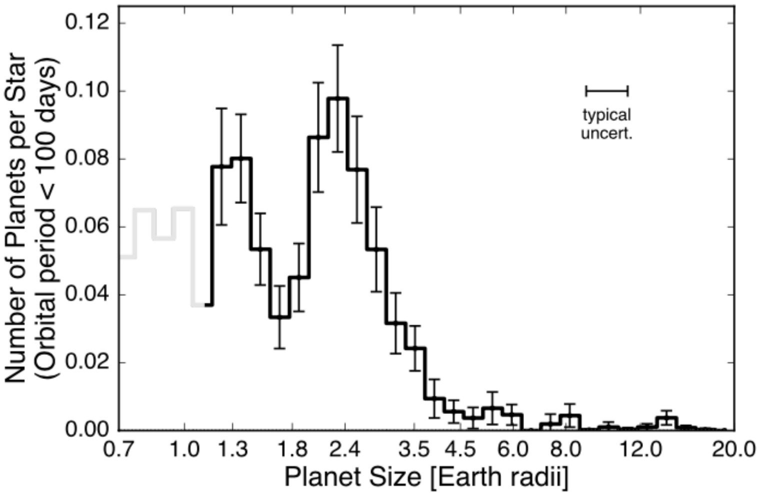

Figure IV.13: Radius Valley from Fulton et al., 2017.
Completeness-corrected histogram of planet radii for planets with orbital periods shorter than 100 days. The light gray region of the histogram for radii smaller than 1.14 R_E suffers from low completeness. The median radius uncertainty is plotted in the upper right portion of the plot.

radius measurements for TESS exoplanet candidates orbiting M dwarfs. We could therefor complement our ExTrA photometric datasets with NIRPS radial velocity measurements to fully characterize these systems as both instruments operate in the near-infrared. Near-infrared observations are particularly interesting for mid-to-late M dwarfs because they provide greater precision than optical instruments. Indeed, visible-light instruments can characterize early M-dwarfs but lack the precision needed for fainter stars. Assuming the TESS survey is complete, ExTrA and NIRPS are the ideal combination for obtaining a statistical view and calculating the occurrence rate of exoplanets orbiting these cooler stars.

The focus of this GTO proposal is therefore on populating the mass-radius diagram with new exoplanets orbiting mid-to-late M dwarfs (stellar type ranging from M3 to M7). Only 12 exoplanets (statistics obtained from Otegi, Bouchy, and Helled, 2020) have been well characterized around these stars when the paper was published. We propose to add 29 new TESS candidates to this sample by measuring their precise mass using NIRPS. We selected all TESS candidates with stellar temperature below $3430K$ and declination below $+20°$ (to be observable from La Silla) and removed exoplanets with already published mass measurements and with radial velocity signals below the m/s. The final candidates have periods ranging between 0 and 40 days and radii between 1 and 4 R_{Earth} (see Figure IV.14). We want to obtain at least 15 measurements for each target to constrain the orbit and estimate that ∼232 hours of observations (without taking into account the overheads for the telescope and instrument) will enable us to obtain a mass measurement for each of these planets with a precision of at least 15%. The targets proposed are presented in Table IV.3. The validated planets have radius with uncertainties displayed and the corresponding orbital period is the published one. The semi-amplitude used to compute the number of measurements needed is the one from the TOI candidate column.

Table IV.3: Targets proposed to populate the Mass-Radius diagram for mid-to-late M dwarfs.

TOI	TESS candidates	H mag	Spectral type	Period (days)	Radius (R_E)	Expected TESS cand. semi-amplitude (m/s)	Number of 20min exposures
4337.01	1	8.59	M3	2.286	2.817	5.8	15
406.01	2	9.13	M3	13.176 - 6.615	1.96 - 1.273	4.74 - 1.35	15
1224.01	1	9.41	M3	4.178	2.183	4.54	15
4336.01	1	8.87	M3	16.336	2.111	3.13	22
4508.01	1	9.71	M3	3.467	2.114	5.19	22
3494.01	1	10.0	M4	7.749	2.217	4.86	19
1078.01	1	8.16	M3	0.518	1.180 ± 0.078	2.14	17
782.01	1	10.11	M3	8.024	2.679	4.86	25
244.01	1	8.25	M3	7.397	1.03 ± 0.08	1.39	40
2441.01	2	10.72	M3	12.890 - 5.551	2.920 - 2.032	4.29 - 3.21	84
654.01	1	10.14	M3	1.528	2.360	6.66	15
210.01	1	10.26	M4	9.011	2.151	3.90	29
521.01	1	10.36	M3	1.543	1.995	5.35	20
4616.01	1	10.71	M3	1.554	1.222	11.37	15
122.01	1	11.02	M3	5.078	2.72 ± 0.18	6.73	32
136.01	1	9.48	M5	0.463	1.32 ± 0.02	7.25	15
4552.01	1	9.66	M3	0.301	1.280	4.93	24
4526.01	1	11.03	M4	2.260	2.45 ± 0.28	8.16	17
4184.01	1	12.11	M4	4.902	2.555	7.40	51
771.01	1	9.96	M4	2.326	1.396	11.56	15
2406.01	1	12.13	M4	3.077	2.94 ± 0.17	12.20	19
2495.01	1	10.10	M3	7.795	1.894	5.42	20
206.01	1	10.28	M3	0.736	1.30 ± 0.05	4.98	23
1080.01	1	10.47	M4	3.965	1.433	7.06	15
4556.01	1	11.00	M6	3.792	1.560	3.83	46
2445.01	1	11.03	M4	0.371	1.25 ± 0.08	6.62	25
736.02	2	10.99	M5	4.990 - 0.948	2.31 ± 0.25 - 1.12 ± 0.13	8.05 - 4.48	43

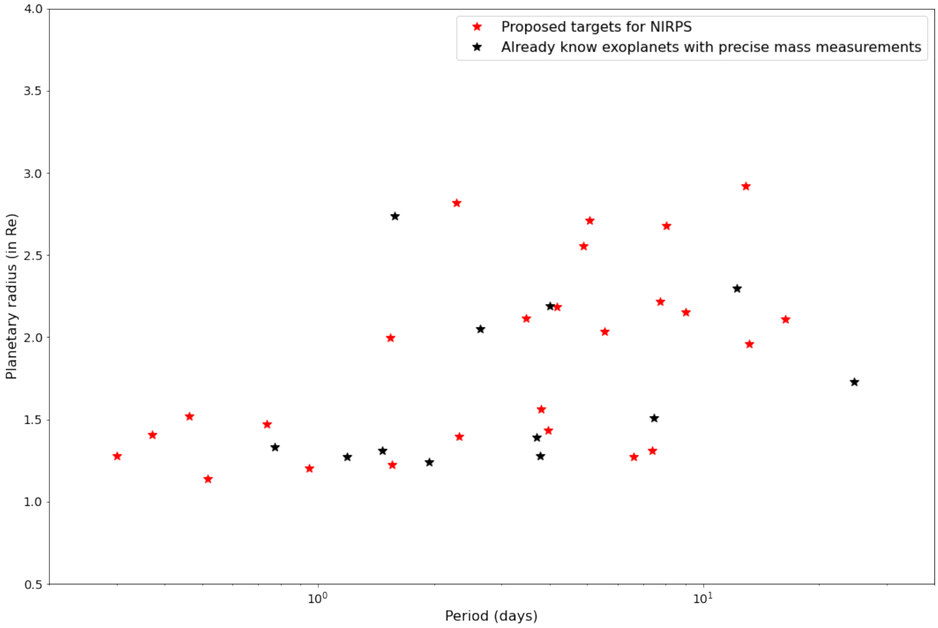

Figure IV.14: Targets proposed for Mass-radius program of NIRPS GTO. Radius-period diagram with already known exoplanets with precise mass measurement in black, and candidates proposed for the GTO to expand the catalog of well characterized exoplanets orbiting mid-to-late M-dwarfs in red.

IV.3 PRELIMINARY RESULTS FROM THE NIRPS COMMISSIONINGS

After its nine commissionings, the NIRPS instrument is finally ready to start observing in April 2023. The first 4 commissionings were dedicated to the front-end, adaptive optics system and fiber train but without the spectrograph. The 5th commissioning in spring 2022 was the first one with the complete instrument. The first light of the NIRPS instrument was made on May 17, 2022 (see Figure IV.15, and ESO Press Release) and some stars were already observed. An example of one of the first NIRPS spectrum of the star Proxima is presented in Figure IV.16.

To test the capabilities of NIRPS during the commissioning phase, different stars were observed to validate different aspects of the instrument. NIRPS observed photometric standards, to measure the transmission of the instrument and photometrically calibrate the spectrograph, telluric standards to implement the telluric correction for all spectra, radial velocity standards to measure the stability of the instrument, stars with planet to test our ability to re-detect known exoplanets, faint targets to push the limits of the instrument, ... I

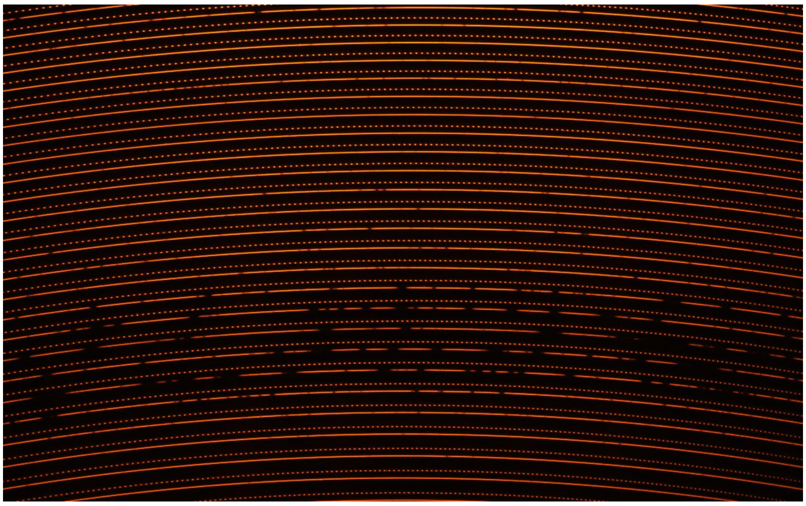

Figure IV.15: NIRPS first light.
First raw data of NIRPS (spectrum of Barnard's star). Each horizontal line corresponds to a narrow region of light that shows both the absorption lines from the star and the absorption lines from the Earth's atmosphere. The dotted lines correspond to the calibration spectrum.

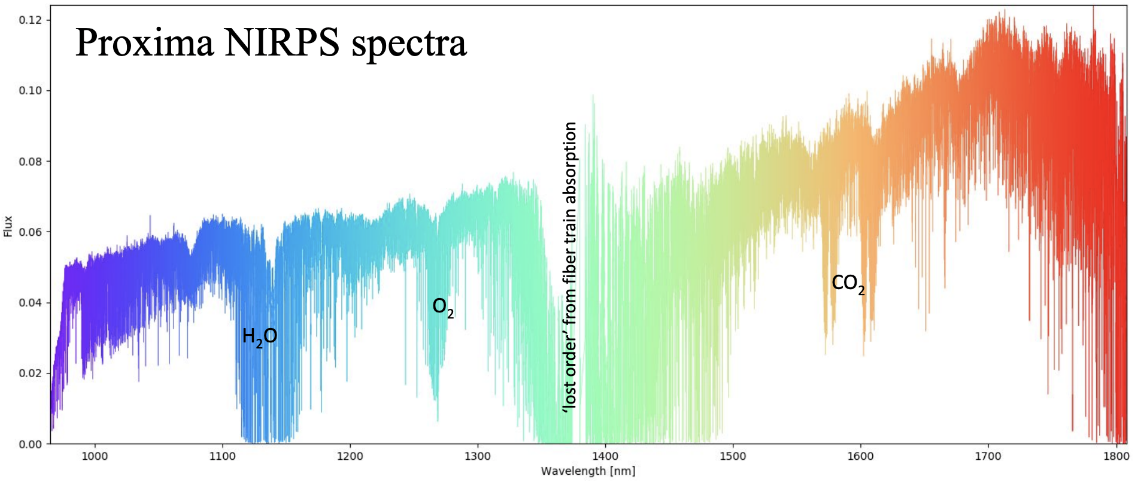

Figure IV.16: Spectrum of Proxima from the NIRPS spectrograph.
The main absorption bands are annotated. An order is lost in the middle of the spectrum due to absorption from the fiber train.

will present hereafter the results for some of these aspects.

During commissioning, NIRPS demonstrated m/s-level radial velocity stability, with performances on the radial velocity standard Proxima consistent with an 80 cm/s noise floor after subtraction of the planetary signal from Faria et al., 2022 (see left panel of the

Figure IV.17). This performance is unprecedented for near-infrared precise radial velocity, outperforming any competitor by a factor of ~ 2.

GJ 581 b is a Neptune-like exoplanet that orbits an M3-type star. This exoplanet has a mass of 15.8 M_{Earth}, and an orbital period of 5.4 days. This system possesses three exoplanets : GJ 581 b discovered by Bonfils et al., 2005, GJ 581 c discovered by Udry et al., 2007 and GJ 581 e discovered by Mayor et al., 2009. Several subsequent studies found that the planetary signal first attributed to GJ 581 d was caused by stellar activity, and the exoplanet does not exist (Robertson et al., 2014). Presented in the right panel of Figure IV.17 are the telluric corrected radial velocities for the HE mode observed with NIRPS. In this figure, we display the combined Keplerian contribution of the exoplanets in the system and the residuals after removal of the major component GJ 581 b.

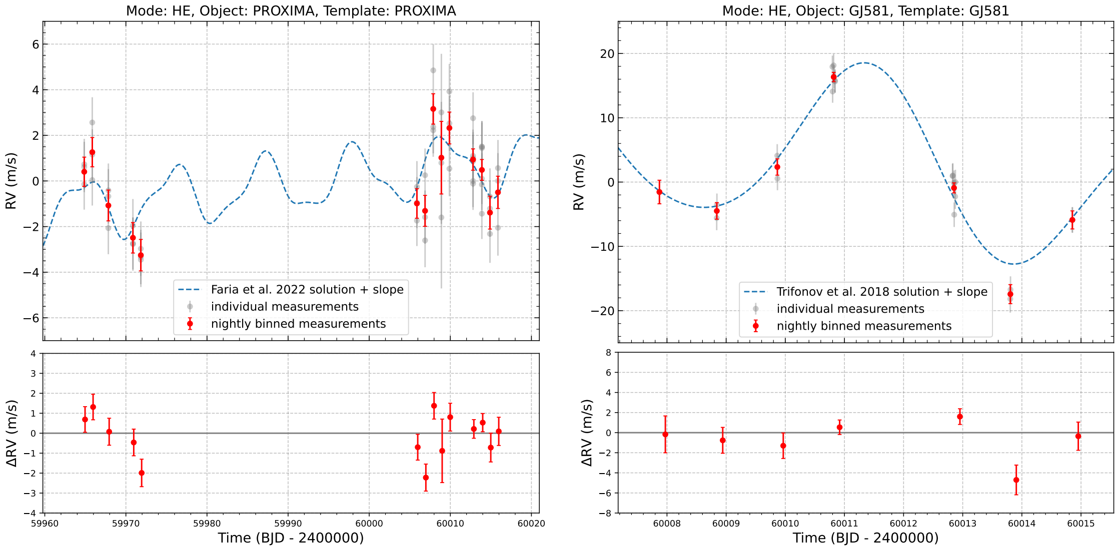

Figure IV.17: Sample RV sequences from COMM 8 & 9 for Proxima and GJ581. The exoplanets in both systems are seen in the NIRPS data (keplerian signals determined from published ephemeris are over-plotted). The unaccounted-for RMS (subtracting errors in quadrature) is at the 80 cm/s level for Proxima and 1.3 m/s for GJ 581.

After the three last commissionings, we noticed that the HE mode is consistently better than the HA mode for < 5 m/s precise radial velocity sequences. The differences between the two modes are at the level of $10 - 20\%$, which corresponds to a difference of telescope efficiency of $20 - 40\%$, equivalent to an additional year of observation time for the NIRPS GTO. This difference between the modes is consistent with a floor from modal noise, but it may be possible to calibrate HA down to the level of HE. HA is however very useful to resolve close binaries of for atmospheric absorption work.

According to our commissioning results (presented in Figure IV.18), a 20-min exposure on target with a H-band magnitude of 8 and 10 will respectively give a S/N of 185 and 70, and a corresponding radial velocity uncertainty of 1.9 m/s and 5 m/s in agreement with the expected radial velocity semi-amplitude of the candidates proposed in the different programs. However, as discussed before, the precision computed in both GTO programs used an older version of the ETC and we expect now to multiply by ∼1.5 the observation time to obtain the precision desired. Some of the targets will only require a few measurements to eliminate brown dwarfs, binaries, false positives, or fast rotating stars. Others will need up to 100 measurements to narrow down the iron core mass fraction of super-Earths.

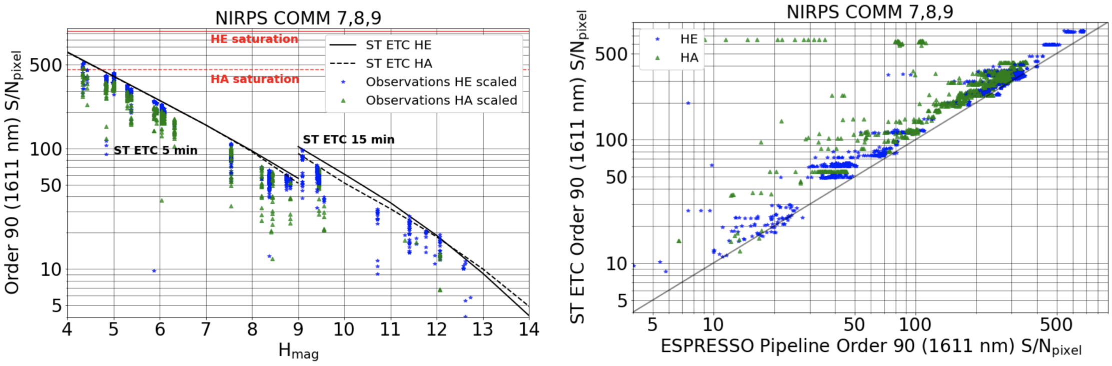

Figure IV.18: Expected and observed S/N during the NIRPS commissionings. *Left*: Signal-to-noise ratio as a function of the H-band magnitude. The black curves correspond to the expected S/N computed using the Science Team Exposure Time Calculator (ST ETC) for 5-min and 15-min exposures depending on the brightness of the star. The blue and green dots correspond to the NIRPS observations in HE and HA mode respectively. *Right*: Comparison between the S/N computed using the Science Team Exposure Time Calculator (ST ETC) and the actual S/N obtained using the ESPRESSO pipeline.

NIRPS's unique capabilities, combined with its coupling with HARPS, make it a unique tool for carrying out the scientific programs described in Sections IV.2.2 and IV.2.3.

V

CONCLUSION

"I was a billion little pieces
'Til you pulled me into focus
Astronomy in reverse
It was me who was discovered"
Venus by Sleeping At Last

During my PhD, I conducted research with a global perspective, which included various stages from selecting the targets, scheduling the observations using different instruments, analyzing the data and interpreting the results. In this section, I will summarize my work with ExTrA and outline potential future work to be done. I will then discuss my involvement in the NIRPS Science team and the programs I proposed for the GTO. I will mention as well the potential synergies between ExTrA transit observations and NIRPS radial velocity measurements. I will present the papers I have contributed to and how they're helping us understand the planetary systems that exist around M dwarfs. Finally, I will conclude with the next steps needed to expand our comprehension of exoplanets orbiting M dwarfs and future missions in this field.

V.1 EXTRA : CONCLUSION AND PERSPECTIVES

My research focuses on the discovery of new exoplanets orbiting M dwarfs. To observed these faint targets, near-infrared observations are preferred as M dwarfs emit most of their energy at these wavelengths. During my thesis, I worked on ExTrA, a facility composed of three 60-cm telescopes and designed to detect and revisit small exoplanets around low mass stars. To accomplish this, I began by planning the observations using a target list based on the planetary candidates found by the TESS mission. I carefully selected targets for ExTrA observations based on their potential to host exoplanets around cool stars, for which other instruments might not be as efficient as ExTrA to detect the transits. I took into account a variety of factors, including the stellar temperature, the declination of the target to be observable with ExTrA at La Silla Observatory, and the previous knowledge obtained from TESS and TESS Follow-up Observing Program (TFOP).

After acquiring the observations, I reduced the data and developed a pipeline to convert the extracted ExTrA spectra into usable light curves. This required a lot of research, trial and error, as I needed to understand how ExTrA worked and adjust various parameters to ensure that the pipeline functioned properly. This step was necessary to ensure that I had accurate and dependable photometry to work with. Along with the light curves, I also created an automatic PDF night report, a useful document to spot any issue during observations that could impact the light curves. Once created, I analyzed and modeled the light curves to look for transit signals. I had to decide on an already existing modeling tool to use (juliet, Espinoza, Kossakowski, and Brahm, 2019), learn the best way to parameterize the model, to identify and remove systematics from the data, and understand the variety of statistical techniques to obtain the posterior distributions of the fit and to estimate the size and orbit of any observed exoplanets. I decided to use Gaussian processes to correct for the systematics present in the ExTrA photometry. As I couldn't determine the origin of these systematics, modeling them with a GP appeared to be the best working solution.

Once the routines to model jointly photometric and velocimetric datasets to constrain the planetary parameters were perfected, I used them to publish two newly discovered systems (TOI-269 b and TOI-663 b, c and d) and worked on finding specific science goals to achieve using the ExTrA facility. I also created generic routines to fit the TESS and ExTrA photometry simultaneously and I am writing a paper summarizing the results of the WP1 of ExTrA on validating TESS planet candidates and improving the planetary radius measurement using ExTrA transits.

Overall, ExTrA is already producing usable light curves and has proven itself a useful tool to validate planetary candidates orbiting low-mass stars. Several published papers (see Section V.4) are using ExTrA observations to confirm the transit in the near-infrared and increase the precision on the planetary parameters.

Nonetheless, we could think about ways to improve the experiment. The process of creating the light curves can still be refine and other members of the ExTrA science team have already helped upgrading the pipeline, but work remains to be done to achieve the best performance of the instrument. Additionally we noticed the presence of systematics in the ExTrA photometry and used Gaussian process on the temporal component to correct for that. However, we could consider using ExTrA spectroscopic information to correct the systematics using the wavelength component instead or in addition to the temporal one.

ExTrA could also be very useful for other science cases than validating transiting candidates and improving on the radius measurements. Preliminary work of the ExTrA WP2 to measure transit timing variations and detect additional planets in TESS multi-planetary systems were done by other members of the ExTrA science team but a lot of observations remained to be analyzed. Moreover we decided to dedicate some observation time to studying very cold stars as ExTrA has demonstrated its ability to achieve good precision when observing these stars. ExTrA may additionally be utilized in non-exoplanet projects such as near-infrared spectro-photometric monitoring campaigns.

The summary of all ExTrA observations will be used in the near future to estimate the performances of the instrument, as well as which stars or planetary systems would benefit from near-infrared ExTrA observations.

V.2 NIRPS : CONCLUSION AND PERSPECTIVES

During the second part of my PhD, I had the opportunity to work on the preparation of the near-infrared spectrograph installed on the 3.6m ESO telescope as a member of the NIRPS science team. NIRPS is a high-precision spectrograph to detect and characterize exoplanets using the radial velocity method. Its objective is to reach the accuracy of current visible spectrographs like HARPS in the near-infrared to better study low mass stars.

I proposed two programs for the NIRPS Guaranteed Time Observations based on the expertise I developed working on TESS planet candidates around M dwarfs and ExTrA photometry. The first program proposes to characterize transiting exoplanets by measuring their precise mass and investigate the mass-radius diagrams of exoplanets orbiting mid-to-late M dwarfs, which could reveal important information about the formation and evolution of these exoplanets. The second program aims to use the deep search strategy to find additional planets in already known TESS systems, by comparing the probability of different systems to host more planets that TESS could have missed, potentially leading to the discovery of new multi-planetary systems.

I also gathered information on all the targets linked to the blind survey of WP1 and the mass measurements of WP2 as part of my involvement in those two work packages. I conducted researches on the targets and analyzed data from various sources to determine the potential scientific value of the targets. With this knowledge, I assisted in the selection of priority targets to observe, which could lead rapidly to the discovery of new interesting exoplanetary systems.

NIRPS operates simultaneously with HARPS on ESO's 3.6m telescope, which enables us to obtain observations in a spectral band that covers the visible to near infrared. Combining the two spectrographs provides a large spectral coverage with HARPS ranging from 378 to 691 nm and NIRPS from 971 to 1875 nm, a way to distinguish between planetary signals and stellar activity, and the ability to detect and characterize a wide range of exoplanets.

NIRPS has already demonstrated his performances during its several commissionings by showcasing excellent intrinsic stability, and a precision of a m/s for bright targets. Therefore, we anticipate that the proposed scientific programs in the Guaranteed Time Observations will be feasible based on its performance. NIRPS has started officially its observations on April 1st 2023. The GTO is spread over 5 years and is filled with many different scientific topics. NIRPS will search for exoplanets around low-mass and ultra-cool dwarf stars in order to identify potential Earth-like planets for future study and to better understand the process of planet formation and the initial conditions in protoplanetary disks. It will also aim to characterize the planetary system architecture around M dwarfs in order to better understand how the exoplanets formed. NIRPS will study small transiting exoplanets orbiting mid-to-late M dwarfs extensively, primarily using TESS candidates, to help pave the mass-radius diagram of multi-planetary systems, provide ultra-precise mass measurements of rocky planets to constrain their core mass fraction, and provide mass measurements of temperate small planets amenable to atmospheric characterization using the James Webb Space Telescope. NIRPS will also participate in the characterization of exoplanet atmospheres, and reshaping the field toward population-based studies using a uniform data acquisition, reduction, and analysis strategy, and providing high-fidelity spectra.

V.3 SYNERGY BETWEEN EXTRA & NIRPS

The transit method and the radial velocity method are two of the most commonly used methods for detecting and characterizing exoplanets. The transit method involves monitoring the brightness of a star over time and looking for small dips in brightness caused by a planet passing in front of the star as seen from Earth. Multiple transits can be used to calculate the planet's size and orbital period. The radial velocity method, on the other hand, measures the speed at which a star is moving towards or away from us caused by the gravitational pull of an orbiting planet. This method can be used to compute the planet's minimum mass, which combined with the transit method giving the inclination of the system leads to the planet mass, as well as its orbital period and eccentricity.

ExTrA and NIRPS are two powerful instruments designed for detecting exoplanets orbiting M dwarfs by observing in the near-infrared. Both instruments are located at La Silla Observatory in Chile and are therefore able to observe the same targets. ExTrA and NIRPS will hopefully help to increase the precision with which we can detect small exoplanets orbiting these low-mass stars. As said previously, combining the photometry of ExTrA and the spectroscopy of NIRPS yields complementary and additional information about exoplanets. ExTrA provides data on the exoplanet's size and NIRPS, on the other hand, provides data on the exoplanet's mass, with additional orbital parameters like the distance to the star, the inclination of the system, the eccentricity. It can also reveal more about the planet's composition, formation history, and atmospheric properties. When these two sets of measurements are combined, they provide a more complete picture of the exoplanet and its properties.

NIRPS and ExTrA will also be used to observe planetary transits simultaneously. The first objective is to refine the transit ephemeris when necessary. The second objective is to check if there are spot-crossing events during the transit. These events bias the transmission spectrum and thus the constraints on the atmospheric parameters and the local stellar line profile necessary to study the Rossiter–McLaughlin, a method for calculating the spin-orbit angle between a planet's orbital plane and its host star's equatorial plane, and the derivation of the stellar parameters. Moreover, the light curve in a wavelength band similar to the high resolution data allows to obtain the limb darkening to properly extract the Rossiter–McLaughlin or the transmission spectrum but simultaneity is not necessary here. Finally, the last objective in observing with ExTrA simultaneously from NIRPS is to study young exoplanets known to be active and with spots. These exoplanets are complex to analyze and having different datasets will allow us to disentangle between stellar and planetary effects.

V.4 PUBLISHED PAPERS AND THEIR CONTRIBUTIONS

During my thesis, I led 2 exoplanet discovery papers (TOI-269 b, Section III.4 and TOI-663 b, c and d, Section II.5) by planning and gathering the observations using ExTrA and other instruments, and analyzing jointly the photometry and radial velocity data using the routines I developed. I also contributed to 7 other exoplanet discovery papers using ExTrA observations, analyzing the photometry and modeling the transit, and finally providing ExTrA light curves to validate the planetary candidate in a near-infrared spectral range, alongside a section describing our observations (see the section Publications).

First, the discovery of a new sub-Neptune transiting the M2 dwarf TOI-269 (Cointepas et al., 2021) near the transition between super-Earths and sub-Neptunes provides an excellent target for atmospheric characterization. Because of its high eccentricity, the exoplanet's orbit could have been caused by planet-planet interactions, providing new insights into the dynamics of exoplanet systems.

The discovery of a transiting, temperate, Neptune-sized exoplanet orbiting the nearby M3 star TOI-1231 (Burt et al., 2021) is significant as it is one of the coolest small planets accessible for atmospheric studies so far. Its host star's bright near-infrared brightness makes it an exciting target for the Hubble Space Telescope and James Webb Space Telescope, and future atmospheric observations would enable the first comparative planetology efforts in the 250-350 K temperature regime via comparisons with K2-18 b (Madhusudhan et al., 2020).

TOI-177 b, a mini-Neptune, was discovered around an M2-dwarf star located at 22 pc (Almenara et al., 2022a). An interior modeling analysis suggests that the planet is expected to have a volatile envelope and a coupled atmospheric and dynamical evolution analysis of the planet favors a heavyweight atmosphere rather than a pure H-He atmosphere. TOI-177 b is the second most favorable mini-Neptune after GJ 1214 b (Berta et al., 2012) for atmospheric characterization. An additional planet candidate was also identified from the radial velocity data, but its transits were not detected.

The validation of a transiting low-density exoplanet orbiting the M2.5 dwarf TOI-620 (Reefe et al., 2022) is also valuable for atmospheric characterization, as it is one of the most amenable exoplanets for such studies validated or confirmed by the TESS mission to date. The discovery of an outer companion allowed for a detailed exploration of possible system architectures, which excluded TOI-620 b to be a circum-secondary planet or a pair of eclipsing binary stars orbiting the host in a hierarchical triple system.

The discovery and validation of two temperate super-Earths transiting the M6 nearby star LP 890-9 (TOI-4306, SPECULOOS-2) (Delrez et al., 2022) provide new insights into the formation and evolution of exoplanet systems. With a overall low density, these planets are likely water-rich with small H-He atmospheres. The discovery of a second outer transiting planet, previously undetected by TESS, highlights the importance of continued monitoring and observations of exoplanet systems.

A sub-Saturn exoplanet TOI-3884 b (Almenara et al., 2022b) was discovered transiting a mid-M dwarf star with a chromatic transit signal. Follow-up observations revealed that the planet transits a large polar spot on the host star. The host star's brightness and small size make it a top target for atmospheric characterization with the James Webb Space Telescope and ground-based telescopes.

A gas giant exoplanet TOI-3235 b (Hobson et al., 2023) was found orbiting an M-dwarf star with a mass close to the critical mass at which stars transition from partially to fully convective. This discovery challenges current planet formation models as gas giants such as TOI-3235 b are not predicted to form around low-mass stars like TOI-3235. With a high transmission spectroscopy metric, TOI-3235 b is one of the best-suited giants orbiting M-dwarfs for atmospheric characterization.

The discovery of a temperate Earth-sized planet orbiting the cool M6 dwarf LP 791-18 (Peterson et al, accepted in Nature) is significant because it offers a rare opportunity to explore the conditions under which planets can develop hospitable climate conditions. LP 791-18 d is part of a co-planar system (Crossfield et al., 2019) and provides a unique opportunity to investigate a temperate exo-Earth in a system with a sub-Neptune that retained its gas or volatile envelope. The gravitational interaction with the sub-Neptune prevents the complete circularization of LP 791-18 d's orbit, resulting in continued tidal heating of its interior and likely strong volcanic activity at the surface.

Finally, the detection and characterization of three exoplanets orbiting the early M dwarf TOI-663 (Cointepas et al. resubmitted) and located just above the radius valley, suggest that these planets are water-rich and have small H-He atmospheres. This discovery supports the recent observation that sub-Neptunes around M dwarfs have lower densities than those around other spectral type stars.

The discovery of these several exoplanets reported here in chronological order has important scientific implications as they cover a wide range of parameters, from Earth-sized planets to gas giants, orbiting early to late M dwarfs on various orbits. The majority of these new exoplanets are excellent candidates for atmospheric characterization. These discoveries also suggest that sub-Neptune exoplanets orbiting M-dwarf stars indeed tend to have a lower density compared to similar exoplanets orbiting other types of stars. This challenges the current understanding of planet formation and evolution but it may help refine the models and better understand the complex interaction of many factors that influence the properties of exoplanets.

V.5 NEXT STEPS OF EXOPLANETS SCIENCE AROUND M DWARFS

Exoplanetary science is a rapidly evolving field that has made significant advances in the last few decades. With the discovery of more exoplanets and the advancement of new techniques and instruments, the future of exoplanetary science will hopeful reveal more information on the formation and evolution of exoplanets, on their internal structure and a detailed characterization of their atmosphere. Discovering potentially habitable exoplanets will continue to be a major focus of exoplanetary science in the future. As new instruments and methods are developed, the number of confirmed exoplanets in the habitable zone of their host stars is expected to grow.

Exoplanet formation and evolution research is still an ongoing process that will be studied in the future to better understand the properties and characteristics of exoplanets. The differences in these mechanisms as a function of the spectral type of the star will specifically be investigated. Exoplanetary system exploration to gain a better understanding of their dynamics, as well as interactions between exoplanets and their host stars, is also becoming of prime interest. This will require the discoveries of new multi-planetary systems, as they provide a unique opportunity for direct comparative planetology (Millholland, Wang, and Laughlin, 2017) because the exoplanets formed within the same protoplanetary disk and evolved around the same host star. Ongoing or future missions will address all of these various scientific questions.

TESS completed its primary mission in July of 2020, then its first extended mission and entered its second extended mission in September 2022. These extensions will enable the detection of longer period exoplanets and help resolve mono-transits and duo-transits. The mission is still an outstanding achievement after five years in space. TESS' cameras have mapped over 93% of the sky, discovered 329 new worlds that led to publication, and identified more than 4300 candidates. Within the massive amount of data that TESS has already collected, new discoveries are waiting to be made. This is a collection of observations that we will study for years, and there is much more to come.

The Gaia mission has already participated in exoplanet science by providing the parallax and proper motion of host stars. In the latest Data Release (Gaia Collaboration et al., 2022), the GDR3 catalog provides celestial positions, proper motions, parallaxes, broad band photometry as well as about 1 million mean spectra from the radial velocity spectrometer. The Gaia measurements will be very useful in identifying false alarms because the accuracy is sufficient to determine that some candidates are double stars rather than stars with an orbiting exoplanet. It is predicted that with an astrometric precision of around 10 micro-arcseconds for the brightest stars, it will be possible to detect tens of thousands of exoplanets out to 500 parsec from the Sun by measuring the wobble caused by their parent stars on the sky (Perryman et al., 2014). According to current estimates of planet distribution and orbits, roughly 1000-1500 of these discoveries are expected to be exoplanets orbiting M-type dwarf stars within 100 parsec. As for the transit method, it is predicted that with the precision of Gaia's photometric measurements, a few hundred to a few thousand transiting massive planets will be discovered. The Gaia DR4, with full astrometric, photometric, and radial-velocity catalogs, and an exoplanet list, is expected but not before the end of 2025.

PLATO's (Rauer et al., 2022) primary goal is to detect exoplanets orbiting in the habitable zone of Sun-like stars and accurately and precisely determine their sizes. It is scheduled to launch late 2026. PLATO will also study host stars using asteroseismology, which will allow us to determine stellar properties with high accuracy, significantly improving our understanding of stellar structure and evolution. PLATO shall also detect terrestrial planets which orbit M dwarf stars at distances that include the star habitable zone. To identify good targets for spectroscopic measurements to investigate planetary atmospheres, PLATO will observe 5 000 M dwarf stars and expect to find a sample of more than 10 exoplanets around bright stars and observe more than 100 planetary transits around M dwarfs from different regions in the sky of good targets for spectroscopic measurements to investigate planetary atmospheres (as described in Plato Definition Study Report).

Exoplanets observed in transits or in radial velocity will be amenable to atmospheric characterization using new instruments such as the James Webb Space Telescope (JWST) and the Extremely Large Telescope (ELT). ANDES at the ELT (previously known as HIRES) will revolutionize the characterization of low-mass planet atmospheres. It will be capable of detecting biomarkers, molecules indicative of life, in exoplanet atmospheres using transmission spectroscopy as well as studying their reflected light (Maiolino et al., 2013; Marconi et al., 2020). Its combination of high-contrast imaging and high-resolution spectroscopy will allow it to distinguish between stellar and planet light even at very close distances, and in the right conditions, detect the presence of oxygen in their atmospheres (Marconi et al., 2020).

For the final words, the results presented in this thesis demonstrated the efficiency of various methods in detecting exoplanets orbiting M dwarfs. The application of photometry and spectroscopy in the near-infrared is yielding important insights into the properties of exoplanetary systems, particularly those orbiting low-mass stars. But many discoveries remain to be done to advance our understanding of exoplanetary system formation and evolution, as well as the potential habitability of exoplanets in M dwarf habitable zones. This study opens up new avenues for further exploration and investigation into the captivating world of exoplanets.

VI

RÉSUMÉ EN FRANÇAIS

VI.1 INTRODUCTION

Des planètes du système solaire aux exoplanètes

L'être humain a toujours été fasciné par ce qui se trouve au-delà de l'horizon terrestre. Depuis l'Antiquité, nous regardons le ciel nocturne et nous nous interrogeons sur les étoiles et les planètes. Cette fascination pour l'espace a conduit au développement de technologies telles que les télescopes et les satellites, dans le but de mieux comprendre l'univers dans lequel nous vivons. Au-delà de notre système solaire, il existe un univers vaste et encore largement inexploré. L'étude des exoplanètes, les planètes en orbite autour d'étoiles situées en dehors de notre système solaire, est l'un des domaines de recherche les plus passionnants de ces dernières années. La première détection d'une exoplanète en orbite autour d'une étoile semblable au Soleil a été faite par Mayor and Queloz, 1995. 51 Peg b a une masse minimale de 0,47 $M_{Jupiter}$, une période orbitale de 4,23 jours et est la première d'une classe d'exoplanètes connues sous le nom de Jupiters chauds. Ce n'est pas le type d'exoplanètes que nous nous attendions à découvrir, car elles n'existent pas dans notre système solaire mais cette découverte a donné le coup d'envoi pour la découverte de nombreuses exoplanètes, toutes plus surprenantes les unes que les autres. Depuis, les progrès réalisés en matière d'instrumentation et d'analyse de données ont permis de détecter des milliers d'exoplanètes au sein d'une grande variété de systèmes planétaires. En outre, la recherche sur les exoplanètes a des implications importantes, car l'étude des propriétés de ces exoplanètes et de leurs atmosphères nous permet d'en apprendre davantage sur la formation et l'évolution des systèmes planétaires, ainsi que sur les origines de notre propre système solaire.

Méthodes de détection

L'un des aspects les plus difficiles de l'étude des exoplanètes est qu'elles sont extrêmement éloignées, ce qui rend l'observation directe de ces objets difficile. C'est pourquoi la majorité des exoplanètes connues ont été découvertes par des méthodes indirectes, où l'on n'observe pas directement l'exoplanète mais où l'on détecte sa présence en mesurant l'atténuation de la lumière de l'étoile causée par le transit d'une planète devant son étoile ou en surveillant les variations de la vitesse radiale de l'étoile que l'exoplanète produit par son influence gravitationnelle.

La méthode des vitesses radiales est une technique qui mesure le mouvement d'une étoile causé par l'attraction gravitationnelle d'une exoplanète. En observant le mouvement de l'étoile, on peut déterminer la masse et l'orbite de l'exoplanète. La méthode des vitesses radiales ou spectroscopie Doppler est une méthode indirecte de détection des exoplanètes basée sur les oscillations qu'elles provoquent dans la vitesse radiale de leur étoile hôte, la vitesse radiale étant la projection en ligne de mire du vecteur vitesse de l'étoile. L'étoile tourne autour du barycentre du système étoile-planète en raison de l'interaction gravitationnelle réciproque étoile-planète. Si le plan orbital n'est pas orthogonal à la ligne de visée, les variations de la vitesse radiale de l'étoile le long de l'orbite entraînent des déplacements périodiques des raies d'absorption dans le spectre de l'étoile, qui peuvent être détectés à l'aide d'un spectrographe sur Terre.

Fischer et al., 2016 et Wright and Robertson, 2017 ont donné un aperçu des instruments Doppler de haute précision dans le visible et le proche infrarouge et des principaux relevés qui leur sont associés. HARPS (High Accuracy Radial Velocity Planet Searcher, Mayor et al., 2003) est situé à l'Observatoire de La Silla au Chili. Il a détecté plus d'une centaine d'exoplanètes et est considéré comme l'un des instruments de détection d'exoplanètes les plus performants. HIRES (High Resolution Echelle Spectrometer, Vogt et al., 1994), situé à l'observatoire Keck à Hawaï, a détecté des dizaines d'exoplanètes, y compris certaines des toutes premières exoplanètes confirmées. ESPRESSO (Echelle SPectrograph for Rocky Exoplanet and Stable Spectroscopic Observations, Pepe et al., 2021) est un spectrographe récent installé à Paranal au Chili et l'un des instruments de recherche de planètes les plus puissants actuellement utilisés. CARMENES (Calar Alto high-Resolution search for M dwarfs with Exo-earths with Near-infrared and optical Echelle Spectrographs, Quirrenbach et al., 2014) est un spectrographe situé à l'observatoire espagnol de Calar Alto et destiné à détecter des exoplanètes en orbite autour d'étoiles de faible masse. Ce ne sont là que quelques-uns des spectrographes qui ont été utilisés pour trouver des exoplanètes. Chaque instrument a ses propres avantages et inconvénients, et ils sont souvent utilisés en tandem avec d'autres instruments et techniques pour confirmer l'existence d'exoplanètes.

La méthode des transits consiste à observer la baisse de luminosité d'une étoile lorsqu'une exoplanète passe devant elle. La taille de l'exoplanète et la profondeur du transit étant liées, des transits plus profonds correspondent à des exoplanètes plus grandes. L'étude des courbes de lumière pour trouver des transits planétaires nous renseignent sur le rayon planétaire et l'inclinaison de l'orbite (en fonction de la forme de la courbe de transit) si les propriétés stellaires sont connues avec précision, et la récurrence du transit permet de contraindre la période orbitale de la planète. Comme seule une fraction des planètes peut être observée en transit, il faut observer un grand nombre d'étoiles pour trouver des exoplanètes, en particulier pour détecter des planètes à de grandes distances de leur étoile. C'est cette raison qui a motivée la création de relevés de transit avec de grands champs d'observation depuis l'espace et depuis le sol.

Les missions spatiales telles que CoRoT (Auvergne et al., 2009; Baglin et al., 2009) lancée en 2006, Kepler et K2 (Borucki et al., 2010; Howell et al., 2014) lancées en 2009 et maintenant TESS (Ricker et al., 2014) lancée en 2018 sont nécessaires pour obtenir une surveillance continue à long terme d'un grand nombre d'étoiles et détecter des milliers de candidats planétaires. D'autre part, les études depuis le sol sur des étoiles individuelles sont essentielles pour valider et confirmer l'existence des exoplanètes détectées par les missions spatiales, pour trouver d'autres exoplanètes dans des systèmes déjà connus et pour détecter des exoplanètes autour d'étoiles moins lumineuses. L'utilisation de ces instruments au sol (comme MEarth, Irwin et al., 2015 ; TRAPPIST, Jehin et al., 2011 ; SPECULOOS, Jehin et al., 2018) pour valider les candidats planétaires et améliorer la précision de la mesure du rayon a conduit à la découverte des premières exoplanètes terrestres orbitant dans la zone habitable de leur étoile comme dans le système TRAPPIST-1 (Gillon et al., 2016, 2017) ou dans le système TOI-700 (Gilbert et al., 2020, 2023).

La combinaison de la méthode des transits et de la méthode des vitesses radiales permet d'obtenir une compréhension plus détaillée des exoplanètes. Nous pouvons confirmer l'existence d'exoplanètes et éliminer les faux positifs en combinant les deux techniques. Par exemple, si une exoplanète est découverte par la méthode du transit, des observations ultérieures par la méthode des vitesses radiales peuvent mesurer sa masse et en déduire sa densité, révélant ainsi des informations importantes sur sa composition et sa structure interne. En outre, la détection d'une planète à l'aide des deux techniques augmente la probabilité qu'il s'agisse d'une véritable exoplanète et non d'un faux positif causé par un autre phénomène.

Exoplanètes autour des naines M

Le type spectral d'une étoile est une lettre donnée en fonction de la forme de son spectre et de l'intensité de ses raies. Il permet de classer les étoiles en fonction de leur température et de leur luminosité. Des types les plus chauds aux plus froids, nous avons 0, B, A, F, G, K, et M. Les naines M sont abondantes dans notre galaxie, représentant 70% des populations d'étoiles dans le voisinage solaire (Henry, Kirkpatrick, and Simons, 1994). Elles couvrent une très large gamme de masses (de 0,07 à 0,6 masse solaire) et de températures (de 2300 à 3800 K) entre les étoiles M9 et M0. Les naines M ont également une durée de vie plus longue que les autres étoiles et peuvent exister pendant des dizaines de milliards d'années. Ces étoiles sont les plus petites et les moins massives de la séquence principale. Le rayon et la masse plus faibles des naines M par rapport aux étoiles comme le Soleil ouvrent la voie à la détection et à la caractérisation de petites exoplanètes comme celles de la taille de la Terre, car le contraste entre l'étoile et l'exoplanète est plus grand, tant pour le transit photométrique que pour la mesure de la vitesse radiale. Un autre aspect intéressant des naines M est le potentiel de détection d'exoplanètes dans la zone habitable de leurs étoiles hôtes. En effet, leur faible luminosité implique une zone habitable plus proche, correspondant à des périodes orbitales relativement courtes (10-30 jours). La zone habitable est définie par

Kopparapu et al., 2013 comme la région autour d'une étoile où l'exoplanète reçoit la bonne quantité d'irradiation pour avoir potentiellement de l'eau liquide à la surface.

Les naines M sont le type d'étoile le plus courant et de nombreuses exoplanètes sont susceptibles d'être découvertes en orbite autour de ces étoiles. Cependant, la détection de petites exoplanètes autour des naines M est difficile en raison de leur faible luminosité intrinsèque. Comme les étoiles de type M émettent la majorité de leur énergie dans le spectre infrarouge, on s'attend à ce que les observations dans le proche infrarouge soient plus efficaces pour détecter les petites exoplanètes en orbite autour de ces étoiles en utilisant les méthodes du transit et de la vitesse radiale. En effet, la luminosité de l'étoile influence la précision mesurée sur la profondeur du transit. En observant l'absorption de la lumière proche infrarouge par des caractéristiques atmosphériques telles que la vapeur d'eau et le méthane, les observations dans le proche infrarouge peuvent également être utilisées pour caractériser les atmosphères des exoplanètes. Les étoiles de type M présentent peu de caractéristiques spectrales dans le domaine visible, ce qui limite la précision des mesures de vitesse radiale. Le proche infrarouge, en revanche, est riche en caractéristiques d'absorption moléculaire qui peuvent être utilisées pour mesurer les vitesses radiales avec une plus grande précision.

Le proche infrarouge est également utile pour atténuer l'effet de l'activité stellaire. En effet, l'observation dans le proche infrarouge permet de distinguer plus facilement les contributions des vitesses radiales des activités planétaires et stellaires. L'amplitude des signaux d'activité est réduite dans le proche infrarouge car le contraste entre les éléments sombres et brillants de la photosphère stellaire diminue entre les longueurs d'onde du visible et celles du proche infrarouge. Le fait de disposer simultanément des vitesses radiales optiques et proche infrarouge (en combinant HARPS et NIRPS par exemple) est encore plus puissant car il permet de distinguer les signaux ayant les mêmes caractéristiques (un signal képlérien d'une planète) dans les deux domaines spectraux et les signaux ayant des caractéristiques différentes (signal d'activité) dans les deux domaines spectraux.

Questions actuelles en exoplanètes

La science des exoplanètes est un domaine en pleine expansion qui cherche à étudier et à comprendre les planètes situées au-delà de notre système solaire. L'analyse combinée des exoplanètes détectées par toutes les méthodes peut fournir des informations intéressantes, mais de nombreuses questions restent sans réponse, et la science des exoplanètes demeure l'un des domaines les plus actifs de la recherche astronomique. L'un des aspects les plus frappants de ce domaine est la diversité des systèmes exoplanétaires. Les exoplanètes varient en taille, en masse et en orbite, des Jupiters chauds aux super-Terres. Nous essayons de comprendre les causes de cette diversité et son lien avec la formation et l'évolution des systèmes exoplanétaires, ainsi que la manière dont le gaz et la poussière présents dans les disques protoplanétaires autour des jeunes étoiles forment des planètes. Nous nous intéressons également à la manière dont les planètes interagissent entre elles et avec leur étoile au fil du temps. Ces connaissances sont essentielles pour comprendre les diverses architectures planétaires observées dans les systèmes exoplanétaires, ainsi que les conditions qui conduisent à la formation des exoplanètes.

En ce qui concerne les systèmes planétaires en orbite autour des naines M, il convient de noter qu'une douzaine de systèmes seulement avaient été bien caractérisés lorsque j'ai commencé ma thèse, et que ce nombre a doublé depuis. Malgré le peu de données disponibles, ces systèmes ont déjà démontré des caractéristiques intrigantes et remarquables, qui seront discutées plus en détail dans les paragraphes suivants.

Des recherches récentes indiquent que les petites exoplanètes ont tendance à être plus fréquentes autour des naines M qu'autour des étoiles de type solaire. Cloutier and Menou, 2020 a constaté une augmentation de la fréquence des planètes rocheuses autour d'étoiles de faible masse, cependant, ils n'ont pas été en mesure d'identifier avec certitude la cause physique de cette tendance. Kubyshkina and Vidotto, 2021 a découvert que l'échappement atmosphérique des exoplanètes ayant la même température d'équilibre se produit plus efficacement autour des étoiles de faible masse. Malgré les preuves suggérant que les naines M ont tendance à former plus de planètes rocheuses que de planètes riches en matériaux volatiles, il semble que les mini-Neptunes autour des naines M soient en fait moins denses que celles autour d'autres étoiles. Déterminer si ces exoplanètes continuent à suivre cette tendance de faible densité ou non fournira des informations critiques pour les scénarios de formation d'exoplanètes autour des naines M.

Dans le régime des petites planètes, la découverte récente d'une distribution bimodale de rayons séparés par une vallée autour de 1,8 R_E a ouvert une nouvelle fenêtre sur la formation planétaire (Bean, Raymond, and Owen, 2021; Fulton et al., 2017). Cette vallée autour des naines M est située à des rayons légèrement plus petits qu'autour des étoiles semblables au Soleil (Cloutier and Menou, 2020) et marque la transition entre les super-Terres rocheuses et les mini-Neptunes qui possèdent des enveloppes H/He (Owen and Wu, 2017). Plusieurs mécanismes physiques ont été proposés pour expliquer cette vallée, notamment la photo-évaporation, la perte de masse alimentée par le noyau (Gupta and Schlichting, 2020; Jin and Mordasini, 2018; Wyatt, Kral, and Sinclair, 2020), ou directement comme un résultat du processus de formation des planètes dans lequel les super-Terres se forment à des moments ultérieurs dans un environnement pauvre en gaz (Lee and Connors, 2021; Lopez and Rice, 2018). La caractérisation de la composition globale d'autres exoplanètes en transit permettra de déterminer si la vallée autour des naines M provient directement de la formation de la planète ou si elle est le résultat d'un échappement atmosphérique après la formation de la planète.

Il a également été remarqué que les exoplanètes de la masse de Jupiter sont extrêmement rares à proximité des naines M. L'absence de Jupiters chauds est particulièrement intrigante car, en raison de leur grande taille et de leur courte période, ces planètes sont les plus faciles à détecter. Par conséquent, leur absence est très probablement réelle et n'est pas due à un biais de détection. Les modèles récents de synthèse des populations planétaires basés sur la théorie de l'accrétion du noyau prédisent un taux d'occurrence très faible des exoplanètes géantes et suggèrent même qu'il devrait diminuer jusqu'à zéro pour la gamme de masse stellaire des naines M (Burn et al., 2021). Cependant, quelques-unes de ces exoplanètes géantes ont été détectées en orbite autour de naines M. Pour fournir plus d'informations sur leur processus de formation, la validation et la mesure des masses d'un plus grand nombre de planètes géantes transitant des naines M sont nécessaires.

Les naines M sont différentes des autres étoiles car elles ont tendance à héberger des systèmes multiplanétaires, qui peuvent fournir des tests beaucoup plus solides pour les théories de formation planétaire que les systèmes à une seule planète (Ballard and Johnson, 2016; Fang and Margot, 2012; Steffen and Hwang, 2015). Selon Otegi, Helled, and Bouchy, 2022 qui a examiné les systèmes multiplanétaires observés par K2 et TESS, pour lesquels les rayons et la masse ont été mesurés avec précision, les systèmes multiplanétaires de naines M présentent plus de similitudes en termes de densité que de masse, ce qui indique un lien possible dans leur mécanisme de formation. Outre les informations encodées dans l'architecture des systèmes multiplanétaires, la structure interne des exoplanètes en orbite autour d'une même étoile hôte est extrêmement précieuse pour contraindre les modèles. Comme elles partagent la même étoile hôte et le même disque d'accrétion, la seule différence de composition est le lieu de formation et l'évolution. La caractérisation de la densité apparente des exoplanètes dans les systèmes multiplanétaires, ainsi que l'estimation de la présence de volatiles et d'eau liquide/solide, nous permettent de tester directement les hypothèses de formation des planètes.

Les mesures de la masse et du rayon des exoplanètes doivent être très précises afin de comprendre leur structure interne et leur atmosphère. Ces mesures peuvent être difficiles car elles nécessitent des observations détaillées et une analyse minutieuse des données, ce qui a motivé la conception de nouveaux instruments comme ExTrA et NIRPS qui pourraient pousser la précision déjà acquise dans le visible jusqu'au domaine du proche infrarouge afin d'obtenir des mesures précises du rayon et de la masse des exoplanètes en orbite autour des naines M.

VI.2 LA MISSION SPATIALE TESS

Après le succès des missions CoRoT (Auvergne et al., 2009; Baglin et al., 2009) et Kepler (Borucki et al., 2010), ainsi que d'autres études depuis le sol sol, l'étape suivante pour la communauté des exoplanètes consistait à concevoir une mission spatiale photométrique couvrant l'ensemble du ciel et permettant la découverte de planètes en transit autour d'étoiles brillantes se prêtant à un suivi en vitesses radiales. Le Transiting Exoplanet Survey Satellite (TESS) représente une avancée significative dans la recherche d'exoplanètes. TESS détecte les exoplanètes en utilisant la méthode des transits et étudie la quasi-totalité du ciel au cours de sa mission, en se concentrant sur des zones différentes chaque année. Même si la mission est encore en cours, TESS apporte déjà des contributions significatives au domaine de la recherche sur les exoplanètes grâce à ses capacités de pointe et à sa vaste zone d'étude. TESS à trouvé des TOIs (TESS Object of Interest, ou candidats planétaires) en orbite autour d'une population stellaire variée, mais dans le cadre de mon doctorat, je m'intéresse aux TOIs en orbite autour des naines M.

Observations de suivi

TESS vise à trouver de petites exoplanètes en orbite autour d'étoiles brillantes qui peuvent être étudiées en détail grâce à des observations de suivi, généralement réalisées depuis le sol. Ces observations de suivi depuis le sol sont nécessaires pour contraindre les éphémérides précises et les paramètres orbitaux de l'objet en transit. Comme TESS a un grand champ de vision, les étoiles situées à moins de 2,5 minutes d'arc les unes des autres sont extrêmement difficiles à distinguer. TESS pourrait attribuer une baisse de flux à une exoplanète en transit, alors qu'il s'agit en fait d'une binaire à éclipses ou d'un événement qui s'est produit sur une étoile proche. Les observations de suivi permettront de valider le candidat planétaire, d'estimer la masse planétaire par des mesures de vitesse radiale (Cloutier et al., 2018) et de caractériser l'atmosphère de l'exoplanète par spectroscopie en transmission (Kempton et al., 2018).

Le programme d'observation de suivi de TESS (TFOP) coordonne la majorité des observations de suivi des TOIs. La plupart des travaux de suivi se répartissent en cinq domaines, chacun d'entre eux ayant son propre sous-groupe (SG). Le SG1 utilise la photométrie pour détecter les faux positifs causés par des binaires à éclipses qui peuvent contaminer l'image TESS. Le SG2 est dédié à la spectroscopie de reconnaissance et fournit des paramètres spectroscopiques qui contraignent plus précisément les masses et les rayons des étoiles hôtes, détecte les faux positifs causés par les binaires spectroscopiques et identifie les étoiles qui ne se prêtent pas à des mesures précises de vitesses radiales. Le SG3 fournit une imagerie à haute résolution afin d'identifier les objets proches qui ne sont pas résolus dans le catalogue TESS. Le SG4 vise à déterminer la masse planétaire par rapport à l'étoile hôte en utilisant des mesures précises de la vitesse radiale. Le SG5 utilise la photométrie spatiale principalement pour confirmer et/ou améliorer les éphémérides des cibles TESS, mais aussi pour fournir de meilleures courbes de lumière. Au cours de mon doctorat, j'ai été impliqué en particulier dans le SG1 en faisant de la photométrie depuis le sol avec ExTrA pour valider la nature planétaire du compagnon et améliorer la mesure du rapport des rayons. Avec ExTrA, nous avons également la possibilité d'observer le transit dans une gamme de longueurs d'onde différente de celle de TESS. J'ai également suivi l'activité du SG4 qui se concentre sur la mesure précise des vitesses radiales pour confirmer et caractériser les exoplanètes.

TOIs autour des naines M

Pour réussir à détecter de nouvelles exoplanètes en orbite autour de naines M avec ExTrA et NIRPS, j'ai d'abord eu besoin d'un échantillon de candidats pour observer et confirmer la présence d'une exoplanète en orbite autour de l'étoile cible. Pour m'organiser, j'ai créé un tableau regroupant tous les candidats TESS autour des naines M que je mets à jour mensuellement avec les nouveaux secteurs TESS, les publications et les résultats du programme de suivi SG1 afin d'optimiser les observations de suivi faites avec ExTrA. Pour trier ces candidats, j'ai sélectionné dans le catalogue des TOIs des systèmes dont la température stellaire est inférieure à 4100 K, et dont le rayon est strictement inférieur à 1 R_{Sun} pour éviter les étoiles géantes rouges et les étoiles à rayon inconnu (qui sont placées automatiquement à 1 R_{Sun} dans TFOP). J'ai rassemblé toutes les TOIs correspondant à ces critères dans un tableau et j'y ai ajouté quelques informations utiles pour les observations de suivi. Sur les 441 TOIs actuellement dans ce tableau, 28 étaient déjà des exoplanètes connues avant que TESS ne les observe, 43 ont été confirmées et publiées avec un rayon et une masse, 36 ont été validées mais sans estimation de masse pour l'instant et 321 sont encore des candidates planétaires.

Une autre utilisation très importante de ce tableau est de rassembler les observations de suivi des différents TOIs. En tant que membre de TFOP, j'ai accès aux informations sur les observations de suivi des instruments photométriques et vélocimétriques que j'ai affichées dans ce tableau, ainsi qu'au rayon et à la masse des planètes obtenus à partir d'articles publiés. J'utilise également ce tableau pour sélectionner les différentes cibles que nous observons avec ExTrA. En partant de nos premiers résultats publiés sur les capacités d'ExTrA (Cointepas et al., 2021), nous avons pu estimer le S/N (rapport signal sur bruit) que nous attendons pour n'importe quelle étoile de la table en fonction de sa magnitude et de la profondeur et durée du transit. Une fois les observations effectuées avec ExTrA, je mets à jour le tableau pour suivre l'évolution de chaque candidat.

Analyses des courbes de lumière

J'ai analysé de manière systématique toutes les courbes de lumière TESS pour les TOIs en orbite autour de naines M afin d'avoir une idée de la qualité des données, des variations dans la photométrie et d'avoir un premier regard sur les transits. Pour modéliser la photométrie de TESS, j'ai utilisé le logiciel juliet développé par Espinoza, Kossakowski, and Brahm, 2019 et disponible publiquement sur GitHub. Le package batman (Kreidberg, 2015) est utilisé pour modéliser le transit, et l'ajustement est fait en utilisant un algorithme d'échantillonnage. J'ai décidé d'utiliser des processus gaussiens (GP) pour corriger les systématiques restantes dans la photométrie de TESS. Deux routines spécifiques ont été créées pour modéliser les courbes de lumière de TESS, l'une pour les données SPOC avec une cadence de 2 minutes et l'autre pour les données QLP avec une cadence de 30 minutes, et fournissent en sortie les paramètres postérieurs de l'ajustement du transit et ainsi que les courbes de lumière et le modèle ajusté.

VI.3 L'INSTALLATION PHOTOMÉTRIQUE EXTRA

J'ai passé la majeure partie de mon doctorat à travailler avec ExTrA, une installation située à l'observatoire de La Silla au Chili. Le projet vise à étendre la précision de la photométrie dans le visible à la photométrie dans le proche infrarouge en utilisant l'information spectroscopique pour sélectionner les meilleures bandes de longueur d'onde et éliminer ce qui pourrait causer des effets de couleur et perturber les observations depuis le sol. Grâce à cette approche unique, ExTrA espère découvrir des planètes rocheuses en transit orbitant dans la zone habitable de naines M proches. Mon travail a consisté à détecter des exoplanètes en transit en examinant les données brutes pour créer des courbes de lumière utilisables. Une fois les courbes de lumière créées, je les ai analysées pour identifier les transits planétaires et les ai modélisées pour obtenir les paramètres de la planètes.

Description de l'instrument et Observations

ExTrA est composé de trois télescopes de 60 cm alimentant un spectrographe proche infrarouge (Bonfils et al., 2015). Les télescopes sont placés dans trois dômes et un bâtiment auxiliaire abrite le spectrographe, le serveur principal, une station météorologique, une caméra sur le ciel et une webcam. Sur chaque télescope, 5 unités de champ (FU) sont utilisées à la place d'une caméra CCD pour capter la lumière de la cible et de 4 étoiles de comparaison. La spectro-photométrie de la cible sera comparée à la spectro-photométrie des quatre étoiles de comparaison. Les FU sont constitués de fibres, positionnées avec précision pour assurer la stabilité photométrique. Les trois télescopes sont indépendants, et toutes les fibres des trois télescopes alimentent un seul spectrographe dans le proche infrarouge avec une faible résolution spectrale, où deux prismes différents sont disponibles avec des résolutions de R$\sim$20 ou R$\sim$200, et une couverture en longueur d'onde de 0,85 à 1,55 microns. Chaque télescope possède 5 FUs, chacun avec 4 fibres scientifiques (2 de 4 arcsec et 2 de 8 arcsec), pour un total de 60 fibres reliant le plan focal des télescopes au spectrographe.

Les observations d'ExTrA sont entièrement réalisées à distance. Nous sélectionnons des cibles et les observons lorsqu'un transit est prévu. Pour ce faire, nous utilisons un outil de prédiction des transits, développé par un membre de l'équipe scientifique d'ExTrA, qui prend en entrée les éphémérides calculées en utilisant la photométrie de TESS ou des éphémérides plus précises et qui affiche pour la nuit sélectionnée les transits visibles depuis l'Observatoire de La Silla ainsi que l'heure et la durée des transits. Quelques cibles, généralement 2 à 3 par nuit, sont alors sélectionnées pour être observées. Au cours des deux premières années d'observation d'ExTrA, nous avons décidé que les trois télescopes observeraient la même cible afin d'estimer correctement les capacités de l'instrument. Les trois télescopes peuvent bien sûr observer des cibles différentes en même temps afin d'augmenter l'efficacité de notre étude.

Analyses de données

Après la phase d'observation, l'étape suivante consiste à effectuer une analyse complète des données acquises. La création et la modélisation d'une courbe de lumière pour trouver un transit impliquent plusieurs étapes. Nous commençons par collecter les données obtenues à partir d'un photomètre ou d'un télescope spatial qui surveille en permanence la luminosité d'une étoile au fil du temps. J'ai principalement travaillé avec les observations des trois télescopes ExTrA et du satellite TESS. Les données d'observation sont ensuite traitées pour éliminer les effets systématiques et le bruit. Il s'agit notamment d'éliminer les valeurs aberrantes, de corriger les tendances systématiques et de normaliser les données. Cette étape correspond à la production des courbes de lumière. Une fois que nos courbes de lumière sont prêtes, nous définissons un modèle qui prend en compte le transit de la planète : sa période orbitale, la taille de la planète, et la forme du transit, et si nécessaire des modèles de bruit. Le modèle est ensuite ajusté à la courbe de lumière à l'aide de méthodes statistiques. La qualité de l'ajustement est évaluée en comparant le modèle aux données ou différents modèles entre eux, et en examinant les résidus de l'ajustement. Une fois que nous avons décidé quel modèle est le plus fiable, les paramètres du transit, tels que la profondeur, la durée et la période orbitale de la planète, peuvent être extraits du modèle. Ces paramètres peuvent ensuite être utilisés pour estimer la taille et les autres propriétés de la planète en transit.

juliet est un outil très utile pour modéliser différents ensembles de données, c'est pourquoi j'ai dû apprendre à le maîtriser pendant mon doctorat car je l'ai utilisé pour toutes les modélisations faites. J'ai créé plusieurs routines qui implémentent juliet, afin de modéliser uniquement la photométrie de TESS, la photométrie de TESS et ExTrA en utilisant une profondeur de transit commune pour les deux instruments et aussi différentes profondeurs pour vérifier la chromaticité du signal de transit et enfin une modélisation conjointe de la photométrie et de la vitesse radiale combinée pour caractériser certaines exoplanètes.

L'une des premières cibles observées par ExTrA est TOI-269, où nous avons pu confirmer la présence d'une mini-Neptune en orbite autour de cette étoile de type M2. Nous l'avons observée 3 nuits avec ExTrA lorsque des transits étaient attendus compte tenu de l'éphéméride calculée avec TESS. D'autres installations avaient obtenu des observations pour cette cible spécifique et je les ai donc toutes rassemblées. L'analyse des données photométriques et vélocimétriques a révélé une orbite excentrique pour TOI-269 b avec presque la valeur la plus élevée pour des planètes de ce type. Nous avons effectué de nombreux tests pour confirmer ce résultat et nous nous sommes ensuite tournés vers des explications possibles telles que la migration de la planète, l'intéraction avec une planète lointaine ou l'échappement atmosphérique.

Cas scientifiques et sélection des cibles

En utilisant la photométrie de transit, le projet ExTrA vise à détecter de petites exoplanètes en orbite autour d'étoiles naines M. Le temps d'observation d'ExTrA a été divisé en différents sous programmes, chacun avec son propre ensemble d'objectifs qui correspondent à un cas scientifique spécifique. Dans chaque sous programme, j'ai soigneusement sélectionné un sous-ensemble de cibles du catalogue TOI qui sont les mieux adaptées pour répondre aux questions scientifiques. En mars 2023, ExTrA a déjà observé $\sim$160 TOIs différents.

Après avoir publié le premier article de validation d'une exoplanète en orbite autour d'une naine M en utilisant la photométrie ExTrA, nous avons réalisé que nous pouvions obtenir la même précision sur les résidus des courbes de lumière ajustées que TESS mais avec moins de transits ExTrA. Ceci a motivé la création du premier sous programme d'ExTrA dédié à la validation des candidats planétaires de TESS en utilisant les observations ExTrA dans le proche infrarouge et en améliorant l'estimation actuelle du rayon planétaire. Nous avons choisi des TOIs autour d'étoiles ayant des températures effectives inférieures à 3800K qui sont visibles par les télescopes ExTrA de l'Observatoire de La Silla. Nous avons sélectionné des cibles pour lesquelles 5 transits ExTrA devraient permettre d'obtenir un rapport signal/bruit similaire ou supérieur à celui de TESS (sans tenir compte des observations futures de TESS ou de la photométrie additionnelle). Nous avons inclus des candidats planétaires qui n'avaient pas encore été validés par un suivi spectroscopique ou photométrique, car nous pensons que la couverture en longueurs d'onde dans le proche infrarouge d'ExTrA permettra d'exclure les binaires à éclipses comme source du signal de transit. Les résultats de cette étude sont actuellement en train d'être résumés dans un article.

Un deuxième sous programme d'ExTrA est consacré aux systèmes multiplanétaires. Les systèmes comportant deux exoplanètes ou plus sont importants pour plusieurs raisons. La découverte de plusieurs exoplanètes dans un même système permet de mieux comprendre la formation et l'évolution des planètes. L'étude des propriétés de ces planètes, telles que leur rayon, leur masse, leur orbite et leur composition, permet d'élaborer et de tester des théories sur la formation des systèmes planétaires. Ces systèmes peuvent présenter une grande variété d'architectures et de propriétés, fournissant ainsi des données pour tester les théories sur la formation et l'évolution des planètes. Les systèmes d'exoplanètes multiples peuvent également nous aider à mieux comprendre le processus de migration des planètes. Les planètes peuvent s'éloigner de leur position initiale à la suite d'interactions gravitationnelles avec d'autres planètes ou avec le disque protoplanétaire. La présence de plusieurs planètes dans un système peut nous aider à limiter les trajectoires de migration possibles et à mieux comprendre les facteurs qui influencent la migration des planètes. En observant plusieurs transits d'une exoplanète, en particulier dans les systèmes multiplanétaires déjà connus, nous pouvons détecter des variations du temps de transit (TTV). Les TTVs sont des déviations dans le temps de transit d'une exoplanète qui peuvent être causées par des interactions gravitationnelles avec d'autres exoplanètes dans le système (Agol and Fabrycky, 2018; Agol et al., 2005; Holman and Murray, 2005). Les TTVs peuvent être utilisés pour détecter des planètes supplémentaires dans un système, ainsi que pour contraindre les propriétés des planètes connues. Pour ce projet, nous avons sélectionné des systèmes multi-planétaires à partir de l'échantillon de naines M de TESS, auquel nous avons ajouté des candidats de TESS avec d'éventuelles exoplanètes supplémentaires détectées en vitesses radiales.

VI.4 LE SPECTROGRAPHE PROCHE INFRAROUGE NIRPS

Dans l'étude et la caractérisation des exoplanètes, les mesures de vitesse radiale sont complémentaires à la photométrie pour obtenir la masse du compagnon planétaire et donc estimer sa densité. Le Near Infrared Planet Searcher, NIRPS, est un spectrographe conçu pour observer dans le domaine spectral du proche infrarouge depuis l'hémisphère sud. L'objectif principal de NIRPS est d'effectuer un suivi précis de la vitesse radiale des candidats planètes en transit identifiés par les missions spatiales, parfois déjà validés à l'aide de la photométrie au sol, et surtout d'observer les naines M afin de trouver et de caractériser les exoplanètes, y compris les exoplanètes rocheuses, dans la zone habitable de leur étoile. En mai 2015, l'ESO a invité l'équipe de NIRPS à adapter la conception originale du spectrographe pour une observation simultanée avec le spectrographe HARPS au foyer Cassegrain du télescope de 3,6 mètres de l'ESO à l'Observatoire de La Silla.

Description de l'instrument

NIRPS est un spectrographe équipé d'une optique adaptative et situé dans un réservoir cryogénique sous vide. NIRPS observe dans les bandes spectrales Y, J et H avec une gamme de longueurs d'onde de 0,971-1,854 μm. Nous nous attendons à ce qu'il fournisse des vitesses radiales avec une précision d'environ 1 m/s. Une description plus détaillée de l'instrument est disponible dans Bouchy et al., 2017; Wildi et al., 2022. NIRPS est composé de quatre sous-systèmes différents : le front-end connecté au télescope de 3,6 m, l'unité d'étalonnage, la liaison par fibre optique et le spectrographe. Le front-end extrait la lumière de 700 nm à 2400 nm du télescope à l'aide d'un dichroïque et corrige la dispersion atmosphérique. NIRPS est le premier spectrographe doté d'un système d'optique adaptative (OA) (Conod et al., 2016). L'instrument est équipé d'une fibre multimode, qui est beaucoup moins affectée par les résidus de correction de l'OA qu'une fibre monomode, ce qui permet d'obtenir une meilleure efficacité (Blind, Conod, and Wildi, 2017). Le spectrographe est très compact grâce au système d'OA, qui permet de réduire d'un facteur deux la taille de la fibre. Le faisceau lumineux est ensuite injecter dans une fibre optique qui transporte la lumière vers le spectrographe, avec la possibilité de brouiller la lumière. NIRPS dispose de deux modes d'observation. Le mode HA, qui utilise une fibre octogonale de 0,4 arcsec pour atteindre une résolution spectrale de ∼82 000 et le mode HE, qui utilise une fibre octogonale de 0,9 arcsec, coupée en deux au niveau de la pupille et alimentant une fibre rectangulaire pour atteindre une résolution spectrale de ∼75 000. La fibre est étirée à l'aide d'un dispositif qui réduit l'impact du bruit modal en modulant rapidement la phase entre les modes et en homogénéisant l'éclairage en sortie.

HARPS et NIRPS observeront simultanément la plupart du temps, même si NIRPS peut être utilisé seul. Cela permettra de construire un spectrographe unique, puissant, à haute résolution et haute fidélité, couvrant la gamme de 0,37 à 1,85 microns. Comme les vitesses radiales dans le proche infrarouge sont moins affectées par les variations des taches stellaires que dans le visible, cette combinaison permettra un meilleur étalonnage de l’activité stellaire.

Observations de temps garanti NIRPS

Les observations de temps garanti (GTO) sont accordées pour la création de matériel ou de logiciels qui améliorent les capacités scientifiques de l’ESO. Le nombre total de nuits GTO accordées à l’équipe NIRPS est de 725 nuits qui seront programmées au cours des cinq premières années d’exploitation de l’instrument (2023 - 2028). NIRPS a été conçu pour étudier les différents aspects offerts par les naines M en tant qu’hôtes d’exoplanètes, en se concentrant sur trois cas scientifiques principaux : le Work Package 1 pour effectuer une recherche d’exoplanètes en aveugle autour des naines M afin de comprendre la formation des planètes, en particulier sa sensibilité aux conditions initiales dans le disque protoplanétaire et trouver des cibles intéressantes pour des études d’imagerie directe avec les futurs imageurs à optique adaptative sur l’ELT, le Work Package 2 pour mesurer la masse et déduire la densité des exoplanètes en transit autour des naines M, et le Work Package 3 pour caractériser les atmosphères des exoplanètes via la spectroscopie de transmission à haute résolution. J’ai contribué au GTO de NIRPS en proposant deux programmes différents liés aux WP1 et WP2. En plus de proposer ces deux programmes, j’ai également participé à la préparation du premier semestre d’observations avec NIRPS en aidant dans la planification et la coordination du calendrier d’observation pour ces deux work packages. J’ai collaboré étroitement avec d’autres membres de l’équipe NIRPS pour veiller à ce que le temps d’observation soit optimisé et alloué de manière appropriée en fonction du niveau de priorité des différentes cibles.

Le premier programme Deep Search pour détecter des planètes additionnelles avec NIRPS a été principalement réalisé pendant le stage d’Augustin Patey intitulé "Vers une stratégie optimale de détection des exo-Terres en transit". Le satellite TESS utilise actuellement la méthode du transit pour détecter les exoplanètes. Ballard, 2019 a proposé une estimation du nombre d’exoplanètes qui auraient été détectées par TESS autour des naines M, ainsi que le nombre d’exoplanètes que TESS aurait manqué. L’idée principale de ce projet était, en utilisant les données TESS dont nous disposons actuellement, d’estimer à nouveau le nombre d’exoplanètes manquées autour des naines M TESS et de calculer le coût de leur détection en utilisant une variété d’instruments vélocimétriques et photométriques. La dernière étape a consisté à déterminer comment utiliser au mieux le temps de télescope donné afin de maximiser le taux de nouvelles détections. En supposant que l’orbite d’une planète ait une orientation uniformément distribuée, la probabilité qu’elle soit orientée pour transiter est telle que seule une fraction des exoplanètes existantes peut être détectée à l’aide de cette méthode. Malgré cette statistique défavorable, les orbites des exoplanètes au sein d’un même système planétaire tendent à être relativement coplanaires. Par conséquent, pour une étoile donnée, la détection d’une exoplanète en transit biaise la statistique des autres exoplanètes potentielles en orbite autour de l’étoile en faveur d’une orbite bien orientée. Nous avons développé une stratégie d’étude qui cible les systèmes connus pour avoir une orientation favorable (c’est-à-dire au moins une exoplanète en transit), en optimisant le taux de nouvelles détections. Contrairement aux recherches traditionnelles à l'aveugle, nous appelons cette stratégie Deep Search.

Le second programme vise à peupler le diagramme Masse-Rayon des exoplanètes autour des naines M les plsu froides en mesurant precisément les masses des planètes détectées en transit. Au cours des trois dernières décennies, plus de 5000 exoplanètes ont été découvertes, et des propriétés statistiques significatives sont apparues. Des recherches antérieures ont suggéré que la distribution de la masse et du rayon des exoplanètes diffère entre les étoiles M et FGK. Divers processus physiques peuvent avoir lieu, et nous pouvons nous demander si la formation de planètes est plus efficace autour des naines M (Ballard, 2019; Ballard and Johnson, 2016; Dressing and Charbonneau, 2015), et si les exoplanètes en orbite autour de ce type d'étoile ont des compositions plus rocheuses (Mulders, Pascucci, and Apai, 2015). Cependant, en regardant le diagramme Mass-Rayon des planètes connues, nous observons que les mini-Neptunes autour des naines M semblent être moins denses que les mini-Neptunes autour d'autres types d'étoiles. Déterminer si ces planètes ont réellement des densités plus faibles ou, au contraire, ont des compositions plus rocheuses fournira des informations critiques pour comprendre le scénario de formation des exoplanètes en orbite autour des naines M. Seules 12 exoplanètes (statistiques obtenues par Otegi, Bouchy, and Helled, 2020) ont été bien caractérisées autour de ces étoiles au moment la préparation du GTO. Nous proposons d'ajouter 29 nouveaux candidats TESS à cet échantillon en mesurant leur masse précisement à l'aide de NIRPS.

En résumé, après avoir réalisé 9 commissionings, l'instrument NIRPS est désormais prêt à débuter ses observations en avril 2023. Suite à la première lumière de l'instrument le 17 mai 2022, quelques étoiles ont déjà été observées avec succès. Les résultats obtenus lors des différentes tests indiquent que la précision de l'instrument est en accord avec les attentes pour mesurer la semi-amplitude de vitesse radiale des candidats proposés dans les différents programmes.

VI.5 CONCLUSION

Au cours de mon doctorat, j'ai mené mes recherches avec une perspective globale, comprenant différentes étapes allant de la sélection des cibles à l'analyse des données et à l'interprétation des résultats, en passant par la programmation des observations à l'aide de différents instruments. Dans cette section, je résumerai mon travail avec ExTrA et je décrirai les travaux potentiels à venir. Je parlerai ensuite de mon implication dans l'équipe scientifique du NIRPS et des programmes que j'ai proposés pour le GTO. Je mentionnerai également les synergies potentielles entre les observations de transit d'ExTrA et les mesures de vitesse radiale de NIRPS. Je présenterai les articles auxquels j'ai contribué et la manière dont ils nous aident à comprendre les systèmes planétaires qui existent autour des naines M. Enfin, je conclurai sur les prochaines étapes nécessaires pour améliorer notre compréhension des exoplanètes en orbite autour des naines M et sur les futures missions dans ce domaine.

ExTrA : conclusion et perspectives

Mes recherches portent sur la découverte de nouvelles exoplanètes en orbite autour de naines M. Pour observer ces cibles peu lumineuses, les observations dans le proche infrarouge sont privilégiées car les naines M émettent la majeure partie de leur énergie à ces longueurs d'onde. Pendant ma thèse, j'ai travaillé sur ExTrA, une installation composée de trois télescopes de 60 cm observant dans le proche infrarouge et conçue pour détecter et valider de petites exoplanètes autour d'étoiles de faible masse. Pour ce faire, j'ai commencé par planifier les observations en utilisant une liste de cibles basée sur les candidats planétaires trouvés par la mission TESS. Après avoir acquis les observations, j'ai réduit les données et développé un code pour convertir les spectres ExTrA en courbes de lumière utilisables. Avec les courbes de lumière, j'ai également créé un rapport de nuit automatique au format PDF, un document utile pour repérer tout problème pendant les observations qui pourrait avoir un impact sur les courbes de lumière. Une fois créées, j'ai analysé et modélisé les courbes de lumière pour rechercher des signaux de transit. J'ai dû choisir un outil de modélisation déjà existant (juliet, Espinoza, Kossakowski, and Brahm, 2019), apprendre la meilleure façon de paramétrer le modèle, d'identifier et de supprimer les systématiques des données, et comprendre la variété des techniques statistiques pour obtenir les distributions postérieures de l'ajustement et pour estimer la taille et l'orbite de toutes les exoplanètes observées. J'ai décidé d'utiliser des processus gaussiens pour corriger les systématiques présentes dans la photométrie ExTrA. Comme je ne pouvais pas déterminer l'origine de ces systématiques, les modéliser avec un processus gaussien semblait être la meilleure solution.

Une fois que les routines pour modéliser conjointement les ensembles de données photométriques et vélocimétriques afin de contraindre les paramètres planétaires ont été perfectionnées, je les ai utilisées pour publier deux systèmes nouvellement découverts (TOI-269 b et TOI-663 b, c et d) et j'ai travaillé sur la recherche d'objectifs scientifiques spécifiques à atteindre en utilisant l'installation ExTrA. J'ai également créé des routines génériques pour ajuster la photométrie de TESS et d'ExTrA simultanément et je suis en train de rédiger un article résumant les résultats du WP1 d'ExTrA sur la validation des candidats planétaires de TESS et l'amélioration de la mesure du rayon planétaire à l'aide des transits d'ExTrA. Dans l'ensemble, ExTrA produit déjà des courbes de lumière utilisables et s'est avéré un outil utile pour valider les candidats planétaires en orbite autour d'étoiles de faible masse. Plusieurs articles publiés utilisent les observations d'ExTrA pour confirmer le transit dans l'infrarouge proche et augmenter la précision des paramètres planétaires.

Le résumé de toutes les observations d'ExTrA sera utilisé dans un futur proche pour estimer les performances de l'instrument, ainsi que pour déterminer quelles étoiles ou quels systèmes planétaires pourraient bénéficier des observations d'ExTrA dans le proche infrarouge.

NIRPS : conclusion et perspectives

Pendant la deuxième partie de mon doctorat, j'ai eu l'occasion de travailler sur la préparation du spectrographe proche infrarouge installé sur le télescope de 3,6 m de l'ESO en tant que membre de l'équipe scientifique NIRPS. NIRPS est un spectrographe de haute précision qui permet de détecter et de caractériser les exoplanètes en utilisant la méthode des vitesses radiales. Son objectif est d'atteindre la précision des spectrographes visibles actuels tels que HARPS dans le proche infrarouge afin de mieux étudier les exoplanètes autour des étoiles de faible masse.

J'ai proposé deux programmes pour le GTO de NIRPS, basés sur l'expertise que j'ai développée en travaillant sur les candidats planètes TESS autour des naines M et sur la photométrie ExTrA. Le premier programme propose de caractériser les exoplanètes en transit en mesurant leur masse précise et d'étudier le diagramme Masse-Rayon des exoplanètes en orbite autour de naines M, ce qui pourrait révéler des informations importantes sur la formation et l'évolution de ces exoplanètes. Le second programme vise à utiliser la stratégie Deep Search pour trouver des planètes supplémentaires dans les systèmes TESS déjà connus, en comparant la probabilité des différents systèmes d'abriter d'autres planètes que TESS aurait pu manquer, ce qui pourrait conduire à la découverte de nouveaux systèmes multi-planétaires.

NIRPS a déjà démontré ses performances au cours des commissionings en montrant une excellente stabilité intrinsèque et une précision d'un m/s pour les cibles brillantes. Par conséquent, nous prévoyons que les programmes scientifiques proposés dans le cadre du GTO seront réalisables sur la base de ces performances. NIRPS a officiellement commencé ses observations le 1er avril 2023. Le GTO s'étale sur 5 ans et comprend de nombreux sujets scientifiques différents. NIRPS recherchera des exoplanètes autour d'étoiles de faible masse et ultra-froides afin d'identifier des planètes potentielles semblables à la Terre pour des études futures et de mieux comprendre le processus de formation des planètes et les conditions initiales dans les disques protoplanétaires. Il s'agira également de caractériser l'architecture des systèmes planétaires autour des naines M afin de mieux comprendre comment les exoplanètes se sont formées. NIRPS étudiera de manière approfondie les petites exoplanètes en transit orbitant autour de naines M, principalement à l'aide des candidates TESS, afin d'aider à tracer le diagramme Masse-Rayon des systèmes multi-planétaires, de fournir des mesures de masse ultra-précises des planètes rocheuses et des petites planètes tempérées se prêtant à une caractérisation atmosphérique à l'aide du télescope spatial James Webb. NIRPS participera également à la caractérisation des atmosphères des exoplanètes en utilisant une stratégie d'acquisition, de réduction et d'analyse des données uniforme, et en fournissant des spectres de haute fidélité.

Synergie entre ExTrA et NIRPS

La méthode du transit et la méthode des vitesses radiales sont deux des méthodes les plus couramment utilisées pour détecter et caractériser les exoplanètes. ExTrA et NIRPS sont deux instruments puissants conçus pour détecter des exoplanètes en orbite autour de naines M en observant dans le proche infrarouge. Les deux instruments sont situés à l'Observatoire de La Silla au Chili et sont donc capables d'observer les mêmes cibles. ExTrA et NIRPS permettront, nous l'espérons, d'accroître la précision avec laquelle nous pouvons détecter de petites exoplanètes en orbite autour de ces étoiles de faible masse. La combinaison de la photométrie d'ExTrA et de la spectroscopie de NIRPS permet d'obtenir des informations complémentaires et supplémentaires sur les exoplanètes. ExTrA fournit des données sur la taille de l'exoplanète et NIRPS, d'autre part, fournit des données sur la masse de l'exoplanète, avec des paramètres orbitaux supplémentaires tels que la distance à l'étoile, l'inclinaison du système, l'excentricité. Elle peut également nous en apprendre davantage sur la composition de la planète, son histoire et ses propriétés atmosphériques. Lorsque ces deux séries de mesures sont combinées, elles fournissent une image plus complète de l'exoplanète et de ses propriétés.

Articles publiés

Pendant ma thèse, j'ai rédigé 2 articles de découverte d'exoplanètes (TOI-269 b et TOI-663 b, c et d) en planifiant et en rassemblant les observations d'ExTrA et d'autres instruments, et en analysant conjointement les données de photométrie et de vitesse radiale à l'aide des codes que j'ai développées. J'ai également contribué à 7 autres articles sur la découverte d'exoplanètes en utilisant les observations ExTrA, en analysant la photométrie et en modélisant le transit, et enfin en fournissant des courbes de lumière ExTrA pour valider le candidat planétaire dans le proche infrarouge, ainsi qu'une section décrivant nos observations.

Tout d'abord, la découverte d'une nouvelle mini-Neptune transitant devant TOI-269 (Cointepas et al., 2021), constitue une excellente cible pour la caractérisation de son atmosphère. En raison de sa forte excentricité, l'orbite de l'exoplanète pourrait avoir été causée par des interactions entre planètes, fournissant de nouvelles informations sur la dynamique des systèmes exoplanétaires.

La découverte d'une exoplanète tempérée de la taille de Neptune en orbite autour de l'étoile TOI-1231 (Burt et al., 2021) est importante car il s'agit de l'une des planètes les plus froides accessibles à ce jour pour les études atmosphériques. La luminosité de son étoile hôte dans le proche infrarouge en fait une cible intéressante pour le télescope spatial Hubble et le télescope spatial James Webb, et les futures observations atmosphériques permettraient les premiers efforts de planétologie comparative dans le régime de température de 250-350 K via des comparaisons avec K2-18 b (Madhusudhan et al., 2020).

TOI-177 b, une mini-Neptune, a été découverte autour d'une naine M située à 22 pc (Almenara et al., 2022a). Une analyse de la modélisation de l'intérieur suggère que la planète devrait avoir une enveloppe volatile et une analyse couplée de l'évolution atmosphérique et dynamique de la planète favorise une atmosphère lourde plutôt qu'une atmosphère d'H-He. TOI-177 b est la deuxième mini-Neptune la plus favorable après GJ 1214 b (Berta et al., 2012) pour la caractérisation atmosphérique. Un autre candidat planétaire a été identifiée à partir des données de vitesse radiale, mais ses transits n'ont pas été détectés.

La validation d'une exoplanète de faible densité en transit autour de TOI-620 (Reefe et al., 2022) est également précieuse pour la caractérisation atmosphérique, car c'est l'une des exoplanètes les plus propices à de telles études validées ou confirmées par la mission TESS à ce jour. La découverte d'un compagnon extérieur a permis une exploration détaillée des architectures possibles du système, qui a exclu que TOI-620 b soit une planète circum-secondaire ou une paire d'étoiles binaires à éclipses orbitant autour de l'hôte dans un système triple.

La découverte et la validation de deux super-Terres tempérées transitant l'étoile voisine LP 890-9 (TOI-4306, SPECULOOS-2) (Delrez et al., 2022) offrent de nouvelles perspectives sur la formation et l'évolution des systèmes d'exoplanètes. Avec une densité globalement faible, ces planètes sont probablement riches en eau avec de petites atmosphères d'Hydrogène-Helium. La découverte d'une deuxième planète externe en transit, qui n'avait pas été détectée par TESS, souligne l'importance de poursuivre la surveillance et l'observation des systèmes exoplanétaires.

Une exoplanète plus petite que Saturne TOI-3884 b (Almenara et al., 2022b) a été découverte transitant une étoile M avec un signal de transit chromatique. Des observations complémentaires ont révélé que la planète transite devant une grande tache située au pole de l'étoile hôte. La luminosité et la petite taille de l'étoile hôte en font une cible de choix pour la caractérisation de l'atmosphère avec le télescope spatial James Webb et les télescopes terrestres.

Une exoplanète géante gazeuse TOI-3235 b (Hobson et al., 2023) a été découverte en orbite autour d'une naine M dont la masse est proche de la masse critique à laquelle les étoiles passent de la convection partielle à la convection totale. Cette découverte remet en question les modèles actuels de formation des planètes, car les géantes gazeuses telles que TOI-3235 b ne devraient pas se former autour d'étoiles de faible masse comme TOI-3235. TOI-3235 b est également l'une des géantes en orbite autour de naines M les mieux adaptées à la caractérisation atmosphérique.

La découverte d'une planète tempérée de la taille de la Terre en orbite autour de la naine M LP 791-18 (Peterson et al, accepté dans Nature) est importante car elle offre une rare opportunité d'explorer les conditions dans lesquelles les planètes peuvent développer des conditions climatiques hospitalières. LP 791-18 d fait partie d'un système coplanaire (Crossfield et al., 2019) et offre une occasion unique d'étudier une exo-Terre tempérée dans un système avec une mini-Neptune qui a conservé son enveloppe gazeuse. L'interaction gravitationnelle avec la mini-Neptune empêche la circularisation complète de l'orbite de LP 791-18 d, ce qui entraîne un réchauffement continu de son intérieur par les marées et probablement une forte activité volcanique à la surface.

Enfin, la détection et la caractérisation de trois exoplanètes en orbite autour de la naine M TOI-663 (Cointepas et al. in prep) suggèrent que ces planètes sont riches en eau et ont de petites atmosphères d'H-He. Cette découverte confirme l'observation récente selon laquelle les mini-Neptunes autour des naines M ont des densités plus faibles que celles autour d'autres étoiles de type spectral différents.

La découverte de ces exoplanètes, présentées ici dans l'ordre chronologique, a d'importantes implications scientifiques car elles couvrent une large gamme de paramètres, allant de planètes de la taille de la Terre à des géantes gazeuses, orbitant autour de naines M plus ou moins froides sur des orbites variées. La majorité de ces nouvelles exoplanètes sont d'excellents candidats pour la caractérisation atmosphérique. Ces découvertes suggèrent également que les exoplanètes sub-neptuniennes en orbite autour de naines M ont en effet tendance à avoir une densité plus faible que les exoplanètes similaires en orbite autour d'autres types d'étoiles. Cela remet en question la compréhension actuelle de la formation et de l'évolution des planètes, mais peut aider à affiner les modèles et à mieux comprendre l'interaction complexe des nombreux facteurs qui influencent les propriétés des exoplanètes.

Prochaines étapes dans la recherche des exoplanètes autour des naines M

La science des exoplanètes est un domaine qui évolue rapidement et qui a fait des progrès significatifs au cours des dernières décennies. Avec la découverte d'un plus grand nombre d'exoplanètes et le progrès de nouvelles techniques et de nouveaux instruments, l'avenir de la science exoplanétaire révélera, on l'espère, davantage d'informations sur la formation et l'évolution des exoplanètes, sur leur structure interne et sur une caractérisation détaillée de leur atmosphère. La découverte d'exoplanètes potentiellement habitables restera l'un des principaux objectifs de la science exoplanétaire à l'avenir. Avec le développement de nouveaux instruments et de nouvelles méthodes, le nombre d'exoplanètes confirmées dans la zone habitable de leur étoile devrait augmenter.

TESS a achevé sa mission principale en juillet 2020, puis sa première mission étendue et a entamé sa deuxième mission étendue en septembre 2022. Ces extensions permettront la détection d'exoplanètes à plus longue période et aideront à résoudre les mono-transits et les duo-transits. Après cinq ans dans l'espace, la mission reste une réussite exceptionnelle.

La mission Gaia a déjà participé à la science des exoplanètes en fournissant la parallaxe et le mouvement propre des étoiles hôtes. Selon les estimations actuelles de la distribution des planètes et de leurs orbites, environ 1000 à 1500 des futures découvertes de Gaia en astrométrie devraient être des exoplanètes orbitant autour d'étoiles naines de type M à moins de 100 parsec. En ce qui concerne la méthode du transit, on prévoit qu'avec la précision des mesures photométriques de Gaia, quelques centaines à quelques milliers de planètes massives en transit seront découvertes.

L'objectif principal de PLATO est de détecter des exoplanètes en orbite dans la zone habitable d'étoiles semblables au Soleil et de déterminer leur taille avec précision. Afin d'identifier de bonnes cibles pour les mesures spectroscopiques visant à étudier les atmosphères planétaires, PLATO observera 5 000 étoiles naines M.

Les exoplanètes observées en transits ou en vitesse radiale pourront être caractérisées sur le plan atmosphérique à l'aide de nouveaux instruments tels que le James Webb Space Telescope (JWST) et l'Extremely Large Telescope (ELT). ANDES sur l'ELT (précédemment connu sous le nom de HIRES) révolutionnera la caractérisation des atmosphères des planètes de faible masse. Il sera capable de détecter des biomarqueurs, des molécules indicatives de la vie, dans les atmosphères d'exoplanètes à l'aide de la spectroscopie par transmission, ainsi que d'étudier leur lumière réfléchie (Marconi et al., 2020).

Pour conclure, les résultats présentés dans cette thèse ont démontré l'efficacité de différentes méthodes dans la détection d'exoplanètes en orbite autour de naines M. L'application de la photométrie et de la spectroscopie dans le proche infrarouge permet d'obtenir des informations importantes sur les propriétés des systèmes exoplanétaires autour d'étoiles de faible masse. Mais de nombreuses découvertes restent à faire pour améliorer notre compréhension de la formation et de l'évolution des systèmes exoplanétaires, ainsi que de l'habitabilité potentielle des exoplanètes autour des naines M. Cette étude ouvre de nouvelles perspectives d'exploration et de recherche dans le monde captivant des exoplanètes.

PUBLICATIONS

This is the full list of publications I have contributed to during my thesis (as of September 2023).

FIRST AUTHOR PAPERS

I led and gathered the observations, analyzed the data and wrote these following papers.

- TOI-269 b: an eccentric sub-Neptune transiting a M2 dwarf revisited with ExTrA.
Cointepas et al., 2021, paper displayed in Section III.4.

- TOI-663 : a newly discovered multi-planetary system with three transiting mini-Neptunes orbiting an early M star.
Paper in prep by Cointepas, Bouchy, Almenara, Bonfils et al., draft displayed in Section II.5.

- Validation of new transiting systems with the ExTrA telescopes in the context of TESS planetary candidates follow-up.
Paper in prep by Cointepas, Almenara, Bonfils, Bouchy et al., draft displayed in Section III.5.1.

EXTRA OBSERVATIONS

I contributed to the following papers by monitoring the TESS planetary candidates and planning the observations with ExTrA when transits were expected to happen, analyzing the photometry and modeling the transit, following the TESS follow-up observation group activities and providing ExTrA light curves to validate the planetary candidate in a near-infrared spectral range, alongside a section describing our observations.

- TOI-1231 b: A Temperate, Neptune-sized Planet Transiting the Nearby M3 Dwarf NLTT 24399.
Burt et al., 2021

- A Close-in Puffy Neptune with Hidden Friends: The Enigma of TOI 620.
Reefe et al., 2022

- Two temperate super-Earths transiting a nearby late-type M dwarf.
Delrez et al., 2022

- TOI-3235 b: A Transiting Giant Planet around an M4 Dwarf Star.
Hobson et al., 2023

- A temperate Earth-sized planet with tidally-heated interior transiting an M6 star.
Peterson et al., accepted in Nature

- A 1.55 R_{Earth} habitable-zone planet hosted by TOI-715, an M4 star near the ecliptic South Pole.
Dransfield et al., 2023

- TOI-2084 b and TOI-4184 b: two new sub-Neptunes around M dwarf stars.
Barkaoui et al., 2023

- TOI-4201 b and TOI-5344 b: Discovery of Two Transiting Giant Planets Around M Dwarf Stars and Revised Parameters for Three Others.
Hartman et al., 2023

OTHERS

- Populating the brown dwarf and stellar boundary: Five stars with transiting companions near the hydrogen-burning mass limit.
Grieves et al., 2021; I helped the first author obtain the data by observing targets using the EULER telescope located at La Silla Observatory in Chile.

- Three new brown dwarfs and a massive hot Jupiter revealed by TESS around early-type stars.
Psaridi et al., 2022; I helped the first author with the understanding and use of the juliet software to fit jointly photometric and radial velocity data.

- TOI-5678 b: a 48-day transiting Neptune-mass planet characterized with CHEOPS and HARPS.
Ulmer-Moll et al., 2023; I helped the first author obtain the data by observing targets using the EULER telescope located at La Silla Observatory in Chile.

- GJ 3090 b: one of the most favourable mini-Neptune for atmospheric characterisation.
Almenara et al., 2022a; I was involved in this paper as part of the ExTrA science team.

- TOI-3884 b: A rare 6-RE planet that transits a low-mass star with a giant and likely polar spot .

Almenara et al., 2022b; I was involved in this paper as part of the ExTrA science team.

- TOI-4860 b, a short-period giant planet transiting an M3.5 dwarf.
Almenara et al., 2023; I was involved in this paper as part of the ExTrA science team.

- Identification of the Top TESS Objects of Interest for Atmospheric Characterization of Transiting Exoplanets with JWST.
Hord et al., 2023; I was invited on this paper as a member of TFOP who contributed to follow-up observations.

A

APPENDIX

APPENDIX 1

Is presented here the general code created to fit jointly TESS and ExTrA photometry (using the same transit depth for both instruments) for any TOIs requested. This routine was developed with the purpose of validating the TESS planetary candidates and improve on the planetary parameters as part of the ExTrA WP1 objective. A similar routine was also created where two different transit depths are used for TESS and ExTrA to check for signs of chromaticity in the transit as TESS and ExTrA observations are made at different wavelength ranges.

```
# FIT JULIET FOR TESS (2-MIN) AND EXTRA PHOTOMETRY WITH GP

import juliet212 as juliet
import numpy as np
import matplotlib.pyplot as plt
from astropy.io import fits as pf
import matplotlib.gridspec as gridspec
from IPython.display import display, Math
import os, glob, sys
from astropy.time import Time
import corner
from astropy import time, coordinates as coord, units as u
from astropy.coordinates import Angle, EarthLocation, AltAz, get_sun
import pickle
from astroquery.mast import Tesscut
from astroquery.mast import Observations
import csv
import pandas as pd
from matplotlib.ticker import (MultipleLocator, FormatStrFormatter,
    ScalarFormatter,AutoMinorLocator)
from dynesty import plotting as dyplot
import datefinder
import regex as re
import datetime
import math
```

```
from itertools import islice


# SELECT TOI
toi_name = input('Faire l\'analyse pour TOI-')

# CHANGE THE NAME IF NOT CALLED TOI IN EXTRA
if toi_name=='667': toi_name_bis = 'GJ1132'
elif toi_name=='136': toi_name_bis = 'LHS3844'
elif toi_name=='455': toi_name_bis = 'GJ3193'
elif toi_name=='2221': toi_name_bis = 'AUMic'
else : toi_name_bis = 'TOI-{}' .format(toi_name)

# KNOWLEDGE FROM TESS
liste=pd.read_csv('exofop_tess_priors.csv',header=0, skiprows=2)  #
    download the table directly from url?

toi = np.float(toi_name)+0.01
for i in range(len(liste['TOI'])):
    if liste['TOI'][i]==toi:
        tic = liste['TIC ID'][i]
        if math.isnan(liste['Stellar Radius (TIC)'][i])==False and math
            .isnan(liste['Stellar Radius (TIC) Unc.'][i])==False:
            radi_star = np.random.normal(liste['Stellar Radius (TIC)'][
                i],liste['Stellar Radius (TIC) Unc.'][i],10000)
            mass_star = np.random.normal(liste['Stellar Mass (TIC)'][i
                ],liste['Stellar Mass (TIC) Unc.'][i],10000)
            rho_est_med = np.median((mass_star*1.3271244e20/6.67408e
                -11)/((4/3)*np.pi*pow(radi_star*6.957e8,3)))
            rho_est_std = np.std((mass_star*1.3271244e20/6.67408e-11)
                /((4/3)*np.pi*pow(radi_star*6.957e8,3)))
        elif math.isnan(liste['Stellar Radius (TIC)'][i])==True or math
            .isnan(liste['Stellar Mass (TIC)'][i])==True:
            print('No stellar density estimation for this TOI.')
            rho_est_med = np.nan
            rho_est_std = np.nan
        elif math.isnan(liste['Stellar Radius (TIC)'][i])==False and
            math.isnan(liste['Stellar Radius (TIC) Unc.'][i])==True:
            rho_est_med = (liste['Stellar Mass (TIC)'][i]*1.3271244e20
                /6.67408e-11)/((4/3)*np.pi*pow(liste['Stellar Radius (
                TIC)'][i]*6.957e8,3))
            rho_est_std = rho_est_med/10
per_est, t0_est, toinumber = [], [], []
per_err_est, t0_err_est = [], []
depth, duration = [], []
for i in range(len(liste['TOI'])):
    if liste['TIC ID'][i]==tic:
        per_est.append(liste['Orbital Period (TOI)'][i])
        per_err_est.append(liste['Orbital Period (TOI) Unc.'][i])
        t0_est.append(liste['Transit Midpoint (TOI)'][i]+57000)
```

```
        t0_err_est.append(liste['Transit Midpoint (TOI) Unc.'][i])
        toinumber.append(liste['TOI'][i])
        depth.append(liste['Transit Depth (TOI)'][i]/1000)
        duration.append(liste['Transit Duration (TOI)'][i])
star_name = "TIC {}".format(tic)

# DOWNLOAD TESS PHOTOMETRY FROM MAST
observations = Observations.query_object(star_name,radius = "0 deg")
obs_wanted = (observations['dataproduct_type'] == 'timeseries') & (
    observations['obs_collection'] == 'TESS')
data_products = Observations.get_product_list(observations[obs_wanted])
products_wanted = Observations.filter_products(data_products,
    productSubGroupDescription=["LC"])
manifest = Observations.download_products(products_wanted)
time, flux, flux_err = [], [], []
for i in range(len(manifest)):
    t,f,ferr = juliet.get_TESS_data(manifest[i][0])
    time.extend(t+57000)
    flux.extend(f)
    flux_err.extend(ferr)

# only use data around transit time to save computing time
phases = juliet.utils.get_phases(np.array(time), per_est[0], t0_est[0])
limphase = (duration[0]/24)/per_est[0]
idx_oot = np.where(np.abs(phases)<2*limphase)[0]
times, fluxes, fluxes_error = {},{},{}
times['TESS'], fluxes['TESS'], fluxes_error['TESS'] = np.array(time)[
    idx_oot],np.array(flux)[idx_oot],np.array(flux_err)[idx_oot]

# COUNT THE APPROXIMATE NUMBER OF TRANSITS IN TESS PHOTOMETRY
nTESS = 0
n = 0
for n in range(int((times['TESS'][-1]-t0_est[0])/per_est[0])+2):
    if np.round(t0_est[0]+per_est[0]*n,2) in np.round(times['TESS'],2):
        nTESS += 1
for n in range(int((t0_est[0]-times['TESS'][0])/per_est[0])+2):
    if n!=0:
        if np.round(t0_est[0]-per_est[0]*n,2) in np.round(times['TESS'
            ],2):
            nTESS += 1

# FILLING THE PRIORS FOR 1 PLANET TO BE FITTED
priors = {}

if len(per_est)==1:
    params = ['P_p1','t0_p1','r1_p1','r2_p1','q1_TESS','q2_TESS','
        ecc_p1','omega_p1','rho', 'mdilution_TESS', 'mflux_TESS', '
        sigma_w_TESS','GP_sigma_TESS', 'GP_rho_TESS']
```

```
    dists = ['normal','normal','uniform','uniform','uniform','uniform',
       'fixed','fixed','normal', 'fixed', 'normal', 'loguniform','
       loguniform', 'loguniform']
    hyperps = [[per_est[0],per_err_est[0]], [t0_est[0],t0_err_est[0]],
       [0.,1.], [0.,1.], [0.,1.], [0.,1.], 0.0, 90.,[rho_est_med,
       rho_est_std], 1.0, [0.0, 0.01], [1., 1000.],[1e-6, 0.1], [1e-3,
       10.]]

for param, dist, hyperp in zip(params, dists, hyperps):
    priors[param] = {}
    priors[param]['distribution'], priors[param]['hyperparameters'] =
       dist, hyperp


# GET ALL EXTRA LIGHTCURVES
path = 'SEQ_new_photometry_3/'
allfiles = [os.path.join(root, name)
             for root, dirs, files in os.walk(path)
             for name in files
             if '{}_'.format(toi_name_bis) in name and name.endswith('.
                fits')]
allfiles.sort(key=os.path.getctime)

# CREATE INSTRUMENT NAME : EXTR-TELESCOPE-n-NIGHT
ni = 0 ; date_past = 0 ; date = 0; nn = 0
ndiff = []; obs_night = []
instruments,instruments_all = [],[]
for file in allfiles:
    if 'T1' in file: tel = '1'
    if 'T2' in file: tel = '2'
    if 'T3' in file: tel = '3'
    match = re.search(r'\d{4}-\d{2}-\d{2}', file)
    date_past = date
    date = datetime.datetime.strptime(match.group(), '%Y-%m-%d').date()
    if date != date_past:
        ni=ni+1
        ndiff.append(nn)
        obs_night.append(date.strftime('%Y-%m-%d'))
    nn=nn+1
    instruments.append('EXTR{}n{}'.format(tel,ni))
    instruments_all.append('EXTR{}n{}'.format(tel,ni))
ndiff.append(len(allfiles))
decoup = []
for i in range(len(ndiff)-1):
    decoup.append(ndiff[i+1]-ndiff[i])

# READ EXTRA LIGHTCURVES
lat = Angle('-29:15:25 degrees')
lon = Angle('-70:44:18 degrees')
height = 2345 * u.meter
```

```
ExTrA = EarthLocation.from_geodetic(lon, lat, height, ellipsoid='WGS84'
    )
# parameters for median filtering
nb=21    #shoud be even number -->  window median filtering (ExTrA is
    60s exposure time)
nbloop = 4  #iterative process -> four loops are usually sufficient
tps = {}

for instrument,starfile in zip(instruments_all,allfiles):
    temps, temps_ini, star, alt = [], [], [], []
    fits = pf.open(starfile)
    headers = []
    headers.append(fits[1].header)
    data = fits[1].data
    fieldH = fits[0].header
    target = fieldH['HIERARCH TARGET'][4:]
    for j in range(5):          #FIND ON WHICH FU IS THE TARGET
        if fieldH['HIERARCH FU{} TYPE'.format(j+1)]=='Target':
            FUtarget = 'StarFU{}'.format(j+1)
            fu = 'FU{}'.format(j+1)
    jmag = fieldH['HIERARCH {} J MAG'.format(fu)]
    for i in range(len(data)):
        temps_ini.append(data[i]['TIME [BJD_TDB]'])
    t_ini = np.array(temps_ini)-2400000                     #ALL
       TIMESTAMPS
    for i in range(len(data)-1):
        if t_ini[i+1]>t_ini[i]:                             #REMOVE
           PROBLEMS CONNECTED TO PEAK IN THE OVERSCAN
            temps.append(data[i]['TIME [BJD_TDB]'])
            star.append(data[i][FUtarget])
    #ADD THE LAST VALUE
    temps.append(data[len(data)-1]['TIME [BJD_TDB]'])
    star.append(data[len(data)-1][FUtarget])
    t = np.array(temps)-2400000
    f = np.array(star)
    #MEDIAN FILTERING TO ESTIMATE THE STD OF THE DATA
    try:
        for i in range(nbloop):
            moy=np.mean(f)
            wff=f/moy
            mm=np.cumsum(wff,dtype='float64')
            mm[nb:]=mm[nb:]-mm[:-nb]
            mm2=moy*mm[nb-1:]*1./(nb*1.)
            mm3=np.concatenate((np.ones(int(nb/2))*mm2[0],mm2,np.ones(
               int(nb/2))*mm2[-1]))
    except IndexError:
        print('Not enough data points for median filtering')
        instruments.remove(instrument)
        continue
    ferr = np.array([np.round(np.std(f/mm3),5)]*len(t))
```

```
    #REMOVE NOISY NIGHTS
    if ferr[0]>0.01:
        instruments.remove(instrument)
        continue

    times[instrument], fluxes[instrument], fluxes_error[instrument] = t, f, ferr
    tps[instrument] = t

    params = ['sigma_w_','mflux_','mdilution_']
    dists = ['loguniform', 'normal', 'fixed']
    hyperps = [[1.,1000], [0.,0.01], 1.0]

    for param, dist, hyperp in zip(params, dists, hyperps):
        priors[param+instrument] = {}
        priors[param+instrument]['distribution'], priors[param+instrument]['hyperparameters'] = dist, hyperp
    print(instrument,starfile)

# ADD GAUSSIAN PROCESS TO EXTRA PHOTOMETRY FOR ALL TELESCOPES
gp_sigma_tel1 = 'GP_sigma' ; gp_sigma_tel2 = 'GP_sigma' ; gp_sigma_tel3 = 'GP_sigma'
gp_rho_tel1 = 'GP_rho' ; gp_rho_tel2 = 'GP_rho' ; gp_rho_tel3 = 'GP_rho'

for instrument in instruments:
    if 'EXTR1' in instrument:
        gp_sigma_tel1 = gp_sigma_tel1+'_'+instrument
        gp_rho_tel1 = gp_rho_tel1+'_'+instrument
    elif 'EXTR2' in instrument:
        gp_sigma_tel2 = gp_sigma_tel2+'_'+instrument
        gp_rho_tel2 = gp_rho_tel2+'_'+instrument
    elif 'EXTR3' in instrument:
        gp_sigma_tel3 = gp_sigma_tel3+'_'+instrument
        gp_rho_tel3 = gp_rho_tel3+'_'+instrument

params = ['q1_EXTR','q2_EXTR',gp_sigma_tel1,gp_sigma_tel2,gp_sigma_tel3,gp_rho_tel1,gp_rho_tel2,gp_rho_tel3]
dists = ['uniform','uniform','loguniform','loguniform','loguniform','loguniform','loguniform']
hyperps = [[0.,1.], [0.,1.],[1e-6, 0.1],[1e-6, 0.1],[1e-6, 0.1],[1e-3, 10.],[1e-3, 10.],[1e-3, 10.]]

#REMOVE NON USED TELESCOPES
excess = False
try :
    params.remove('GP_sigma')
    params.remove('GP_rho')
    excess = True
except : ValueError
```

```
if excess:
    hyperps.remove([1e-6,0.1])
    hyperps.remove([1e-3, 10])
    dists.remove(’loguniform’)
    dists.remove(’loguniform’)

excess = False
try :
    params.remove(’GP_sigma’)
    params.remove(’GP_rho’)
    excess = True
except : ValueError
if excess:
    hyperps.remove([1e-6, 0.1])
    hyperps.remove([1e-3, 10.])
    dists.remove(’loguniform’)
    dists.remove(’loguniform’)

for param, dist, hyperp in zip(params, dists, hyperps):
    priors[param] = {}
    priors[param][’distribution’], priors[param][’hyperparameters’] =
       dist, hyperp

# COUNT THE NUMBER OF TRANSITS IN ExTrA PHOTOMETRY
nEXTR = 0
n = 0
for instrument in instruments:
    for n in range(int((times[instrument][-1]-t0_est[0])/per_est[0])+2)
       :
        if np.round(t0_est[0]+per_est[0]*n,2) in np.round(times[
           instrument],2):
            nEXTR += 1
    for n in range(int((t0_est[0]-times[instrument][0])/per_est[0])+2):
        if n!=0:
            if np.round(t0_est[0]-per_est[0]*n,2) in np.round(times[
               instrument],2):
                nEXTR += 1

# PRINT ALL PARAMETERS OF THE FIT
freeparams = 0
k = 1
for ii in priors.keys():
    print(’{} : {} : {} : {}’.format(k, ii, priors[ii][’distribution’],
        priors[ii][’hyperparameters’]))
    k = k+1
    if priors[ii][’distribution’] != ’fixed’:
        freeparams += 1
print(’#{} free parameters’.format(freeparams))

# RUN THE FIT
```

```
dataset = juliet.load(priors=priors, t_lc = times, y_lc = fluxes,
   yerr_lc = fluxes_error, GP_regressors_lc = times, out_folder = 'toi
   {}_TESSxExTrA_samedepth_v2'.format(toi_name))
results = dataset.fit(sampler='dynesty', dynamic=False, bound='single',
    sample='slice', nthreads=40, n_live_points=freeparams*5, ecclim
   =0.9, pl=0.0, pu=1.0, nsave=10000000)

# PLOT THE RESULTS
## GET THE MAXIMUM A POSTERIORI AND 1000 RANDOM MODELS FROM THE SAMPLES
params = list(results.posteriors['posterior_samples'].keys())
params.remove('unnamed')
params.remove('loglike')
maxp = {}
for ii, param in enumerate(params):
    maxp[param] = results.posteriors['posterior_samples']['unnamed'
       ][-1, ii]
for key in dataset.priors.keys():
    if dataset.priors[key]['distribution'] == 'fixed':
        maxp[key] = dataset.priors[key]['hyperparameters']
for key in maxp.keys():
    maxp[key] = np.array([maxp[key],])
maxp

np.random.seed(28964)
nsamples = 1000
inds = np.random.uniform(0, np.shape(results.posteriors['
   posterior_samples']['P_p1'])[0] - 1, nsamples).astype(np.int)
random = {}
for ii, param in enumerate(params):
    random[param] = results.posteriors['posterior_samples']['unnamed'][
       inds, ii]
for key in dataset.priors.keys():
    if dataset.priors[key]['distribution'] == 'fixed':
        random[key] = np.repeat(dataset.priors[key]['hyperparameters'],
            nsamples)

## TIME OF TESS AND EXTRA OBSERVATIONS
fig = plt.figure(figsize=(24,6))
plt.errorbar(dataset.times_lc['TESS'], dataset.data_lc['TESS'],yerr =
   dataset.errors_lc['TESS'], fmt = '.' , alpha = 0.1)
for instrument in instruments:
    plt.errorbar(dataset.times_lc[instrument], dataset.data_lc[
       instrument],yerr = dataset.errors_lc[instrument], fmt = '.' ,
       alpha = 0.1,color='red')
plt.title('TESS (blue) and ExTrA (red) observations')
plt.xlabel('Time (BJD-2400000)')
plt.ylabel('Flux')
plt.savefig('toi{}_TESSxExTrA_samedepth_v2/toi{}_TESS_ExTrA_data.png'.
   format(toi_name,toi_name));
```

```
## PHASED LIGHTCURVES OF TESS AND EXTRA
for l in range(len(depth)):
    planet = l+1
    f = plt.figure(figsize=(18,8))

    P, t0 = maxp[’P_p{}’.format(planet)],maxp[’t0_p{}’.format(planet)]
    # SCALING OF THE DATA
    y1 = 1-5*depth[planet-1]/1000
    y2 = 1+5*depth[planet-1]/1000
    x1 = -1.5*(duration[planet-1]/24)/P
    x2 = 1.5*(duration[planet-1]/24)/P
    ph0 = x1  #limit in phase
    bww = (duration[planet-1]*60/6)/24/60/P  #bin size in phase (1/6 of
         the transit duration)

    #TESS PHOTOMETRY
    ax1 = f.add_axes([0.1,0.23,0.4,0.65])
    ax2 = f.add_axes([0.1,0.11,0.4,0.12])

    phases = juliet.get_phases(dataset.times_lc[’TESS’],P, t0)
    i_allm = np.zeros(len(dataset.data_lc[’TESS’]))
    i_transitm = np.zeros(len(dataset.data_lc[’TESS’]))
    i_gpm = np.zeros(len(dataset.data_lc[’TESS’]))
    i_allm = results.lc.evaluate(’TESS’, parameter_values=maxp,
        nsamples=1)
    i_transitm = results.lc.model[’TESS’][’deterministic’]
    i_gpm = results.lc.model[’TESS’][’GP’]
    newfluxT,newresT,newph=[],[],[]
    newferr,newferres = [],[]
    while ph0<=x2:
        indi = np.where(np.logical_and(phases>=ph0,phases<ph0+bww))
        newfluxT.append(np.mean((dataset.data_lc[’TESS’]-i_gpm)[indi]))
        newresT.append(np.mean((dataset.data_lc[’TESS’]-i_gpm-
            i_transitm)[indi]))
        newferr.append(np.std(dataset.data_lc[’TESS’][indi])/np.sqrt(np
            .size(indi)))
        newferres.append(np.std((dataset.data_lc[’TESS’]-i_transitm)[
            indi])/np.sqrt(np.size(indi)))
        ph0 = ph0 + bww
        newph.append(ph0-(bww/2))
    ax1.errorbar(phases, (dataset.data_lc[’TESS’]-i_gpm)*(1+maxp[’
        mflux_TESS’]), yerr = dataset.errors_lc[’TESS’], fmt = ’.’,
        alpha = 0.3)
    idx = np.argsort(phases)
    ax1.plot(phases[idx],i_transitm[idx]*(1+maxp[’mflux_TESS’]), color=
        ’black’,zorder=10)
    ax1.errorbar(newph,newfluxT,yerr = newferr,fmt = ’o’,color = ’black
        ’,zorder=11)
    ax1.set_xlim([x1,x2])
    ax1.set_ylim([y1,y2])
```

```
ax1.set_title('P = {0:.1f} days \n TESS (10cm, space) \n {1:}
    transits'.format(P[0],nTESS),pad=10,fontsize=16)
ax1.set_ylabel('Relative flux', fontsize=14)
ax1.tick_params(axis='y', which='major', labelsize=14, length=7,
    width=1.4)
ax1.yaxis.set_minor_locator(MultipleLocator(0.0025))
ax1.tick_params(axis='y', which='minor', length=5)
ax1.tick_params(axis='x', colors='white')
ax2.errorbar(phases, (dataset.data_lc['TESS'] - i_gpm) - i_transitm
    , yerr = dataset.errors_lc['TESS'], fmt = '.', alpha = 0.3)
ax2.errorbar(newph,newresT,yerr = newferres,fmt = 'o',color = '
    black',zorder=11)
ax2.set_xlabel('Phases',labelpad=8, fontsize=14)
ax2.set_xlim([x1,x2])
y3 = -2.5*np.nanstd((dataset.data_lc['TESS'] - i_gpm) - i_transitm)
y4 = 2.5*np.nanstd((dataset.data_lc['TESS'] - i_gpm) - i_transitm)
ax2.set_ylim([y3,y4])
ax2.set_xlim(ax1.get_xlim())
ax2.set_ylabel('Residuals', fontsize=14)
ax2.axhline(0,zorder=10,color = 'grey',alpha=0.7)
ax2.tick_params(axis='y', which='major', labelsize=14, length=7,
    width=1.4)
ax2.tick_params(axis='x', which='major', labelsize=14, length=7,
    width=1.4)
ax2.xaxis.set_minor_locator(MultipleLocator(0.005))
ax2.tick_params(axis='x', which='minor', length=5)
ax2.yaxis.set_minor_locator(MultipleLocator(0.01))
ax2.tick_params(axis='y', which='minor', length=5)

#EXTRA PHOTOMETRY
ax3 = f.add_axes([0.58,0.23,0.4,0.65])
ax4 = f.add_axes([0.58,0.11,0.4,0.12])
binflux = []

ph0 = x1  #limite phase
newfluxE = []
newresE = []
newferrE = []
newferresE = []
newphE = []
while ph0<=x2:
    valeur=0
    err=0
    erres=0
    valeurres=0
    ll=0
    for instrument in instruments:
        phaseE = juliet.get_phases(dataset.times_lc[instrument], P,
            t0)
            #calcul du modele pour chaque nuit/tel ExTrA
```

```
        i_allm = np.zeros(len(dataset.data_lc[instrument]))
        i_transitm = np.zeros(len(dataset.data_lc[instrument]))
        i_gpm = np.zeros(len(dataset.data_lc[instrument]))
        i_allm = results.lc.evaluate(instrument, parameter_values=
           maxp, nsamples=1)
        i_transitm = results.lc.model[instrument]['deterministic']
        i_gpm = results.lc.model[instrument]['GP']

        dfs = (dataset.data_lc[instrument] - i_gpm)*(1+maxp['mflux_
           '+instrument])#- i_transitm
        dfsres = (dataset.data_lc[instrument] - i_gpm)- i_transitm
        indiE = np.where(np.logical_and(phaseE>=ph0,phaseE<ph0+bww)
           )
        valeur = valeur + np.sum(dfs[indiE])
        err = err + np.std(dfs[indiE])/np.sqrt(np.size(indiE))
        erres = erres + np.std(dfsres[indiE])/np.sqrt(np.size(indiE
           ))
        valeurres = valeurres + np.sum(dfsres[indiE]) #ajout de
           toutes les valeurs de r sidus des differents nuit/tel d
           'un m me bin
        ll = ll + len(dfs[indiE])   #nombre de valeur par bin
    newfluxE.append(valeur/ll)
    newferrE.append(err/ll)
    newresE.append(valeurres/ll)  #moyenne des r sidus
    newferresE.append(erres/ll)
    ph0 = ph0 + bww  #changement de phase par pas de 'taille du bin
       '
    newphE.append(ph0-(bww/2))
ax3.errorbar(newphE,newfluxE,yerr = newferrE,fmt = 'o',color = '
   black',zorder=11)
ax4.errorbar(newphE,newresE,yerr = newferresE,fmt = 'o',color = '
   black',zorder=11)
std = {}
for instrument in instruments:
    i_allm = np.zeros(len(dataset.data_lc[instrument]))
    i_transitm = np.zeros(len(dataset.data_lc[instrument]))
    i_gpm = np.zeros(len(dataset.data_lc[instrument]))
    i_allm = results.lc.evaluate(instrument, parameter_values=maxp,
        nsamples=1)
    i_transitm = results.lc.model[instrument]['deterministic']
    i_gpm = results.lc.model[instrument]['GP']
    phases = juliet.get_phases(dataset.times_lc[instrument], P, t0)
    ax3.errorbar(phases, (dataset.data_lc[instrument]-i_gpm)*(1+
       maxp['mflux_'+instrument]), yerr = dataset.errors_lc[
       instrument], fmt = '.', alpha = 0.3)
    idx = np.argsort(phases)
    ax3.plot(phases[idx],i_transitm[idx]*(1+maxp['mflux_'+
       instrument]), color='black',zorder=10)
```

```
    ax4.errorbar(phases, (dataset.data_lc[instrument] - i_gpm) -
        i_transitm, yerr = dataset.errors_lc[instrument], fmt = '.',
        alpha = 0.3)
    std[instrument] = np.std((dataset.data_lc[instrument] - i_gpm -
        i_transitm)*(1+maxp['mflux_'+instrument]))
ax3.set_xlim([x1,x2])
ax3.set_ylim([y1,y2])
ax3.tick_params(axis='x', colors='white')
ax3.set_title('ExTrA (60cm, ground) \n {} transits'.format(nEXTR),
    pad=10, fontsize=16)
ax4.set_xlabel('Phases',labelpad=8,fontsize=14)
ax4.set_xlim([x1,x2])
ax4.set_ylim([y3,y4])
ax4.set_xlim(ax3.get_xlim())
ax4.axhline(0,zorder=10,color = 'grey',alpha=0.7)
ax3.tick_params(axis='y', which='major', labelsize=14, length=7,
    width=1.4)
ax3.yaxis.set_minor_locator(MultipleLocator(0.0025))
ax3.tick_params(axis='y', which='minor', length=5)
ax4.yaxis.set_minor_locator(MultipleLocator(0.01))
ax4.tick_params(axis='y', which='minor', length=5)
ax4.tick_params(axis='y', which='major', labelsize=14, length=7,
    width=1.4)
ax4.tick_params(axis='x', which='major', labelsize=14, length=7,
    width=1.4)
ax4.xaxis.set_minor_locator(MultipleLocator(0.005))
ax4.tick_params(axis='x', which='minor', length=5)

plt.savefig('toi{}_TESSxExTrA_samedepth_v2/toi{}
    _TESS_ExTrA_phased_planet{}.png'.format(toi_name,toi_name,planet
    ));


#INSTRUMENTS PRECISION FOR DIFFERENT BIN SIZES
f = plt.figure(figsize=(12,12))
ax = f.add_axes([0.1,0.2,0.8,0.7])

i_allT = results.lc.evaluate('TESS', parameter_values=maxp,
    nsamples=1)
i_transitT = results.lc.model['TESS']['deterministic']
i_gpmT = results.lc.model['TESS']['GP']
errbE = [];errbT = []; binw = []

for bwidth in [2,4,8,16,32,64]:
    bww = bwidth/(P*24*60)  #binsize in phase
    ph0 = x1
    newfluxE = []; newfluxT = []
    while ph0<=x2:
        valeur=0; ll=0
```

```
        #EXTRA
        for instrument in instruments:
            phaseE = juliet.get_phases(dataset.times_lc[instrument
               ], P, t0)
            #MODEL COMPUTATION FOR EACH NIGHT/TEL
            i_allm = np.zeros(len(dataset.data_lc[instrument]))
            i_transitm = np.zeros(len(dataset.data_lc[instrument]))
            i_gpm = np.zeros(len(dataset.data_lc[instrument]))
            i_allm = results.lc.evaluate(instrument,
               parameter_values=maxp, nsamples=1)
            i_transitm = results.lc.model[instrument]['
               deterministic']
            i_gpm = results.lc.model[instrument]['GP']
            dfs = (dataset.data_lc[instrument] - i_gpm) -
               i_transitm
            indiE = np.where(np.logical_and(phaseE>=ph0,phaseE<ph0+
               bww))
            if dfs[indiE].size!=0:
                valeur = valeur + np.sum(dfs[indiE])  #sum of all
                   the residuals values of all night/tel for a same
                    bin
                ll = ll + len(dfs[indiE])   #number of values per
                   bin
        if ll!=0:
            newfluxE.append(valeur/ll)   #mean of the residuals

        #TESS
        phaseT = juliet.get_phases(dataset.times_lc['TESS'], P, t0)
        indiT = np.where(np.logical_and(phaseT>=ph0,phaseT<ph0+bww)
           )  #index of all datapoints in the bin
        newfluxT.append(np.mean(dataset.data_lc['TESS'][indiT]-
           i_gpmT[indiT]-i_transitT[indiT]))  #mean of the
           residuals
        ph0 = ph0 + bww  #change of phase by binsize
    binw.append(bww*(P*24*60))  #binsize in minutes
    errbE.append((np.std(np.array(newfluxE)))*1000.)
    errbT.append((np.std(np.array(newfluxT)))*1000.)
    #KEEP THE PRECISION VALUE FOR 8-MIN BIN
    if bwidth==8:
        precision_eight_E = np.std(np.array(newfluxE))*1000.*np.
           sqrt(len(instruments))
        precision_eight_T = np.std(np.array(newfluxT))*1000.*np.
           sqrt(nTESS)


ax.plot(binw,errbT,'b',label='TESS - {} transits'.format(nTESS))
ax.plot(binw,errbE,'r',label='ExTrA - {} transits'.format(nEXTR))
ax.set_xscale('log')
ax.set_xlabel('Bin Width (minutes)',fontsize=22,labelpad=10)
ax.set_ylabel('Error (mmag)',fontsize=22,labelpad=10)
```

```
ax.legend(bbox_to_anchor=(1., 1),fontsize=22)
ax.tick_params(axis=’x’, which=’major’, labelsize=20, length=7,
    width=1.4)
ax.tick_params(axis=’x’, which=’minor’, length=7, width=1.)
ax.tick_params(axis=’y’, which=’minor’, length=7, width=1.)
ax.tick_params(axis=’y’, which=’major’, labelsize=20, length=7,
    width=1.4)
ax.set_xticks([2,5,10,20,30,50])
ax.get_xaxis().set_major_formatter(ScalarFormatter());
plt.savefig(’toi{}_TESSxExTrA_samedepth_v2/toi{}
    _TESS_ExTrA_precision_planet{}.png’.format(toi_name,toi_name,
    planet));

#PLANETARY RADIUS
f = open(’TESS_GP_TOI-{}_1/_dynesty_NS_posteriors.pkl’.format(
    toi_name), ’rb’)
results_TESS = pickle.load(f)
f.close()
r1, r2 = results_TESS[’posterior_samples’][’r1_p{}’.format(planet)
    ],results_TESS[’posterior_samples’][’r2_p{}’.format(planet)]
b_TESS,p_TESS = juliet.utils.reverse_bp(r1, r2, 0., 1.)
Rstar_T = np.random.normal(np.median(radi_star),np.std(radi_star),
    len(p_TESS))
rp_TESS = p_TESS*Rstar_T*6.957e8/6.3781e6
rm1_T,ru1_T,rl1_T = juliet.utils.get_quantiles(rp_TESS)

r1, r2 = results.posteriors[’posterior_samples’][’r1_p{}’.format(
    planet)],results.posteriors[’posterior_samples’][’r2_p{}’.format
    (planet)]
b_TESSxEXTR,p_TESSxEXTR = juliet.utils.reverse_bp(r1, r2, 0., 1.)
Rstar = np.random.normal(np.median(radi_star),np.std(radi_star),len
    (p_TESSxEXTR))
rp_TESSxEXTR = p_TESSxEXTR*Rstar*6.957e8/6.3781e6
rm1_E,ru1_E,rl1_E = juliet.utils.get_quantiles(rp_TESSxEXTR)

f = plt.figure(figsize=(14,12))
ax = f.add_axes([0.08,0.08,0.9,0.9])
plt.hist(rp_TESS,’auto’,color=’blue’,alpha=0.7,density=True,label=’
    TESS - {} transits - {:.3f}+-{:.3f}’.format(nTESS,rm1_T,(ru1_T-
    rl1_T)/2))
plt.hist(rp_TESSxEXTR,’auto’,color=’purple’,alpha=0.6,density=True,
    label=’TESSxExTrA - {} transits - {:.3f}+-{:.3f}’.format(nTESS+
    nEXTR,rm1_E,(ru1_E-rl1_E)/2))
plt.xlabel(’$R_p$ in $R_{Earth}$’,fontsize=18)
ax.tick_params(axis=’x’, which=’major’, labelsize=16, length=7,
    width=1.4)
ax.tick_params(axis=’y’, which=’minor’, labelsize=18, length=7,
    width=1.)
plt.legend(fontsize=16)
```

```
    plt.savefig('toi{}_TESSxExTrA_samedepth_v2/toi{}
        _TESS_TESSxExTrA_radius_planet{}.png'.format(toi_name,toi_name,
        planet));

    r1, r2 = results_TESS['posterior_samples']['r1_p{}'.format(planet)
        ],results_TESS['posterior_samples']['r2_p{}'.format(planet)]
    b_TESS,p_TESS = juliet.utils.reverse_bp(r1, r2, 0., 1.)
    rp_TESS = p_TESS
    rm1_T,ru1_T,rl1_T = juliet.utils.get_quantiles(rp_TESS)

    r1, r2 = results.posteriors['posterior_samples']['r1_p{}'.format(
        planet)],results.posteriors['posterior_samples']['r2_p{}'.format
        (planet)]
    b_TESSxEXTR,p_TESSxEXTR = juliet.utils.reverse_bp(r1, r2, 0., 1.)
    rp_TESSxEXTR = p_TESSxEXTR
    rm1_E,ru1_E,rl1_E = juliet.utils.get_quantiles(rp_TESSxEXTR)

    f = plt.figure(figsize=(14,12))
    ax = f.add_axes([0.08,0.08,0.9,0.9])
    plt.hist(rp_TESS,'auto',color='cornflowerblue',alpha=0.7,density=
        True,label='TESS - {} transits - {:.4f}+-{:.4f}'.format(nTESS,
        rm1_T,(ru1_T-rl1_T)/2))
    plt.hist(rp_TESSxEXTR,'auto',color='plum',alpha=0.6,density=True,
        label='TESSxExTrA - {} transits - {:.4f}+-{:.4f}'.format(nTESS+
        nEXTR,rm1_E,(ru1_E-rl1_E)/2))
    plt.xlabel('Radius ratio',fontsize=18)
    ax.tick_params(axis='x', which='major', labelsize=16, length=7,
        width=1.4)
    ax.tick_params(axis='y', which='minor', labelsize=18, length=7,
        width=1.)
    plt.legend(fontsize=16);
    plt.savefig('toi{}_TESSxExTrA_samedepth_v2/toi{}
        _TESS_TESSxExTrA_radiusratio_planet{}.png'.format(toi_name,
        toi_name,planet));

## PLOT EACH NIGHT EXTRA
#CUT BY NIGHT (ONE FIGURE FOR EACH NIGHT)
Inputt = iter(instruments_all)
output = [list(islice(Inputt, elem))
          for elem in decoup]

m = 0
t = 0
nsamples = 1000
for n in range(len(output)):
    fig = plt.figure(figsize=(9,16))

    #SIZE OF THE FIGURE DEPENDING ON THE NUMBER OF TELESCOPES FOR EACH
        NIGHT
    if len(output[n])==1:
```

```
    x0 = 0.18 ; y0 = 0.2 ; yres = 0.1
    width = 0.8 ; height = 0.4 ; heightres = 0.1
    t=1
    mstep = 0
elif len(output[n])==2:
    x0 = 0.18 ; y0 = 0.55 ; yres = 0.5
    width = 0.8 ; height = 0.4 ; heightres = 0.05
    mstep = 0.45
elif len(output[n])==3:
    x0 = 0.18 ; y0 = 0.7 ; yres = 0.67
    width = 0.8 ; height = 0.28 ; heightres = 0.03
    mstep = 0.31

output[n].sort()
for instrument in output[n]:
    t = t+1
    try:
        i_all = np.zeros((len(dataset.data_lc[instrument]),nsamples
           ))
    except KeyError:
        continue
    i_transit = np.zeros((len(dataset.data_lc[instrument]),nsamples
       ))
    i_gp = np.zeros((len(dataset.data_lc[instrument]),nsamples))
    mflux = []
    i_allm = np.zeros(len(dataset.data_lc[instrument]))
    i_transitm = np.zeros(len(dataset.data_lc[instrument]))
    i_gpm = np.zeros(len(dataset.data_lc[instrument]))
    for ii in range(nsamples):
        iparams = {}
        for key in random.keys():
            iparams[key] = np.array([random[key][ii],])
        mflux.append(iparams['mflux_'+instrument])
        i_all[:,ii] = results.lc.evaluate(instrument,
           parameter_values=iparams, nsamples=1)
        i_transit[:,ii] = results.lc.model[instrument]['
           deterministic']
        i_gp[:,ii] = results.lc.model[instrument]['GP']
    i_allm = results.lc.evaluate(instrument, parameter_values=maxp,
        nsamples=1)
    i_transitm = results.lc.model[instrument]['deterministic']
    i_gpm = results.lc.model[instrument]['GP']
    upper = np.zeros(len(dataset.data_lc[instrument]))
    lower = np.zeros(len(dataset.data_lc[instrument]))
    for i in range(len(dataset.data_lc[instrument])):
        med,u,l = juliet.utils.get_quantiles(i_all[i,:])
        upper[i]=u
        lower[i]=l
    ax1 = fig.add_axes([x0,y0-m,width,height])
```

```
        ax1.errorbar(dataset.times_lc[instrument], dataset.data_lc[
           instrument], yerr = dataset.errors_lc[instrument], fmt = '.'
           , alpha = 0.2, label = 'Data')
        ax1.plot(dataset.times_lc[instrument], np.median(i_all,axis=1),
            color='black',zorder=10, label = 'Transit + GP model')
        ax1.fill_between(dataset.times_lc[instrument],lower,upper,
           zorder=0,alpha = 0.3, color='black')
        ax1.errorbar(dataset.times_lc[instrument], (dataset.data_lc[
           instrument]-i_gpm)*(1+maxp['mflux_'+instrument]), yerr =
           dataset.errors_lc[instrument], fmt = '.', color='grey',alpha
            = 0.3,zorder=10, label = '(Data - GP model)*(1+Offset
           relative flux)')
        ax1.plot(dataset.times_lc[instrument],i_transitm*(1+maxp['
           mflux_'+instrument]),'r',label = 'Transit model*(1+Offset
           relative flux)')
        ax1.set_ylabel('Relative flux of tel {}'.format(instrument
           [4:5]),labelpad=8,fontsize=16)
        ax2 = fig.add_axes([x0,yres-m,width,heightres])
        ax2.plot(dataset.times_lc[instrument], (dataset.data_lc[
           instrument]-i_gpm)*(1+maxp['mflux_'+instrument]) -
           i_transitm*(1+maxp['mflux_'+instrument]),'k.',alpha = 0.2,
           zorder=10)  #RESIDUALS GREY-RED CURVES
        ax2.set_xlabel('Time (BJD - 2400000)',labelpad=10,fontsize=16)
        ax2.set_ylabel('Residuals',labelpad=8,fontsize=14)
        ax2.set_xlim(ax1.get_xlim())
        ax2.axhline(0,zorder=10,color = 'grey',alpha=0.7)
        m = m+mstep
        ax1.tick_params(axis='x', colors='white')
        ax1.tick_params(axis='y', which='major', labelsize=12, length
           =5)
        ax2.tick_params(axis='x', which='major', labelsize=12, length
           =5)
        ax1.yaxis.set_minor_locator(MultipleLocator(0.005))
        ax1.tick_params(axis='y', which='minor', length=5)
        ax2.xaxis.set_minor_locator(MultipleLocator(0.01))
        ax2.tick_params(axis='x', which='minor', length=5)
        if t==1:
            ax2.tick_params(axis='x', colors='white')
        ax2.tick_params(axis='y', colors='grey', labelsize=10,length=5)
    m = 0
    t = 0
    ax1.legend(fontsize=12)
    plt.tight_layout()
    plt.savefig('toi{}_TESSxExTrA_samedepth_v2/toi{}_ExTrA_{}.png'.
       format(toi_name,toi_name,obs_night[n]));

## PLOT THE POSTERIOR DISTRIBUTIONS WITH DYNESTY TOOL
f = open('toi{}_TESSxExTrA_samedepth_v2/_dynesty_NS_posteriors.pkl'.
   format(toi_name), 'rb')
results_P = pickle.load(f)
```

```
f.close()
dresults = results_P['dynesty_output']
params = list(results_P['posterior_samples'].keys())
params.remove('unnamed')
params.remove('loglike')
tfig, taxes = dyplot.traceplot(dresults, show_titles=True,title_fmt='.7
    f',labels=params, max_n_ticks=7)
plt.tight_layout()
plt.savefig('toi{}_TESSxExTrA_samedepth_v2/toi{}_dyplot.png'.format(
    toi_name,toi_name));
```

APPENDIX 2

Is presented here the table gathering all the TOIs orbiting M dwarfs.

TIC ID	TOI	SG1 Disposition	Vmag	Jmag	RA_J2000 hh:mm:ss	DEC_J2000 dd:mm:ss	Epoch (BJD-2400000)	Depth (mmag)	P (days)	Rp (Re)	Teff (Mann relations, color)	Rstar (GAIA DR2, Mann relations)	Mstar (GAIA DR2, Mann relations)	Predicted K (m/s)	TESS Sectors	SNR TESS	SNR ExTrA	Articles
231702397	122.01	VP	15.53	11.53	22:11:47	-58:56:42	58329.12025	6.676	5.078	2.709	3303	0.3342+/-0.0101	0.3167+/-0.0077	6.27	1,27,28	13	30	https://arxiv.org/pdf/2010.15905.pdf
234523599	127.01	P	16.44	12.61	1:02:12	-61:45:22	58325.6506	58.299	3.796	10.326	3445	0.4449+/-0.0136	0.4446+/-0.0110	53.7	1,2,28,29	96	204	https://arxiv.org/pdf/1812.09406.pdf
234994474	134.01	P	11.01	7.94	23:20:08	-60:03:55	58326.03316	0.672	1.402	1.74	3735	0.5974+/-0.0182	0.5904+/-0.0149	3	1,28	16	4	https://arxiv.org/pdf/1812.08145.pdf https://arxiv.org/pdf/2001.09175.pdf
410153553	136.01	VP	15.24	10.05	22:41:58	-69:10:08	59036.32368	4.886	0.463	1.517	2994	0.1883+/-0.0057	0.1552+/-0.0038	8.25	1,27	26	20	https://arxiv.org/pdf/1809.07242.pdf
425934411	142.01	VPC+	16.64	13.36	0:18:25	-62:50:52	58325.48619	28.032	0.853	12.694	3644	0.6073+/-0.0191	0.5984+/-0.0156	102.87	1,2,28,29	21	51	
307210830	175.01	P	11.69	7.93	8:18:08	-68:18:47	59363.75306	1.897	3.691	1.322	3422	0.3143+/-0.0094	0.2931+/-0.0070	2.16	2,5,8,9,10,11,12,28,29,32,35,36,37,38,39	69	11	https://arxiv.org/pdf/1903.08017.pdf https://arxiv.org/pdf/1905.10669.pdf https://arxiv.org/pdf/2108.03323.pdf
307210830	175.02	P	11.69	7.93	8:18:08	-68:18:47	59338.78409	1.478	7.451	1.537	3422	0.3143+/-0.0094	0.2931+/-0.0070	2.21	2,5,8,9,10,11,12,28,29,32,35,36,37,38	141	6	https://arxiv.org/pdf/1903.08017.pdf https://arxiv.org/pdf/1905.10669.pdf https://arxiv.org/pdf/2108.03323.pdf
307210830	175.03	VP	11.69	7.93	8:18:08	-68:18:47	59362.04588	0.732	2.253	0.952	3422	0.3143+/-0.0094	0.2931+/-0.0069	0.9	2,5,8,9,10,11,12,28,29,32,35,36,37,38,39	31	4	https://arxiv.org/pdf/1903.08017.pdf https://arxiv.org/pdf/1905.10669.pdf https://arxiv.org/pdf/2108.03323.pdf
262530407	177.01	P	11.4	8.17	1:21:45	-46:42:52	58356.15323	1.725	2.853	2.127	3670	0.5184+/-0.0156	0.5204+/-0.0128	3.63	2,3,29	29	10	https://arxiv.org/abs/2207.14121
12421862	198.01	VPC	11.69	8.65	0:09:04	-27:07:20	58356.3672	1.08	10.215	1.478	3673	0.4467+/-0.0133	0.4466+/-0.0106	1.41	2,29	11	8	paper in prep by Oddo et al. (CHEOPS)
55650590	206.01	VP	14.94	10.87	4:54:57	-62:31:21	58325.54367	1.384	0.736	1.471	3334	0.3517+/-0.0106	0.3374+/-0.0082	4.05	1,2,3,4,5,6,7,8,9,10,11,12,13,27,28,29,30,31,32,33,34,35,36,37,38,39	17	6	https://arxiv.org/abs/2201.12661
141608198	210.01	VPC+	15.37	10.87	5:55:51	-73:59:05	59338.99312	4.488	9.011	2.151	3220	0.3308+/-0.0100	0.3126+/-0.0077	3.53	1,2,3,4,5,7,8,9,10,11,12,13,27,28,29,30,31,32,33,34,35,37,38,39	40	33	
206609630	212.01	APC	14.88	10.58	1:30:12	-59:35:00	58325.49	20.807	0.335	4.484	3293	nan+/- nan	nan+/- nan	38.3	1,2,28,29	85	94	
32090583	218.01	VPC+	16.45	11.68	3:53:41	-68:44:22	58325.54019	0.22	0.438	0.439	3126	0.2841+/-0.0085	0.2579+/-0.0063	0.11	1,2,3,4,6,7,8,9,10,11,12,13,27,28,29,30,31,32,33,34,36,37,38,39	1	1	
2760710	227.01	STPC	18.44	12.13	23:46:07	-16:41:28	58364.10207	33.518	100	4.587	2811	0.2413+/-0.0074	0.2098+/-0.0054	1.6	2	inf	126	
415969908	233.01	VPC+	13.34	9.94	22:54:50	-18:54:42	58365.26099	3.113	11.67	2.018	3581	0.3804+/-0.0115	0.3713+/-0.0090	2.59	2,29,42	17	24	paper in prep by Almenara
415969908	233.02	VPC	13.34	9.94	22:54:50	-18:54:42	58359.46257	2.16	7.202	1.706	3581	0.3804+/-0.0115	0.3712+/-0.0091	2.29	2,29,42	11	14	
12423815	234.01	VPC+	16.52	13.22	0:10:16	-26:16:57	58356.08801	39.749	2.839	11.158	3656	0.5499+/-0.0175	0.5496+/-0.0145	58.68	2,29	25	92	paper in prep by HATSouth team
305048087	237.01	VP	16.37	11.74	23:32:58	-29:24:54	58355.24981	7.114	5.434	1.72	3139	0.2110+/-0.0066	0.1778+/-0.0046	4.11	2	8	28	https://arxiv.org/pdf/2010.15905.pdf
118327550	244.01	VPC+	12.86	8.83	0:42:17	-36:43:05	58357.36469	1.104	7.397	1.312	3340	0.4071+/-0.0125	0.4022+/-0.0101	1.38	2,29	9	6	https://arxiv.org/abs/2301.08162 paper in prep CHEOPS and ESPRESSO
179985715	249.01	VPC	12.53	10.10	0:56:19	-38:56:55	58359.53852	1.48	6.615	2.283	4130	0.5960+/-0.0177	0.5893+/-0.0145	2.71	2,29	10	12	
322063810	253.01	CPC-	10.77	8.16	0:57:16	-51:35:05	58355.61907	0.339	3.51	1.335	4007	0.6311+/-0.0187	0.6173+/-0.0152	1.34	2,29	9	3	
92226327	256.01	KP	14.15	9.61	0:44:59	-15:16:17	58399.92864	7.146	24.737	1.844	3144	0.2156+/-0.0066	0.1826+/-0.0046	2.75	3,30	22	55	https://arxiv.org/pdf/2010.06928.pdf
92226327	256.02	KP	14.15	9.61	0:44:59	-15:16:17	59141.10049	3.773	3.778	1.566	3144	0.2156+/-0.0066	0.1826+/-0.0046	3.9	3,30	8	25	https://arxiv.org/pdf/2010.06928.pdf
37749396	260.01	CPC	9.9	7.38	0:19:06	-9:57:53	58392.29375	0.762	13.476	1.68	4110	0.6069+/-0.0180	0.5982+/-0.0147	1.27	3,42	11	6	
220479565	269.01	P	14.37	10.91	5:03:23	-54:10:38	58381.84498	5.102	3.698	2.917	3555	0.3979+/-0.0120	0.3917+/-0.0095	6.87	3,4,5,6,10,13,30,31,32,33,36	35	26	https://arxiv.org/abs/2104.14782
259377017	270.01	P	12.6	9.10	4:33:40	-51:57:22	59198.96145	4.195	5.661	2.407	3514	0.3745+/-0.0115	0.3643+/-0.0093	4.51	3,4,5,30,32	58	29	https://arxiv.org/pdf/1903.06107.pdf https://arxiv.org/pdf/2004.12475.pdf https://arxiv.org/pdf/2101.01593.pdf
259377017	270.02	P	12.6	9.10	4:33:40	-51:57:22	58389.67934	3.422	11.38	2.254	3514	0.3745+/-0.0115	0.3643+/-0.0093	3.2	3,4,5,30,32	41	27	https://arxiv.org/pdf/1903.06107.pdf https://arxiv.org/pdf/2004.12475.pdf https://arxiv.org/pdf/2101.01593.pdf
259377017	270.03	P	12.6	9.10	4:33:40	-51:57:22	58383.73321	1.057	3.36	1.184	3514	0.3745+/-0.0115	0.3643+/-0.0093	1.5	3,4,5,30,32	17	7	https://arxiv.org/pdf/1903.06107.pdf https://arxiv.org/pdf/2004.12475.pdf https://arxiv.org/pdf/2101.01593.pdf
439456714	277.01	VPC+	13.63	10.40	1:16:19	-20:57:08	58385.03631	6.318	3.993	4.256	3669	0.5226+/-0.0157	0.5244+/-0.0127	10.49	3,30	23	47	paper in prep by Jose https://arxiv.org/abs/2211.08490
220459976	285.01	STPC	13.81	10.98	4:58:47	-56:23:39	58361.66393	2.637	100	3.17	3888	0.6430+/-0.0190	0.6263+/-0.0154	2.81	2,3	8	25	
153065527	406.01	VPC+	13.77	9.70	3:17:03	-42:14:33	58388.56746	2.695	13.176	1.96	3323	0.3883+/-0.0116	0.3806+/-0.0091	2.33	3,4,30,31	19	21	
153065527	406.02	PC	13.77	9.70	3:17:03	-42:14:33	58385.38837	1.152	6.615	1.273	3323	0.3883+/-0.0116	0.3805+/-0.0091	1.41	3,4,30,31	5	6	
44647437	435.01	VPC+	14.34	11.75	3:57:39	-25:11:24	58411.84477	4.575	3.353	5.293	4043	0.6378+/-0.0189	0.6224+/-0.0153	14.15	4,5,31	14	26	
70899085	442.01	P	12.49	9.49	4:16:46	-12:05:02	59196.11534	6.002	4.052	4.952	3800	0.6070+/-0.0182	0.5983+/-0.0149	12.36	5,32	49	40	https://arxiv.org/pdf/2011.01716.pdf
98796344	455.01	P	10.59	7.29	3:01:51	-16:35:36	59168.29527	2.945	5.359	1.445	3558	0.2755+/-0.0083	0.2480+/-0.0060	2.48	4,31	20	18	https://arxiv.org/pdf/1906.10147.pdf https://arxiv.org/abs/2107.14737 https://arxiv.org/abs/2210.09713 https://arxiv.org/abs/2301.08162
89256802	457.01	VPC-	17.04	11.90	3:54:54	-26:25:25	58411.56054	16.279	1.176	7.719	3054	nan+/- nan	nan+/- nan	43.93	4,31	12	55	

TIC ID	TOI	SG1 Disposition	Vmag	Jmag	RA_J2000 hh:mm:ss	DEC_J2000 dd:mm:ss	Epoch (BJD-2400000)	Depth (mmag)	P (days)	Rp (Re)	Teff (Mann relations, color)	Rstar (GAIA DR2, Mann relations)	Mstar (GAIA DR2, Mann relations)	Predicted K (m/s)	TESS Sectors	SNR TESS	SNR ExTrA	Articles
33521996	468.01	KP	15.04	12.05	5:52:35	-19:01:54	59220.8204	38.391	3.325	11.504	3799	0.5975+/-0.0180	0.5906+/-0.0147	55.88	6,32,33	97	175	https://arxiv.org/abs/1408.1758
100608026	475.01	PPC	12.2	9.66	5:47:00	-32:31:59	58442.48655	1.541	8.262	2.341	4079	0.6106+/-0.0181	0.6012+/-0.0148	2.65	5,6,32,33	19	13	
260708537	486.01	CPC	11.62	7.90	6:33:50	-58:31:43	59387.75899	0.174	1.745	0.661	3448	0.4267+/-0.0128	0.4244+/-0.0102	0.21	1,2,3,4,5,6,8,9,10,11,12,13,27,28,29,30,31,32,33,34,35,36,37,38	84	1	
452866790	488.01	P	13.74	9.63	8:02:23	+03:20:19.68	59228.97809	1.057	1.198	1.122	3307	0.3544+/-0.0107	0.3406+/-0.0084	1.81	7,34	9	6	https://arxiv.org/pdf/2009.10432.pdf
348538431	507.01	VPC+	16.3	11.65	8:06:31	-15:45:53	58492.09617	65.759	0.899	17.12	3142	0.5046+/-0.0153	0.5069+/-0.0124	331.51	7,34	94	275	tli-color analysis by Parviainen (see TOI-5
218795833	519.01	VP	17.35	12.85	8:18:26	-19:39:46	58491.87197	124.589	1.265	12.166	3229	0.3554+/-0.0110	0.3418+/-0.0088	121.73	7,34	76	315	https://arxiv.org/pdf/2011.11458.pdf
27649847	521.01	VPC+	14.69	10.92	8:13:23	+12:13:18.12	59575.79663	2.272	1.543	1.995	3413	0.4199+/-0.0125	0.4168+/-0.0099	4.63	7,34,44,45,46	426	13	/
387690507	530.01	P	15.4	12.11	6:53:39	+12:52:54.48	59530.54351	26.07	6.388	8.435	3649	0.5444+/-0.0164	0.5447+/-0.0134	27.98	6,33,44,45	38	127	https://arxiv.org/abs/2110.04220
144700903	532.01	P	14.41	11.47	5:40:19	+11:33:46.44	58470.5763	9.359	2.327	5.774	3875	0.6231+/-0.0187	0.6110+/-0.0152	19.04	6	23	50	https://arxiv.org/abs/2107.13670
200322593	540.01	VP	14.82	9.76	5:05:14	-47:56:15	59175.14165	2.52	1.239	0.965	3042	0.1971+/-0.0059	0.1639+/-0.0040	1.69	4,5,6,31,32	17	9	https://arxiv.org/pdf/2009.13623.pdf
192826603	551.01	KP	15.67	12.70	5:30:51	-36:37:51	59203.14917	23.451	2.647	10.613	3802	0.5672+/-0.0172	0.5649+/-0.0141	54.09	5,6,32,33	22	61	https://arxiv.org/abs/1710.11099
44737596	552.01	P	15.69	12.48	4:03:48	-25:24:32	58413.06043	28.982	2.789	9.665	3744	0.5878+/-0.0176	0.5826+/-0.0144	44.48	4,5,31	55	104	https://arxiv.org/abs/2112.01928
170849515	555.01	P	16.68	13.69	4:41:22	-32:19:13	58438.14751	36.372	1.942	11.757	3837	0.6340+/-0.0203	0.6195+/-0.0164	67.15	5,31,32	33	76	https://arxiv.org/abs/2112.01928
55488511	557.01	VPC	13.34	10.40	3:56:04	-10:16:19	58439.54965	1.521	3.345	2.254	3800	0.5741+/-0.0171	0.5710+/-0.0140	3.57	5,31	9	9	
413248763	562.01	P	10.91	7.34	9:36:02	-21:39:39	59272.67589	1.225	3.931	1.217	3509	0.3608+/-0.0107	0.3482+/-0.0082	1.61	8,35	20	7	https://arxiv.org/pdf/1904.12818.pdf (juliet) https://arxiv.org/abs/2301.08162
296739893	620.01	VP	12.26	8.84	9:28:42	-12:09:56	58518.00571	3.072	5.099	2.926	3594	0.5481+/-0.0166	0.5481+/-0.0136	4.97	8,35	21	17	https://arxiv.org/abs/2204.03108
35009898	654.01	VPC+	14.54	10.74	10:58:54	-5:32:47	59576.06792	3.077	1.528	2.36	3429	0.4276+/-0.0128	0.4255+/-0.0102	6.09	9,36,45,46	591	17	
36734222	656.01	KP	12.3	9.99	10:19:38	-9:48:23	59279.79745	29.293	0.813	13.16	4231	0.6920+/-0.0208	0.6625+/-0.0164	104.73	9,35	319	174	https://arxiv.org/abs/1104.2823
54962195	663.01	VPC+	13.67	10.45	10:40:16	-8:30:39	58544.38897	2.129	2.599	2.288	3666	0.5119+/-0.0153	0.5141+/-0.0124	4.27	9,35	13	14	
54962195	663.02	VPC+	13.67	10.45	10:40:16	-8:30:39	58543.40453	2.188	4.696	2.415	3666	0.5119+/-0.0153	0.5140+/-0.0124	3.84	9,35	10	16	
54962195	663.03	PC	13.67	10.45	10:40:16	-8:30:39	58547.11079	1.555	7.103	1.95	3666	0.5119+/-0.0153	0.5140+/-0.0124	2.33	9,35	8	12	
101955023	667.01	KP	13.68	9.24	10:14:52	-47:09:24	59280.9894	2.731	1.629	1.215	3212	0.2266+/-0.0070	0.1940+/-0.0050	3.14	9,10,36	26	13	https://arxiv.org/pdf/1511.03550.pdf https://arxiv.org/pdf/1806.03870.pdf
151825527	672.01	VPC+	13.58	10.36	11:11:58	-39:19:40	58546.47998	9.443	3.634	5.092	3694	0.5436+/-0.0163	0.5439+/-0.0133	14.33	9,10,36	61	67	
158588995	674.01	P	14.2	10.36	10:58:21	-36:51:29	59301.77814	15.27	1.977	5.057	3432	0.4218+/-0.0126	0.4190+/-0.0099	20.64	9,10,36	100	83	https://arxiv.org/pdf/2106.01246.pdf
77156829	696.01	VP	12.6	9.02	4:32:43	-39:47:12	58411.47363	0.782	0.86	0.972	3450	0.3387+/-0.0105	0.3220+/-0.0083	1.26	4,5,31,32	11	3	https://arxiv.org/abs/2110.12079#
77156829	696.02	VP	12.6	9.02	4:32:43	-39:47:12	58411.06752	0.905	3.694	1.043	3450	0.3387+/-0.0105	0.3220+/-0.0083	1	4,5,31,32	13	5	https://arxiv.org/abs/2110.12079#
77156829	696.03	VPC	12.6	9.02	4:32:43	-39:47:12	58414.56293	0.688	4.965	0.857	3450	0.3387+/-0.0105	0.3220+/-0.0083	0.45	4,5,31,32	6	4	https://arxiv.org/abs/2110.12079#
141527579	698.01	VPC+?	14.24	10.71	5:50:57	-76:37:13	59385.01574	2.102	15.087	2.102	3527	0.4718+/-0.0142	0.4735+/-0.0114	2.18	1,2,3,4,5,7,8,9,10,11,12,13,27,28,29,30,31,32,33,34,35,36,37,38,39	21	16	
150428135	700.01	VP	13.15	9.47	6:28:23	-65:34:46	59303.15706	3.084	16.051	2.602	3454	0.4200+/-0.0126	0.4169+/-0.0101	3.33	1,3,4,5,6,7,8,9,10,11,13,27,28,30,31,33,34,35,36,37,38	33	19	https://arxiv.org/pdf/2001.00952.pdf
150428135	700.02	VP	13.15	9.47	6:28:23	-65:34:46	58330.47508	0.799	37.424	1.145	3454	0.4200+/-0.0126	0.4169+/-0.0100	0.54	1,3,4,5,6,7,8,9,10,11,13,27,28,30,31,33,34,35,36,37,38	11	8	https://arxiv.org/pdf/2001.00952.pdf
150428135	700.03	VP	13.15	9.47	6:28:23	-65:34:46	59349.03688	0.577	9.977	0.971	3454	0.4200+/-0.0126	0.4170+/-0.0100	0.47	1,3,4,5,6,7,8,9,10,11,13,27,28,30,31,33,34,35,36,37,38	10	4	https://arxiv.org/pdf/2001.00952.pdf https://arxiv.org/pdf/2005.11587.pdf
150428135	700.04	VP	13.15	9.47	6:28:23	-65:34:46	58352.99122	0.492	27.809	0.954	3454	0.4200+/-0.0126	0.4169+/-0.0100	0.31	1,3,4,5,6,7,8,9,10,11,13,27,28,30,31,33,34,35,36,37,38	8	5	https://arxiv.org/abs/2301.03617
237914496	702.01	VPC	13.25	10.66	3:44:42	-65:11:57	58326.81413	1.007	3.568	2.07	4076	0.5828+/-0.0173	0.5784+/-0.0142	2.85	1,2,3,4,7,11,27,29,30,31,34,37	13	6	
260004324	704.01	VP	12.17	8.80	6:04:20	-55:18:47	59319.12878	0.495	3.814	1.091	3580	0.5046+/-0.0150	0.5069+/-0.0121	0.86	1,2,3,4,5,7,8,9,10,11,12,13,27,28,29,30,31,32,33,34,35,36,37,38,39	18	3	https://arxiv.org/pdf/2003.04525.pdf
219195044	714.01	VPC	13.31	10.24	6:09:34	-53:49:25	59355.44308	0.978	4.324	1.49	3695	0.4728+/-0.0142	0.4746+/-0.0114	1.83	1,2,4,5,6,7,8,11,12,28,31,32,33,34,35,38	635	6	
219195044	714.02	VPC	13.31	10.24	6:09:34	-53:49:25	58419.10785	1.036	10.178	1.554	3695	0.4728+/-0.0142	0.4746+/-0.0114	1.48	4,5,6,7,8,11,12,28,31,32,33,34,35,38	14	8	
271971130	715.01	VPC+	16.68	11.81	7:35:24	-73:34:39	58327.55132	5.004	19.288	1.595	3066	0.2296+/-0.0069	0.1972+/-0.0047	2.22	1,2,3,4,5,6,7,8,9,10,11,12,13,27,29,30,31,32,33,34,35,36,37,39	17	26	paper in prep by Dransfield

TIC ID	TOI	SG1 Disposition	Vmag	Jmag	RA_J2000 hh:mm:ss	DEC_J2000 dd:mm:ss	Epoch (BJD-2400000)	Depth (mmag)	P (days)	Rp (Re)	Teff (Mann relations, color)	Rstar (GAIA DR2, Mann relations)	Mstar (GAIA DR2, Mann relations)	Predicted K (m/s)	TESS Sectors	SNR TESS	SNR ExTrA	Articles
38509907	722.01	VPC+	13.32	10.76	4:09:31	-62:51:05	58339.13817	1.401	15.3	1.296	4047	0.4200+/-0.0236	0.4167+/-0.0247	0.78	1,2,3,4,5,7,8,9,10,11,12,27,28,29,30,31,32,34,35,37,38,39	18	13	
149788158	727.01	LEPC	12.68	9.66	8:42:57	-2:29:53	59245.51846	1.608	4.724	1.965	3734	0.4967+/-0.0148	0.4991+/-0.0119	2.75	8,34	58	9	
11561667	730.01	P	16.2	13.78	9:59:18	-27:23:34	58543.86942	45.963	3.088	14.053	4236	0.6621+/-0.0226	0.6405+/-0.0178	75.84	9,35	27	98	https://arxiv.org/abs/2112.01928
34068865	731.01	P	10.15	6.63	9:44:30	-45:46:35	59304.83753	0.398	0.322	1.028	3517	0.4577+/-0.0136	0.4586+/-0.0108	1.69	9,35,36	17	2	https://arxiv.org/abs/2112.01309 https://arxiv.org/abs/2201.12661
36724087	732.01	P	13.14	9.01	10:18:35	-11:43:00	58543.90665	0.982	0.768	1.141	3303	0.3747+/-0.0112	0.3645+/-0.0088	2.14	9,35	10	5	https://arxiv.org/pdf/2003.01136.pdf https://arxiv.org/pdf/2003.01140.pdf
36724087	732.02	P	13.14	9.01	10:18:35	-11:43:00	58546.8496	3.254	12.252	2.075	3303	0.3747+/-0.0112	0.3646+/-0.0088	2.71	9,35	12	20	https://arxiv.org/pdf/2003.01136.pdf https://arxiv.org/pdf/2003.01140.pdf
146846569	734.01	VPC+	18.26	13.10	10:43:34	-44:37:21	58545.4485	284.387	4.754	11.849	3011	nan+/- nan	nan+/- nan	118.74	9,10,36	19	576	
181804752	736.01	VP	16.91	11.56	11:02:46	-16:24:22	59285.0148	19.139	4.99	2.284	2946	0.1717+/-0.0052	0.1396+/-0.0034	8.05	9,36	22	80	https://arxiv.org/pdf/1906.09267.pdf
181804752	736.02	VP	16.91	11.56	11:02:46	-16:24:22	58543.55772	4.652	0.948	1.201	2946	0.1717+/-0.0052	0.1396+/-0.0034	4.48	9,36	8	14	https://arxiv.org/pdf/1906.09267.pdf
219189765	737.01	P	17.26	13.25	11:24:04	-19:33:26	58544.43094	39.511	1.732	11.689	3395	0.6154+/-0.0210	0.6048+/-0.0170	70.17	9,36	36	93	https://arxiv.org/abs/2112.01928
359271092	741.01	PC	9.49	6.44	9:21:38	-60:16:55	58544.08415	0.315	7.577	0.972	3764	0.5248+/-0.0156	0.5265+/-0.0127	0.44	9,10,36,37	13	3	
73649615	756.01	VPC+	14.61	11.14	12:48:25	-45:28:14	59308.00435	3.02	1.239	2.867	3563	0.5083+/-0.0152	0.5105+/-0.0123	8.07	10,11,37	14	16	
165317334	761.01	PC	12.25	9.77	11:57:03	-38:06:17	58576.38561	1.58	10.556	2.59	4106	0.6384+/-0.0190	0.6229+/-0.0153	2.87	10,37	12	14	
178709444	762.01	VPC	16	12.00	11:04:18	-47:49:17	59329.50563	33.77	3.472	8.027	3401	0.4274+/-0.0131	0.4252+/-0.0106	37.2	10,36,37	38	129	https://arxiv.org/abs/2303.00659
277634430	771.01	VPC+	14.89	10.51	10:56:27	-72:59:05	59335.35229	3.567	2.326	1.396	3217	0.2422+/-0.0073	0.2108+/-0.0051	3.44	10,11,12,37,38	20	19	
306996324	776.01	P	11.54	8.48	11:54:18	-37:33:10	59324.53476	1.375	15.665	1.923	3728	0.5322+/-0.0158	0.5334+/-0.0129	1.7	10,37	15	13	https://arxiv.org/pdf/2009.08338.pdf
306996324	776.02	P	11.54	8.48	11:54:18	-37:33:10	59321.85862	0.902	8.247	1.548	3728	0.5322+/-0.0158	0.5334+/-0.0128	1.46	10,37	431	8	https://arxiv.org/pdf/2009.08338.pdf
429358906	782.01	VPC+	14.83	10.68	12:15:41	-18:54:37	58577.04189	4.438	8.024	2.679	3298	0.4065+/-0.0123	0.4015+/-0.0098	4.52	10,36	12	31	Hori et al. in prep
374829238	785.01	PC	13.34	10.22	5:53:21	-65:38:02	58363.82145	0.461	18.626	1.178	3716	0.5618+/-0.0167	0.5603+/-0.0137	0.62	2,3,6,7,9,10,12,13,27,29,30,33,34,36,37,39	9	10	
300710077	789.01	VPC	14.23	10.51	7:41:04	-71:18:16	58329.11244	0.906	5.447	1.077	3426	0.3717+/-0.0112	0.3610+/-0.0088	0.91	1,2,3,5,6,7,8,9,10,11,12,13,27,28,29,30,31,32,33,35,36,37,38,39	10	6	/
300710077	789.02	CPC	14.23	10.51	7:41:04	-71:18:16	58334.76948	1.288	12.971	1.284	3426	0.3717+/-0.0112	0.3610+/-0.0088	1.18	1,2,3,5,6,7,8,9,10,11,12,13,27,28,29,30,31,32,33,35,36,37,38,39	10	10	
300710077	789.03	VPC	14.23	10.51	7:41:04	-71:18:16	58329.96143	0.766	8.043	1.017	3426	0.3717+/-0.0112	0.3610+/-0.0088	0.65	1,2,3,5,6,7,8,9,10,11,12,13,27,28,29,30,31,32,33,35,36,37,38,39	11	7	
271596225	797.01	VPC	13.69	10.41	7:14:15	-74:36:09	58326.81719	0.751	1.801	1.286	3644	0.4732+/-0.0141	0.4750+/-0.0113	1.91	1,2,3,4,5,6,7,8,9,10,11,12,13,27,28,29,30,31,32,33,34,35,36,37,38,39	16	4	
271596225	797.02	VPC	13.69	10.41	7:14:15	-74:36:09	58327.41688	0.803	4.14	1.297	3644	0.4732+/-0.0141	0.4749+/-0.0113	1.47	1,2,3,4,5,6,7,8,9,10,11,12,13,27,28,29,30,31,32,33,34,35,36	9	4	
271596225	797.03	PC	13.69	10.41	7:14:15	-74:36:09	58327.46597	0.423	2.731	1.043	3644	0.4732+/-0.0141	0.4750+/-0.0113	0.85	1,2,3,4,5,6,7,8,9,10,11,12,13,27,28,29,30,31,32,33,34,35,36,37,38,39	9	3	
38460940	805.01	VPC	15.63	11.58	4:04:32	-62:59:14	59357.99304	2.117	4.118	1.276	3310	0.2809+/-0.0086	0.2542+/-0.0064	2.15	1,3,4,5,7,8,11,12,27,28,29,30,31,32,34,35,37,38	12	9	
33831980	806.01	VPC	13.27	10.85	4:13:40	-76:05:52	59354.18418	1.354	21.917	2.282	4179	0.6197+/-0.0185	0.6084+/-0.0151	1.78	1,2,3,5,6,8,9,12,13,27,28,29,32,33,35,36,38,39	14	14	
362249359	833.01	VP	11.72	8.97	9:42:35	-62:28:35	58544.11999	0.537	1.042	1.352	3914	0.6026+/-0.0178	0.5947+/-0.0146	2.15	9,10,11,36,37	14	3	https://arxiv.org/abs/2201.12661
231728511	864.01	VPC	13.8	10.05	5:25:47	-51:21:25	58411.15308	0.681	0.521	1.005	3440	0.3985+/-0.0121	0.3923+/-0.0096	1.47	4,5,6,27,31,32,33,37	9	3	
219229644	870.01	VPC+	12.54	9.55	4:13:16	-50:56:40	58390.80078	1.312	22.038	2.335	3842	0.6104+/-0.0181	0.6010+/-0.0148	1.95	3,4,5,30,31,32	13	11	
237920046	873.01	VPC?	14	10.85	3:46:56	-63:20:14	58326.22271	0.995	5.931	1.688	3718	0.5206+/-0.0155	0.5224+/-0.0126	1.92	1,2,3,4,11,28,29,30,31,34,38	10	8	
261257684	904.01	VPC	12.59	9.61	5:57:29	-83:07:49	59366.62864	2.032	10.877	2.556	3816	0.5318+/-0.0158	0.5330+/-0.0129	3.12	12,13,27,38,39	22	19	paper in prep
261257684	904.02	PC	12.59	9.61	5:57:29	-83:07:49	58714.35119	2.146	84	2.378	3816	0.5318+/-0.0158	0.5330+/-0.0129	1.4	12,13,27,38,39	10	26	paper in prep
369327947	910.01	VPC	13	8.55	19:20:54	-82:33:16	59389.14572	1.062	2.029	0.929	3190	0.2871+/-0.0095	0.2613+/-0.0079	0.92	12,13,27,39	13	5	https://arxiv.org/abs/2304.01920
406941612	912.01	VPC+	12.67	9.09	15:17:22	-80:28:22	59386.25425	1.521	4.678	1.796	3521	0.4271+/-0.0128	0.4248+/-0.0102	2.64	12,13,39	967	10	paper in prep by Almenara
351601843	1075.01	P	12.62	9.94	20:39:53	-65:26:58	58654.25001	0.991	0.605	1.667	3980	0.5795+/-0.0173	0.5755+/-0.0142	3.76	13,27	12	5	https://arxiv.org/abs/2201.12661 https://arxiv.org/abs/2210.14901

TIC ID	TOI	SG1 Disposition	Vmag	Jmag	RA_J2000 hh:mm:ss	DEC_J2000 dd:mm:ss	Epoch (BJD-2400000)	Depth (mmag)	P (days)	Rp (Re)	Teff (Mann relations, color)	Rstar (GAIA DR2, Mann relations)	Mstar (GAIA DR2, Mann relations)	Predicted K (m/s)	TESS Sectors	SNR TESS	SNR ExTrA	Articles
370133522	1078.01	VP	12.68	8.70	20:27:42	-56:27:26	58654.10545	0.866	0.518	1.14	3329	0.3903+/-0.0118	0.3828+/-0.0093	2.35	13,27	17	4	https://arxiv.org/pdf/1912.05556.pdf https://arxiv.org/abs/2208.09479
161032923	1080.01	VPC+?	15.35	11.04	18:25:29	-52:12:51	58654.06003	5.192	3.965	1.433	3250	0.2000+/-0.0060	0.1667+/-0.0040	3.5	13	8	26	paper in prep by Chew
261108236	1082.01	PC	13.22	10.71	5:33:06	-80:48:56	59165.53801	2.254	16.347	2.928	4071	0.6236+/-0.0186	0.6113+/-0.0151	3.02	1,4,8,11,12,13,27,28,31,38,39	15	22	
322270620	1083.01	VPC	14.16	10.70	19:47:19	-87:19:18	58627.91634	3.135	12.98	3.208	3575	0.4912+/-0.0147	0.4934+/-0.0119	4.56	12,13,39	7	28	
29960110	1201.01	P	12.26	9.53	2:48:59	-14:32:15	58411.67088	2.276	2.492	2.219	3951	0.4817+/-0.0147	0.4838+/-0.0120	4.28	4,31	16	15	https://arxiv.org/abs/2109.09346
453260209	1215.01	CPC-	12.31	8.38	9:47:31	-77:17:46	58570.39677	0.441	1.212	0.927	3412	0.6432+/-0.0193	0.6264+/-0.0156	0.66	10,11,12,37,38,39	8	2	
141527965	1216.01	PC	12.75	10.44	5:50:51	-75:41:20	58325.4441	0.221	4.554	0.903	4256	0.6760+/-0.0203	0.6508+/-0.0161	0.34	1,2,3,4,5,7,8,9,10,11,12,13,27,28,29,30,31,32,33,34,35,36,37,38,39	10	3	
299798795	1224.01	VPC+?	13.95	10.02	2:28:46	-80:53:57	59363.91652	2.819	4.178	2.183	3397	0.4050+/-0.0121	0.3998+/-0.0094	3.98	1,13,27,28,39	15	20	
360156606	1227.01	VP	17	11.89	12:27:04	-72:27:06	58617.47608	23.767	27.363	6.545	3020	0.4419+/-0.0133	0.4413+/-0.0107	12.89	11,12,38	13	165	https://arxiv.org/abs/2110.09531
447061717	1231.01	P	12.36	8.88	10:26:59	-52:28:10	58563.88906	6.834	24.246	3.71	3539	0.4651+/-0.0141	0.4665+/-0.0114	4.92	9,10,36	57	66	paper in prep by Burt
90504905	1234.01	LEPC	16.27	12.17	19:22:17	+26:19:10.40	58685.61315	16.431	2.265	5.194	3335	0.4112+/-0.0124	0.4069+/-0.0099	21.04	14,40	9	96	
103633434	1235.01	P	11.49	8.71	10:08:52	+69:16:35.56	59603.35433	0.782	3.445	1.753	3907	0.6301+/-0.0188	0.6165+/-0.0152	2.19	14,20,21,40,41,47	1152	6	https://arxiv.org/pdf/2004.06682.pdf https://arxiv.org/pdf/2004.06218.pdf
153951307	1238.01	VPC-?	12.8	10.04	13:25:32	+68:50:10.56	59659.5369	1.434	3.295	2.373	3959	0.6240+/-0.0183	0.6117+/-0.0149	3.74	14,15,21,22,41,49	670	10	https://arxiv.org/abs/2111.14602
153951307	1238.02	CPC-	12.8	10.04	13:25:32	+68:50:10.56	59662.76933	0.413	0.765	1.342	3959	0.6240+/-0.0183	0.6117+/-0.0149	2.31	14,15,21,22,41,49	158	2	https://arxiv.org/abs/2111.14602
219698776	1243.01	VPC+	13.43	9.73	9:02:56	+71:38:13.31	59598.14316	1.499	4.659	4.498	3489	0.4904+/-0.0145	0.4927+/-0.0115	11.41	14,20,40,47	1	6	
229781583	1245.01	VPC	14.37	10.86	18:54:09	+69:37:59.88	59764.32932	2.097	4.82	2.388	3558	0.5251+/-0.0156	0.5267+/-0.0126	3.68	14,15,16,17,18,19,20,21,22,23,25,26,40,41,47,48,49,50,51,52	1292	15	
233211762	1252.01	VPC	13.5	10.76	17:46:45	+70:47:03.79	59662.04288	5.279	1.122	9.713	3947	nan+/- nan	nan+/- nan	54.81	14,15,16,17,18,19,21,22,24,25,26,41,47,48,49	3	23	
467179528	1266.01	VP	12.94	9.71	13:12:00	+65:50:01.70	59649.7513	3.445	10.895	2.469	3677	0.4357+/-0.0130	0.4345+/-0.0103	3.37	14,15,21,22,41,48,49	38	27	https://arxiv.org/pdf/2006.11180.pdf https://arxiv.org/pdf/2009.04317.pdf
467179528	1266.02	VP	12.94	9.71	13:12:00	+65:50:01.70	59630.04643	1.833	18.802	1.911	3677	0.4357+/-0.0130	0.4345+/-0.0103	1.82	14,15,21,22,41,48,49	15	14	https://arxiv.org/pdf/2006.11180.pdf https://arxiv.org/pdf/2009.04317.pdf https://arxiv.org/abs/2109.10838
235683377	1442.01	VP	15.39	10.93	19:09:10	+74:10:20.22	59768.70842	1.26	0.409	1.651	3222	0.3087+/-0.0093	0.2865+/-0.0069	6.67	14,15,16,17,18,19,20,21,22,23,24,25,26,40,41,47,48,49,50,51,52	5	4	https://arxiv.org/abs/2201.13274 https://arxiv.org/abs/2201.12661
343628284	1448.01	VPC	15.68	11.60	21:05:18	+57:46:16.94	58713.33373	8.022	8.114	3.791	3316	0.3809+/-0.0114	0.3718+/-0.0089	8.53	15,16	7	48	Hori et al. in prep
356158613	1449.02	VPC+	12.52	9.52	20:02:50	+39:40:05.34	58683.58523	0.791	2.369	1.689	3820	0.6195+/-0.0184	0.6082+/-0.0150	2.38	14,15,41	9	5	
377293776	1450.01	VPC	12.28	8.46	19:07:25	+59:05:09.36	59662.33557	0.434	2.044	1.035	3450	0.4728+/-0.0140	0.4746+/-0.0111	0.91	14,15,16,17,18,19,20,21,22,23,24,25,26,40,41,47,49	389	2	
420112589	1452.01	P	14.35	10.60	19:20:42	+73:11:43.54	59731.35931	2.74	11.062	1.448	3428	0.2754+/-0.0094	0.2478+/-0.0078	1.95	14,15,16,17,19,20,21,22,23,24,25,26,40,41,47,49,50,51,52	305	19	https://arxiv.org/abs/2208.06333
240968774	1467.01	VPC+	12.29	9.38	1:16:27	+49:14:01.61	58766.98373	1.492	5.973	1.827	3797	0.4904+/-0.0146	0.4927+/-0.0117	2.27	17	8	10	
243185500	1468.01	VPC	12.5	9.34	1:06:37	+19:13:33.16	59450.35603	3.194	15.532	2.014	3649	0.3689+/-0.0109	0.3578+/-0.0084	2.41	17,42,43	20	23	https://arxiv.org/abs/2208.10351
243185500	1468.02	VPC+	12.5	9.34	1:06:37	+19:13:33.16	59448.30816	1.319	1.881	1.455	3649	0.3689+/-0.0109	0.3578+/-0.0084	2.8	17,42,43	12	8	https://arxiv.org/abs/2208.10351
284441182	1470.01	VPC+	13.46	10.15	0:40:21	+61:12:49.05	58766.46865	2.089	2.527	2.165	3636	0.4906+/-0.0146	0.4929+/-0.0117	4.04	17,18,24	12	13	
201186294	1634.01	P	13.22	9.48	3:45:34	+37:06:44.00	58791.515	1.651	0.989	1.83	3472	0.4653+/-0.0137	0.4666+/-0.0108	4.3	18	11	9	https://arxiv.org/pdf/2103.12790.pdf https://arxiv.org/pdf/2103.12760.pdf
312862941	1638.01	VPC+	13.85	10.89	1:01:17	+55:41:52.61	58791.14637	5.979	0.915	8.637	3825	0.7010+/-0.0206	0.6690+/-0.0163	48.51	18	12	28	
396562848	1640.01	P	13.3	9.62	2:57:18	+76:33:11.25	59767.37311	1.543	1.95	2.63	3464	0.2599+/-0.0079	0.2303+/-0.0057	10.07	18,19,25,26,52	1	5	https://arxiv.org/pdf/2102.11640.pdf
259168516	1680.01	VPC+	15.87	11.64	19:29:15	+65:58:27.72	59657.39407	4.341	4.803	1.447	3227	0.2135+/-0.0064	0.1804+/-0.0044	3.17	14,15,16,17,18,19,20,21,22,23,24,25,40,41,47,48,49	415	18	paper in prep by Ghachoui
28900646	1685.01	P	13.38	9.62	4:34:22	+43:02:14.69	58816.22502	1.084	0.669	1.469	3453	0.4621+/-0.0138	0.4632+/-0.0110	3.39	19	8	6	https://arxiv.org/pdf/2103.01016.pdf https://arxiv.org/pdf/2103.12760.pdf
353475866	1693.01	VP	12.96	9.19	6:01:14	+34:46:23.40	59549.0973	0.893	1.767	1.415	3479	0.4614+/-0.0138	0.4625+/-0.0110	2.31	19,43,44,45	14	6	https://arxiv.org/abs/2201.12661
422756130	1695.01	VPC+	12.99	9.64	1:27:41	+72:17:47.19	58791.51935	1.313	3.134	1.819	3634	0.5158+/-0.0154	0.5178+/-0.0124	2.7	18,19,24,25	14	8	https://arxiv.org/abs/2211.06205 https://arxiv.org/abs/2211.06445
470381900	1696.01	VP	16.82	12.23	4:21:07	+48:49:11.69	58816.69771	12.023	2.501	2.969	3203	0.2806+/-0.0086	0.2538+/-0.0064	10.71	19	7	35	https://arxiv.org/abs/2203.02694 https://arxiv.org/abs/2204.09063

TIC ID	TOI	SG1 Disposition	Vmag	Jmag	RA_J2000 hh:mm:ss	DEC_J2000 dd:mm:ss	Epoch (BJD-2400000)	Depth (mmag)	P (days)	Rp (Re)	Teff (Mann relations, color)	Rstar (GAIA DR2, Mann relations)	Mstar (GAIA DR2, Mann relations)	Predicted K (m/s)	TESS Sectors	SNR TESS	SNR ExTrA	Articles
1884091865	1697.01	VPC-	12.5	9.92	19:20:26	+61:05:06.19	59755.17474	1.391	10.717	2.665	4084	nan+/- nan	nan+/- nan	2.97	14,15,16,17,18,19,20,21,22,23,24,25,26,40,41,47,48,49,50,51,52	1357	13	
285048486	1728.01	P	12.39	9.64	8:02:27	+64:47:48.93	59604.39909	5.879	3.491	4.964	3962	0.6337+/-0.0188	0.6193+/-0.0152	12.76	20,47	4254	42	https://arxiv.org/pdf/2006.14546.pdf
318022259	1730.01	PC	12.23	9.06	7:11:28	+48:19:49.40	59603.96341	1.304	6.226	1.953	3703	0.5326+/-0.0159	0.5338+/-0.0129	2.38	20,47	446	9	paper in prep by Wilson
318022259	1730.02	VPC	12.23	9.06	7:11:28	+48:19:49.40	59603.31333	0.739	2.156	1.499	3703	0.5326+/-0.0159	0.5338+/-0.0129	2.16	20,47	221	5	paper in prep by Wilson
318022259	1730.03	VPC	12.23	9.06	7:11:28	+48:19:49.40	59598.36814	2.369	12.566	2.636	3703	0.5326+/-0.0159	0.5338+/-0.0129	3.14	20,47	1059	21	
470987100	1732.01	PC	12.89	10.13	7:27:12	+53:02:42.31	59601.2399	1.76	4.119	2.565	3945	0.6316+/-0.0188	0.6177+/-0.0152	3.93	20,47	452	13	
104208182	1738.01	VPC	14.07	11.31	3:38:00	+50:57:19.75	58792.66061	3.126	3.697	3.586	3967	0.6686+/-0.0197	0.6454+/-0.0157	7	18,19	9	17	
219860288	1743.01	VPC+	14.97	10.81	17:10:59	+71:52:17.01	59660.49421	1.847	4.266	3.306	3289	0.3200+/-0.0094	0.2998+/-0.0070	9.65	15,16,17,18,19,20,21,22,23,24,25,26,40,41,47,48,49	1	8	
232635922	1745.01	PC	14.52	11.52	18:44:33	+54:57:00.40	59653.47836	2.783	5.985	2.163	3755	0.4239+/-0.0126	0.4213+/-0.0099	3.35	14,15,16,18,19,22,25,26,40,41,48,49	357	15	
232650365	1746.01	VPC-	14.24	10.28	18:47:04	+54:54:37.34	58684.78135	1.21	2.525	1.377	3350	nan+/- nan	nan+/- nan	2.13	14,15,16,19,22,25,26,40,41	7	7	
232650365	1746.02	VPC-	14.24	10.28	18:47:04	+54:54:37.34	59660.64099	1.282	3.878	1.348	3350	nan+/- nan	nan+/- nan	1.78	14,15,16,19,22,25,26,40,41,49	89	7	
233602827	1749.01	VP	13.86	11.07	18:50:57	+64:25:09.12	59763.32306	1.391	4.489	2.077	3892	0.5614+/-0.0166	0.5599+/-0.0136	2.85	14,15,16,17,18,19,20,21,23,24,25,26,40,41,47,48,49,50,51,52	682	9	https://arxiv.org/pdf/2107.05430.pdf
233602827	1749.02	VP	13.86	11.07	18:50:57	+64:25:09.12	59647.5152	1.662	9.045	2.215	3892	0.5614+/-0.0166	0.5599+/-0.0136	2.52	14,15,16,17,18,19,20,21,23,24,25,26,40,41,47,48,49,50	14	11	https://arxiv.org/pdf/2107.05430.pdf
287139872	1752.01	VPC+	14.62	11.37	16:53:51	+60:42:32.69	59662.73117	1.097	0.935	2.305	3634	0.5278+/-0.0157	0.5293+/-0.0128	5.97	14,15,16,17,18,19,20,21,22,23,24,25,26,40,41,47,48,49	41	3	paper in prep by Morello
287139872	1752.02	PC	14.62	11.37	16:53:51	+60:42:32.69	58704.62898	1.984	32.716	2.217	3634	0.5278+/-0.0157	0.5294+/-0.0128	1.71	14,15,16,17,18,19,20,21,22,23,24,25,26,40,41	9	17	
332477926	1754.01	VPC+	13.26	10.48	17:42:23	+57:26:52.17	59662.80222	1.652	16.214	2.479	3931	0.5927+/-0.0176	0.5866+/-0.0145	2.43	14,15,16,17,18,19,20,21,23,24,25,26,40,41,47,48,49	273	16	
364074068	1756.01	VPC	13.88	10.81	20:25:19	+77:38:10.28	58764.85082	1.071	2.783	1.776	3776	0.5631+/-0.0166	0.5615+/-0.0135	2.56	17,18,19,24,40	9	7	
408636441	1759.01	P	11.93	8.77	21:47:25	+62:45:13.90	59838.74502	2.74	18.85	3.256	3717	0.6271+/-0.0186	0.6141+/-0.0151	3.57	16,17,24,56	15	28	https://arxiv.org/abs/2202.01259 https://arxiv.org/abs/2202.01240
441739871	1763.01	VPC+	15.63	11.39	17:18:15	+74:18:10.39	59657.04834	1.597	3.798	2.295	3328	0.4726+/-0.0140	0.4743+/-0.0112	3.99	14,15,16,17,18,19,20,21,22,23,24,25,26,41,47,48,49	20	5	
67646988	1779.01	KP	15.44	10.58	9:51:05	+35:58:09.47	59633.11987	113.513	1.882	10.842	3120	0.3064+/-0.0092	0.2838+/-0.0069	98.93	21,48	141186	675	https://arxiv.org/pdf/1808.03243.pdf
138819293	1796.01	KP	10.67	6.90	11:42:11	+26:42:23.66	59639.96333	6.976	2.644	3.812	3426	0.4259+/-0.0126	0.4235+/-0.0098	11.52	22,49	100	37	w.aanda.org/articles/aa/pdf/2007/35/aa77 + others
119584412	1801.01	VPC+	11.58	8.65	11:42:18	+23:01:36.68	59648.61974	1.347	10.644	1.973	3828	0.5464+/-0.0165	0.5466+/-0.0135	1.99	22,49	561	12	paper in prep by Mallorquin
138762614	1802.01	VPC	12.76	9.94	10:57:01	+24:52:56.73	58904.1545	1.974	16.796	2.507	3897	0.5817+/-0.0172	0.5774+/-0.0141	2.48	22	9	20	
166648874	1806.01	VPC	15.19	10.93	11:04:29	+30:27:31.50	58909.5468	6.077	15.145	3.41	3322	0.4010+/-0.0120	0.3953+/-0.0094	5.56	22	8	52	
166648874	1806.02	VPC	15.19	10.93	11:04:29	+30:27:31.50	58905.22825	5.114	8.196	2.766	3322	0.4010+/-0.0120	0.3952+/-0.0093	4.78	22,48	10	33	
390651552	1827.01	P	11.39	7.20	12:47:57	+09:45:05.03	59691.14934	1.685	1.467	1.324	3260	0.3317+/-0.0099	0.3137+/-0.0074	2.83	23,50	34	9	https://arxiv.org/pdf/2103.04950.pdf
198385543	1846.01	VPC+	13.97	10.38	17:11:49	+54:31:36.98	59601.33452	1.586	3.931	1.691	3485	0.4109+/-0.0121	0.4066+/-0.0094	2.6	17,20,23,24,25,26,40,47	358	10	paper in prep by Soubkiou (MuSCAT3)
359357695	1880.01	VPC	16.48	11.23	12:10:54	-75:07:55	59363.24703	11.021	1.726	8.438	2963	0.5554+/-0.0167	0.5545+/-0.0138	42.77	11,12,38,39	20	68	
348755728	1883.01	VPC+	15.79	11.87	8:56:21	-12:55:50	59256.84605	13.504	4.506	5.899	3415	0.4942+/-0.0150	0.4965+/-0.0122	18.23	8,35	12	67	
229586455	1887.01	VPC+	13.42	11.13	18:05:29	+75:08:42.81	59662.05882	1.478	2.2	2.798	4279	0.6806+/-0.0201	0.6543+/-0.0159	5.39	14,15,16,17,18,19,20,21,22,23,24,25,26,40,41,47,48,49	584	9	
172370679	1899.01	P	14.88	11.34	19:57:42	+40:08:35.75	59439.21525	41.568	29.09	12.183	3573	0.6177+/-0.0182	0.6068+/-0.0149	29.33	14,15,41,53	58	394	https://arxiv.org/pdf/2007.07098.pdf
166184426	1955.01	NPC	12.91	9.59	13:44:25	-40:20:12	58600.45092	2.718	16.336	2.238	3574	0.3105+/-0.0093	0.2887+/-0.0070	3.26	11	8	21	paper in prep by Timmermans
188589164	2013.01	P	12.68	8.69	15:58:19	+35:24:24.28	58956.39632	1.217	2.616	1.097	3360	0.3255+/-0.0097	0.3064+/-0.0074	1.38	24,25	12	7	https://arxiv.org/abs/2202.00970
368287008	2015.01	VPC+	16.11	11.12	15:28:32	+27:21:38.87	59712.92891	7.857	3.349	5.447	3069	0.3245+/-0.0097	0.3052+/-0.0073	24.19	24,51	2	42	
417931300	2068.01	VPC	13.01	9.87	12:25:06	+60:25:06.14	59623.46416	1.141	7.769	1.783	3710	0.5421+/-0.0162	0.5426+/-0.0132	1.87	14,15,21,22,41,48	383	9	
23814735	2075.01	VPC+	12.39	9.97	14:00:11	+38:42:20.78	59690.29232	1.142	4.798	2.313	4172	0.6491+/-0.0191	0.6309+/-0.0154	3.05	16,23,50	10	9	
224298134	2079.01	VPC	12.82	9.46	12:21:21	+57:45:08.88	59634.22067	0.597	1.492	1.212	3611	0.4805+/-0.0141	0.4826+/-0.0112	1.77	15,21,22,41,48	251	3	
224298134	2079.02	VPC	12.82	9.46	12:21:21	+57:45:08.88	59633.661	1.271	9.317	1.936	3611	0.4806+/-0.0141	0.4827+/-0.0112	2.19	15,21,22,41,48	377	9	

TIC ID	TOI	SG1 Disposition	Vmag	Jmag	RA_J2000 hh:mm:ss	DEC_J2000 dd:mm:ss	Epoch (BJD-2400000)	Depth (mmag)	P (days)	Rp (Re)	Teff (Mann relations, color)	Rstar (GAIA DR2, Mann relations)	Mstar (GAIA DR2, Mann relations)	Predicted K (m/s)	TESS Sectors	SNR TESS	SNR ExTrA	Articles
321669174	2081.01	VP	13.37	10.36	17:37:13	+53:01:32.53	59757.44461	1.343	10.505	1.838	3760	0.5161+/-0.0154	0.5181+/-0.0124	1.84	14,17,20,21,24,25,26, 40,41,47,50	14	11	https://arxiv.org/abs/2206.10643
441738827	2084.01	VPC+	15.12	11.96	17:17:01	+72:44:48.71	59652.83438	1.967	6.078	2.06	3680	0.4665+/-0.0139	0.4678+/-0.0111	2.87	15,16,18,19,20,21,22, 23,24,25,47,48,49	203	9	paper in prep by Barkaoui
356016119	2094.01	VPC+	14.41	10.80	16:56:34	+70:01:38.34	58691.32907	1.568	18.792	1.441	3491	0.3768+/-0.0113	0.3670+/-0.0088	1.26	14,15,16,17,19,20,21, 22,23,24,25,26,40	7	10	
235678745	2095.01	VPC?	13.19	9.80	19:02:32	+75:25:06.98	59752.69391	0.728	17.665	1.26	3588	0.4629+/-0.0136	0.4641+/-0.0108	0.88	14,15,16,17,18,19,20, 21,22,23,24,26,40,41, 47,48,49,50,51,52	382	6	paper in prep by Quintana paper in prep by Murgas (CARMENES)
235678745	2095.02	VPC?	13.19	9.80	19:02:32	+75:25:06.98	59718.49345	0.891	28.172	1.326	3588	0.4629+/-0.0136	0.4641+/-0.0108	0.82	14,15,16,17,18,19,20, 21,22,23,24,26,40,41, 47,48,49,50,51,52	341	9	paper in prep by Quintana paper in prep by Murgas (CARMENES)
142748283	2096.01	VPC	15.92	11.88	10:06:29	+74:49:39.12	59601.84617	3.632	3.119	1.602	3339	0.2474+/-0.0074	0.2165+/-0.0051	3.86	14,20,21,40,41,47	89	12	https://arxiv.org/abs/2303.08174
142748283	2096.02	VPC	15.92	11.88	10:06:29	+74:49:39.12	58687.53815	6.858	6.388	2.101	3339	0.2474+/-0.0074	0.2165+/-0.0051	4.83	14,20,21,40,41	12	28	https://arxiv.org/abs/2303.08174
389900760	2120.01	VPC+	15.65	11.10	1:34:01	+65:30:53.70	58795.82271	10.201	5.8	2.582	3231	0.2398+/-0.0073	0.2081+/-0.0052	7.24	18,24,25	12	48	Hori et al. in prep
336128819	2136.01	VP	14.32	10.18	18:44:42	+36:33:44.53	59394.59373	4.214	7.852	2.171	3304	0.3443+/-0.0104	0.3286+/-0.0080	3.63	26,40	15	29	https://arxiv.org/abs/2202.10182 https://arxiv.org/abs/2202.10024 https://arxiv.org/abs/2204.09063
44313455	2142.01	VPC+	13.28	9.61	17:48:11	+15:58:46.74	59014.83313	1.727	9.302	1.461	3454	0.3636+/-0.0109	0.3515+/-0.0084	1.67	26	7	14	
260298958	2205.01	VPC+	16.54	13.73	6:17:16	-56:30:36	59361.95575	45.931	0.889	14.253	3926	0.6506+/-0.0208	0.6321+/-0.0166	119.26	27,28,29,31,35,36,37, 38,39	54	74	
38680052	2208.01	VPC+	17.9	14.11	4:22:07	-61:22:07	59362.15356	118.808	0.674	12.472	3434	0.3222+/-0.0109	0.3024+/-0.0095	169.69	27,28,29,31,35,36,37, 38,39	53	139	paper in prep by Dransfield et al.
441420236	2221.01	P	8.81	5.44	20:45:10	-31:20:27	59041.28175	3.123	8.463	4.027	3593	0.6895+/-0.0204	0.6607+/-0.0161	6.33	27	13	32	/arxiv.org/ftp/arxiv/papers/2006/2006.132 https://arxiv.org/abs/2109.03924 https://arxiv.org/abs/2202.04308 https://arxiv.org/abs/2302.04922
198485881	2257.01	VP	15.21	11.47	12:58:58	+77:39:41.69	59606.20289	4.924	35.19	2.225	3435	0.3273+/-0.0097	0.3085+/-0.0072	2.4	14,20,21,26,40,41,47, 48	13	37	https://arxiv.org/abs/2111.01749#
8348911	2266.01	VPC+	16.54	11.84	16:21:07	+31:34:36.76	58957.92717	4.531	2.326	1.698	3123	0.2608+/-0.0079	0.2314+/-0.0057	4.5	24,25	6	16	paper in prep by Parviainen
459837008	2267.01	VPC-	15.56	10.35	4:20:13	+84:54:06.36	58816.15396	2.344	3.495	1.258	2996	nan+/- nan	nan+/- nan	2.51	19,20,25,26,40	9	12	paper in prep by Gunther
459837008	2267.03	VPC-	15.56	10.35	4:20:13	+84:54:06.36	58818.07497	1.812	2.289	1.024	2996	nan+/- nan	nan+/- nan	1.44	19,20,25,26,40	7	9	
441798995	2269.02	VPC+	13.48	10.77	17:36:35	+77:07:34.04	58684.77666	0.671	2.841	1.486	3970	0.5481+/-0.0162	0.5481+/-0.0132	1.91	14,15,16,17,18,19,20, 21,22,23,24,25,26,40, 41	11	5	
441798995	2269.03	CPC-	13.48	10.77	17:36:35	+77:07:34.04	58686.45244	0.978	10.403	1.651	3970	0.5481+/-0.0162	0.5481+/-0.0132	1.48	14,15,16,17,18,19,20, 21,22,23,24,25,26,40, 41	8	6	
289164482	2274.01	VPC-+	11.99	9.19	18:29:50	+40:32:27.72	59392.78584	1.08	2.68	2.525	3880	0.6311+/-0.0186	0.6172+/-0.0151	4.43	14,26,40	8	6	
289164482	2274.02	PC	11.99	9.19	18:29:50	+40:32:27.72	58684.28476	0.446	1.119	1.346	3880	0.6311+/-0.0186	0.6172+/-0.0151	2.03	14,26,40	6	2	
243313296	2278.01	VPC+	14.89	10.89	19:18:03	+56:14:09.78	59690.58368	0.999	1.466	1.887	3343	0.3221+/-0.0098	0.3024+/-0.0075	5.28	14,15,16,20,23,26,40, 41,49,50	1	4	
198211976	2283.01	CPC?	13.16	9.86	16:33:20	+63:31:26.49	58683.72445	0.121	0.402	0.553	3636	0.5194+/-0.0153	0.5214+/-0.0123	0.16	14,15,16,17,18,19,20, 21,22,23,24,25,26	5	1	
329148988	2285.01	VP	13.4	9.86	22:10:15	+58:42:22.26	58747.18318	1.842	27.27	1.904	3519	0.4606+/-0.0138	0.4617+/-0.0110	1.54	16,17,24	8	15	https://arxiv.org/abs/2110.10215
462615350	2288.01	VPC	14.06	11.52	16:44:29	+60:05:09.98	58740.4232	2.621	8.917	3.046	4094	0.5947+/-0.0177	0.5882+/-0.0145	3.98	16,24,25,40,41	11	17	
321688498	2290.01	CPC	12.63	9.90	21:26:24	+68:38:25.28	58764.98874	0.653	0.386	1.486	3938	0.5667+/-0.0170	0.5645+/-0.0139	3.64	17,18,24,25	10	3	https://arxiv.org/abs/2201.12661
236934937	2291.01	VPC	13.64	10.77	20:17:12	+65:52:15.60	59620.20422	1.315	9.406	3.754	3826	0.4760+/-0.0140	0.4779+/-0.0111	6.78	15,16,17,18,21,22,24, 25,41,48	1	8	
71347873	2293.01	VPC-	13.68	10.47	7:42:22	+70:24:16.55	59600.31453	1.619	6.068	2.033	3684	0.4987+/-0.0149	0.5010+/-0.0120	2.68	20,26,40,47	272	11	
362220495	2299.01	VPC?	9.62	7.59	19:04:53	+79:45:19.08	58798.44087	2.972	165.021	3.832	4477	nan+/- nan	nan+/- nan	2.04	14,17,18,20,21,24,25, 26,40,41	7	30	
100267480	2341.01	VPC	15.03	11.25	20:27:22	-53:13:14	58681.75145	13.163	0.877	8.552	3484	0.6173+/-0.0184	0.6065+/-0.0151	51.67	13	373	41	
201177276	2379.01	VPC+	15.55	12.39	23:52:22	-53:02:35	59062.46415	35.167	5.469	11.453	3742	0.6384+/-0.0191	0.6228+/-0.0155	45.28	28,29	42	129	
382602147	2384.01	VPC-+	15.1	12.00	2:24:37	-65:00:00	59062.34169	31.759	2.136	11.499	3772	0.6664+/-0.0203	0.6438+/-0.0162	61.02	28,29	92	142	
231297123	2405.01	VPC	13.87	11.33	3:00:35	-51:47:37	59117.31837	2.305	1.979	3.454	4069	0.6874+/-0.0204	0.6592+/-0.0161	8.27	30	9	12	
212957629	2406.01	VP	16.66	12.63	0:35:13	-3:22:14	59475.94605	20.824	3.077	2.779	3288	0.1969+/-0.0061	0.1637+/-0.0042	11.89	30,42,43	17	57	https://arxiv.org/abs/2107.14125 Hori et al. in prep
153078576	2407.01	VPC+?	14.68	11.13	3:18:59	-46:27:27	59116.62063	5.587	2.703	3.794	3497	0.5252+/-0.0157	0.5269+/-0.0128	9.81	3,4,30,31	26	35	https://arxiv.org/abs/2211.08490
10837041	2411.01	VP	11.27	9.33	1:23:42	-8:42:05	59116.01286	0.564	0.783	1.747	4727	0.6768+/-0.0202	0.6514+/-0.0160	3.46	30	10	3	https://arxiv.org/abs/2201.12661
161223358	2415.01	VPC	17	13.48	22:43:54	-53:25:42	59062.02582	44.374	0.515	12.429	3595	0.6181+/-0.0204	0.6069+/-0.0165	116.45	28	27	75	
142937186	2427.01	VP	10.29	7.89	3:29:10	-31:21:47	59169.61994	0.608	1.306	1.995	4203	0.6538+/-0.0195	0.6345+/-0.0156	3.66	31	24	3	https://arxiv.org/abs/2201.12661

TIC ID	TOI	SG1 Disposition	Vmag	Jmag	RA_J2000 hh:mm:ss	DEC_J2000 dd:mm:ss	Epoch (BJD-2400000)	Depth (mmag)	P (days)	Rp (Re)	Teff (Mann relations, color)	Rstar (GAIA DR2, Mann relations)	Mstar (GAIA DR2, Mann relations)	Predicted K (m/s)	TESS Sectors	SNR TESS	SNR ExTrA	Articles
258804746	2431.01	VPC	10.9	8.36	2:31:03	+08:22:55.18	59498.17216	0.586	0.224	5.566	4067	0.6556+/-0.0195	0.6358+/-0.0157	37.67	31,42,43	1	2	paper in prep by Malavolta
405763009	2433.01	STPC	14.54	10.43	19:57:45	+56:58:14.13	58746.35624	3.673	100	1.81	3299	0.3092+/-0.0093	0.2871+/-0.0069	0.27	14,15,16,41	8	33	
219175972	2441.01	VPC	15.26	11.33	6:05:39	-51:40:49	58335.50141	4.2	12.89	2.92	3390	0.4680+/-0.0141	0.4695+/-0.0113	4.03	1,5,7,11,28,31,32,33,34,38	16	27	
219175972	2441.02	VPC?	15.26	11.33	6:05:39	-51:40:49	58325.90859	1.393	5.551	2.032	3390	0.4680+/-0.0141	0.4695+/-0.0113	2.88	1,5,7,11,28,31,32,33,34	6	9	
29959760	2444.01	VPC+	15.38	12.30	2:49:03	-16:33:35	59145.04113	35.677	1.647	15.736	3689	0.5937+/-0.0183	0.5873+/-0.0150	245.56	31	16	116	
439867639	2445.01	VP	15.69	11.55	2:53:16	+00:03:08.78	58411.21733	2.525	0.371	1.406	3264	0.2721+/-0.0082	0.2441+/-0.0060	5.82	4,31	7	7	https://arxiv.org/abs/2201.13274 https://arxiv.org/abs/2201.12661
59128183	2453.01	VPC	14.41	11.04	4:59:21	+12:56:11.21	59516.81735	3.175	4.441	3.036	3613	0.5017+/-0.0148	0.5040+/-0.0118	5.85	5,32,43,44	274	17	
434260570	2455.01	VPC-+	15.14	11.51	4:16:59	+14:46:18.46	59474.58529	52.026	4.72	14.327	3525	nan+/- nan	nan+/- nan	194.66	5,32,43,44	57	286	
117799904	2457.01	VPC	12.15	9.74	4:40:40	-12:53:27	59175.25507	2.02	14.199	2.759	4158	0.6136+/-0.0182	0.6035+/-0.0149	2.9	32	9	17	
33091590	2495.01	VPC	14.73	10.66	6:59:18	-4:49:42	59208.3845	3.027	7.795	1.894	3312	0.3525+/-0.0107	0.3384+/-0.0084	2.83	33	7	21	
160328683	2496.01	VPC+	nan	12.50	6:04:47	-32:34:49	59175.52063	87.588	1.575	22.958		0.5805+/-0.0181	0.5764+/-0.0149	252.69	32,33	48	314	
134471108	2501.01	PC	12.94	10.53	7:12:16	-44:01:39	59203.65523	1.97	5.326	2.905	4164	0.6400+/-0.0191	0.6241+/-0.0154	4.34	6,7,8,33,34	11	16	
354518617	2540.01	VPC	9.91	7.15	5:30:14	-42:41:50	58480.9438	1.243	12.719	2.592	3951	0.6376+/-0.0189	0.6222+/-0.0153	2.7	6,33	13	12	
354518617	2540.02	FA?	9.91	7.15	5:30:14	-42:41:50	59223.1456	1.107	22.082	2.291	3951	0.6376+/-0.0189	0.6222+/-0.0153	1.82	6,33	825	10	
31515092	2552.01	PC	14.47	10.66	7:43:41	-10:15:26	59230.69684	2.118	2.369	3.009	3461	0.6525+/-0.0195	0.6335+/-0.0156	6.12	34	9	16	
176772671	2603.01	VPC+	15.53	12.70	9:30:16	-18:50:35	59255.82309	42.81	1.333	11.728	3879	nan+/- nan	nan+/- nan	78.49	35	37	127	
146776480	2605.01	VPC	12.16	9.26	8:17:25	-34:27:53	58536.5519	13.225	20.601	8.178	3804	0.4939+/-0.0147	0.4962+/-0.0119	19.11	8,34,35	40	86	
268914377	2610.01	NPC	nan	14.03	7:52:12	-48:29:55	59229.716	110.015	2.154	16.017		0.4832+/-0.0206	0.4851+/-0.0190	255.02	34,35	17	208	
135036669	2640.01	PC	nan	13.77	10:01:06	-52:26:09	59307.40102	80.016	0.911	7.393		0.2754+/-0.0090	0.2479+/-0.0072	71.88	36,37	16	164	
443556801	2768.01	VPC?	12.66	10.19	6:37:27	-15:28:54	59225.64663	1.945	1.508	3.001	4159	0.6306+/-0.0187	0.6169+/-0.0152	7.05	6,33	385	11	
317417916	2781.01	VPC-+	14.53	11.69	5:51:17	-13:22:51	59226.42805	6.938	2.764	5.926	3876	nan+/- nan	nan+/- nan	17.73	6,33	461	29	
141141249	2911.01	VPC-	16.54	12.31	8:36:19	-46:21:57	59301.84746	18.616	1.77	8.341	3366	nan+/- nan	nan+/- nan	45.57	8,9,35,36	1302	60	
302527524	2952.01	VPC	14.75	11.20	8:56:46	-68:30:38	59351.6677	15.032	10.784	6.253	3527	0.5087+/-0.0152	0.5109+/-0.0123	14.74	9,10,11,36,37,38	1820	100	
243641947	3235.01	VPC+	15.16	11.71	13:49:54	-46:03:58	59355.55402	88.42	2.593	11.08	3562	0.3721+/-0.0113	0.3615+/-0.0090	78.78	11,38	4575	370	https://arxiv.org/abs/2302.10008 https://arxiv.org/abs/2303.00659
79920467	3288.01	VPC+	14.98	12.04	19:48:26	-43:01:04	59057.73076	34.594	1.434	12.383	3802	0.6703+/-0.0203	0.6466+/-0.0161	78.83	13,27	3907	140	
154616309	3397.01	VPC	15.02	12.07	8:08:52	-28:56:16	59248.5087	12.427	3.625	6.79	3838	0.6275+/-0.0187	0.6144+/-0.0152	21.55	7,8,34	635	58	
165827520	3494.01	VPC+	15.04	10.55	13:37:34	-37:11:00	59310.02063	5.579	7.749	2.217	3182	0.3083+/-0.0092	0.2861+/-0.0069	4.14	11,37	11	35	paper in prep by Almenara
455784423	3629.01	VPC+	14.64	11.42	23:59:10	+39:18:51.30	58784.25613	18.152	3.938	8.184	3712	0.6154+/-0.0183	0.6050+/-0.0149	29.12	17	1628	113	https://arxiv.org/abs/2201.09963
155867025	3714.01	VPC+	15.7	11.74	4:38:13	+39:27:29.91	58840.51086	50.993	2.155	11.144	3436	0.5087+/-0.0151	0.5110+/-0.0122	67.39	19	3263	232	https://arxiv.org/abs/2201.09963
468777766	3750.01	PC	14.76	11.74	5:05:42	+67:49:13.46	58826.42586	18.76	12.484	8.49	3818	0.6287+/-0.0187	0.6154+/-0.0152	20.84	19	810	115	
445751830	3757.01	P	14.81	12.00	6:04:01	+55:01:12.59	58838.77232	35.435	3.439	11.919	3926	0.6376+/-0.0191	0.6222+/-0.0154	56.64	19	466	149	https://arxiv.org/abs/2203.07178
458419328	3785.01	PC	14.6	11.05	8:43:36	+63:04:41.34	59604.77275	8.94	4.675	4.714	3561	0.4988+/-0.0149	0.5012+/-0.0121	12.22	20,47	1094	57	
86263325	3884.01	VPC+?	15.74	11.13	12:06:17	+12:30:24.89	59656.49982	33.899	4.545	5.778	3164	0.3031+/-0.0091	0.2800+/-0.0067	25.52	22,46,49	2965	198	https://arxiv.org/abs/2210.10909 https://arxiv.org/abs/2302.04757
20182780	3984.01	VPC+?	15.69	11.93	15:05:21	+36:47:12.45	59715.02249	23.864	4.353	7.244	3450	0.4649+/-0.0139	0.4662+/-0.0111	27.25	23,24,50,51	2099	110	https://arxiv.org/abs/2302.07714
232632239	4107.01	VPC	14.22	11.63	17:56:58	+58:52:57.35	59660.46146	2.663	3.532	3.423	4042	0.6331+/-0.0189	0.6188+/-0.0153	6.68	14,15,16,17,18,19,20,21,22,23,24,25,26,40,41,47,48,49	730	14	
230084146	4109.01	PC	13.92	11.58	16:25:28	+66:21:04.81	59746.88065	6.305	12.32	5.128	4245	0.6375+/-0.0188	0.6221+/-0.0152	8.6	15,16,17,18,20,21,22,23,24,25,26,40,41,47,48,50,51,52	1577	38	
229408913	4114.01	VPC	13.54	11.14	19:31:52	+61:52:55.71	59657.5357	2.239	4.804	3.213	4174	0.6642+/-0.0196	0.6422+/-0.0156	5.34	14,15,16,17,18,19,20,21,23,24,25,26,40,41,47,48,49	358	16	
394357918	4184.01	VPC+?	17.12	12.62	2:55:18	-79:24:55	58326.78969	11.762	4.902	2.555	3150	0.2405+/-0.0074	0.2090+/-0.0054	7.51	1,28,39	11	33	paper in prep by Barkaoui
95057860	4201.01	VPC+	15.16	12.26	6:01:54	-13:27:41	58485.28631	40.765	3.581	12.125	3879	0.6138+/-0.0185	0.6037+/-0.0151	58.68	6	1923	173	
44898913	4306.01	VPC+	18	12.26	4:16:31	-28:18:53	58413.19188	8.095	2.73	1.351	2852	0.1557+/-0.0047	0.1252+/-0.0031	4.33	4,5,31,32	7	21	https://arxiv.org/abs/2209.02831
251086776	4312.01	PC	12.17	9.27	2:30:11	-3:24:18	58434.86494	1.856	726.118	2.439	3834	0.5509+/-0.0174	0.5505+/-0.0144	0.7	4,31	10	15	
408416746	4324.01	VPC?	11.97	8.30	9:42:36	-19:14:05	58518.99542	0.869	6.251	1.312	3457	0.3947+/-0.0119	0.3880+/-0.0095	1.49	8,35	8	5	
202185707	4325.01	VPC	13.12	10.34	6:47:24	+06:07:45.84	58469.36888	2.946	1.65	2.399	3900	0.4548+/-0.0139	0.4554+/-0.0113	5.85	6,33	8	15	
140687214	4327.01	VPC	14.04	10.81	4:52:50	-76:20:24	59387.01775	0.739	0.83	3.422	3713	0.5651+/-0.0168	0.5632+/-0.0138	11.66	1,2,3,4,5,6,7,8,9,10,11,12,13,27,28,29,30,31,32,33,34,35,36,37,38,39	1	3	
166184428	4336.01	VPC+	13.6	9.45	13:44:25	-40:20:16	59335.5726	4.493	16.336	2.111	3305	0.3268+/-0.0099	0.3079+/-0.0077	2.83	38	13	34	paper in prep by Timmermans
399642071	4337.01	PC	12.67	9.05	10:57:10	-69:58:46	59335.38779	2.273	2.286	2.817	3398	0.7237+/-0.0255	0.6853+/-0.0199	5.58	37,38	13	27	

TIC ID	TOI	SG1 Disposition	Vmag	Jmag	RA_J2000 hh:mm:ss	DEC_J2000 dd:mm:ss	Epoch (BJD-2400000)	Depth (mmag)	P (days)	Rp (Re)	Teff (Mann relations, color)	Rstar (GAIA DR2, Mann relations)	Mstar (GAIA DR2, Mann relations)	Predicted K (m/s)	TESS Sectors	SNR TESS	SNR ExTrA	Articles
7439481	4339.01	NPC	15.54	12.55	14:11:43	-29:58:27	59333.969	74.162	1.254	10.349	3756	0.3993+/-0.0125	0.3932+/-0.0104	84.54	38	49	217	
354944123	4342.01	VPC	12.67	9.83	21:37:33	-77:58:44	58654.53243	1.529	5.538	2.272	3881	0.5978+/-0.0178	0.5908+/-0.0146	2.99	13,27	11	12	https://arxiv.org/abs/2301.01370
354944123	4342.02	VPC	12.67	9.83	21:37:33	-77:58:44	58659.34802	1.631	10.689	2.464	3881	0.5978+/-0.0178	0.5908+/-0.0145	2.76	13,27	9	14	https://arxiv.org/abs/2301.01370
313889049	4349.01	PC	13.39	10.40	0:00:31	-26:13:54	58355.68965	1.903	749.161	2.344	3795	0.5719+/-0.0172	0.5691+/-0.0141	0.61	2,29	9	23	
176797879	4353.01	PC	12.31	8.98	3:14:20	-34:02:03	58427.01974	1.058	718.181	1.365	3607	0.4253+/-0.0127	0.4229+/-0.0101	0.31	4,31	8	10	
52307802	4360.01	PC	15.67	11.04	1:26:53	-68:38:03	58328.29436	1.8	3.075	1.295	3131	0.3082+/-0.0092	0.2860+/-0.0069	2.26	1,2,27,28,29	8	10	
325682877	4363.01	VPC?	12.68	10.06	2:28:27	-12:32:56	58412.27724	0.722	2.119	1.833	4049	0.6536+/-0.0194	0.6343+/-0.0156	2.75	4,31	7	5	
4070275	4364.01	VPC	13.56	9.95	5:20:16	-4:14:22	58439.34024	1.92	5.424	2.094	3525	0.4666+/-0.0141	0.4679+/-0.0113	3.07	5,32	10	13	
22233480	4438.01	VPC	13.69	9.70	18:01:16	+35:35:50.49	59396.41313	4.11	7.445	2.335	3348	0.3757+/-0.0112	0.3658+/-0.0086	3.9	40	20	31	
137899948	4446.01	KP	16.74	13.75	19:31:29	+41:03:51.36	59420.80367	50.927	2.455	13.647	3813	0.6152+/-0.0198	0.6047+/-0.0161	81.31	40,41	21	100	
230129753	4459.01	PC	16.15	13.09	16:47:19	+67:17:52.46	59581.82224	10.586	5.749	5.718	3757	0.5775+/-0.0175	0.5738+/-0.0144	14.46	40,41,47,48,49	15	29	
75262942	4469.01	KP	15.56	12.97	19:56:12	+17:34:11.89	59421.46179	40.134	2.664	13.253	4036	0.6535+/-0.0198	0.6342+/-0.0158	72.57	41	23	111	
126606859	4479.01	VP	15.18	11.44	21:04:23	+24:39:15.10	59797.40634	4.084	1.159	2.649	3445	0.4269+/-0.0127	0.4247+/-0.0101	8.14	15,41,55	11	18	https://arxiv.org/abs/2206.10643
239332587	4481.01	VPC+	10.79	7.33	20:45:04	+44:29:56.64	59823.51516	1.054	0.926	1.678	3524	0.4256+/-0.0126	0.4232+/-0.0098	4.05	15,41,55	4	5	https://arxiv.org/abs/2301.06873
193336820	4491.01	PC	11.52	9.24	20:22:45	+47:18:27.86	59829.76204	1.249	5.007	2.12	4283	0.5960+/-0.0175	0.5893+/-0.0144	2.62	14,15,41,56	482	8	
434105094	4506.01	VPC	17.02	11.46	23:37:38	-12:50:28	58357.51752	25.89	5.411	2.89	2936	nan+/- nan	nan+/- nan	11.04	2,29,42	9	86	
170789802	4508.01	VPC+	14.23	10.31	4:38:27	-31:11:22	58438.0121	3.978	3.467	2.114	3389	0.3324+/-0.0100	0.3146+/-0.0076	4.69	5,32	9	14	
39926974	4526.01	KP	16.53	11.70	22:22:30	-7:57:20	59448.65423	6.676	2.26	2.726	3166	0.3405+/-0.0104	0.3242+/-0.0081	8.16	42	7	25	https://arxiv.org/abs/1801.10177
380887434	4527.01	PC	10.92	7.84	1:17:53	+05:28:26.15	59474.20024	0.359	0.399	0.909	3716	0.4859+/-0.0144	0.4881+/-0.0115	0.97	42,43	13	2	
384888319	4529.01	PC	12.21	8.79	1:07:52	+12:52:51.79	59495.54356	1.391	5.879	1.815	3577	0.4934+/-0.0148	0.4957+/-0.0120	2.25	42,43	744	11	
248250955	4552.01	VPC	14.44	10.26	17:38:52	-47:38:06	59361.88234	1.584	0.301	1.28	3309	0.2856+/-0.0086	0.2596+/-0.0063	5.1	39	8	7	
107018378	4556.01	VPC	18.26	11.51	12:11:42	-32:31:53	58570.93493	4.029	3.792	1.56	2757	0.2185+/-0.0066	0.1855+/-0.0045	3.83	10,37	6	18	
381897917	4565.01	VPC	12.32	8.93	18:00:26	-48:28:23	58676.61007	1.967	692.515	2.278	3629	0.5318+/-0.0158	0.5330+/-0.0129	0.64	13,39	12	17	
307849973	4567.01	PC	13.6	10.67	8:34:01	-66:46:06	58543.8625	0.572	0.841	1.413	3830	0.6083+/-0.0181	0.5993+/-0.0148	2.48	9,11,35,36,37,38	7	3	
307849973	4567.02	PC	13.6	10.67	8:34:01	-66:46:06	58548.58541	1.411	23.542	2.562	3830	0.6083+/-0.0181	0.5993+/-0.0148	2.24	9,11,35,36,37,38	7	14	
154940895	4572.01	PC	13.74	10.59	14:00:07	+88:36:42.15	58836.17783	1.182	26.951	1.805	3663	0.4692+/-0.0140	0.4708+/-0.0112	1.39	19,20,25,26,40	7	10	
298428237	4574.01	VPC	13.56	10.46	20:48:16	+24:29:04.31	59823.5267	0.945	0.769	2.025	3766	0.5422+/-0.0161	0.5427+/-0.0131	5.02	14,15,41,55	2	4	
137683938	4587.01	KP	16.6	13.14	19:30:19	+37:22:35.01	59393.6605	16.63	3.29	7.067	3576	0.5676+/-0.0176	0.5653+/-0.0145	25.22	40,41	7	39	
307809773	4599.01	P	9.63	6.67	6:37:11	+17:33:53.33	59547.76105	0.706	2.77	1.459	3805	0.4659+/-0.0140	0.4672+/-0.0113	2.08	43,44,45	169	4	https://arxiv.org/abs/2204.10261
307809773	4599.02	P	9.63	6.67	6:37:11	+17:33:53.33	59547.42294	0.902	5.706	3.546	3805	0.4659+/-0.0140	0.4672+/-0.0113	7.38	43,44,45	2	5	https://arxiv.org/abs/2204.10261
1950736	4610.01	PC	11.26	8.96	5:16:11	+30:35:07.37	59548.16751	0.543	3.113	1.545	4262	0.6590+/-0.0194	0.6383+/-0.0155	1.77	19,43,44,45	443	4	
258796169	4616.01	VPC+	14.75	11.32	0:59:16	+13:51:36.09	59448.70699	3.622	1.554	1.222	3567	0.1927+/-0.0058	0.1596+/-0.0039	3.71	17,42,43	7	16	paper in prep by Wells et al.
284326455	4618.01	KP	13.4	11.14	6:39:36	+25:28:57.16	59544.3795	30.332	3.8	13.264	4320	0.6990+/-0.0207	0.6676+/-0.0163	63.69	43,44,45	7445	174	
94727308	4622.01	FA?	nan	14.21	4:00:54	+31:41:27.94	59474.77337	58.205	1.297	11.286		0.4640+/-0.0213	0.4649+/-0.0204	86.87	43,44	11	127	
336961891	4642.01	VPC	14.75	10.34	2:03:32	+06:48:59.02	59449.12955	2.424	3.602	1.167	3196	0.2418+/-0.0074	0.2104+/-0.0053	1.98	42,43	7	13	
270355392	4643.01	PC	12.32	9.40	2:08:52	+04:18:23.09	59451.70042	0.712	5.026	1.367	3833	0.5180+/-0.0154	0.5199+/-0.0125	1.42	4,31,42,43	10	5	
270355392	4643.02	PC	12.32	9.40	2:08:52	+04:18:23.09	58415.85615	0.839	10.739	1.446	3833	0.5180+/-0.0154	0.5200+/-0.0125	1.21	4,31,42,43	5	5	
165202476	4666.01	VPC+	15.33	11.98	3:45:10	-39:03:47	59168.47637	50.173	2.909	12.795	3659	0.5857+/-0.0176	0.5808+/-0.0145	70.68	31	2858	237	
142938659	4668.01	PC	nan	12.10	3:30:35	-35:12:13	59169.29941	9.378	1.005	5.225		0.4222+/-0.0127	0.4194+/-0.0102	27.3	31	7	28	
404506270	4670.01	PC	17.37	13.37	4:06:40	-39:26:40	59150.61756	102.48	15.501	10.71	3363	nan+/- nan	nan+/- nan	42.45	31	611	229	
279095914	4675.01	PC	12.41	9.86	3:22:10	-4:06:42	59165.52615	0.902	3.578	2.136	4086	0.5949+/-0.0177	0.5884+/-0.0145	3	4,31	197	6	
186470968	4832.01	PC	15.16	12.54	8:50:44	-34:46:58	59275.70288	17.292	2.781	8.787	4055	0.6777+/-0.0204	0.6521+/-0.0161	35.06	35	248	54	
428685938	4856.01	PC	18.84	12.83	12:00:56	-23:38:05	59283.35875	44.401	14.49	7.649	2805	0.3545+/-0.0111	0.3407+/-0.0090	24.6	36	431	135	
262499797	4858.01	VPC	17.36	13.19	7:19:31	-55:43:41	59303.19612	68.186	1.751	12.323	3227	0.4441+/-0.0138	0.4437+/-0.0113	94.09	35,36	236	136	
335590096	4860.01	VPC	16.47	12.06	12:14:16	-13:10:29	59304.24561	64.942	1.523	9.07	3259	0.3522+/-0.0110	0.3381+/-0.0089	69.85	36	573	225	https://arxiv.org/abs/2303.00659
143032776	4863.01	VPC	16.88	13.15	11:09:01	-10:11:18	59289.28185	75.61	12.486	12.163	3434	0.4462+/-0.0144	0.4460+/-0.0121	47.59	36	297	231	
124235800	4898.01	PC	13.62	10.68	13:09:22	-32:49:45	59330.01077	2.598	2.765	3.482	3840	0.6393+/-0.0190	0.6236+/-0.0153	7.51	10,37	394	16	https://arxiv.org/abs/2211.08490
445392860	4988.01	VPC	16.06	13.60	7:29:50	-51:59:27	59277.22097	51.323	2.37	23.851	4163	0.6976+/-0.0224	0.6665+/-0.0174	200.02	35	33047	82	
247180220	4991.01	VPC	16.62	13.17	16:54:48	-45:22:03	59385.80449	32.097	0.77	13.623	3620	0.6841+/-0.0229	0.6567+/-0.0178	112.88	39	57	56	
424196109	5007.01	VPC	15.33	12.23	15:44:15	-61:02:28	59384.64412	23.376	2.543	10.55	3785	0.6549+/-0.0195	0.6353+/-0.0156	50.16	39	137	72	
276735500	5010.01	VPC	16.3	13.48	18:01:22	-79:21:11	59376.39698	32.366	6.711	12.913	3944	0.7032+/-0.0220	0.6705+/-0.0172	49.37	39	138	62	
213111428	5023.01	PC	nan	13.22	17:08:30	-51:31:53	59386.47128	77.393	2.275	17.111		0.3214+/-0.0100	0.3015+/-0.0080	342.46	39	53596	114	
318180448	5033.01	PC	13.93	10.28	20:37:35	-83:05:32	59389.28989	1.739	5.47	1.398	3482	0.3613+/-0.0109	0.3488+/-0.0085	1.86	13,27,39	203	10	
324609476	5041.01	VPC	17.27	13.37	20:50:24	-81:26:35	59388.71896	47.255	0.734	12.084	3411	0.4382+/-0.0140	0.4372+/-0.0118	122.65	39	50	57	
5882269	5083.01	KP	13.27	10.87	5:16:34	+20:15:18.36	59542.11431	2.478	4.795	3.082	4202	0.6286+/-0.0186	0.6153+/-0.0151	4.98	43,44,45	1602	19	https://arxiv.org/abs/1801.07320
184892124	5090.01	KP	nan	14.35	8:42:39	+19:24:51.90	59552.22239	160.108	1.983	11.295		0.2929+/-0.0116	0.2680+/-0.0110	108.12	44,45,46	26	195	https://arxiv.org/abs/1706.03084
19028197	5094.01	KP	12.33	8.79	7:59:06	+15:23:29.24	59577.27877	7.113	3.337	4.361	3509	0.4995+/-0.0150	0.5018+/-0.0121	11.96	44,45,46	43639	51	https://arxiv.org/abs/1812.08241

TIC ID	TOI	SG1 Disposition	Vmag	Jmag	RA_J2000 hh:mm:ss	DEC_J2000 dd:mm:ss	Epoch (BJD-2400000)	Depth (mmag)	P (days)	Rp (Re)	Teff (Mann relations, color)	Rstar (GAIA DR2, Mann relations)	Mstar (GAIA DR2, Mann relations)	Predicted K (m/s)	TESS Sectors	SNR TESS	SNR ExTrA	Articles
434226736	5095.01	KP	16.21	11.30	4:13:06	+15:14:52.01	59501.77407	12.385	3.485	3.114	3070	0.2907+/-0.0087	0.2654+/-0.0064	10.11	44	11	47	https://arxiv.org/abs/2007.12766
203214081	5097.01	KP	13.82	10.06	8:58:52	+21:04:34.20	59572.27802	3.97	5.746	2.031	3461	0.3154+/-0.0094	0.2945+/-0.0070	3.86	44,45,46	55918	23	https://arxiv.org/abs/1912.00291 https://arxiv.org/abs/2208.07287
203289099	5111.01	KP	13.42	10.50	9:05:27	+21:40:07.32	59548.77567	1.151	3.356	1.929	3829	0.5613+/-0.0169	0.5598+/-0.0139	2.77	44,45	9362	8	https://arxiv.org/abs/2108.05621
337385330	5112.01	PC	11.49	9.03	7:21:13	+17:35:19.72	59577.84725	1.173	15.532	2.015	4112	0.6059+/-0.0181	0.5973+/-0.0148	1.72	44,45,46	580	12	
95337971	5139.01	PC	14.39	11.50	10:13:32	+19:56:54.62	59626.88302	3.85	5.947	7.107	3848	0.5969+/-0.0180	0.5901+/-0.0148	20.3	45,46,48	2	20	
173103335	5146.01	KP	12.17	9.42	11:29:20	-1:27:17	59528.16829	1.823	10.054	2.259	3911	0.5510+/-0.0165	0.5507+/-0.0135	2.54	45,46	11	14	https://arxiv.org/abs/1812.08241
388811663	5155.01	KP	12.98	10.63	1:13:42	+03:05:48.97	59495.56445	1.945	9.794	3.049	4210	0.6743+/-0.0204	0.6496+/-0.0162	3.81	42,43	1684	17	https://arxiv.org/abs/2108.08889
437054764	5176.01	VPC?	16.52	13.36	9:00:05	+13:16:25.76	59553.71434	41.498	20.355	10.508	3689	0.5399+/-0.0170	0.5405+/-0.0140	27.8	44,45,46	18	135	
419411415	5205.01	P	15.9	11.93	20:55:05	+24:21:38.71	59443.47067	76.518	1.631	11.045	3437	0.3970+/-0.0120	0.3906+/-0.0096	86.87	41	1901	282	https://arxiv.org/abs/2209.11160
147892178	5207.01	PC	14.87	12.05	9:30:55	+71:44:25.35	59585.83898	14.526	24.695	6.463	3893	0.5643+/-0.0167	0.5624+/-0.0136	11.1	14,20,40,41,47	964	89	
259172249	5218.01	PC	16.04	13.34	19:30:39	+71:45:46.39	59662.32268	20.872	4.291	9.242	3974	0.6749+/-0.0206	0.6500+/-0.0163	33.13	41,47,48,49	861	54	
202468443	5268.01	VPC	nan	12.82	15:16:02	+62:43:06.05	59690.59682	42.13	2.069	12.408		0.3079+/-0.0094	0.2856+/-0.0072	120.26	41,48,49,50	32991	73	https://arxiv.org/abs/2303.00659
264301607	5278.01	VPC+	17.46	13.31	19:43:14	+66:34:17.50	59768.53606	115.709	0.435	21.276	3317	0.3835+/-0.0118	0.3749+/-0.0096	515.61	41,47,48,49,50,51,52	127293	144	
250330564	5285.01	VPC?	13.13	11.71	22:43:53	-1:50:17	59469.31445	19.81	4.385	10.204	5446	0.6987+/-0.0242	0.6673+/-0.0187	39.25	42	729	109	
33397739	5292.01	PC	16.42	13.63	22:56:53	-8:07:11	59469.42431	48.889	2.023	13.355	3928	0.5858+/-0.0199	0.5807+/-0.0164	85.82	42	49	80	
250111245	5293.01	VPC+	16.19	12.46	23:43:19	-2:02:42	59466.49666	56.64	2.93	11.951	3453	0.5089+/-0.0161	0.5111+/-0.0133	65.22	42	1550	195	https://arxiv.org/abs/2302.07714
4619242	5295.01	VPC	15.2	11.53	23:17:09	-9:26:06	59467.50731	33.16	4.302	10.332	3467	nan+/- nan	nan+/- nan	43.28	42	1232	168	
369477998	5307.01	VPC	13.41	10.90	1:03:33	+09:54:50.39	59490.96374	4.264	5.298	4.026	4096	0.6139+/-0.0185	0.6037+/-0.0151	7.65	42,43	590	30	
306401382	5311.01	VPC	15.19	12.37	2:09:20	+21:27:07.22	59453.71507	36.4	39.054	13.481	3923	0.6979+/-0.0210	0.6667+/-0.0165	29.66	42,43	384	149	
126982221	5315.01	VPC	16.89	12.97	1:37:12	+16:01:08.67	59493.47004	45.963	2.47	17.062	3344	nan+/- nan	nan+/- nan	266.08	42,43	37308	93	
246965431	5319.01	VPC-	13.95	10.35	2:20:51	+23:31:14.93	59496.58733	4.93	4.079	3.782	3533	0.5043+/-0.0154	0.5066+/-0.0126	8.75	18,42,43	113	33	
16005254	5344.01	VPC	15.4	11.80	4:13:04	+20:54:54.91	59522.82521	26.865	3.793	9.72	3579	0.5834+/-0.0176	0.5788+/-0.0145	40.68	43,44	1503	116	
26054627	5349.01	VPC	15.69	12.43	3:30:51	+20:52:46.96	59521.81383	27.5	3.318	9.366	3704	0.5869+/-0.0178	0.5817+/-0.0146	39.83	42,43,44	1218	98	
90767677	5359.01	VPC	nan	13.04	3:36:16	+30:12:21.73	59522.00405	17.369	1.682	9.278		0.4691+/-0.0158	0.4706+/-0.0136	56.58	42,43,44	5	24	
71268730	5375.01	VPC+	14.06	11.17	7:35:08	+71:24:02.13	59580.73615	36.884	1.722	11.705	3880	0.6338+/-0.0188	0.6193+/-0.0152	69.39	47	64	231	https://arxiv.org/abs/2303.16193
407591297	5388.01	VPC	12.73	9.17	10:08:42	+35:32:49.14	59630.89575	1.162	2.595	1.912	3480	0.3129+/-0.0094	0.2915+/-0.0071	4.58	21,48	4	3	
39143128	5389.01	VPC	17.09	13.40	11:15:12	+39:21:32.84	59609.44541	47.881	10.401	8.811	3459	0.4222+/-0.0142	0.4192+/-0.0124	30.52	48	15	127	
56798909	5404.01	PC	14.57	11.98	6:45:27	+22:17:26.35	59546.13094	4.842	2.177	4.081	4024	0.5745+/-0.0172	0.5713+/-0.0141	11.3	44,45	159	25	
371164829	5414.01	VPC	15.78	13.14	7:17:28	+31:28:54.99	59529.14955	29.227	10.783	15.503	4011	0.7026+/-0.0223	0.6701+/-0.0174	120.2	44,45	10	112	
87405719	5416.01	PC	14.56	11.66	6:52:02	+25:12:07.32	59537.05296	20.496	13.015	7.37	3823	0.5196+/-0.0156	0.5215+/-0.0127	18.06	45	292	140	
75697959	5433.01	VPC	16.43	13.68	5:42:30	+28:32:59.47	59544.29374	28.814	4.146	12.112	3929	0.7056+/-0.0240	0.6721+/-0.0186	51.89	43,44,45	467	70	
171646471	5464.01	VPC	17.24	13.57	10:35:06	+19:07:05.82	59635.5598	35.816	1.161	9.876	3477	0.5283+/-0.0176	0.5296+/-0.0148	65.88	45,48	542	63	
291109653	5486.01	PC	14.3	10.98	12:42:12	+03:47:20.47	59691.06297	4.777	2.025	3.818	3634	0.5532+/-0.0165	0.5527+/-0.0135	10.57	23,46,50	857	29	paper in prep by Esparza-Borges
468983280	5489.01	VPC?	13.82	10.28	8:34:46	+11:29:22.20	59578.0699	1.141	3.152	1.439	3517	0.4164+/-0.0125	0.4128+/-0.0099	2.11	7,34,44,45,46	279	7	
377097547	5507.01	VPC	12.98	9.39	9:54:25	+06:38:45.53	59577.45512	0.825	1.507	1.07	3505	0.3565+/-0.0106	0.3431+/-0.0082	1.41	45,46	62	4	
389040826	5511.01	VPC	14.83	11.50	9:27:59	+04:12:48.13	59575.04248	12.58	4.717	5.823	3635	0.5143+/-0.0153	0.5164+/-0.0124	17.09	8,35,45,46	1364	56	
443582629	5519.01	CPC	14.27	10.21	11:10:55	-3:14:33	59576.96322	1.195	5.851	1.292	3317	0.3652+/-0.0112	0.3534+/-0.0089	1.58	9,36,45,46	134	9	
443616612	5523.01	STPC	15.75	12.42	11:16:28	-3:58:32	59533.35413	31.038	100	9.504	3680	0.5625+/-0.0173	0.5608+/-0.0142	2.89	36,45,46	20	306	
443616612	5523.02	KP	15.75	12.42	11:16:28	-3:58:32	59281.4095	6.682	3.471	4.835	3680	0.5625+/-0.0173	0.5608+/-0.0142	13.05	36,45,46	9	28	
277833995	5524.01	KP	13.68	10.46	10:25:37	+02:30:51.67	58518.11936	1.125	2.298	2.033	3695	0.5900+/-0.0176	0.5843+/-0.0144	3.34	8,45,46	6	6	https://arxiv.org/abs/2007.12744
345450130	5525.01	CPC	14.47	10.17	3:51:30	+09:43:44.15	58440.19991	1.114	2.752	1.382	3239	0.4185+/-0.0125	0.4152+/-0.0098	2.05	5,42,43,44	5	6	
458686847	5528.01	KP	14.64	11.45	8:55:25	+10:28:08.90	59230.01404	1.593	1.292	2.101	3698	0.5146+/-0.0155	0.5166+/-0.0127	4.65	34,44,45,46	8	7	https://arxiv.org/abs/1703.07416
244170332	5530.01	PC	13.01	10.19	0:25:57	-5:41:49	58382.17093	0.46	0.477	1.118	3847	0.5254+/-0.0159	0.5270+/-0.0130	1.83	3,30,42	5	2	
318836983	5532.01	PC	13.07	10.36	2:45:31	+05:09:03.83	58412.25985	1.12	5.654	2.155	3966	0.6615+/-0.0196	0.6402+/-0.0157	2.57	4,42,43	9	10	
387974148	5551.01	VPC?	14.09	11.16	5:48:30	+18:10:46.29	59474.72141	1.39	2.405	2.005	3802	0.5536+/-0.0164	0.5530+/-0.0134	3.34	43,44,45	7	8	
91287873	5554.01	PC	11.09	8.66	6:58:59	+28:42:58.56	59515.17161	2.015	26.694	2.685	4155	0.6263+/-0.0187	0.6135+/-0.0152	2.29	44,45	15	21	
388804061	5555.01	KP	13.48	9.76	11:30:15	+07:35:18.26	59537.24962	3.499	32.938	2.532	3473	0.4444+/-0.0132	0.4441+/-0.0104	2.4	45,46	13	28	
323687123	5557.01	PC	15.33	10.74	9:08:49	+11:51:41.12	59502.34327	3.082	4.018	1.042	3165	0.1943+/-0.0059	0.1611+/-0.0040	1.52	44,45,46	9	16	https://arxiv.org/abs/2302.00699
330637910	5561.01	VPC	17.53	13.74	9:04:48	+13:47:44.64	59502.14819	22.682	2.007	7.164	3437	0.4906+/-0.0173	0.4928+/-0.0150	33.35	44,45,46	10	32	
17307715	5562.01	KP	12.77	10.27	4:21:52	+21:21:12.94	59476.99484	1.358	13.852	2.365	4065	0.5773+/-0.0171	0.5736+/-0.0140	2.32	43,44	8	13	
459762279	5573.01	PC	15.51	12.30	9:05:42	+55:18:26.55	59600.45002	25.364	8.796	9.217	3693	0.5940+/-0.0179	0.5877+/-0.0146	27.79	47	1098	113	
268405086	5574.01	PC	14.26	10.45	18:34:12	+86:33:24.36	59598.13767	0.76	6.824	2.243	3492	0.7481+/-0.0221	0.7032+/-0.0184	2.62	18,19,20,25,26,40,47	311	7	
160162137	5575.01	PC	17.01	12.28	16:05:00	+85:12:14.97	59747.65944	170.898	32.074	9.486	3115	0.2398+/-0.0072	0.2081+/-0.0050	37.42	41,47,52,53	182	747	
252928337	5579.01	VPC	15.56	12.17	7:03:17	+52:31:03.34	59583.26095	34.123	19.863	7.81	3553	0.4295+/-0.0129	0.4276+/-0.0102	19.77	47	593	143	
357244603	5583.01	PC	16.16	12.92	7:10:32	+74:29:09.06	59601.81425	25.475	3.065	11.209	3687	nan+/- nan	nan+/- nan	50.74	40,47	458	67	
29169215	5584.01	PC	11.83	9.62	9:01:18	+47:27:08.66	59580.44833	1.76	18.63	2.995	4348	0.6753+/-0.0199	0.6503+/-0.0158	3.01	21,47	556	17	

TIC ID	TOI	SG1 Disposition	Vmag	Jmag	RA_J2000 hh:mm:ss	DEC_J2000 dd:mm:ss	Epoch (BJD-2400000)	Depth (mmag)	P (days)	Rp (Re)	Teff (Mann relations, color)	Rstar (GAIA DR2, Mann relations)	Mstar (GAIA DR2, Mann relations)	Predicted K (m/s)	TESS Sectors	SNR TESS	SNR ExTrA	Articles
302908969	5595.01	PC	13.32	11.05	7:21:51	+35:13:19.68	59598.86942	4.003	5.99	4.738	4293	0.6884+/-0.0206	0.6598+/-0.0162	9.53	20,47	549	29	
237108775	5598.01	PC	16.88	13.38	17:09:16	+80:24:57.71	59623.67858	18.097	6.295	7.387	3575	0.5278+/-0.0164	0.5292+/-0.0135	22.88	41,47,48	270	40	
252481136	5610.01	PC	16.84	13.60	10:24:06	+48:14:54.85	59628.93716	40.574	7.945	9.866	3667	0.5098+/-0.0164	0.5119+/-0.0137	35.41	48	154	77	
154220877	5616.01	VPC	16.74	13.57	12:19:36	+48:40:59.40	59634.53513	27.11	2.003	11.008	3750	0.6542+/-0.0205	0.6347+/-0.0163	58.48	48	240	49	
119585136	5634.01	VPC	16.85	13.70	11:42:35	+20:57:55.45	59663.42258	31.147	2.205	9.608	3703	0.5270+/-0.0199	0.5282+/-0.0172	50.82	49	195	59	
141202786	5641.01	VPC+	17.06	12.99	12:03:38	+42:32:15.48	59663.47835	26.142	2.181	7.604	3315	nan+/- nan	nan+/- nan	36.63	49	295	62	
119178132	5658.01	PC	16.72	13.09	14:03:06	-1:28:49	59689.09596	29.696	1.606	11.757	3524	0.6318+/-0.0205	0.6176+/-0.0165	71.6	50	47	57	
422217860	5662.01	VPC-	13.79	10.56	12:44:21	+05:41:18.36	59689.67307	1.869	2.314	2.72	3682	0.6209+/-0.0186	0.6093+/-0.0151	5.31	23,46,50	334	12	
23863105	5671.01	VPC	16.27	13.25	14:04:02	+38:37:05.76	59685.75335	91.924	3.308	11.93	3740	0.4087+/-0.0126	0.4040+/-0.0102	76.62	50	598	217	
155949264	5683.01	PC	16.62	13.33	15:26:02	+44:49:28.93	59716.68551	23.065	0.775	17.264	3646	nan+/- nan	nan+/- nan	302.17	50,51	8	27	
193634953	5688.01	VPC	15.78	12.86	17:47:42	+47:42:17.17	59750.62301	26.476	2.948	9.382	3886	0.5778+/-0.0174	0.5741+/-0.0143	41.88	51	689	73	
23638678	5694.01	VPC	16.29	13.02	14:27:19	-7:32:51	59717.46832	57.04	1.154	17.047	3646	0.6244+/-0.0202	0.6120+/-0.0164	269.08	51	118	105	
103865797	5695.01	VPC+	nan	12.47	16:08:37	+19:15:12.15	59740.63147	34.975	2.223	9.328		0.3589+/-0.0109	0.3459+/-0.0086	63.74	51	25	74	
286813592	5709.01	PC	13.16	9.79	10:58:36	+14:37:25.88	58899.96983	0.866	3.381	1.498	3612	0.4956+/-0.0146	0.4979+/-0.0117	1.95	22,45,46,49	9	6	
441804533	5711.01	PC	13.25	10.18	17:41:49	+72:13:05.08	58753.18387	1.231	16.304	2.341	3743	nan+/- nan	nan+/- nan	2.08	16,17,22,47,48,49,50	10	12	
219041246	5713.01	PC	15.36	11.07	13:53:50	+52:36:10.25	58745.67796	4.343	10.442	1.861	3277	0.2921+/-0.0087	0.2671+/-0.0063	2.9	16,22,23,49	8	28	
147923561	5715.01	PC	13.12	10.22	11:02:58	+69:54:58.70	58684.15874	0.647	6.282	1.308	3818	0.5001+/-0.0148	0.5024+/-0.0119	1.25	14,20,21,40,41,47,48	8	5	
298074836	5716.01	PC	15.83	11.57	13:27:36	+73:10:42.12	58683.61197	2.432	6.766	1.25	3241	0.2261+/-0.0069	0.1935+/-0.0048	2.11	14,15,20,21,22,40,47, 48	7	11	
17932757	5718.01	PC	12.31	9.62	11:21:06	+41:34:35.43	58903.53945	1.698	716.843	2.649	3962	0.6715+/-0.0198	0.6475+/-0.0158	0.72	22,48	11	19	
230055368	5720.01	PC	13.85	10.12	11:21:16	+25:16:25.28	58900.64503	1.117	1.434	1.393	3477	0.3708+/-0.0110	0.3599+/-0.0084	2.83	22,49	6	6	
1042432	5725.01	PC	12.88	10.23	10:15:43	+28:21:18.64	58882.10682	1.816	746.955	2.718	3998	0.6238+/-0.0184	0.6116+/-0.0150	0.77	21,48	7	16	
219875976	5728.01	PC	15.02	11.00	17:21:24	+67:32:59.05	58685.09717	0.916	11.497	1.127	3348	0.3760+/-0.0112	0.3661+/-0.0087	0.83	14,15,16,17,18,19,20, 21,23,24,25,26,40,41, 47,48,49,50	8	7	
103605399	5729.01	PC	14.14	11.42	10:04:51	+69:09:59.22	58886.83654	6.598	554.499	3.888	3875	0.4234+/-0.0126	0.4207+/-0.0100	2.01	14,20,21,40,41,47	7	48	
138820713	5730.01	PC	13.19	9.76	11:42:16	+24:11:35.52	58900.38758	0.976	1.927	1.426	3557	0.4646+/-0.0138	0.4659+/-0.0110	2.26	22,49	8	6	
157769780	5735.01	VPC	15	10.65	9:48:30	+77:23:21.44	58683.54479	1.298	2.121	0.859	3252	0.2107+/-0.0064	0.1776+/-0.0044	0.88	14,20,26,40,47	6	6	
310380289	5736.01	PC	13.55	10.83	14:15:02	+49:30:04.66	58738.8986	0.61	0.649	1.617	3970	0.5802+/-0.0173	0.5762+/-0.0142	3.49	16,49,50	5	3	
229618478	5737.01	PC	13.72	11.16	18:35:37	+77:44:07.50	58698.86756	1.248	19.448	2.109	4063	0.6186+/-0.0182	0.6075+/-0.0149	1.7	14,17,18,19,21,22,23, 24,25,26,40,47,48,50	9	11	
198162530	5738.01	PC	13.99	10.87	16:15:38	+61:55:34.91	58683.64323	0.32	0.768	0.992	3727	0.5701+/-0.0169	0.5675+/-0.0139	0.97	14,15,16,17,18,19,21, 22,23,24,25,47,48,49, 50	5	2	
4918918	5747.01	VPC?	13.02	9.31	9:53:31	+35:34:16.72	58870.47457	0.889	0.573	1.497	3479	0.4202+/-0.0124	0.4172+/-0.0097	3.94	21,48	9	5	
310262516	5750.01	VPC?	16.11	13.45	16:34:08	+24:19:20.79	59741.11834	34.415	1.904	12.878	3992	0.6318+/-0.0197	0.6178+/-0.0160	78.99	51,52	152	56	
72889156	5756.01	PC	16.27	12.59	16:56:40	+37:46:59.46	59742.75951	25.319	7.641	9.382	3473	nan+/- nan	nan+/- nan	31.17	51,52	179	62	
289666986	5775.01	PC	16.71	13.53	3:44:58	+77:27:53.34	59765.10528	28.814	2.437	7.137	3698	0.4076+/-0.0129	0.4028+/-0.0108	35.5	52,53	15	92	
264468702	5778.01	VPC	15.72	12.76	21:42:57	+83:18:42.05	59762.21289	23.62	6.096	9.062	3858	0.5986+/-0.0181	0.5914+/-0.0149	30.37	52,53	653	74	
328081248	5799.01	PC	13.29	9.74	20:06:31	+15:59:17.13	59772.33448	2.84	4.165	1.988	3481	0.3436+/-0.0103	0.3278+/-0.0079	3.87	54	12	19	
243921117	5801.01	KP	11.84	9.22	20:12:40	-2:08:39	59770.02675	38.161	3.068	11.8	4063	0.6368+/-0.0190	0.6216+/-0.0154	57.87	54	296	296	
354727907	5836.01	VPC	17.12	12.94	19:17:48	+19:08:52.58	59786.40429	80.417	8.45	11.607	3326	0.4078+/-0.0134	0.4030+/-0.0115	53.54	54	11	226	
151728428	5850.01	PC	12.56	9.70	20:19:32	-8:17:54	59786.27101	8.13	4	13.852	3875	0.6390+/-0.0192	0.6233+/-0.0155	69.47	54	0	27	
114947483	5859.01	PC	14.82	11.87	19:01:27	+29:01:17.03	59794.55631	10.342	3.379	6.342	3839	0.6283+/-0.0187	0.6150+/-0.0152	19.65	14,40,53,54	15	48	
380517859	5867.01	PC	16.56	13.56	20:14:40	+30:46:33.88	59823.57011	29.986	1.109	10.293	3766	0.4904+/-0.0161	0.4926+/-0.0136	75.24	54,55	1	78	
353146308	5873.01	VPC	15.87	12.66	21:39:57	+01:17:36.55	59823.92212	24.086	0.413	12.245	3658	0.5015+/-0.0164	0.5037+/-0.0138	138.43	55	1	35	
258037656	5879.01	PC	17.05	12.72	21:53:24	+21:24:51.84	59823.90112	37.332	4.033	9.927	3277	0.4794+/-0.0153	0.4814+/-0.0128	46.74	55	9	100	
14956304	5896.01	PNEB?	16.33	13.27	20:26:02	+36:12:54.63	59823.40176	15.616	0.997	6.85	3772	0.5786+/-0.0182	0.5747+/-0.0150	35.19	41,55	12	46	
329709756	5915.01	PC	15.64	13.12	20:59:00	+47:32:30.55	59824.05164	56.697	12.542	13.465	4135	0.5854+/-0.0184	0.5805+/-0.0151	47.4	55	15	201	
305506996	5916.01	VPC+	16.6	13.12	21:41:12	+09:35:56.99	59817.68967	54.206	2.368	10.823	3597	0.4865+/-0.0159	0.4885+/-0.0135	64.06	55	13	144	
296898634	5940.01	PC	16.04	12.86	20:48:18	+47:55:50.20	59820.77863	17.071	2.849	6.385	3678	0.5181+/-0.0157	0.5200+/-0.0128	23.55	55	9	87	
236785891	5956.01	PC	nan	13.98	18:53:16	+59:49:02.91	59825.95876	49.362	0.929	15.079		0.4865+/-0.0166	0.4886+/-0.0142	336.49	56	10	70	
262689575	5961.01	CPC	10.51	7.86	23:16:52	+05:41:45.61	59826.27769	0.373	1.617	1.32	3992	0.6237+/-0.0183	0.6115+/-0.0149	1.76	56	9	2	
354173595	5974.01	VPC	13.02	9.42	23:19:04	+07:54:58.12	59826.05116	1.152	1.726	1.227	3495	0.3714+/-0.0111	0.3607+/-0.0087	2.13	56	8	6	
12938488	5977.01	PC	nan	12.87	19:54:10	+26:52:44.30	59419.98927	21.33	0.432	8.494		0.5893+/-0.0188	0.5837+/-0.0154	66.38	41,54,55	15	43	
120045750	5981.01	PC	14.42	10.50	18:55:52	+39:03:42.14	59423.51717	2.029	7.014	2.395	3409	0.5400+/-0.0159	0.5407+/-0.0129	3.21	41,53,54	13	18	
356871098	5983.01	PC	15.4	11.24	18:24:13	+66:56:08.54	58683.8199	0.937	1.027	1.376	3323	0.4004+/-0.0120	0.3945+/-0.0094	2.92	14,15,16,17,18,19,21, 22,24,25,26,40,47,48, 49,51,52,53,54,55	10	4	

TIC ID	TOI	SG1 Disposition	Vmag	Jmag	RA_J2000 hh:mm:ss	DEC_J2000 dd:mm:ss	Epoch (BJD-2400000)	Depth (mmag)	P (days)	Rp (Re)	Teff (Mann relations, color)	Rstar (GAIA DR2, Mann relations)	Mstar (GAIA DR2, Mann relations)	Predicted K (m/s)	TESS Sectors	SNR TESS	SNR ExTrA	Articles
284900292	5987.01	PC	13.91	11.26	17:23:55	+57:28:09.34	58769.9818	1.749	48.713	2.488	4048	0.6222+/-0.0184	0.6103+/-0.0150	1.65	17,19,20,22,23,24,25, 26,40,41,47,48,49,50	10	17	
370907864	5998.01	PC	12.78	10.37	19:30:18	+18:23:41.26	59397.78857	1.925	9.338	3.093	4210	0.6708+/-0.0198	0.6471+/-0.0158	4	40,54	10	17	
259233660	6000.01	PC	15.45	11.66	19:30:26	+68:09:16.36	58683.57604	0.733	0.449	1.015	3388	0.3770+/-0.0113	0.3672+/-0.0087	1.67	14,15,16,17,18,19,20, 21,22,23,24,25,26,40, 47,48,49,51,52,53,54, 55	7	2	
102734241	6002.01	PC	14.6	11.00	19:58:27	+32:17:19.18	58692.75995	4.385	10.905	1.549	3481	0.2416+/-0.0072	0.2102+/-0.0050	2.45	14,41,54,55	7	28	
48353358	6004.01	KP	13.86	10.65	18:54:31	+48:23:27.66	58685.7784	1.879	9.879	2.108	3705	nan+/- nan	nan+/- nan	2.21	14,26,40,41,53,54,55	11	14	
279922257	6007.01	PC	13.94	10.40	2:36:42	+78:39:07.78	58799.85258	3.294	949.791	2.863	3549	0.4239+/-0.0127	0.4213+/-0.0101	1	18,19,25,26,52,53	5	36	
286201103	6008.01	PC	15.97	10.42	20:41:47	+49:38:48.15	58711.37016	1.622	0.857	0.916	2909	0.2351+/-0.0070	0.2032+/-0.0048	1.38	15,16,41,55	5	6	
455947620	6022.01	PC	16.63	12.10	22:40:00	+60:49:23.43	59854.58918	124.403	1.928	13.366	3221	0.3701+/-0.0110	0.3592+/-0.0085	120.19	57	49	447	
388076422	6034.01	VPC+	15.19	11.90	21:11:36	+68:24:07.55	59883.90547	61.679	2.576	12.537	3641	0.4973+/-0.0149	0.4996+/-0.0121	78.64	58	35	263	

BIBLIOGRAPHY

Adibekyan, Vardan, Caroline Dorn, et al. (Oct. 2021). “A compositional link between rocky exoplanets and their host stars”. In: *Science* 374.6565, pp. 330–332. DOI: `10.1126/science.abg8794`. arXiv: `2102.12444 [astro-ph.EP]` (Cited on page 145).

Agol, Eric and Daniel C. Fabrycky (2018). “Transit-Timing and Duration Variations for the Discovery and Characterization of Exoplanets”. In: *Handbook of Exoplanets*. Ed. by Hans J. Deeg and Juan Antonio Belmonte, 7, p. 7. DOI: `10.1007/978-3-319-55333-7_7` (Cited on pages 122, 187).

Agol, Eric, Jason Steffen, et al. (May 2005). “On detecting terrestrial planets with timing of giant planet transits”. In: *MNRAS* 359.2, pp. 567–579. DOI: `10.1111/j.1365-2966.2005.08922.x` (Cited on pages 122, 187).

Airapetian, V. S., R. Barnes, et al. (Apr. 2020). “Impact of space weather on climate and habitability of terrestrial-type exoplanets”. In: *International Journal of Astrobiology* 19.2, pp. 136–194. DOI: `10.1017/S1473550419000132`. arXiv: `1905.05093 [astro-ph.EP]` (Cited on page 146).

Alibert, Y., I. Baraffe, et al. (Aug. 2006). “Formation and structure of the three Neptune-mass planets system around HD 69830”. In: *A&A* 455.2, pp. L25–L28. DOI: `10.1051/0004-6361:20065697`. arXiv: `astro-ph/0607175 [astro-ph]` (Cited on page 142).

Alibert, Y. and W. Benz (Feb. 2017). “Formation and composition of planets around very low mass stars”. In: *A&A* 598, L5, p. L5. DOI: `10.1051/0004-6361/201629671`. arXiv: `1610.03460 [astro-ph.EP]` (Cited on page 142).

Almenara, J. M., X. Bonfils, et al. (Sept. 2022a). “GJ 3090 b: one of the most favourable mini-Neptune for atmospheric characterisation”. In: *A&A* 665, A91, A91. DOI: `10.1051/0004-6361/202243975`. arXiv: `2207.14121 [astro-ph.EP]` (Cited on pages 129, 171, 193, 198).

Almenara, J. M., X. Bonfils, et al. (Nov. 2022b). “TOI-3884 b: A rare 6-R$_E$ planet that transits a low-mass star with a giant and likely polar spot”. In: *A&A* 667, L11, p. L11. DOI: `10.1051/0004-6361/202244791`. arXiv: `2210.10909 [astro-ph.EP]` (Cited on pages 129, 172, 194, 199).

Almenara, J. M., X. Bonfils, et al. (Aug. 2023). “TOI-4860 b, a short-period giant planet transiting an M3.5 dwarf”. In: *arXiv e-prints*, arXiv:2308.01454, arXiv:2308.01454. DOI: `10.48550/arXiv.2308.01454`. arXiv: `2308.01454 [astro-ph.EP]` (Cited on page 199).

Andrews, Sean M. (Aug. 2020). “Observations of Protoplanetary Disk Structures”. In: *ARA&A* 58, pp. 483–528. DOI: `10.1146/annurev-astro-031220-010302`. arXiv: `2001.05007 [astro-ph.EP]` (Cited on page 14).

Anglada-Escudé, Guillem, Pedro J. Amado, et al. (Aug. 2016). “A terrestrial planet candidate in a temperate orbit around Proxima Centauri”. In: *Nature* 536.7617, pp. 437–

440. DOI: 10.1038/nature19106. arXiv: 1609.03449 [astro-ph.EP] (Cited on page 141).

Artigau, Étienne, Driss Kouach, et al. (July 2014). "SPIRou: the near-infrared spectropolarimeter/high-precision velocimeter for the Canada-France-Hawaii telescope". In: *Ground-based and Airborne Instrumentation for Astronomy V*. Ed. by Suzanne K. Ramsay, Ian S. McLean, and Hideki Takami. Vol. 9147. Society of Photo-Optical Instrumentation Engineers (SPIE) Conference Series, 914715, p. 914715. DOI: 10.1117/12.2055663. arXiv: 1406.6992 [astro-ph.IM] (Cited on page 17).

Astudillo-Defru, N., T. Forveille, et al. (June 2017). "The HARPS search for southern extra-solar planets. XLI. A dozen planets around the M dwarfs GJ 3138, GJ 3323, GJ 273, GJ 628, and GJ 3293". In: *A&A* 602, A88, A88. DOI: 10.1051/0004-6361/201630153. arXiv: 1703.05386 [astro-ph.EP] (Cited on page 141).

Auvergne, M., P. Bodin, et al. (Oct. 2009). "The CoRoT satellite in flight: description and performance". In: *A&A* 506.1, pp. 411–424. DOI: 10.1051/0004-6361/200810860. arXiv: 0901.2206 [astro-ph.SR] (Cited on pages 11, 25, 179, 182).

Baglin, Annie, Michel Auvergne, et al. (Feb. 2009). "CoRoT: Description of the Mission and Early Results". In: *Transiting Planets*. Ed. by Frédéric Pont, Dimitar Sasselov, and Matthew J. Holman. Vol. 253, pp. 71–81. DOI: 10.1017/S1743921308026252 (Cited on pages 11, 25, 179, 182).

Ballard, Sarah (Mar. 2019). "Predicted Number, Multiplicity, and Orbital Dynamics of TESS M-dwarf Exoplanets". In: *AJ* 157.3, 113, p. 113. DOI: 10.3847/1538-3881/aaf477. arXiv: 1801.04949 [astro-ph.EP] (Cited on pages 149, 157, 189, 190).

Ballard, Sarah, Jessie L. Christiansen, et al. (May 2011). "A Search for Additional Planets in Five of the Exoplanetary Systems Studied by the NASA EPOXI Mission". In: *ApJ* 732.1, 41, p. 41. DOI: 10.1088/0004-637X/732/1/41. arXiv: 1103.0010 [astro-ph.EP] (Cited on page 142).

Ballard, Sarah and John Asher Johnson (Jan. 2016). "The Kepler Dichotomy among the M Dwarfs: Half of Systems Contain Five or More Coplanar Planets". In: *ApJ* 816.2, 66, p. 66. DOI: 10.3847/0004-637X/816/2/66. arXiv: 1410.4192 [astro-ph.EP] (Cited on pages 20, 145, 149, 150, 157, 182, 190).

Barkaoui, K., M. Timmermans, et al. (Sept. 2023). "TOI-2084 b and TOI-4184 b: Two new sub-Neptunes around M dwarf stars". In: *A&A* 677, A38, A38. DOI: 10.1051/0004-6361/202346838. arXiv: 2306.15095 [astro-ph.EP] (Cited on pages 130, 198).

Baruteau, C., A. Crida, et al. (Jan. 2014). "Planet-Disk Interactions and Early Evolution of Planetary Systems". In: *Protostars and Planets VI*. Ed. by Henrik Beuther, Ralf S. Klessen, et al., pp. 667–689. DOI: 10.2458/azu_uapress_9780816531240-ch029. arXiv: 1312.4293 [astro-ph.EP] (Cited on page 142).

Batalha, Natasha E., Taylor Lewis, et al. (Nov. 2019). "The Precision of Mass Measurements Required for Robust Atmospheric Characterization of Transiting Exoplanets". In: *ApJ* 885.1, L25, p. L25. DOI: 10.3847/2041-8213/ab4909. arXiv: 1910.00076 [astro-ph.EP] (Cited on page 145).

Bean, Jacob L., Sean N. Raymond, and James E. Owen (Jan. 2021). "The Nature and Origins of Sub-Neptune Size Planets". In: *Journal of Geophysical Research (Planets)* 126.1, e06639, e06639. DOI: 10.1029/2020JE006639. arXiv: 2010.11867 [astro-ph.EP] (Cited on pages 18, 181).

Beatty, Thomas G. and Sara Seager (Apr. 2010). "Transit Probabilities for Stars with Stellar Inclination Constraints". In: *ApJ* 712.2, pp. 1433–1442. DOI: 10.1088/0004-637X/712/2/1433. arXiv: 1002.3168 [astro-ph.EP] (Cited on page 152).

Bedell, Megan, Jacob L. Bean, et al. (Sept. 2018). "The Chemical Homogeneity of Sun-like Stars in the Solar Neighborhood". In: *ApJ* 865.1, 68, p. 68. DOI: 10.3847/1538-4357/aad908. arXiv: 1802.02576 [astro-ph.SR] (Cited on page 145).

Berger, Travis A., Daniel Huber, et al. (Sept. 2020). "The Gaia-Kepler Stellar Properties Catalog. II. Planet Radius Demographics as a Function of Stellar Mass and Age". In: *AJ* 160.3, 108, p. 108. DOI: 10.3847/1538-3881/aba18a. arXiv: 2005.14671 [astro-ph.EP] (Cited on page 146).

Berta-Thompson, Zachory K., Jonathan Irwin, et al. (Nov. 2015). "A rocky planet transiting a nearby low-mass star". In: *Nature* 527.7577, pp. 204–207. DOI: 10.1038/nature15762. arXiv: 1511.03550 [astro-ph.EP] (Cited on page 127).

Berta, Zachory K., David Charbonneau, et al. (Mar. 2012). "The Flat Transmission Spectrum of the Super-Earth GJ1214b from Wide Field Camera 3 on the Hubble Space Telescope". In: *ApJ* 747.1, 35, p. 35. DOI: 10.1088/0004-637X/747/1/35. arXiv: 1111.5621 [astro-ph.EP] (Cited on pages 30, 171, 193).

Beuzit, Jean-Luc, Markus Feldt, et al. (July 2008). "SPHERE: a 'Planet Finder' instrument for the VLT". In: *Ground-based and Airborne Instrumentation for Astronomy II*. Ed. by Ian S. McLean and Mark M. Casali. Vol. 7014. Society of Photo-Optical Instrumentation Engineers (SPIE) Conference Series, 701418, p. 701418. DOI: 10.1117/12.790120 (Cited on page 5).

Birkby, J., R. de Kok, et al. (Dec. 2013). "Characterising Exoplanet Atmospheres with High-resolution Spectroscopy". In: *The Messenger* 154, pp. 57–61 (Cited on page 141).

Blind, N., U. Conod, and F. Wildi (Nov. 2017). "Few-mode fibers and AO-assisted high resolution spectroscopy: coupling efficiency and modal noise mitigation". In: *arXiv e-prints*, arXiv:1711.00835, arXiv:1711.00835. DOI: 10.48550/arXiv.1711.00835. arXiv: 1711.00835 [astro-ph.IM] (Cited on pages 136, 137, 188).

Blind, N., U. Conod, et al. (Aug. 2022). "NIRPS front-end: design, performance, and lessons learned". In: *Ground-based and Airborne Instrumentation for Astronomy IX*. Ed. by Christopher J. Evans, Julia J. Bryant, and Kentaro Motohara. Vol. 12184. Society of Photo-Optical Instrumentation Engineers (SPIE) Conference Series, 121844H, 121844H. DOI: 10.1117/12.2628321. arXiv: 2207.14143 [astro-ph.IM] (Cited on pages 136, 138).

Bonfils, X., J. M. Almenara, et al. (Sept. 2015). "ExTrA: Exoplanets in transit and their atmospheres". In: *Techniques and Instrumentation for Detection of Exoplanets VII*. Ed. by Stuart Shaklan. Vol. 9605. Society of Photo-Optical Instrumentation Engineers (SPIE) Conference Series, 96051L, p. 96051L. DOI: 10.1117/12.2186999. arXiv: 1508.06601 [astro-ph.IM] (Cited on pages 17, 61, 185).

Bonfils, X., X. Delfosse, et al. (Jan. 2013). "The HARPS search for southern extra-solar planets. XXXI. The M-dwarf sample". In: *A&A* 549, A109, A109. DOI: 10.1051/0004-

6361/201014704. arXiv: 1111.5019 [astro-ph.EP] (Cited on pages 18, 141, 142, 144, 157).

Bonfils, X., T. Forveille, et al. (Dec. 2005). "The HARPS search for southern extra-solar planets. VI. A Neptune-mass planet around the nearby M dwarf Gl 581". In: *A&A* 443.3, pp. L15–L18. DOI: 10.1051/0004-6361:200500193. arXiv: astro-ph/0509211 [astro-ph] (Cited on page 164).

Borucki, William J., David Koch, et al. (Feb. 2010). "Kepler Planet-Detection Mission: Introduction and First Results". In: *Science* 327.5968, p. 977. DOI: 10.1126/science.1185402 (Cited on pages 11, 25, 179, 182).

Bouchy, F., R. Doyon, et al. (Sept. 2017). "Near-InfraRed Planet Searcher to Join HARPS on the ESO 3.6-metre Telescope". In: *The Messenger* 169, pp. 21–27. DOI: 10.18727/0722-6691/5034 (Cited on pages 17, 136, 188).

Bouvier, J., A. Sousa, et al. (Apr. 2023). "Stable accretion and episodic outflows in the young transition disk system GM Aurigae. A semester-long optical and near-infrared spectrophotometric monitoring campaign". In: *A&A* 672, A5, A5. DOI: 10.1051/0004-6361/202245342. arXiv: 2301.13568 [astro-ph.SR] (Cited on pages 125, 127).

Bowler, Brendan P. (Oct. 2016). "Imaging Extrasolar Giant Planets". In: *PASP* 128.968, p. 102001. DOI: 10.1088/1538-3873/128/968/102001. arXiv: 1605.02731 [astro-ph.EP] (Cited on page 5).

Bryant, Edward M., Daniel Bayliss, and Vincent Van Eylen (Mar. 2023). "The occurrence rate of giant planets orbiting low-mass stars with TESS". In: *MNRAS*. DOI: 10.1093/mnras/stad626. arXiv: 2303.00659 [astro-ph.EP] (Cited on page 144).

Buchhave, Lars A., David W. Latham, et al. (Nov. 2011). "Kepler-14b: A Massive Hot Jupiter Transiting an F Star in a Close Visual Binary". In: *ApJS* 197.1, 3, p. 3. DOI: 10.1088/0067-0049/197/1/3. arXiv: 1106.5510 [astro-ph.EP] (Cited on page 30).

Burn, R., M. Schlecker, et al. (Dec. 2021). "The New Generation Planetary Population Synthesis (NGPPS). IV. Planetary systems around low-mass stars". In: *A&A* 656, A72, A72. DOI: 10.1051/0004-6361/202140390. arXiv: 2105.04596 [astro-ph.EP] (Cited on pages 20, 144, 182).

Burt, Jennifer A., Diana Dragomir, et al. (Sept. 2021). "TOI-1231 b: A Temperate, Neptune-sized Planet Transiting the Nearby M3 Dwarf NLTT 24399". In: *AJ* 162.3, 87, p. 87. DOI: 10.3847/1538-3881/ac0432. arXiv: 2105.08077 [astro-ph.EP] (Cited on pages 130, 171, 193, 197).

Cabral, Alexandre, Bachar Wehbé, et al. (Aug. 2022). "NIRPS - the Near Infra-Red Planet Searcher: design, integration, and tests of the atmospheric dispersion corrector". In: *Ground-based and Airborne Instrumentation for Astronomy IX*. Ed. by Christopher J. Evans, Julia J. Bryant, and Kentaro Motohara. Vol. 12184. Society of Photo-Optical Instrumentation Engineers (SPIE) Conference Series, 121844M, p. 121844M. DOI: 10.1117/12.2628930 (Cited on page 136).

Cale, Bryson L., Michael Reefe, et al. (Dec. 2021). "Diving Beneath the Sea of Stellar Activity: Chromatic Radial Velocities of the Young AU Mic Planetary System". In: *AJ* 162.6, 295,

p. 295. DOI: 10.3847/1538-3881/ac2c80. arXiv: 2109.13996 [astro-ph.EP] (Cited on page 142).

Carleo, I., L. Malavolta, et al. (June 2020). "The GAPS Programme at TNG. XXI. A GIARPS case study of known young planetary candidates: confirmation of HD 285507 b and refutation of AD Leonis b". In: *A&A* 638, A5, A5. DOI: 10.1051/0004-6361/201937369. arXiv: 2002.10562 [astro-ph.EP] (Cited on page 146).

Carmona, A., X. Delfosse, et al. (Mar. 2023). "Near-IR and optical radial velocities of the active M-dwarf star Gl 388 (AD Leo) with SPIRou at CFHT and SOPHIE at OHP". In: *arXiv e-prints*, arXiv:2303.16712, arXiv:2303.16712. DOI: 10.48550/arXiv.2303.16712. arXiv: 2303.16712 [astro-ph.SR] (Cited on page 16).

Carter, Joshua A., Eric Agol, et al. (Aug. 2012). "Kepler-36: A Pair of Planets with Neighboring Orbits and Dissimilar Densities". In: *Science* 337.6094, p. 556. DOI: 10.1126/science.1223269. arXiv: 1206.4718 [astro-ph.EP] (Cited on page 122).

Castelli, F. and R. L. Kurucz (Jan. 2003). "New Grids of ATLAS9 Model Atmospheres". In: *Modelling of Stellar Atmospheres*. Ed. by N. Piskunov, W. W. Weiss, and D. F. Gray. Vol. 210, A20. DOI: 10.48550/arXiv.astro-ph/0405087. arXiv: astro-ph/0405087 [astro-ph] (Cited on page 15).

Charbonneau, David, Zachory K. Berta, et al. (Dec. 2009). "A super-Earth transiting a nearby low-mass star". In: *Nature* 462.7275, pp. 891–894. DOI: 10.1038/nature08679. arXiv: 0912.3229 [astro-ph.EP] (Cited on page 127).

Charbonneau, David, Timothy M. Brown, et al. (Jan. 2000). "Detection of Planetary Transits Across a Sun-like Star". In: *ApJ* 529.1, pp. L45–L48. DOI: 10.1086/312457. arXiv: astro-ph/9911436 [astro-ph] (Cited on page 9).

Chen, Jingjing and David Kipping (Jan. 2017). "Probabilistic Forecasting of the Masses and Radii of Other Worlds". In: *ApJ* 834.1, 17, p. 17. DOI: 10.3847/1538-4357/834/1/17. arXiv: 1603.08614 [astro-ph.EP] (Cited on pages 32, 34).

Chiang, Eugene and Gregory Laughlin (June 2013). "The minimum-mass extrasolar nebula: in situ formation of close-in super-Earths". In: *MNRAS* 431.4, pp. 3444–3455. DOI: 10.1093/mnras/stt424. arXiv: 1211.1673 [astro-ph.EP] (Cited on page 142).

Claret, A. (Nov. 2000). "A new non-linear limb-darkening law for LTE stellar atmosphere models. Calculations for -5.0 <= log[M/H] <= +1, 2000 K <= T_{eff} <= 50000 K at several surface gravities". In: *A&A* 363, pp. 1081–1190 (Cited on page 10).

Cloutier, Ryan, René Doyon, et al. (Aug. 2018). "Quantifying the Observational Effort Required for the Radial Velocity Characterization of TESS Planets". In: *AJ* 156.2, 82, p. 82. DOI: 10.3847/1538-3881/aacea9. arXiv: 1807.01263 [astro-ph.EP] (Cited on pages 29, 153, 157, 183).

Cloutier, Ryan and Kristen Menou (May 2020). "Evolution of the Radius Valley around Low-mass Stars from Kepler and K2". In: *AJ* 159.5, 211, p. 211. DOI: 10.3847/1538-3881/ab8237. arXiv: 1912.02170 [astro-ph.EP] (Cited on pages 18–20, 144, 145, 157, 181).

Cointepas, M., J. M. Almenara, et al. (June 2021). "TOI-269 b: an eccentric sub-Neptune transiting a M2 dwarf revisited with ExTrA". In: *A&A* 650, A145, A145. DOI: 10.1051/0004-6361/202140328. arXiv: 2104.14782 [astro-ph.EP] (Cited on pages 171, 184, 193, 197).

Conod, U., N. Blind, et al. (July 2016). "Adaptive optics for high resolution spectroscopy: a direct application with the future NIRPS spectrograph". In: *Adaptive Optics Systems V*. Ed. by Enrico Marchetti, Laird M. Close, and Jean-Pierre Véran. Vol. 9909. Society of Photo-Optical Instrumentation Engineers (SPIE) Conference Series, 990941, p. 990941. DOI: `10.1117/12.2233651`. arXiv: `1608.01124 [astro-ph.IM]` (Cited on pages 136, 188).

Crossfield, Ian J. M., William Waalkes, et al. (Sept. 2019). "A Super-Earth and Sub-Neptune Transiting the Late-type M Dwarf LP 791-18". In: *ApJ* 883.1, L16, p. L16. DOI: `10.3847/2041-8213/ab3d30`. arXiv: `1906.09267 [astro-ph.EP]` (Cited on pages 172, 194).

Delrez, L., C. A. Murray, et al. (Nov. 2022). "Two temperate super-Earths transiting a nearby late-type M dwarf". In: *A&A* 667, A59, A59. DOI: `10.1051/0004-6361/202244041`. arXiv: `2209.02831 [astro-ph.EP]` (Cited on pages 128, 130, 172, 194, 198).

Delrez, Laetitia, Michaël. Gillon, et al. (July 2018). "SPECULOOS: a network of robotic telescopes to hunt for terrestrial planets around the nearest ultracool dwarfs". In: *Ground-based and Airborne Telescopes VII*. Ed. by Heather K. Marshall and Jason Spyromilio. Vol. 10700. Society of Photo-Optical Instrumentation Engineers (SPIE) Conference Series, 107001I, p. 107001I. DOI: `10.1117/12.2312475`. arXiv: `1806.11205 [astro-ph.IM]` (Cited on pages 17, 128).

Dittmann, Jason A., Jonathan M. Irwin, et al. (Apr. 2017). "A temperate rocky super-Earth transiting a nearby cool star". In: *Nature* 544.7650, pp. 333–336. DOI: `10.1038/nature22055`. arXiv: `1704.05556 [astro-ph.EP]` (Cited on page 127).

Donati, J. F., D. Kouach, et al. (Nov. 2020). "SPIRou: NIR velocimetry and spectropolarimetry at the CFHT". In: *MNRAS* 498.4, pp. 5684–5703. DOI: `10.1093/mnras/staa2569`. arXiv: `2008.08949 [astro-ph.IM]` (Cited on page 139).

Donati, J. F., C. Moutou, et al. (June 2016). "A hot Jupiter orbiting a 2-million-year-old solar-mass T Tauri star". In: *Nature* 534.7609, pp. 662–666. DOI: `10.1038/nature18305`. arXiv: `1606.06236 [astro-ph.SR]` (Cited on page 142).

Dorn, Caroline, Julia Venturini, et al. (Jan. 2017). "A generalized Bayesian inference method for constraining the interiors of super Earths and sub-Neptunes". In: *A&A* 597, A37, A37. DOI: `10.1051/0004-6361/201628708`. arXiv: `1609.03908 [astro-ph.IM]` (Cited on page 21).

Dransfield, Georgina, Mathilde Timmermans, et al. (May 2023). "A 1.55 R habitable-zone planet hosted by TOI-715, an M4 star near the ecliptic South Pole". In: *MNRAS*. DOI: `10.1093/mnras/stad1439`. arXiv: `2305.06206 [astro-ph.EP]` (Cited on pages 130, 198).

Dressing, Courtney D. and David Charbonneau (July 2015). "The Occurrence of Potentially Habitable Planets Orbiting M Dwarfs Estimated from the Full Kepler Dataset and an Empirical Measurement of the Detection Sensitivity". In: *ApJ* 807.1, 45, p. 45. DOI: `10.1088/0004-637X/807/1/45`. arXiv: `1501.01623 [astro-ph.EP]` (Cited on pages 18, 144, 149–151, 157, 190).

Espinoza, Néstor (Nov. 2018). "Efficient Joint Sampling of Impact Parameters and Transit Depths in Transiting Exoplanet Light Curves". In: *Research Notes of the American*

Astronomical Society 2.4, 209, p. 209. DOI: 10.3847/2515-5172/aaef38. arXiv: 1811.04859 [astro-ph.EP] (Cited on page 74).

Espinoza, Néstor, Diana Kossakowski, and Rafael Brahm (Dec. 2019). "juliet: a versatile modelling tool for transiting and non-transiting exoplanetary systems". In: *MNRAS* 490.2, pp. 2262–2283. DOI: 10.1093/mnras/stz2688. arXiv: 1812.08549 [astro-ph.EP] (Cited on pages 37, 72, 168, 184, 191).

Fang, Julia and Jean-Luc Margot (Dec. 2012). "Architecture of Planetary Systems Based on Kepler Data: Number of Planets and Coplanarity". In: *ApJ* 761.2, 92, p. 92. DOI: 10.1088/0004-637X/761/2/92. arXiv: 1207.5250 [astro-ph.EP] (Cited on pages 20, 145, 182).

Faria, J. P., A. Suárez Mascareño, et al. (Feb. 2022). "A candidate short-period sub-Earth orbiting Proxima Centauri". In: *A&A* 658, A115, A115. DOI: 10.1051/0004-6361/202142337. arXiv: 2202.05188 [astro-ph.EP] (Cited on page 163).

Fischer, Debra A., Guillem Anglada-Escude, et al. (June 2016). "State of the Field: Extreme Precision Radial Velocities". In: *PASP* 128.964, p. 066001. DOI: 10.1088/1538-3873/128/964/066001. arXiv: 1602.07939 [astro-ph.IM] (Cited on pages 8, 178).

Foreman-Mackey, Daniel, Eric Agol, et al. (Dec. 2017). "Fast and Scalable Gaussian Process Modeling with Applications to Astronomical Time Series". In: *AJ* 154.6, 220, p. 220. DOI: 10.3847/1538-3881/aa9332. arXiv: 1703.09710 [astro-ph.IM] (Cited on page 77).

Foreman-Mackey, Daniel, David W. Hogg, et al. (Mar. 2013). "emcee: The MCMC Hammer". In: *PASP* 125.925, p. 306. DOI: 10.1086/670067. arXiv: 1202.3665 [astro-ph.IM] (Cited on page 75).

Fortney, Jonathan J. (Apr. 2018). "Modeling Exoplanetary Atmospheres: An Overview". In: *arXiv e-prints*, arXiv:1804.08149, arXiv:1804.08149. DOI: 10.48550/arXiv.1804.08149. arXiv: 1804.08149 [astro-ph.EP] (Cited on page 21).

Fulton, Benjamin J., Erik A. Petigura, et al. (Sept. 2017). "The California-Kepler Survey. III. A Gap in the Radius Distribution of Small Planets". In: *AJ* 154.3, 109, p. 109. DOI: 10.3847/1538-3881/aa80eb. arXiv: 1703.10375 [astro-ph.EP] (Cited on pages 4, 18, 143, 144, 157, 159, 181).

Fulton, Benjamin J., Erik A. Petigura, et al. (Apr. 2018). "RadVel: The Radial Velocity Modeling Toolkit". In: *PASP* 130.986, p. 044504. DOI: 10.1088/1538-3873/aaaaa8. arXiv: 1801.01947 [astro-ph.IM] (Cited on page 74).

Gaia Collaboration, A. G. A. Brown, et al. (Aug. 2018). "Gaia Data Release 2. Summary of the contents and survey properties". In: *A&A* 616, A1, A1. DOI: 10.1051/0004-6361/201833051. arXiv: 1804.09365 [astro-ph.GA] (Cited on pages 26, 32).

Gaia Collaboration, A. Vallenari, et al. (July 2022). "Gaia Data Release 3: Summary of the content and survey properties". In: *arXiv e-prints*, arXiv:2208.00211, arXiv:2208.00211. DOI: 10.48550/arXiv.2208.00211. arXiv: 2208.00211 [astro-ph.GA] (Cited on page 173).

Gaidos, E. (Sept. 2017). "A minimum mass nebula for M dwarfs". In: *MNRAS* 470.1, pp. L1–L5. DOI: 10.1093/mnrasl/slx063. arXiv: 1704.03265 [astro-ph.EP] (Cited on page 14).

Gaidos, E., A. W. Mann, et al. (Apr. 2016). "They are small worlds after all: revised properties of Kepler M dwarf stars and their planets". In: *MNRAS* 457.3, pp. 2877–2899. DOI: `10.1093/mnras/stw097`. arXiv: `1512.04437 [astro-ph.EP]` (Cited on page 157).

Gilbert, Emily A., Thomas Barclay, et al. (Sept. 2020). "The First Habitable-zone Earth-sized Planet from TESS. I. Validation of the TOI-700 System". In: *AJ* 160.3, 116, p. 116. DOI: `10.3847/1538-3881/aba4b2`. arXiv: `2001.00952 [astro-ph.EP]` (Cited on pages 11, 28, 179).

Gilbert, Emily A., Andrew Vanderburg, et al. (Feb. 2023). "A Second Earth-sized Planet in the Habitable Zone of the M Dwarf, TOI-700". In: *ApJ* 944.2, L35, p. L35. DOI: `10.3847/2041-8213/acb599`. arXiv: `2301.03617 [astro-ph.EP]` (Cited on pages 11, 179).

Gillon, M., E. Jehin, et al. (Feb. 2011). "TRAPPIST: a robotic telescope dedicated to the study of planetary systems". In: *European Physical Journal Web of Conferences*. Vol. 11. European Physical Journal Web of Conferences, 06002, p. 06002. DOI: `10.1051/epjconf/20101106002`. arXiv: `1101.5807 [astro-ph.EP]` (Cited on page 128).

Gillon, Michaël, Emmanuël Jehin, et al. (May 2016). "Temperate Earth-sized planets transiting a nearby ultracool dwarf star". In: *Nature* 533.7602, pp. 221–224. DOI: `10.1038/nature17448`. arXiv: `1605.07211 [astro-ph.EP]` (Cited on pages 11, 128, 179).

Gillon, Michaël, Amaury H. M. J. Triaud, et al. (Feb. 2017). "Seven temperate terrestrial planets around the nearby ultracool dwarf star TRAPPIST-1". In: *Nature* 542.7642, pp. 456–460. DOI: `10.1038/nature21360`. arXiv: `1703.01424 [astro-ph.EP]` (Cited on pages 11, 149, 179).

Gladman, Brett (Nov. 1993). "Dynamics of Systems of Two Close Planets". In: *Icarus* 106.1, pp. 247–263. DOI: `10.1006/icar.1993.1169` (Cited on page 149).

Grieves, Nolan, François Bouchy, et al. (Aug. 2021). "Populating the brown dwarf and stellar boundary: Five stars with transiting companions near the hydrogen-burning mass limit". In: *A&A* 652, A127, A127. DOI: `10.1051/0004-6361/202141145`. arXiv: `2107.03480 [astro-ph.SR]` (Cited on page 198).

Grimm, Simon L., Brice-Olivier Demory, et al. (May 2018). "The nature of the TRAPPIST-1 exoplanets". In: *A&A* 613, A68, A68. DOI: `10.1051/0004-6361/201732233`. arXiv: `1802.01377 [astro-ph.EP]` (Cited on page 122).

Guerrero, Natalia M., S. Seager, et al. (June 2021). "The TESS Objects of Interest Catalog from the TESS Prime Mission". In: *ApJS* 254.2, 39, p. 39. DOI: `10.3847/1538-4365/abefe1`. arXiv: `2103.12538 [astro-ph.EP]` (Cited on pages 28, 37).

Gupta, Akash and Hilke E. Schlichting (Mar. 2020). "Signatures of the core-powered mass-loss mechanism in the exoplanet population: dependence on stellar properties and observational predictions". In: *MNRAS* 493.1, pp. 792–806. DOI: `10.1093/mnras/staa315`. arXiv: `1907.03732 [astro-ph.EP]` (Cited on pages 18, 20, 144, 181).

Haghighipour, Nader (2015). "Planet Detection: Transit Timing Variation". In: *Encyclopedia of Astrobiology*. Ed. by Muriel Gargaud, William M. Irvine, et al. Berlin, Heidelberg: Springer Berlin Heidelberg, pp. 1906–1909. ISBN: 978-3-662-44185-5. DOI: `10.1007/978-3-662-44185-5_5290`. URL: `https://doi.org/10.1007/978-3-662-44185-5_5290` (Cited on page 123).

Hartman, J. D., G. Á. Bakos, et al. (July 2023). "TOI 4201 b and TOI 5344 b: Discovery of Two Transiting Giant Planets Around M Dwarf Stars and Revised Parameters for Three Others". In: *arXiv e-prints*, arXiv:2307.06809, arXiv:2307.06809. DOI: `10.48550/arXiv.2307.06809`. arXiv: `2307.06809 [astro-ph.EP]` (Cited on pages 130, 198).

He, Matthias Y., Eric B. Ford, et al. (Dec. 2020). "Architectures of Exoplanetary Systems. III. Eccentricity and Mutual Inclination Distributions of AMD-stable Planetary Systems". In: *AJ* 160.6, 276, p. 276. DOI: `10.3847/1538-3881/abba18`. arXiv: `2007.14473 [astro-ph.EP]` (Cited on page 150).

Henry, Gregory W., Geoffrey W. Marcy, et al. (Jan. 2000). "A Transiting "51 Peg-like" Planet". In: *ApJ* 529.1, pp. L41–L44. DOI: `10.1086/312458` (Cited on page 9).

Henry, Todd J., J. Davy Kirkpatrick, and Douglas A. Simons (Oct. 1994). "The Solar Neighborhood. I. Standard Spectral Types (K5-M8) for Northern Dwarfs Within Eight Parsecs". In: *AJ* 108, p. 1437. DOI: `10.1086/117167` (Cited on pages 12, 179).

Hirano, Teruyuki, Masayuki Kuzuhara, et al. (Dec. 2020). "Precision radial velocity measurements by the forward-modeling technique in the near-infrared". In: *PASJ* 72.6, 93, p. 93. DOI: `10.1093/pasj/psaa085`. arXiv: `2007.11013 [astro-ph.EP]` (Cited on page 139).

Hobson, Melissa J., Andrés Jordán, et al. (Feb. 2023). "TOI-3235 b: a transiting giant planet around an M4 dwarf star". In: *arXiv e-prints*, arXiv:2302.10008, arXiv:2302.10008. DOI: `10.48550/arXiv.2302.10008`. arXiv: `2302.10008 [astro-ph.EP]` (Cited on pages 130, 172, 194, 198).

Holman, Matthew J. and Norman W. Murray (Feb. 2005). "The Use of Transit Timing to Detect Terrestrial-Mass Extrasolar Planets". In: *Science* 307.5713, pp. 1288–1291. DOI: `10.1126/science.1107822`. arXiv: `astro-ph/0412028 [astro-ph]` (Cited on pages 122, 187).

Hord, Benjamin J., Eliza M. R. Kempton, et al. (Aug. 2023). "Identification of the Top TESS Objects of Interest for Atmospheric Characterization of Transiting Exoplanets with JWST". In: *arXiv e-prints*, arXiv:2308.09617, arXiv:2308.09617. DOI: `10.48550/arXiv.2308.09617`. arXiv: `2308.09617 [astro-ph.EP]` (Cited on page 199).

Howell, Steve B., Charlie Sobeck, et al. (Apr. 2014). "The K2 Mission: Characterization and Early Results". In: *PASP* 126.938, p. 398. DOI: `10.1086/676406`. arXiv: `1402.5163 [astro-ph.IM]` (Cited on pages 11, 179).

Huang, Chelsea X., Andrew Vanderburg, et al. (Nov. 2020a). "Photometry of 10 Million Stars from the First Two Years of TESS Full Frame Images: Part I". In: *Research Notes of the American Astronomical Society* 4.11, 204, p. 204. DOI: `10.3847/2515-5172/abca2e`. arXiv: `2011.06459 [astro-ph.EP]` (Cited on pages 27, 37).

— (Nov. 2020b). "Photometry of 10 Million Stars from the First Two Years of TESS Full Frame Images: Part II". In: *Research Notes of the American Astronomical Society* 4.11, 206, p. 206. DOI: `10.3847/2515-5172/abca2d` (Cited on pages 27, 37).

Irwin, Jonathan, Zachory K. Berta-Thompson, et al. (Jan. 2015). "The MEarth project: an all-sky survey for transiting Earth-like exoplanets orbiting nearby M-dwarfs". In: *American Astronomical Society Meeting Abstracts #225*. Vol. 225. American Astronomical Society Meeting Abstracts, 258.01, p. 258.01 (Cited on pages 11, 127, 179).

JWST Transiting Exoplanet Community Early Release Science Team, Eva-Maria Ahrer, et al. (Feb. 2023). "Identification of carbon dioxide in an exoplanet atmosphere". In: *Nature* 614.7949, pp. 649–652. DOI: `10.1038/s41586-022-05269-w`. arXiv: `2208.11692 [astro-ph.EP]` (Cited on page 21).

Jehin, E., M. Gillon, et al. (Sept. 2011). "TRAPPIST: TRAnsiting Planets and PlanetesImals Small Telescope". In: *The Messenger* 145, pp. 2–6 (Cited on pages 11, 179).

Jehin, E., M. Gillon, et al. (Dec. 2018). "The SPECULOOS Southern Observatory Begins its Hunt for Rocky Planets". In: *The Messenger* 174, pp. 2–7. DOI: `10.18727/0722-6691/5105` (Cited on pages 11, 128, 179).

Jenkins, Jon M. (Aug. 2002). "The Impact of Solar-like Variability on the Detectability of Transiting Terrestrial Planets". In: *ApJ* 575.1, pp. 493–505. DOI: `10.1086/341136` (Cited on page 37).

Jenkins, Jon M., Hema Chandrasekaran, et al. (July 2010). "Transiting planet search in the Kepler pipeline". In: *Software and Cyberinfrastructure for Astronomy*. Ed. by Nicole M. Radziwill and Alan Bridger. Vol. 7740. Society of Photo-Optical Instrumentation Engineers (SPIE) Conference Series, 77400D, p. 77400D. DOI: `10.1117/12.856764` (Cited on page 37).

Jenkins, Jon M., Joseph D. Twicken, et al. (Aug. 2016). "The TESS science processing operations center". In: *Software and Cyberinfrastructure for Astronomy IV*. Ed. by Gianluca Chiozzi and Juan C. Guzman. Vol. 9913. Society of Photo-Optical Instrumentation Engineers (SPIE) Conference Series, 99133E, 99133E. DOI: `10.1117/12.2233418` (Cited on pages 27, 37).

Jin, Sheng and Christoph Mordasini (Feb. 2018). "Compositional Imprints in Density-Distance-Time: A Rocky Composition for Close-in Low-mass Exoplanets from the Location of the Valley of Evaporation". In: *ApJ* 853.2, 163, p. 163. DOI: `10.3847/1538-4357/aa9f1e`. arXiv: `1706.00251 [astro-ph.EP]` (Cited on pages 18, 144, 181).

Johansen, Anders, Melvyn B. Davies, et al. (Oct. 2012). "Can Planetary Instability Explain the Kepler Dichotomy?" In: *ApJ* 758.1, 39, p. 39. DOI: `10.1088/0004-637X/758/1/39`. arXiv: `1206.6898 [astro-ph.EP]` (Cited on page 150).

Kanodia, Shubham, Suvrath Mahadevan, et al. (Aug. 2018). "Overview of the spectrometer optical fiber feed for the habitable-zone planet finder". In: *Ground-based and Airborne Instrumentation for Astronomy VII*. Ed. by Christopher J. Evans, Luc Simard, and Hideki Takami. Vol. 10702. Society of Photo-Optical Instrumentation Engineers (SPIE) Conference Series, 107026Q, 107026Q. DOI: `10.1117/12.2313491`. arXiv: `1808.00557 [astro-ph.IM]` (Cited on page 139).

Kempton, Eliza M. R., Jacob L. Bean, et al. (Nov. 2018). "A Framework for Prioritizing the TESS Planetary Candidates Most Amenable to Atmospheric Characterization". In: *PASP* 130.993, p. 114401. DOI: `10.1088/1538-3873/aadf6f`. arXiv: `1805.03671 [astro-ph.EP]` (Cited on pages 29, 32, 34, 183).

Kipping, David M. (Nov. 2013). "Efficient, uninformative sampling of limb darkening coefficients for two-parameter laws". In: *MNRAS* 435.3, pp. 2152–2160. DOI: `10.1093/mnras/stt1435`. arXiv: `1308.0009 [astro-ph.SR]` (Cited on page 74).

Kopparapu, Ravi Kumar, Ramses Ramirez, et al. (Mar. 2013). “Habitable Zones around Main-sequence Stars: New Estimates”. In: *ApJ* 765.2, 131, p. 131. DOI: `10.1088/0004-637X/765/2/131`. arXiv: `1301.6674 [astro-ph.EP]` (Cited on pages 14, 180).

Kotani, Takayuki, Motohide Tamura, et al. (July 2018). “The infrared Doppler (IRD) instrument for the Subaru telescope: instrument description and commissioning results”. In: *Ground-based and Airborne Instrumentation for Astronomy VII*. Ed. by Christopher J. Evans, Luc Simard, and Hideki Takami. Vol. 10702. Society of Photo-Optical Instrumentation Engineers (SPIE) Conference Series, 1070211, p. 1070211. DOI: `10.1117/12.2311836` (Cited on page 139).

Kreidberg, Laura (Nov. 2015). “batman: BAsic Transit Model cAlculatioN in Python”. In: *PASP* 127.957, p. 1161. DOI: `10.1086/683602`. arXiv: `1507.08285 [astro-ph.EP]` (Cited on pages 37, 74, 184).

Kubyshkina, Daria and Aline A. Vidotto (June 2021). “How does the mass and activity history of the host star affect the population of low-mass planets?” In: *MNRAS* 504.2, pp. 2034–2050. DOI: `10.1093/mnras/stab897`. arXiv: `2103.13117 [astro-ph.EP]` (Cited on pages 18, 144, 181).

Laughlin, Gregory, Peter Bodenheimer, and Fred C. Adams (Sept. 2004). “The Core Accretion Model Predicts Few Jovian-Mass Planets Orbiting Red Dwarfs”. In: *ApJ* 612.1, pp. L73–L76. DOI: `10.1086/424384`. arXiv: `astro-ph/0407309 [astro-ph]` (Cited on pages 20, 144).

Lecavelier Des Etangs, A. (Jan. 2007). “A diagram to determine the evaporation status of extrasolar planets”. In: *A&A* 461.3, pp. 1185–1193. DOI: `10.1051/0004-6361:20065014`. arXiv: `astro-ph/0609744 [astro-ph]` (Cited on page 4).

Lee, Eve J. and Nicholas J. Connors (Feb. 2021). “Primordial Radius Gap and Potentially Broad Core Mass Distributions of Super-Earths and Sub-Neptunes”. In: *ApJ* 908.1, 32, p. 32. DOI: `10.3847/1538-4357/abd6c7`. arXiv: `2008.01105 [astro-ph.EP]` (Cited on pages 19, 144, 181).

Li, Jie, Peter Tenenbaum, et al. (Feb. 2019). “Kepler Data Validation II-Transit Model Fitting and Multiple-planet Search”. In: *PASP* 131.996, p. 024506. DOI: `10.1088/1538-3873/aaf44d`. arXiv: `1812.00103 [astro-ph.IM]` (Cited on page 37).

Lillo-Box, J., P. Figueira, et al. (Oct. 2020). “Planetary system LHS 1140 revisited with ESPRESSO and TESS”. In: *A&A* 642, A121, A121. DOI: `10.1051/0004-6361/202038922`. arXiv: `2010.06928 [astro-ph.EP]` (Cited on pages 14, 145, 149).

Limbach, Mary Anne and Edwin L. Turner (Jan. 2015). “Exoplanet orbital eccentricity: Multiplicity relation and the Solar System”. In: *Proceedings of the National Academy of Science* 112.1, pp. 20–24. DOI: `10.1073/pnas.1406545111`. arXiv: `1404.2552 [astro-ph.EP]` (Cited on page 150).

Lopez, Eric D. and Ken Rice (Oct. 2018). “How formation time-scales affect the period dependence of the transition between rocky super-Earths and gaseous sub-Neptunesand implications for $\eta_\oplus$”. In: *MNRAS* 479.4, pp. 5303–5311. DOI: `10.1093/mnras/sty1707`. arXiv: `1610.09390 [astro-ph.EP]` (Cited on pages 19, 20, 144, 181).

Luger, Rodrigo, Marko Sestovic, et al. (June 2017). “A seven-planet resonant chain in TRAPPIST-1”. In: *Nature Astronomy* 1, 0129, p. 0129. DOI: `10.1038/s41550-017-0129`. arXiv: `1703.04166 [astro-ph.EP]` (Cited on page 149).

Madhusudhan, Nikku, Matthew C. Nixon, et al. (Mar. 2020). "The Interior and Atmosphere of the Habitable-zone Exoplanet K2-18b". In: *ApJ* 891.1, L7, p. L7. DOI: `10.3847/2041-8213/ab7229`. arXiv: `2002.11115 [astro-ph.EP]` (Cited on pages 171, 193).

Madhusudhan, Nikku, Anjali A. A. Piette, and Savvas Constantinou (Sept. 2021). "Habitability and Biosignatures of Hycean Worlds". In: *ApJ* 918.1, 1, p. 1. DOI: `10.3847/1538-4357/abfd9c`. arXiv: `2108.10888 [astro-ph.EP]` (Cited on pages 14, 145).

Mahadevan, Suvrath, Lawrence Ramsey, et al. (Sept. 2012). "The habitable-zone planet finder: a stabilized fiber-fed NIR spectrograph for the Hobby-Eberly Telescope". In: *Ground-based and Airborne Instrumentation for Astronomy IV*. Ed. by Ian S. McLean, Suzanne K. Ramsay, and Hideki Takami. Vol. 8446. Society of Photo-Optical Instrumentation Engineers (SPIE) Conference Series, 84461S, 84461S. DOI: `10.1117/12.926102`. arXiv: `1209.1686 [astro-ph.EP]` (Cited on page 17).

Maiolino, R., M. Haehnelt, et al. (Oct. 2013). "A Community Science Case for E-ELT HIRES". In: *arXiv e-prints*, arXiv:1310.3163, arXiv:1310.3163. DOI: `10.48550/arXiv.1310.3163`. arXiv: `1310.3163 [astro-ph.IM]` (Cited on page 174).

Malavolta, L., V. Nascimbeni, et al. (Apr. 2016). "The GAPS programme with HARPS-N at TNG. XI. Pr 0211 in M 44: the first multi-planet system in an open cluster". In: *A&A* 588, A118, A118. DOI: `10.1051/0004-6361/201527933`. arXiv: `1602.00009 [astro-ph.EP]` (Cited on page 30).

Mann, Andrew W., Trent Dupuy, et al. (Jan. 2019). "How to Constrain Your M Dwarf. II. The Mass-Luminosity-Metallicity Relation from 0.075 to 0.70 Solar Masses". In: *ApJ* 871.1, 63, p. 63. DOI: `10.3847/1538-4357/aaf3bc`. arXiv: `1811.06938 [astro-ph.SR]` (Cited on pages 33, 34).

Mann, Andrew W., Gregory A. Feiden, et al. (May 2015). "How to Constrain Your M Dwarf: Measuring Effective Temperature, Bolometric Luminosity, Mass, and Radius". In: *ApJ* 804.1, 64, p. 64. DOI: `10.1088/0004-637X/804/1/64`. arXiv: `1501.01635 [astro-ph.SR]` (Cited on pages 32–34).

Mann, Andrew W., Eric Gaidos, and Megan Ansdell (Dec. 2013). "Spectro-thermometry of M Dwarfs and Their Candidate Planets: Too Hot, Too Cool, or Just Right?" In: *ApJ* 779.2, 188, p. 188. DOI: `10.1088/0004-637X/779/2/188`. arXiv: `1311.0003 [astro-ph.EP]` (Cited on page 33).

Marconi, A., M. Abreu, et al. (Dec. 2020). "ELT-HIRES, the high resolution spectrograph for the ELT: the Phase A study and the path to construction". In: *Ground-based and Airborne Instrumentation for Astronomy VIII*. Ed. by Christopher J. Evans, Julia J. Bryant, and Kentaro Motohara. Vol. 11447. Society of Photo-Optical Instrumentation Engineers (SPIE) Conference Series, 1144726, p. 1144726. DOI: `10.1117/12.2560489` (Cited on pages 141, 174, 196).

Mayor, M., X. Bonfils, et al. (Nov. 2009). "The HARPS search for southern extra-solar planets. XVIII. An Earth-mass planet in the GJ 581 planetary system". In: *A&A* 507.1, pp. 487–494. DOI: `10.1051/0004-6361/200912172`. arXiv: `0906.2780 [astro-ph.EP]` (Cited on page 164).

Mayor, M., F. Pepe, et al. (Dec. 2003). "Setting New Standards with HARPS". In: *The Messenger* 114, pp. 20–24 (Cited on pages 8, 178).

Mayor, Michel and Didier Queloz (Nov. 1995). “A Jupiter-mass companion to a solar-type star”. In: *Nature* 378.6555, pp. 355–359. DOI: `10.1038/378355a0` (Cited on pages 3, 6, 177).

Mazeh, T., T. Holczer, and S. Faigler (May 2016). “Dearth of short-period Neptunian exoplanets: A desert in period-mass and period-radius planes”. In: *A&A* 589, A75, A75. DOI: `10.1051/0004-6361/201528065`. arXiv: `1602.07843 [astro-ph.EP]` (Cited on page 4).

Mercer, Anthony and Dimitris Stamatellos (Jan. 2020). “Planet formation around M dwarfs via disc instability. Fragmentation conditions and protoplanet properties”. In: *A&A* 633, A116, A116. DOI: `10.1051/0004-6361/201936954`. arXiv: `2001.10062 [astro-ph.SR]` (Cited on page 14).

Millholland, Sarah, Songhu Wang, and Gregory Laughlin (Nov. 2017). “Kepler Multi-planet Systems Exhibit Unexpected Intra-system Uniformity in Mass and Radius”. In: *ApJ* 849.2, L33, p. L33. DOI: `10.3847/2041-8213/aa9714`. arXiv: `1710.11152 [astro-ph.EP]` (Cited on page 173).

Mordasini, C., Y. Alibert, et al. (May 2012). “Extrasolar planet population synthesis . IV. Correlations with disk metallicity, mass, and lifetime”. In: *A&A* 541, A97, A97. DOI: `10.1051/0004-6361/201117350`. arXiv: `1201.1036 [astro-ph.EP]` (Cited on page 14).

Morris, Robert L., Joseph D. Twicken, et al. (Jan. 2017). *Kepler Data Processing Handbook: Photometric Analysis*. Kepler Science Document KSCI-19081-002, id. 6. Edited by Jon M. Jenkins. (Cited on page 37).

Mulders, Gijs D., Joanna Drążkowska, et al. (Oct. 2021). “Why Do M Dwarfs Have More Transiting Planets?” In: *ApJ* 920.1, L1, p. L1. DOI: `10.3847/2041-8213/ac2947`. arXiv: `2110.02971 [astro-ph.EP]` (Cited on page 14).

Mulders, Gijs D., Ilaria Pascucci, and Dániel Apai (Dec. 2015). “An Increase in the Mass of Planetary Systems around Lower-mass Stars”. In: *ApJ* 814.2, 130, p. 130. DOI: `10.1088/0004-637X/814/2/130`. arXiv: `1510.02481 [astro-ph.EP]` (Cited on pages 157, 190).

Origlia, L., E. Oliva, et al. (July 2014). “High resolution near IR spectroscopy with GIANO-TNG”. In: *Ground-based and Airborne Instrumentation for Astronomy V*. Ed. by Suzanne K. Ramsay, Ian S. McLean, and Hideki Takami. Vol. 9147. Society of Photo-Optical Instrumentation Engineers (SPIE) Conference Series, 91471E, 91471E. DOI: `10.1117/12.2054743` (Cited on page 139).

Otegi, J. F., F. Bouchy, and R. Helled (Feb. 2020). “Revisited mass-radius relations for exoplanets below 120 $M_{\oplus}$”. In: *A&A* 634, A43, A43. DOI: `10.1051/0004-6361/201936482`. arXiv: `1911.04745 [astro-ph.EP]` (Cited on pages 33, 34, 147, 150, 160, 190).

Otegi, J. F., C. Dorn, et al. (Aug. 2020). “Impact of the measured parameters of exoplanets on the inferred internal structure”. In: *A&A* 640, A135, A135. DOI: `10.1051/0004-6361/202038006`. arXiv: `2006.12353 [astro-ph.EP]` (Cited on page 21).

Otegi, J. F., R. Helled, and F. Bouchy (Feb. 2022). “The similarity of multi-planet systems”. In: *A&A* 658, A107, A107. DOI: `10.1051/0004-6361/202142110` (Cited on pages 21, 145, 182).

Owen, James E. and Yanqin Wu (Oct. 2013). "Kepler Planets: A Tale of Evaporation". In: *ApJ* 775.2, 105, p. 105. DOI: `10.1088/0004-637X/775/2/105`. arXiv: `1303.3899 [astro-ph.EP]` (Cited on page 146).

— (Sept. 2017). "The Evaporation Valley in the Kepler Planets". In: *ApJ* 847.1, 29, p. 29. DOI: `10.3847/1538-4357/aa890a`. arXiv: `1705.10810 [astro-ph.EP]` (Cited on pages 18, 156, 157, 181).

Paegert, Martin, Keivan G. Stassun, et al. (Aug. 2021). "TESS Input Catalog versions 8.1 and 8.2: Phantoms in the 8.0 Catalog and How to Handle Them". In: *arXiv e-prints*, arXiv:2108.04778, arXiv:2108.04778. arXiv: `2108.04778 [astro-ph.EP]` (Cited on page 32).

Pascucci, I., G. Laughlin, et al. (Dec. 2011). "Planet Formation Around M-dwarf Stars: From Young Disks to Planets". In: *16th Cambridge Workshop on Cool Stars, Stellar Systems, and the Sun*. Ed. by Christopher Johns-Krull, Matthew K. Browning, and Andrew A. West. Vol. 448. Astronomical Society of the Pacific Conference Series, p. 469. DOI: `10.48550/arXiv.1101.1913`. arXiv: `1101.1913 [astro-ph.EP]` (Cited on page 14).

Patat, F. (Dec. 2004). "Observing During Bright Time: Tips and Tricks". In: *The Messenger* 118, pp. 11–14 (Cited on page 66).

Pepe, F., S. Cristiani, et al. (Jan. 2021). "ESPRESSO at VLT. On-sky performance and first results". In: *A&A* 645, A96, A96. DOI: `10.1051/0004-6361/202038306`. arXiv: `2010.00316 [astro-ph.IM]` (Cited on pages 9, 138, 139, 178).

Pepe, F., M. Mayor, et al. (Dec. 2002). "HARPS: ESO's coming planet searcher. Chasing exoplanets with the La Silla 3.6-m telescope". In: *The Messenger* 110, pp. 9–14 (Cited on page 139).

Perryman, Michael (2011). *The Exoplanet Handbook* (Cited on page 11).

Perryman, Michael, Joel Hartman, et al. (Dec. 2014). "Astrometric Exoplanet Detection with Gaia". In: *ApJ* 797.1, 14, p. 14. DOI: `10.1088/0004-637X/797/1/14`. arXiv: `1411.1173 [astro-ph.EP]` (Cited on page 174).

Plavchan, Peter, Thomas Barclay, et al. (June 2020). "A planet within the debris disk around the pre-main-sequence star AU Microscopii". In: *Nature* 582.7813, pp. 497–500. DOI: `10.1038/s41586-020-2400-z`. arXiv: `2006.13248 [astro-ph.EP]` (Cited on page 146).

Plotnykov, Mykhaylo and Diana Valencia (Nov. 2020). "Chemical fingerprints of formation in rocky super-Earths' data". In: *MNRAS* 499.1, pp. 932–947. DOI: `10.1093/mnras/staa2615`. arXiv: `2010.06480 [astro-ph.EP]` (Cited on page 145).

Psaridi, Angelica, François Bouchy, et al. (Aug. 2022). "Three new brown dwarfs and a massive hot Jupiter revealed by TESS around early-type stars". In: *A&A* 664, A94, A94. DOI: `10.1051/0004-6361/202243454`. arXiv: `2205.10854 [astro-ph.EP]` (Cited on page 198).

Queloz, D., G. W. Henry, et al. (Nov. 2001). "No planet for HD 166435". In: *A&A* 379, pp. 279–287. DOI: `10.1051/0004-6361:20011308`. arXiv: `astro-ph/0109491 [astro-ph]` (Cited on page 16).

Quirrenbach, A., P. J. Amado, et al. (July 2014). "CARMENES instrument overview". In: *Ground-based and Airborne Instrumentation for Astronomy V*. Ed. by Suzanne K. Ramsay, Ian S. McLean, and Hideki Takami. Vol. 9147. Society of Photo-Optical Instrumentation Engineers (SPIE) Conference Series, 91471F, 91471F. DOI: `10.1117/12.2056453` (Cited on pages 9, 178).

Quirrenbach, A., P. J. Amado, et al. (July 2018). "CARMENES: high-resolution spectra and precise radial velocities in the red and infrared". In: *Ground-based and Airborne Instrumentation for Astronomy VII*. Ed. by Christopher J. Evans, Luc Simard, and Hideki Takami. Vol. 10702. Society of Photo-Optical Instrumentation Engineers (SPIE) Conference Series, 107020W, 107020W. DOI: `10.1117/12.2313689` (Cited on page 17).

Rauer, Heike, Conny Aerts, et al. (Sept. 2022). "The PLATO Mission". In: *European Planetary Science Congress*, EPSC2022-453, EPSC2022–453. DOI: `10.5194/epsc2022-453` (Cited on page 174).

Reefe, Michael A., Rafael Luque, et al. (June 2022). "A Close-in Puffy Neptune with Hidden Friends: The Enigma of TOI 620". In: *AJ* 163.6, 269, p. 269. DOI: `10.3847/1538-3881/ac658b`. arXiv: `2204.03108 [astro-ph.EP]` (Cited on pages 130, 172, 194, 197).

Ricker, George R., Joshua N. Winn, et al. (Aug. 2014). "Transiting Exoplanet Survey Satellite (TESS)". In: *Space Telescopes and Instrumentation 2014: Optical, Infrared, and Millimeter Wave*. Ed. by Jr. Oschmann Jacobus M., Mark Clampin, et al. Vol. 9143. Society of Photo-Optical Instrumentation Engineers (SPIE) Conference Series, 914320, p. 914320. DOI: `10.1117/12.2063489`. arXiv: `1406.0151 [astro-ph.EP]` (Cited on pages 11, 17, 25, 179).

Robertson, Paul and Suvrath Mahadevan (Oct. 2014a). "Disentangling Planets and Stellar Activity for Gliese 667C". In: *ApJ* 793.2, L24, p. L24. DOI: `10.1088/2041-8205/793/2/L24`. arXiv: `1409.0021 [astro-ph.EP]` (Cited on page 16).

— (Oct. 2014b). "Disentangling Planets and Stellar Activity for Gliese 667C". In: *ApJ* 793.2, L24, p. L24. DOI: `10.1088/2041-8205/793/2/L24`. arXiv: `1409.0021 [astro-ph.EP]` (Cited on page 142).

Robertson, Paul, Suvrath Mahadevan, et al. (July 2014). "Stellar activity masquerading as planets in the habitable zone of the M dwarf Gliese 581". In: *Science* 345.6195, pp. 440–444. DOI: `10.1126/science.1253253`. arXiv: `1407.1049 [astro-ph.EP]` (Cited on pages 16, 164).

Rodriguez, Joseph E., Andrew Vanderburg, et al. (Sept. 2020). "The First Habitable-zone Earth-sized Planet from TESS. II. Spitzer Confirms TOI-700 d". In: *AJ* 160.3, 117, p. 117. DOI: `10.3847/1538-3881/aba4b3`. arXiv: `2001.00954 [astro-ph.EP]` (Cited on page 28).

Sabotta, S., M. Schlecker, et al. (Sept. 2021). "The CARMENES search for exoplanets around M dwarfs. Planet occurrence rates from a subsample of 71 stars". In: *A&A* 653, A114, A114. DOI: `10.1051/0004-6361/202140968`. arXiv: `2107.03802 [astro-ph.EP]` (Cited on page 142).

Seager, Sara and Drake Deming (Sept. 2010). "Exoplanet Atmospheres". In: *ARA&A* 48, pp. 631–672. DOI: `10.1146/annurev-astro-081309-130837`. arXiv: `1005.4037 [astro-ph.EP]` (Cited on page 21).

Sebastian, D., M. Gillon, et al. (Jan. 2021). “SPECULOOS: Ultracool dwarf transit survey. Target list and strategy”. In: *A&A* 645, A100, A100. DOI: 10.1051/0004-6361/202038827. arXiv: 2011.02069 [astro-ph.EP] (Cited on page 124).

Skrutskie, M. F., R. M. Cutri, et al. (Feb. 2006). “The Two Micron All Sky Survey (2MASS)”. In: *AJ* 131.2, pp. 1163–1183. DOI: 10.1086/498708 (Cited on page 32).

Smette, A., H. Sana, et al. (Apr. 2015). “Molecfit: A general tool for telluric absorption correction. I. Method and application to ESO instruments”. In: *A&A* 576, A77, A77. DOI: 10.1051/0004-6361/201423932. arXiv: 1501.07239 [astro-ph.IM] (Cited on page 17).

Snellen, I. A. G., R. J. de Kok, et al. (Feb. 2013). “Finding Extraterrestrial Life Using Ground-based High-dispersion Spectroscopy”. In: *ApJ* 764.2, 182, p. 182. DOI: 10.1088/0004-637X/764/2/182. arXiv: 1302.3251 [astro-ph.EP] (Cited on page 6).

Snellen, I., R. de Kok, et al. (Apr. 2015). “Combining high-dispersion spectroscopy with high contrast imaging: Probing rocky planets around our nearest neighbors”. In: *A&A* 576, A59, A59. DOI: 10.1051/0004-6361/201425018. arXiv: 1503.01136 [astro-ph.EP] (Cited on pages 6, 141).

Speagle, Joshua S. (Apr. 2020). “DYNESTY: a dynamic nested sampling package for estimating Bayesian posteriors and evidences”. In: *MNRAS* 493.3, pp. 3132–3158. DOI: 10.1093/mnras/staa278. arXiv: 1904.02180 [astro-ph.IM] (Cited on page 75).

Stassun, Keivan G., Ryan J. Oelkers, et al. (Sept. 2018). “The TESS Input Catalog and Candidate Target List”. In: *AJ* 156.3, 102, p. 102. DOI: 10.3847/1538-3881/aad050. arXiv: 1706.00495 [astro-ph.EP] (Cited on page 26).

Stassun, Keivan G., Ryan J. Oelkers, et al. (Oct. 2019). “The Revised TESS Input Catalog and Candidate Target List”. In: *AJ* 158.4, 138, p. 138. DOI: 10.3847/1538-3881/ab3467. arXiv: 1905.10694 [astro-ph.SR] (Cited on pages 26, 33).

Steffen, Jason H. and Jason A. Hwang (Apr. 2015). “The period ratio distribution of Kepler’s candidate multiplanet systems”. In: *MNRAS* 448.2, pp. 1956–1972. DOI: 10.1093/mnras/stv104. arXiv: 1409.3320 [astro-ph.EP] (Cited on pages 20, 145, 182).

Stumpe, Martin C., Jeffrey C. Smith, et al. (Sept. 2012). “Kepler Presearch Data Conditioning I—Architecture and Algorithms for Error Correction in Kepler Light Curves”. In: *PASP* 124.919, p. 985. DOI: 10.1086/667698. arXiv: 1203.1382 [astro-ph.IM] (Cited on page 37).

Suissa, Gabrielle, Eric T. Wolf, et al. (Sept. 2020). “The First Habitable-zone Earth-sized Planet from TESS. III. Climate States and Characterization Prospects for TOI-700 d”. In: *AJ* 160.3, 118, p. 118. DOI: 10.3847/1538-3881/aba4b4. arXiv: 2001.00955 [astro-ph.EP] (Cited on page 28).

Thibault, Simon, Denis Brousseau, et al. (Aug. 2022). “NIRPS back-end: design and performance”. In: *Ground-based and Airborne Instrumentation for Astronomy IX*. Ed. by Christopher J. Evans, Julia J. Bryant, and Kentaro Motohara. Vol. 12184. Society of Photo-Optical Instrumentation Engineers (SPIE) Conference Series, 1218454, p. 1218454. DOI: 10.1117/12.2630640 (Cited on page 138).

Twicken, Joseph D., Joseph H. Catanzarite, et al. (June 2018). “Kepler Data Validation I—Architecture, Diagnostic Tests, and Data Products for Vetting Transiting Planet

Candidates”. In: *PASP* 130.988, p. 064502. DOI: `10.1088/1538-3873/aab694`. arXiv: `1803.04526 [astro-ph.EP]` (Cited on page 37).

Udry, S., X. Bonfils, et al. (July 2007). “The HARPS search for southern extra-solar planets. XI. Super-Earths (5 and 8 M{⊕}) in a 3-planet system”. In: *A&A* 469.3, pp. L43–L47. DOI: `10.1051/0004-6361:20077612`. arXiv: `0704.3841 [astro-ph]` (Cited on page 164).

Ulmer-Moll, S., H. P. Osborn, et al. (June 2023). “TOI-5678b: A 48-day transiting Neptune-mass planet characterized with CHEOPS and HARPS”. In: *A&A* 674, A43, A43. DOI: `10.1051/0004-6361/202245478`. arXiv: `2306.04295 [astro-ph.EP]` (Cited on page 198).

Van Eylen, V., Camilla Agentoft, et al. (Oct. 2018). “An asteroseismic view of the radius valley: stripped cores, not born rocky”. In: *MNRAS* 479.4, pp. 4786–4795. DOI: `10.1093/mnras/sty1783`. arXiv: `1710.05398 [astro-ph.EP]` (Cited on pages 156, 157).

Vanderburg, Andrew and John Asher Johnson (Oct. 2014). “A Technique for Extracting Highly Precise Photometry for the Two-Wheeled Kepler Mission”. In: *PASP* 126.944, p. 948. DOI: `10.1086/678764`. arXiv: `1408.3853 [astro-ph.IM]` (Cited on page 37).

Vogt, S. S., S. L. Allen, et al. (June 1994). “HIRES: the high-resolution echelle spectrometer on the Keck 10-m Telescope”. In: *Instrumentation in Astronomy VIII*. Ed. by David L. Crawford and Eric R. Craine. Vol. 2198. Society of Photo-Optical Instrumentation Engineers (SPIE) Conference Series, p. 362. DOI: `10.1117/12.176725` (Cited on pages 9, 178).

Weiss, Lauren M., Geoffrey W. Marcy, et al. (Jan. 2018). “The California-Kepler Survey. V. Peas in a Pod: Planets in a Kepler Multi-planet System Are Similar in Size and Regularly Spaced”. In: *AJ* 155.1, 48, p. 48. DOI: `10.3847/1538-3881/aa9ff6`. arXiv: `1706.06204 [astro-ph.EP]` (Cited on page 20).

Wildi, F., N. Blind, et al. (Sept. 2017). “NIRPS: an adaptive-optics assisted radial velocity spectrograph to chase exoplanets around M-stars”. In: *Society of Photo-Optical Instrumentation Engineers (SPIE) Conference Series*. Ed. by Stuart Shaklan. Vol. 10400. Society of Photo-Optical Instrumentation Engineers (SPIE) Conference Series, 1040018, p. 1040018. DOI: `10.1117/12.2275660` (Cited on page 137).

Wildi, François, François Bouchy, et al. (Aug. 2022). “First light of NIRPS, the near-infrared adaptive-optics assisted high resolution spectrograph for the ESO 3.6m”. In: *Ground-based and Airborne Instrumentation for Astronomy IX*. Ed. by Christopher J. Evans, Julia J. Bryant, and Kentaro Motohara. Vol. 12184. Society of Photo-Optical Instrumentation Engineers (SPIE) Conference Series, 121841H, 121841H. DOI: `10.1117/12.2630016` (Cited on pages 136, 188).

Wright, Jason T. and Paul Robertson (Dec. 2017). “The Third Workshop on Extremely Precise Radial Velocities: The New Instruments”. In: *Research Notes of the American Astronomical Society* 1.1, 51, p. 51. DOI: `10.3847/2515-5172/aaa12e`. arXiv: `1801.05383 [astro-ph.IM]` (Cited on pages 8, 178).

Wyatt, M. C., Q. Kral, and C. A. Sinclair (Jan. 2020). “Susceptibility of planetary atmospheres to mass-loss and growth by planetesimal impacts: the impact shoreline”. In:

MNRAS 491.1, pp. 782–802. DOI: `10.1093/mnras/stz3052`. arXiv: `1910.10731 [astro-ph.EP]` (Cited on pages 18, 144, 181).

Zeng, Li, Stein B. Jacobsen, et al. (May 2019). “Growth model interpretation of planet size distribution”. In: *Proceedings of the National Academy of Science* 116.20, pp. 9723–9728. DOI: `10.1073/pnas.1812905116`. arXiv: `1906.04253 [astro-ph.EP]` (Cited on page 157).